ISSN 0288-4534
CODEN: KPPJAD

KONA Powder and Particle Journal

No.35 (2018)

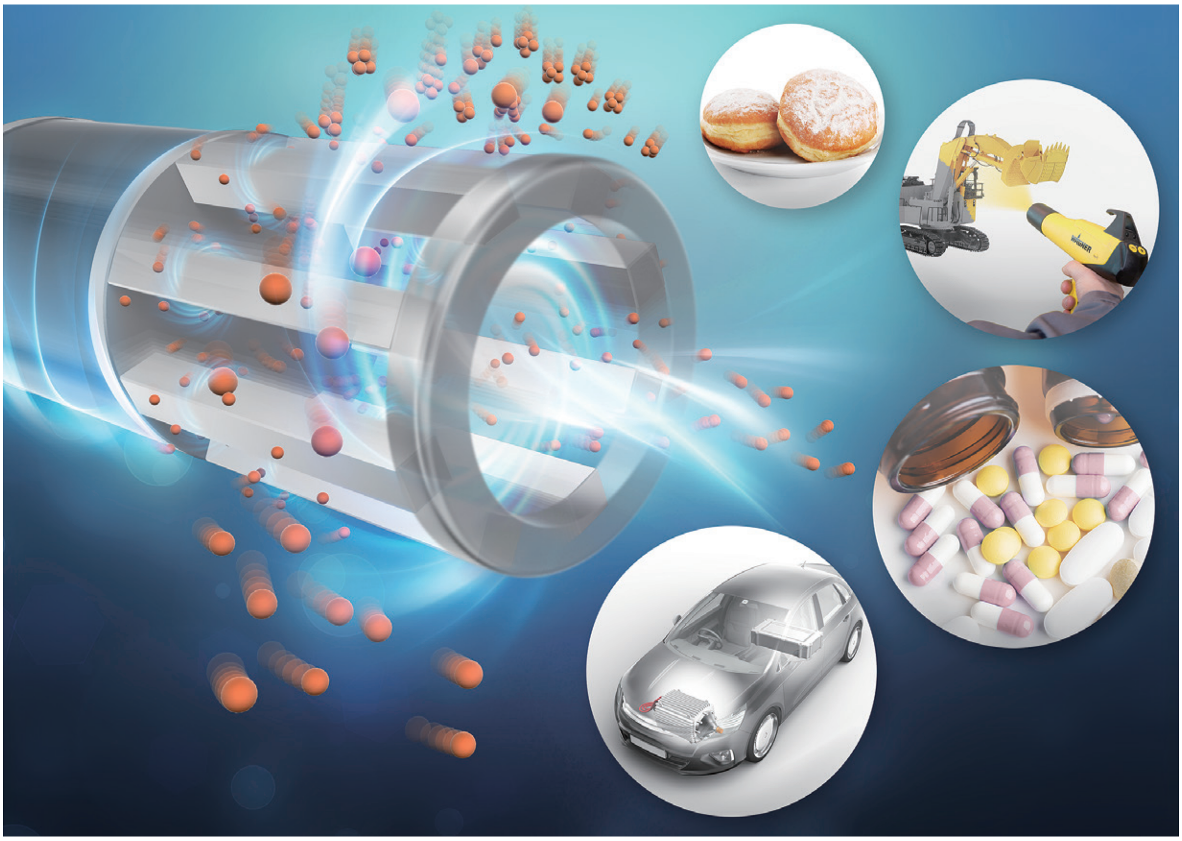

Hosokawa Powder Technology Foundation

available online-www.kona.or.jp

About this Journal

KONA Powder and Particle Journal is a refereed scientific journal that publishes articles on powder and particle science and technology. This journal has been published annually since 1983 and is distributed free of charge to researchers, members of the scientific communities, universities and research libraries throughout the world, by Hosokawa Powder Technology Foundation (http://www.kona.or.jp/) established by Mr. Masuo Hosokawa in 1991.

The Chinese character “粉” in the cover is pronounced “KONA” in Japanese, and means “Powder”. The hand written “粉” is after the late Mr. Eiichi Hosokawa, founder of the Hosokawa Micron Corporation (http://www.hosokawa-micron.co.jp).

About the Cover

Air classification is an important step in production of many industrial powders. Among various types of equipment, the deflector wheel classifier, where coarse particles are deflected on the outer edge of the deflector wheel and fine particles follow the air flow through the deflector wheel, is the dominant separation device for obtaining fine powders of a given size and narrow size distribution of color pigments, abrasive powders and so on. Using high-speed camera, effective particle behavior in separation process of deflector wheel classifier was analyzed at high particle loading condition focusing on the particle-particle and particle-wall collisions. In addition, the influence of process parameters such as revolution rate and mass loading on the separation efficiency was presented with the consistent theoretical model. Please read the paper on pp.172–185.

Headquarters of Hosokawa Micron Corporation

Editorial Board

■ Publication Office
Hosokawa Powder Technology Foundation (http://www.kona.or.jp)
(in the headquarters building of Hosokawa Micron Corporation)
1-9, Shodaitajika, Hirakata-shi, Osaka 573-1132, Japan
E-mail: contact_zainq@hmc.hosokawa.com

■ Printing Office: Nakanishi Printing Co., Ltd., Japan

■ Publication Date: 10 January 2018

<Editorial>

<Review Papers>

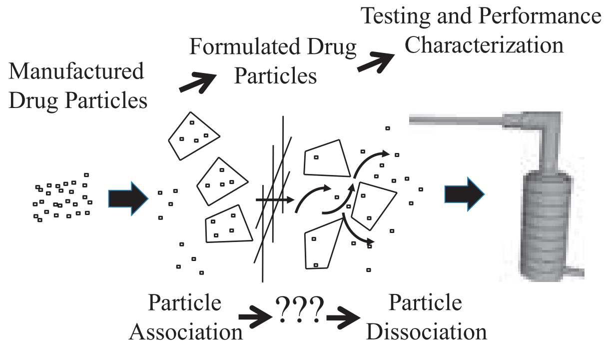
Testing and Performance Characterization
Formulated Drug Particles
Manufactured Drug Particles
Particle Association
???
Particle Dissociation

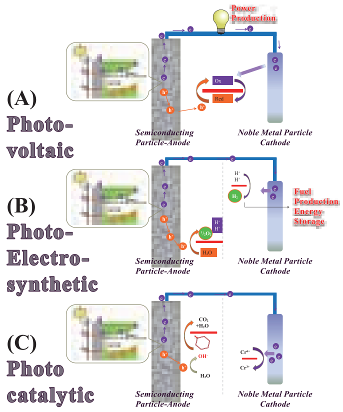
Power Production
(A) Photo-voltaic
Ox
Red
Semiconducting Particle-Anode
Noble Metal Particle Cathode
(B) Photo-Electro-synthetic
H⁺
H⁺
H₂
Fuel Production Energy Storage
½O₂
H₂O
Semiconducting Particle-Anode
Noble Metal Particle Cathode
(C) Photo catalytic
CO₂ +H₂O
OH⁻
H₂O
Cr⁶⁺
Cr³⁺
Semiconducting Particle-Anode
Noble Metal Particle Cathode

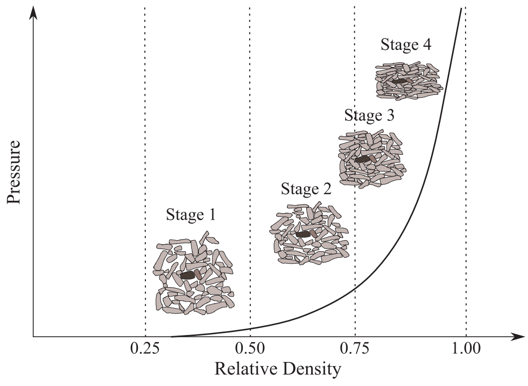
Pressure
Stage 1
Stage 2
Stage 3
Stage 4
0.25
0.50
0.75
1.00
Relative Density

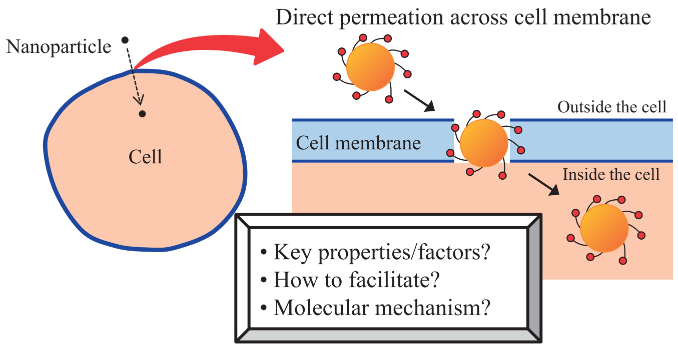
Direct permeation across cell membrane
Nanoparticle
Cell
Outside the cell
Cell membrane
Inside the cell
• Key properties/factors?
• How to facilitate?
• Molecular mechanism?

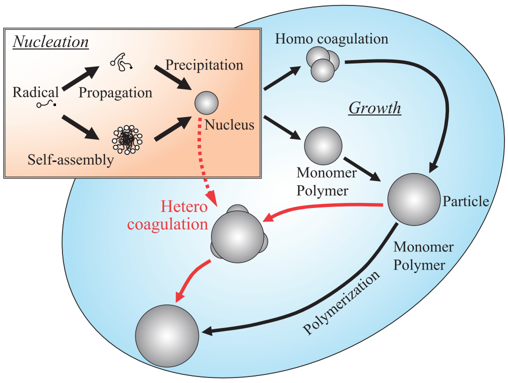
Nucleation
Radical
Propagation
Precipitation
Nucleus
Self-assembly
Homo coagulation
Growth
Monomer
Polymer
Particle
Hetero coagulation
Monomer
Polymer
Polymerization

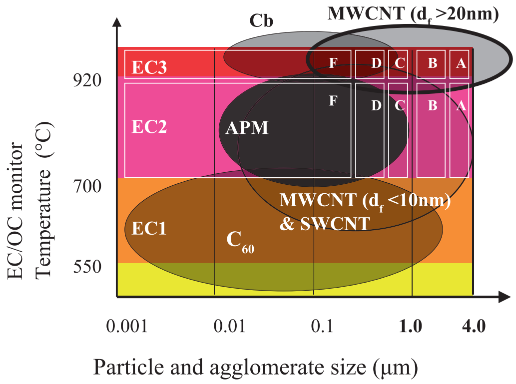
Cb
MWCNT (d_f >20nm)
EC3
F D C B A
920
EC2
APM
F D C B A
700
MWCNT (d_f <10nm) & SWCNT
EC1
C_{60}
550
EC/OC monitor Temperature (°C)
0.001
0.01
0.1
1.0
4.0
Particle and agglomerate size (µm)

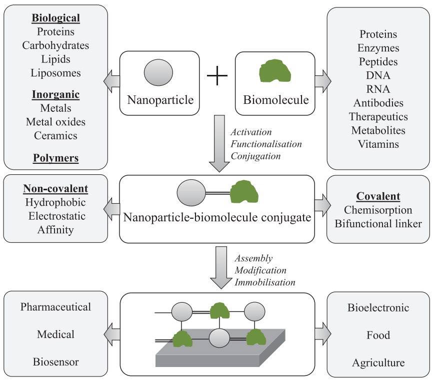
Biological
Proteins
Carbohydrates
Lipids
Liposomes
Inorganic
Metals
Metal oxides
Ceramics
Polymers
Nanoparticle
+
Biomolecule
Proteins
Enzymes
Peptides
DNA
RNA
Antibodies
Therapeutics
Metabolites
Vitamins
Activation
Functionalisation
Conjugation
Non-covalent
Hydrophobic
Electrostatic
Affinity
Nanoparticle-biomolecule conjugate
Covalent
Chemisorption
Bifunctional linker
Assembly
Modification
Immobilisation
Pharmaceutical
Medical
Biosensor
Bioelectronic
Food
Agriculture

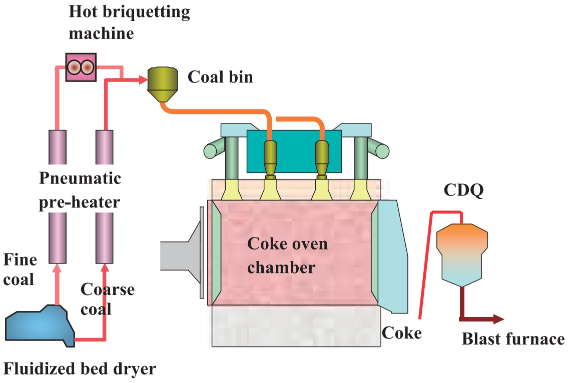
Hot briquetting machine
Coal bin
Pneumatic pre-heater
CDQ
Coke oven chamber
Fine coal
Coarse coal
Coke
Blast furnace
Fluidized bed dryer

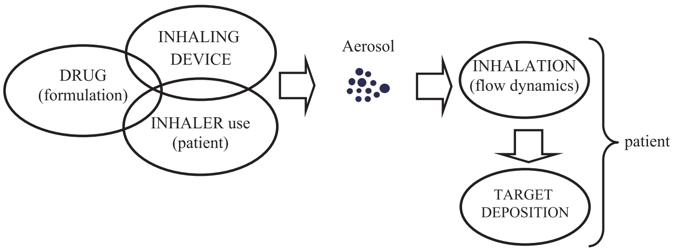
INHALING DEVICE
DRUG (formulation)
INHALER use (patient)
Aerosol
INHALATION (flow dynamics)
TARGET DEPOSITION
patient

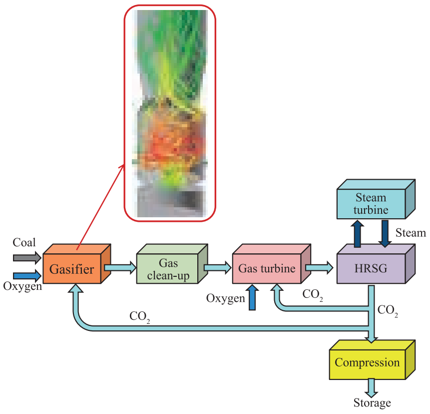
Steam turbine
Steam
Coal
Oxygen
Gasifier
Gas clean-up
Gas turbine
HRSG
Oxygen
CO_2
CO_2
CO_2
Compression
Storage

<Special Contribution>

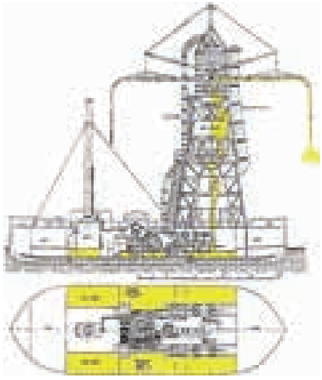

<Original Research Papers>

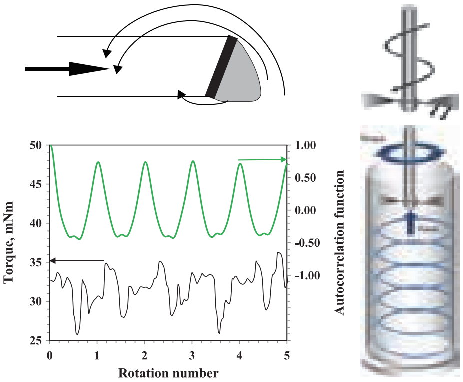
Torque, mNm
50
45
40
35
30
25
0
1
2
3
4
5
Rotation number
1.00
0.50
0.00
-0.50
-1.00
Autocorrelation function

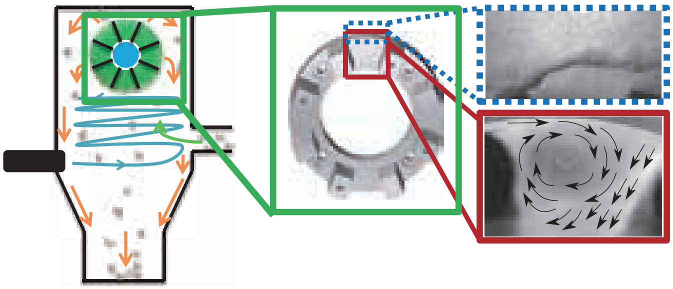

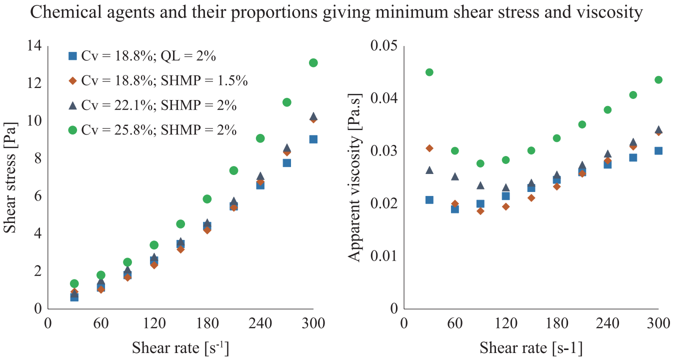
Chemical agents and their proportions giving minimum shear stress and viscosity
■ Cv = 18.8%; QL = 2%
◆ Cv = 18.8%; SHMP = 1.5%
▲ Cv = 22.1%; SHMP = 2%
● Cv = 25.8%; SHMP = 2%
Shear stress [Pa]
0
2
4
6
8
10
12
14
Shear rate [s-1]
0
60
120
180
240
300
Apparent viscosity [Pa.s]
0
0.01
0.02
0.03
0.04
0.05
Shear rate [s-1]
0
60
120
180
240
300

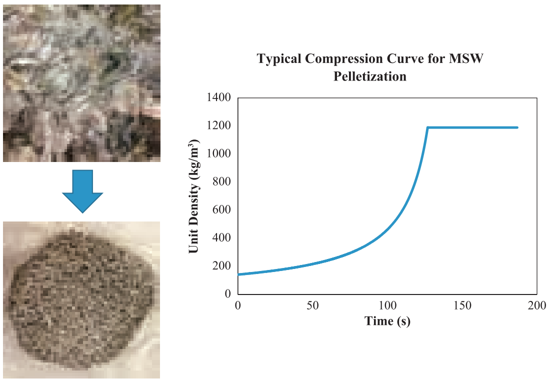
Typical Compression Curve for MSW Pelletization
Unit Density (kg/m³)
0
200
400
600
800
1000
1200
1400
Time (s)
0
50
100
150
200

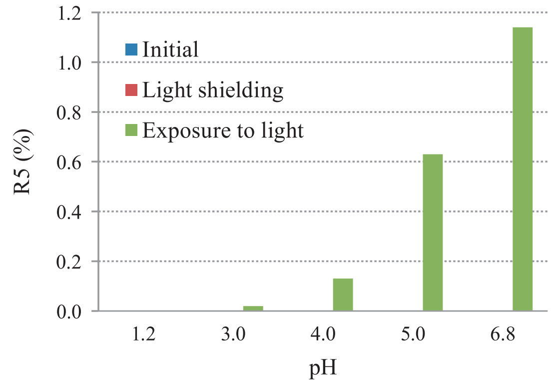
R5 (%)
1.2
1.0
0.8
0.6
0.4
0.2
0.0
🟦 Initial
🟥 Light shielding
🟩 Exposure to light
1.2
3.0
4.0
5.0
6.8
pH

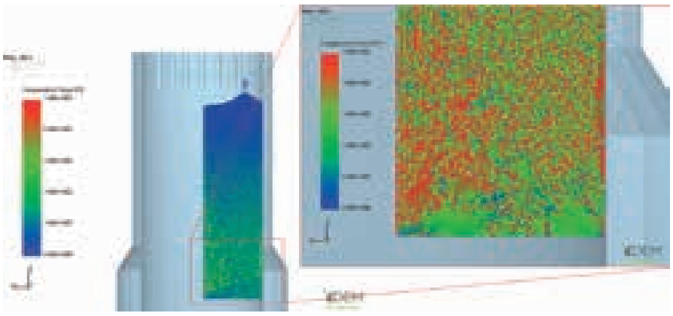

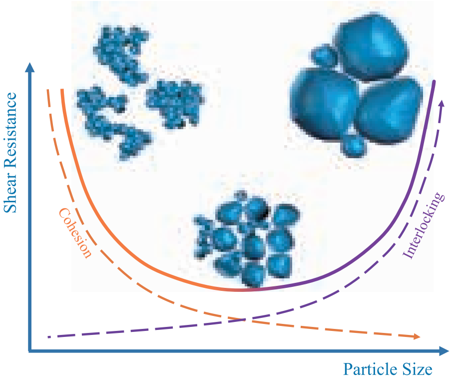
Shear Resistance
Cohesion
Interlocking
Particle Size

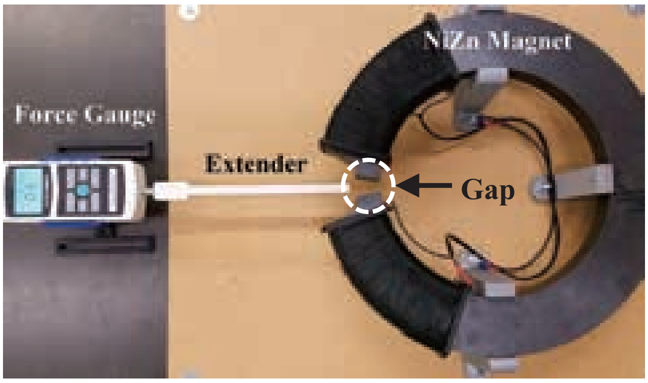
NiZn Magnet
Force Gauge
Extender
Gap

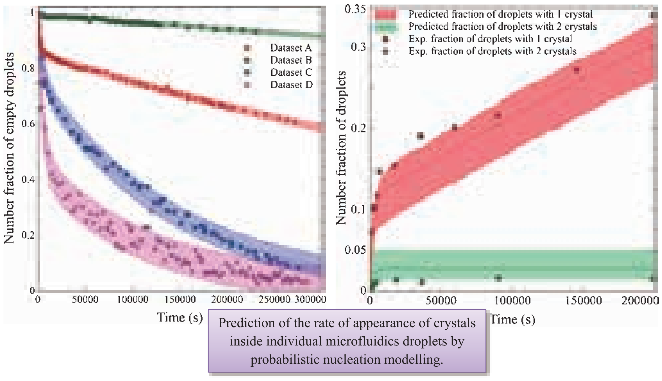

Prediction of the rate of appearance of crystals inside individual microfluidics droplets by probabilistic nucleation modelling.

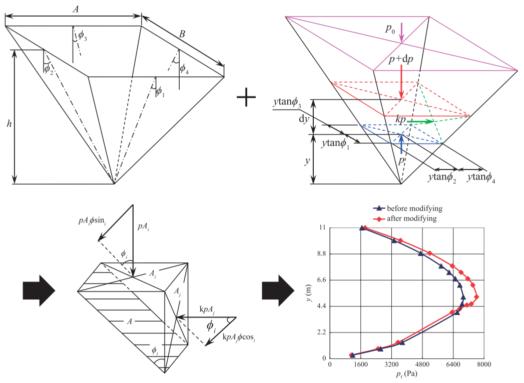

<Information Articles>

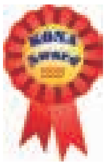

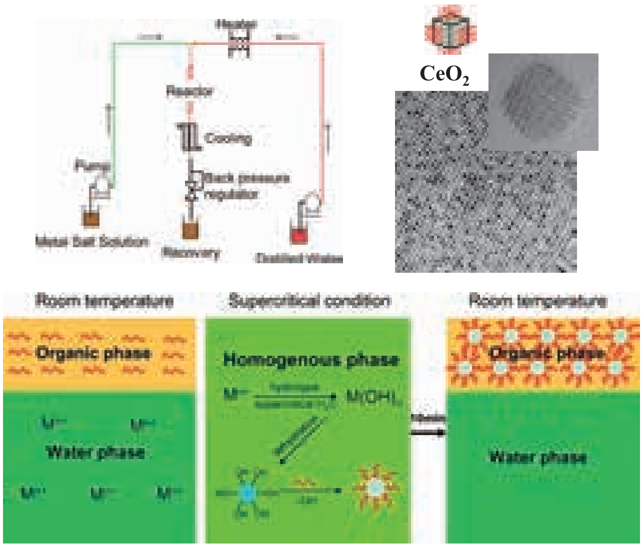

Some achievements of the research for the 24th KONA Award—Continuous production of organic modified nanoparticles by supercritical hydrothermal synthesis (p.286).

KONA Powder and Particle Journal No. 35 (2018) 1–2/Doi:10.14356/kona.2018022 Editorial

Editor’s Preface

Kikuo Okuyama, Editor-in-Chief

Hiroshima University, Japan

As the Editor-in-Chief, I am pleased to introduce the KONA Powder & Particle Journal, Issue No.35. Continuing the years’ tradition, this issue contains high quality reviews and original research articles focusing on the industry-oriented powder and particle technology. It is clear that continuous improvement has always been one of the spirits of this Journal to meet the demand of the powder and particle technology society. Three years ago, this journal was introduced to the J-STAGE (Japan Science and Technology Information Aggregator Electronic) to support better transmission to the readers, continued with the introduction of the Open Access policy last year.

The Editorial Committee, consisting of three editorial boards located in Europe, America, and Asia/Oceania, received more than 50 high-quality articles this year and anticipate to receive more in the future. To accommodate this trend, the Editorial Manager® (EM) system was used to facilitate easy manuscript submission, reviewing, and tracking. The EM system allows the submitted articles to be immediately assessed by the Editorial Committee members, thereby allowing the contributors to receive the decisions at their earliest opportunity and have sufficient time to improve their manuscripts.

The increasing number of articles received by the editorial office reflects the growing research efforts concerning powder and particle technology. The interest ranges from the fields of basic sciences of physics, chemistry, and biology, to the applied fields such as chemical and process engineering. This is in conjunction with the vast-growing applications of powder and particle technology, such as heat-resistant materials, memory and recording media, photo functional materials, and energy-supplying devices. The demand for high performance materials is escalating even more with the emerge of artificial intelligence and the Internet of Things. This is something that needs to be anticipated and further explored by the powder and particle technology community. Researchers and engineers in this field need to continuously develop efficient, scalable, and environmentally friendly manufacturing processes for high performance materials. This also includes post-processing handling technology to realize fully functionalized materials with high purity. This is the message that we tried to convey through this year’s issue.

Our aim is to introduce high quality research throughout the world. In-line with the rapid advancement of the powder and particle technology, we attempt to increase the publication frequency of this journal in the near future while keeping the quality of the published articles. In the meantime, I hope this issue would be a valuable platform for the discourse of powder and particle technology advancement.

Finally, I would like to thank Dr. Jusuke Hidaka, emeritus professor of Doshisha University, Japan, for his continuous dedication as the former Editor-in-Chief of KONA Powder and Particle Journal.

Reviewer Appreciation

I express our gratitude to the reviewers for the publication of this KONA Powder and Particle Journal. Thanks to the generous contributions of the volunteer reviewers as well as the interest of researchers in our journal, the number of submission to this journal is increasing after the registration on the major international journal platforms and its level is further improving. Because of the limited space of this annual journal, the number of papers published there is regrettably rather restricted. Therefore the papers of good quality need to be selected for the journal and further improved and refined by the reviewing.

The editorial team of KONA Journal would like to take this opportunity to gratefully acknowledge the reviewers here and deeply appreciate their valuable time and professional contributions to the KONA Journal. We apologize to any reviewer who may have inadvertently been omitted from this list. We are sincerely grateful to all who have been of any assistance to the publication of this journal.

BAŁDYGA, Jerzy
BISCANS, Béatrice
CASTRO, José Adilson de
COPPENS, Marc-Olivier
FURSE, Cynthia
GARCIA-CONTRERAS, Lucila
GOTOH, Kuniaki
GRADOŃ, Leon
HICKEY, Anthony
HUANG, Ching-Chung
INOUE, Yohei
KANDA, Yoshiteru
KANO, Junya
KAWASAKI, Akira
KLINZING, George E.
KWADE, Arno
MAKINO, Hisao
MATSUSAKA, Shuji
MEESTERS, Gabriel
MILANI, Paolo
MORI, Yasushige
MOUDGIL, Brij
NAGAO, Daisuke
NAKAMURA, Hideya
OKUYAMA, Kikuo
PURI, Virendra
RAJAMANI, Raj
RASTEIRO, Maria da Graça
ROSATO, Anthony D.
SAITO, Fumio
SAKAI, Mikio
SEN, Surajit
SHINTO, Hiroyuki
SHIRAKAWA, Yoshiyuki
SUZUKI, Hiroshi
TAVARES, Luis Marcelo
TOKORO, Chiharu
TSUJI, Takuya
VALVERDE, Jose Manuel
YOKOYAMA, Toyokazu
YOSHIDA, Mikio

Kikuo Okuyama

Kikuo Okuyama
Editor-in-Chief
Prof. emeritus, Hiroshima University
October 2017

KONA Powder and Particle Journal No. 35 (2018) 3–13/Doi:10.14356/kona.2018007 Review Paper

Complexity in Pharmaceutical Powders for Inhalation: A perspective[†]

Anthony J. Hickey

[1] *RTI International, USA*

Abstract

Pharmaceutical aerosol powders intended for inhalation are required to have unique performance characteristics that are highly dependent on their physico-chemical properties. A wide range of analytical methods have been applied to study particle structure, size distribution, surface properties and subsequent behaviour of powders with the intention of predicting their performance. However, particle interactions are dictated by complex fundamental forces that impact on the efficiency and reproducibility of delivery and thereby the quality, efficacy and safety of the final product. This manuscript reviews the interplay of physico-chemical properties of powder and the complex process and analytical variables that must be monitored and controlled to effectively predict powder performance.

Keywords: powder, particle, drug, inhalation, characterization

1. Introduction

Understanding the role of powder properties in their performance can be likened to the aphorism of the blind men and the elephant (Shah I., 1993). All methods, applied correctly, describe a specific feature of the particle or powder. However, without knowledge of all of the features that define the whole object or population of objects the conclusions about it/them may be misleading. The challenge to the pharmaceutical research and development community has been to collect sufficient information on powder properties to allow prediction of behavior.

Interest in powder properties with respect to ensuring efficient and reproducible performance in delivering drugs from inhalers has driven an enormous research effort over a period of more than 50 years. The complex interaction of fundamental aspects of physical chemistry, mechanical engineering, aerosol physics and the ability to identify and consider all relevant variables has limited the development of comprehensive predictive models of product behavior (Hickey A., 2003). The current capacity to use the knowledge of key parameters to guide product optimization appears to involve systematic consideration of the most important factors but requires iteration with respect to unidentified variables or confounding of known variables that lead to sub-optimal performance (Hickey A. and Xu Z., 2013).

It is important to recognize that dry powders are non-equilibrium systems (although time scales can be long) at all dimensional scales of scrutiny. The historical view of individual particles as essentially unchanging objects has to be revised to reflect their ability to respond to manufacturing, storage and general environmental conditions. This has implications for their interaction with each other and the container or conveyor which influences bulk powder properties.

The intent of this review is to describe the factors known to contribute to dry powder inhaler product performance and then to discuss approaches to characterization that might account for interactions of these variables or for unknown variables to contribution.

2. Methods of manufacture and particle morphology

2.1 Milling

Milling has a history that can be traced through centuries for the processing of raw materials for food and pharmaceutical products. The desired particles size for aerosol delivery of drugs to the lungs requires a high-energy method to overcome the forces of attraction between molecules usually in the crystalline solid state to create a large surface area (Hickey A. and Ganderton D., 2001; Shur J. et al., 2012). The method, as depicted in **Fig. 1**,

---

[†] Received 21 December 2016; Accepted 15 February 2017

[1] 3040 Cornwallis Road, Research Triangle Park, NC 27709, USA
E-mail: ahickey@unc.edu
TEL: +1-919-541-6771 FAX: +1-919-541-6936

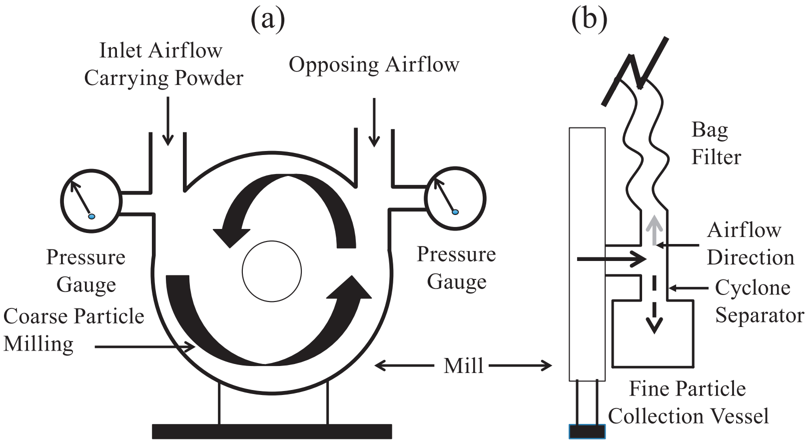

Fig. 1 Schematics of **(a)** front view of an air jet mill and **(b)** side view showing the filter and collection vessel separated by the cyclone behind the mill.

employed throughout modern times is air jet milling in which particles are carried on high a velocity gas stream (usually air or nitrogen) into an opposing high velocity gas stream such that particles impinge on each other and the walls of the mill shattering ultimately into respirable sizes (1–5 μm) (**Fig. 1a**). These respirable particles are collected by elutriation, in the figure passing into the plane of the image through a central tube and entering a cyclone separator as shown in **Fig. 1b** (Hickey A., 1993). In the example shown air then passes to a bag filter and exits while powder under the influence of impaction and sedimentation forces is collected in a vessel directly below the filter. This process can be continued for as long as necessary to the capacity of the collection vessel and with attention to occlusion of the filter.

The production of particles by milling can be controlled in terms of the processing variables of gas flow and temperature but cannot readily be controlled at the level of the individual particle production and the outcome of the process is highly dependent on the starting material in terms of both composition and state which makes it a difficult process from which to extract general principles. Each drug treated in this manner requires full characterization in order to guarantee quality and performance in the final product.

2.2 Spray drying

Spray drying has been of increasing interest since over the last 20 years as it became evident that the technique resulted in particles and powders with unique physicochemical and performance properties (Vehring R., 2008; Van Oort M. and Sacchetti M., 2007). The ability to create low-density particles promoted the ability to efficiently disperse particles. Since most spray dried material is amorphous in nature the influence on stability needs to be addressed. For proteins and peptides this is a desirable solid-state form and is likely to be stable on storage. For small molecular weight drugs the amorphous form is unlikely to be the most stable with respect to fluctuations in moisture and temperature (Carstensen J., 1990). Consequently, since most drugs are of small molecular weight, packaging considerations are required to ensure the stability of the final product most notably the use of moisture impermeable wrapping, e.g. aluminum, or inclusion of desiccant where the response to equilibrium moisture content and fluctuations are more modest (Atkins P. and Crowder T., 2004).

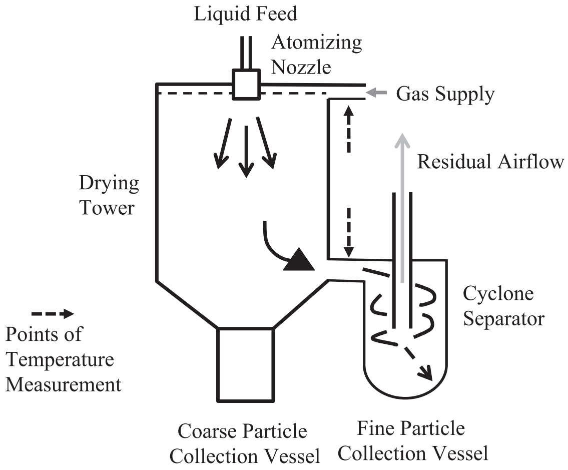

Fig. 2 Schematic of a spray drier illustrating the key elements of solution feed, gas supply, temperature control and monitoring and collection vessels before and after the size selective cyclone separator.

Fig. 2 illustrates the key components of a spray drier including the liquid feed to the atomization nozzle, drying gas supply, the drying tower, cyclone separator and collection vessels for coarse and fine particles. This is a simplified image as it does not show condensers, heater/cooler, recycling and feedback electronics that are integral parts of this equipment.

2.3 Supercritical fluid manufacture

Supercritical fluid manufacture showed great promise as a means of accurately and reproducibly controlling particle size and morphology when it first appeared as an approach to the manufacture of drug particles in the 1990s (Van Oort M. and Sacchetti M., 2007). Several methods were developed each of which had its merits but all of which required multiple small batch production cycles to achieve pilot or production scale quantities of processed drug. Rapid expansion supercritical solutions or antisolvent techniques are the most prominent methods using supercritical gases such as carbon dioxide.

2.4 Mixing/Blending

The modern history of dry powder inhalers can be traced back to the 1960s in particular to the Cromolyn Sodium product delivered from a Spinhaler (Pfisons) (Sanders M., 2011). From the outset mixing/blending was a central element of the powder formulation and the concept of attaching milled respirable particles to the surface of lactose carrier particles became the standard, which remains most common to this day. The importance of the mixing process cannot be understated as it dictates both the ability to fill the dosing containment unit (e.g. capsule, blister or reservoir) and the efficiency with which the drug particles can be detached and enter the entraining air supply (Stewart P., 1986; Young P. et al., 2007).

3. Physico-chemical properties

3.1 Primary particle size and distribution

Primary particle size and distribution is an important property to measure for aerosol products. The aerodynamic performance of aerosols depends on the ability to input energy usually from the patient's inspiratory airflow to move the powder and disperse it into particles that can enter the lungs. This non-equilibrium phenomenon rarely disperses drug completely into primary particle sizes. However, by measuring the primary particle size and distribution an important metric for underlying quality as well as a target for complete dispersion is established. Primary particle size can be evaluated by two complementary methods an indirect population measurement. Laser diffraction measurement can be conducted to assess particles in liquid suspension or dry powders at high-pressure drop, to allow sufficient shear to break the powders in individual particles (Behara S. et al., 2012; Jaffari S. et al., 2013; 2014). Scanning electron microscopy allows imaging on a scale to visualize particles in respirable size ranges (Hickey A. and Xu Z., 2013). Individual particles can be distinguished from aggregates. However, microscopy generally does not allow sufficient numbers of particles to be measured for quantitative statistical representation of the population of particles (Allen T., 1990).

3.2 Shape and density

Particle shape is an important property dictating their behavior. **Fig. 3** illustrates schematically important features of particle surfaces. While the ideal particle is spherical (**Fig. 3a(i)**) and is the basis for most measures of particle size (equivalent spheres) most drug particles deviate from sphericity and exhibit some form of surface rugosity (**Fig. 3a(ii)**) (Chew N. and Chan H-K., 2001). In the extreme the shape of the particle can be significantly distorted in one (needle or fiber, **Fig. 3a(iii)**) or two (plate or flake) dimensions (Mullin J., 1993). The latter usually occurs because of restriction of crystal growth in one (plate or flake) or two (needle or fiber) dimensions. The shape of the particle and surface functionality are inextricably

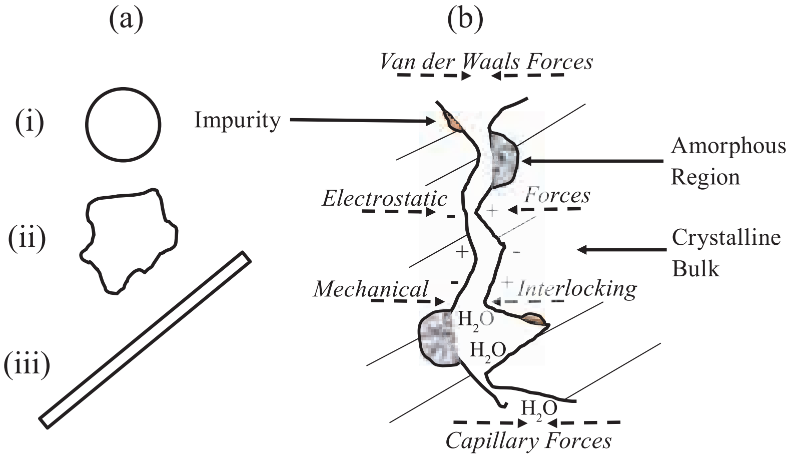

Fig. 3 Schematics illustrating **(a) (i)** spherical, **(ii)** rugose or **(iii)** elongated Particle morphology and **(b)** Forces of interaction at the interface between two particle surfaces.

linked since the surface may exhibit specific features based on the action of impurities during crystallization or the presence of different polymorphs or moisture at the surface. **Fig. 3b** illustrates a variety of surface phenomena resulting from the presence of moisture, crystallinity, electrostatics, discontinuities and, impurities. These surface functions increase the interaction of particles beyond that resulting from the innate van der Waals forces.

Once features exist the way in which they border three-dimensional space with edges or corners creates both a physical and energetic differential that impacts on the likelihood of interaction with other surfaces.

Some mathematical approaches have been taken to depicting irregularly shaped particles with a view to correlating the numerical descriptor with subsequent behavior. **Fig. 4** shows two methods that have been applied. The first is to inscribe the image of the particle periphery with radii from a central point that can then be described in polar co-ordinates, distance from the origin for designated angles, from which Fourier coefficients can be derived that are correlated with a variety of shapes (Tian Y. et al., 1994; Hickey A. and Concessio N., 1997). First, second, third, etc. Fourier coefficients are considered to represent roundness, squareness, triangularity, and so on.

Fractal analysis has been applied to the shape of particles as a means of expanding shape considerations beyond conventional simple shape factors more descriptive terms such as Fourier coefficients based on polar co-ordinates (Hickey A. and Concessio N., 1997). The Fractal dimension introduced for the first time the notion of non-integer dimensions $< 3D$ to convey greater information about the particle than the usual one or two dimensional descriptors obtained from imaging individual particles and subsequently statistically aggregated into particle population data represented by the number of particles observed and then described in terms of average and distribution.

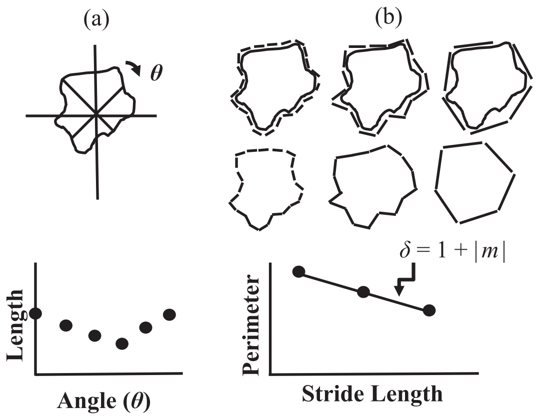

Fig. 4 Depiction of **(a)** Polar co-ordinate image and the data derived for analysis that would be fit to a Fourier series to obtain coefficients and **(b)** The use of different scales, top, to measure the surface by connecting chords around the periphery, middle, to allow estimates of the perimeter length to be plotted against the stride length on a log-log scale, bottom, from which the Fractal Dimension, δ, is measured.

The aerodynamic behavior of aerosol particles is dictated by the particle size and other physical properties including shape and density as described by Stokes' equation. The importance of these properties was overlooked until relatively recently when the potential to modify them to enhance aerosol performance was realized (Crowder T. et al., 2002).

Spray drying may be employed to produce low-density particles. The method involves the spraying of hollow shell or highly porous particles (whiffle ball) that present delicate membrane-like surfaces in various geometric structures permeated by air (Vehring R., 2008; Van Oort M. and Sacchetti M., 2007). These particles due to their low density (somewhere between the true density of a solid particle and the density of air) may be quite large but have a small aerodynamic diameter as described by Stokes' Law. In addition, the distance between the molecules of drug in the particle and those in adjacent particles means that the van der Waals forces are much lower than a solid particle due to the reduced Lennard Jones potential (Telko M. and Hickey A., 2005; Dunbar C. et al., 1998). Consequently, these particles require very little energy to disperse as an aerosol. Indeed, if placed on a flat surface in room air the local convective air movement may be sufficient to generate the aerosol.

Elongated particles are known to orientate longitudinally into the direction of the airflow (Davies C., 1979; Gonda I. and el Khalik A., 1988; Fults K. et al., 1997). Consequently, for specific length, cross-sectional area diameter and aspect ratio they have the capacity to move in air predominantly as a function of their cross-sectional area diameter suggesting a limited radius of gyration while in motion in the two dimensions represented by the cross section (Lippmann M., 1990).

Most dry powder inhaler products employ blends of drug with lactose. The surface properties of the drug and the lactose play a significant role in their interaction and, thereby, in the energy required to separate and disperse them into primary drug and lactose particles (Xu Z. et al. 2011). The use of ∝-lactose monohydrate a monoclinic crystal presents proportionately large flat surfaces to the smaller drug particles (Hickey A. et al., 2007a and 2007b). These surfaces are deceptive in their apparent uniformity in that they can become discontinuous through the presence of impurities (Crowder T. et al., 2003). The presence of impurities, moisture, amorphous lactose or β-lactose monohydrate at the surface creates variable surface energy densities for interaction with the drug (**Fig. 3b**) (Hickey A. et al., 2007a). The potential for variation in nature and extent of drug binding gives rise to non-uniformity in performance, which has implications for both quality and therapy (Telko M. and Hickey A., 2005; Dunbar C. et al., 1998).

A variety of methods of analysis have been evaluated for their utility in characterizing surface forces including thermal analysis (bulk polymorphic forms) inverse gas chromatography (surface polar and non-polar forces, (Telko M. and Hickey A., 2007)), atomic force microscopy (surface free energy, (Begat P. et al., 2004)), static (Carstensen J., 1993) and dynamic (Hickey A. and Concessio N., 1996) angle of repose (bulk flow properties as a measure of particle interaction), Faraday cage (standing electrostatic charge, (Smyth H. et al., 2004)), electronic samplers for charge determination as a function of aerodynamic particle size (Telko M. et al. 2007; Telko M. and Hickey A., 2014; Wong J. et al., 2015).

4. Complexity

The ability to predict powder performance has clear implications for ensuring the quality and efficacy of a pharmaceutical aerosol formulation. In addition, accurate prediction would allow efficient and cost-effective product development with a high probability of meeting with regulatory approval by accommodating the desire for quality by design.

It would be scientifically elegant to approach the desire to predict powder performance from the perspective of the fundamental underlying forces of interaction between particles discussed earlier. However, the inability to separate these forces in the heterogeneous systems of which pharmaceutical formulations are composed has confounded efforts to reduce the problem to basic principles. Various groups have chosen to examine the problem from the perspective of probing powder systems experimentally to derive data on performance that can inform models that allow prediction of behavior (Hickey A. and Xu Z., 2013; Steckel H. and Bolzen N., 2004; Jones M. and Price R., 2006; Grasmeijer F. et al., 2013, 2014).

The powders employed for inhalation consist predominantly of blends with lactose or as spray-dried particles. It is important in considering the dispersion properties of a powder to consider it as a function of quantifiable descriptors of the energy imparted by the airflow such as Reynolds' number, resistance or shear stress. These terms can easily be described for most devices but it should be noted that all devices include design features intended to aid in deaggregation such as baffles, tortuous channels or other impaction surfaces (Telko M. and Hickey A., 2005). Consequently, when considering terms such as pressure drop (at a fixed airflow rate) or airflow rate (at the defined device pressure drop) across or through the device as a reference term for the energy imparted the design features may make the data deviate from quantitative generalizable relationships while giving qualitative information about formulation performance.

Fig. 5 illustrates a model of the proposed interactions between drug and lactose assuming regions of different surface energy density exist to which drug particles exhibit a range of binding properties. When subject to shear and turbulence in air, in the mouthpiece or when passing through or around a tortuous air path feature, impacting on device surfaces and with other particles drug is liberated from the surface of lactose by the action of airflow and constraints of the air path. Incomplete dispersion may be explained by the heterogeneity of the surface energy density.

Fig. 6 illustrates a second model proposed for interactions between drug and lactose assuming that not only is drug associated directly with lactose but through cohesion and incomplete mixing aggregates exist at the surface of lactose that because of their larger size are stripped more readily from the surface and then deaggregated by the shear, turbulence and impaction described earlier. This model is not mutually exclusive with respect to the first model but adds a layer of additional information that might help in formulation that being the cohesive or adhesive nature of the component particles.

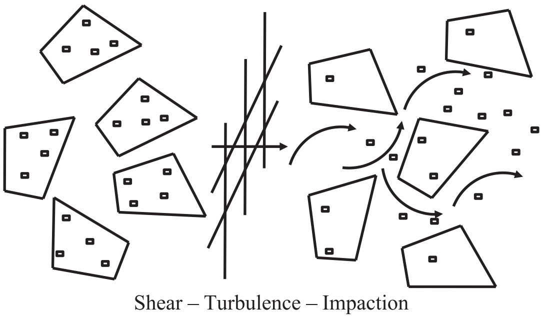

Fig. 5 Schematic of small drug particles at the surface of large lactose carrier particle depicting their liberation as a function of airflow and air path features.

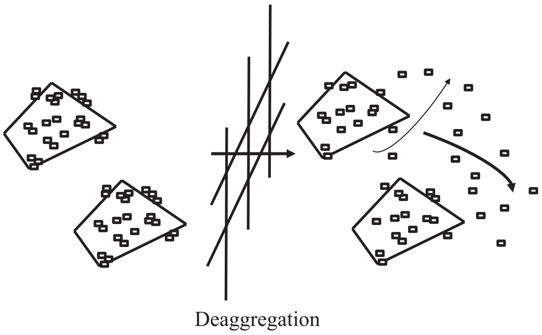

Fig. 6 Schematic of small drug particles at the surface of large lactose carrier particles some in the form of aggregates depicting their liberation initially as a deaggregation phenomenon in response to airflow.

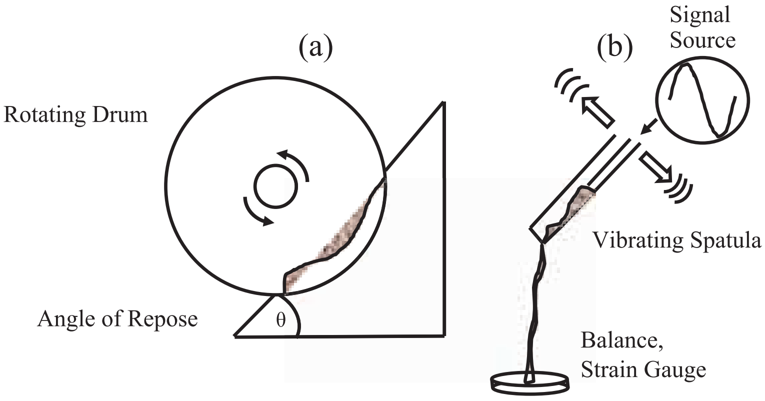

Fig. 7 Diagrams of **(a)** the rotating drum dynamic angle of repose measurement technique and **(b)** vibrating spatula with mass detection.

4.1 Powder flow

The movement of most pharmaceutical powders is irregular but almost all processes in which powders play a role would be better served by uniform flow and behavior including aerosol generation. Since the nature of powder movement can vary it can be inferred that knowledge of this phenomenon would be useful in predicting a variety of powder properties such as dilation followed by generation for aerosol formulations.

There are several methods for evaluating powder flow properties and their underlying physics including rotating drum (Hickey A. and Concessio N., 1996; Crowder T. et al., 1999, Crowder, T. and Hickey A., 1999), vibrating spatula (Hickey A. and Concessio N., 1994; Crowder T. and Hickey A., 1999) and critical orifice (Flodex, (Taylor M. et al., 2000)). When oscillations in the motion of powder in a rotating drum or delivery from a vibrating spatula, as depicted in **Fig. 7**, are plotted in phase space a typical attractor is observed that can be characterized by a Fractal Dimension (δ) or Lyupanov Exponent reflecting the divergence of each successive data point from the previous one. This single dimension, which can be viewed as a measure of irregularity in microflow can then be correlated with the ability to disperse powders as aerosols (Concessio N. et al., 1999; Crowder T. and Hickey A., 2006). The predictive nature of this approach renders it a potentially useful tool for the characterization of powder blends. Formulation optimization might be performed by ranking powders in terms of flow (powders with small δ flow better than those with large δ) as a predictor of their ability to effectively be disperse as aerosols.

4.2 Cohesive adhesive balance

The cohesive adhesive balance (CAB) model refers to the interaction between drug and lactose in the blend that influence the energy required for detachment of particles from each other and surfaces during the aerosolization process (Begat P. et al., 2004; Behara S. et al., 2011a; 2011b; 2011c). Drug entrainment onto the inspiratory flow of the patient is influenced by these interactions and consequently may result in variable efficacy (Grasmeijer F. et al., 2013; Behara S. et al., 2011d).

4.3 Powder aerosol dispersion equation

Collecting experimental data and developing a working model, rather than a physical model might circumvent the physical complexity of the models of interaction between particles in a blend. One approach to measuring the interaction of particles and data collection is to investigate the energy required to separate them in a standardized airflow using an entrainment tube (**Fig. 8a**) and inertial impactor for aerodynamic particle size measurement (**Fig. 8b**). This approach has been explored for several drugs in lactose blends (Mansour H. et al., 2010; Xu Z. et al., 2010a, 2010b, 2010c). The detachment in response to applied shear stress was considered analogous to desorption phenomena in which particles are removed from low energy binding sites and increasing quantities are removed at high shear as higher energy binding sites are evacuated (Xu Z. et al., 2010c). These experiments resulted in the proposal of a powder aerosol dispersion equation (PADE) (Xu Z. et al., 2010c).

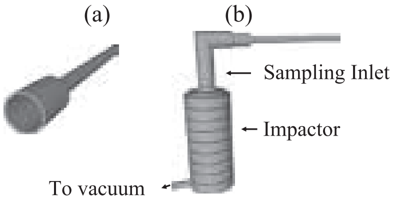

Fig. 8 Illustrations of **(a)** a standardized entrainment tube and; **(b)** its position with respect to a stacked, cascade impactor for aerodynamic particle size determination.

5. Aerosol performance

5.1 Laser diffraction volume diameter determination

Laser diffraction instruments are used routinely for measurement of particle size distribution of aerosol powders. When used with powder dispersion systems operating at different pressure drops or when dispersed in suspending liquid particles may be separated into primary sizes to establish the limit of efficient dispersion possible with an effective dry powder inhaler (Young P. et al., 2007; Behara S. et al., 2012). The particle size obtained at different dispersing pressure drops may be used to characterize the ease of deaggregation (resistance to deaggregation due to particle interactions).

5.2 Aerodynamic particle size distribution

The aerodynamic particle size distribution (APSD) is generally measured by inertial impaction (Tougas T. et al., 2013). Inertial impactors size segregate powders using a series of jets of decreasing orifice size through which air is drawn, at a fixed rate by a vacuum. An increasing linear velocity at each successive collection stage is thereby established. The combination of the mass of particles in the distribution and range of linear velocities results in samples of decreasing particle size being sampled as an aerosol passes through each successive stage of the impactor.

5.3 Delivered dose

The dose delivered from the inhaler is that which leaves the mouthpiece of the device for which a proportion, the fine particle dose, is considered in a size that is relevant to pulmonary delivery (USP, 2011). The fine particle dose should not be confused with the respirable dose. The fine particle dose is designated as the entire dose below a specific particle size, usually 5mm unless otherwise stated, that is thought to be broadly relevant for pulmonary drugs as a quality measure (Hickey A., 2004). The respirable dose is derived from theoretical and experimental data on lung deposition and considers the probability of particles over a range of sizes to penetrate to the lungs. Various public and occupational health agencies have specific definitions for respirable dose (Hinds W., 1999). The fact that a single fine particle doses is equivalent to a range of respirable doses based on the particle size distribution has been considered elsewhere (Martonen T. et al., 1992) It is important to note that caution must be exercised in interpreting fine particle dose, a quality measure, as a predictor of lung delivery.

5.4 Aerosol delivery rate

In evaluating the performance of DPIs the importance of aerosol delivery rate (ADR) is often overlooked. The APSD and delivered dose uniformity (DDU) are clearly important quality measures for the product performance but the relevance of ADR may not be as evident. The relevance of ADR only becomes obvious when the purpose of a DPI is considered. Drug delivered as an aerosol from a DPI is intended, within reasonable limits, to be controlled with respect to the characteristics that may be important in lung delivery and, therefore, in therapeutic effect. The portion of the inspiratory flow on which the aerosol is delivered is critical to its site of deposition and the ADR, or mass of aerosol powder delivered at different times with respect to initiation of airflow is an important indicator of performance in patients (Ziffels S. et al., 2015). **Fig. 9** illustrates this point by adopting an approach of following obscuration of a light source placed perpendicularly to the direction of aerosol delivery as sampling into an inertial impactor is performed (**Fig. 9a**). For illustration the aerosol dispersion is separated into three periods initially visualizing increasing mass, followed by peak mass and terminating in declining mass delivery (**Fig. 9b**). This is measured by a detector in which obscuration is the reciprocal of light detected. Differences in the shape of the obscuration curve indicate differences in ADR (**Fig. 9c**).

The complexity of dry powder inhalers can only be fully grasped when the need for control at all scales spatial and temporal scrutiny is considered. **Fig. 10** summarizes the dimensions, the properties, the processes and the control variables that can be employed to influence each of the systems. There are points in the preparation of dry powders for inhalation where certain properties are known to positively influence the aerosol performance of the powder. Arguably, great progress has been made with regard to qualitative understanding of which factors may be important in supporting product development and by iteration performance can be optimized sufficiently to meet regulatory requirements.

Particle surface treatments such as smoothing (Young P. et al., 2002), mechanical coating (Zhou Q. et al., 2013), corrugation (Chew N. and Chan K-K., 2001) and the use of fines to obscure high surface energy density sites (Jones M. and Price R., 2006) are among the promising strategies to limit the influence of formulation variables on performance. The use of standardized techniques to evaluate the formulation independently of the device allows initial optimization (Louey M. et al., 2006) and the use of inspiratory flow profiles in sampling may be more sensitive to performance variation than constant flow rates currently used (Dunbar C. et al., 2000). Ultimately, the device and formulation combination must be evaluated (Behara S. et al., 2011d; Adams W. et al., 2012) to

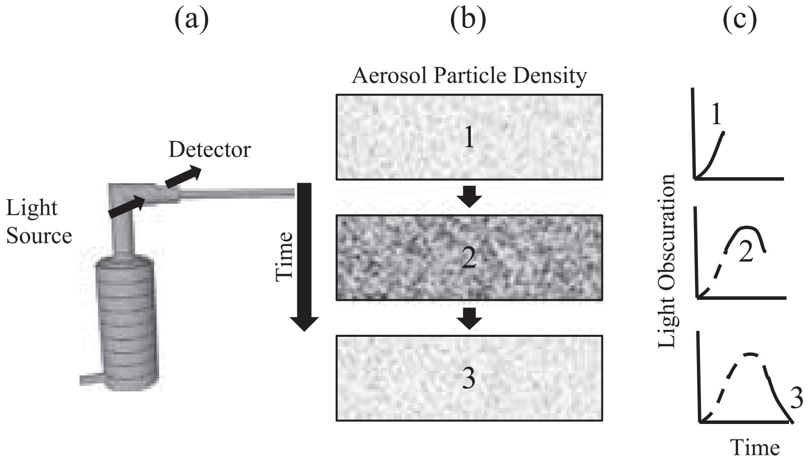

Fig. 9 **(a)** Arrangement of apparatus to follow light obscuration at the inlet to an inertial impactor; **(b)** Depiction of the density of particles in air (dictating light obscuration) at three intervals after (top to bottom) initiation of aerosol delivery during aerosol delivery; **(c)** The real-time measurement of obscuration at the detector corresponding with **(b)**, initial, middle and end (top to bottom).

SCALE	PROCESS	PROPERTY	PROCESS CONTROL
Molecular	Crystallization	Crystal System (lattice spacing)	Mixing conditions
	Precipitation	Crystal Habit (shape)	Use of solvents/ Other Additives
		True Density	
	Spray	Solubility	Temperature
	Drying	Initial Particle Size and Distribution (PSD)	
Particle	Milling	Modified PSD	
		Modified Shape	Energy to break
	↓	Intrinsic Surface Geometry	Initial Particle
		Intrinsic Surface Functionality	Environmental
	[Coating]	[Modified Surface Geometry]	Temperature
	↓	[Modified Surface Functionality]	Humidity
Powder	Unprocessed	Bulk/Tapped Density	
	↓	Aggregation (cohesion)	
	Mixing/Blending	Aggregation (cohesion/adhesion)	
	↓	Surface interactions	
	Filling	Flow (low shear motion)	Energy
	Aerosol Generation	Dispersion (high shear motion)	to induce motion

DESIRED PERFORMANCE CHARACTERISTICS

Fig. 10 Properties with respect to scale of scrutiny of a pharmaceutical dry powder aerosol formulation and the processes and variables that must be controlled to optimize desired performance characteristics with respect to quality, safety and efficacy.

meet the regulatory requirements (US FDA, 1998). The US Food and Drug Administration Guidance on a specific dry powder product (combined fluticasone propionate and salmeterol xinofoate) dry powder inhaler intended to lead to in vitro and in vivo bioequivalence (Apiou-Sbirlea G. et al., 2013) serves to emphasize the importance of understanding and controlling all phenomena described above (US FDA 2013). Greater progress is required in linking the spectrum of known properties to defined process variables if sufficient knowledge and understanding is to be gained to predict and efficiently control performance.

6. Conclusion

The complexity of powder behavior in DPIs can be considered at several levels. The first is the composition and structure of individual particles. The second is the composition and structure of populations of particles at rest. The third is the motion of particles as a partially dilated flowing mass. The fourth is the motion of particles as fully dilated dispersed aerosols. Each of these elements is intricately woven into the overall performance of the product dictating the delivered dose and its aerodynamic particle size distribution. These performance measures in conjunction with pulmonary function, anatomy and physiology dictate efficacy and bioavailability of deposited drug.

Acknowledging that complexity at all levels of scrutiny in powder properties and behavior emphasizes the difficulty of attempting to control static variables and expecting controlled product performance. A comprehensive understanding of the dynamics is central to managing performance within acceptable limits.

References

Adams W.P., Lee S.L., Plourde R., Lionberger R.A., Bertha C.M., Doub W.H., Bovet J.-M., Hickey A.J., Effects of device and formulation on in vitro performance of dry powder inhalers, The AAPS Journal, 14 (2012) 400–409.

Allen T.A., Microscopy, in: Particle Size Measurement, fourth ed., Chapman and Hall, New York, 1990, pp. 217–248.

Apiou-Sbirlea G., Newman S., Fleming J., Siekmeier R., Ehrmann S., Scheuch G., Hochhaus G., Hickey A., Bioequivalence of inhaled drugs: Fundamentals, challenges and perspectives, Therapeutic Delivery, 4 (2013) 343–367.

Atkins P.J., Crowder T.M., The design and development of inhalation drug delivery systems, in: Pharmaceutical Inhalation Aerosol Technology, second ed., Hickey A.J. (Ed.), Informa Healthcare, New York, 2004, pp. 279–309.

Begat P., Morton D.A.V., Staniforth J.N., Price R., The cohesive-adhesive balances in dry powder inhaler formulations I: Direct quantification by atomic force microscopy, Pharmaceutical Research, 21 (2004) 1591–1597.

Behara S.R.B., Larson I., Kippax P., Stewart P., Morton D.A.V., Insight into pressure drop dependent efficiencies of dry powder inhalers, European Journal of Pharmaceutical Sciences, 46 (2012) 142–148.

Behara S.R.B., Kippax P., McIntosh M.P., Morton D.A.V., Larson I., Stewart P., Structural influence of cohesive mixtures of salbutamol sulphate and lactose on aerosolisation and de-agglomeration behaviour under dynamic conditions, European Journal of Pharmaceutical Sciences, 42 (2011a) 210–219.

Behara S.R.B., Larson I., Kippax P., Morton D.A.V., Stewart P., An approach to characterising the cohesive behaviour of powders using a flow titration aerosolisation based methodology, Chemical Engineering Science, 66 (2011b) 1640–1648.

Behara S.R.B., Larson I., Kippax P., Morton D.A.V., Stewart P., The kinetics of cohesive powder de-agglomeration from three inhaler devices, International Journal of Pharmaceutics, 421 (2011c) 72–81.

Behara S.R.B., Kippax P., Larson I., Morton D.A.V., Stewart P., Kinetics of emitted mass—a study with three dry powder inhaler devices, Chemical Engineering Science, 66 (2011d) 5284–5292.

Carstensen J., Solid state stability, in: McGinity J.W. (Ed.), Drug Stability: Principles and Practices, Marcel Dekker, Inc., New York, 1990, pp. 129–164

Carstensen J.T., Angle of repose, in: Carstensen J.T. (Ed.) Pharmaceutical Principles of Solid Dosage Forms, Technomic Publishing Co, Inc., Lancaster, 1993, pp. 27–29.

Chew N.Y.K., Chan H.-K., Use of solid corrugated particles to enhance powder aerosol performance, Pharmaceutical Research, 18 (2001) 1570–1577.

Concessio N.M., VanOort M.M., Knowles M.R., Hickey A.J., Pharmaceutical dry powder aerosols: Correlation of powder properties with dose delivery and implications for pharmacodynamic effect, Pharmaceutical Research, 16 (1999) 828–834.

Crowder T.M., Hickey A.J., An instrument for rapid powder flow measurement and temporal fractal analysis, Particle & Particle Systems Characterization, 16 (1999) 32–34.

Crowder T.M., Hickey A.J., The physics of powder flow: Applied to pharmaceutical solids, Pharmaceutical technology., 24 (2000) 50–58.

Crowder T.M., Hickey A.J., Louey M.D., Orr N., Particulate systems: manufacture and characterization, Interpharm/CRC, Boca Raton, FL, 2003, pp. 9–26.

Crowder T., Hickey A., Powder specific active dispersion for generation of pharmaceutical aerosols, International Journal of Pharmaceutics, 327 (2006) 65–72.

Crowder T.M., Rosati J.A., Schroeter J.D., Hickey A.J., Martonen T.B., Fundamental effects of particle morphology on lung delivery: Predictions of stokes' law and the particular relevance to dry powder inhaler formulation and development, Pharmaceutical Research, 19 (2002) 239–245.

Crowder T.M., Sethuraman V., Fields T.B., Hickey A.J., Signal processing and analysis applied to powder behavior in a rotating drum, Particle & Particle Systems Characterization, 16 (1999) 191–196.

Davies C.N., Particle fluid interactions, J. Aerosol Sci., 10 (1979) 477–513.

Dunbar C.A., Hickey A.J., Holzner P., Dispersion and characterization of pharmaceutical dry powder aerosols, KONA Powder and Particle Journal, 16 (1998) 7–45.

Dunbar C.A., Morgan B., Van Oort M., Hickey A.J., comparison of dry powder inhaler dose delivery characteristics using a power criterion, PDA Journal of Pharmaceutical Science and Technology, 54 (2000) 478–484.

Fults K.A., Miller I.F., Hickey A.J., Effect of particle morphology on emitted dose of fatty acid-treated disodium cromoglycate powder aerosols, Pharmaceutical Development and Technology, 2 (1997) 67–79.

Gonda I., el Khalik A.F.A., Aerodynamic properties of different crystal forms of hexamethylmelamine, The Annals of Occupational Hygiene, 32 (1988) 379–390.

Grasmeijer F., Hagedoorn P., Frijlink H.W., de Boer A.H., Drug content effects on the dispersion performance of adhesive mixtures for inhalation, PLoS ONE, 8 (2013) e71339.

Grasmeijer F., Lexmond A.J., Maarten V., Hagedoorn P., Hickey A.J., Frijlink H.W., de Boer A.H., New mechanisms to explain the effects of added lactose fines on the dispersion performance of adhesive mixtures for inhalation, PLoS One, 9 (2014) 1–11.

Hickey A.J., Lung deposition and clearance of pharmaceutical aerosols: What can be learned from inhalation toxicology and industrial hygiene?, Aerosol Science and Technology, 18 (1993) 290–304.

Hickey A.J., Pharmaceutical inhalation aerosol powder dispersion—An unbalancing act, American Pharmaceutical Review, 6 (2003) 106–110.

Hickey A.J., Summary of common approaches to pharmaceutical aerosol administration, in: Pharmaceutical Inhalation Aerosol Technology, second ed., A.J. Hickey (Ed.), Marcel Dekker, Inc., New York, NY, 2004, pp. 385–421.

Hickey A.J., Concessio N.M., Flow properties of selected pharmaceutical powders from a vibrating spatula, Particle & Particle Systems Characterization, 11 (1994) 457–462.

Hickey A.J., Concessio N.M., Chaos in rotating lactose powder beds, Particulate Science and Technology, 14 (1996) 15–25.

Hickey A.J., Concessio N.M., Descriptors of irregular particle morphology and powder properties, Advanced Drug Delivery Reviews, 26 (1997) 29–40.

Hickey A.J., Ganderton D. (Eds.), Size reduction and classification, in: Pharmaceutical Process Engineering, Informa Healthcare, New York, 2001, pp. 174–197.

Hickey A.J., Mansour H.M., Telko M.J., Xu Z., Smyth H.D.C., Mulder T., McLean R., Langridge J., Papadopoulos D., Physical characterization of component particles included in dry powder inhalers. I. Strategy review and static characteristics, J Pharm Sci, 96 (2007a) 1282–1301.

Hickey A.J., Mansour H.M., Telko M.J., Xu Z., Smyth H.D.C., Mulder T., McLean R., Langridge J., Papadopoulos D., Physical characterization of component particles included in dry powder inhalers. II. Dynamic characteristics, J Pharm Sci, 96 (2007b) 1302–1319.

Hickey A.J., Xu Z., Balancing particle properties to achieve effective inhaled drug delivery, Pharm Tech Japan, 29 (2013) 183–188.

Hinds W.C., Aerosol technology: Properties and Behavior and Measurement of Airborne Particles, second ed., John Wiley and Sons, New York, 1999, p. 251.

Jaffari S., Forbes B., Collins E., Barlow D.J., Martin G.P., Murnane D., Rapid characterisation of the inherent dispersibility of respirable powders using dry dispersion laser diffraction, International Journal of Pharmaceutics, 447 (2013) 124–131.

Jaffari S., Forbes B., Collins E., Khoo J., Martin G.P., Murnane D., Evidence for the existence of powder sub-populations in micronized materials: Aerodynamic size-fractions of aerosolized powders possess distinct physicochemical properties, Pharmaceutical Research, 31 (2014) 3251–3264.

Jones M.D., Price R., The influence of fine excipient particles on the performance of carrier-based dry powder inhalation formulations, Pharmaceutical Research, 23 (2006) 1665–1674.

Lippmann M., Effects of fiber characteristics on lung deposition, retention, and disease, Environmental health perspectives, 88 (1990) 311–317.

Louey M.D., Van Oort M., Hickey A.J., Standardized entrainment tubes for the evaluation of pharmaceutical dry powder dispersion, Journal of Aerosol Science, 37 (2006) 1520–1531.

Mansour H.M., Xu Z., Hickey A.J., Dry powder aerosols generated by standardized entrainment tubes from alternative sugar blends: 3. Trehalose dihydrate and D-mannitol carriers, Journal of Pharmaceutical Sciences, 99 (2010) 3430–3441.

Martonen T.B., Katz I., Fults K., Hickey A.J., Use of analytically defined estimates of aerosol respirable fraction to predict lung deposition patterns, Pharmaceutical Research, 9 (1992) 1634–1639.

Mullin J.W., Crystallization, third ed., Butterworth-Heinemann, Oxford, 1993.

Sanders M., Pulmonary drug delivery: An historical overview, in: Smyth H.D.C., Hickey A.J. (Eds.), Controlled pulmonary drug delivery, Springer New York, New York, NY (2011) pp. 51–73.

Shah I., The blind ones and the matter of the elephant, in: Tales of the Dervishes, Arkana, London, 1993, pp. 25–26.

Shur J., Kubavat H.A., Ruecroft G., Hipkiss D., Price R., Influence of crystal form of ipratropium bromide on micronisation and aerosolisation behaviour in dry powder inhaler formulations, Journal of Pharmacy and Pharmacology, 64 (2012) 1326–1336.

Smyth H.D.C., Cooney D.J., Garmise R.J., Zimmerer R.O., Pipkin J.D., Hickey A.J., Dynamic electrostatic charge determinations of dry powder blends for inhalation: correlations with dispersion performance influence of physical form of captisol, in: Respiratory Drug Delivery IX, Volume III, Dalby R.N., Byron P.R., Peart J., Suman J.D. and Farr S.J. (Eds.), Davis Healthcare International Publishing, LLC, River Grove, IL, 2004, pp. 805–807.

Steckel H., Bolzen N., Alternative sugars as potential carriers for dry powder inhalations, International Journal of Pharmaceutics, 270 (2004) 297–306.

Stewart P.J., Particle interaction in pharmaceutical systems, Pharmaceutical International, 7 (1986) 146–149.

Taylor M.K., Ginsburg J., Hickey A.J., Gheyas F., Composite method to quantify powder flow as a screening method in early tablet or capsule formulation development, AAPS PharmSciTech, 1 (2000) 20–30.

Telko M.J., Hickey A.J., Dry powder inhaler formulation, Respiratory Care, 50 (2005) 1209–1227.

Telko M.J., Hickey A.J., Critical assessment of inverse gas chromatography as means of assessing surface free energy and acid–base interaction of pharmaceutical powders, Journal of Pharmaceutical Sciences, 96 (2007) 2647–2654.

Telko M.J., Hickey A.J., Aerodynamic and electrostatic properties of model dry powder aerosols: A comprehensive study of formulation factors, AAPS PharmSciTech, 15 (2014) 1378–1397.

Telko M.J., Kujanpää J., Hickey A.J., Investigation of triboelectric charging in dry powder inhalers using electrical low pressure impactor (ELPI™), International Journal of Pharmaceutics, 336 (2007) 352–360.

Tian Y., Parasrampuria D., Kanke M., Hickey A.J., Manufacture and in-vitro assessment of bromsulphthalein and phenolphthalein loaded polyester microspheres, Drug Development and Industrial Pharmacy, 20 (1994) 1159–1178.

Tougas T.P., Mitchell J.P., Lyapustina S.A., Good Casacade Impactor Practices, AIM and EDA for Orally Inhaled Products, Springer, NY, 2013.

US FDA (Food and Drug Adminstration), November 1998, Draft Guidance for the Industry, Metered Dose inhaler (MDI and Dry Powder Inhaler (DPI) Chemistry, Manufacturing and Controls Documentation.

US FDA (Food and Drug Administration), Draft Guidance on Fluticasone Propionate; Salmeterol Xinafoate, September 2013.

USP (United States Pharmacopoeia), General Chapter <601> Aerosols, Nasal Sprays, Metered Dose Inhalers, and Dry Powder Inhalers, USP Rockville, MD, 34 (2011) pp. 218–239.

Van Oort M.M., Sacchetti M., Spray drying and supercritical fluid particle generation techniques, in: Inhalation Aerosols, Physical and Biological Basis for Therapy, Second Edition, A.J. Hickey (Eds.), Informa Healthcare, New York, 2007, pp. 307–346.

Vehring R., Pharmaceutical particle engineering *via* spray drying, Pharmaceutical Research, 25 (2008) 999–1022.

Wong J., Lin Y.-W., Kwok P.C.L., Niemelä V., Crapper J., Chan H.-K., Measuring bipolar charge and mass distributions of powder aerosols by a novel tool (BOLAR)., Molecular Pharmaceutics, 12 (2015) 3433–3440.

Xu Z., Mansour H.M., Hickey A.J., Particle interactions in dry powder inhaler unit processes: A review, Journal of Adhesion Science and Technology, 25 (2011) 451–482.

Xu Z., Mansour H.M., Mulder T., McLean R., Langridge J., Hickey A.J., Dry powder aerosols generated by standardized entrainment tubes from drug blends with lactose monohydrate: 1. Albuterol sulfate and disodium cromoglycate, Journal of Pharmaceutical Sciences, 99 (2010a) 3398–3414.

Xu Z., Mansour H.M., Mulder T., McLean R., Langridge J., Hickey A.J., Dry powder aerosols generated by standardized entrainment tubes from drug blends with lactose monohydrate: 2. Ipratropium bromide monohydrate and fluticasone propionate, Journal of Pharmaceutical Sciences, 99 (2010b) 3415–3429.

Xu Z., Mansour H.M., Mulder T., McLean R., Langridge J., Hickey A.J., Heterogeneous particle deaggregation and its implication for therapeutic aerosol performance, Journal of Pharmaceutical Sciences, 99 (2010c) 3442–3461.

Young P.M., Chan H.-k., Chiou H., Edge S., Tee T.H.S., Traini D., The influence of mechanical processing of dry powder inhaler carriers on drug aerosolization performance, Journal of Pharmaceutical Sciences, 96 (2007) 1331–1341.

Young P.M., Cocconi D., Colombo P., Bettini R., Price R., Steele D.F., Tobyn M.J., Characterization of a surface modified dry powder inhalation carrier prepared by “particle smoothing”, Journal of Pharmacy and Pharmacology, 54 (2002) 1339–1344.

Zhou Q., Qu L., Gengenbach T., Larson I., Stewart P.J., Morton D.A.V., Effect of surface coating with magnesium stearate via mechanical dry powder coating approach on the aerosol performance of micronized drug powders from dry powder inhalers, AAPS PharmSciTech, 14 (2013) 38–44.

Ziffels S., Bemelmans N.L., Durham P.G., Hickey A.J., In vitro dry powder inhaler formulation performance considerations, Journal of Controlled Release, 199 (2015) 45–52.

Author’s short biography

Anthony J. Hickey

Dr. Hickey is Distinguished RTI Fellow, at RTI International, Emeritus Professor of Molecular Pharmaceutics of the Eshelman School of Pharmacy, and Adjunct Professor Biomedical Engineering in the School of Medicine, at the University of North Carolina at Chapel Hill. He obtained Ph.D. and D.Sc. degrees in pharmaceutical sciences from Aston University, Birmingham, UK. He is a Fellow of the Royal Society of Biology, the American Association of Pharmaceutical Scientists and the American Association for the Advancement of Science. He received the Research Achievement Award of the Particulate Presentations and Design Division of the Powder Technology Society of Japan and the David W Grant Award in Physical Pharmacy of the American Association of Pharmaceutical Scientists. He is a member of the Pharmaceutical Dosage Forms Expert Committee of the United States Pharmacopeia.

KONA Powder and Particle Journal No. 35 (2018) 14–31/Doi:10.14356/kona.2018004 Review Paper

Nanomaterials for Environmental Solar Energy Technologies: Applications & Limitations †

Yiannis Deligiannakis

[1] *Laboratory of Physical Chemistry of Materials and Environment, Department of Physics, University of Ioannina, Greece*

Abstract

Environmental remediation and energy production are currently listed among the priority tasks by administration bodies, stakeholders and market competition. In this context, nanomaterials present competitive advantages in terms of performance and production costs. In the present critical review, the current state of the art of nanomaterials used in environmentally benign technologies exploiting solar irradiation such as H_2 production, water-splitting and photocatalysis are discussed. Factors determining the overall efficiency are articulated in a single "photophysical efficiency" equation. The physical meaning, limits and constraints of each factor are analyzed, updated and examples are discussed. The article highlights the main structure-function relationships in tandem with the limitations posed by the particle's physicochemical properties, production method, and the prerequisites posed by regulatory bodies and market needs. Several misconceptions are highlighted with regard to performance and yields that ultimately impact the end use of the nanomaterials. Current targets/limitations posed by the US Department of Energy are discussed as case studies. For context-coherence reasons, the present review focuses on metal and metal-oxide nanoparticles, i.e. carbon nanomaterials are not covered herein.

Keywords: nanomaterials, semiconductor, H_2, O_2, photocatalysis, heterojunction

1. Introduction

The interconversion of different forms of energy ultimately determines environmentally benign technologies that are quantifiable in a product/byproduct/cost balance (Chen X. et al., 2010; Froschl T. et al., 2012; Holdren J.P., 2007; Kamat P.V, 2010). Research on interactions of solar photons at particle interfaces or electrode surfaces boosts technology, the economy, as well as environmental policy interests. The energy content of the earth's sunlight is 0.9 to 3.2 electron volts (eV) photon, i.e. 87 to 308 kilojoules per einstein, i.e. "mole" of photons. On average, this makes a total maximum ~120.000 TW of solar radiation arriving on the earth's surface (Lewis N.S. and Nocera D.G., 2006). Today, the world's energy consumption is 15 TW, which is estimated to rise to 30 TW by 2050 (Lewis N.S. and Nocera D.G., 2006). In this context, if properly exploited, solar energy input could provide a significant contribution to our energy needs. This requires efficient/low-cost/environmentally sustainable technologies utilizing readily available materials for the solar-conversion process. Hydrogen (H_2) combustion emits only water vapor without carbon emissions, thus it is an ideal fuel. H_2 has the highest energy density of all fuels (143 kJ kg^{-1}), i.e. ideally 1 kg of H_2 can replace 2.6 kg of gasoline (Holdren J.P., 2007; Lewis N.S. and Nocera D.G., 2006). Today, however, 96 % of the global demand for H_2 is produced from fossil fuels (gasoline, coal). In this context, nanophotocatalytic materials emerge as being among the most promising solutions for photonic-energy storage in the form of H_2. As we discuss herein, the same photophysical machinery can be used to catalyze the degradation/transformation of environmental pollutants such as toxic organics of high-valency metals (Dong S. et al., 2015; Fagan R. et al., 2016).

In the present critical review, the current state of the art of nanomaterials used in environmentally benign technologies exploiting solar irradiation via H_2 production, water-splitting and photocatalysis are discussed, using a unified nanomaterials-technology view as originally envisaged by A. Bard (Bard A.J., 1980). Solar photoelectrochemical (PEC) hydrogen production, since its original conception in 1972 (Fujishima and Honda, 1972), surpassed the limit of 12 % efficiency in 1998 (Khaselev O. and Turner J.A., 1998). Today, photocatalysis is envisaged as a technology that can potentially provide a clean, cost-effective, domestically produced energy vector using solar energy (Lewis N.S and Nocera D.G., 2006; ENERGY.

---

† Received 13 July 2016; Accepted 31 August 2016

[1] 45110 Ioannina, Greece
E-mail: ideligia@cc.uoi.gr
TEL: +30-265-100-8662

GOV, 2015). It should be underlined, however, that currently (2016), low-temperature (< 80 °C) H_2 production experiences strong research interest aimed at setting up standards and parameters in parallel with cost reduction and factory-scale economy. In the 2015 report of the US Department of Energy on hydrogen production technologies (ENERGY.GOV, 2015), it is stated that photoelectrochemical H_2 production based on semiconductor photoelectrodes or photocatalysts is at an early stage of development. Thus it requires advances in materials development and reactor concept development. The progress on these fronts is envisaged through priority-ranked tasks: (a) in an initial stage, the study/development of high-efficiency, probably high-cost, materials to establish performance parameters, (b) attain a fundamental understanding of PEC hydrogen production vs. corrosion mechanisms, (c) then, in a later stage, the study of durable, low-cost, probably lower-performance materials to improve efficiency by mitigating loss mechanisms, (d) finally, development of complex multicomponent devices capable of achieving water splitting via optimization [light absorption]–[electron-hole transport]–[interfacial catalysis]. In this context, the fabrication of artificial photosynthetic systems can be directed towards two targets: [a] direct conversion of abundant materials, e.g. H_2O and CO_2 to fuels (H_2, HCOOH, CH_3OH), (Chen Z. et al., 2010; Lianos P., 2011; Miller E.L. et. al., 2010), or [b] production of electricity. Moreover, photochemical reactions could be employed to replace other energy-consuming chemical processes, for example, for pollution abatement or in chemical synthesis.

The present article is a review on the current status of photoactive nanomaterials used in such environmental technologies. The aim is to highlight the common (nano) photophysical properties that determine their performance, limitations and potential in technological applications. Emphasis is focused on the materials' physicochemical properties in an effort to highlight the main factors that determine nanomaterials' production targets and limitations. A detailed tabulation of the literature data per material is beyond the scope of the present review. The interested reader is encouraged to consult pertinent reviews on photocatalysis (Teo W.Y. et al., 2012), heterogeneous photocatalytic water treatment using visible light-responsive photocatalysts (Dong S. et al., 2015), solar and visible-light-active TiO_2 photocatalysis for treating biocontaminants (Fagan R. et al., 2016), N-TiO_2 for green energy applications under UV/visible light (Devi L.G. and Kavitha R., 2014), as well as alternative photocatalysts to TiO_2 (Hernandez-Alonso et al., 2012). Moreover, the interested reader is encouraged to visit a virtual issue published by the American Chemical Society (JPCCSVI, 2016) where a comprehensive set of review articles—up to 2013—is available.

2. The general photo-nano-technology concept

Solar electromagnetic radiation is consistent with that of a black body at $T = 5800$ K with a radiation spectrum peak at 0.8 eV. A significant part of this spectrum is in the visible range of the spectrum (400–700 nm). The fraction of solar light which reaches the earth's surface has a maximum power density of ~100 mW/cm^2 (Holdren J.P., 2007; Lewis N.S. and Nocera D.G., 2006). However, only photons with hν exceeding the semiconductors band gap (E_g), generate electron-hole (e^-/h^+) pairs. The overall power-conversion efficiency of single crystalline p-n solar cells ranges from 10 to 30 %, yielding 10 to 30 mW/cm^2. On the other hand, when pursuing visible-light photocatalysts, Maeda and Domen (2007) have proposed that, before commercial development, photocatalysts must reach a quantum yield of 30 % at 600 nm. This seems a bold challenge at present, however, as we discuss herein, this is exactly the driving-force for science and technology in this field (ENERGY.GOV, 2015).

There are three main technology/research approaches for the exploitation of solar photons. The common basis of these was originally conceptualized by Bard A. (1980), as depicted schematically in **Fig. 1**.

Photoelectrochemical cells (PEC): In this general scheme, **Fig. 1**, the archetypical Fujishima-Honda photoelectrochemical cell (PEC) (Fujishima and Honda, 1972) is the combination of the n-type semiconductor as the anode and an inert electrode as the cathode immersed in the electrolyte solution, see **Fig. 1(A)**. PEC provides both the required field for e^-/h^+ separation as well as considerable spatial separation of the products to minimize recombination hurdles or unwanted product reaction. Until today, the nanophotoelectrodes used are of n-type. Fewer examples of p-type nanophotoelectrodes exist, i.e. CuO, Co-phosphates, IrO_2, that will be discussed hereafter. The definitions on efficiency for PEC devices are aligned with those used for photovoltaics (PV) because the two fields share many common characteristics, and they are in agreement with previous analyses of efficiencies for PEC water splitting (Chen Z. et al., 2010; Rocheleau R. and Miller E., 1997). In energy terms, in a PEC it is light that pumps the electrons "uphill" and provides the required energy. Note that the PEC provides both the required field for e^-/h^+ separation as well as the considerable spatial separation of the reaction products to minimize unwanted back-reactions.

The concept of PEC for H_2O splitting for H_2 production has been discussed for decades since its first demonstration in 1972 (Fujishima and Honda, 1972), but the world-record solar-to-hydrogen (STH) efficiency of 12.4 % was achieved almost two decades ago in 1998 (Khaselev O. and Turner J.A., 1998). This technology combines the harvesting of solar energy and the electrolysis of water

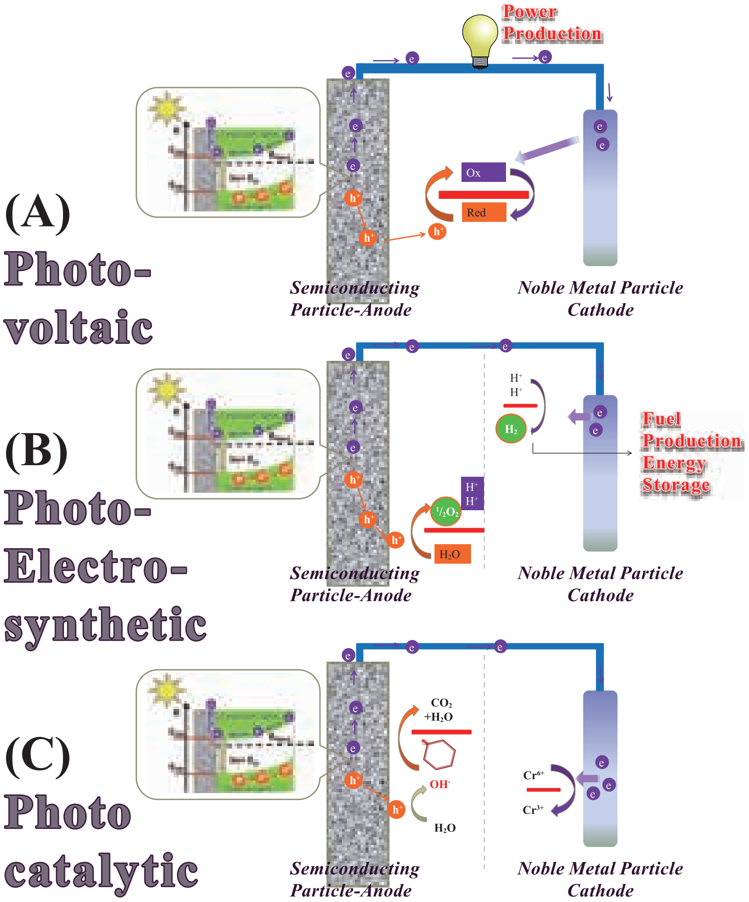

Fig. 1 Schematic description of the fundamental photoactive nanocatalytic systems. A fundamental difference is the positioning of the energy levels of the redox couples vs. the photo-induced electrons' and holes' energy levels. For simplicity, external bias voltage is not included in these schemes. External bias, depending on polarity and voltage, will shift upwards or downwards the energy levels of e^- and h^+.

into a single device. When a semiconductor—with the right set of properties—is immersed in an aqueous electrolyte and irradiated with sunlight, the photon energy is converted to electrical energy which is directly used to split water into hydrogen and oxygen (chemical energy), **Fig. 1B**. Thus, intermittent energy from sunlight is converted into an inherently more storable form of energy, i.e. that of chemical bonds. An excellent account on the physicochemical, technical and economical issues of PECs is given by Chen et al. (2010).

For the direct PEC decomposition of water to occur, several key criteria must be met simultaneously: (i) the semiconductor system must generate sufficient voltage upon photo-excitation to split H_2O; (ii) the bulk band gap, E_g, must match the energy of solar photons, preferably in the visible spectrum, i.e. 2.0–3.0 eV; (iii) the band-edge potentials at the surfaces must encompass the H^+/H_2 and H_2O/O_2 redox potentials; (iv) the system must exhibit physicochemical resilience in aqueous electrolytes; (v) for H_2O splitting, the charge transfer from the surface of the semiconductor to the solution must avoid corrosion and be energetically/kinetically facile enough to reduce energy losses due to kinetic overpotential. So far, *no cost-effective material* satisfies *all* of these technical requirements (Chen Z. et al., 2010). Here, we present a survey on some of the key factors that may influence the efficiency.

Overal quantum yield vs. efficiency in PECs: Photo-induced e-transfer reactions are now well understood. High quantum yields for photochemical e^-/h^+ separation are very often reported. When these systems are coupled to sacrificial electron donors, such as methanol, or acceptors, such as persulfate, then H_2 or O_2 can be produced from H_2O (Chen Z. et al., 2010; Harriman A. et al., 1988).

When practical energy conversion is considered in real systems, the use of sacrificial systems gives a simplistic "efficiency" that should be revised when taking into account electrolyte redox-couple cycling. However, such sacrificial donors are useful in mechanistic studies because [a] they minimize e^-/h^+ recombination and [b] they permit the examination of a light-driven half-cell reaction, i.e. oxidation or reduction, separately. Thus, from the practical point of view, estimating separately the quantum yield of H_2 or O_2 evolution in sacrificial half-cycles is also an effective method for rapidly screening new catalysts

(Chen Z. et al., 2010; Goldsmith J. et al., 2005).

Achieving high quantum yields in sacrificial half-cycles implies the use of efficient key components (catalytic material/redox mediators/photosensitisers) that allow a proof-of-concept level for overall water splitting. The problem is to combine them in such a way that diminishes e^{-}/h^{+} and H_2/O_2 recombination. Control of e^{-}/h^{+} recombination is a complex process, even in the simplest of such systems, such as a Pt^0-loaded *n*-semiconductor particle coupled to an O_2-evolving catalyst, see **Fig. 1B**. A high quantum yield can be achieved only if the forward electron transfer rate (solid arrows in **Fig. 1B**) *at each branch in the chain* is faster than the *sum of all the reverse rates*. For example, in **Fig. 1B**, the forward electron transfer from the semiconductor to the H_2-evolving catalyst must compete effectively with e^{-}/h^{+} recombination and also with e-transfer to the H_2O-oxidation catalyst. Here, a key hurdle is that the reverse reactions are fast because the reverse pathways have much higher driving forces than the forward ones. However, because e^{-}/h^{+} recombination rates are also strongly distance-dependent, it should be possible to arrange the components *in space* in such a way that the forward pathway becomes kinetically competitive or even dominant. Photosynthesis is living proof of this principle. On this front, the use of heterostructural nanoparticles containing all components (O_2-evolving particle, main photo-excitable semiconductor, and e-accumulating particle) is a very attractive technology that we discuss hereafter.

Photocatalysis: The concept of photocatalysis for environmental remediation, depicted in **Fig. 1C**, implies that photons are converted in a first step to chemical intermediates that are highly energetic, thus very reactive. Typically, these are hydroxyl radicals ($^{\bullet}OH$) or superoxide radicals ($^{\bullet}OO$) and, in more rare cases, singlet-oxygen radicals ($^{\bullet}O$) that are generated at the particle-solution interface (Teo W.Y. et al., 2012; Linsebigler A.L. et al., 1995), see **Fig. 2**.

When a semiconductor surface is irradiated by light ($h\nu \geq E_g$), there is a generation of electron/hole pairs (e^{-}/h^{+}) via the promotion of an e^{-} from the valence band (lower energy level) to the conduction band (higher energy level). The surface water molecules and/or hydroxyl ions react with the holes on the valence band to generate hydroxyl radicals ($^{\bullet}OH$), which are a powerful oxidizing agent (+ 2.80 V). In **Fig. 1(C)**, this shows that a strong ΔG gradient has to be overcomed for the degradation of persistent organic pollutants: notice the energy level-positioning differences in **Figs. 1A, B, C**.

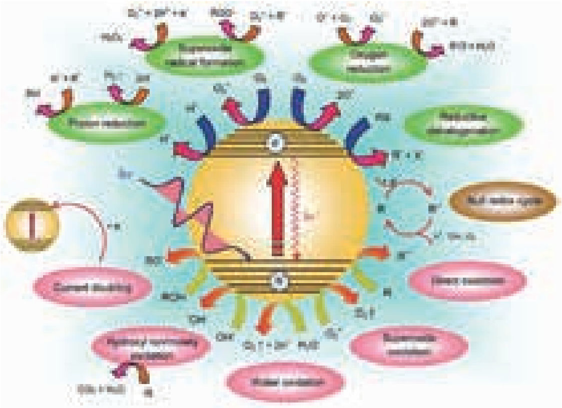

Fig. 2 Photo-induced reactions and radical transient species produced arising from the excitation of a photocatalyst particle in aqueous solution. Reprinted with permission from Ref. (Teo W.Y. et al., 2012). Copyright: (2012) American Chemical Society.

3. Basic photophysical principles-characteristics of photocatalytic nanomaterials

In the context of photocatalysis, a reference solar spectrum (atmospheric mass, AM1.5) is commonly considered. 1.5 atmosphere thickness corresponds to a solar zenith angle of $z = 48.2°$. Therefore, AM1.5 is useful to represent the overall yearly average for mid-latitudes on Earth. The solar intensity versus air mass (AM) is given by

$$I = 1.1 \times I_0 \times 0.7^{(0.678\mathrm{AM})}$$

where solar intensity external to the earth's atmosphere, $I_0 = 1.353\ \mathrm{kW/m^2}$, and the factor 1.1 is derived assuming that the diffuse component of sunlight is 10 % of the direct component. For AM1.5 this results in a solar power density ~930 $\mathrm{W/m^2}$ (Würfel P., 2005)

In the fundamental Shockley-Queisser model, it is assumed that photons with energy below the band gap ($h\nu < E_g$) are not absorbed at all, while photons with energy far above the band gap ($h\nu > E_g$) are absorbed, but all that excess energy is wasted as thermal energy (Shockley W. and Queisser H. J., 1961).

Here, we notice that for ($h\nu >> E_g$), electrons are excited to an energy-level far above the conduction-band minimum, and holes far below the valence-band maximum. After such an excitation, e^{-} and h^{+} relax to the band edges very rapidly ($t <$ ns). If this relaxation could be stopped, then the highly energetic "hot" h^{+}/e^{-} pair efficiency can theoretically considerably exceed the existing theoretical limits posed by Shockley and Queisser for *p-n* junction photovoltaics (Shockley W. and Queisser H.J., 1961). In practice, this is very difficult; thus far, even a proof-of-principle laboratory demonstration of a complete hot-electron device is lacking.

3.1 Formulation of the Photophysical Efficiency Concept

In their report, Chen et al. (2010) make clear that solar-to-hydrogen (STH) efficiency should be used as a common reference benchmark reporting. Other efficiency parameters can also be used, providing insight into the functionality and limitations of a device; definitions are reviewed in (Chen Z. et al., 2010; ENERGY.GOV, 2015; Lianos P., 2011). In all technological applications of photocatalysts, the photophysical efficiency of a given material is the core parameter that will determine its ultimate eligibility. Then, scalability, cost and life-cycle issues have to be taken into account to permit an industrial-scale consideration. The two main parameters are:

- **Quantum efficiency** = molecules of product produced per photon absorbed;
- **Solar efficiency** = molecules of product produced per incident solar photon.

Focusing on the h^+/e^- production efficiency of a given material, without reference to the subsequent interfacial or liquid-phase reactions, we may use a 'photophysical efficiency parameter'. The photophysical efficiency of a photocatalyst concerns all processes *inside the particle* that include the photon absorption until migration of the electron and the hole to their first *interfacial* acceptors.

As detailed by Bolton (1978, 1985), the photophysical efficiency parameter can provide a common base of discussion for all photodevices described in **Fig. 1** (Bard A.J., 1980). In this context, the overall catalytic efficiency of a given photocatalyst can be formulated as follows:

$$\text{Photophysical Efficiency} = f_{\text{particle}} \cdot \text{ELP} \tag{1}$$

where the two factors f_{particle} and ELP are defined as follows:

- f_{particle} = efficiency of electron-hole photoproduction
- ELP = energy level positioning of the e^-/h^+ relative to their interfacial electron-acceptor and hole-acceptor, respectively.

The ELP factor takes into account the efficiency of energy-level alignment for the elementary-step, for example from a TiO_2 nanoparticle to Pt^0, in the TiO_2-Pt^0 system. Equation (1) can be further expanded by considering that $\boldsymbol{f}_{\text{particle}}$ consists of two factors:

$$f_{\text{particle}} = f_{\text{structural}} \cdot R_{\text{kinetic}} \tag{2a}$$

where the two factors $f_{\text{structural}}$ and R_{kinetic} are defined as follows

$$f_{\text{structural}} = ([\alpha]/[\text{SSA}]\ [\text{catalyst mass}]) \tag{2b}$$

$$R_{\text{kinetic}} = ([M_e][M_h]/[\text{RR}]) \tag{2c}$$

with

α = solar-light absorbance efficiency

RR = h^+/e^- recombination rate

M_e, M_h = mobilities of the electrons and the holes

and SSA=specific surface area of the catlyst.

3.2 Direct vs. Indirect Band-Gap Semiconductors:

[A]-*Direct band-gap semiconductor*: For a direct band-gap semiconductor, α is related to the frequency of the light, v, according to the following formula:

$$\alpha \cong A^* \sqrt{hv - E_g} \tag{3a}$$

where α is the light-absorption coefficient, v = light frequency, h = Plank's constant, E_g is the semiconductor's band-gap energy, A^* is a frequency-independent constant, with formula (Würfel P., 2005)

$$A^* = \frac{(2m_r)^{\frac{3}{2}} q x_{vc}^2}{\lambda_0 \in_0 \hbar^3 n} \tag{3b}$$

and

$$m_r = \frac{m_h{}^* m_e{}^*}{m_h{}^* + m_e{}^*} \tag{3c}$$

is the *reduced mass*, based on the effective masses m_e* and m_h* of the hole and the electron, respectively. n is the real part of the refraction index of the material, $\chi_{\upsilon c}$ is a crystal-matrix parameter usually taken equal to the lattice constant for each material. q and ε_0 are the electron charge and vacuum permittivity, respectively. This formula is valid only for light with photon energy larger, but not too much larger, than the band gap (more specifically, this formula assumes the bands are approximately parabolic), and ignores all other sources of absorption other than the band-to-band absorption in question, as well as the electrical attraction between the newly created electron and hole.

[B]-*Indirect band-gap semiconductor*: On the other hand, for an *indirect* band gap, the formula is:

$$\alpha \propto \frac{\left(hv - E_g + E_p\right)^2}{\exp\left(\frac{E_p}{kT}\right) - 1} + \frac{\left(hv - E_g - E_p\right)^2}{1 - \exp\left(-\frac{E_p}{kT}\right)} \tag{4}$$

where E_p the energy of the *phonon* i.e. a lattice vibrational state, that assists in the transition; kT is the Boltzmann thermal factor. This differentiates a so-called direct from an indirect semiconductor.

A direct band-gap semiconductor is formed when the minimum energy of the conduction band is at the same k-position in the Brillouin zone to the maximum of the valence-band, see **Fig. 3**. *The notion of direct vs. indirect band gap has profound impact on the e^-/h^+ lifetime and*

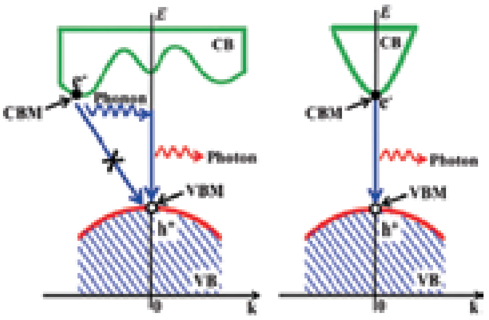

(a) Anatase (b) Rutile

Fig. 3 *Indirect* (Anatase TiO_2) and *direct* (Rutile TiO_2) band-gap semiconductors. Reprinted with permission from Ref. (Zhang J. et al., 2014). Copyright: (2014) Royal Society of Chemistry.

recombination dynamics: when the excited electrons come back from the conduction band to the valence band due to recombination of photogenerated e^-/h^+, they will *release* their extra energy as photons of frequency v, i.e.

$$hv = E_g \tag{5a}$$

Moreover, the excited electrons must meet the transition selection rule of momentum conservation,

$$\hbar \boldsymbol{k}_{\mathrm{e(conduction\ band)}} - \hbar \boldsymbol{k}_{\mathrm{e(valence\ band)}} = \hbar \boldsymbol{q}_{\mathrm{phonon}} \quad \text{(indirect band gap } e^-/h^+ \text{ recombination)} \tag{5b}$$

where $\hbar$ is the reduced Planck constant, $\boldsymbol{k}_{\mathrm{e(conduction\ band)}}$, $\boldsymbol{k}_{\mathrm{e(valence\ band)}}$ are the electron wave vectors at the conduction band and valence band, respectively, $\boldsymbol{q}$ is the wave vector of the assisted phonon (Zhang J. et al., 2014). Using this formulation, for a direct band-gap semiconductor:

$$\hbar \boldsymbol{k}_{\mathrm{e(conduction\ band)}} = \hbar \boldsymbol{k}_{\mathrm{e(valence\ band)}} \Rightarrow \hbar \boldsymbol{q}_{\mathrm{phonon}} = 0 \quad \text{(direct band gap } e^-/h^+ \text{ recombination)} \tag{5c}$$

i.e. only a photon *without phonon* is involved in e^-/h^+ recombination (Zhang J. et al., 2014). Examples are rutile and brookite: an electron only emits a photon following recombination of photogenerated e^-/h^+. However, the recombination of photoexcited electron and hole in anatase is assisted by a phonon, because $\hbar \boldsymbol{k}_{\mathrm{e(conduction\ band)}} \neq \hbar \boldsymbol{k}_{\mathrm{e(valence\ band)}}$ for this indirect band-gap semiconductor (Zhang J. et al., 2014). Thus, the excited electrons cannot recombine directly with holes, resulting in an increase of the photogenerated electron–hole lifetime in anatase, relative to that of rutile and brookite. As a result, the diffusion length and reaction time of the electron and hole excited in anatase also increase.

In this context, in general, direct band-gap semiconductors are expected to have *higher* h^+/e^- *recombination rates* (shorter e^-/h^+ lifetimes) than indirect band-gap semiconductors. Examples of common direct band-gap semiconductors include ZnO and GaAs, while crystalline Si forms indirect band-gap semiconductors. All quantum dots are direct band-gap materials.

The direct or indirect band-gap character of $BiVO_4$ has been a matter of debate (Cooper J.K. et al. 2015; Walsh A. et al., 2009). In an earlier report, Walsh et al. (2009) reported $BiVO_4$ to be a direct-band-gap material, with a direct band-gap $E_g = 2.4$ eV, however recent data by Cooper et al. (2015) suggest that $BiVO_4$ is an indirect band-gap semiconductor with a transition located at 0.2 eV below the direct one at 2.4 eV. This very small energy-positioning difference dictates the difficulty for its detection (Cooper J.K. et al., 2015; Walsh A. et al., 2009). Experimentally, the direct and indirect band gaps can result in resolvable differences in UV-vis transitions. Thus direct and indirect band gaps can be estimated by the so-called Tauc analysis (Tauc et al. 1970) as follows: using the UV-vis data for a given semiconducting material, we typically plot $(\alpha hv)^n$ versus (hv) where α is the measured absorption coefficient in the UV-vis spectrum. To do this, we have to convert the x-axis from wavelength (λ) to eV using the relation

$$hv(\mathrm{eV}) = 1240/\lambda \text{ in nm} \tag{6}$$

This method can determine the optical bulk band gap (E_g) and, ideally, can distinguish between allowed direct ($n = 2$) and allowed indirect ($n = 1/2$) transitions (Tauc et al 1970; Elliott R.J., 1957).

3.3 Effective mass-effect on e^-/h^+ transfer rates

The quantum efficiency of a photocatalyst is also affected by the transfer rate of photogenerated electrons and holes (Linsebigler A.L. et al., 1995). The transfer rate of h^+/e^- can be indirectly assessed by the effective mass (m^*) of electrons and holes (Linsebigler A.L. et al., 1995). In general, the transfer rate of photogenerated h^+/e^- is inversely proportional to their effective masses, i.e. the larger the effective mass of photogenerated carriers, the slower their transfer rate. Thus the small effective mass can promote the migration of charge carriers and inhibit their recombination. For example, the effective mass of photogenerated electrons and holes in $CaZrTi_2O_7$ have been estimated to be $m_e^* = 1.35m_0$ and $m_h^* = 1.23m_0$, respectively (Liu J.J. et al., 2012). In $NaBiO_3$, effective masses of $m_e^* = 0.14m_0$ and $m_h^* = 1.1m_0$ have been estimated, respectively (Liu J.J. et al., 2012; Zhang J., 2014). For anatase TiO_2, effective masses of $m_e^* = 0.0948$ and $m_h^* = 0.1995$ have been calculated (Zhang J., 2014). This correlates with the fact that anatase TiO_2 has a higher photocatalytic activity than $CaZrTi_2O_7$ and $NaBiO_3$ (Liu J.J. et al., 2012, 2013; Zhang J., 2014).

Mobility-diffusion is intimately related with the e^-/h^+ separation efficiency or the recombination rate RR in equation (2b). The case of Fe_2O_3 is very instructive: This material has a great advantage in that it absorbs visible

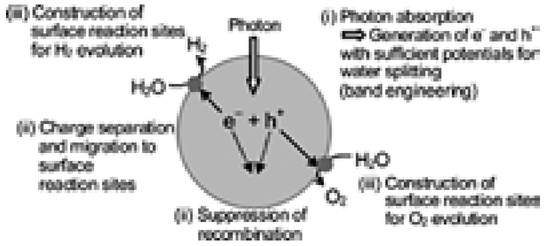

Fig. 4 Efficiency determining reactions in a photo-induced e^-/h^+ generation on a semiconductor nanoparticle. Reprinted with permission from Ref. (Kudo A. et al., 2009). Copyright: (2009) Royal Society of Chemistry.

light $E_g = 2.2$ eV (Miyauchi M. et al., 2002), but it suffers from a short hole-diffusion length (2–4 nm) (Formal F.L. et al., 2010).

In summary, formulas (1–2) entail that the overall photophysical efficiency (PPE) is determined by three main terms:

– $f_{\text{structural}}$ is determined by the energetic and solid-state properties of a given photocatalyst. These are physical properties determined by the solid-state characteristics of a given particle.

– R_{kinetic} is determined by the dynamic, kinetic characteristics of photogenerated e^-/h^+ in the photocatalyst. These are determined by the crystal structure and also by the defects, dopings, etc.

– the energy level positioning (ELP) factor describes the efficiency of the electron/hole transfer from the particle to the first interfacial acceptor. These factors are often described in texts and visualized in pertinent reaction schemes such as in **Fig. 4**.

Thus, equations (1, 2) offer a simple, compact form allowing an overview of the e^-/h^+ photogeneration efficiency. They indicate that in a given nanoparticle type, the factors $f_{\text{particle}} = f_{\text{structural}} \cdot R_{\text{kinetic}}$ are determined uniquely by its structure. Then, when in contact with an exogenous agent, electron level positioning will have to be determined for each type of application, since the types of acceptors will be different in different experiments.

4. Practical Issues: Examples of common limitations in data acquisition and analysis

4.1 Efficiency estimates

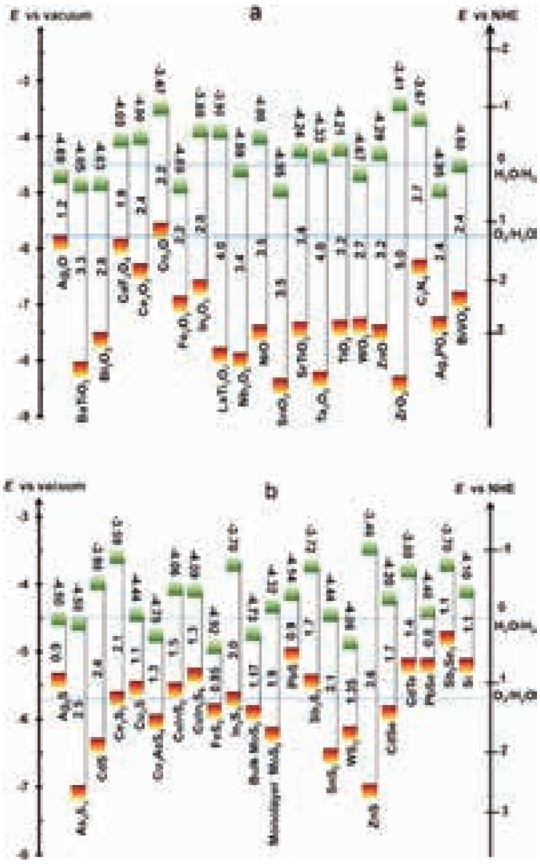

Fig. 5 Conduction-band and valence-band edge positions (in eV units) for selected semiconductors at pH 0.Left Y-axes provide energies vs. the vacuum energy level. Right Y-axes provide energies vs. the NHE energy level. Reprinted with permission from Ref. (Li and Wu, 2015). Copyright: (2015) Royal Society of Chemistry.

The energy levels of the conduction and valence bands, as determined form their ideal structures and compiled by Li and Wu (2015), are displayed in **Fig. 5**. Bolton et al. (1985) considered the thermodynamics of photochemical water splitting in detail and concluded that it is possible to store about 12 % of the incident solar energy in the form of hydrogen, allowing for reasonable losses (a total of 1.0 eV) in the electron transfer steps and the catalytic reactions of water splitting. In practice, there have been very few reports of photocatalytic water splitting using visible light (Hernandez-Alonso M.D. et al., 2009; Maeda K. et al., 2006; Zou Z. et.al., 2001), and the best reported quantum yield is so far about 6 % (Maeda K. and Domen K., 2008).

The solar power conversion based on semiconductor p-n junctions and semiconductor-liquid junctions can be quite efficient. In such p-n junctions, charge recombination is inhibited by the electric field that separates the light-generated minority and majority carriers (Hernandez-Alonso M.D., et al., 2009).

Photon-to-electron quantum yields approaching unity and power conversion efficiencies up to 18 % have been reported with single-crystal photoelectrodes (Khaselev O. et al., 1998). As noted above, if charge recombination reactions could be suppressed, then photocatalytic water splitting could become similarly efficient. On this front, significant advances have been made towards understanding photo-induced charge separation and interfacial charge-transfer processes in semiconductor photocatalyst assemblies (Tang J.W. et al., 2011). Thermodynamic and kinetic limitations determine the efficiency of electron and hole transfer in semiconductor systems. The existence of shallow surface traps may enhance the overall efficiency by increasing the e^-/h^+ lifetime. In any case, it is worth emphasizing that as much as 90 % of the electron–hole pairs recombine in less than 10 ns and consequently, photogenerated carriers available for surface reactions are quite limited. Values of quantum yield vary broadly with the process considered.

As an example, for TiO_2 reactions in solution, quantum yields are typically around 1 % (Wang C. et al., 2002) but they can exceed 5 % for some gas-phase reactions (Coronado J.M. et al., 2008). These values depend, as dictated by relations (1) and (2), on e^-/h^+ transfer at the particle interface and the surface characteristics, but considering exclusively the photoactivation process, TiO_2 shows a limited performance. Thus in contrast to silicon, which presents an internal quantum efficiency (IQE) close to 100 % under illumination at 600 nm (Svrcek V., 2004), in TiO_2, the absorbed photon-to-current efficiency is about 30 % at 360 nm (Lindgren T. et al., 2004).

4.2 Experimental Issues

Using diffuse-reflectance UV-vis spectroscopy, we typically measure the optical bulk band gap E_g of the semiconducting particles. One has to discriminate between a direct or indirect band gap, allowed or forbidden transition.

As described in Section 3.2, UV-vis data are routinely analyzed using Tauc plots (Tauc J. et al., 1970), i.e. $(\alpha h\nu)^n$ versus $(h\nu)$ and fitting the data with the appropriate n-value, we can decide if we have allowed direct ($n = 2$), forbidden direct ($n = 2/3$), allowed indirect ($n = 1/2$), and forbidden indirect ($n = 1/3$) transitions. An example is given in **Fig. 6** where absorption data for a Cu_2O material are analyzed in the form of Tauc plots (Tauc J. et al., 1970). By plotting the $(\alpha h\nu)^2$ versus $(h\nu)$, the band gap for the allowed direct transitions is determined to be $E_g^{\text{direct}} = 2.4$ eV, **Fig. 6**.

By plotting $(\alpha h\nu)^{1/2}$ versus $(h\nu)$, the indirect optical band gap is determined $E_g^{\text{indirect}} = 2.0$ eV, **Fig. 6c**. Attention should be paid to the fact that in nanoparticles, a UV-vis-derived band gap for the bulk is not necessarily valid for the surface. Moreover, the slope of the tangent to the data is prone to subjective error and should be treated with caution.

Typical error-prone cases are the verification of 'visible light absorbance'. In cases where a semiconducting particle is just covered or intermixed with a colored substance, this will give a change in the UV-vis profile. If this spectrum is analyzed by a typical Tauc plot, then this will result in the erroneous conclusion that the band gap of TiO_2 has been narrowed, whereas it is just an overlap of two UV-vis spectra.

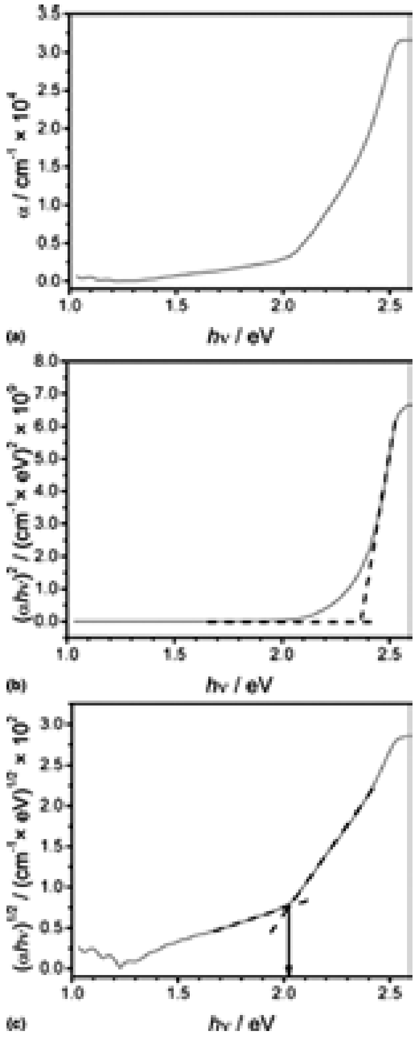

Fig. 6 (a) $(\alpha h\nu)^2$ versus $(h\nu)$ for Cu_2O sample. (b) The band gap for the allowed direct transitions is determined to be $E_g^{\text{direct}} = 2.4$ eV. (c) By plotting $(\alpha h\nu)^{1/2}$ versus $(h\nu)$, the indirect optical band gap is determined $E_g^{\text{indirect}} = 2.0$ eV. Reprinted with permission from Ref. (Chen, Z. et al, 2010). Copyright: (2010) Cambridge University Press.

This can be a common mistake even for the common TiO_2-Pt^0 particle characterization where Pt^0 particles are deposited on the TiO_2 surface for H_2-generation applications. The color of Pt^0 particles causes a shift of the TiO_2 UV-vis, however this should not be interpreted as band-gap narrowing (Giannakas A. et al., 2016). Similarly, in dye-sensitized solar cells (DSCC), the dye-covered particles give a visible-light absorbance band, however this is not due to band-gap narrowing, see the example in **Fig. 7**. As explained by Grätzel M. (2005), the basic mechanism of DSSC involves photoexcitation of the dye, donation of electrons by the dye on the conduction band of the semiconductor, and filling of the dye-hole via the counter-electrode/electrolyte circuit.

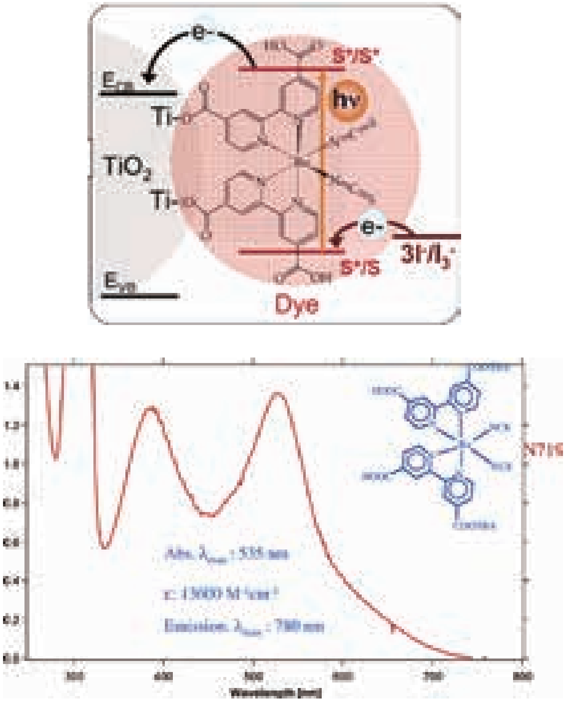

Fig. 7 The UV-vis spectrum of a Ru-based dye entails strong absorbance bands at visible wave lengths, with no TiO_2 band gap narrowing. Reprinted with permission from Ref. (Grätzel M., 2005). Copyright: (2005) American Chemical Society.

As a general guideline, the most interesting materials will exhibit a band gap, E_g, of between 1.5 and 3.5 V, because it needs to be large enough to account for the thermodynamic energy requirements of water splitting (1.23 V). In addition, conduction and valence-band potentials should encompass the hydrogen and oxygen evolution reactions, both the reduction of protons ($E_{NHE(H/H_2)} = 0.0$ eV) and the oxidation of water ($E_{NHE(O_2/H_2O)} = 1.2$ eV) (Kamat P.V., 2010).

Open-circuit potential is the maximum potential that a PEC can provide under zero current flow. This is the simplest commonly used method to measure conductivity and flat-band potential $V_{FB.}$ In practical terms, to obtain measurable V_{FB} data for a photoactive material, one has to use high illumination intensities. However, depending on the type of material, high photon flux may cause photocorrosion or surface alteration of the material. This is evidenced as a non-linear change in the measured mVolts at increased photon flux. Chen et al. (2010) exemplified this effect for a p-GaAsPN material using a tungsten 150-W lamp, where for illumination intensities from 100 mW/cm^2 to 600 mW/cm^2, the measured potential changed from ~430 mV to 600 mV (Chen X. et al., 2010).

H_2/O_2 ratios are used in standard test protocols to prove that H_2O splitting occurs. This requires perfect gas-shielding of the reactor components and thermal stability of the reaction set-up, particularly the illumination set-up. Stability tests often take days of repetitive use (Kudo A. and Miseki Y., 2009). In water splitting, both H_2 and O_2 should form with a stoichiometric amount, 2:1, in the absence of a sacrificial agent. Often H_2 is observed with a lack of O_2 evolution. In this case, the amount of H_2 evolution is usually small compared with the amount of a photocatalyst. It is not clear if such a reaction is photocatalytic water splitting, and it is important to clarify that it is not a sacrificial reaction (Froschl T. et al., 2012; Kudo A. and Miseki Y., 2009). Because the photocatalytic activity depends on the experimental conditions such as the light source and type of reaction cell, the activities cannot be compared with each other if the reaction conditions are different from each other. Therefore, determination of a quantum yield is important. The number of incident photons can be measured using a solid-state photodiode under non-saturating light-flux conditions. In a particle dispersion/slurry system, the real flux of photons absorbed by a photocatalyst will be lower than the incident photons because of scattering. So the obtained quantum yield is an *apparent* quantum yield (Kudo A. and Miseki Y., 2009). The apparent quantum yield is estimated to be smaller than the real quantum yield because the number of absorbed photons is usually smaller than that of incident light (Lewis N.S. and Nocera D.G., 2006).

In many cases, the most common test protocols in photocatalysis involve comparison versus the commercial Degussa-P25-TiO_2 for the degradation of dyes. However, extracting meaningful conclusions by such studies requires a complete data set that assesses the solid-state, interface and solution parameters. Ryu and Choi (2008) have compared the photocatalytic performance of 8 commercial types of TiO_2 for 19 different substrates. They concluded that not one of the tested TiO_2 is best for all the substrate types. As suggested (Ryu and Choi, 2008), multivariant statistical analysis, taking into account the key physicochemical properties of the photocatalyst in relation to the photocatalytic mechanistics, may provide a meaningful insight into the real performance of a photocatalyst. Useful details of experimental design for general photocatalysis can be found in Ohtani B. (2008).

Deactivation of surface sites. Deactivation of surface sites may occur in photocatalytic materials due to various reasons such as surface (photo) corrosion or surface fouling, or due to adsorption of reaction products on the surface. This phenomenon, however small it may be, has to be considered carefully (Dong S. et al., 2015).

Both these events result in deactivation of surface sites. As an example, if we have a loss of L % in each catalytic cycle, then, after k cycles, the remaining active sites are given by equation (7)

$$N_{\text{remaining}} = N_{\text{intial}}(1 - L)^k \tag{7}$$

Fig. 8 reveals that after just 100 cycles, a $L = 0.01$ % will

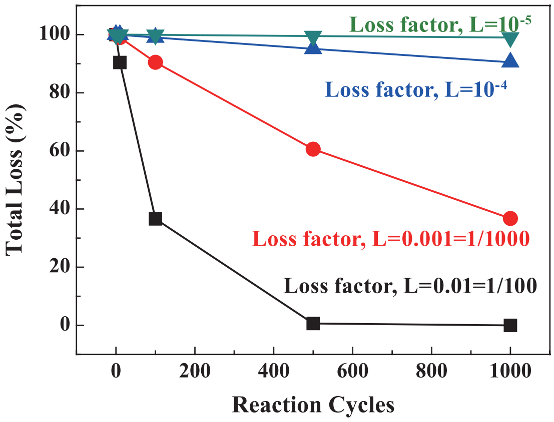

Fig. 8 Total loss of surface sites, for a [loss/per cycle] factor L, after N reaction cycles, estimated from equation (7). After just 100 cycles, *L* = 0.01 % will result in the loss of ~ 40 % of the active surface sites.

result in more than 40 % loss of active surface sites.

4.3 Dispersed Powders vs. Electrodes

In nanosized materials, the ability to manipulate the particle size permits the chemical properties in nanoparticles to be tuned. Thus, size control has tremendously extended the potential of nanomaterials. It is well known that in its simplest form, water-splitting is the transformation of the energy of photons in electrons and holes and ultimately to H_2 and O_2. Thus it is easy to anticipate that if 100 % of input electrons (e^-) can be successfully put to work and not lost, then a maximum amount of photons is transferred and stored in H_2 molecules. Ideally, maximizing the surface of the cathode and anode materials, a maximum conversion of photons to e^-/h^+ pairs and ultimately to H_2/O_2 is feasible. Thus, using nanoparticles instead of bulk materials should boost the fundamental e^-/h^+ transfer efficiency and therefore, in water splitting, see **Fig. 9** (Teo W.Y., 2012). In this context, the know-how gained from studies of PEC cells with bulk semiconductor electrodes can be applied to the design of systems in which semiconductor nanoparticles are used (Chen X. et al., 2010; Getoff N., 1990; Kudo A. and Miseki Y., 2009). For example, using powders of TiO_2 with platinum dispersed on the TiO_2-surface, each particle can be pictured as a "short-circuited" PEC cell (Bard A.J., 1980; Chen X. et al., 2010; Teo W.Y et al., 2012), where the TiO_2-electrode and Pt-counter electrode are in physical contact (Chen X., et al., 2010; Bard A.J., 1980; Teo W.Y et al., 2012). Irradiation of such nanoparticulate systems still involves the e^-/h^+ pair formation and surface oxidation/reduction reactions, found in the cells but without external current flow.

Although nanopowders are obviously much simpler to use, the advantage of the large spatial *separation* between the oxidation and reduction sites that occurs in bulk electrodes used in PEC, remains a weak point of the nanopowders (Teo W.Y. et. al., 2012). However, at a molecular scale, the distance between oxidation and reduction sites on large-enough particles is still probably large compared to those found in solution-phase photochemical redox reactions (Teo W.Y. et al., 2012) where the redox products are in close proximity within the same solvent cage. Keeping this in mind, the know-how of PEC electrodes can serve as a useful guide to the design of the particle-based catalytic devices.

5. Choice of photocatalyst material

So far, nanocrystalline TiO_2 is the most commonly used photoactive material to build a photoanode. However, other oxides and other n-type semiconductors have been studied as well. Man I. et al. (2011) have explored trends in electrocatalytic activity of the oxygen evolution

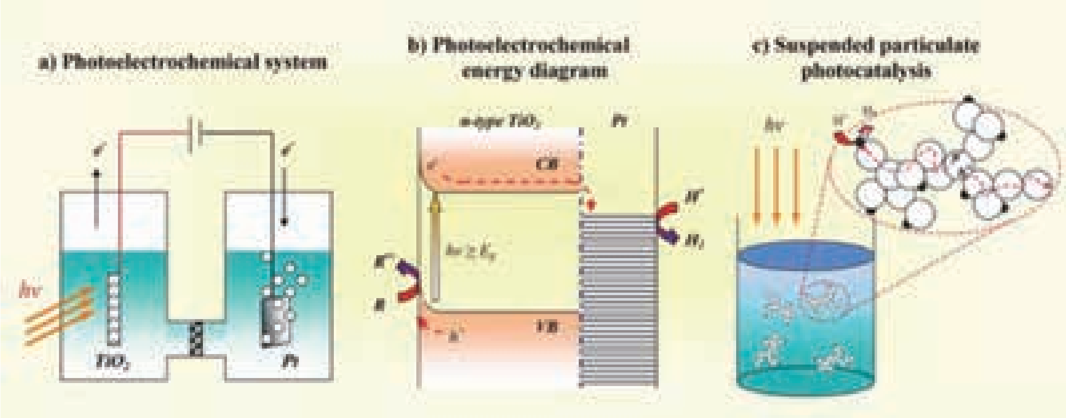

Fig. 9 Conceptualization of the equivalence of a suspended nanoparticle system as a miniaturized PEC. Reprinted with permission from Ref. (Teo W.Y. et al., 2012). Copyright: (2012) American Chemical Society.

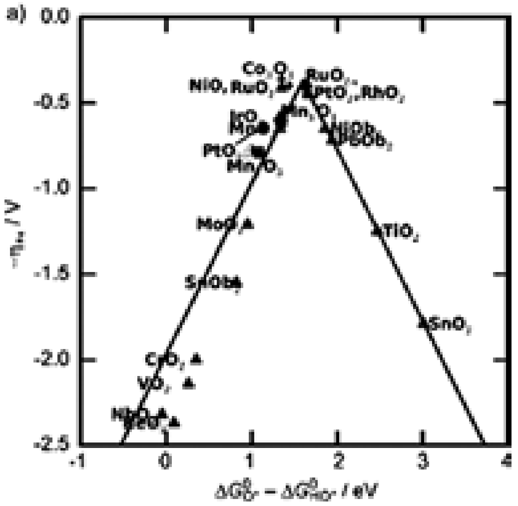

Fig. 10 Oxygen evolution efficiency plot for various metal oxides. Reprinted with permission from Ref. (Man I. et al., 2011). Copyright: (2011) Royal Society of Chemistry.

reaction (OER) investigated on the basis of a large database of $HO^\bullet$ and $HOO^\bullet$ adsorption energies on oxide surfaces. Based on theoretically calculated overpotentials (Man I. et al. 2011), they have derived a universal scaling relation between the adsorption energies of $HOO^\bullet$ *vs.* HO. Then, based on this, they have analyzed the reaction-free energy diagrams, ΔG, of many oxides and derived an "activity volcano", see **Fig. 10**. This plot can provide a universal descriptor for the oxygen evolution activity.

Fig. 10 suggests a fundamental limitation on the maximum oxygen evolution activity of oxide catalysts. For example, **Fig. 10** suggests that Mn-oxide and Co-oxide, i.e. much cheaper oxides than RuO_2 or IrO_2, should be promising co-catalysts for the O_2 production reactions in water-splitting heterostructures.

A similar "volcano activity" plot has been derived by Morales-Guio C.G. et al. (2014), see **Fig. 11**, for the electron-accepting particles. This shows that the—expensive—Pt^0, Pd^0, Rh^0 particles are the most efficient for H_2 production technologies. Cu^0, Ni^0, Co^0—as low-cost alternatives—are worth exploiting; however, avoiding their surface oxidation is a great limitation at present. Non-oxide chalcogenide n-type semiconductors such as ZnS, CdS, CdSe, etc. have been extensively studied for application in the photocatalytic (Kakuta N. et al., 1985) and photoelectrochemical (Hodes G. et al., 1976) production of H_2.

The reason is that, with the exception of ZnS, they absorb visible light. However, these substances are vulnerable to oxidation (for example, $CdS + 2H^+ \rightarrow Cd^{2+} + H_2S$), which dissolves the material and destroys it. In the presence of a sacrificial agent, it is possible to harvest h^+, thus restricting the particle degradation in solution. Also, chalcogenide materials can be synthesized in the form of core-shell nanostructures (Amirav L. and Alivisatos A.P., 2010) which have greater stability. ZnS—in spite of its highest Eg among all halcogenides—has been a popular research target since its CB and VB levels are favorably placed, as can be seen in **Fig. 5**. Thus, ZnS possesses strong oxidant and reductant power. It combines with CdS, so that, by changing their proportions, the overall light-absorbance can be tuned within a wide range. In the most advanced Z-scheme concept, the combination of two semiconductors assists electron–hole separation anyway (see Section 4.1.5).

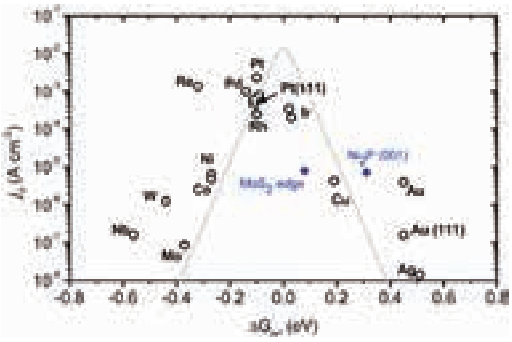

Fig. 11 H_2 evolution efficiency plot for various metal co-catalysts. Reprinted with permission from Ref. (Morales-Guio C. G. et al., 2014). Copyright: (2014) Royal Society of Chemistry.

5.1 Bi-Vanadate-Based Nanostructures

Monoclinic sheelite $BiVO_4$ is an n-type semiconductor with a direct band gap of 2.4 eV, thus it absorbs visible light, $\lambda = 420–530$ nm, and is stable in neutral electrolyte, non-toxic and relatively cheap (Kudo A. et al., 1999).

$BiVO_4$ has an optical penetration depth of $lp = 100–500$ nm at $\lambda = 420–530$ nm. Compared to other common O_2-evolving photocatalysts such as WO_3 or Fe_2O_3, $BiVO_4$ has a relatively high CB edge (+ 0.02 eV) (Kudo A. and Miseki Y., 2009; Park Y., et al., 2013) and, as a consequence, requires less bias potential to raise the potential of photoelectrons above the H^+/H^2 reduction potential (0.0 V). $BiVO_4$ is thermodynamically favorable for the half-reaction of H_2O oxidation, but requires an externally applied bias (Kudo A. and Miseki Y., 2009; Park Y. et al., 2013) for the water reduction half-reaction. The theoretical maximum STH efficiency is 9.1 % and the theoretical maximum photocurrent is 7.4 A/cm^2 (Park Y. et al., 2013). In the last decade, $BiVO_4$ has arisen among the main materials for visible-light photocatalysis, despite its shortcomings, i.e. low e-conductivity and poor H_2O-oxidation kinetics. These undesired properties may be improved by modifications, including the formation of heterostructures with another semiconductor, charge mediator, or use of a co-catalyst (Kudo A. et al., 1999; Kudo A. and Miseki Y., 2009). So far, the theoretical maximum STH efficiency

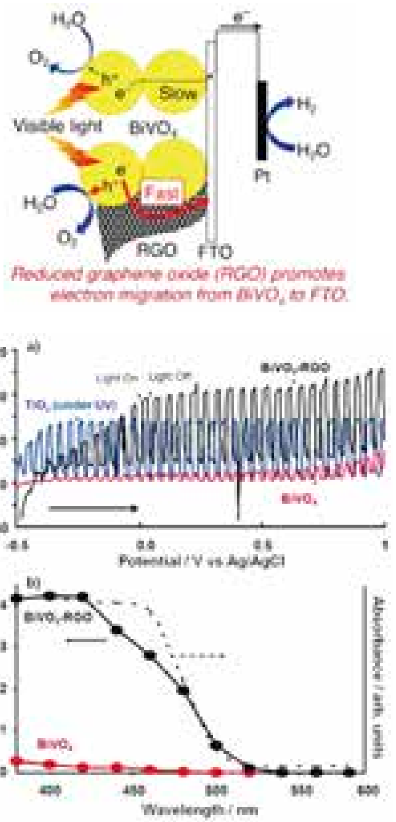

Fig. 12 Reduced graphene oxide on a visible-light $BiVO_4$ photocatalyst for enhanced photoelectrochemical water splitting. Reprinted with permission from Ref. (Ng Y.H., et al., 2010). (Copyright: (2010) American Chemical Society.

9.1 % cannot be achieved due to serious charge recombination and low water oxidation kinetics. $BiVO_4$ has an electron-diffusion length of only ~10 nm and a hole-diffusion length of ~100–200 nm (Hong S.J., et al., 2011; Li Z., et al., 2013). This causes excessive consumption of electrons by charge recombination. Doping $BiVO_4$ with Mo and W can significantly increase its electron- diffusion length to ~300 nm (Kudo A. et al., 1999). Poor kinetics for O_2 evolution at the $BiVO_4$ surface constrains its efficiency. This can be improved by co-catalyst loading on $BiVO_4$.

In an innovative approach, Amal's and Kudo's groups (Ng Y.H., et al., 2010) demonstrated that a reduced graphene oxide RGO/$BiVO_4$ nanocomposite, see **Fig. 12**, can achieve almost an 80-fold [i-V] enhancement in the photoelectrochemical water splitting reaction. In the same work (Ng Y.H. et al., 2010), $BiVO_4$ was used successfully as a visible-light-photocatalyst to photocatalytically reduce GO to reduced graphene oxide. Recently, Kim et al. (2014) demonstrated that a nanoporous $BiVO_4$ (SSA = 31.8 m^2/g) effectively suppresses bulk carrier recombination of $BiVO_4$ without additional doping, manifesting an electron-hole separation yield of 0.90 at 1.23 V. Use of two different oxygen evolution catalyst (OEC) layers, FeOOH and NiOOH, resulted in a $BiVO_4$/FeOOH/NiOOH photoanode that achieved a photocurrent density of 2.73 mA/cm^2 at a potential as low as 0.6 V. The use of FeOOH and NiOOH reduces interface recombination at the $BiVO_4$/OEC junction, while creating a more favorable Helmholtz layer potential drop at the OEC/electrolyte junction, Kim et al. (2014).

5.2 Z-Scheme Nano Photo Structures

A "Z-scheme" (Sasakia Y. et al., 2008) can be considered a special type of PEC-PEC tandem cell that imitates the architecture of the two natural photo systems of green plants, i.e. photosystem I and photosystem II. In the nano-Z-scheme approach, see **Fig. 13**, two semiconductors, I and II, are bridged with a redox particle or a liquid-redox couple mediator. Energetic considerations of the photodecomposition of water by semiconductor systems using sunlight suggest that a *single* light-absorbing system necessitates the use of a semiconductor with a rather large band gap of 2.5 to 3.0 eV (Chen X. et al., 2010; Kubacka A. et al., 2012; Sasakia Y. et al., 2008). This stems from the fact that the requisite energy and driving forces must suffice to overcome the redox barrier of 1.23 eV for water splitting, see **Fig. 13**.

Alternatively, efficient utilization of solar energy for water splitting may imitate the successful strategy of green plants, that is, the use of two photo systems with the absorption of *two photons* of lower energy per electron transferred. So far, several Z-schemes with two-heterostructured photocatalysts have been investigated in H_2 and O_2 production from water using solar energy (Chen X. et al., 2010; Kubacka A. et al., 2012; Sasakia Y. et al., 2008).

These works have established that overall water splitting can be achieved by constructing a Z-scheme photocatalytic system using photocatalysts, each one being active only for one of the half-reactions of water splitting (H_2 or O_2 evolution reactions) in the absence of sacrificial

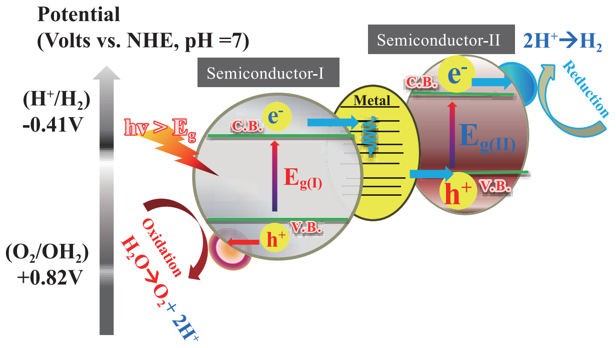

Fig. 13 An all-solid-state Z-scheme heterostructure.

reagents. In general, a redox mediator is required to couple with two photosystems. In a further leap forward, to eliminate undesirable backward reactions caused by redox mediators (such as Fe^{3+}/Fe^{2+}), a Z-scheme system without an electron mediator, i.e. an all-solid-state Z-scheme photocatalyst, has attracted much attention, see **Fig. 13**. This advanced Z-scheme retards back-reactions and increases the reaction efficiency. A number of all-solid-state Z-scheme photocatalysts (Chen X. et al., 2010; Kubacka A. et al., 2012) such as CdS-Au-TiO_2 (Tada H. et al., 2006) have been demonstrated to exhibit high photocatalytic activity, far exceeding that of the single-component systems. In all these multi-component Z-scheme photocatalyst systems without exception, the separation of e^-/h^+ pairs is promoted within the two semiconductors and further improved by the coupled metal particle that acts as the electron-transfer mediator, **Fig. 13**.

5.3 Visible-Light Energy Production

Visible light water splitting is a long-standing challenge in photochemistry (Chen X., 2010; Grätzel M., 2001; Youngblood W.J. et al., 2009). As shown in **Fig. 14**, the band structure of the particle determines the spectral range of light absorption and the theoretical maximum STH efficiency (Chen Z., 2010; Li J. and Wu N., 2015). For example, the theoretical maximum STH efficiency is only 0.22 % for $SrTiO_3$ ($E_g = 3.7$ eV) and 1.3 % for anatase TiO_2 ($E_g = 3.2$ eV) (Li J. and Wu N., 2015; Miller E.L. et al., 2010; Youngblood W.J. et al., 2009).

TiO_2 is a benchmark semiconductor, but it has a wide band gap (3.2 eV for anatase). Hence it can only absorb UV light, which accounts for less than 5 % of total solar radiation (Grätzel M., 2001; Miller E.L. et al., 2010). The most effective approach to increase the STH efficiency is to decrease the E_g in order to extend the light absorption spectral range into the visible-light region (~43 % of total solar radiation) and even the near-infrared light region (~80 % of total solar radiation). However, the band gap must be large enough to meet the thermodynamic and kinetic requirements for water splitting. Thermodynamics dictate the minimum energy required to overcome the standard Gibbs free energy change (1.23 eV) for water splitting. Thermodynamic losses (0.3–0.5 eV) should be added to this value. Thus an overpotential of 0.4–0.6 eV is required to enable a fast reaction (Asashi R. et al., 2001; Liu G. et al., 2012). Therefore, an ideal band gap is 1.9–2.3 eV.

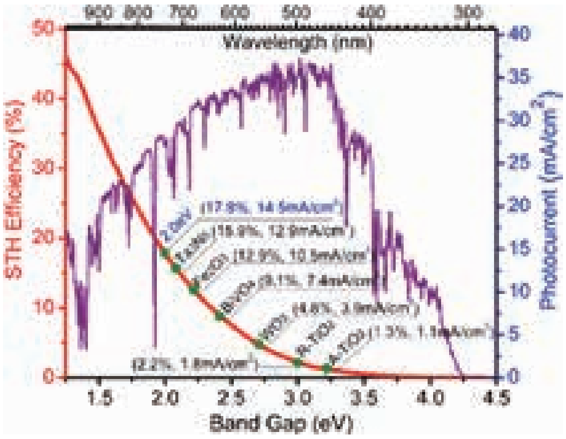

Fig. 14 Solar-to-hydrogen (STH) efficiency and maximum photocurrent trends vs. the band gap for photoactive semiconductors. Reprinted with permission from Ref. (Li J. and Wu N., 2015).Copyright: (2015) Royal Society of Chemistry.

Nitrogen-doping of TiO_2 (Asashi R. et al., 2001) has boosted research in visible-light photocatalysis. Other examples of innovative visible-light structures involve the following:

i) "Red anatase" TiO_2, which has been prepared by heating anatase TiO_2 microspheres with a pre-doped interstitial boron shell to between 580 and 620 °C in a gaseous NH_3 atmosphere.

This material has achieved a high photoelectrochemical water splitting activity (Liu G., et al., 2012). The UV-vis absorption spectrum of red anatase TiO_2 shows an extended absorption edge up to 700 nm, covering the full visible-light spectrum due to a band-gap gradient which varies from 1.94 eV on the surface to 3.22 eV in the core by gradually elevating the VB maximum, **Fig. 15**. The approach for producing this red-TiO_2 involved a predoping step, i.e. introduction of an interstitial boron gradient (Liu G. et al., 2012). This in turn improved the incorporation of substitutional N in the TiO_2 bulk without introducing Ti^{3+} impurity levels (Liu G. et al., 2012). Structurally, the interstitial boron dopant effectively weakened the surrounding Ti-O bonds to facilitate easier N-substitution and increased the chemical stability of B-N co-doped

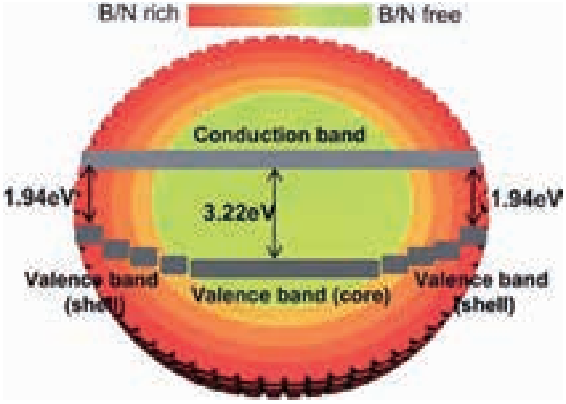

Fig. 15 Structural characteristics of red anatase, prepared by N-B-TiO_2 sequential doping of TiO_2. Reprinted with permission from Ref. (Liu G. et al., 2012). Copyright: (2012) Royal Society of Chemistry.

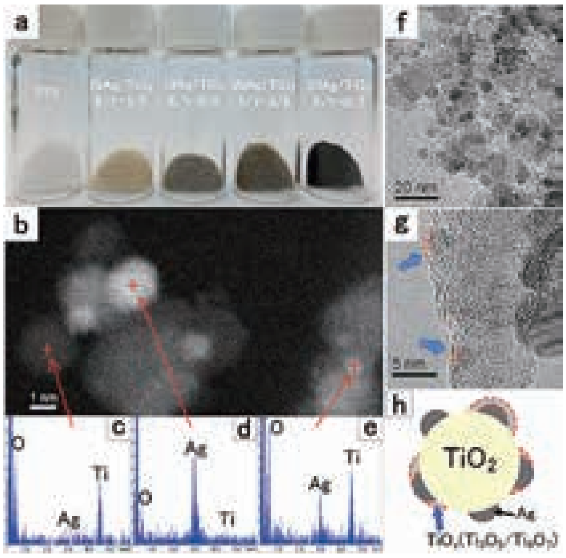

Fig. 16 Black TiO_2 suboxide produced via flame spray pyrolysis. Reprinted with permission from Ref. (Fujiwara K., et al., 2014). Copyright: (2014) Elsevier.

TiO_2. Moreover, the extra electrons from B-atoms compensated for the charge difference between the lattice oxygen and a substituted ion to maintain charge neutrality.

ii) "Black TiO_2" can be produced by two different technologies: treatment of TiO_2 particles under H_2 at high pressures and temperatures (Chen X. et al., 2011), which results in the formation of a Ti^{3+} shell by reduction of the Ti^{4+}. This Ti^{3+} shell has a distorted structure, which in turn creates additional interband states. This results in light absorbance in the visible wavelengths (Chen X. et al., 2011).

Recently, we have discovered that a black TiO_2 can be produced by a scalable flame spray pyrolysis process in one step (Fujiwara K. et al., 2014), **Fig. 16**. Reductant combustion intermediates present during flame synthesis of these materials partially induce strong TiO_2 metal support interactions (SMSI), resulting in crystalline Ti-suboxides (Ti_3O_5, Ti_4O_7). The growth of such suboxides can be controlled via control of the flame spray pyrolysis conditions, allowing the light absorption intensity in the visible spectrum to be tuned.

6. The notion of "renewable H_2" production

Currently, industrial electrolysis uses clean water in order to prevent the fouling of system components. However, the need for clean water prevents the exploitation of large-body sources such as seawater, industrial waste and municipal waste as water feed. This poses the challenge that the use of cheaper, alternative sources of water instead of purified distilled water should be envisioned as the next target for truly unlimited production of "renewable H_2". At the consumer scale, H_2 can be either produced centrally or on-site. The market for on-site generation systems is growing due to certain advantages associated with not needing transportation and delivery. Currently, most of industrial-use H_2 is produced by the steam reforming of natural gas or CH_4 (Conway, B.E, and Tilak, B.V. 2002; Holdren J.P., 2007) due to the availability and low prices of natural gas at present. Next, after the steam reforming of natural gas, the partial oxidation of petroleum oil is second in H_2 production capacity.

So far, with regard to biofuels, most researchers choose to study methanol, ethanol or glycerol as model fuels (Chen X. et al., 2010; Lianos P., 2011). There are three main reasons for this: (1) methanol, ethanol or glycerol give the highest yield; (2) they have been extensively studied, so a lot of data and know-how on their use exists; and (3) they can be cost-efficient products of biomass. Thus in a mature biomass-based market, methanol, ethanol or glycerol should be available and renewable. As an example, glycerol, a waste byproduct material of biodiesel production (Lianos P., 2011), is available in mass-produced quantities. In addition to small alcohols, other organics such as sugars and organic acids have also been a popular choice for photocatalytic H_2 production (Chen X. et al., 2010; Lianos P., 2011).

Thus truly "renewable H_2" production can be achieved if the photocatalytic technology can exploit seawater or wastewater feed or via the use of small organics produced via a sustainable process.

7. Next-decade targets

Currently, the long-term objective aimed at by the US Department of Energy is the photocatalytic H_2 production based on a durable, semiconductor-based, solar-driven water-splitting device with the following specifications:

(1) solar-to-hydrogen (STH) efficiency > 20 %,
(2) that can operate under at least 10–15 times solar concentration, and generate renewable hydrogen for < \$2/kg .(ENERGY.GOV, 2015)

In the same context, the US-DoE near-future objectives specify the nanomaterials' physicochemical standards as follows: development of surface modifications that will make the materials viable at high current densities. This is related to the need for highly efficient, durable materials for PEC water splitting using concentrated solar energy. This is important since in order to minimise H_2-production costs, operation under high photon and electron flows is identified as the most significant driver. Mechanical surface durability can be improved through the crystal structure and surface engineering. To this end, surface defects should be engineered in a balanced way, since surface defects might be desirable for enhanced reactivity; however, at the same time, too many surface defects might decrease the durability of a nanocrystal.

In parallel, the optimization of existing materials or the discovery of novel materials should incorporate the predictive power of theory and modeling. The target of 20 % STH efficiency targeted by the US-DoE is a feasible goal. As a reference, a 10-fold solar light concentration with a 20 % STH gives approximately 160 mA/cm^2 (Conway, B.E and Tilak, B.V., 2002; Lewis N.S. and Nocera D.G., 2006). However, although the current H_2 oxidation reaction rates in fuel cells achieve this range, i.e. 100–1000 mA/cm^2, a severe rate-limiting step is imposed by the very slow O_2 reduction reaction that typically imposes low rates, i.e. as low as 10^{-6}–10^{-11} A/cm^2 (Conway, B.E and Tilak, B.V., 2002; Lewis N.S. and Nocera D.G., 2006). Thus intensive research on novel or improved O_2-reduction materials is in high demand.

The US-DoE targeted (by 2018) an increase in *chemical conversion process efficiency* for PEC from 4 % to 12 % (ENERGY.GOV, 2015; Miller E.L., et al., 2010). This will require significant breakthroughs in the development of new materials. The challenge can be seen through **Fig. 14**, which allows an estimate of the fundamental solar absorption limitations in H_2 production in PEC for a number of the tested metal-oxide semiconductors (Li J. and Wu N., 2015; Miller E.L. et al., 2010). In **Fig. 14**, the potentially achievable photocurrent levels and STH conversion efficiencies of a given semiconductor/electrolyte interface are related to the semiconductor band gap. This is based on an idealized case where 100 % of the photons in the solar spectrum with energies exceeding the band gap are absorbed and converted. It must be strongly emphasized that the STH efficiencies, as shown in **Fig. 14**, are only defined in stand-alone material systems with sufficient photo-induced potential to thermodynamically split water. To date, only very high-band-gap materials have exhibited stand-alone water-splitting in single junction configurations, as seen in **Fig. 14**. It is seen that the resulting STH efficiencies of these materials is *less than 1 %* (Li J. and Wu N., 2015; Miller E.L., et al., 2010; Rocheleau R. and Miller E., 1997). Interestingly, today's PEC performance status of a STH = 4 % has been achieved in *multi-junction configurations* (Grätzel M., 2001), not in a single-particle system. Thus, it is important to emphasize that Z-scheme, multi-junction configurations are the way forward to create stand-alone water-splitting systems. This will allow the use of some of the low-E_g materials under a proper "branching" of the CB/VB levels, see the concept in **Fig. 13**. If this is the case with Z-scheme configurations, the photo-generated currents and therefore their STH efficiencies will not be constrained by the E_g value or e^-/h^+ transfer rates, but rather by the *semiconductor/electrolyte interface* limitations. Even in such Z-scheme configurations, achieving STH performance ~15 % will require development of efficient and stable semiconductors with the E_g near 2.0 eV. Ultimately, after the lab work, marketing of the most competitive materials or devices will require low-cost nanomaterials production and device synthesis. On this front, scalable one-step particle production technologies such as flame spray pyrolysis (Teoh W.Y. et al 2012; Ng, Y. et al., 2010; Fujiwara K. et al., 2014), would contribute decisively.

8. Conclusions

Photoactive nanomaterials hold great potential for environmental technologies. These include the production of electricity, energy-fuel production and photocatalytic water remediation. Current targets posed by the US Department of Energy are discussed based on a 2015 report. In contrast to the case of p-n junction photovoltaics where the manufacturing cost of the required high-purity single crystals emerges as the main objective (mostly commercial, rather than fundamental research), a key target for the field of photoelectrochemical nanotechnology is the discovery and development of *new materials* to advance the field. These include:

- raising the solar to hydrogen yields > 15 %,
- manufacturing of all-solid-state Z-scheme photoactive materials,
- optmized materials for visible-light absorbance with enhanced quantum yields.

Nomenclature

Symbols and units should be listed in alphabetical order with their definition and dimensions in SI units.

PEC	Photoelectrochemical cell
DoE	Department of Energy
NHE	Normal hydrogen electrode
RGO	Reduced graphene oxide
AM	Atmospheric mass

References

Amirav L., Alivisatos A.P., Photocatalytic hydrogen production with tunable nanorod heterostructures, Journal of Physical Chemistry Letter, 1 (2010) 1051–1054.

Asashi R., Morikawa T., Ohwaki T., Aoki K., Taga Y., Visible-light photocatalysis in nitrogen-doped titanium oxides, Science, 293 (2001) 269–271.

Bard A.J., Photoelectrochemistry, Science, 207 (1980) 139–144.

Bolton J.R., The production of energy-rich compounds by the photochemical conversion and storage of solar energy, Solar Fuels Science, 202 (1978) 705–711.

Bolton J.R., Strickler S.J., Connolly J.S., Limiting and realizable efficiencies of solar photolysis of water, Nature, 316 (1985) 495–500.

Chen X., Shen S., Guo L., Mao S.S., Semiconductor-based photocatalytic hydrogen generation, Chemical Review, 110 (2010) 6503–6570.

Chen X., Liu L., Yu P.Y., Mao S.S., Increasing solar absorption for photocatalysis with black hydrogenated titanium dioxide nanocrystals, Science, 331 (2011) 746–750.

Chen Z., Jaramillo T.F., Deutsch T.G., Kleiman-Shwarsctein A., Forman A.J., Gaillard N., Garland R., Takanabe K., Heske C., Sunkara M., McFarland E.W., Domen K., Miller E.L., Turner J.A., Dinh H.N., Accelerating materials development for photoelectrochemical hydrogen production: Standards for methods, definitions, and reporting protocols, Journal of Materials Research, 25 (2010) 3–16.

Conway B.E, Tilak B.V., Interfacial processes involving electrocatalytic evolution and oxidation of H^+ and the role of chemisorbed H^+, Electrochemical Acta, 47 (2002) 3571–3594.

Cooper J.K., Gul S., Toma F.M., Chen L., Liu Y., Guo J., Ager J.W., Yano J., Ian D., Sharp On the Indirect Bandgap and Optical Properties of Monoclinic Bismuth Vanadate Journal of Physical Chemistry C, 119 (2015) 2969–2974.

Coronado J.M., Sanchez B., Portela R., Suarez S., Journal of Solar Energy & Engineering, Solar photocatalysis for the elimination of trichloroethylene in the gas phase, 130 (2008) 011–016.

Devi L.G., Kavitha R., Review on modified N-TiO_2 for green energy applications under UV/visible light: selected results and reaction mechanisms, RSC Advances, 4 (2014) 28265–28299.

Dong S., Feng J., Fan M., Pi Y., Hu L., Han X., Liu M., Sun J., Recent developments in heterogeneous photocatalytic water treatment using visible light-responsive photocatalysts: A review, RSC Advances, 5 (2015) 14610–14630.

Elliott R.J., Intensity of optical absorption by excitons, Physical Review, 108 (1957) 1384–1389.

ENERGY.GOV (U.S. Department of Energy), US-DoE Efficiency and Renewable Energy, Hydrogen, Fuel Cells and Infrastructure Technologies Program—Multi-Year Research, Development and Demonstration Plan; 2015. <https://energy.gov/sites/prod/files/2015/06/f23/fcto_myrdd_production.pdf> accessed 21.12.2016.

Fagan R., McCormack D.E., Dionysiou D.D., Pillai S.C., A review of solar and visible light active TiO_2 photocatalysis for treating bacteria, cyanotoxins and contaminants of emerging concern, Materials Science in Semiconductor Processing, 42 (2016) 2–14.

Formal F.L., Gratzel M., Sivula K., Controlling photoactivity in ultrathin hematite films for solar water-splitting, Advanced Functions Materials, 20 (2010) 1099–1107.

Froschl T., Behm R. J., Hormann U., Husing N., Kubiak P., Kaiser U., Kucerova G., Landfester K., Pfanzelt M., Weiss C.K., Wohlfahrt-Mehrens M., High surface area crystalline titanium dioxide: potential and limits in electrochemical energy storage and catalysis, Chemical Society Review, 41 (2012) 5313–5360.

Fujishima A., Honda K., Electrochemical Photolysis of Water at a Semiconductor Electrode., Nature, 38 (1972) 37–38.

Fujiwara K., Deligiannakis Y., Skoutelis C.G., Pratsinis S.E., Visible-light active black TiO_2-Ag/TiO_x particles, Applied Catalysis B-Environmental, 9 (2014) 154–155.

Getoff N., Photoelectrochemical and photocatalytic methods of hydrogen production: a short review, International Journal of Hydrogen Energy, 15 (1990) 407–417.

Giannakas A., Antonopoulou M., Konstantinou I., Deligiannakis Y., EPR and Photocatalytic Study of Pt-Loaded N-TiO_2, NF-TiO_2, ACS Catalysis, (2016) Submitted.

Goldsmith J.I., Hudson W.R., Lowry M.S., Anderson T.H., Bernhard S., Discovery and high-throughput screening of heteroleptic iridium complexes for photoinduced hydrogen production, Journal of American Chemical Society, 127 (2005) 7502–7510.

Grätzel M., Photoelectrochemical cells, Nature, 414 (2001) 338–344.

Grätzel M., Solar Energy Conversion by Dye-Sensitized Photovoltaic Cells Inorganic Chemistry, 44 (2005) 6841–6851.

Harriman A., Pickering I.J., Thomas J.M., Christensen P.A., Metal oxides as heterogeneous catalysts for oxygen evolution under photochemical conditions, Journal of Chemistry Society, Faraday Transactions I, 84 (1988) 2795–2806.

Hernandez-Alonso M.D., Fresno F., Sureza S., Coronado J.M., Development of alternative photocatalysts to TiO_2:Challenges and opportunities, Energy Environmental Science, 2 (2009) 1231–1257.

Hodes G., Manassen J., Cahen D., Photoelectrochemical energy conversion and storage using polycrystalline chalcogenide electrodes, Nature, 261 (1976) 403–404.

Holdren J.P., Energy and sustainability, Science, 315 (2007) 737.

Hong S.J., Lee S., Jang J.S., Lee J.S., Heterojunction $BiVO_4$/WO_3 electrodes for enhanced photoactivity of water oxidation Energy Environmental Science, 4 (2011) 1781–1787.

JPCCSVI (Journal of Physical Chemistry C Special Virtual Issue), Solar Fuels. Photocatalytic Hydrogen Generation, <http://pubs.acs.org/page/jpccck/vi/solarfuels.html> accessed 21.12.2016.

Kakuta N., Park K.H., Finlayson M.F., Ueno A., Bard A.J., Campion A., Fox M.A., Webber S.E., White J.M., Photoassisted hydrogen production using visible light and coprecipitated ZnS-CdS without a noble metal, Journal of Physical Chemistry, 89 (1985) 732–734.

Kamat P.V., Environmentally Benign Photocatalysts in: Anpo M. (Eds), Springer, 2010.

Khaselev O., Turner J.A., A monolithic photovoltaic-photoelectrochemical device for hydrogen production via water splitting, Science, 280 (1998) 425–427.

Kim, T.W., Choi K-S., Photoanodes with Dual-Layer Oxygen Evolution Nanoporous $BiVO_4$ Catalysts for Solar Water Splitting, Science, 343 (2014) 190–194.

Kubacka A., Fernández-García M., Colón G., Advanced nanoarchitectures for solar photocatalytic applications, Chemical Reviews, 112 (2012) 1555–1614.

Kudo A., Omori K., Kato H., A novel aqueous process for preparation of crystal form-controlled and highly crystalline $BiVO_4$ powder from layered vanadates at room temperature and its photocatalytic and photophysical properties, Journal of American Chemistry Society, 121, (1999) 11459–11467.

Kudo A., Miseki Y., Heterogeneous photocatalyst materials for water splitting, Chemical Society Review, 38 (2009) 253–278.

Lewis N.S., Nocera D.G., Powering the planet: Chemical challenges in solar energy utilization, Proceedings of the National Academy of Science of the United States America, 103 (2006) 15729–15735.

Li J., Wu N., Semiconductor-based photocatalysts and photoelectrochemical cells for solar fuel generation: a review, Catalysis Science Technology, 5 (2015) 1360–1384.

Li Z., Luo W., Zhang M., Feng J., Zou Z., Photoelectrochemical cells for solar hydrogen production: current state of promising photoelectrodes, methods to improve their properties, and outlook, Energy Environmental Science, 6 (2013) 347–370.

Lianos P., Production of electricity and hydrogen by photocatalytic degradation of organic wastes in a photoelectrochemical cell: The concept of the Photo fuel cell: A review of a re-emerging research field, Journal of Hazardous Materials, 185 (2011) 575–590.

Licht S., Wang B., Mukerji S., Soga T., Umeno M., Tributsch H., Over 18 % solar energy conversion to generation of hydrogen fuel: theory and experiment for efficient solar water splitting, International Journal of Hydrogen Energy, 26 (2001) 653–659.

Lindgren T., Lu J., Hoel A., Granqvist C.G., Torres G.R., Lindquist S.E., Photoelectrochemical study of sputtered nitrogen-doped titanium dioxide thin films in aqueous electrolyte, Solar Energy Materials & Solar Cells, 84 (2004) 145–157.

Linsebigler A.L., Lu G.Q., Yates J.T., Photocatalysis on TiO_2 Surfaces-Principles, Mechanisms, and Selected Results, Chemical Reviews, 95 (1995) 735–758.

Liu G., Yin L., Wang J., Niu P., Zhen C., Xie Y. Cheng H., A red anatase TiO_2 photocatalyst for solar energy conversion, Energy & Environmental Science, 5 (2012) 9603–9610.

Liu J.J., Chen S., Zhu Y., Electronic structures and effective masses of photogenerated carriers of $CaZrTi_2O_7$ photocatalyst: First-principles calculations, Solid State Communication, 152 (2012) 1650–1654.

Liu J.J., Chen S.F., Liu Q.Z., Zhu Y.F., Zhang J.F., Correlation of crystal structures and electronic structures with visible light photocatalytic properties of $NaBiO_3$, Chemical Physics Letters, 572 (2013) 101–105.

Maeda K., Teramura K., Lu D., Takata T., Saito N., Inoue Y., Domen K., Photocatalysts releasing hydrogen from water, Nature, 440 (2006) 295.

Maeda K., Domen K., New Non-Oxide Photocatalysts Designed for Overall Water Splitting under Visible Light, Journal of Physical Chemistry C, 111 (2007) 7851–7861.

Maeda K., Domen K., Effect of post calcination on photocatalytic activity of $(Ga_{1-x}Zn_x)(N_{1-x}O)$ solid solution for overall water splitting under visible light, Journal of Catalysis, 254 (2008) 198–204.

Man I., Su H.-Y., Vallejo F., Hansen H., Martinez J., Inoglu N., Kitchin J., Jaramillo T., Norskov J., Rossmeis, Universality in Oxygen Evolution Electrocatalysis on Oxide Surfaces, ChemCatChem Catalysis, 3 (2011) 1159–1165.

Miller E.L., Gaillard N., Kaneshiro J., DeAngelis A., Garland R., Progress in new semiconductor materials classes for solar photoelectrolysis, International Journal of Energy Research, 34 (2010) 1215–1222.

Miyauchi M., Nakajima A., Watanabe T., Hashimoto K., Photocatalysis and photoinduced hydrophilicity of various metal oxide thin films, Chemical Materials, 14 (2002) 2812–2816.

Morales-Guio C.G., Stern L-A, Hu X., Nanostructured hydrotreating catalysts for electrochemical hydrogen evolution, Chemical Society Review, 43 (2014) 6555–6569.

Ng Y.H., Iwase A., Kudo A., Amal R., Reducing Graphene Oxide on a Visible-Light $BiVO_4$ Photocatalyst for an Enhanced Photoelectrochemical Water Splitting, Journal of Physical Chemistry Letter, 1 (2010) 2607–2612.

Ohtani B., Preparing Articles on Photocatalysis-Beyond the Illusions, Misconceptions, and Speculation, Chemistry Letters, 37 (2008) 216–229.

Paracchino A., Laporte V., Sivula K., Grätzel M., Thimsen E., Highly active oxide photocathode for photoelectrochemical water reduction, Nature Materials, 10 (2011) 456–461.

Park Y., McDonald K.L., Choi K., Progress in bismuth vanadate photoanodes for use in solar water oxidation, Chemical Society Review, 42 (2013), 2321–2337.

Rocheleau R., Miller E., Photoelectrochemical production of hydrogen: engineering loss analysis, International Journal Hydrogen Energy, 22 (1997) 771–782.

Ryu J., Choi W., Substrate Specific Photocatalytic Activities of TiO_2 and Multiactivity Test for Water Treatment Application, Environmental Science Technology, 42 (2008) 294–300.

Sasakia Y., Iwasea A., Katoa H., Kudo A., The effect of co-catalysts for Z-scheme photocatalysis systems with an Fe electron mediator on overall water splitting under visible light irradiation, Journal of Catalysis, 259 (2008) 133–137.

Shockley W., Queisser H.J., Detailed Balance Limit of Efficiency of p-n Junction Solar Cells, Journal of Applied Physics, 32 (1961) 510.

Svrcek V., Slaoui A., Muller J.-C., Silicon nanocrystals as light converter for solar cells, Thin Solid Films, 451 (2004) 384–388.

Tada H., Mitsui T., Kiyonaga T., Akita T., Tanaka K., All-solid-state Z-scheme in CdS–Au–TiO_2 three-component nanojunction system, Nature Materials 5, (2006) 782–786.

Tang J.W., Cowan A.J., Durrant J.R., Klug D.R., Mechanism of O_2 Production from Water Splitting: Nature of Charge Carriers in Nitrogen Doped Nanocrystalline TiO_2 Films and Factors Limiting O_2 Production, Journal of Physical Chemistry C, 115 (2011) 3143–3150.

Tauc J., Menth A., Wood D.L., Optical and magnetic investigations of localized states in semiconducting glasses, Physical Review Letter, 25 (1970) 749–752.

Teo W.Y., Scott J.A., Amal R., Progress in Heterogeneous Photocatalysis: From Classical Radical Chemistry to Engineering Nanomaterials and Solar Reactors, The Journal of Physical Chemistry Letters, 3 (2012) 629–639.

Walsh A., Yan Y., Huda M.N., Al-Jassim M.M, Wei S., Band Edge Electronic Structure of $BiVO_4$: Elucidating the Role of the Bi s and V d Orbitals, Chemical Material, 21 (2009) 547–551.

Wang C., Rabani J., Bahnemann D.W., Dohrmann J.K., Photonic efficiency and quantum yield of formaldehyde formation from methanol in the presence of various TiO_2 photocatalysts, Journal of Photochemistry and Photobiology A, 148 (2002) 169–176.

Wang L. Wei H., Fan Y., Liu X., Zhan J., Synthesis, optical properties and photocatalytic activity of one–dimensional CdS@ZnS core-shell nanocomposites, Nanoscale Research Letters, 4 (2009) 558–564.

Würfel P. The Physics of Solar Cells. Weinheim: Wiley-VCH (2005).

Youngblood W.J., Lee S.A., Maeda K. Mallouk T.E., Accounts of Chemical Research Visible Light Water Splitting Using Dye Sensitized Oxide Semiconductors, 42 (2009) 1966–1973.

Zhang J., Zhou P., Liu J., Yu J., New understanding of the difference of photocatalytic activity among anatase, rutile and brookite TiO_2, Physical Chemistry Chemical Physics, 16 (2014) 20382–20386.

Zou Z., Ye J., Sayama K., Arakawa H., Direct splitting of water under visible light irradiation with an oxide semiconductor photocatalyst, Nature, 414 (2001) 625–626.

Author's short biography

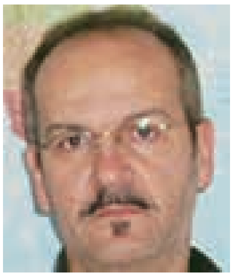

Yiannis Deligiannakis

Yiannis Deligiannakis is currently a full professor and head of the Lab of Physical Chemistry of Materials & Environment, Dept. of Physics at the University of Ioannina, Greece. He earned his PhD at the National Centre for Scientific Research "Demokritos", Athens, Greece (1991). Between 1991 and 2000, he worked as research associate at the Section de Bioenergetique, CEA, Saclay, Paris, France. In 2012-2013, he was a visiting professor at the Particle Technology Laboratory, ETH Zurich, lab of Prof. S. Pratsinis. He has published over 140 ISI papers in materials science, catalysis, EPR spectroscopy, flame spray pyrolysis. He holds 7 patents on nanomaterials and applications in environment-related technologies.

KONA Powder and Particle Journal No. 35 (2018) 32–48/Doi:10.14356/kona.2018006 Review Paper

Critical Review on Engineering Mechanical Quality of Green Compacts using Powder Properties [†]

Hojae Yi [1]*, Anuranjan Pandeya [2], Apoorva Karamchandani [1] and Virendra M. Puri [1]

[1] *Department of Agricultural and Biological Engineering, Pennsylvania State University, USA*
[2] *Scientific and Digital Systems Delhi, India*

Abstract

For processes involving particulate materials, mechanical properties of green compacts are of great interest when they are final or intermediate products. Optimal quality of green compacts is achieved usually with empirical approaches, *i.e.*, unexpected issues in processes or products' quality are usually mitigated by time and resource consuming trial-and-error methods. Issues of the powder compaction are commonly observed when there are problems in feed materials or operational conditions even without any substantial change in a formula. Such divergent behavior of particulate materials is especially problematic for product developments and reliable operations. It has been widely accepted hypothesis that properties of particles are determinants of mechanical behavior of powder during compaction and the quality of resulting compacts. With recent developments in nanotechnology, characterization and engineering of individual particles at a microscopic or sub-microscopic scale are now feasible. Leveraging recent technological advancements, there has been a good progress in regard to quantitative understanding of mechanical relationships between properties of particles, particle system and final product. This review highlights the recent developments and gaps in engineering mechanical quality of powder compacts in conjunction with the characterization of particle systems and compaction at multiple scales.

Keywords: powder compaction, green compacts, compact quality, powder properties, particle properties

1. Introduction

Compaction is often employed as a terminal process for manufacturing consumer goods and it affects the quality of final products in the most direct way. Mechanical properties of compacts are especially important in post-production processes such as packaging, transportation, and end-use by consumers. For example, medicinal tablets should not only maintain its integrity throughout packaging and subsequent handling but also provide appropriate disintegration characteristics when administered into human body. Likewise, biomass pellets should preserve their shape and size to ensure desired handling characteristics throughout transportation with minimal crumbliness. On the other hand, cosmetic compacts need to have desired friability for consumer use as well as enough strength so that they do not develop aesthetic defects during shipping and handling. Therefore, achieving and maintaining desired quality of compact is of great importance as a final consumer product. Compaction is also utilized as a critical intermediate process, whose product's properties are crucial in reliable and efficient downstream processes such as sintering of ceramic or compacted metal powders.

Ideally, compaction behavior and quality should be reasonably predicted during product development process, *e.g.*, formulation, and novel particulate materials development. In reality, producing compact with minimal operational anomalies and desirable quality metrics is very much an art. Manufacturers regularly search for an efficient and sustainable window of operational parameters that will reliably produce compacts' characteristics satisfying often conflicting quality metrics. Balances between operational maneuver, different mechanical quality metrics, and performance characteristics of compacts are usually achieved by tedious trial-and-error approaches due to the lack of adequate scientific understanding of or a systematic approach to the powder compaction. One of major reasons why compaction operation remains empirical, is because the fundamental understanding of powder compaction is still elusive and, as a result, experiential knowledge plays an essential role. However, the extent, to

---

[†] Received 26 December 2016; Accepted 20 January 2017

[1] 249 Agricultural Engineering Building, University Park, PA 16802, USA

[2] IDA House, R K R K Puram, Sector 4, RK Puram, New Delhi, Delhi 110022, India

* Corresponding author: Hojae Yi
E-mail: huy1@psu.edu
TEL: +1-814-865-2807 FAX: +1-814-863-1031

which such empiricism can be applied, is limited because of particulate materials' innate heterogeneity and variability. Novel materials or upstream processes require extended time in identifying optimal process parameters from scratch (Bell, 2005; Merrow, 1988). To address this issue and enable a systematic approach in compaction process and quality control, it is essential to expand our knowledge of the fundamental mechanics of powder compaction and to develop quantitative relationships between feed particulate materials' properties, densification process parameters, and the mechanical quality metrics of final products.

In addition to insufficient fundamental knowledge of powder compaction, subjective quality metrics of compacts impose challenges to the consideration of the end product quality. Many of quality metrics that are employed by industry have been developed and employed reflecting specific usages of particular products. For example, to evaluate adequate strengths of compacts for logistics or end use, one may use a 'pass or fail' test, in which a product is dropped from a certain height to determine breakages. Such tests provide only binary information that may provide limited usage as a quantifiable quality metrics. Similar tests can be re-designed to measure mass and height, at which the product begins to break. Obviously such a quality measurement requires more effort and resources, but it will eventually pay-off when one has the means to predict the quality of products based on quantitative relationships taking properties of feed materials and operational parameters into the consideration. Ideally, these types of tests can be replaced with a set of standardized tests that reflect various scenarios of logistical events, *e.g.*, durability, friability, hardness, and solubility that may be relevant to a specific powder compact product depending on the end use of the compacts.

Another challenge to the powder compaction process is the quantitative powder properties characterization. In regard to properties of particulate feed materials, there are two categories of properties that are relevant and meaningful in our context, namely physical and mechanical properties. Physical properties include bulk density, tap density, particle density, particle size distribution, particle shape, and so on. Even though these are fundamental properties of particulate materials, direct relationships between these and the final product's properties are difficult to establish because of the stochastic properties of particulate materials, insufficient knowledge on the mechanics of the powder compaction process, and limited understanding of how physical and mechanical properties of the powders affect the powder compaction process and properties of compacts. Nonetheless, because of the dominant importance of mechanical properties of powder *en masse* in the evolution of mechanical properties of compacts, there have been good amount of studies concerning mechanical aspects of powder compaction especially at the microscopic scale. Reflecting these, this review attempts to assess the current knowledge and to identify subjects, studying which will aid the fundamental understanding of the powder compaction process and will enable a systematic engineering approach in efficient and reliable powder compact production. To that end, this review focuses on the quality metrics' *status quo* with emphasis on how fundamental approach can help with predicting and controlling the quality of compacts.

2. Compaction as a powder processing operation

Unit operations involving particulate materials as raw materials, have been well known to be prone to issues that are difficult to mitigate through quantitative engineering approaches (Ennis et al., 1994; Merrow, 1984, 1988). Furthermore, powder compaction is one of less addressed powder processes in spite of its critical role in industrial manufacturing. Powder compaction is utilized as a final production process in various industries including pharmaceutical and nutraceutical tablets, cosmetic consumer goods, biomass pellets, as well as an intermediate process in ceramics and powder metallurgy. Compaction of powders is performed by mechanically pressing powder *en masse* in dies to form a densified powder mass with enough mechanical integrity that can withstand external loads during expected lifecycle. Green compacts are made typically at ambient temperature through following stages (**Fig. 1**): 1) Rearrangement of the particles by filling large pores accompanied with the increase in number of contacts (coordination number); 2) packing of particles resulting in decrease in porosity with the formation of localized agglomeration of particles, namely secondary and higher order particle structures; 3) increase in the contact area between particles accompanying elastic deformation of particles; and 4) contact enlargement through plastic deformation of particles (Azami and Khoei, 2006; Bortzmeyer, 1992; Castellanos et al., 2005; Cunningham et al., 2004; Fayed and Otten, 1984; German, 2014; Yi et al., 2001).

Even though these stages of powder compaction have been established for decades, quantitative and fundamental understanding of how these stages contribute to the formation of green compacts is yet to be fully elucidated. This is mainly due to the multiscale nature of the compaction process, which evolves towards different scales of scrutiny, *i.e.*, microscale (single particle, particle-particle interactions), mesoscale (secondary and tertiary particle structures), and macroscale (bulk powder system). Furthermore, due to powder system's intrinsic stochasticity in particle shapes and sizes in addition to the multiscale

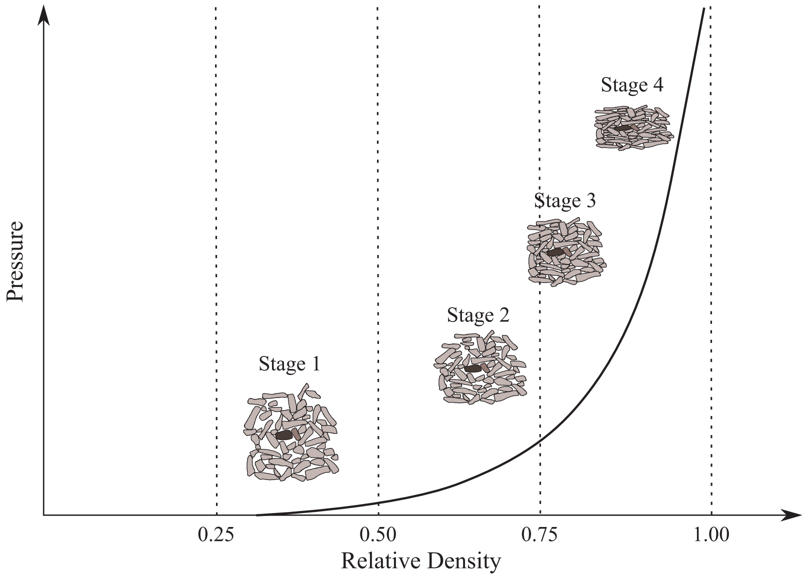

Fig. 1 Four stages of powder compaction. In the initial stage (Stage 1) of compaction, rearrangement of the particles by filling large pores accompanied with the increase in number of contacts (coordination number). When the rearrangement of particles completes, volume of powder mass further decreases due to the packing of particles with the formation of localized agglomeration of particles (Stage 2). Powder compaction advances with the increase in the contact area between particles accompanying elastic deformation of particles (Stage 3), then particle-particle contacts enlarge through plastic deformations of particles (Stage 4). As pressure increases further, the bulk density of powder mass gets close to the true density of particles, which leads to the relative density of 1.0. Actual mechanisms of compaction overlaps in real-world compaction and the relative density, at which each stage initiates, varies depending on various particle properties.

and multiphase nature, powder system is considered to be an inherently complex system (de Gennes, 1999). As a result, many investigations of powder compaction are more or less of troubleshooting nature. For example, issues of powder compaction have been identified by Blumenthal et al. (1997) in regards to powder metallurgy, by Alderborn and Nystrom (1996) for pharmaceutical powder, and by Ennis et al. (1994) for general granular materials.

On the other hand, there are established quantitative models describing powder compaction. Some phenomenological models include Heckel (Ilkka and Paronen, 1993), Kawakita (Kawakita and Lüdde, 1971), and Cooper-Eaton model (Cooper and Eaton, 1962). More physically and mathematically rigorous models describe powder compaction as a macroscopic phenomenon. Such a constitutive model includes Cam-clay models (Dimaggio and Sandler, 1971; Schofield and Wroth, 1968). Unfortunately, existing powder compaction models do not provide fundamental understanding on how underlying particle's properties and particle interactions evolves up to macroscopic behavior of powder system during compaction. Therefore, there exists inevitable limitation when one employs existing powder compaction models in predicting and controlling powder compaction process and compact properties.

3. Green compact quality

This review focuses on mechanical aspects of compact properties among many quality metrics of powder compacts. This section briefly summarizes which mechanical properties of powder compacts are reviewed. A quantified and systematic approach in determining the quality of green compacts is an important step in engineering powder compaction. Accordingly, studies on powder compacts quality metrics are reviewed. Quality metrics of powder compacts include fundamental metrics such as density, strength, hardness as well as secondary or phenomenological properties including friability and other defects of powder compacts (**Fig. 2**).

One of the most important mechanical properties of compact is strength, *i.e.*, the stress level at which a compact loses its mechanical integrity. Compact strength is related to the constitutive structure of a compact originating from the presence of ingredients, how homogeneously different ingredients are mixed, deposited, and compressed. While the measurement of compact strength is usually performed at the macroscopic level, the origin of defects develop and grow when a compact is subjected to a certain level of mechanical loading, which can often be predicted by relative density distributions. The observation that the corresponding mechanical behavior is closely

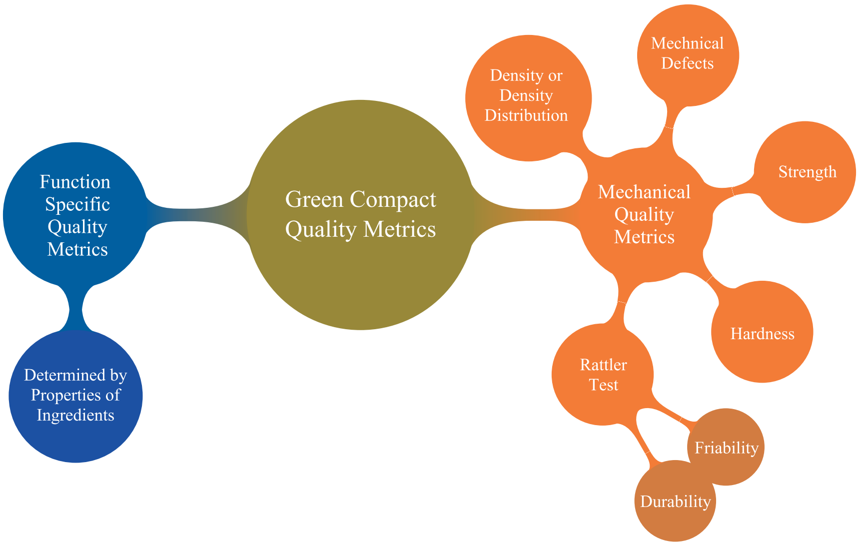

Fig. 2 Green compact quality metrics. Right side branches include mechanical quality metrics that are reviewed in this study. Quality metrics specific to compacts' end users, which are in blue and on left branches, are not reviewed.

related to the heterogeneous relative density distribution of a compact, suggests that the strength of compacts develops in relation to loaded powder system's characteristic stress distribution development pattern inside a powder system. Since it is not practical to measure stress distribution of powder compacts during the compaction process, compaction behavior has long been described by change in relative density of compact to the true density of particles. Relative density of a powder compact has been one of actively investigated and widely used powder compact quality metrics. Therefore, studies on powder compacts' density are reviewed first.

In following sections, studies involving powder compacts' mechanical strengths from a more rigorous perspective are reviewed. In regard to quantitative mechanical properties of powder compacts, their integrity presents two distinctive aspects *i.e.*, development of discontinuity of a compact and localized breakage of powders at the surface of a compact. The former relates more to defects of compacts in a somewhat empirical sense. Considering it wide usage, it is important to recognize empirical quality metrics. For example, mechanical quality metrics of compacts are often described or determined by inspecting a presence of surface defects such as crack or capping. In addition, such mechanical defects of powder compacts often arise from irregular or undesirable mechanical properties of compacts meaning that these can be regarded as indicators of mechanical strength of powder compacts. Moreover, mechanical strength of compacts can be determined in a more empirical way. For example, one can simply conduct a fail or pass test as a result of dropping a product from a certain height. This type of test provides a binary result under very specific circumstances. Recognizing broad usage of such approaches, studies involving mechanical defects of powder compacts are reviewed. Subsequently, studies involving mechanical strengths of powder compacts involving breakage or quantitative mechanical properties, which includes elastic moduli, parameters of powder compaction models, are reviewed. In addition, mechanical strength of a compact's surface has been widely used as an indicator of mechanical properties of the entirety of powder compacts. Compacts surface's mechanical characteristic itself is of importance in some cases. Therefore, studies involving hardness tests or surface indentation test are also reviewed.

In addition, the properties of end product, *i.e.*, powder compacts, are often determined in the secondary or tertiary ways, most notably Rattler methods such as friability or durability test. In industry, mechanical strengths of products in compressed powder form, are determined in such empirical ways. For pharmaceutical products and densified biomass, friability or durability test are commonly used to determine the level of mechanical integrity of products when they are subjected to a predetermined sustained mechanical impacts. These type of tests generate quantitative quality metrics, but it is hard to correlate them to fundamental properties of compacts, bulk powder, or particles because those tests represent specific mechanical environments. Nonetheless, considering its popularity and frequent usage, studies involving Rattler tests are reviewed.

3.1 Quality; Density and density distribution

Density is the most basic and fundamental property of powder compacts. The term 'bulk density' is often used to clarify that powder compact that inherently includes voids between particles. Referring to the densities of ingredients, terms like 'true density' or 'solid density' are used. The relative density, *i.e.*, ratio between bulk density achieved by compression and 'true density' of particles, is often used as a parameter indicating the degree of compaction or compaction behavior. Measurement of bulk density of loose and compressed powders are rather straightforward but ASTM D6683-14 (ASTM Standard and D18.24 Committee, 2014) and ASTM D7481-09 (ASTM Standard and D18.24 Committee, 2009) describe standardized measurement procedures.

Considering that the density of bulk solid is determined by its weight and volume whereas volume of bulk solid changes upon compression, density can be an indicator of a degree of compaction. Therefore, macroscopic volume change of bulk solid has long been used to describe powder compaction or as an indicator of a degree of compaction. Some of most widely used descriptors of powder compaction using macroscopic volume change and applied load includes Heckel, Kawakita, and Cooper-Eaton equations (Alderborn and Nystrom, 1996; Fayed and Otten, 1984). Compressibility, which is based on the relative density of powder as described above, is still widely used as a straightforward descriptor of mechanical behavior of powder in industry as well as researches. For example, Bonaccorsi and Proverbio (2006) measured relative density (termed as green density) as an indicator of compaction quality for metallic powder compaction. Perez-Gandarillas et al. (2015)'s study used relative density change to explain tensile strength gain of compacts for different granulated pharmaceutical formula. Due to the straightforward measurement of relative density, which can be determined using Pycnometer and simple weight measurement with known volume, in addition to the volume change during compaction makes this approach attractive especially from the practical point of view. Similarly, Yohannes et al. (2015) used relative density change in investigating compaction behavior of powders with different particle size distributions focusing on the role of fines. They report that fines do not affect the compressibility and strength past initial rearrangement state and therefore fines can be disregarded in computational modeling using discrete particle approach. These recent studies show the utility of bulk density of powder compaction. However, limitations of macroscopic relative density of powder compaction exist as it lacks an ability to predict or indicate local defects such as crack or capping. It is simply because bulk density is a lumped macroscopic measurement and does not explain underlying mechanism of compaction. This can be complemented by measuring density distribution in compacts.

In addition, density or density distribution of compact often used as measurement to validate compaction model. For example, Huang and Puri (2000) used density in validation of Adachi-Oka model implemented in a finite element approach (**Fig. 3**), Borowski (2011) Kadiri et al. (2005) Michrafy et al. (2002), and Sinka et al. (2003) used density in validation of Drucker-Prager model solved with finite element models, and Aydin et al. (1994) and Michrafy et al. (2004) used density in validation of non-linear elastic problem with finite element model by successive incremental solution. In addition, Kong and Lannutti (2000) used density to validate discrete element model.

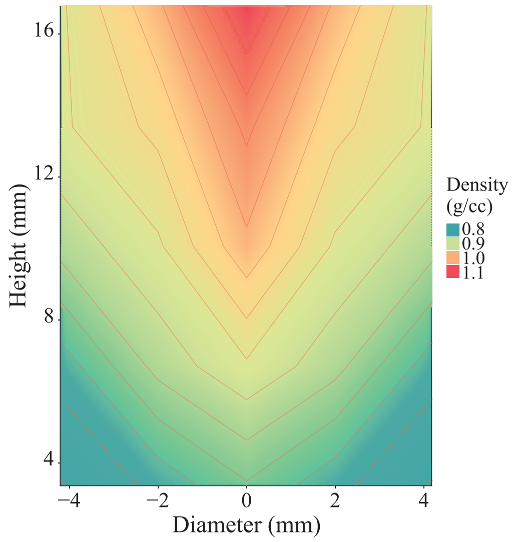

Fig. 3 Apparent density distribution measured from cylindrical compacts of microcrystalline cellulose under 14 MPa when pressed from top. Recreated with the permission from Huang and Puri (2000). Copyright: (2000) Taylor & Francis, Inc.

To this end, determination of density distribution of powder compacts is an important characterization that is necessary in fundamental understanding of powder compaction. Density of compacts can be measured with instrumented compaction unit, which can precisely trace the change of height, therefore density can be determined using known weight of charge. This approach is used in very early studies such as Train (1956) and recent studies such as Michrafy et al. (2003). As one of the earliest efforts of using density distribution in powder compaction study, Train (1956) demonstrated that density of compact is not homogeneous and neighbor of a stationary lower punch wall has higher density compared to upper central region. This difference of density is more pronounced with unlubricated die and attributes to defects of compacts such as capping. Therefore, the relationship between density distribution and defects of compact has been viewed as a quantitative predictor of compact quality.

One of major contribution to the developing density gradient during compaction is die-wall friction. This relationship was investigated by Michrafy et al. (2003). This study shows that friction between wall and die decreases while compaction progressed for different types of microcrystalline cellulose powders (PH101, PH102, and PH105) by determining the friction coefficient between compact and die wall using the transmission ratio (applied pressure/transmitted pressure), the transfer ratio (radial pressure/axial pressure) and the aspect ratio (height/diameter of tablet). Small caveat of this measurement is the use of published value for the transfer ratio based on the stress measured at the upper punch instead of mean axial stress at a respective depth. In addition, Michrafy et al. (2003)'s study also shows that measured relative densities are lower than both the Heckel equation, which is an exponential relation between applied stress by a punch and relative density, and a predictive model accounting for the exponentially decaying mean axial stress inside a compact away from the surface, on which a stress is applied. The gap between the measured value and predicted values of Heckel equation increases when the depth increases. This observation suggests that stress decreases exponentially inside a powder compact during compaction. However, quantitative contribution of die wall friction to the compaction behavior remains to be investigated since relative densities are experimentally determined only for unlubricated case.

Alternatively, a destructive indentation hardness can be used in determining compact density. However, indentation hardness test is prone to breaking brittle compacts during experiments. In addition, these methods cannot characterize horizontal variability of compact densities, which arises from the interactions with a die wall. Due to such limitations in regard to the accurate characterization of density distributions, research on this particular subject has been limited in spite of the importance of quantitative measurement of powder compacts' density distribution as fundamental metrics of powder compaction.

Development of non-destructive (or non-invasive) methods has enabled determining the density of compacts without mechanical disruptions of the test subject. X-ray tomography (including computed tomography, namely CT, or computerized axial tomography, namely CAT), Nuclear magnetic resonance (NMR), Magnetic Resonance Imaging (MRI), and Ultrasound are most widely accepted methods in non-destructive testing of materials (Banhart, 2008).

For example, the development of X-ray tomography has been utilized in quantitative density distribution analysis of compacts. Density distribution of alumina compact was determined using X-ray imaging tracing embedded lead balls (Aydin et al., 1994). Finite element model developed using their measurement demonstrated the contribution of the wall friction to the density distribution. However, there were a substantial disagreement between predicted and measured higher versus lower density regions that are attributed to assumed non-homogeneous internal angle of friction throughout the assembly. This heterogeneity of internal angle of friction of powder assembly is yet to be substantiated. Kong and Lannutti, (2000) utilized X-ray Computed Tomography (CT) to determine variances of density in alumina compacts especially for early compaction stages. To trace compaction, they used tungsten marker, which may have interfered during compaction. Richard et al. (2003) utilized X-ray micro-tomography to investigate packing and compaction of glass beads based on void ratio. Although this is not a direct measurement of compact density, it can be useful approach applicable to other types of particulate materials, whose density can be determined with about 10 µm resolution. Sinka et al. (2004) explored the use of X-ray CT scan in measurement of density distribution in microcrystalline cellulose compacts and showed spatial density distribution can be determined quantitatively. Busignies et al. (2006) also measured a density profile in microcrystalline cellulose compacts using X-ray tomography to study the heterogeneous density of compacts and to investigate a correlation between mechanical properties of compacts and compact densities. However, X-ray tomography does not show clear density gradient inside binary mixture compacts. However, this study reports preferential localization of a specific ingredient implying the origin of difference between mechanical properties of whole compact versus mechanical properties of compact surface, such as indentation hardness. It should be noted that the root cause of such preferential localization of an ingredient is not clarified, which can be a result of less than ideal mixing or segregation during deposition of mixture in a die. Miguélez-Morán et al. (2009) used X-ray CT to characterize roller-compacted ribbons of microcrystalline cellulose showing higher compression in the middle than edges. In addition, they developed correlation between the relative density and localized indentation that follows a log-normal relationship.

Nuclear magnetic resonance (NMR) also has been used in studying density distribution of compacts as shown in Djemai and Sinka (2006) but NMR is not as widely used in this field. Caveats of NMR and X-ray based tomography techniques still exists that they are time-consuming and costly. Additional point to X-ray is that the measurement depends on the chemical composition of the test subject and a specific calibration for subject material is required for different formulations, which can be less than straightforward for industries using multi-ingredients. In another effort, Garino et al. (1995) utilized MRI to determine density variations in powder compacts. In addition, Glass and Ewsuk (1995) used ultrasound to determine relative density of alumina compact. Akseli et al. (2011) used both ultrasound and X-ray CT to determine density distribution of ribbon compacted microcrystalline cellulose in investigation of mechanical properties. They showed that both methods have resolution to distinguish spatially distributed density in compacts. More interestingly, correlation between ultrasonic measurement and tablet's mechanical strength (tensile strength) was found; which was used in other materials whose mechanical properties are difficult to measure. It should be noted that the listed non-destructive characterization techniques are still confined by limitations regarding resolutions high enough to distinguish individual particles.

3.2 Quality: Mechanical defects

Some of major issues of compacts include defects including crack, capping, and uneven surface (**Fig. 4**). These defects are more qualitative in nature and often examined with a binary designation *i.e.*, pass or fail. In many cases, local irregularity evolves into defective compacts, it is not straightforward to predict or prevent powder compacts' mechanical defects without fundamental understanding of powder compaction taking the stochasticity of particulate materials into consideration. This is especially problematic during development of products since it is hard to know the risk of defective products *a priori* and higher defect rate is found after they are fully formulated. Then this situation requires an extensive investigation relying on trial-and-error approach to identify optimal (or working) recipe of process parameters even without finding out actual causes. As an effort to mitigate this issue, Akseli et al. (2014) presents a relationship between capping and process parameters including formulations. In addition, Kuppuswamy et al. (2001)'s study is an attempt to predict the risk of capping by indentation hardness and observe crack development. Kuppuswamy et al. (2001) investigated detection of formula prone to capping using indentation hardness test attributing capping to the residual die-wall pressure introducing microscopic cracks, which is hypothesized to develop into cracks, therefore capping due to insufficient plasticity. This study suggests that the plasticity of particles is related to localized defect development. This idea is in line with that too much elastic rebound after or during unloading may introduce local defects or failure of compacts.

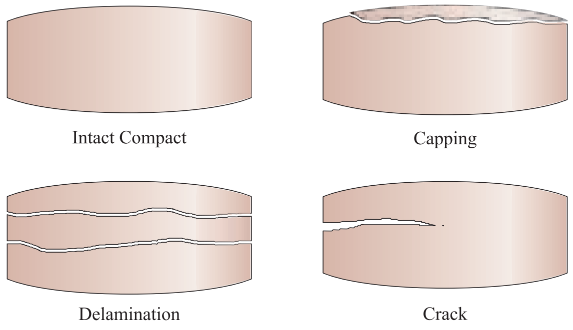

Fig. 4 Typical compacts with no or common mechanical defects including capping, delamination, and crack.

There have been studies to understand where these defects originate. In studying a relationship between smoothness of surface and mechanical characteristics of compacts, Narayan and Hancock (2003) suggests that brittle bulk powder may indicate their propensity to be vulnerable to cracks or surface defects. It should be noted that Narayan and Hancock (2003)'s study seems to refer to bulk powder's brittleness or ductility to their failure behavior when compressed. In addition, this study did not investigate the underlying mechanism of how brittleness of compact can be related to cracks or surface defects. However, authors suggest roles of particle size distribution, shape, and bonding interactions in initial packing. In addition, this study also implicitly connects brittleness or ductility of compact (or powder mass under compaction) to the same properties of particles, which would be interesting to find out how these are correlated. Recent advancement of experimental methods, which can determine mechanical properties of sub-micrometer sized test specimen, definitely allow quantitative investigation of particles (Govedarica et al., 2012; Karamchandani et al., 2016).

Related to this subject, Ashby and Hallam (1986) and Ashby and Sammis (1990) report theoretical investigation on how microcracks develop and induce failure in solids. Since powder compacts usually bear defects including microcracks, application of such theories to powder compacts may assist quantitative prediction and control of powder compact's mechanical integrity. More fundamental origin of compact defects, excessive pores, were reported by Shinohara et al. (1999), in which the voids created from the dimples of alumina particles, grain boundaries, prominently larger particles are proposed as major culprits. Correlation between those major causes and defects in the compacts were reported based on observatory investigation and it is expected that modeling approach that can included such information at particle scale and simulate larger scale compaction behavior will further substantiate this hypothesized origin of defects. In addition, considering alumina particle surface being smooth and spherical, the effect of asperity of more irregular particles on defective compact would be interesting.

In a more recent study, Garner et al. (2014) investigated the mechanism of crack development during ejection of microcrystalline compacts using Druker-Prager model implemented with a finite element method. Their study suggests that microcracks develop during unloading as a mechanism of relieving the radial wall stress. Also surface cracks develops when a compact is exiting die due to abrupt decreases of stresses following the elastic expansion whose rate can be controlled by adding tapper at the end of die. Recent advancement of nano-technology and computational power is expected to allow linking approaches taken by Garner et al. (2014) with the observation of Shinohara et al. (1999), which will elucidate the origin and mechanism of defects development during powder compaction process.

3.3 Quality: Strength

Mechanical strength of powder compacts is one of most widely used quantitative metrics (Bonaccorsi and Proverbio, 2006; Hayashi et al., 2013; Krycer et al., 1983a, 1983b; Mazel et al., 2014; Perez-Gandarillas et al., 2015; Russell et al., 2015; Yohannes et al., 2015). Compact's mechanical strength is influenced by many parameters including temperature (Rouèche et al., 2006) or properties of particle including particle size (Narayan and Hancock, 2005) in case of tensile strength. Finer particles tend to result in stronger compacts owing to higher surface area (Alderborn and Nystrom, 1996). However, it is notable that the degree of this increase in compact strength varies for different materials.

Compact strength is largely determined by compression pressure (**Fig. 5**). A positive correlation between these two are empirically known (Sinka et al., 2009), but exact relationship is yet to be elucidated as there are many additional parameters to determine exact compact strength such as loading rate, amount of charge (therefore the dimension of final compact), etc. A basic approach of determining mechanical strength of medicinal tablets can be found in United States Pharmacopeial Convention (2011). Detailed procedure of mechanical tests are reviewed by Amorós et al. (2008) and Podczeck, 2012. Mazel et al. (2014)'s study is notable since they attempted to link practical engineering strength test to more rigorous Drucker-Prager yield criteria.

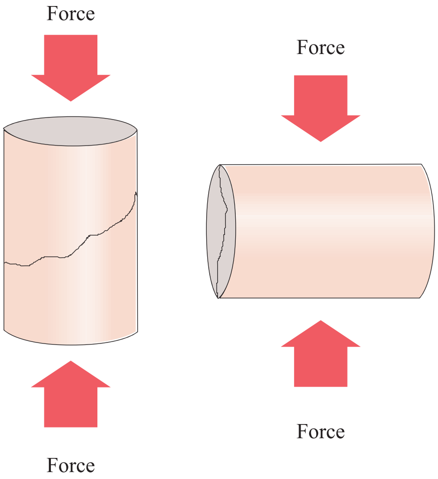

Fig. 5 Typical mechanical tests to determine strength of compacts. Loading in the major axis direction is used in determining compressive strength of compacts (left), whereas loading in the minor (or radial) axis direction is used in determining tensile strength (right). The latter is often referred as a diametral test.

Sinka et al. (2009)'s study lists processing parameters affecting eventual strength of compact. Notably, they suggested that the compaction behavior and ultimate properties of compacts originates from particle's properties. However, Sinka et al. (2009)'s have reported such causal relations in a qualitative way. It is simply because of the daunting numbers of intertwined parameters affecting the compaction process. To be quantitative includes identifying dominant parameters and how large their contribution is and finding out how compaction is happening including the die-wall and loading-rate effects, and possibly mechanics at a scale, in which individual particles are scrutinized. Some specific aspect of processing parameter, such as temperature, has been specifically shown to influence mechanical properties of pharmaceutical compacts York and Pilpel (1973). Nonetheless, this generally accepted conjecture on causal relationship between particle's properties and compacts' properties have been actively investigated. For example, Zhang et al. (2014)'s study demonstrated an implicit effects of ingredients on a biomass pellets. Similar result is shown for binders commonly used by Zhang et al. (2003) or major ingredients of pharmaceutical compacts (Akseli, 2009; Pandeya and Puri, 2012).

Furthermore, relationships between surface area of particles and medicinal tablet's tensile strength have been studied extensively (Fell and Newton, 1970; Jetzer, 1986; Leuenberger, 1982; Riepma et al., 1990, 1991, 1992). Particle's morphology and ductility of compacts has been reported by Galen and Zavaliangos (2005). Galen and Zavaliangos (2005) examined the anisotropic strength of compacts and attributed the anisotropy especially in the ductile powder compacts to the microscopic architectural structure of deformed particles after the compaction. For example, mechanism is different in each case. For ductile powders, compaction involves the flattening of particles which results in greater strength in the transverse direction due to increased crack deflection that results from greater particle overlap. For the brittle powder, it is proposed that particle fragmentation occurring along the compaction direction weakens strength in the transverse direction. Actual quantification of such a claim was not substantiated but it should be possible now due to the development of nano-technology and microscopy. This idea is investigated further by Wang (2007).

In addition, particle size or particle size distribution's effect on a compaction process have been actively studied (Jiang et al., 2001; Kaerger et al., 2004; Koynov et al., 2013; Morsi et al., 2006). Effect of particle size on compact strength has been well documented (Khan and Pilpel, 1986; McKenna and McCafferty, 1982). In addition, effect of particle shape on a powder system has been investigated in detail, as well (de Bono and McDowell, 2016; Mittal et al., 2001; Yi et al., 2002; Yi et al., 2001). However, study on the relationship between particle shape and compact's properties is scarce, which is thought to be because of the difficulty in quantification of particle shape. Studies on discrete element model require a quantitative and direct description of particle morphology and this need has prompted recent studies on quantitative descriptions of particles (Amberger et al., 2012; Coetzee, 2016; Favier et al., 1999; Garcia et al., 2009; Kruggel-Emden et al., 2008; Křupka and Říha, 2015; Li et al., 2015; Rickman et al., 2016; Wu et al., 2016; Zhao and Wang, 2016).

One of notable properties that has not been studied from this perspective include actual mechanical properties of individual particle and evolution of contacts between particles during compaction in relation to bulk responses of powder *en masse* during compaction or mechanical properties of resulting compacts. Recently, there have been attempts to investigate mechanical properties of particle with powder compaction using nanoindentation as a mean to determine particle's mechanical property (Cao et al., 2010; Govedarica et al., 2012). Furthermore Portnikov and Kalman (2015) investigated the effect of temperature on elastic properties individual particles and showed that the effective modulus of elasticity decreases while temperature of particles increases. Unfortunately, this approach is not widely performed probably due to the lack of a clear understanding on how one can use such information in predicting or controlling compaction operations.

In addition, one of the challenges of quantitative characterization of mechanical strength of compact is its stochastic nature originating from stochasticity of particle sizes and shape of powder system. Such distributed nature of mechanical strength of compacts can be characterized using Weibull distribution as shown in Phani (1987). Portnikov and Kalman (2014) established a mathematical model describing the distribution of the effective modulus of elasticity of individual particles including salt, potash, granulated gold nano particles (GNP), zirconium spheres, and glass spheres. Russell et al. (2015)'s study demonstrates how stochastic strength of particle system can be quantitatively investigated using synthetic zeolitic granules whose D_{50} is 1.75 mm.

There also have been studies on the evolution of coordination number during powder compaction (German, 2014). Nonetheless, knowledge on how coordination number and overall interaction between particles contributes powder compacts' mechanical integrity and responses is generally lacking. It is expected that efforts to elucidate laws governing the evolution of mechanical properties powder compacts from particle scale based on individual particles and interparticle mechanics will expand leveraging those recent developments.

3.4 Quality: Hardness

The indentation hardness has been very widely used in industry as a measure of the mechanical property of powder compacts owing to its straightforward and speedy procedure. Accordingly, many studies used the indentation hardness as a characterization method of mechanical properties of compacts (Bonaccorsi and Proverbio, 2006; Chtourou et al., 2002; Kuppuswamy et al., 2001; Tehrani et al., 2010) as well as an evaluation metrics of a compaction process (Chtourou et al., 2002).

Although the indentation hardness is not a fundamental mechanical experiment procedure, relationships between indentation hardness and mechanical properties have been actively developed and widely accepted. Few examples of such studies can be found in Gent (1958), Gubicza et al. (1996), Oliver and Pharr (1992), and Pavlina and Tyne (2008). It should be noted that, these relationships are specific to tip geometry of an indentor (**Fig. 6**) and subjected compacts especially in relation to the surface roughness (Laitinen et al., 2013). Furthermore, it is more difficult to establish relationships between hardness measurements and fundamental mechanical properties of materials with inelastic or stochastic mechanical responses (Ma et al., 2009) or when the indentation tip material and subject material have comparable mechanical stiffness

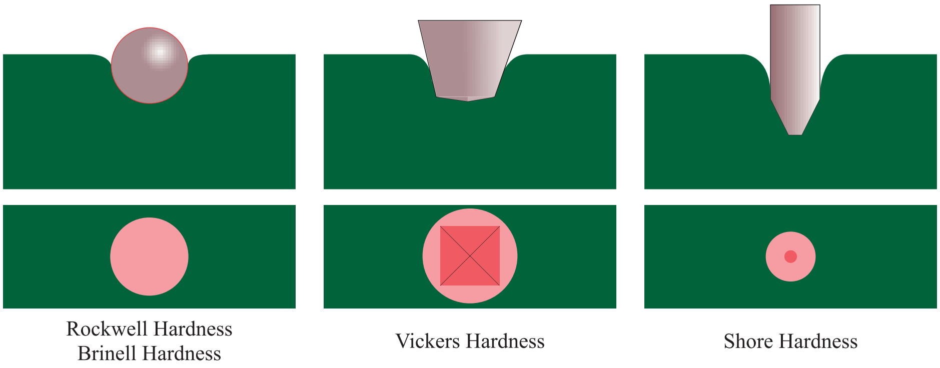

Fig. 6 Commonly used indentation hardness tip shapes shown from the front (top row) and the shape of indentation shown from the top (bottom row). Indentation hardness is measured by the depth of indentation when subject surface is indented by a tip with specific geometry with a pre-set force.

(Skrinjar et al., 2005). In other words, it is required for an indentation tip to be much harder than subjected powder compacts with large enough dimension compared to the indentation to ensure an accurate hardness measurement, which is not always straightforward to implement especially for novel materials or materials with less known surface characteristics or mechanical properties.

Indentation hardness has been recognized as a useful and promising tool in mechanical characterization of particles with the recent development in micro-indentation tester, especially for the advancement of Atomic Force Microscopy (AFM) (Cao et al., 2010; Masterson and Cao, 2008; Meier et al., 2009; Willems et al., 1993) or nanoindenter (Gibson et al., 2015; Govedarica et al., 2012; Taylor et al., 2004). In general, a caution should be exercised when fundamental mechanical properties, such as Young's modulus and Poisson's ratio when the simplest elasticity is assumed, are estimated from indentation hardness test results. For example, Govedarica et al. (2012) used Sneddon (1965)'s equations which assumes semi-infinite half-space of subject material compared to the indentor geometry. Taylor et al. (2004) used Duncan-Hewitt and Weatherly (1989)'s study based on a semi-empirical fracture mechanics to estimate brittleness based on the ratio of the hardness and elastic modulus based on the indentation geometry of a conventional Vickers Hardness test. Gibson et al. (2015) used a finite element modeling to estimate Young's modulus and Poisson's ratio using a nanoindentation tests on micron-sized silica (SiO_2) particles. It should be noted that Gibson et al. (2015) assumed non-slip contact, which should be further substantiated as assumptions on contact may have a significant effect especially at the microscopic scales (Briscoe and Adams, 1987; Skrinjar et al., 2005; Thornton and Ning, 1998).

Despite above mentioned caveats, there have been efforts focused on the development of relationship between particle's properties and powder system's behavior during compaction or properties of compact. Most notably, Cao et al. (2010) performed AFM nanoindentation on individual pharmaceutical particles, *e.g.*, acetaminophen crystallites, ibuprofen crystallites, sodium acetate trihydrate, microcrystalline cellulose, ascorbic acid, tartaric acid and the hydropropyl methylcellulose. They used film sample for hydropropyl methylcellulose whereas other materials were tested as crystalline particles. Elastic modulus was determined based on the measured stiffness and contact area following the Hertzian contact law. Correlating particle hardness and powder compact hardness, which is also determined by AFM nanoindentation, a quantitative relationship between particle hardness with powder compaction performance is obtained. It should be noted that the powder compaction performance has been determined based on quantitative metrics of mechanical properties of compacts. It is clear that there exist apparent cluster of ingredients resulting compacts with poor or good mechanical quality in relation to the hardness of particles. Cao et al. (2010) study is notable as the first attempt to correlate individual particle's mechanical properties with the macroscopic powder compacts' properties. There are plentiful opportunities for further investigation such as appropriate contact mechanics theory for AFM nanoindentation on crystalline particles. For example, due to AFM nanoindentor's small geometry and unknown asperity of contact surfaces of subject materials, Hertzian contact mechanics may not be appropriate to estimate mechanical properties of particles (Carrillo and Dobrynin, 2012; Johnson, 1987; Kendall, 1987). In addition, degree of crystallinity and effects of crystallographic properties, as Cao et al. (2010) and Willems et al. (1993) assumed for the dominant face of the crystal to play a major role on powder compaction, are yet to be fully understood as actively investigated for cellulose (Pinto, 1999; French and Johnson, 2009; Glasser et al., 2012). Further studies will produce quantitative correlation between macroscopic powder compacts mechanical performance and individual particle's properties.

Development of AFM also opened other *in situ* characterization of powder compacts as shown in Miguélez-Morán et al. (2009). In addition, it should be noted that particle interactions have been widely studied using AFM (Cleaver and Looi, 2007; Dobryden et al., 2013; M. Götzinger and Peukert, 2004; Martin Götzinger and Peukert, 2003; Jones et al., 2003; Kani et al., 2007; Tanaka et al., 2008; Tsukada et al., 2004) but mechanical properties of a single particle has not been studied as actively. This is probably due to the mechanism of AFM's measurement, which relies on the interactive force between AFM cantilever tip and subject surface including mechanical contact force, van der Waals force, chemical bonding, electrostatic force, magnetic forces, and so forth.

3.5 Quality: Rattler test

Rattler test is originally used to test paving bricks. It was adopted to determine strength of metallurgic powder compacts (Blumenthal et al., 1997). Typical rattler test designates number and size of compacts to be tumbled inside a chamber of predetermined dimension. After a specific number of revolutions at a specified speed, the loss of weight including samples, which are broken during the procedure, is recorded and compared to the original weight of intact samples. Similar approach is used to measure of how green compact maintains its mechanical integrity. Such methods include friability test for pharmaceutical tablets, which is described in (USP29, 2016) and durability test for biomass compacts (**Fig. 7**), which is described in ASABE Standard S269.4 (2002).

Some studies used durability to control or predict the

Fig. 7 Durability tester (left) fabricated in accordance with the ASABE Standard S269.4 (2002) and a friability tester (right) fabricated in accordance with US Pharmacopia standard.

quality of biomass compacts (Kaliyan and Morey, 2009; Karamchandani, 2013; Wilson, 2010). Similar approaches were used for pharmaceutical compacts (Vinogradov and Komarova, 1962) using the fundamental idea of friability and not the standardized friability test (Krycer et al., 1983a; Sinka et al., 2009).

Since the friability test procedure's simple concept and its ability to mimic conditions of handling of compacts, durability or friability provide good quantitative measures of mechanical property of compacts. However, the tertiary nature of the test procedure makes this test to be highly dependent on the dimension of the test device, speed of the rotation, and the size of compacts in one test. Furthermore, the accuracy of this test method is not fully examined. The procedure of durability or friability test is well established and the number of samples and repetition is as well defined. Such dependency of test procedures and equipment for biomass compacts are studied by Temmerman et al. (2006). No similar study is reported for friability of smaller and lighter powder compacts. Furthermore, establishing correlative relationship between friability and other mechanical properties may be of interest to overcome the caveat of this type of test.

4. Summary

As reviewed in this article, studies on powder mechanics research have shown the feasibility of developing predictive relationships between mechanical properties and quality metrics of few types of powders. For example, pharmaceutical tablets are formed using powder ingredients such as filler, binder, disintegrant, and active pharmaceutical ingredient, either by dry blending the ingredients or wet granulation of the powder mix followed by compaction. Pandeya and Puri (2012)'s study reports that a set of mechanical properties of powder *en masse*, such as springback index, compression index, and bulk modulus, were found most suitable for predicting diametral strength, indentation hardness, and friability of compacts. This was found by developing predictive correlations for tablet quality vs. dry and granulated powder's mechanical properties that were determined using a medium pressure flexible boundary cubical triaxial tester and mechanical quality metrics of compacts.

In another study, similar approach was applied to biomass pelleting: Karamchandani et al. (2015) demonstrated that ground biomass pellet's quality can be related to mechanical properties of ground biomass. Especially, this study showed that the fundamental mechanical properties at low pressure range of compaction is capable of predicting properties of compacts produced at much higher pressure, which is thought to be due to the importance of early stage of compaction including rearrangement and elastic responses. This informs the significant importance of measuring fundamental mechanical properties at low pressure range as it is much more practical in industrial laboratory than the measurement at higher pressure range, *i.e.*, over 1 MPa.

5. Looking ahead: The role of microscale interactions

The above-mentioned two studies demonstrate that the quality of compacts can be rationally predicted based on the characterization of feed materials' mechanical properties. The key to these studies is employing quantitative approaches both in the measurements of quality metrics and characterization of feed materials. This quantitative approach is the first step toward systematically establishing optimal compaction processes to produce compacts with optimal quality; avoiding overshooting production operation parameters as can be the case when using trial-and-error. To achieve this ultimate goal, one needs to understand particle properties' role in and contribution to the mechanical behavior of powder during densification. The ability to predict behavior of powder during compaction based on mechanical characteristics of individual particles and their interactions will provide a means to implement quality control by design that takes the characteristics of the feedstock into account.

An analytical model, which describes how macroscopic compaction mechanics evolves from mechanics of the underlying scales, is absent largely because of the lack of an adequate method to examine mechanics at the scale where individual particles can be scrutinized. The compaction process evolves towards different scales of scrutiny, *i.e.*, microscale (single particle, particle-particle interactions), mesoscale (secondary and tertiary particle structures), and macroscale (bulk powder system). Accordingly, a research question can be posed as how do a single particle's properties and particle-particle interactions govern the evolution of compaction in powders (and powder mixtures) at different scales? For example, the change in formulation with similar (or same) base material is shown to result in different characteristics of compacts (Souriou et al., 2009). Overall, recent advances in nano-technology, computational capacity and modeling approach, such as a discrete element modeling (DEM), have been actively explored in studies of many aspects of powder processing. We believe that similar multi-scale approaches can be successfully employed in addressing this question on the powder compaction. In a multi-scale framework, properties of single particle and particle-particle interaction characterized using Nano or MicroElectroMechanical Systems (NEMS/MEMS) devices form the foundation of a mesoscopic and macroscopic governing principles of powder compaction. Ultimately, such characterization are hypothesized to be linked to fundamental mechanical properties of bulk particulate materials during compaction. This can be done using a fundamental tester such as a true Cubical Triaxial Tester (CTT) that is free of the confounding effect of samples' boundary conditions. Through this approach, we believe that it is possible to formulate rational principles of compaction of powder *en masse* based on the governing laws at multiple scales employing the mechanical properties of underlying scales, and to develop and validate a multi-scale and multi-physics computational model of the evolution of compacts. We envision that this approach will enable systematically engineering the optimization of powder compaction processes so that one can quantitatively predict and control a compact's mechanical quality properties through the design and characterization of the powders that are used as raw materials of powder processing.

References

Akseli I., Nano/micro/meso scale interactions in mechanics of pharmaceutical solid dosage forms, PhD Thesis, (2009). Retrieved from http://adsabs.harvard.edu/abs/2009PhDT........18A.

Akseli I., Iyer S., Lee H.P., Cuitiño A.M., A quantitative correlation of the effect of density distributions in roller-compacted ribbons on the mechanical properties of tablets using ultrasonics and X-ray tomography, AAPS PharmSciTech, 12 (2011) 834–853. DOI:10.1208/s12249-011-9640-z.

Akseli I., Stecuła A., He X., Ladyzhynsky, N., Quantitative correlation of the effect of process conditions on the capping tendencies of tablet formulations, J. Pharm. Sci., 103 (2014) 1652–1663. DOI:10.1002/jps.23951.

Alderborn G., Nystrom C., Pharmaceutical powder compaction technology, Marcel Dekker, Inc., 1996. Retrieved from http://www.diva-portal.org/smash/record.jsf?pid=diva2:87597.

Amberger S., Friedl M., Goniva C., Pirker S., Kloss C., Approximation of objects by spheres for multisphere simulations in DEM, In ECCOMAS 2012, 2012.

Amorós J.L., Cantavella V., Jarque J.C., Felíu C., Green strength testing of pressed compacts: An analysis of the different methods, J. Eur. Ceram. Soc., 28 (2008) 701–710. DOI:10.1016/j.jeurceramsoc.2007.09.040.

ASABE Standard S269.4, A., Cubes, pellets, and crumbles-definitions and methods for determining density, durability, and moisture content, (No. S269. 4).

Ashby M.F., Hallam S.D. (Née C., The failure of brittle solids containing small cracks under compressive stress states, Acta Metall., 34 (1986) 497–510. DOI:10.1016/0001-6160(86)90086-6.

Ashby M.F., Sammis C.G., The damage mechanics of brittle solids in compression, Pure Appl. Geophys., 133 (1990) 489–521. DOI:10.1007/BF00878002.

ASTM Standard, and D18.24 Committee, Standard test methods for determining loose and tapped bulk densities of powders using a graduated cylinder (Standard No. D7481-09) (p. 4), West Conshohocken, PA: ASTM International, 2009. DOI: 10.1520/D7481-09

ASTM Standard, and D18.24 Committee, Standard test method for measuring bulk density values of powders and other bulk solids as function of compressive stress (Standard No. D6683-14) (p. 5), West Conshohocken, PA: ASTM International, 2014. DOI: 10.1520/D6683-14

Aydin İ., Briscoe B.J., Şanlitürk K.Y., Density distributions during the compaction of alumina powders: A comparison of a computational prediction with experiment, Comput. Mater. Sci., 3 (1994) 55–68.

Azami A.R., Khoei A.R., 3D computational modeling of powder compaction processes using a three-invariant hardening cap plasticity model, Finite Elem. Anal. Des., 42 (2006) 792–807. DOI:10.1016/j.finel.2006.01.011.

Banhart J., Advanced tomographic methods in materials research and engineering, OUP Oxford, 2008.

Bell T.A., Challenges in the scale-up of particulate processes—an industrial perspective, Powder Technol., 150 (2005) 60–71. DOI:10.1016/j.powtec.2004.11.023.

Blumenthal W.R., Sheinberg H., Bingert S.A., Compaction issues in powder metallurgy, MRS Bull., 22 (1997) 29–33. DOI:10.1557/S0883769400034710.

Bonaccorsi L., Proverbio E., Powder compaction effect on foaming behavior of uni-axial pressed PM precursors, Adv. Eng. Mater., 8 (2006) 864–869. DOI:10.1002/adem.200600082.

Borowski G., Effect of friction for density distribution in die compaction of powders, Postępy Nauki Tech., 10 (2011) 159–168.

Bortzmeyer D., Modelling ceramic powder compaction, Powder Technol., 70 (1992) 131–139. DOI:10.1016/0032-5910(92)85040-3.

Briscoe B.J., Adams M.J. (Eds.), Tribology in particulate technology, A. Hilger, Bristol, England; Philadelphia, 1987.

Busignies V., Leclerc B., Porion P., Evesque P., Couarraze G., Tchoreloff P., Quantitative measurements of localized density variations in cylindrical tablets using X-ray microtomography, Eur. J. Pharm. Biopharm., 64 (2006) 38–50.

DOI:10.1016/j.ejpb.2006.02.007.

Cao X., Morganti M., Hancock B.C., Masterson V.M., Correlating particle hardness with powder compaction performance, J. Pharm. Sci., 99 (2010) 4307–4316. DOI:10.1002/jps.22130.

Carrillo J.-M.Y., Dobrynin A.V., Contact mechanics of nanoparticles, Langmuir, 28 (2012) 10881–10890. DOI:10.1021/la301657c.

Castellanos A., Valverde J.M., Quintanilla M.A.S., Physics of compaction of fine cohesive particles, Phys. Rev. Lett., 94 (2005) 075501. DOI:10.1103/PhysRevLett.94.075501.

Chtourou H., Guillot M., Gakwaya A., Modeling of the metal powder compaction process using the cap model. Part I. Experimental material characterization and validation, Int. J. Solids Struct., 39 (2002) 1059–1075. DOI:10.1016/S0020-7683(01)00255-4.

Cleaver J.A.S., Looi L., AFM study of adhesion between polystyrene particles;—The influence of relative humidity and applied load, Powder Technol., 174 (2007) 34–37. DOI:10.1016/j.powtec.2006.10.017.

Coetzee C.J., Calibration of the discrete element method and the effect of particle shape, Powder Technol., 297 (2016) 50–70. DOI:10.1016/j.powtec.2016.04.003.

Cooper A.R., Eaton L.E., Compaction Behavior of Several Ceramic Powders, J. Am. Ceram. Soc., 45 (1962) 97–101. DOI:10.1111/j.1151-2916.1962.tb11092.x.

Cunningham J.C., Sinka I.C., Zavaliangos A., Analysis of tablet compaction. I. Characterization of mechanical behavior of powder and powder/tooling friction, J. Pharm. Sci., 93 (2004) 2022–2039. DOI:10.1002/jps.20110.

de Bono J.P., McDowell G.R., Investigating the effects of particle shape on normal compression and overconsolidation using DEM, Granul. Matter, 18 (2016). DOI:10.1007/s10035-016-0605-5.

de Gennes P.-G., Granular matter: a tentative view, Rev. Mod. Phys., 71 (1999) S374. DOI:10.1103/RevModPhys.71.S374; J1: RMP.

Dimaggio F.L., Sandler I.S., Material model for granular soils, J. Eng. Mech., (1971). Retrieved from/view.aspx?id=124117.

Djemai A., Sinka I.C., NMR imaging of density distributions in tablets, Int. J. Pharm., 319 (2006) 55–62. DOI:10.1016/j.ijpharm.2006.03.049.

Dobryden I., Yang X., Almqvist N., Holmgren A., Weber H., An atomic force microscopy study of the interaction between magnetite particles: The effect of Ca^{2+} ions and pH, Powder Technol., 233 (2013) 116–122. DOI:10.1016/j.powtec.2012.09.003.

Duncan-Hewitt W.C., Weatherly G.C., Evaluating the hardness, Young's modulus and fracture toughness of some pharmaceutical crystals using microindentation techniques, J. Mater. Sci. Lett., 8 (1989) 1350–1352.

Ennis B.J., Green J., Davies R., The legacy of neglect in the United-States, Chem. Eng. Prog., 90 (1994) 32–43.

Favier J.F., Abbaspour-Fard M.H., Kremmer M., Raji A.O., Shape representation of axi-symmetrical, non-spherical particles in discrete element simulation using multi-element model particles, Eng. Comput., 16 (1999) 467–480.

Fayed M.E., Otten L., Handbook of powder science and technology, Van Nostrand Reinhold Company Inc, New York, NY 10020, 1984.

Fell J.T., Newton J.M., The prediction of the tensile strength of tablets, J. Pharm. Pharmacol., 22 (1970) 247–248. DOI:10.1111/j.2042-7158.1970.tb08513.x.

French A.D., Johnson G.P., Cellulose and the twofold screw axis: modeling and experimental arguments, Cellulose, 16 (2009) 959–973. DOI:10.1007/s10570-009-9347-4.

Galen S., Zavaliangos A., Strength anisotropy in cold compacted ductile and brittle powders, Acta Mater., 53 (2005) 4801–4815. DOI:10.1016/j.actamat.2005.06.023.

Garcia X., Xiang J., Latham J.-P., Harrison J.P., A clustered overlapping sphere algorithm to represent real particles in discrete element modelling, Géotechnique, 59 (2009) 779–784. DOI:10.1680/geot.8.T.037.

Garino T., Mahoney M., Readey M., Ewsuk K., Gieske J., Stoker G., Min S., Characterization techniques to validate models of density variations in pressed powder compacts (No. SAND--95-1615C; CONF-951033--12), Sandia National Labs., Albuquerque, NM (United States). Retrieved from http://www.osti.gov/scitech/biblio/100203.

Garner S., Ruiz E., Strong J., Zavaliangos A., Mechanisms of crack formation in die compacted powders during unloading and ejection: An experimental and modeling comparison between standard straight and tapered dies, Powder Technol., 264 (2014) 114–127. DOI:10.1016/j.powtec.2014.04.086.

Gent A.N., On the relation between indentation hardness and Young's modulus, Rubber Chem. Technol., 31 (1958) 896–906. DOI:10.5254/1.3542351.

German R.M., Coordination number changes during powder densification, Powder Technol., 253 (2014) 368–376. DOI:10.1016/j.powtec.2013.12.006.

Gibson R.F., Jang H.-K., Simkhada S., Yu Q., Kim H.-I., Suhr J., Use of nanoindentation, finite element simulations, and a combined experimental/numerical approach to characterize elastic moduli of individual porous silica particles, Part. Sci. Technol., 33 (2015) 213–218. DOI:10.1080/02726351.2014.950396.

Glass S.J., Ewsuk K.G., Ceramic powder compaction (No. SAND--95-1804C; CONF-9511208--1), Sandia National Labs., Albuquerque, NM (United States). Retrieved from http://www.osti.gov/energycitations/product.biblio.jsp?osti_id=234692.

Glasser W.G., Atalla R.H., Blackwell J., Malcolm Brown R., Burchard W., French A.D., Klemm D.O., Nishiyama Y., About the structure of cellulose: debating the Lindman hypothesis, Cellulose, 19 (2012) 589–598. DOI:10.1007/s10570-012-9691-7.

Götzinger M., Peukert W., Dispersive forces of particle–surface interactions: direct AFM measurements and modelling, Powder Technol., 130 (2003) 102–109. DOI:10.1016/S0032-5910(02)00234-6.

Götzinger M., Peukert W., Particle adhesion force distributions on rough surfaces, Langmuir, 20 (2004) 5298–5303. DOI:10.1021/la049914f.

Govedarica B., Ilić I., Šibanc R., Dreu R., Srčič S., The use of single particle mechanical properties for predicting the compressibility of pharmaceutical materials, Powder Technol., 225 (2012) 43–51. DOI:10.1016/j.powtec.2012.03.030.

Gubicza J., Juhász A., Tasnádi P., Arató P., Vörös G., Determination of the hardness and elastic modulus from continuous vickers indentation testing, J. Mater. Sci., 31 (1996) 3109–3114. DOI:10.1007/BF00354655.

Hayashi Y., Miura T., Shimada T., Onuki Y., Obata Y., Takayama K., Prediction of tablet characteristics from residual stress distribution estimated by the finite element method, J. Pharm. Sci., 102 (2013) 3678–3686. DOI:10.1002/jps.23675.

Huang L., Puri V.M., A three-dimensional finite element model for powder compaction: Time-dependent formulation and validation, Part. Sci. Technol., 18 (2000) 257–274. DOI:10.1080/02726350008906838.

Ilkka J., Paronen P., Prediction of the compression behaviour of powder mixtures by the Heckel equation, Int. J. Pharm., 94 (1993) 181–187. DOI:10.1016/0378-5173(93)90022-8.

Jetzer W.E., Compaction characteristics of binary mixtures, Int. J. Pharm., 31 (1986) 201–207. DOI:10.1016/0378-5173(86)90154-7.

Jiang G., Daehn G.S., Wagoner R.H., Inclusion particle size effects on the cyclic compaction of powder composites, Scr. Mater., 44 (2001) 1117–1123.

Johnson K.L., Contact mechanics, Cambridge university press, 1987.

Jones R., Pollock H.M., Geldart D., Verlinden A., Inter-particle forces in cohesive powders studied by AFM: effects of relative humidity, particle size and wall adhesion, Powder Technol., 132 (2003) 196–210. DOI:10.1016/S0032-5910(03)00072-X.

Kadiri M.S., Michrafy A., Dodds J.A., Pharmaceutical powders compaction: Experimental and numerical analysis of the density distribution, Powder Technol., 157 (2005) 176–182. DOI:10.1016/j.powtec.2005.05.025.

Kaerger J.S., Edge S., Price R., Influence of particle size and shape on flowability and compactibility of binary mixtures of paracetamol and microcrystalline cellulose, Eur. J. Pharm. Sci., 22 (2004) 173–179. DOI:10.1016/j.ejps.2004.03.005.

Kaliyan N., Morey V.R., Factors affecting strength and durability of densified biomass products, Biomass Bioenergy, 33 (2009) 337–359. DOI:10.1016/j.biombioe.2008.08.005.

Kani T., Tamonoki M., Suzuki T., Tsukada M., Kamiya H., Influence of surface-adhered nanoparticles and nanoporous structure on particle–particle interaction of silica, Powder Technol., 176 (2007) 99–107. DOI:10.1016/j.powtec.2007.02.006.

Karamchandani A., Predictive relationships for quality assessment of densified biomass using fundamental mechanical properties of ground corn stover, switchgrass, and willow (master of science dissertation), Pennsylvania State University, 2013.

Karamchandani A., Yi H., Puri V.M., Fundamental mechanical properties of ground switchgrass for quality assessment of pellets, Powder Technol., 283 (2015) 48–56. DOI:10.1016/j.powtec.2015.04.069.

Karamchandani A., Yi H., Puri V.M., Single particle mechanical characterization of ground switchgrass in air dry and wet states using a microextensometer, Powder Technol., 301 (2016) 568–574. DOI:10.1016/j.powtec.2016.06.041.

Kawakita K., Lüdde K.-H., Some considerations on powder compression equations, Powder Technol., 4 (1971) 61–68. DOI:10.1016/0032-5910(71)80001-3.

Kendall K., Relevance of contact mechanics to powders-elasticity, friction and agglomerate strength, Tribol. Part. Technol., (1987) 110–122.

Khan F., Pilpel N., The effect of particle size and moisture on the tensile strength of microcrystalline cellulose powder, Powder Technol., 48 (1986) 145–150.

Kong C.M., Lannutti J.J., Localized densification during the compaction of alumina granules: The Stage I—II transition, J. Am. Ceram. Soc., 83 (2000) 685–690.

Koynov A., Romanski F., Cuitiño A.M., Effects of particle size disparity on the compaction behavior of binary mixtures of pharmaceutical powders, Powder Technol., 236 (2013) 5–11. DOI:10.1016/j.powtec.2012.07.046.

Kruggel-Emden H., Rickelt S., Wirtz S., Scherer V., A study on the validity of the multi-sphere Discrete Element Method, Powder Technol., 188 (2008) 153–165. DOI:10.1016/j.powtec.2008.04.037.

Křupka A., Říha K., Minimal prerequisites for measuring two-dimensional contour roundness in a particle classification context, Powder Technol., 284 (2015) 486–495. DOI:10.1016/j.powtec.2015.07.018.

Krycer I., Pope D.G., Hersey J.A., An evaluation of tablet binding agents part I. Solution binders, Powder Technol., 34 (1983a) 39–51. DOI:10.1016/0032-5910(83)87026-0.

Krycer I., Pope D.G., Hersey J.A., An evaluation of tablet binding agents part II. Pressure binders, Powder Technol., 34 (1983b) 53–56. DOI:10.1016/0032-5910(83)87027-2.

Kuppuswamy R., Anderson S.R., Augsburger L.L., Hoag S.W., Estimation of capping incidence by indentation fracture tests, Aaps PharmSci, 3 (2001) 54–65.

Laitinen O., Bauer K., Niinimäki J., Peuker U.A., Validity of the Rumpf and the Rabinovich adhesion force models for alumina substrates with nanoscale roughness, Powder Technol., 246 (2013) 545–552. DOI:10.1016/j.powtec.2013.05.051.

Leuenberger H., The compressibility and compactibility of powder systems, Int. J. Pharm., 12 (1982) 41–55. DOI:10.1016/0378-5173(82)90132-6.

Li C.-Q., Xu W.-J., Meng Q.-S., Multi-sphere approximation of real particles for DEM simulation based on a modified greedy heuristic algorithm, Powder Technol., 286 (2015) 478–487. DOI:10.1016/j.powtec.2015.08.026.

Ma D., Ong C.W., Zhang T., An Instrumented Indentation Method for Young's Modulus Measurement with Accuracy Estimation, Exp. Mech., 49 (2009) 719–729. DOI:10.1007/s11340-008-9177-6.

Masterson V.M., Cao X., Evaluating particle hardness of pharmaceutical solids using AFM nanoindentation, Int. J. Pharm., 362 (2008) 163–171. DOI:10.1016/j.ijpharm.2008.06.015.

Mazel V., Diarra H., Busignies V., Tchoreloff P., Comparison of different failure tests for pharmaceutical tablets: Applicability of the Drucker–Prager failure criterion, Int. J. Pharm., 470 (2014) 63–69. DOI:10.1016/j.ijpharm.2014.05.006.

McKenna A., McCafferty D.F., Effect of particle size on the compaction mechanism and tensile strength of tablets, J. Pharm. Pharmacol., 34 (1982) 347–351. DOI:10.1111/j.2042-7158.1982.tb04727.x.

Meier M., John E., Wieckhusen D., Wirth W., Peukert W., Influence of mechanical properties on impact fracture: Prediction of the milling behaviour of pharmaceutical powders by nanoindentation, Powder Technol., 188 (2009) 301–313. DOI:10.1016/j.powtec.2008.05.009.

Merrow E.W., Linking R&D to problems experienced in solids processing (product page No. P-7034), Rand Corporation. Retrieved from http://www.rand.org/pubs/papers/P7034.html.

Merrow E.W., Estimating startup times for solids-processing plants, Chem. Eng., 95 (1988) 89–89.

Michrafy A., Dodds J.A., Kadiri M.S., Wall friction in the compaction of pharmaceutical powders: measurement and effect on the density distribution, Powder Technol., 148 (2004) 53–55. DOI:10.1016/j.powtec.2004.09.021.

Michrafy A., Kadiri M.S., Dodds J.A., Wall friction and its effects on the density distribution in the compaction of pharmaceutical excipients, Chem. Eng. Res. Des., 81 (2003) 946–952. DOI:10.1205/026387603322482185.

Michrafy A., Ringenbacher D., Tchoreloff P., Modelling the compaction behaviour of powders: application to pharmaceutical powders, Powder Technol., 127 (2002) 257–266.

Miguélez-Morán A.M., Wu C.-Y., Dong H., Seville J.P.K., Characterisation of density distributions in roller-compacted ribbons using micro-indentation and X-ray micro-computed tomography, Eur. J. Pharm. Biopharm., 72 (2009) 173–182. DOI:10.1016/j.ejpb.2008.12.005.

Mittal B., Yi H., Puri V.M., McNitt A.S., Mancino C.F., Measurement of bulk mechanical properties and modeling the load-response of rootzone sands. Part 2: Effect of moisture on continuous sand mixtures, Part. Sci. Technol., 19 (2001) 369–386. DOI:10.1080/02726350290057895.

Morsi K., Shinde S., Olevsky E.A., Effect of nickel particle size on the compaction behavior of rotator mixed and mechanically alloyed nickel and aluminum powders, Mater. Sci. Eng. A, 426 (2006) 283–288. DOI:10.1016/j.msea.2006.04.027.

Narayan P., Hancock B.C., The relationship between the particle properties, mechanical behavior, and surface roughness of some pharmaceutical excipient compacts, Mater. Sci. Eng. A, 355 (2003) 24–36; 24.

Narayan P., Hancock B.C., The influence of particle size on the surface roughness of pharmaceutical excipient compacts, Mater. Sci. Eng. A, 407 (2005) 226–233; 226.

Oliver W.C., Pharr G.M., An improved technique for determining hardness and elastic modulus using load and displacement sensing indentation experiments, J. Mater. Res., 7 (1992) 1564–1583. DOI:10.1557/JMR.1992.1564.

Pandeya A., Puri V.M., Relationships between tablet physical quality parameters and granulated powder properties: feasibility study, Part. Sci. Technol., 30 (2012) 482–496.

Pavlina E.J., Tyne C.J.V., Correlation of yield strength and tensile strength with hardness for steels, J. Mater. Eng. Perform., 17 (2008) 888–893. DOI:10.1007/s11665-008-9225-5.

Perez-Gandarillas L., Mazor A., Souriou D., Lecoq O., Michrafy A., Compaction behaviour of dry granulated binary mixtures, Powder Technol., 285 (2015) 62–67. DOI:10.1016/j.powtec.2015.05.003.

Phani K.K., A new modified Weibull distribution function, J. Am. Ceram. Soc., 70 (1987) C-182. DOI:10.1111/j.1151-2916.1987.tb05719.x.

Pinto B.M., Carbohydrates and their derivatives including tannins, cellulose, and related lignins, in: Barton S.D., Nakanishi K., Meth-Cohn O. (Eds.) , Comprehensive natural products chemistry, Volume 3, Pergamon, Oxford, 1999., Elsevier, 1999.

Podczeck F., Methods for the practical determination of the mechanical strength of tablets—From empiricism to science, Int. J. Pharm., 436 (2012) 214–232. DOI:10.1016/j.ijpharm.2012.06.059.

Portnikov D., Kalman H., Determination of elastic properties of particles using single particle compression test, Powder Technol., 268 (2014) 244–252. DOI:10.1016/j.powtec.2014.08.011.

Portnikov D., Kalman H., The effect of temperature on elastical properties of individual particles, presented at the 8th international conference for conveying and handling of particulate solids, Tel-Aviv, Israel, 2015.

Richard P., Philippe P., Barbe F., Bourl S. Hane, Thibault X., Bideau D., Analysis by X-ray microtomography of a granular packing undergoing compaction, Phys. Rev. E, 68 (2003) 020301.

Rickman D., Lohn-Wiley B., Knicely J., Hannan B., Probabilistic solid form determined from 2D shape measurement, Powder Technol., 291 (2016) 466–472. DOI:10.1016/j.powtec.2015.10.044.

Riepma K.A., Lerk C.F., de Boer A.H., Bolhuis G.K., Kussendrager K.D., Consolidation and compaction of powder mixtures. I. Binary mixtures of same particle size fractions of different types of crystalline lactose, Int. J. Pharm., 66 (1990) 47–52. DOI:10.1016/0378-5173(90)90383-F.

Riepma K.A., Veenstra J., de Boer A.H., Bolhuis G.K., Zuurman K., Lerk C.F., Vromans H., Consolidation and compaction of powder mixtures: II. Binary mixtures of different particle size fractions of α-lactose monohydrate, Int. J. Pharm., 76 (1991) 9–15. DOI:10.1016/0378-5173(91)90338-O.

Riepma K.A., Zuurman K., Bolhuis G.K., de Boer A.H., Lerk C.F., Consolidation and compaction of powder mixtures: III. Binary mixtures of different particle size fractions of different types of crystalline lactose, Int. J. Pharm., 85 (1992) 121–128. DOI:10.1016/0378-5173(92)90141-N.

Rouèche E., Serris E., Thomas G., Périer-Camby L., Influence of temperature on the compaction of an organic powder and the mechanical strength of tablets, Powder Technol., 162 (2006) 138–144. DOI:10.1016/j.powtec.2005.12.005.

Russell A., Schmelzer J., Müller P., Krüger M., Tomas J., Mechanical properties and failure probability of compact agglomerates, Powder Technol., 286 (2015) 546–556. DOI:10.1016/j.powtec.2015.08.045.

Schofield A., Wroth P., Critical state soil mechanics, McGraw-Hill, London, New York etc., 1968.

Shinohara N., Okumiya M., Hotta T., Nakahira K., Naito M., Uematsu K., Formation mechanisms of processing defects and their relevance to the strength in alumina ceramics made by powder compaction process, J. Mater. Sci., 34 (1999) 4271–4277. DOI:10.1023/A:1004611105281.

Sinka I., Cunningham J., Zavaliangos A., The effect of wall friction in the compaction of pharmaceutical tablets with curved faces: a validation study of the Drucker–Prager Cap model, Powder Technol., 133 (2003) 33–43. DOI:10.1016/S0032-5910(03)00094-9.

Sinka I.C., Burch S.F., Tweed J.H., Cunningham J.C., Measurement of density variations in tablets using X-ray computed tomography, Int. J. Pharm., 271 (2004) 215–224. DOI:10.1016/j.ijpharm.2003.11.022.

Sinka I.C., Motazedian F., Cocks A.C.F., Pitt K.G., The effect of processing parameters on pharmaceutical tablet properties, Powder Technol., 189 (2009) 276–284. DOI:10.1016/j.powtec.2008.04.020.

Skrinjar O., Larsson P.-L., Storåkers B., Local contact compliance relations at compaction of composite powders, J. Appl. Mech., 74 (2005) 164–168. DOI:10.1115/1.2165240.

Sneddon I.N., The relation between load and penetration in the axisymmetric Boussinesq problem for a punch of arbitrary profile, Int. J. Eng. Sci., 3 (1965) 47–57. DOI:10.1016/0020-7225(65)90019-4.

Souriou D., Goeuriot P., Bonnefoy O., Thomas G., Doré F., Influence of the formulation of an alumina powder on compaction, Powder Technol., 190 (2009) 152–159. DOI:10.1016/j.powtec.2008.04.074.

Tanaka M., Komagata M., Tsukada M., Kamiya H., Evaluation of the particle–particle interactions in a toner by colloid probe AFM, Powder Technol., 183 (2008) 273–281. DOI:10.1016/j.powtec.2007.07.039.

Taylor L.J., Papadopoulos D.G., Dunn P.J., Bentham A.C., Mitchell J.C., Snowden M.J., Mechanical characterisation of powders using nanoindentation, Powder Technol., 143–144 (2004) 179–185. DOI:10.1016/j.powtec.2004.04.012.

Tehrani M., Al-Haik M.S., Dyck C., Khraishi T., A practical route for the characterization of zinc powder compacts with the aid of instrumented indentation and scratch tests, Mater. Sci. Eng. A, 528 (2010) 494–499. DOI:10.1016/j.msea.2010.09.033.

Temmerman M., Rabier F., Jensen P.D., Hartmann H., Böhm T., Comparative study of durability test methods for pellets and briquettes, Biomass Bioenergy, 30 (2006) 964–972. DOI:10.1016/j.biombioe.2006.06.008.

Thornton C., Ning Z., A theoretical model for the stick/bounce behaviour of adhesive, elastic-plastic spheres, Powder Technol., 99 (1998) 154–162. DOI:10.1016/S0032-5910(98)00099-0.

Train D., An investigation into the compaction of powders, J. Pharm. Pharmacol., 8 (1956) 745–761.

Tsukada M., Irie R., Yonemochi Y., Noda R., Kamiya H., Watanabe W., Kauppinen E.I., Adhesion force measurement of a DPI size pharmaceutical particle by colloid probe atomic force microscopy, Powder Technol., 141 (2004) 262–269. DOI:10.1016/j.powtec.2004.03.008.

United States Pharmacopeial Convention, USP35 NF30, 2012: U. S. Pharmacopoeia National Formulary, United States Pharmacopeial, 2011.

USP29, General Chapters: <1216> Tablet friability, USP29-NF24, United States Pharmacopeial Convention, Retrieved July 14, 2016, from http://www.pharmacopeia.cn/v29240/usp29nf24s0_c1216.html.

Vinogradov G.A., Komarova L.M., Investigation of the friability of metal powders in connection with rolling conditions, Sov. Powder Metall. Met. Ceram., 1 (1962) 17–22. DOI:10.1007/BF01135025.

Wang W., Towards an improved understanding of strength and anisotropy of cold compacted powder, PhD Thesis, (2007). Retrieved from http://adsabs.harvard.edu/abs/2007PhDT.......106W.

Willems G., Celis J.-P., Lambrechts P., Braem M., Vanherle G., Hardness and Young's modulus determined by nanoindentation technique of filler particles of dental restorative materials compared with human enamel, J. Biomed. Mater. Res., 27 (1993) 747–755.

Wilson T.O., Factors affecting wood pellet durability (Master of Science Dissertation), The Pennsylvania State University, 2010.

Wu Y., Wu X., Yao L., Brunel M., Coëtmellec S., Lebrun D., Gréhan G., Cen K., 3D boundary line measurement of irregular particle with digital holography, Powder Technol., 295 (2016) 96–103. DOI:10.1016/j.powtec.2015.11.061.

Yi H., Mittal B., Puri V.M., Li F., Mancino C.F., Measurement of bulk mechanical properties and modeling the load-response of rootzone sands. Part 1: Round and angular monosize and binary mixtures, Part. Sci. Technol., 19 (2001) 145–173.

Yi H., Mittal B., Puri V.M., MCNitt A.S., Mancino C.F., Measurement of bulk mechanical properties and modeling the load response of rootzone sands. Part 3: Effect of organics and moisture content on continuous sand mixtures, Part. Sci. Technol., 20 (2002) 125–157. DOI:10.1080/02726350215335.

Yohannes B., Gonzalez M., Abebe A., Sprockel O., Nikfar F., Kang S., Cuitino A.M., The role of fine particles on compaction and tensile strength of pharmaceutical powders, Powder Technol., 274 (2015) 372–378. DOI:10.1016/j.powtec.2015.01.035.

York P., Pilpel N., The tensile strength and compression behaviour of lactose, four fatty acids, and their mixtures in relation to tableting., J. Pharm. Pharmacol., 25 (1973) Suppl:1P-11P.

Zhang L., Xu C.C., Lei H., Wang H.L., Ning T.T., Hao W., Hu X.D., Effects of addition of various ingredients during pelletizing on physical characteristics of green tea residue pellets, Appl. Eng. Agric., 30 (2014) 49–53. DOI:10.13031/aea.30.10160.

Zhang Y., Law Y., Chakrabarti S., Physical properties and compact analysis of commonly used direct compression binders, AAPS PharmSciTech, 4 (2003) 489–499. DOI:10.1208/pt040462.

Zhao B., Wang J., 3D quantitative shape analysis on form, roundness, and compactness with μCT, Powder Technol., 291 (2016) 262–275. DOI:10.1016/j.powtec.2015.12.029.

Author’s short biography

Hojae Yi

Dr. Hojae Yi is a Research Associate at the Pennsylvania State University. He earned his Ph.D. degree from the Seoul National University in 2003. He joined the Pennsylvania State University as a visiting scholar in 2000 for one year where he started his researches on powder mechanics. Dr. Hojae Yi has been working at Department of Agricultural and Biological Engineering of the Pennsylvania State University since 2006. His current research interests include experimental studies and mathematical modeling on compaction and flow behavior of particulate materials with emphasis on the multiscale approach.

Anuranjan Pandeya

Dr. Anuranjan Pandeya is currently working at Scientific and Digital Systems Delhi, consulting and catering Food/Pharmaceutical research organizations and industry for their instrumentation need. He is also guest faculty at Birla Institute of Technology, Mesra (India). Dr. Pandeya has been involved in research in the area of powder flow and compaction, particle characterization, and milling behavior of powders, presently and earlier as Ph.D. and post-doctoral scholar at Penn State University. Dr. Pandeya has co-authored several papers in the area of powder and particulate science. He also presented paper and gave technical talks to industries and research institutes.

Apoorva Karamchandani

Apoorva Karamchandani is a doctoral candidate in the department of Agricultural and Biological Engineering at Pennsylvania State University, working under the supervision of distinguished professor Virendra Puri. She received a B. Tech. degree in agricultural engineering from G.B. Pant University, Uttrakhand, India and a master’s degree from Penn State in the same discipline. At Penn State, Apoorva is working in the field of powder mechanics including physical and mechanical characterization of particulates and compaction. Her research explores the ways to improve the efficiency of biomass densification process by developing a fundamental framework to predict end product quality.

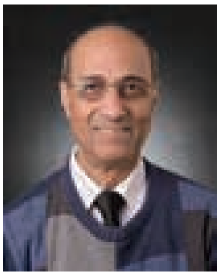

Virendra M. Puri

Dr. Virendra M. Puri, University Distinguished Professor, has researched in the field of powder mechanics for over three decades. He served as Acting Director of the Particulate Materials Center and co-authored numerous publications. He is co-inventor and holder of patents in powder flow, deposition, and compaction and has copyright for multi-purpose computational software on powder processing. Dr. Puri has served on several Editorial Boards, International Advisory Boards, and Chairpersons of bulk solids-related publications and professional activities. Professor Puri is member of KONA North Americas Editorial Board and Co-Editor-in-Chief of *Particulate Science and Technology*. He has received several teaching and research awards.

KONA Powder and Particle Journal No. 35 (2018) 49–65/Doi:10.14356/kona.2018011 Review Paper

Direct Permeation of Nanoparticles Across Cell Membrane: A Review[†]

Hideya Nakamura* **and Satoru Watano**

[1] *Department of Chemical Engineering, Osaka Prefecture University, Japan*

Abstract

Nanoparticles have attracted much attention as a key material for new biomedical and pharmaceutical applications. For success in these applications, the nanoparticles are required to translocate across the cell membrane and to reach to inside of the cell. Among several translocation pathways of nanoparticles, the direct permeation pathway has a great advantage due to its high delivery efficacy. However, despite many research efforts, key properties and factors for driving the direct permeation of nanoparticle and its underlying mechanisms are far from being understood. In this article, experimental and computational studies regarding the direct permeation of nanoparticles across a cell membrane will be reviewed. Firstly, experimental studies on the nanoparticle-cell interactions, where spontaneous direct permeation of nanoparticles was observed, are reviewed. From the experimental studies, potential key physico-chemical properties of nanoparticles for their direct permeation are discussed. Secondly, physical methods such as electroporation and sonoporation for delivering nanoparticles into cells are reviewed. Current status of technologies for facilitating the direct permeation of nanoparticle is presented. Finally, we review molecular dynamics simulation studies and present the latest findings on the underlying molecular mechanisms of the direct permeation of nanoparticle.

Keywords: nanoparticle, direct permeation, cell membrane, non-endocytosis, physical delivery, computer simulation

1. Introduction

With recent advances in nanoscience and nanotechnology, nanoparticles (NPs) have attracted much attention as a key material for the new biomedical and pharmaceutical applications. The NPs, defined as materials with at least one dimension in the size range smaller than 100 nm, exhibit significant unique properties that can be useful for the biomedical and pharmaceutical applications. The highly tunable size, structure, and surface properties of NPs at a nanometer scale can be exploited as carrier platforms for drug-, gene-, macromolecule-deliveries (Rana et al., 2012; Shao et al., 2015; Wilczewska et al., 2012). The fluorescence properties of semiconductor NPs can be used for bioimaging (Ekimov et al., 1985; Luo et al., 2012; Weller et al., 1986; Yuan et al., 2013). The unique plasmonic properties of metal NPs can be exploited for simultaneous imaging and photothermal therapies (Dreaden et al., 2011; Huang et al., 2006; Jaque et al., 2014; Kennedy et al., 2011; Périgo et al., 2015; Xiong et al., 2014). The magnetic properties of metal and metal-oxide NPs can be utilized for magnetic resonance imaging and magnetic fluid hyperthermia treatment for cancer therapy (Fortin et al., 2007; Veiseh et al., 2011). Meanwhile, many experimental investigations suggest that use of NPs can cause harmful effects: concerns about nanotoxicity have been elicited. It has been reported that NPs can cause cell membrane disruptions and significant increase in cell death at cellular level (Kahru and Ivask, 2013; Pietroiusti, 2012). NPs can also cause negative physiological effects such as inflammatory and immunological responses, resulting in adverse effects even at in vivo levels (Kim et al., 2013).

For success in the biomedical and pharmaceutical applications (i.e., for maximizing the NPs' beneficial effects and minimizing their potential adverse effects), the NPs are required to be transported into the cell and localized at targeted cellular component without any damage to the cell. When the NPs are transported into the cell, the most critical barrier is the cell membrane. The cell membrane is a fundamental biological barrier and mainly composed of a lipid bilayer with membrane proteins. Transport of extracellular matters into a cell is selectively regulated by the cell membrane. Therefore, a key issue to realize the

---

[†] Received 5 April 2017; Accepted 20 June 2017
J-STAGE Advance published online 30 July 2017

[1] 1-1 Gakuen-cho, Naka-ku, Sakai, Osaka 599-8531, Japan
* Corresponding author: Hideya Nakamura;
E-mail: hnakamura@chemeng.osakafu-u.ac.jp
TEL: +81-72-254-9451 FAX: +81-72-254-9451

potential applications of NPs is development of a technology that can control the NP translocation across the cell membrane. To develop such a technology, understanding of mechanisms of the NP translocation across a cell membrane is necessary.

Through many research efforts up to now, it has been found that translocation of NPs across a cell membrane can be classified into two major pathways: endocytosis and direct permeation (Beddoes et al., 2015; Ding and Ma, 2015; Qu et al., 2013). **Fig. 1** shows a schematic illustration of the NP translocation pathways. Endocytosis is an intrinsic cellular function to take up extracellular substances into the cell. In the endocytosis, a small portion of the cell membrane deforms and wraps extracellular NPs. Subsequently, the cell membrane pinches off and an endocytic vesicle which encloses the NPs is formed. The NPs enclosed by the endocytic vesicle are finally transported into the cell, leading to the NP translocation across the cell membrane. The direct permeation is defined as a non-endocytic translocation pathway. In this pathway, NPs permeates across the cell membrane without confinement of the NPs by the endocytic vesicles, leading to direct delivery of the NPs into the cell.

According to the reviews of experimental investigations (Beddoes et al., 2015; Qu et al., 2013; Zhu et al., 2013), it has been recognized that the endocytosis is a major translocation pathway when NPs interact with the cells, while the direct permeation is a minor one. However, the endocytosis possesses a significant drawback for the biomedical and pharmaceutical applications. The endocytosed NPs cannot often escape from the endocytic vesicles and cannot reach to the targeted cellular component even after translocating across the cell membrane (Ding and Ma, 2015). This leads to low delivery efficacy that is a critical issue for the biomedical and pharmaceutical applications. By contrast, in the direct permeation, NPs reach to inside of the cell without entrapment of NPs by vesicles, resulting in high delivery efficacy. This is a great advantage over the endocytosis, while the direct permeation is a rare event as compared to the endocytosis. To overcome this issue and facilitate the direct permeation, some physical methods, where external forces such as electric field or ultrasound are applied to the cell, are promising (Al-Dosari and Gao, 2009; Mehierhumbert and Guy, 2005). The physical methods were originally developed for gene transfer into cells. Recently, these are exploited for the direct delivery of NPs (Carrasco et al., 2016; Huang et al., 2014; Kawano et al., 2006; Kim et al., 2011; Lin et al., 2009; Wang et al., 2014; Yang et al., 2011; Zu et al., 2014).

Understanding of the mechanism of the direct permeation of NPs across the cell membrane with or without external forces can greatly contribute to realize an ideal NP delivery method with both high delivery efficacy and less damage to the cell. The direct permeation of NPs can be controlled by two potential key factors: physicochemical properties of the NPs; nature and conditions of the external forces. However, despite many research efforts, it is still very challenging to control the direct permeation of NPs across a cell membrane. The key properties and factors for controlling the NP direct permeation and its underlying mechanisms are far from being understood. This lack of understanding hinders the development of new technology which can control the NP direct permeation, and also hinders the design of NPs with suitable properties for their applications.

In this article, the existing studies regarding the direct permeation of NPs across the cell membrane will be reviewed. Our aim is to present (i) potential key physicochemical properties of NPs for their direct permeation; (ii) potential physical methods for facilitating the NP direct permeation; (iii) current understanding of the molecular

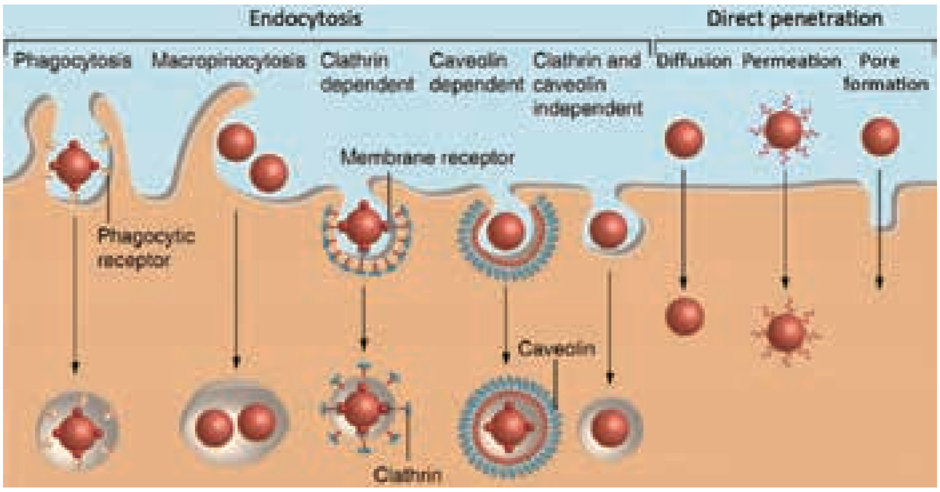

Fig. 1 Translocation pathways of nanoparticles across cell membrane. Reprinted with permission from Ref. (Qu et al., 2013). Copyright: (2013) Future Science Group.

mechanisms of the NP direct permeation. Firstly, experimental studies on the nanoparticle-cell interactions, where the direct permeation of NPs without applying external forces were reported, will be reviewed. From this review, we will extract insights into key physico-chemical properties of NPs for their direct permeation. Subsequently, potential physical methods such as electroporation and sonoporation for facilitating the NP direct permeation are reviewed. Finally, computational studies will also be reviewed, and the latest findings on the underlying molecular mechanisms of the NP direct permeation will be presented.

2. Key physico-chemical properties of NPs for their direct permeation: insights from experimental studies

There are many factors that can affect the NP-cell membrane interactions. Among the potential key factors, physico-chemical properties of the NPs (e.g., size, shape, charge, hydrophobicity/hydrophilicity, surface chemistry, and others) can highly influence the NP-cell membrane interactions. Although there are some reviews on the key NP properties for the NP-cell membrane interactions including adhesion, endocytosis, and membrane disruption (Beddoes et al., 2015; Qu et al., 2013; Verma and Stellacci, 2010; Zhu et al., 2013), the potential key properties for the NP direct permeation have not been reviewed. Herein, we have surveyed numerous experimental studies and will discuss the potential key physico-chemical properties for their direct permeation across cell membranes. In this section, we will only focus on the NP direct permeation without applying external forces, i.e., passive permeation of NPs.

Table 1 shows a summary of experimental studies in which the direct permeation of NPs across a cell membrane was observed. First of all, size of the NPs can be an important factor. In general, for NPs in the size range from several tens to hundreds of nanometers, endocytosis is a major mode of NPs' translocation across a cell membrane. However, for very small NPs, it can be considered that the endocytosis may be unfavorable. Yi et al. (2011) calculated an energy change resulting from the membrane wrapping of a single NP using a thermodynamic theory proposed by Helfrich (1973). Their results exhibited that a higher energy cost was required for the membrane wrapping of a smaller NP, while the membrane wrapping of a larger NP was energetically favorable. Thus, it is expected that for the smaller NPs the direct permeation can be favorable (Ding and Ma, 2015). In fact, as seen in **Table 1**, the size of NPs that exhibited the direct permeation is mostly less than 20 nm. Van Lehn et al. (2013) showed that even with very tiny decrease in the NP size from 5.8 nm to 2.4 nm, amount of NPs entering into cells by the direct permeation significantly increased. Jiang et al. (2015) also reported that the uptake amount of NPs through the direct permeation showed significant dependence on the NP size within a small range of 2 to 6 nm. Although there is no general consensus yet, the experimental results imply that for delivering NPs into cells by the direct permeation mode, size of the NPs seems to be desired to be smaller than 50 nm at least. NPs smaller than 10 nm are more preferred.

The surface charge of NPs can also affect the NP-cell membrane interactions. Many studies regarding NP-cell interactions have pointed out that positively charged NPs are more likely to provide significant influence on the cell as compared to neutral or negatively charged NPs due to attractive electrostatic interactions with the negatively charged cell membranes (Beddoes et al., 2015; Cho et al., 2009; Verma and Stellacci, 2010). However, as shown in **Table 1**, the direct permeation of NPs has been observed regardless of the surface charge of the NPs: i.e., the NPs' surface charge may not be determinant for the direct permeation. As seen in **Table 1**, a positively charged NP exhibited higher uptake through the direct penetration pathway than neutral and negatively charged NPs (Arvizo et al., 2010; Cho et al., 2009), while a negatively charged NP exhibited the direct permeation (Jewell et al., 2011; Lund et al., 2011; Van Lehn et al., 2013; Verma et al., 2008). Van Lehn et al. (2013) reported that the negatively charged gold NP directly penetrates into the synthetic vesicle without disruption of the vesicle membrane, while other studies reported that positively charged NPs can induce disruption of cell membranes, leading to cell death (Hong et al., 2004, 2006). Jiang et al. (2015) observed that the zwitterionic NP was primarily uptaken by the direct permeation, while the positively and negatively charged NPs were primarily uptaken by endocytic pathways. In summary, from the current experimental findings it can be considered that the NPs' surface charge is not likely to be a determinant of the NP direct permeation.

Hydrophobicity/hydrophilicity of the NPs can be an important property, because the cell membranes are composed of amphiphilic phospholipid molecules. Goda et al. (2010) found that their synthesized NP composed of amphiphilic random copolymer exhibited the direct permeation, while another NP composed of solely hydrophilic polymer failed to penetrate into the cell. Liu et al. (2013) reported that temperature sensitive pNIPAM particles with a size of 3 μm, which is much larger size, can directly penetrate into phospholipid vesicles and Hela cells. They considered that this is due to phase transition of the pNIPAM from hydrophilic to hydrophobic at an elevated temperature above its phase transition criterion. From these studies, amphiphilic nature seems to be favorable for the direct permeation, although further investigations are necessary.

Table 1 Summary of experimental studies in which direct permeation of nanoparticles across cell membrane was observed.

Reference	Nanoparticle properties				Types of cell/ membrane[a]	Culture/ dispersion medium[b] and presence/absence of serum[c]	Comments
	Material	Size (nm)	Surface modification	Surface charge/ potential			
Arvizo et al. (2010)	Gold	10	Ligand terminals with: (i) cationic (ii) neutral (iii) anionic (iv) zwitterionic	(i) 24 mV (ii) –1 mV (iii) –38 mV (iv) –2 mV	• CP70 and A2780 • BEC • ASM	• Serum-free DMEM • Serum-free BEGM	• (i) showed higher cellular uptake • (i) directly penetrated into cells without endosomal trap
Cho et al. (2009)	Gold	18	(i) PAA (ii) Citrate (iii) PVA	(i) 20 mV (ii) –10 mV (iii) –4 mV	SK-BR-3	• McCoy's 5a with FBS	(i) showed direct permeation
Geiser et al. (2005)	Gold	25	—	—	• Porcine lung macrophage • Human RBC	RPMI1640 with FBS	NP directly penetrated into both of cells
Goda et al. (2010)	Amphiphilic co-polymer	10–12	—	2 to 4 mV	HepG2	DMEM with FBS	NP showed direct permeation
Hong et al. (2004, 2006)	Cationic dendrimers	10–100	Amine terminated surface	Positively charged	• Supported DMPC bilayer • KB and Rat2	• NaCl aq. • RPMI1640 and DMEM with FBS	NP formed holes on membranes, followed by direct permeation
Jewell et al. (2011)	Gold	5	(i) Structured anionic and neutral ligands (ii) Neutral ligands	Negatively charged (both)	B16-F0	Serum-free DMEM	(i) was uptaken by direct permeation, whereas (ii) was uptaken by endocytosis
Jiang et al. (2015)	Gold	2–6	Ligand terminals with: (i) cationic (ii) zwitterionic (iii) anionic	(i) 18 mV (ii) –7 mV (iii) –43 mV	Hela cell	Serum-free DMEM	• NP uptake decreased in larger NP size at (i) and (iii), whereas the uptake increased in larger NP at (ii) • (ii) was uptaken by direct permeation, while (i) and (iii) were uptaken by endocytosis
Leroueil et al. (2008)	Gold	5	Alkylamine	Positively charged	Supported DMPC bilayer	NaCl aq.	NP formed holes on membrane, followed by direct permeation
Leroueil et al. (2008)	SiO_2	50	Amine terminated surface	Positively charged	Supported DMPC bilayer	NaCl aq.	NP formed holes on membrane, followed by direct permeation
Liu et al. (2013)	pNIPAM	2700	—	—	• DOPC and DOTAP GUV • Hela cell	• Sucrose buffer solution • DMEM	Direct permeation was observed at an elevated temperature, inducing phase transition of NP from hydrophilic to hydrophobic
Lund et al. (2011)	Gold	4	(i) Glucose ligands (ii) Glucose-glutathione mixed ligands	(i) Neutral (ii) Negatively charged	HCT-116, HT 29, LS154T, and SW640	DMEM	NPs directly penetrated into cell
Mu et al. (2012)	SiO_2	14	—	—	A549	DMEM with FBS	NP directly penetrated into cell
Nativo et al. (2008)	Gold	16	Coated with cell penetrating peptides	—	Hela cell	DMEM with FBS	NP directly penetrated into cell
Rothen-Rutishauser et al. (2006)	Gold	25	(i) BSA coated (ii) Cationic ligand	—	Human RBC	RPMI1640 with human serum	Both of NPs directly penetrated into cell
Rothen-Rutishauser et al. (2006)	TiO_2 (anatase)	20–30	—	—	Human RBC	RPMI1640 with human serum	NP directly penetrated into cell

Table 1 Summary of experimental studies in which direct permeation of nanoparticles across cell membrane was observed (contd.).

Reference	Nanoparticle properties				Types of cell/ membrane[a]	Culture/ dispersion medium[b] and presence/absence of serum[c]	Comments
	Material	Size (nm)	Surface modification	Surface charge/ potential			
Van Lehn et al. (2013)	Gold	2.4–5.8	Anionic ligand	Negatively charged	Hela cell	—	• NPs directly penetrated into cell regardless of the size • NPs smaller than 3 nm showed significant increase in uptake amount
Van Lehn et al. (2013)	Gold	2.2	Anionic and neutral ligands	Negatively charged	DOPC vesicle	Sucrose aq.	• NPs directly penetrated into vesicles without disruption of bilayers
Veiseh et al. (2011)	Iron oxide	54	Coated with PEG and poly-arginine	—	• C6 • MCF7	DMEM with FBS	• NP directly penetrated into cell
Verma et al. (2008)	Gold	5	(i) Structured or (ii) unstructured anionic and neutral ligands	(i) –30 mV (ii) –30 mV	DC2.4	Serum-free RPMI640	(i) directly penetrated into cells without membrane disruption, whereas (ii) was trapped in endosomes
Wang et al. (2012)	CdSe/ZnS quantum dots	8	Zwitterionic ligand	—	Human RBC	Serum-free PBS	NP directly penetrated into cell
Yu et al. (2007)	Silver	—	Designed peptide	—	NIH 3T3	Serum-free DMEM	NP directly penetrated into cell

[a] CP70 and A2780: human ovarian cancer cell lines. BEC: human bronchial epithelial cell line. ASM: human airway smooth muscle cell line. SK-BR-3: human breast cancer cell line. RBC: red blood cell. HepG2: human hepatocyte carcinoma cell line. KB: human epithelial cell line. Rat2: rat fibroblasts cell line. B16-F0: mouse melanoma cell line. Hela cell: human cervical cancer cell line. DMPC: 1,2-dimyristoyl-sn-glycero-3-phosphocholine. DOPC: 1,2-dioleoyl-sn-glycero-3-phosphocholine. DOTAP: 1,2-dioleoyl-3-trimethylammonium-propane. GUV: giant unilamellar vesicle. HCT-116, HT 29, LS154T, and SW640: human colorectal cell lines. A549: human lung epithelial cell line. C6: rat glioma cell line. MCF7: human adenocarcinoma cell line. DC2.4: mouse dendritic cell line. NIH 3T3: mouse embryonic fibroblasts cell line.

[b] DMEM: Dulbecco's modified Eagle's medium. BEGM: bronchial epithelial growth medium. RPMI1640: Roswell Park Memorial Institute 1640 medium. PBS: phosphate buffered saline.

[c] FBS: fetal bovine serum.

Surface modification of NPs is effective to control the NP direct permeation. As seen in **Table 1**, variety of functional groups, ligands, biomolecules, polymers have been investigated as surface modifiers to facilitate the NP direct penetration. It has also been found that not only types of modifiers but also their structural arrangement can be a key factor for the NP direct permeation. Verma et al. (2008) synthesized two kinds of gold nanoparticles coated by anionic and neutral ligands with same size, same surface charge, and same ligand composition. One particle was coated in an ordered striped arrangement of anionic and neutral ligands, while the another particle was coated with the same two ligands in a random arrangement. They found that the former particle with the ordered arrangement can directly permeate across the cell membrane without the membrane disruption, whereas the latter particle with the random arrangement was mostly trapped in endosomes by the endocytosis. A similar result has been observed in Jewell et al. (2011). A possible explanation on this effect is that the ligand pattern in the ordered arrangement may be assumed to be more rigid, resulting in the direct permeation across the cell membrane (a more fluid layer) without the membrane disruption, which is similar mechanism for cell penetrating peptides (Verma et al., 2008).

With regard to material of the NPs, it seems that gold is likely to exhibit the direct permeation across cell membranes as compared to other materials (**Table 1**). However, we are speculating that this is not attributed to the material but to the size requirement for the direct permeation. Size of the gold NPs is generally highly tunable. Synthesis of gold NPs smaller than 10 nm is facile as compared to other materials. This may be a possible reason behind the specificity of gold shown in **Table 1**.

The membrane properties can be important factors for the NP direct permeation. Moreover, external environmental conditions such as pH, osmotic pressure, ionic strength, and presence of serum proteins can also be important factors. However, influences of these factors on the NP direct permeation have not been investigated.

3. Physical methods for NP direct delivery

For direct delivery of extracellular objects into the cell, some physical methods have been developed. The physical methods here refer to physical manipulations to improve the efficacy (rate and extent) of the delivery of extracellular objects. Over the past two decades, the following physical methods have been developed for the gene delivery into cells: electroporation; sonoporation; laser irradiation; magnetofection; etc. (Al-Dosari and Gao, 2009; Mehierhumbert and Guy, 2005). In these methods, the cells are exposed to each type of external force fields, forming transient defects and pores in the cell membrane. This results in temporal enhancement of permeability of the cell membrane, leading to direct permeation of extracellular objects in the surrounding medium across the cell membrane. Meanwhile, an increase in cellular mortality can often be a great concern in these physical methods, if cells are subjected to the excess stress derived from the applied external forces. With regard to the direct delivery of NPs, the electroporation (Huang et al., 2014; Kawano et al., 2006; Kim et al., 2011; Lin et al., 2009; Zu et al., 2014) and sonoporation (Carrasco et al., 2016; Wang et al., 2014; Yang et al., 2011) have been utilized in recent. In the following, these studies will be reviewed.

Electroporation is a technique where an electric field (a high intensity electric pulse) is applied to cells. The electric pulse can cause local destabilization of the cell membranes followed by electric field-induced transient pores, resulting in the direct delivery of extracellular objects into the cell. More details of fundamental physics of the electroporation can be found in many literatures (e.g., Al-Dosari and Gao, 2009; Gehl, 2003; Kotnik et al., 2015; Mehierhumbert and Guy, 2005). The electroporation treatment is able to be applied to cells adhered on a culture dish as well as cells suspended in a culture media. Several types of electrodes for both types of cells have been developed and commercially available.

Recently, the electroporation has been utilized for delivery of NPs into cells. These NPs include DNA-conjugated gold NPs with 100 to 200 nm diameter (Huang et al., 2014; Kawano et al., 2006; Zu et al., 2014), silver NPs with 80 nm diameter (Lin et al., 2009), and hollow metal NPs coated with mesoporous silica layer with 65 nm diameter (Kim et al., 2011). These experimental studies demonstrated significant enhancement of delivery efficacy of NPs with the electroporation treatment. Huang et al. (2014) and Zu et al. (2014) showed that with the electroporation treatment the dominant NP delivery pathway into cells shifted from the endocytosis to the direct permeation. It should be noted that even NPs with relatively large particle size (ca. 100 nm) can be directly delivered into cells through the direct permeation pathway using the electroporation. However, negative impacts on cellular functions such as viability and cell differentiation were somewhat found after the electroporation (Huang et al., 2014; Kim et al., 2011). To overcome this disadvantage, some efforts have been reported. Zu et al. (2014) found that both of high delivery efficacy of DNA-conjugated NPs and low cell mortality can be achieved by adding pristine gold NPs as an additive. They considered that this is due to decreasing the electric resistance of the medium with highly conducting gold NPs, resulting in much lower applied intensity required for the delivery. A new electroporation system integrated with microfluidic devices has also been proposed (Geng and Lu, 2013; Wang et al., 2010). In the microfluidic electroporation system, a single cell can be manipulated and be exposed to uniform electric field, as compared to conventional batch electroporation where electric pulse is applied to a bulk cell suspension. This can provide a precise control of electric field per single cell, leading to improvement on the delivery efficacy and less cellular damage.

In order to realize an ideal electroporation-assisted NP delivery with high delivery efficacy and less cellular damage, it is necessary to understand the mechanism underlying the NP permeation in an electric field. In particular, role of NPs' physico-chemical properties on the mechanism of the NP permeation remains subject of investigation. Elucidation of this mechanism can greatly contribute to optimize design of the NPs and operating conditions of the electroporation (e.g., strength and frequency of the electric current, number of electric pulses, and so on).

Sonoporation is a technique where an ultrasound is applied to a suspension of cells and microbubbles. It has been considered that an acoustic cavitation is a central cause of enhancement of the permeability of the cell membranes. Acoustic cavitation generated by the ultrasound irradiation can cause generation, oscillation, and collapse of active bubbles. This results in a release of associated mechanical stresses such as radiation force, micro-streaming, micro-jets, or shock waves, leading to the transient pore formation across adjacent cell membranes. According to this mechanism, the ultrasound-mediated bubbles are necessary for the sonoporation. In clinical applications, ultrasound contrast agents consisting of microbubbles stabilized by surface active molecules such as proteins, polymers, and lipids have often been used for the sonoporation-assisting agents. More details of fundamentals and historical development of the sonoporation can be found in many literatures (e.g., Al-Dosari and Gao, 2009; Kodama et al., 2006; Mehierhumbert and Guy, 2005; Zhou et al., 2014).

Recently, sonoporation-assisted NP deliveries have been investigated. Carrasco et al. (2016) employed a shock wave irradiation for delivery of mesoporous silica NPs into human embryo kidney cells. Although no microbubble additives were used, they verified that the shock wave irradiation significantly enhanced the delivery of the mesoporous silica NPs with 200 nm diameter. Another approach in which NPs/microbubble composites are synthesized and utilized for better delivery of NPs has also been investigated. Wang et al. (2014) synthesized a gold nanorod (AuNR)-microbubble composite, in which AuNRs were encapsulated in perfluorocarbon gas filled microbubbles (3 to 5 µm diameter) covered with a protein/antibody shell. Amount of the AuNRs delivered into tumor cells showed significant increase when the AuNR/microbubble composite was used with a sonoporation treatment as compared to the control condition (without encapsulation of AuNRs in microbubbles). This study suggests that encapsulation of NPs in microbubbles can enhance the delivery performance of NPs in the sonoporation treatment. Yang et al. (2011) synthesized NP-embedded microbubbles composite in which Fe_3O_4 nanoparticles (12 nm diameter) were embedded in a polymer layer covering microbubble (3 to 5 µm diameter). They showed that amount of Fe_3O_4 nanoparticles delivered into tumor cells significantly increased by the ultrasound irradiation. They also found that the Fe_3O_4-embedded microbubbles exhibited higher cell viability as compared to a control condition under the same ultra sound intensity. This suggests that NPs/microbubble composites can reduce damage to the cells associated with the sonoporation.

Many questions and issues still remain unsolved in the sonoporation-assisted NP permeation. Operating conditions of the sonoporation treatment (e.g., intensity, frequency, duration of the ultrasound irradiation) can be key factors. Wang et al. (2014) and Yang et al. (2011) suggested that NP delivery rate can be controlled by the intensity and number of the ultrasound irradiation. Physico-chemical properties of NPs can also be important factors. Carrasco et al. (2016) found that a surface coating of NP with cationic lipid molecules attenuate the decrease in the cell viability after the sonoporation treatment. Interaction between NPs and microbubble is also important subject of investigation, when NPs/microbubble composites will be employed. Role of these potential key factors should be investigated to optimize the sonoporation-assisted NP permeation.

4. Molecular mechanisms of the NP direct permeation: insights from molecular dynamics simulations

Understanding of the mechanism of the direct permeation of NPs across a cell membrane can greatly contribute to synthesizing new NPs and to developing a new NP delivery technique with high delivery efficacy and less cellular damage. However, the molecular mechanism underlying the NP direct permeation is poorly understood. Although a lot of experimental studies on the NP–cell membrane interactions have been conducted, it is still difficult to investigate the molecular mechanism using current experimental techniques. One of the potential ways to investigate the NP–cell membrane interactions is a computational modeling. In particular, molecular dynamics (MD) simulations can be a powerful approach. In the MD simulations, trajectories of individual atom can be calculated so that dynamic evolution of the system consisting of the NP, lipid molecules, and solvents can be simulated at the molecular scale. This can provide deep insights into the understanding of the NP-cell membrane interactions. Coarse-grained MD methods have often been adapted for the NP-cell membrane interactions. In the coarse-grained MD methods, small groups of atoms are represented by a single interaction sites as coarse-grained sites. This can greatly reduce the computational load and enables to simulate the NP-cell membrane interactions with appropriate system size (larger than ten nanometers) and length of time (longer than a few hundred nanoseconds). More details of the MD simulation methods for the NP-cell membrane interactions can be found in the literatures (Ding and Ma, 2015; Qu et al., 2013; Rossi and Monticelli, 2016).

We surveyed MD simulation studies reported so far, and simulated final fates of NPs after interacting with a lipid bilayer (model cell membrane) will be reviewed. **Fig. 2** shows summary of the final fates of NPs reported in previous studies. The MD simulation studies suggest that the final fates of the NPs will become either adhesion, penetration, or wrapping (**Fig. 2(a)**). Here, it should be noted that the further permeation of the NPs across the membrane cannot be observed unless applying external force on the NP (**Fig. 2(b)**) or adopting some additional settings (**Fig. 2(c)**). This review is focusing on the direct permeation, thus, we will review the MD simulation studies which can be classified into groups of **Fig. 2(b)** and **(c)**. We here define the terms to distinguish between these two groups: "biased" and "unbiased" MD simulations. The biased MD simulations correspond to **Fig. 2(b)**, where a NP was artificially forced to permeate across the membrane. Although this is far from a reality, the biased MD simulations can provide insights into that how the NPs can be designed to achieve high permeability and low cellular damage. On the other hand, the unbiased MD simulations correspond to **Fig. 2(c)**, where any external forces are not exerted on the NP, but other additional settings are adopted. The unbiased MD simulations can provide insight into physical requirements for the direct permeation of NPs across a lipid bilayer. In the following sections, the biased and unbiased MD simulation studies will be reviewed, respectively.

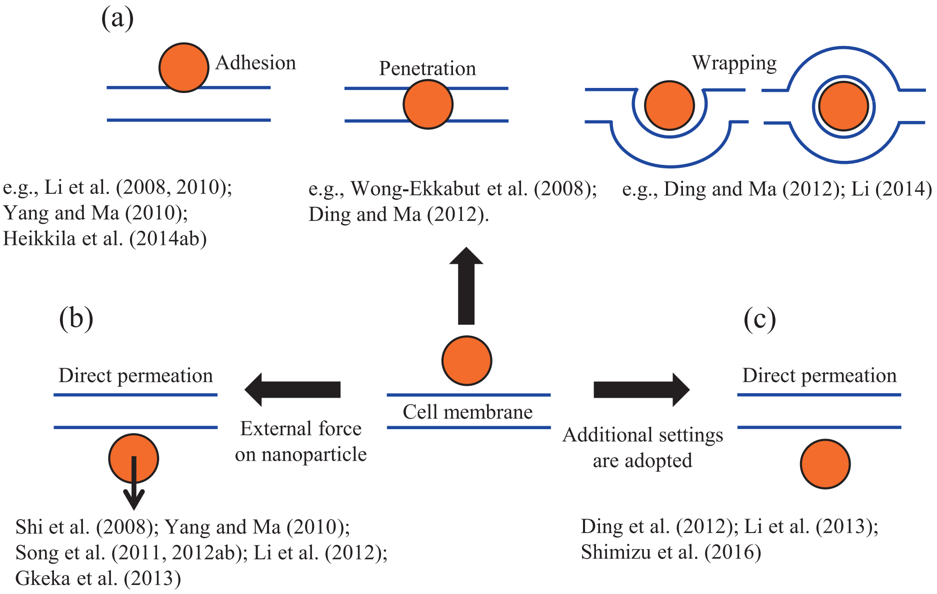

	(a)	(b)	(c)
External force on nanoparticle	No	Yes	No
Other additional settings*	No	No	Yes

*Including transmembrane potential, multiple NPs, and reversible reaction

Fig. 2 Summary of final fates of nanoparticles after interacting with lipid bilayer reported in MD simulation studies.

4.1 Biased MD simulation studies

As mentioned above, the biased MD simulations, where the NP is forced to permeate across the membrane by applying an external force to the NP, have been conducted for investigating potential key NP properties for the NP direct permeation across a cell membrane. The permeation process has been characterized by physical and thermodynamic properties such as the minimal driving force required for the NPs to permeate lipid bilayers and the potential of mean force (i.e., the free energy change) along the NP permeation across the cell membrane.

Song et al. (2011) investigated influence of NP size on the direct permeation across a phospholipid bilayer by means of the biased MD simulation. They used gold NPs in the range of 0.8 to 2.5 nm diameter and with nearly spherical shape. They calculated the minimum driving force required to permeate a DPPC bilayer at various NP sizes. With a decrease in the size of gold NP, the driving force was smaller. This result is similar with an experimental observation presented in Section 2: the smaller the nanoparticle, the easier it is for the direct permeation. The minimum force for permeating whole bilayer (both first and second monolayers) was ca. 100 to 500 pN in the range of the size of 0.8 to 2.5 nm. Song et al. (2011) also reported that the minimum force calculated from their unbiased MD simulations showed an agreement with an experimental result obtained from an atomic force microscopy (Vakarelski et al., 2007), although further investigations seem to be needed. They also calculated the minimum driving pressure, which was defined by the minimum force per cross-sectional area of the NP. They found that the pressure required to permeate whole bilayer deceased with an increase in the nanoparticle size.

Shape of the NP is another key property. Some computational modeling studies on the role of particle shape in the NP permeation have been performed. From the previous studies, a consensus has been addressed: the sharp shape can be advantageous for the NP direct permeation. Yang and Ma (2010) performed a MD simulation of the NP permeation across a lipid bilayer (**Fig. 3(a)**). They calculated the minimum driving force of NPs with various shapes (**Fig. 3(b)**) by means of the biased MD simulation. Their result (**Fig. 3(c)**) revealed that the higher minimum driving force was required at larger radius *r* (i.e., larger contact area between particle and bilayer), while the minimum driving force was less sensitive to the particle height *h*. Interestingly, the minimum driving force significantly decreased even at higher particle height in the case of the V-shaped particle (the green circle plot in **Fig. 3(c)**), where the local curvature at the contact surface between the NP and bilayer was much higher and the disruption area due to the particle permeation gradually increased as the NP permeated into the membrane. The authors con-

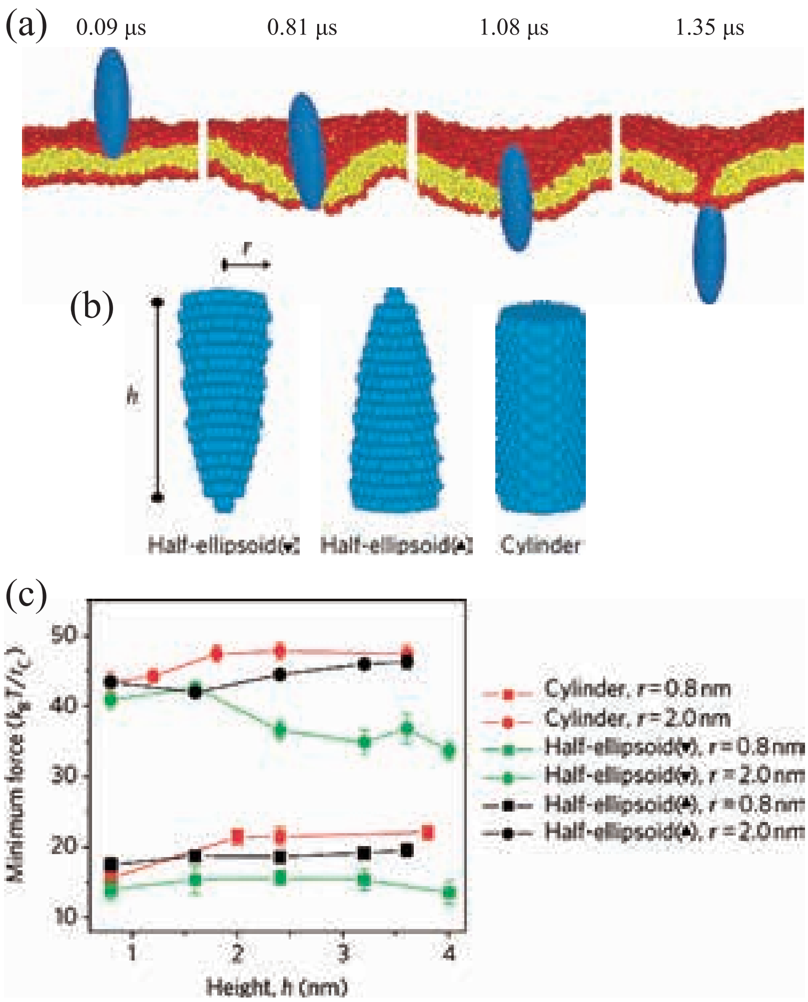

Fig. 3 **(a)** Permeation behavior of elongated nanoparticle in biased MD simulation. **(b)** Various particle shapes and **(c)** minimum driving force for their direct permeation across lipid bilayer. Reprinted with permission from Ref. (Yang and Ma, 2010). Copyright: (2010) Nature Publishing Group.

cluded that the permeability of nanoparticles with anisotropic shapes can be determined by the contact area and the local curvature: i.e., the direct permeation can be more likely to occur at the smaller contact area and the higher local curvature. They also demonstrated that the initial orientation of the NP toward the lipid bilayer strongly relates to the capability of the NP direct permeation across the lipid bilayer. Shi et al. (2008) investigated permeation behavior of carbon nanotubes (CNTs) with different tube diameters. Their simulation result showed the tube diameter can be a determinant of the permeation mode of the CNTs: a CNT with smaller tube diameter (single-walled CNT) can directly permeate the bilayer via a piercing mode, while a CNT with larger tube diameter (multi-walled CNT) is likely to translocate the lipid bilayer via a wrapping mode. Moreover, they proposed theoretical models for the piercing and wrapping modes based on a vacancy diffusion theory and a fluid mechanics theory for an imcompressible viscous fluid. As a result, they successfully explained that the dominant permeation mode can switch from the piercing to the wrapping at a critical radius as the tube radius increases.

In most of the biomedical and pharmaceutical applications utilizing NPs, surface modifications of the NPs have been frequently conducted to modify surface properties such as surface charge, hydrophilicity/ hydrophobicity, and specific interactions with cells. This can control the NP translocation across the cell membrane. Some biased MD simulation studies have investigated that how surface modifications of NP affect its permeation across a lipid bilayer. Song et al. (2012a) performed a MD simulation of permeation behavior of ligand-coated nanoparticles across a DPPC bilayer. They used alkanethiol-coated gold nanoparticles with different alkyl chain lengths. By means of a biased MD simulation, influence of the ligand length on the minimum driving force to permeate the bilayer was investigated. With an increase in the ligand length, the minimum driving force for permeating the first layer of the lipid bilayer was reduced, while the higher driving force was required to permeate the second layer and whole lipid bilayer. This is due to the favorable interactions between the hydrophobic lipid tails and hydrophobic ligands on the NP. This hydrophobic interaction becomes higher at longer ligand length, resulting in reducing the minimum force for permeating the first layer (from hydrophilic to hydrophobic) and increasing the minimum force for permeating the second layer (from hydrophobic to hydrophilic). As presented in Section 2, some experimental studies exhibited that the NP direct permeation can be enhanced by surface modifications with orderly arranged ligand structural pattern (Jewell et al., 2011; Verma et al., 2008), while its mechanism is still unknown. This issue has been investigated by MD simulation studies. Li et al. (2012) investigated the direct permeation of ligand-coated NPs with two different types of ligand structural patterns: striated pattern with orderly arranged hydrophilic and hydrophobic domains (“St” in **Fig. 4(a)**), and randomly arranged pattern at the same ratio of the hydrophilic and hydrophobic ligands (“Rand” in **Fig. 4(a)**). The simulation results demonstrated that the ligand structural pattern significantly affects the critical force for permeation of NPs across the lipid bilayer, and the striated ligand pattern results in the lowest critical force (**Fig. 4(b)**). They also investigated the free energy change associated with the permeation of NPs across the lipid bilayer, (**Fig. 4(c)**). The NP with random ligand pattern encountered substantial energy minimum at the center of bilayer, while the NP with striated ligand pattern flattened the energy minimum. This means that NP with striated ligand pattern is likely to permeate the lipid bilayer as compared to the NP with random ligand pattern, which can be trapped in the hydrophobic region of the bilayer. The similar free energy change induced by switching from random ligand structure to ordered ligand structure has been also reported by Gkeka et al. (2013). Li et al. (2012) conducted further analysis for understanding why the NP with striated ligand pattern exhibited the higher permeability. They indicated that the shallow energy minimum of the striated NP is attributed to lower degree of freedom for rotation of the striated NP in the hydrophobic region of the bilayer. The rotation of the striated NP during permeation across the bilayer was found to be constrained as compared to the NP with random ligand pattern due to the anisotropic ligand pattern. This prevented the NP from further fitting with the hydrophobic tails of lipid molecules, avoiding to be trapped into a deeper energy minimum when the NP passes across the hydrophobic region of the lipid bilayer.

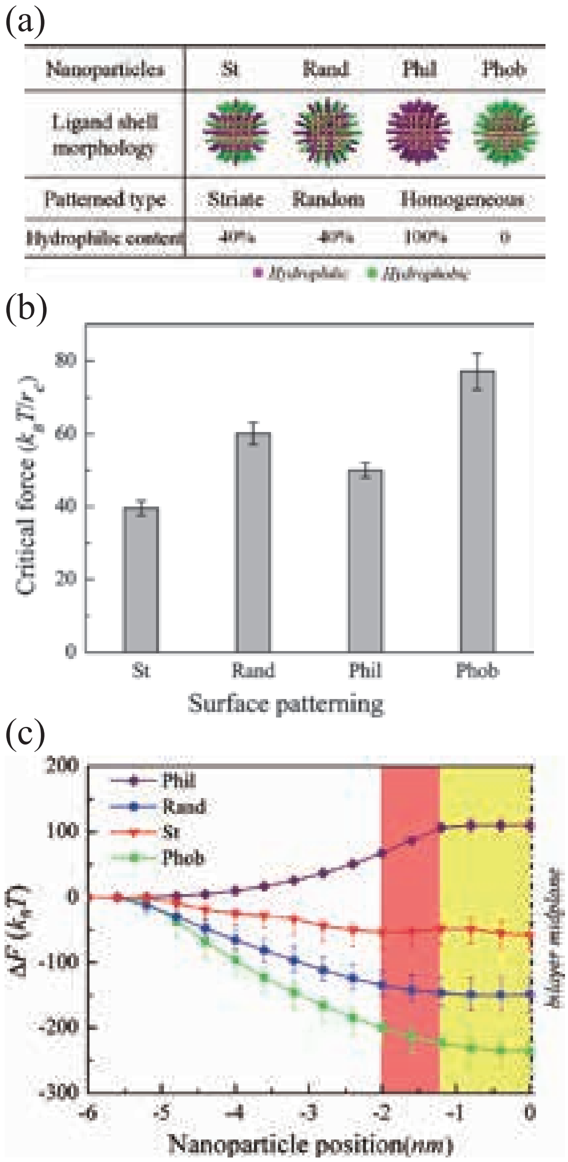

Fig. 4 **(a)** Ligand-coated nanoparticles with different surface structural patterns. **(b)** Critical force for permeating lipid bilayer at each nanoparticle with different surface ligand patterns. **(c)** Free energy change associated with permeation of various nanoparticles with different surface ligand patterns. Reprinted with permission from Ref. (Li et al., 2012). Copyright: (2012) The Royal Society of Chemistry.

Although biased MD simulations reported so far have provided deep insights into the molecular mechanism of the NP direct permeation across cell membranes, many aspects of the mechanism are still unknown. For example, role of physicochemical properties of the NPs such as surface charge and mechanical properties (soft/rigid) on the direct permeation across a cell membrane should be further investigated. Although many MD simulation studies regarding these properties have been reported, most of the previous studies have not focused on the permeation, while they have focused on adhesion or penetration into a lipid bilayer. Impact of the membrane properties such as composition of lipid molecules, bilayer phase, charge property, membrane surface tension should also be analyzed using a biased MD simulation. Moreover, not only the permeability of NPs but also changes of the lipid bilayer’s properties are important subjects to be investigated. From biased MD simulations, it has been observed that significant structural changes of the lipid bilayer such as pore formation and lipid flip-flop were induced by the NP permeation, followed by excessive leakage of waters and ions across the lipid bilayer (Oroskar et al., 2015; Song et al., 2012b). Such membrane disruption induced by the NP permeation should be analyzed further, providing important insights into the cellular damage and toxicity caused by the NP permeation.

4.2 Unbiased MD simulation studies

As mentioned before, the MD simulation studies suggest that NPs cannot permeate across a lipid bilayer unless exerting an external force to the NP. However, experimental studies demonstrated that NPs can directly permeate across a cell membrane without exerting external force on the NP. Thus, a fundamental question remains unsolved: what are the physico-chemical requirements leading to the NP direct permeation? A few unbiased MD simulation studies have investigated to solve this issue. These unbiased MD simulations demonstrated that when some additional settings are adopted, an NP can directly permeate across a lipid bilayer. So far, the following special settings have been found to induce the NP direct permeation: the reversible reaction between NP and ligands (Ding et al., 2012), multiple NPs (Li et al., 2013), application of an external electric field (Shimizu et al., 2016).

Ding et al. (2012) proposed a new type of ligand-coated NP and demonstrated that their NP can directly permeate across a lipid bilayer (**Fig. 5**). Their ligand-coated NP consists of hydrophilic rigid core and amphiphilic ligands. As their uniqueness, they adopted a reversible reaction between the core particle and the ligands. In an aqueous environment, the hydrophilic head of the ligand binds onto the surface of the core particle. This results in the hydrophobic surface of the ligand-coated NP before interacting with a lipid bilayer. Due to this hydrophobic nature, the NP can spontaneously penetrate into the hydrophobic region of the membrane at first. Meanwhile, the ligand starts to break off in the hydrophobic region of the membrane due to reversible reaction responding the hydrophobic environment surrounding NP. Once the ligands leave from surface of the core particle, the hydrophilic surface of the core particle is exposed. Since the hydrophilic nature is unfavorable to stay in the hydrophobic region of the membrane, the NP is spontaneously pushed away and finally permeates across whole lipid bilayer. Although it is actually hard to synthesize such type of ligand-coated NPs, this study provides deep insight into a strategy of the particle design for the NP direct permeation pathway.

In reality, number of NPs interacting with a cell membrane is huge. Moreover, the NPs may form an aggregation, and this aggregation may interact with a cell. This situation can be very different from a situation when the single primary NP interacts with a cell membrane. Thus, understanding of the NP-cell membrane interactions

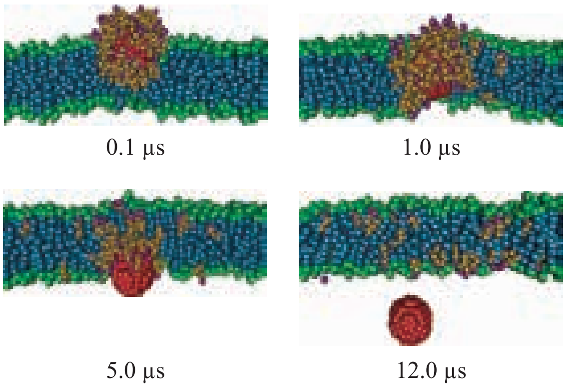

Fig. 5 Direct permeation behavior of ligand-coated nanoparticle by adopting a reversible reaction between nanoparticle and ligands. Reprinted with permission from Ref. (Ding et al., 2012). Copyright: (2012) American Chemical Society.

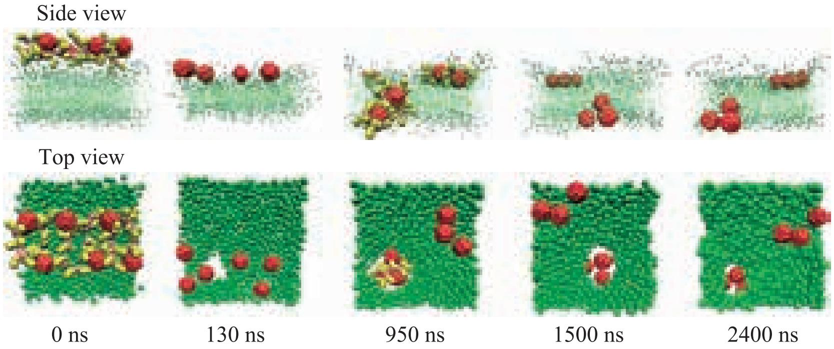

Fig. 6 Interaction of multiple peptide-conjugated nanoparticles with a lipid bilayer. Core of the nanoparticle is in red. The peptides are in yellow and pink. For the clarity, the peptides are not displayed at 130 ns, 1500 ns, and 2400 ns. Reprinted with permission from Ref. (Li et al., 2013). Copyright: (2013) The Royal Society of Chemistry.

when there are multiple NPs is an important issue. Li et al., (2013) performed an unbiased MD simulation study on the interactions of peptide-conjugated NPs with a lipid bilayer (**Fig. 6**). The simulation result showed that when the NP interacted with a bilayer as a single particle any permeation of the NP was not observed. However, they found that when multiple NPs interact with a bilayer some NPs can permeate across the bilayer (**Fig. 6**). This NP permeation was induced by a pore-mediated process: i.e., multiple NPs cooperatively interact with a membrane and form a transmembrane pore. This is the similar mechanism of the transmembrane pore formation induced by multiple antimicrobial peptides (Leontiadou et al., 2006). Such cooperative interaction can be one of the potential mechanisms of the NP direct permeation.

As reviewed in Section 3, application of external force fields can be an effective way to directly deliver NPs into a cell, although its mechanism is largely unknown. We

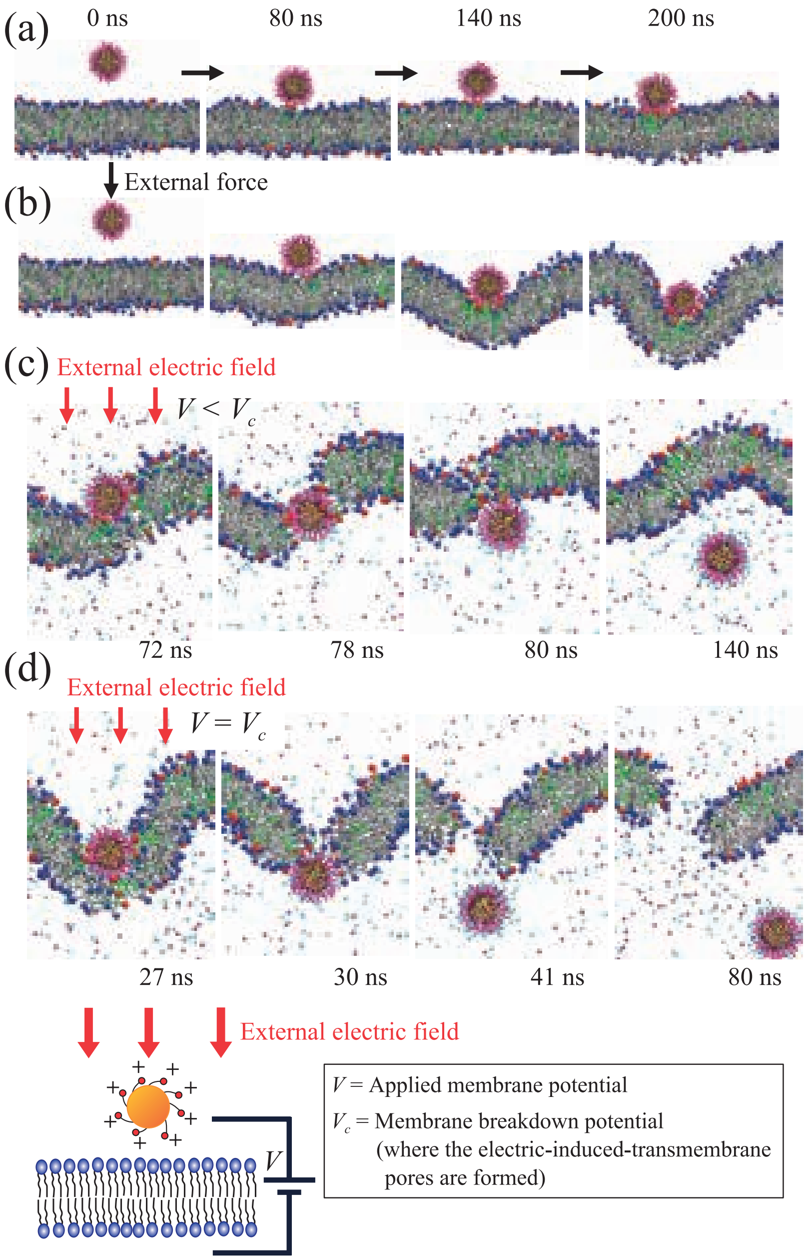

Fig. 7. **(a)** Nanoparticle behavior without both external force on particle and electric field. **(b)** Nanoparticle behavior with external force on particle but without external electric field. **(c)** Nanoparticle behavior with external electric field but without external force on particle. Membrane potential that lower than the membrane breakdown intensity was applied ($V = 0.8V_c$). **(d)** Nanoparticle behavior under excessive applied membrane potential that is equal to the membrane breakdown intensity ($V = V_c$). Waters were not shown for clarity in **(a)** to **(d)**. Ions were not shown in **(a)** and **(b)**. Reprinted with permission from Ref. (Shimizu et al., 2016). Copyright: (2016) The Royal Society of Chemistry.

focused on the electroporation-assisted NP delivery and investigated for the first time the NP permeation across a lipid bilayer under an external electric field by means of an unbiased MD simulation (Shimizu et al., 2016). We used an alkanethiol-coated cationic gold nanoparticle with 4 nm diameter for the simulation. This is a typical NP for the biomedical and the pharmaceutical applications, and the direct permeation of this type of NP across a cell membrane have been observed (**Table 1**). Our study will be introduced in the following.

First of all, we investigated the NP behavior without the external electric field. The final fate of the NP was adhesion on the hydrophilic surface of the lipid bilayer, and the NP permeation across the bilayer was not observed (**Fig. 7(a)**). We also performed a biased MD simulation, i.e., the NP was forced to move downward across the bilayer by applying external force, while the electric field was not applied. Even in this case, the NP did not permeate across the bilayer, and partial wrapping of the NP by the bilayer was observed (**Fig. 7(b)**). Consequently, it was confirmed that the NP cannot permeate across a lipid bilayer without an external electric field. However, a drastic change of the NP behavior was observed when an external electric field was applied: the NP directly permeated across the lipid bilayer (**Fig. 7(c)** and **(d)**). Detail of this permeation process was as follows: (i) the NP adhered onto the hydrophilic surface of the bilayer; (ii) the NP penetrated into the bilayer while forming a hydrophilic pore in the membrane around the periphery of the NP; (iii) the NP finally permeated across the whole bilayer through the hydrophilic pore without membrane wrapping and pulling out of lipid molecules. Interestingly, as shown in **Fig. 7(c)**, this NP direct permeation can be induced even under a lower applied membrane potential than the membrane breakdown potential. This implies that prior application of excessive electric field to form transmembrane pores before delivering NPs may not be necessary. Moreover, under a lower membrane potential than the membrane breakdown intensity (**Fig. 7(c)**) the transmembrane pore generated by the NP permeation immediately resealed after the NP permeation, while the persistent transmembrane pore was formed under an excessive membrane potential that is equal to the membrane breakdown potential (**Fig. 7(d)**). We also evaluated degree of the membrane disruption caused by the NP permeation by analyzing the lipid flip-flop and permeation amount of waters and ions across the membrane. The degree of the membrane disruption in the direct permeation pathway with self-resealing of the membrane (**Fig. 7(c)**) was significantly less and negligible as compare to the direct permeation with persistent transmembrane poration (**Fig. 7(d)**).

To investigate a key factor in the direct permeation of the NP, combined effects of the intensity of applied membrane potential and affinity of the NP for the membrane surface were investigated. Unbiased MD simulations using three different lipid bilayers (LB-1, LB-2, and LB-3 in **Fig. 8**) were conducted. Through the potential-of-mean-force analysis, we confirmed that the NP used in our study has a strong affinity with surface of the LB-3 (DPPC/DPPG leaflet), while less affinity with surfaces of the LB-1 and LB-2 (DPPC leaflet). We then conducted systematic unbiased MD simulations in each lipid bilayer under various applied membrane potentials. **Fig. 8** shows a summary of the results. Following four modes of the NP behaviors were observed: (a) no adhesion; (b) adhesion on the membrane surface; (c) direct permeation with self-resealing of membrane; (d) direct permeation with persistent transmembrane poration. As shown in the result, occurrence probability of these four modes can strongly depend on affinity of the NP with membrane as well as applied membrane potential intensity. In particular, when we focused on the direct permeation pathway with self-resealing of membrane (the blue bar in **Fig. 8**), this ideal pathway is likely to occur in the LB-3: i.e., the case in which there is a strong affinity between the NP and surface of the membrane. The strong affinity can result in exclusion of the water and ions at the interface between the NP and the hydrophilic head group of the membrane. This leads to less remaining water and ions in the transmembrane pore during the NP permeation, preventing nucleation of the persistent hydrophobic pore and enhancing the self-resealing of the membrane after the NP permeation. In summary, our finding from the unbiased MD simulation with external electric field suggests that by controlling the external electric field as well as the NP surface properties in a suitable range, an ideal NP delivery pathway, where the NP can be directly delivered into the cell with high delivery efficacy and less cellular damage, can be achieved.

Our study can also provide insights into the issue of what the physico-chemical requirements can lead to the NP direct permeation. One of the key requirements may be “gradient” across the cell membrane. In actual NP-cell system, many intrinsic gradients such as pH difference, osmotic pressure, ionic concentration, resting transmembrane potential can be observed between outside and inside of the cell. These gradients can be a key for the NP direct permeation. Lin and Alexander-Katz (2013) demonstrated that a NP can directly permeate across a lipid bilayer under a transmembrane potential induced by the ionic imbalance across the bilayer. It is also well known that lipid composition of the two leaflets of the biological cell membrane is highly asymmetric. This asymmetric lipid composition can be a potential key property for the NP direct permeation. Role of these gradients and its combined effects with the NP physico-chemical properties in the NP direct permeation across a cell membrane should be investigated in further studies.

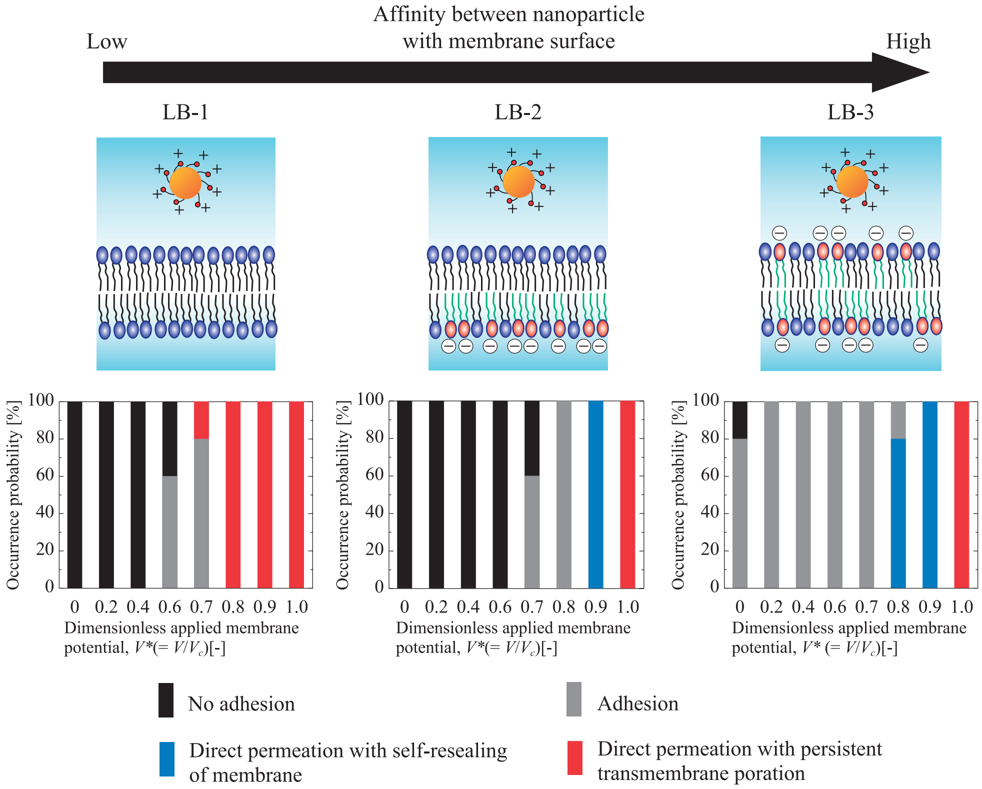

Fig. 8 Occurrence probabilities of four modes of NP behaviors as a function of dimensionless applied membrane potential at different affinities between NP and membrane surface. V is applied membrane potential. V_c is the membrane breakdown potential. Results were within five independent simulation runs. Reprinted with permission from Ref. (Shimizu et al., 2016). Copyright: (2016) The Royal Society of Chemistry.

5. Summary

In this article, we focused on the direct permeation of nanoparticles (NPs) across a cell membrane and reviewed the related literatures on both experimental and modeling studies. First of all, we surveyed experimental studies where a spontaneous direct permeation of NPs across a cell membrane was observed, and reviewed the potential key physico-chemical properties of NPs for the direct permeation (Section 2). The experimental studies suggest that size, hydrophobicity/hydrophilicity, and structural arrangement of surface ligands can be critical NP properties for the direct permeation: much smaller size (smaller than 10 nm), amphiphilic nature, and ordered ligand pattern can be favorable for the NP direct permeation. However, a general consensus of the NP properties is not yet obtained and further investigations are necessary. Subsequently, potential physical methods for facilitating the NP direct permeation were surveyed (Section 3). Among them, electroporation- and sonoporation- assisted NP delivery were reviewed. Many studies demonstrated that by utilizing these physical methods a variety of NPs can be directly delivered into cells and the delivery efficacy of NPs can be significantly enhanced, while cellular damages are always concerned. To overcome this negative impact, it is necessary to investigate the mechanism underlying the NP permeation under external force fields. In particular, role of NPs' physico-chemical properties on the mechanism of the NP direct delivery by the physical methods is an important issue to be solved. Finally, MD simulation studies on the NP permeation across a lipid bilayer were reviewed (Section 4). From review of the biased MD simulations, potential key NP properties for the direct permeation were discussed. The size, shape, and structural arrangement of surface ligands can be key properties for the direct permeation, although many aspects of the mechanism are still unknown. From the unbiased MD simulations, potential physico-chemical requirements leading to the NP direct permeation were reviewed. According to the recent MD simulation studies, the reversible reaction between NP and ligands during the permeation, cooperative interaction induced by multiple NPs, and application of an external electric field can result in the direct permeation of NPs across a cell membrane.

Despite the recent experimental and theoretical progress on the NP-cell membrane interactions, many questions remain and many issues are still unsolved. For example, it is necessary to perform the experimental investigation and computational study under an identical system and condition. This will enable to validate the simulation results with the experimental results. New experimental systems and techniques as well as new computational methods are necessary to fill the gap between "the real system" and "the ideal system". This will greatly contribute to the comprehensive understanding of the NP direct permeation and the development of new direct delivery technology with high delivery efficacy and less cellular damage.

Acknowledgements

This work was supported by the Hosokawa Powder Technology Foundation Research Grant. This work was also supported by the Japan Society for the Promotion of Science, KAKENHI Grant Number 1281208200 and 1581210400.

References

Al-Dosari M.S., Gao X., Nonviral gene delivery: principle, limitations, and recent progress, The AAPS journal, 11 (2009) 671–681.

Arvizo R.R., Miranda O.R., Thompson M.A., Pabelick C.M., Bhattacharya R., David Robertson J., Rotello V.M., Prakash Y.S., Mukherjee P., Effect of nanoparticle surface charge at the plasma membrane and beyond, Nano Letters, 10 (2010) 2543–2548.

Beddoes C.M., Case C.P., Briscoe W.H., Understanding nanoparticle cellular entry: A physicochemical perspective, Advances in Colloid and Interface Science, 218 (2015) 48–68.

Carrasco G., López-Marín L.M., Fernández F., Salas P., Loske A.M., Millán-Chiu B.E., Biomimetic coat enables the use of sonoporation to assist delivery of silica nanoparticle-cargoes into human cells, Biointerphases, 11 (2016) 04B303.

Cho E.C., Xie J., Wurm P.A., Xia Y., Understanding the role of surface charges in cellular adsorption versus internalization by selectively removing gold nanoparticles on the cell surface with a I_2/KI etchant, Nano Letters, 9 (2009) 1080–1084.

Ding H., Ma Y., Theoretical and computational investigations of nanoparticle-biomembrane interactions in cellular delivery, Small, 11 (2015) 1055–1071.

Ding H.M., Tian W. De, Ma Y.Q., Designing nanoparticle translocation through membranes by computer simulations, ACS Nano, 6 (2012) 1230–1238.

Dreaden E.C., Mackey M.A., Huang X., Kang B., El-Sayed M.A., Beating cancer in multiple ways using nanogold, Chemical Society Reviews, 40 (2011) 3391.

Ekimov A.I., Efros A.L., Onushchenko A.A., Quantum size effect in semiconductor microcrystals, Solid State Communications, 56 (1985) 921–924.

Fortin J.-P., Wilhelm C., Servais J., Ménager C., Bacri J.-C., Gazeau F., Size-sorted anionic iron oxide nanomagnets as colloidal mediators for magnetic hyperthermia, Journal of the American Chemical Society, 129 (2007) 2628–2635.

Gehl J., Electroporation: theory and methods, perspectives for drug delivery, gene therapy and research, Acta Physiologica Scandinavica, 177 (2003) 437–447.

Geng T., Lu C., Microfluidic electroporation for cellular analysis and delivery, Lab Chip, 13 (2013) 3803–3821.

Gkeka P., Sarkisov L., Angelikopoulos P., Homogeneous hydrophobic–hydrophilic surface patterns enhance permeation of nanoparticles through lipid membranes, The Journal of Physical Chemistry Letters, 4 (2013) 1907–1912.

Goda T., Goto Y., Ishihara K., Cell-penetrating macromolecules: Direct penetration of amphipathic phospholipid polymers across plasma membrane of living cells, Biomaterials, 31 (2010) 2380–2387.

Helfrich W., Elastic properties of lipid bilayers: theory and possible experiments, Zeitschrift für Naturforschung C, 28 (1973) 693–703.

Hong S., Bielinska A.U., Mecke A., Keszler B., Beals J.L., Shi X., Balogh L., Orr B.G., Baker Jr J.R., Holl M.M.B., Interaction of poly (amidoamine) dendrimers with supported lipid bilayers and cells: hole formation and the relation to transport, Bioconjugate chemistry, 15 (2004) 774–782.

Hong S., Leroueil P.R., Elizabeth K., Peters J.L., Kober M.M., Islam M.T., Orr B.G., Baker Jr J.R., Holl M.M.B., Interaction of polycationic polymers with supported lipid bilayers and cells: nanoscale hole formation and enhanced membrane permeability, Bioconjugate chemistry, 17 (2006) 728–734.

Huang S., Deshmukh H., Rajagopalan K.K., Wang S., Gold nanoparticles electroporation enhanced polyplex delivery to mammalian cells, Electrophoresis, 35 (2014) 1837–1845.

Huang X., El-Sayed I.H., Qian W., El-Sayed M.A., Cancer cell imaging and photothermal therapy in the near-infrared region by using gold nanorods, Journal of the American Chemical Society, 128 (2006) 2115–2120.

Jaque D., Martínez Maestro L., del Rosal B., Haro-Gonzalez P., Benayas A., Plaza J.L., Martín Rodríguez E., García Solé J., Nanoparticles for photothermal therapies, Nanoscale, 6 (2014) 9494.

Jewell C.M., Jung J.M., Atukorale P.U., Carney R.P., Stellacci F., Irvine D.J., Oligonucleotide delivery by cell-penetrating "striped" nanoparticles, Angewandte Chemie—International Edition, 50 (2011) 12312–12315.

Jiang Y., Huo S., Mizuhara T., Das R., Lee Y., Hou S., Moyano D.F., Duncan B., Liang X., Rotello V.M., The interplay of size and surface functionality on the cellular uptake of sub-10 nm gold nanoparticles, ACS Nano, 9 (2015) 9986–9993.

Kahru A., Ivask A., Mapping the dawn of nanoecotoxicological research, Accounts of Chemical Research, 46 (2013) 823–833.

Kawano T., Yamagata M., Takahashi H., Niidome Y., Yamada S., Katayama Y., Niidome T., Stabilizing of plasmid DNA in vivo by PEG-modified cationic gold nanoparticles and the gene expression assisted with electrical pulses, Journal of Controlled Release, 111 (2006) 382–389.

Kennedy L.C., Bickford L.R., Lewinski N.A., Coughlin A.J., Hu Y., Day E.S., West J.L., Drezek R.A., A new era for cancer treatment: gold-nanoparticle-mediated thermal therapies, Small, 7 (2011) 169–183.

Kim S.T., Saha K., Kim C., Rotello V.M., The role of surface functionality in determining nanoparticle cytotoxicity, Accounts of Chemical Research, 46 (2013) 681–691.

Kim T., Momin E., Choi J., Yuan K., Zaidi H., Kim J., Park M., Lee N., McMahon M.T., Quinones-Hinojosa A., Bulte J.W.M., Hyeon T., Gilad A.A., Mesoporous silica-coated hollow manganese oxide nanoparticles as positive T1 contrast agents for labeling and MRI tracking of adipose-derived mesenchymal stem cells, Journal of the American Chemical Society, 133 (2011) 2955–2961.

Kodama T., Tomita Y., Koshiyama K., Blomley M.J.K., Transfection effect of microbubbles on cells in superposed ultrasound waves and behavior of cavitation bubble, Ultrasound in Medicine & Biology, 32 (2006) 905–914.

Kotnik T., Frey W., Sack M., Haberl Meglič S., Peterka M., Miklavčič D., Electroporation-based applications in biotechnology, Trends in Biotechnology, 33 (2015) 480–488.

Leontiadou H., Mark A.E., Marrink S.J., Antimicrobial peptides in action, Journal of the American Chemical Society, 128 (2006) 12156–12161.

Li Y., Li X., Li Z., Gao H., Surface-structure-regulated penetration of nanoparticles across a cell membrane, Nanoscale, 4 (2012) 3768.

Li Y., Computer simulation studies on passive recruitment dynamics of lipids induced by the adsorption of charged nanoparticles, Physical Chemistry Chemical Physics, 16 (2014) 12818.

Li Z., Ding H., Ma Y., Translocation of polyarginines and conjugated nanoparticles across asymmetric membranes, Soft Matter, 9 (2013) 1281–1286.

Lin J., Alexander-Katz A., Cell membranes open “doors” for cationic nanoparticles/biomolecules: insights into uptake kinetics, ACS Nano, 7 (2013) 10799–808.

Lin J., Chen R., Feng S., Li Y., Huang Z., Xie S., Yu Y., Cheng M., Zeng H., Rapid delivery of silver nanoparticles into living cells by electroporation for surface-enhanced Raman spectroscopy, Biosensors and Bioelectronics, 25 (2009) 388–394.

Liu J., Lu N., Li J., Weng Y., Yuan B., Yang K., Ma Y., Influence of surface chemistry on particle internalization into giant unilamellar vesicles, Langmuir, 29 (2013) 8039–8045.

Lund T., Callaghan M.F., Williams P., Turmaine M., Bachmann C., Rademacher T., Roitt I.M., Bayford R., The influence of ligand organization on the rate of uptake of gold nanoparticles by colorectal cancer cells, Biomaterials, 32 (2011) 9776–9784.

Luo Z., Yuan X., Yu Y., Zhang Q., Leong D.T., Lee J.Y., Xie J., From aggregation-induced emission of Au(I)–thiolate complexes to ultrabright Au(0)@Au(I)–thiolate core–shell nanoclusters, Journal of the American Chemical Society, 134 (2012) 16662–16670.

Mehierhumbert S., Guy R., Physical methods for gene transfer: Improving the kinetics of gene delivery into cells, Advanced Drug Delivery Reviews, 57 (2005) 733–753.

Oroskar P.A., Jameson C.J., Murad S., Surface-functionalized nanoparticle permeation triggers lipid displacement and water and ion leakage, Langmuir, 31 (2015) 1074–1085.

Périgo E.A., Hemery G., Sandre O., Ortega D., Garaio E., Plazaola F., Teran F.J., Fundamentals and advances in magnetic hyperthermia, Applied Physics Reviews, 2 (2015) .

Pietroiusti A., Health implications of engineered nanomaterials, Nanoscale, 4 (2012) 1231.

Qu Z.G., He X.C., Lin M., Sha B.Y., Shi X.H., Lu T.J., Xu F., Advances in the understanding of nanomaterial–biomembrane interactions and their mathematical and numerical modeling, Nanomedicine, 8 (2013) 995–1011.

Rana S., Bajaj A., Mout R., Rotello V.M., Monolayer coated gold nanoparticles for delivery applications, Advanced Drug Delivery Reviews, 64 (2012) 200–216.

Rossi G., Monticelli L., Gold nanoparticles in model biological membranes: A computational perspective, Biochimica et Biophysica Acta (BBA)—Biomembranes, 1858 (2016) 2380–2389.

Shao K., Singha S., Clemente-Casares X., Tsai S., Yang Y., Santamaria P., Nanoparticle-based immunotherapy for cancer, ACS Nano, 9 (2015) 16–30.

Shi X., Kong Y., Gao H., Coarse grained molecular dynamics and theoretical studies of carbon nanotubes entering cell membrane, Acta Mechanica Sinica, 24 (2008) 161–169.

Shimizu K., Nakamura H., Watano S., MD simulation study of direct permeation of a nanoparticle across the cell membrane under an external electric field, Nanoscale, 8 (2016) 11897–11906.

Song B., Yuan H., Jameson C.J., Murad S., Role of surface ligands in nanoparticle permeation through a model membrane: a coarse-grained molecular dynamics simulations study, Molecular Physics, 110 (2012a) 2181–2195.

Song B., Yuan H., Jameson C.J., Murad S., Permeation of nanocrystals across lipid membranes, Molecular Physics, 109 (2011) 1511–1526.

Song B., Yuan H., Pham S.V, Jameson C.J., Murad S., Nanoparticle permeation induces water penetration, ion transport, and lipid flip-flop, Langmuir, 28 (2012b) 16989–17000.

Vakarelski I.U., Brown S.C., Higashitani K., Moudgil B.M., Penetration of living cell membranes with fortified carbon nanotube tips, Langmuir, 23 (2007) 10893–10896.

Van Lehn R.C., Atukorale P.U., Carney R.P., Yang Y.-S., Stellacci F., Irvine D.J., Alexander-Katz A., Effect of particle diameter and surface composition on the spontaneous fusion of monolayer-protected gold nanoparticles with lipid bilayers, Nano Letters, 13 (2013) 4060–4067.

Veiseh O., Kievit F.M., Mok H., Ayesh J., Clark C., Fang C., Leung M., Arami H., Park J.O., Zhang M., Cell transcytosing poly-arginine coated magnetic nanovector for safe and effective siRNA delivery, Biomaterials, 32 (2011) 5717–5725.

Verma A., Stellacci F., Effect of surface properties on nanoparticle-cell interactions, Small, 6 (2010) 12–21.

Verma A., Uzun O., Hu Y., Hu Y., Han H.-S., Watson N., Chen S., Irvine D.J., Stellacci F., Surface-structure-regulated cell-membrane penetration by monolayer-protected nanoparticles, Nature Materials, 7 (2008) 588–595.

Wang S., Zhang X., Yu B., Lee R.J., Lee L.J., Targeted nanoparticles enhanced flow electroporation of antisense oligonucleotides in leukemia cells, Biosensors and Bioelectronics, 26 (2010) 778–783.

Wang Y.H., Chen S.P., Liao A.H., Yang Y.C., Lee C.R., Wu C.H., Wu P.C., Liu T.M., Wang C.R.C., Li P.C., Synergistic delivery of gold nanorods using multifunctional microbubbles for enhanced plasmonic photothermal therapy, Scientific Reports, 4 (2014).

Weller H., Schmidt H.M., Koch U., Fojtik A., Baral S., Henglein A., Kunath W., Weiss K., Dieman E., Photochemistry of colloidal semiconductors. Onset of light absorption as a function of size of extremely small CdS particles, Chemical Physics Letters, 124 (1986) 557–560.

Wilczewska A.Z., Niemirowicz K., Markiewicz K.H., Car H., Nanoparticles as drug delivery systems, Pharmacological Reports, 64 (2012) 1020–1037.

Xiong R., Raemdonck K., Peynshaert K., Lentacker I., De Cock I., Demeester J., De Smedt S.C., Skirtach A.G., Braeckmans K., Comparison of gold nanoparticle mediated photoporation: vapor nanobubbles outperform direct heating for delivering macromolecules in live cells, ACS Nano, 8 (2014) 6288–6296.

Yang F., Zhang M., He W., Chen P., Cai X., Yang L., Gu N., Wu J., Controlled release of Fe3O4 nanoparticles in encapsulated microbubbles to tumor cells via sonoporation and associated cellular bioeffects, Small, 7 (2011) 902–910.

Yang K., Ma Y.-Q., Computer simulation of the translocation of nanoparticles with different shapes across a lipid bilayer, Nature Nanotechnology, 5 (2010) 579–583.

Yi X., Shi X., Gao H., Cellular uptake of elastic nanoparticles, Physical Review Letters, 107 (2011) 98101.

Yuan X., Tay Y., Dou X., Luo Z., Leong D.T., Xie J., Glutathione-protected silver nanoclusters as cysteine-selective fluorometric and colorimetric probe, Analytical Chemistry, 85 (2013) 1913–1919.

Zhou Q.L., Chen Z.Y., Wang Y.X., Yang F., Lin Y., Liao Y.Y., Ultrasound-mediated local drug and gene delivery using nanocarriers, BioMed Research International, 2014 (2014) 1–13.

Zhu M., Nie G., Meng H., Xia T., Nel A., Zhao Y., Physicochemical properties determine nanomaterial cellular uptake, transport, and fate, Accounts of Chemical Research, 46 (2013) 622–631.

Zu Y., Huang S., Liao W.-C., Lu Y., Wang S., Gold nanoparticles enhanced electroporation for mammalian cell transfection, Journal of Biomedical Nanotechnology, 10 (2014) 982–992.

Author’s short biography

Hideya Nakamura

Dr. Hideya Nakamura is an Associate Professor at Department of Chemical Engineering in Osaka Prefecture University. He received his Ph.D. in 2008 from Osaka Prefecture University. He then worked as a Post doc associate in Particle Engineering Research Center (PERC), University of Florida. From 2010, he started his carrier as a faculty at Osaka Prefecture University. He is currently working on modelling and experimental studies on nanoparticle-cell membrane interactions. His current projects also include computational modelling of powder handling processes as well as functionalization of particulate materials for next generation secondary batteries.

Satoru Watano

Prof. Satoru Watano, specialized in Chemical Engineering, received his Ph.D. from Osaka Prefecture University (OPU) in 1995. He became professor at OPU in 2005. Currently, he is the vice dean of College of Engineering at OPU. He is the board directors of The Society of Powder Technology Japan and the council member of Japan Society of Pharmaceutical Machinery and Engineering. His research area covers (i) measurement, control, optimization of powder handling processes (ii) particle design and modification of surface properties, (iii) design and handling of nano-particles, (iv) numerical modeling and simulation of particulate systems, and (v) development of innovative powder handling processes.

KONA Powder and Particle Journal No. 35 (2018) 66–79/Doi:10.14356/kona.2018012 Review Paper

Size Control of Polymeric Particle in Soap-Free Emulsion Polymerization†

Tetsuya Yamamoto[1]* **and Ko Higashitani**[2]

[1] *Department of Materials and Design Innovation Engineering, Nagoya University, Japan*
[2] *Department of Chemical Engineering, Kyoto University-Katsura, Japan*

Abstract

The process of synthesis of polymeric particle in soap-free system was observed in-situ on the molecular scale by using an atomic force microscope (AFM). Using cationic water-soluble initiators enabled all of the polymeric materials to be adsorbed on the mica surface electrostatically. This adsorption technique of polymeric materials in the bulk obtained the AFM images of them throughout the reaction and to discuss the real growth mechanism of polymeric particles. The followings are found; the polymeric materials are continuously generated in the bulk throughout the reaction; and they make a contribution to the particle growth. Furthermore, soap-free emulsion polymerization (SFEP) of aromatic vinyl monomer using oil-soluble initiators was studied to synthesize micron-sized particles. Oil-soluble initiator, such as AIBN, worked like a water-soluble initiator in SFEP to prepare monodispersed particles with negative charges, probably because of the pi electron cloud of phenyl ring in a monomer. The addition of an electrolyte enabled secondary particles in the bulk to enhance hetero-coagulation rate for particle growth. Changing the concentration and valence of electrolyte enabled us to control the size in SFEP using AIBN. These methods enabled reaction time to be reduced for the synthesis of micron-sized polymeric particles in soap-free system.

Keywords: soap-free emulsion polymerization (SFEP), AFM, initiator, electrolyte, size control, coagulation

1. Introduction

Polymeric particles are widely used as materials for the making the functional products in many industries, such as toner particles, medicines, cosmetics, and so on (Svec F. and Frechet J.M.J., 1996). Emulsion polymerization is one of the most popular and typical methods in the polymerization for synthesis of the polymeric particles. However, the polydisperse particles were prepared. Because the performance of the products depends on the uniformity of the raw materials, the development of the classification technique for particle size was indispensable for enhancement of the quality of the products (Yamamoto T. et al., 2009; Yamamoto T. et al., 2011; Yoshida H. et al., 2010). The low density of the polymeric particles prevented the precise classification from being successful. Although the soap-free emulsion polymerization (SFEP), where the surfactants were not utilized, was synthesis method for sub-micron polymeric particles with small standard deviation of the size (Arai M. et al., 1979; Goodall A.R. et al., 1977), it was difficult to make the micron-sized particles by this method. The micron-sized particles have generally been synthesized by dispersion polymerization using organic solvents and stabilizers (Kawaguchi H., 2000; Lok K.P. and Ober C.K., 1985; Song J.S. et al., 2006; Tseng C.M. et al., 1986; Ugelstad J. et al., 1992). Recently, using 2,2’-azobis[*N*-(2-carboxyethyl)-2-2-methylpropionami dine] hydrate as a water-soluble initiator in SFEP enabled to synthesize micron-sized polymeric particles (Gu S. et al., 2004; Gu S.C. et al., 2002; Yamada Y. et al., 2005). Thus, the size of polymeric particle was controlled by the various polymerization methods.

Because it was too difficult to observe the synthesis process of particle directly with molecular scale (Hergeth W.-D. et al., 1992; Shouldice G.T.D. et al., 1995), the growth mechanism in the polymerizations was discussed by many studies using the macroscopic data, such as the change of particle number concentration with reaction time, the mass balance, the measurement of particle size using an electron microscopy (Feeney P.J. et al., 1984; Fitch R.M., 1997; Harkins W.D., 1947; Smith W.V., 1948; Song Z.Q. and Poehlein G.W., 1989). These macroscopic data give us some fundamentals to estimate the macro-

---

† Received 23 May 2017; Accepted 4 July 2017

[1] Furo-cho, Chikusa-ku, Nagoya 464-8603, Japan
[2] Kyoto University-Katsura, Nishikyo-ku, Kyoto 615-8510, Japan
* Corresponding author: Tetsuya Yamamoto
E-mail: yamamoto.tetsuya@material.nagoya-u.ac.jp
TEL: +81-52-789-3378 FAX: +81-52-789-3271

scopic mechanism, but were not enough to make the real growth mechanism clarified with molecular scale. Hence, we still did not know the role of polymeric materials remained in the bulk solution, such as oligomers. However, in 2003, a single polymer were able to be observed in-situ by atomic force microscope (AFM) (Arita T. et al., 2003; Arita T. et al., 2004). That was to say that the direct observation of the growth process of polymer particle would be possible. In this paper, a SFEP of styrene in water was studied on the molecular scale by using an AFM to clarify the growth mechanism. A water-soluble cationic initiator was used for all the polymeric products to adsorbed on the negatively-charged mica surface electrostatically and for all the adsorbates to be observable directly by in-situ AFM method.

Furthermore, on the basis of the growth mechanism with molecular scale, the size of the polymeric particles in SFEP could be changed from sub-microns to microns. Hence, to investigate the effect of the solubility of initiator in water on particle size, 2,2’-azobis(2-methylpropionamidine) dihydrochloride (V-50) was used as a water-soluble initiator, 2,2’-azobis(2-methylpropionit rile) (AIBN), dimethyl 2,2’-azobis(2-methylpropionate) (V-601) and 2,2’-Azobis(2-methylbutyronitrile) (V-59) as an oil-soluble initiator in SFEP. AIBN, V-601, and V-59 (Yoshida E., 2010a, b) were dissolved slightly in water to change the number of radicals decomposed from the initiator in water and the generation rate of the particles in bulk. When using oil-soluble initiator for SFEP, the influence of the addition of the electrolytes, other monomer, and water-soluble initiator to the system on particle properties were also investigated.

Thus, this paper describes further two experimental results: 1) investigation of the preparation of polymeric particles through SFEP using an oil-soluble initiator, and 2) development of a synthesis technique for size control of polymeric particles through SFEP with an oil-soluble initiator.

2. Experimental

2.1 Materials

The water was purified using the Milli-Q purification system (Millipore), and, nitrogen gas was then bubbled into the water to remove the dissolved oxygen gas. A styrene monomer (Tokyo Chemical Industry) was washed with a 10 % sodium hydroxide (Wako Pure Chemical) solution to remove the polymerization inhibitors, and was then purified by distillation under reduced pressure using a rotary evaporator (EYELA). 4-Fluorostyrene, 4-bromostyrene, 4-chlorostyrene, 2,3,4,5,6-pentafluorovinylbenzene, vinylcyclohexane, methyl methacrylate (MMA), and benzyl methacrylate (BMA) (Tokyo Chemical Industry), were also used, as received, as a monomer in SFEP by oil-soluble initiator.

A water-soluble initiator, V-50 (Wako Pure Chemical), 4,4’-azobis(4-cyanovaleric acid) (V-501, Wako Pure Chemical), and a oil-soluble initiator, AIBN (Sigma Aldrich), V-601 (Wako Pure Chemical), V-59 (Wako Pure Chemical), were also used as radical initiators without further purification. They were monomers and azo compounds with chemical structures as shown in **Fig. 1**. AIBN, V-601, and V-59 do not dissolve in water as thoroughly as V-50, which was used as an initiator in emulsion polymerization (Qiu J. et al., 1999), as shown in **Table 1**. Therefore, they are not generally used as initiators for SFEP. In this study, the solubility of the initiator in water is an important factor to control the generation rate of secondary particles in bulk for size control of polymeric particle, hence these three initiators were used as radical initiators for the SFEP of styrene.

Potassium chloride, anhydrous calcium chloride (Katayama Chemical), and anhydrous aluminum chloride (Kishida Chemical) were used as electrolytes without further purification to promote the coagulation for the particle growth.

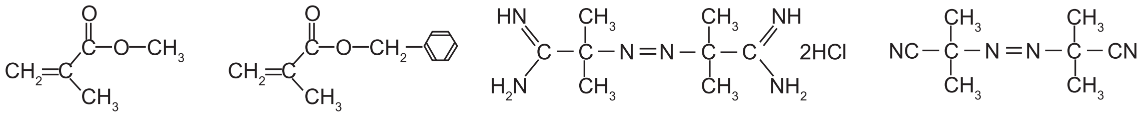
(a) MMA **(b)** BMA **(c)** V-50 **(d)** AIBN

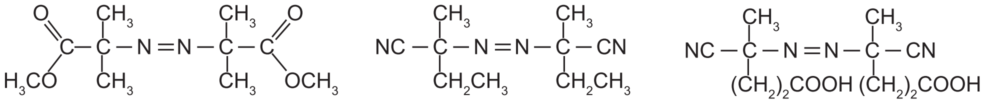
(e) V-601 **(f)** V-59 **(g)** V-501

Fig. 1 Chemical structure of the following monomers and initiators: **(a)** MMA; **(b)** BMA; **(c)** V-50; **(d)** AIBN; **(e)** V-601; **(f)** V-59; **(g)** V-501.

Table 1 Solubility in water and constant rate of decomposition of V-50, AIBN, V-601, V-59, and V-501.

	V-50	AIBN	V-601	V-59	V-501
Solubility in water [wt%]	23.2 (20 °C)	0.04×10^{-3} (25 °C)	0.3 (30 °C)	water- insoluble	soluble in hot water
Constant rate of decomposing [s^{-1}]	1.2×10^{-4} (70 °C)[a]	4.0×10^{-5} (toluene at 70 °C)[b]	4.6×10^{-5} (toluene at 70 °C)	2.3×10^{-5} (toluene at 70 °C)[c]	1.9×10^{-5} (69 °C)

[a] (Anon., 1985). [b](Talât-Erben M. and Bywater S., 1955). [c](Overberger C.G. et al., 1949).

Table 2 Experimental conditions of SFEP of styrene to observe the growth processes by AFM.

Water [g]	Styrene [g]	V-50 [g/10g-water]	Temperature [°C]
120	5.88	0.186	70

Table 3 Experimental conditions of SFEP for synthesis of micron-sized particle.

Water [g]	Monomer [mmol/L]	Initiator [mmol/L]	Electrolyte [mmol/L]	Temperature [°C]
15	64	2.03	0~7	70

2.2 Polymerization reaction

For the observations of the growth processes by AFM, the SFEP of styrene was carried out in a reactor of 500 mL with four necks for stirring mechanically with a Teflon turbine blade, purging the nitrogen gas, condensing the reflux with cold water, and sampling an aliquot of the solution with a pipette. The temperature of the reactor was controlled with a water bath. The experimental conditions of SFEP of styrene employed are listed in **Table 2**. The polymerization reactions were performed as follows. First, a given amount of pure water was poured into the reactor under nitrogen atmosphere, and heated up to a given temperature, agitating with the impeller speed of 180 rpm. Secondary, styrene monomer was added in the reactor after the temperature and agitation were settled. At last, a solution with water and V-50 was added for starting the reaction.

For size control of polymeric particle, the SFEP of various monomers using mainly oil-soluble initiator was carried out in a 30 ml reactor. The rotation speed of the impeller in the reactor and temperature of the reactor were controlled by a heater equipped with a magnetic stirrer (EYELA, RCH-20L). The experimental conditions for the polymerization employed are listed in **Table 3**. Similarly, as the above paragraph, the polymerization reactions were examined as follows. Given amounts of pure water, initiators, and electrolytes, (whose concentration was defined as C_e), were poured into the reactor, and monomer was then added. The reactor was agitated with a 130 rpm impeller by a magnetic stirrer, where the surface between the water and monomer phases was not disturbed to prevent the formation and solidification of any monomer droplets with the dissolved oil-soluble initiators. And then, the reactor was heated up to 70 °C by an electric heater. About setting the monomer concentration in the polymerization, when the concentrations of styrene and aluminum chloride were 640 mmol/L and 0.07 mmol/L, respectively, 89.5 wt% of the monomers were not consumed to form the particles and were solidified by AIBN to obtain the polymeric plate. Thus, the monomer concentration was determined to be 64 mmol/L. Because the synthesized particles did not exhibit good dispersion stability at a reaction time, $t_r > 420$ min after starting polymerization with electrolytes, the longest reaction time was 360 min.

2.3 In-situ observation by atomic force microscopy

Observation of the in-situ molecular-scale images of all the material transferred on the mica surface was examined by the atomic force microscope (AFM), a Nanoscope III (Digital Instruments). Samples were prepared as follows. A drop of the solution was taken from the reactor at t_r and then cast on the mica surface in water, such that cationic polymers synthesized by V-50 initiator were adsorbed on the mica surface with negative charges electrostatically (Hahn J. and Webber S.E., 2004). After setting the mica plate to the AFM liquid cell, the excessive polymeric materials were removed by injection of pure water into the cell to terminate the reaction.

Three dimensional and height images of polymeric products adsorbed on the mica surface were obtained by the tapping-mode procedure. The in-situ interaction forces between the AFM probe tip and surface of polystyrene particle fixed on the mica surface were measured following the contact-mode procedure, where the cantilever with a spring constant of 0.58 N/m was used. All the experiments using AFM were examined at the room temperature of 25 ± 2 °C.

2.4 Measurement of size and zeta potential of particle

The field emission scanning electron microscope (FE-SEM) (JSM-6340FS, JEOL, S-5200, Hitachi High-Technologies) was operated to determine the particle size. The samples were prepared as follows; a small amount of solution was taken from the reactor at t_r and then a drop of the solution cast on the freshly cleaved mica plate. The specimen was dried, and then covered with a thin platinum or osmium film using the chemical vapor deposition method (E-1030, Hitachi High-Technologies, Osmium Plasma Coater OPC60A, Filgen). The number-averaged particle size, D_p, was calculated using averaging the data from 200 to 1000 particles in SEM photographs. The coefficient of variation of the particle size distribution, C_v, was then calculated using D_p and standard deviation (Gu S. et al., 2004).

The ZETASIZER (ZETASIZER 2000, MALVER N Co., Ltd.) was used to evaluate the surface potential of the synthesized particles. The sample of polymer colloid was diluted with the deionized water at a pH of ca. 7.5.

3. Results and discussion

3.1 Growth curve at reaction temperature 70 °C and observation of particle growth by AFM

The growth curve of PSL particles prepared by SFEP using V-50 is shown in **Fig. 2**. Because it was found that particle continued to grow at least up to $t_r = 300$ min, the polymeric products at $t_r < 300$ min was observed by AFM to clarify the growth mechanism.

Fig. 3a shows the three-dimensional AFM image of particle at $t_r = 100$ min. **Fig. 3b** shows the interactions between the AFM probe tip and the top of particle surface. It was found that the AFM images of particle tops were very smooth at $t_r = 100$ min as shown in **Fig. 3a**. The features obtained from these data showed that (A) particles were formed by the hard core covered with the soft shell composed of polymeric materials, such as monomers for swelling, oligomers, embryos, and nuclei, and (B) the thickness of the soft shell was measured to be ca. 4 nm at $t_r = 100$ min as the yellow area drawn in **Fig. 3b** indicated.

To study what kind of molecular-scale polymeric products existing in the bulk, the polymeric materials at $t_r = 100$ min adsorbed on the mica surface were observed by in-situ AFM. **Fig. 4** showed that a lot of non-spherical nanoparticulates were observed, and the average height of the nanoparticulates at $t_r = 150$ min coincided approximately with the surface roughness of the particle as shown in **Fig. 5**. From these observations, it was found that polymeric particulates generated continuously in the bulk solution during the polymerization reaction. As far as the monomers and initiator radicals existed in the bulk, the nucleation of particles always occurred throughout this process. The above results indicated that the deposition of the polymeric materials formed in the bulk on the particle surface as well as the growth by swelling mono-

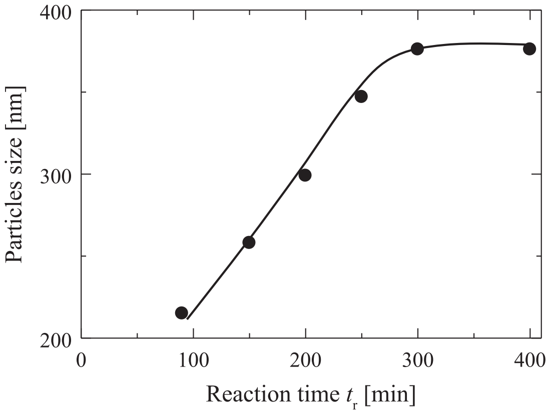

Fig. 2 Growth curve of polystyrene particles synthesized with V-50 in SFEP evaluated by FE-SEM.

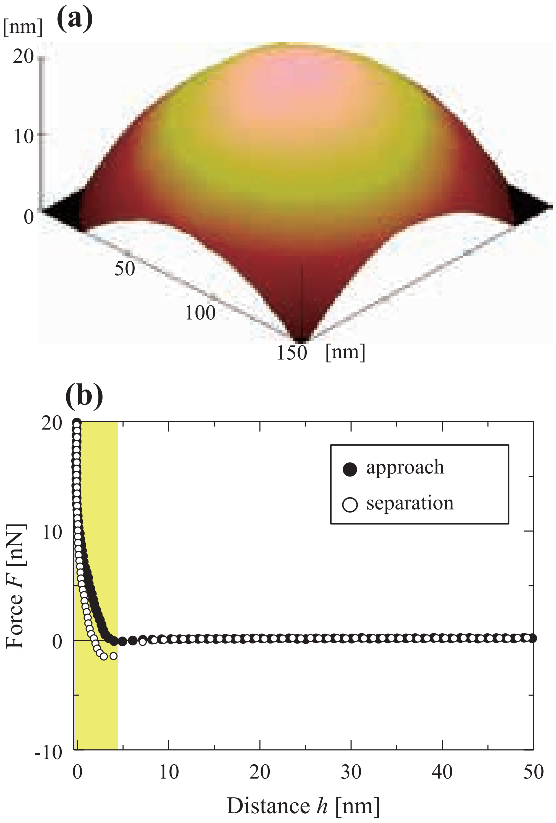

Fig. 3 AFM analysis of the particle at $t_r = 100$ min: **(a)** AFM three-dimensional image of particles top and **(b)** the corresponding force curves between a probe tip and a particle top. **(a)** Reprinted with permission from Ref. (Yamamoto et al., 2005). Copyright: (2005) Elsevier B.V.

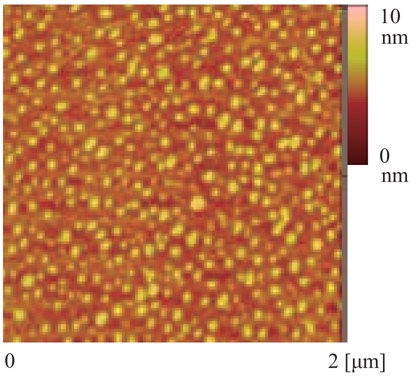

Fig. 4 AFM image of polymeric materials at t_r = 150 min.

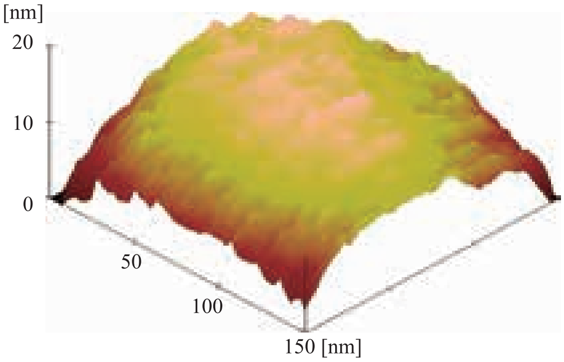

Fig. 5 AFM image of particle top at t_r = 150 min.

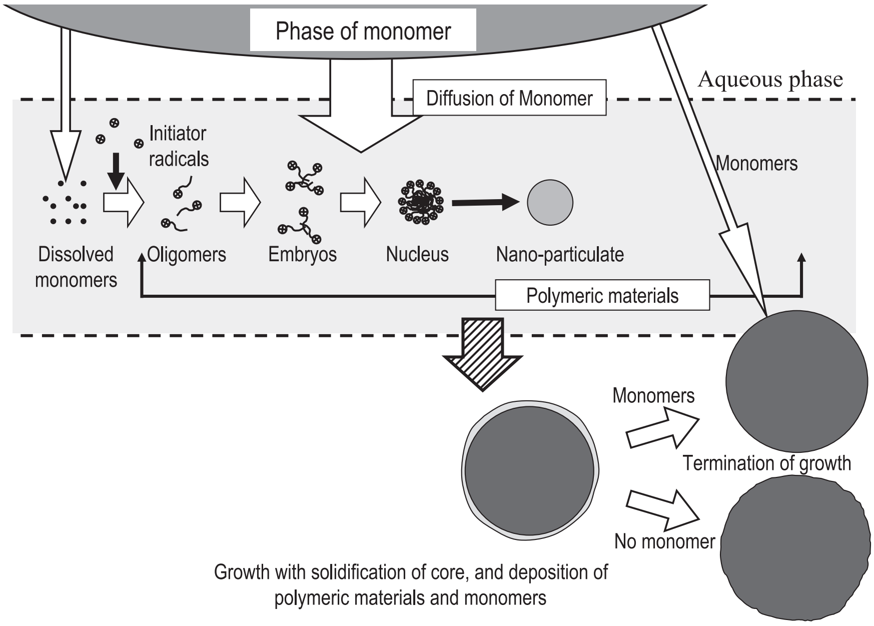

Fig. 6 Schematic representation of particle growth mechanism in SFEP by water-soluble initiator.

mers resulted in the rapid growth of particles around t_r = 150 min. This was confirmed by the fact that the particle surface had some roughness as indicated by **Fig. 5**. As far as the most of monomers were remained in the bulk at the beginning of the reaction, the deposition of nano polymeric materials and swelling by monomers would be occurred simultaneously. That was why particles grew with a smooth and soft shell surface as shown in **Fig. 3**. However, when the most of monomers was consumed, the thickness of the soft shell became thin and the deposited polymeric materials kept their shape as they were, because the amount of monomers in the bulk was too small to make deposited polymers dissolved, as shown in **Fig. 5** (Yamamoto T. et al., 2005; Yamamoto T. et al., 2004).

3.2 Growth mechanism of polystyrene particles and control of particle size with water-soluble initiator concentration

We summarized the experimental results obtained so far and proposed the molecular-scale growth mechanism for particles in SFEP of styrene by V-50, as shown in **Fig. 6** (Yamamoto T. and Higashitani K., 2007; Yamamoto T. et al., 2006a; Yamamoto T. et al., 2006b). When the growth of particles was not observed in terms of the growth plot, the particle surface did not become smooth. Although the polymeric materials still remained in the bulk, they could not make a contribution to the particle growth probably because hydrophobic interaction between the surfaces of particles swollen by monomers in the bulk did not work.

Herein, about the size control of polystyrene particle, the effect of the initiator concentration on the particle size was discussed. Assuming that the final particle size became smaller with initiator concentration increasing has been accepted widely in many processes of particle formation. LaMer diagram (Lamer V.K. and Dinegar R.H., 1950) indicated that the nucleation had to be terminated within the period of particle formation to prepare particles with uniform size. On the other hand, it was well known that the final size of particles became larger as initiator concentration increased in the case of SFEP of styrene. This tendency was reverse to the case as the above description and was also obtained in our experiments, as shown in **Fig. 7**.

The experimental data in this study explained the reason for this reverse tendency. As discussed so far, the nucleation occurred in the bulk throughout the polymerization reaction. However, the total number of particles was determined at least the end of the nucleation period, where the particle growth was so rapid because of the absorption of monomers from the bulk and the simultaneous coagulation among polymeric products. The size of growing particles became different from that of nuclei at this period. Therefore, the polymeric materials nucleated secondary adsorbed on the surface of larger particles, rather than coagulated with each other, probably because the system would be stabilized by their adsorption according to the Ostwald-Ripening law (Wagner C., 1961). If this mechanism is true, almost all the polymeric materials synthesized after nucleation will make a contribution to the growth of particles. The number of the polymeric materials was enlarged with concentration of initiator increased. That was why the final particle size became larger as initiator concentration increased.

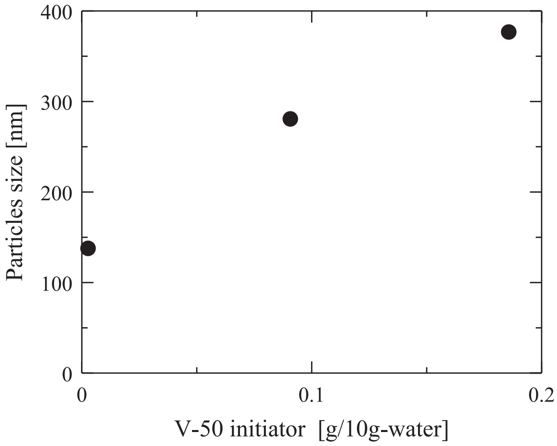

Fig. 7 Influence of V-50 concentration on particle size.

3.3 SFEP of aromatic vinyl monomer using AIBN

From here, the oil-soluble initiator was used in SFEP replacing water-soluble initiator. Firstly, the polystyrene particle was prepared by SFEP using oil-soluble initiator, AIBN. The polymerizations were performed under the conditions listed in **Table 3**, without electrolytes. The monodispersed particles with a diameter of 340 nm and a zeta potential of –44.8 mV were prepared as shown in **Fig. 8a** and **Table 4** (Yamamoto T., 2012). The surface potential was so negative that the polystyrene particles showed good dispersion stability after the polymerization. It was believed that, generally, the origin of charge of the particles synthesized by SFEP was the functional group decomposed from the initiator, such as sulfate group, to show good dispersed stability. Although the nitrile group, which was decomposed from AIBN, was electron-attractive functional group, it did not have such negative charges compared with the ionic functional group originated from a water-soluble initiator, such as potassium persulfate (Arai M. et al., 1979; Munro D. et al., 1979). Hence, to investigate why the synthesized polystyrene particles by AIBN were charged negatively in water, the influence of the pi electron cloud of the aromatic vinyl monomer on surface properties of the particle synthesized through SFEP was studied changing kind of monomer for

Table 4 Zeta potential of the particles and particle size measured by FE-SEM in SFEP using aromatic vinyl monomer and AIBN at $C_e = 0$.

Monomer	Zeta potential [mV]	Particle size [nm]
Styrene	–44.8	340
MMA	0.00	1000
BMA	–38.8	900

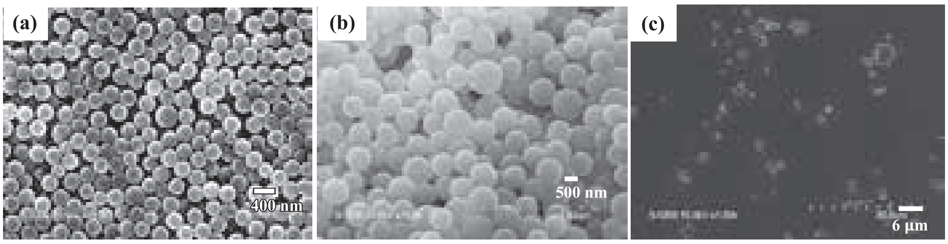

Fig. 8 FE-SEM photographs of polymeric particles prepared by AIBN with the following monomers at $t_r = 360$ min: **(a)** styrene; **(b)** MMA; **(c)** BMA. When vinylcyclohexane was used as a monomer, the particle was not synthesized.

the SFEP using AIBN.

Secondary, the SFEP of MMA using AIBN was examined according to the experimental recipes listed in **Table 3**. As the SEM image (**Fig. 8b**) showed, the synthesized particles were spherical and the average size was about 1.0 μm. However, the dispersion stability was unstable because of the low surface potential, therefore, the particles were coagulated with each other and sedimented soon after finishing the polymerization. Another methacrylic monomers, BMA, which included phenyl ring (**Fig. 1b**), were polymerized in SFEP replacing MMAs to improve the dispersion stability. SFEP of BMA with AIBN was examined according to the conditions listed in **Table 3**. As indicated in **Fig. 8c** and **Table 4**, the particles with a size of 0.90 μm and a zeta potential of –38.8 mV were synthesized under the same conditions. This zeta potential would be originated from pi electron cloud in BMA monomer (Yamamoto T., 2013).

Finally, 4-fluorostyrene, whose pi electron density in the phenyl ring was smaller compared with styrene monomer because the electron could be attracted by functional group of fluorine atom from the pi electron cloud on the phenyl ring, was applied to the system of SFEP by AIBN as a monomer. 4-Bromostyrene, or 4-chlorostyrene was also selected as a monomer in the polymerization for the same reason. In addition, 2,3,4,5,6-pentafluorovinylbenzene, whose pi electron density on the phenyl ring was much smaller because the five fluorine atoms on the phenyl ring attracted pi electron, and vinylcyclohexane, which did not have pi electron cloud, were chosen as a monomer for the SFEP. SFEP of these monomers were conducted by AIBN under the conditions listed in **Table 3** at $C_e = 0$. When vinylcyclohexane was used as a monomer, the particles were not detected by FE-SEM. As summarized in **Fig. 9**, as the number of fluorine atoms on a phenyl ring increased or the electron negativity of the functional group was strengthened, the surface potential of the particle was reduced with its size larger because the electron density did not concentrate on phenyl ring but was delocalized more attracting from the fluorine atoms and the electron density in the phenyl ring became lower. Clearly, the electron density in phenyl ring in the monomer was related strongly with the zeta potential of the synthesized particle through SFEP by AIBN.

From these results, it was possible to think that the particles with good dispersion stability were not able to be synthesized in the SFEP using AIBN and monomer without the phenyl ring. That was to say the pi electron cloud of the phenyl ring in the monomer was one of the origins of the negative charge of the polystyrene particles. The present study made it clear that the electron density of the pi electron cloud in the aromatic monomer used in SFEP influenced the surface charge of the particles prepared with AIBN (Yamamoto T., 2015). Thus, change of the pi electron density on the phenyl ring in the monomer for SFEP by AIBN enabled the size of the particle to be controllable.

In this way, the polymeric particles were able to be synthesized even using oil-soluble initiator in SFEP. The advantage of using oil-soluble initiator in SFEP was that the ions were not generated in the bulk. In the case of ionic initiator with high water solubility, although the particles were charged by the initiator, the counter ions were in the bulk. Hence, the influence of the ions in the bulk on the experimental results did not need to be considered. The polymer colloid prepared through this method using oi-soluble initiator was appropriate for the fundamental research.

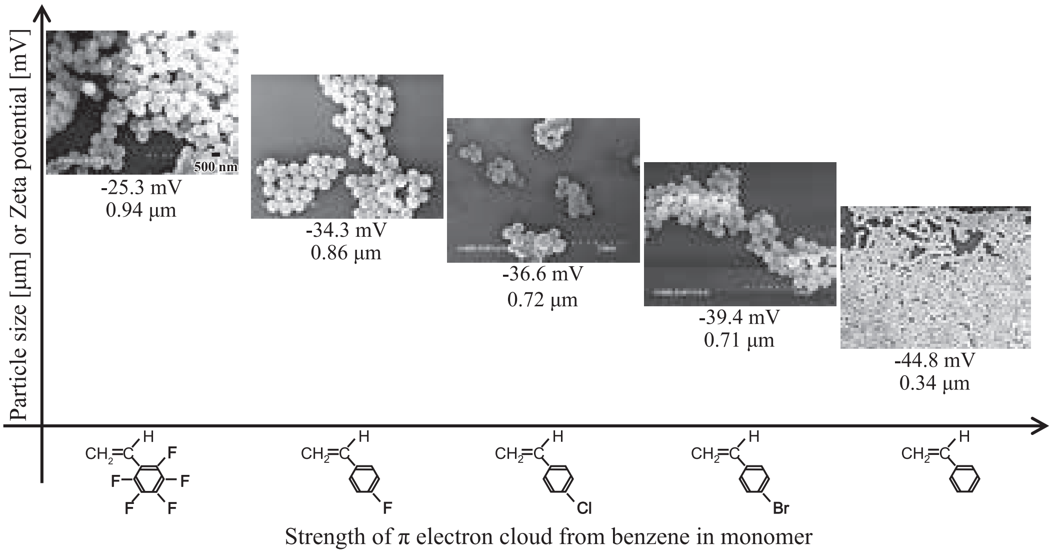

Fig. 9 Schematic representation for influence of the strength of the pi electron cloud of the aromatic vinyl monomer on negative charged particle for the SFEP using AIBN.

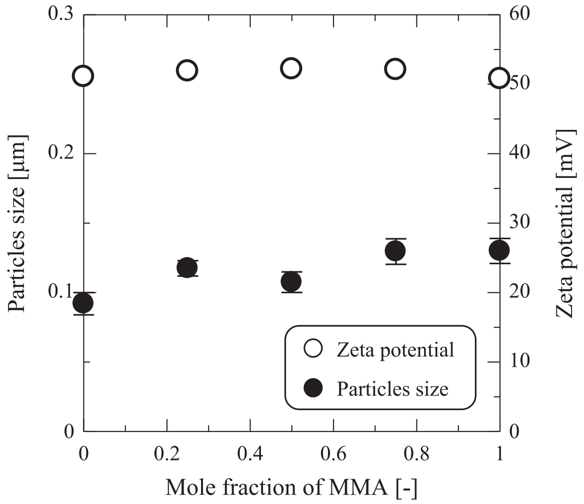

Fig. 10 Particle size or zeta potential as a function of the monomer mole fraction of MMA for the soap-free emulsion copolymerization of MMA and styrene by V-50.

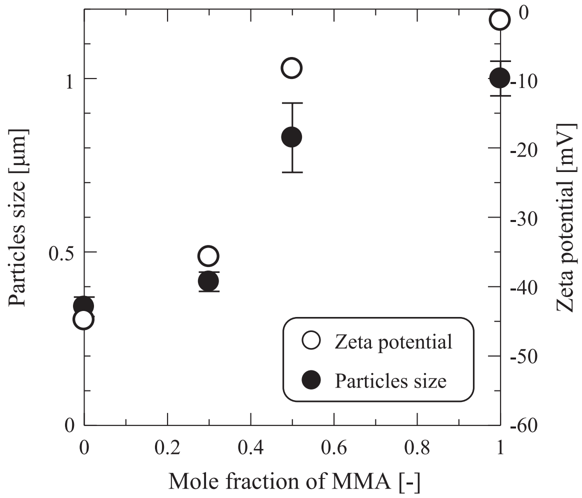

Fig. 11 Particle size or zeta potential as a function of the monomer mole fraction of MMA for the soap-free emulsion copolymerization of MMA and styrene by AIBN.

3.4 Size control by copolymerization in SFEP

In this section, the technique for controlling of particle size in SFEP was developed by changing the mole fraction of MMA in copolymerization of styrene and MMA without surfactant. At first, **Fig. 10** shows the particle size or zeta potential as a function of the monomer mole fraction of MMA in the copolymerization of styrene and MMA using a typical initiator, V-50, under the conditions listed in **Table 3** at $C_e = 0$. Particle size showed nearly constant with the mole fraction of MMA increased. The dispersion stability of the synthesized particles showed so stable, and the zeta potential exhibited no dependency on the mole fraction of MMA. Positive value of zeta potential of the particles was originated from the functional groups of the V-50 water-soluble initiator and so high that the coagulation for the enlargement of particle size were not occurred. Hence, the size of particle became constant as the mole fraction of MMA increased.

In contrast, in the case of this copolymerization by AIBN, the dispersion stability of the synthesized particle depended on the monomer used in the copolymerization. **Fig. 11** shows the effect on surface properties of the MMA monomer ratio to the total monomers for the copolymerization of MMA and styrene; the particle size increased with increasing mole fraction of MMA. The surface potential of the synthesized particles became smaller with the mole fraction of MMA increasing because the proportion of phenyl rings in the particle, which was attribute to the styrene monomers and would be the origin of the negative charge, decreased. Hence, coagulation between particles during the copolymerization was promoted for size enlargement as the ratio of MMA increased (Yamamoto T. and Kawaguchi K., 2016).

Table 5 Zeta potential of the polystyrene particles and particle size measured by FE-SEM in SFEP using V-50, AIBN, V-601, and V-59.

Initiator	Zeta potential [mV]	Particle size [nm]
V-50	53.4	160
AIBN	–44.8	340
V-601	–47.9	310
V-59	–41.5	460

3.5 SFEP of styrene with various oil-soluble initiators

To study the influence of oil-soluble initiator on particle properties; zeta potential and particle size, in the SFEP of styrene, V-601 or V-59 was used as an initiator according to the recipe as listed in **Table 3** at $C_e = 0$. The experimental data are summarized in **Table 5**. Each polymeric particle showed the dispersion stabile at $t_r > 360$ min because of high surface potential.

The atoms of nitrogen and oxygen in negatively polarized were included in V-59 and V-601, respectively. Thus, they also could function like AIBN initiator. We thought that the AIBN was more hydrophilic than V-59 because V-59 obtained two more hydrophobic groups, CH_2, than AIBN to prepare more hydrophobic particle and its size became larger for the coagulation. In the case of the SFEP using V-601, the electron more can be attracted by the functional group of the decomposed initiator, carbonyl group, from the pi electron cloud on the phenyl ring in styrene monomer because the electronegativity of oxygen atom was higher than those of atoms composed of the initiators. Hence, the surface potential of the particles by

V-601 was the highest in **Table 5** to synthesize the smallest particle among oil-soluble initiators in the present research. These experimental data suggested that the surface properties of the particle prepared through SFEP with oil-soluble initiator were controlled by electronegativity of the component atoms of the initiator.

These experimental data showed one of the reasons why the particles with negative charge was synthesized in SFEP even using AIBN, although it was not clarified completely yet. In addition, the functional group decomposed from the oil-soluble initiator or changing the electron density of the phenyl ring by substituent group of the phenyl ring could explain the results about surface properties of the particles prepared with oil-soluble initiators, qualitatively. Hence, it was found that the pi electron cloud on the phenyl ring in the monomer was related strongly with negative value of zeta potential of the polystyrene particle prepared through SFEP with AIBN.

3.6 Size control by electrolyte in SFEP

On the basis of the above experimental data, discussion, and proposed growth mechanism, oil-soluble initiator enabled the surface potential of the synthesized particles to be smaller and the coagulation to be occurred easily during growth process to make the size enlarged. To study the influence of cationic ion on particle size, SFEP of styrene with potassium chloride, calcium chloride, or aluminum chloride at $C_e = 0.7$ mmol/L was performed for 360 min using AIBN by the experimental recipes listed in **Table 3**. **Fig. 12** shows the FE-SEM photographs of the synthesized polystyrene particles. It was found that the sizes became larger with the help of electrolyte compared with **Fig. 8a**. The addition of an electrolyte helped to reduce the surface potential and the electrical double layer by counter ions against the charge of the particles, as DLVO theory indicated (Verwey E.J.W. and Overbeek J.T.G., 1948), hence, the surface potentials were reduced. Repulsive interactions between the particles formed in the bulk were weakened, and coagulations between the particles occurred easily, so the size of the particle became larger according to our proposed growth model (Yamamoto T. and Kawaguchi K., 2015; Yamamoto T. et al., 2006b; Yamamoto T. and Yokoyama T., 2015). As Schulze-Hardy rule indicated (Overbeek J.T.G., 1980), the coagulating effect was larger at the same concentration of electrolyte with increasing the valence of the ion (Verwey E.J.W. and Overbeek J.T.G., 1948). Here, as divalent or trivalent electrolytes, calcium chloride or aluminum chloride was applied to the SFEP to research the coagulation effect on particle growth. FE-SEM images in **Figs. 12b** and **c** show the particles synthesized at $t_r = 360$ min by SFEP with calcium chloride and aluminum chloride, respectively, under the condition of $C_e = 0.7$ mmol/L. The size of the particles prepared with calcium and aluminum chlorides became enlarged compared with those prepared with potassium chloride, compared with **Fig. 12a**. Particles with a number-averaged size of 2.17 μm and a C_v of 11.1 % were able to be synthesized even at $t_r = 360$ min, by the addition of aluminum chloride as shown in **Fig. 12c**. These data showed that the size of particle was larger with the valence of electrolyte increasing, which agreed with the DLVO theory from the point of the coagulation.

Similarly, the previous research showed that an electrolyte, such as sodium chloride, helped the silica particle size to be enlarged (Nakabayashi H. et al., 2010). The coagulation process controlled by the solubility of the initiator and the electrolyte concentration in the aqueous phase played an important role to make micron-sized particles in SFEP.

Fig. 13 shows the influence of the concentration of potassium chloride on size of the particle synthesized by SFEP with AIBN for 360 min changing the concentration of potassium chloride from 0.007 mmol/L to 7 mmol/L, under the experimental conditions in **Table 3**. It was found that the particle size became larger with the concentration increasing. When the concentration of potassium chloride was at $C_e = 7$ mmol/L, a number-averaged size and C_v of the synthesized particles were 2.04 μm and 5.4 %, respectively. This experimental data showed that the reaction time for making micron-sized monodispersed particles in a one-batch system was reduced. Thus, in the system of SFEP of styrene using AIBN, controlling the size of the polystyrene particles size was achieved changing the valance of electrolyte and its concentration.

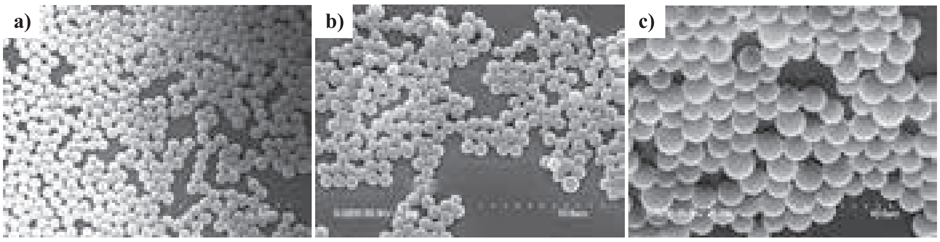

Fig. 12 Effect of the following electrolyte at the concentration of 0.7 mmol/L on particle size through SFEP of styrene using AIBN. **(a)** KCl ($D_p = 0.97$ μm); **(b)** $CaCl_2$ ($D_p = 1.04$ μm); **(c)** $AlCl_3$ ($D_p = 2.17$ μm).

The amount of polymeric radicals at the beginning of the polymerization using AIBN was much smaller than that of V-50 because both the decomposition rate and water solubility of AIBN were much smaller than those of V-50, as listed in **Table 1**. Hence, the number of particles at the beginning of the polymerization of AIBN was much smaller than that at the beginning of the polymerization of V-50, and the consumption rate of the monomer was smaller in the case of AIBN. This makes it possible to think that the size was smaller, $D_p = 0.23$ µm, even when the electrolytes were added to the system by V-50 because the number concentration of final particles in the polymer colloid using V-50 was larger, and the period for particle growth was reduced. Secondary particles were formed continuously in the bulk and deposited on the large particle surface to make a contribution to particle growth in both cases. However, the rate of generation of polymeric radicals in the case of SFEP by AIBN was so slower that particles continued to grow for a longer time and became larger. Also, the electrolyte in the system worked like a catalyst for promotion of the particle growth because secondary particles hetero-coagulations were occurred for the growth efficiently by reduction of the thickness of the electrical double layer, and prevented their self-growth.

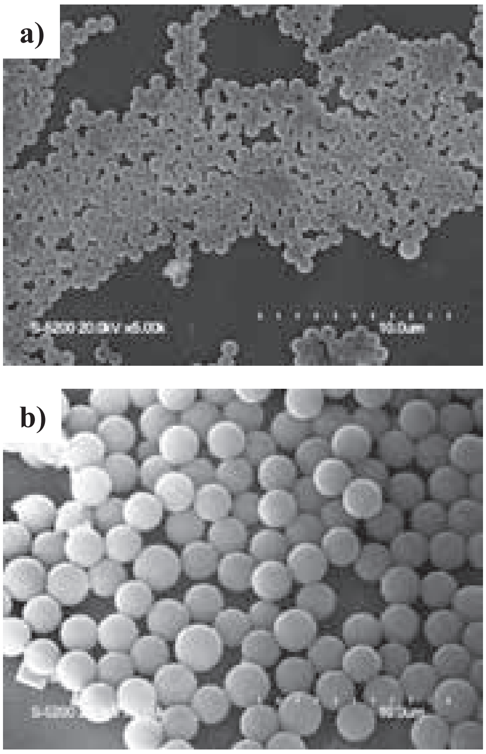

Fig. 13 Influence of concentration of potassium chloride on particle size through SFEP of styrene using AIBN. **(a)** $C_e = 0.007$ mmol/L ($D_p = 0.78$ µm); **(b)** $C_e = 7$ mmol/L ($D_p = 2.04$ µm).

This technique using an oil-soluble initiator and electrolyte for the preparation of micron-sized particles in water would be effective in the field of industry, because organic solvents and surfactants were not included in the system.

From these experimental results, it was possible to say that the cationic ion in electrolyte played an important role to control particle size in SFEP using oil-soluble initiator (Yamamoto T. and Kawaguchi K., 2015). Furthermore, nano particles with the size under 100 nm were successfully synthesized taking ionic radius of the counters ion in a water-soluble initiator into consideration (Yamamoto T. and Yokoyama T., 2015).

3.7 Size control using oil- and water-soluble initiators in SFEP

From the results obtained so far, oil-soluble initiators played the same role as typical initiator in the conventional SFEP. In this section, SFEP of styrene using both oil- and water-soluble initiators was examined. To study the effect of the concentration of V-501, C_i, on particle properties, SFEPs of styrene were carried out changing C_i at the constant concentrations of styrene monomer and AIBN. The reason why V-501 was selected was that the particles were synthesized in the SFEP using water-soluble initiator with carboxyl groups at high pH because of ionized initiator radicals derived from the initiators (Gu S. et al., 2004; Moribe H. et al., 2011; Yamada Y. et al., 2005). It was confirmed that the particles were not able to be formed independently by V-501 in normal water. Hence, the polystyrene particles were synthesized by AIBN in this system. As shown in **Fig. 14**, the particle size became enlarged as C_i was increased because of the

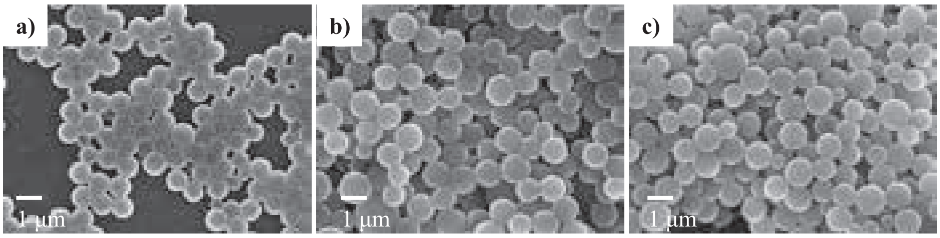

Fig. 14 SEM images of polystyrene particles through SFEP using AIBN with V-501 at the following concentration: **(a)** $C_i = 0.7$ mmol/L ($D_p = 0.80$ µm); **(b)** $C_i = 1.4$ mmol/L ($D_p = 0.86$ µm); **(c)** $C_i = 2.0$ mmol/L ($D_p = 0.95$ µm).

reduction of surface potential with low pH. Similarly, the particle size became larger through the hetero coagulation mechanism even increasing the concentration of initiator in the conventional SFEP of styrene by water-soluble initiator, such as V-50 and potassium persulfate (Goodall A.R. et al., 1977; Munro D. et al., 1979; Yamamoto T. et al., 2004). This kind of growth improvement using V-501 could also be accepted with the hetero coagulation (Liu B. et al., 2017; Yamamoto T. et al., 2016). Increase of the concentration of oil-soluble initiator made the monomer phase solidified furthermore. Thus, the addition of water-soluble initiator to the SFEP using oil-soluble initiator was effective for making the particle size enlarged.

4. Conclusions

The molecular-scale investigation on the growth process of polystyrene particles in SFEP with a cationic and water-soluble initiator by in-situ AFM method gave us some followings at least qualitatively.

- Tiny polymeric particulates were generated in the bulk throughout the polymerization, and their deposition on the larger particle surface resulted in the particle growth.
- The particle size was increased with the water-soluble initiator increased according to our proposed growth mechanism through hetero coagulation.
- Even though the tiny polymeric particulates were in the bulk, the particle growth was not observed when the monomers were consumed. The roughness of the surface depended on the balance of the polymeric nano particulates and the amount of monomers dosed.

SFEPs of aromatic vinyl monomer using oil-soluble initiators were carried out to develop the technique for controlling particle size. Preparation of micron-sized polystyrene particles through SFEP using oil-soluble initiators with electrolytes or water-soluble initiator was achieved. The conclusions were as followings.

- When an oil soluble initiator, such as AIBN, V-59, and V-601, was used in SFEP of styrene, the initiator was dissolved a little in water and the monodispersed polymeric particles were prepared as the conventional SFEP. The monodispersed particles showed negative charges, which would be originated from the pi electron density of phenyl ring in styrene and the polarization of the functional groups decomposed from the oil-soluble initiators. Thus, even oil-soluble initiator was useful for SFEP assuming that the negative charges were given to the synthesized particles by aromatic vinyl monomer used in the polymerization and made a contribution to keeping their dispersion stability good.
- Surface charge and particle size were able to be controlled changing the pi electron density of aromatic vinyl monomer with functional groups.
- Addition of an electrolyte was an effective method for enlargement of particle size because the secondary particles formed in the bulk made an contribution to particle growth through hetero-coagulation by reduction of surface potential, and prevented their self-growth. The larger effect by this method was obtained in the case of the polymerization by an initiator with lower water solubility.
- The particle size became larger with the concentration of electrolyte increasing in SFEP with an oil-soluble initiator.
- At the same concentration of electrolyte for enlargement of particle size in SFEP, the coagulation for particle growth effect became larger with the valence of the electrolyte increasing.
- Particle size in SFEP of styrene using AIBN was controllable changing the valence of electrolyte and its concentration.
- When the copolymerization of styrene and MMA using AIBN in the soap-free system, the surface charge and particle size could be controlled changing the monomer fraction of MMA.
- In addition of a water-soluble initiator, V-501, to the system using AIBN, the particle size became larger due to the grow promotion through coagulation between particles because of the reduction of surface potential by weak acid of V-501 as the concentration of V-501 was increased and the polymerization was proceeded.

From the above conclusions, it was possible to say that the technique for control of size of the particle was developed through the polymerization in SFEP using electrolyte or initiators or combination of monomers with and without phenyl ring or water- and oil-soluble initiators.

Acknowledgement

This study was financially supported in part by Grants-in-Aid for Young Scientists (B) (No.23760721) and Grant-in-Aid for Scientific Research (C) (No.25420817) from the Ministry of Education, Culture, Sports, Science and Technology of Japan.

Nomenclature

C_e	concentration of electrolyte (mmol/L)
C_i	concertation of V-501 (mmol/L)
D_p	number-averaged particle size (µm)
h	distance between surfaces (nm)
F	force (nN)
t_r	reaction time (min)

References

Anon., Product Bulletin V-50, Wako Chemicals, USA, 1985.

Arai M., Arai K., Saito S., Polymer particle formation in soapless emulsion polymerization, Journal of Polymer Science: Polymer Chemistry Edition, 17 (1979) 3655–3665.

Arita T., Kanda Y., Hamabe H., Ueno T., Watanabe Y., Higashitani K., In situ morphology of cationic flocculants adsorbed on surfaces and their interaction forces investigated by atomic force microscopy, Langmuir, 19 (2003) 6723–6729.

Arita T., Kanda Y., Higashitani K., In situ observation of single polymers adsorbed onto mica surfaces in water, Journal of Colloid and Interface Science, 273 (2004) 102–105.

Feeney P.J., Napper D.H., Gilbert R.G., Coagulative nucleation and particle-size distributions in emulsion polymerization, Macromolecules, 17 (1984) 2520–2529.

Fitch R.M., Ed., Polymer colloids: A comprehensive introduction, Academic Press, London, 1997.

Goodall A.R., Wilkinson M.C., Hearn J., Mechanism of emulsion polymerization of styrene in soap-free systems, Journal of Polymer Science: Polymer Chemistry Edition, 15 (1977) 2193–2218.

Gu S., Akama H., Nagao D., Kobayashi Y., Konno M., Preparation of micrometer-sized poly(methyl methacrylate) particles with amphoteric initiator in aqueous media, Langmuir, 20 (2004) 7948–7951.

Gu S.C., Inukai S., Konno M., Preparation of monodisperse, micron-sized polystyrene particles with an amphoteric initiator in soapfree polymerization, Journal of Chemical Engineering of Japan, 35 (2002) 977–981.

Hahn J., Webber S.E., Deposition of cationic polymer micelles on planar SiO_2 surfaces, Langmuir, 20 (2004) 4211–4219.

Harkins W.D., A general theory of the mechanism of emulsion polymerization, Journal of the American Chemical Society, 69 (1947) 1428–1444.

Hergeth W.-D., Lebek W., Stettin E., Witkowski K., Schmutzler K., Particle formation in emulsion polymerization, 2. Aggregation of primary particles, Die Makromolekulare Chemie, 193 (1992) 1607–1621.

Kawaguchi H., Functional polymer microspheres, Progress in Polymer Science, 25 (2000) 1171–1210.

Lamer V.K., Dinegar R.H., Theory, production and mechanism of formation of monodispersed hydrosols, Journal of the American Chemical Society, 72 (1950) 4847–4854.

Liu B., Fu Z., Han Y., Zhang M., Zhang H., Facile synthesis of large sized and monodispersed polymer particles using particle coagulation mechanism: an overview, Colloid and Polymer Science, 295 (2017) 749-757.

Lok K.P., Ober C.K., Particle-size control in dispersion polymerization of polystyrene, Canadian Journal of Chemistry, 63 (1985) 209–216.

Moribe H., Kitayama Y., Suzuki T., Okubo M., Effect of stirring rate on particle formation in emulsifier-free, organotellurium-mediated living radical emulsion polymerization (emulsion TERP) of styrene, Polymer Journal, 44 (2011) 205–210.

Munro D., Goodall A.R., Wilkinson M.C., Randle K., Hearn J., Study of particle nucleation, flocculation, and growth in the emulsifier-free polymerization of styrene in water by total intensity light scattering and photon correlation spectroscopy, Journal of Colloid and Interface Science, 68 (1979) 1–13.

Nakabayashi H., Yamada A., Noba M., Kobayashi Y., Konno M., Nagao D., Electrolyte-added one-pot synthesis for producing monodisperse, micrometer-sized silica particles up to 7 microm, Langmuir, 26 (2010) 7512–7515.

Overbeek J.T.G., The rule of schulze and hardy, Pure and Applied Chemistry, 52 (1980) 1151–1161.

Overberger C.G., Oshaughnessy M.T., Shalit H., The preparation of some aliphatic azo nitriles and their decomposition in solution, Journal of the American Chemical Society, 71 (1949) 2661–2666.

Qiu J., Gaynor S.G., Matyjaszewski K., Emulsion polymerization of n-butyl methacrylate by reverse atom transfer radical polymerization, Macromolecules, 32 (1999) 2872–2875.

Shouldice G.T.D., Choi P.Y., Koene B.E., Nazar L.F., Rudin A., A novel way to study the initial stages of soap-free emulsion polymerizations: The intercalation of polystyrene oligomers into hydrotalcite, Journal of Polymer Science Part A: Polymer Chemistry, 33 (1995) 1409–1417.

Smith W.V., The kinetics of styrene emulsion polymerization, Journal of the American Chemical Society, 70 (1948) 3695–3702.

Song J.S., Chagal L., Winnik M.A., Monodisperse micrometer-size carboxyl-functionalized polystyrene particles obtained by two-stage dispersion polymerization, Macromolecules, 39 (2006) 5729–5737.

Song Z.Q., Poehlein G.W., Particle formation in emulsifier-free aqueous-phase polymerization of styrene, Journal of Colloid and Interface Science, 128 (1989) 501–510.

Svec F., Frechet J.M.J., New designs of macroporous polymers and supports: From separation to biocatalysis, Science, 273 (1996) 205–211.

Talât-Erben M., Bywater S., The thermal decomposition of 2,2'-Azo-bis-isobutyronitrile. Part II. Kinetics of the reaction, Journal of the American Chemical Society, 77 (1955) 3712–3714.

Tseng C.M., Lu Y.Y., El-Aasser M.S., Vanderhoff J.W., Uniform polymer particles by dispersion polymerization in alcohol, Journal of Polymer Science Part A: Polymer Chemistry, 24 (1986) 2995–3007.

Ugelstad J., Berge A., Ellingsen T., Schmid R., Nilsen T.N., Mork P.C., Stenstad P., Hornes E., Olsvik O., Preparation and application of new monosized polymer particles, Progress in Polymer Science, 17 (1992) 87–161.

Verwey E.J.W., Overbeek J.T.G., Eds., Theory of the stability of lyophobic colloids, Elsevier Publishing Company, New York, 1948.

Wagner C., Theorie der alterung von niederschlagen durch umlosen (ostwald-reifung), Zeitschrift für Elektrochemie, Berichte der Bunsengesellschaft für physikalische Chemie, 65 (1961) 581–591.

Yamada Y., Sakamoto T., Gu S., Konno M., Soap-free synthesis for producing highly monodisperse, micrometer-sized polystyrene particles up to 6 μm, Journal of Colloid and Interface Science, 281 (2005) 249–252.

Yamamoto T., Synthesis of micron-sized polymeric particles in soap-free emulsion polymerization using oil-soluble initiators and electrolytes, Colloid and Polymer Science, 290 (2012) 1023–1031.

Yamamoto T., Synthesis of nearly micron-sized particles by soap-free emulsion polymerization of methacrylic monomer using an oil-soluble initiator, Colloid and Polymer Science, 291 (2013) 2741–2744.

Yamamoto T., Effect of the Amount of π; Electrons in aromatic monomer on the surface potential of polymeric particles obtained through soap-free emulsion polymerization using AIBN, Chemistry Letters, 44 (2015) 1555–1556.

Yamamoto T., Fukushima T., Kanda Y., Higashitani K., Molecular-scale observation of the surface of polystyrene particles by AFM, Journal of Colloid and Interface Science, 292 (2005) 392–396.

Yamamoto T., Harada Y., Fukui K., Yoshida H., Classification of particles dispersed by bead milling using electrical field-flow fractionation, Journal of Chemical Engineering of Japan, 42 (2009) 720–727.

Yamamoto T., Harada Y., Tsuyama T., Fukui K., Yoshida H., Classification of particles dispersed by bead milling with electrophoresis, KONA Powder and Particle Journal, (2011) 125–133.

Yamamoto T., Higashitani K., Growth processes of poly methylmethacrylate particles investigated by atomic force microscopy, Advanced Powder Technology, 18 (2007) 567–577.

Yamamoto T., Inoue M., Kanda Y., Higashitani K., AFM observation of growing poly isobutyl methacrylate (PiBMA) particles, Chemistry Letters, 33 (2004) 1440–1441.

Yamamoto T., Kanda Y., Higashitani K., Nucleation and growth process of polystyrene particle investigated by AFM, Journal of Chemical Engineering of Japan, 39 (2006a) 596–603.

Yamamoto T., Kawaguchi K., Effect of electrolyte species on size of particle through soap-free emulsion polymerization of styrene using AIBN and electrolyte, Colloid and Polymer Science, 293 (2015) 1003–1006.

Yamamoto T., Kawaguchi K., Relationship between surface potential and particle size in soap-free emulsion copolymerization of styrene and methyl methacrylate using a water- or oil-soluble initiator, Colloid and Polymer Science, 294 (2016) 281–284.

Yamamoto T., Kawaguchi K., Takahashi Y., Particle size control in the soap-free emulsion polymerization of styrene by an oil-soluble initiator with a weakly acidic water-soluble initiator, Colloids and Surfaces A: Physicochemical and Engineering Aspects, 502 (2016) 1–5.

Yamamoto T., Nakayama M., Kanda Y., Higashitani K., Growth mechanism of soap-free polymerization of styrene investigated by AFM, Journal of Colloid and Interface Science, 297 (2006b) 112–121.

Yamamoto T., Yokoyama T., Effect of counter ionic radius in initiator on particle size in soap-free emulsion polymerization of styrene, Chemistry Letters, 44 (2015) 824–825.

Yoshida E., Effect of azoinitiators on nitroxide-mediated photo-living radical polymerization of methyl methacrylate, Colloid and Polymer Science, 288 (2010a) 341–345.

Yoshida E., Effects of initiators and photo-acid generators on nitroxide-mediated photo-living radical polymerization of methyl methacrylate, Colloid and Polymer Science, 288 (2010b) 901–905.

Yoshida H., Nishimura Y., Fukui K., Yamamoto T., Effect of apex cone shape on fine particle classification of gas-cyclone, Powder Technology, 204 (2010) 54–62.

Author’s short biography

Tetsuya Yamamoto

Tetsuya Yamamoto is an Associate Professor of the Department of Materials Innovation Design Engineering, Nagoya University. After he received his Ph.D. from Department of Chemical Engineering, Kyoto University in 2005, he worked as an Assistant Professor, Hiroshima University from 2005 to 2014. He was also a guest researcher in Max Planck Institute for Polymer Research in 2012.

His research is in the field of synthesis of polymer particle and surface control engineering. He received awards for outstanding young researchers from The Society of Chemical Engineering, Japan, from The Society of Powder Technology, Japan, and from The Nagai Foundation for Science and Technology.

Ko Higashitani

Ko Higashitani graduated from Department of Chemical Engineering, Kyoto University, Japan in 1968. He worked on Viscoelastic Fluids as a Ph.D. student under the supervision of Prof. A.S. Lodge in Department of Chemical Engineering, University of Wisconsin-Madison, USA. After he received a Ph.D. degree in 1973, he joined Department of Applied Chemistry, Kyushu Institute of Technology, Japan, as a lecturer, and then became a professor in 1983. He moved to Department of Chemical Engineering, Kyoto University in 1992. He is now an Emeritus Professor, Kyoto University.

His major research interests are the correlations between macroscopic behaviours of colloidal particles in solutions, such as particle formation, particle stability, suspension rheology etc. with the molecular-scale characteristics of particles which can be evaluated by the Atomic Force Microscope, and so on

KONA Powder and Particle Journal No. 35 (2018) 80–88/Doi:10.14356/kona.2018013 Review Paper

Review; Risk Assessment of Aerosolized SWCNTs, MWCNTs, Fullerenes and Carbon Black[†]

Toshihiko Myojo[1*] **and Mariko Ono-Ogasawara**[2]

[1] *Institute of Industrial Ecological Sciences, University of Occupational and Environmental Health, Japan*
[2] *Work Environment Research Group, National Institute of Occupational Safety and Health, Japan*

Abstract

In this paper we review the risk assessment of carbonaceous nanomaterials, such as single-wall carbon nanotubes (SWCNTs), multi-walled carbon nanotubes (MWCNTs), fullerenes and carbon black, and summarize elemental carbon (EC) analyses for the determination of the those nanomaterials, focusing on the inhalation exposure of airborne nanomaterials. In the reports of hazard assessment, the proposed OELs (Occupational Exposure Limits) of MWCNTs and SWCNTs ranged from 1 to 50 μg/m^3. The fullerenes and carbon black seem to be less toxic than the CNTs. In the reports of exposure assessment, the aerosol concentrations of MWCNTs and SWCNTs in work environments were from less than 0.1 to more than 100 μg/m^3. The expected minimum concentration of airborne MWCNTs in the EC analyses was around 1 μg/m^3, but the concentrations of EC in ambient particulate matters (APM) were more than 1 μg/m^3 in urban environments. The EC analysis introduced in this paper is a convenient method to quantify the carbonaceous nanomaterials in the samples, but size-classification of aerosol samples by cascade impactor and observation using electron microscopes are needed to confirm the characteristics of the nanomaterials.

Keywords: nanomaterials, SWCNTs, MWCNTs, fullerenes, carbon black, thermal carbon analysis

1. Introduction

Ten years ago, Maynard (2007) wrote “Nanotechnology is clearly a concept whose time has come. Yet it is now being promoted in the scientific and popular press as a major technological breakthrough, heralding the next industrial revolution.” He also foresaw, “At the same time, there are increasing concerns that new nanotechnologies will bring about new risks to human health and the environment.” That is, nanotechnology will have both benefits and risks. How can we avoid the risks and obtain the benefits? In this paper, we review the risk-management of carbonaceous nanomaterials, as shown in **Fig. 1**.

Carbon black (CB), a representative carbonaceous nanomaterial, has a long history and is mass-produced worldwide. Primary CB particles are produced during partial combustion or thermal decomposition of hydrocarbons by gas-to-particle conversion. The sizes of primary particles range from 10 nm to 100 nm. A few to many tens of primary particles immediately form highly branched chains of primary particles called aggregates. CB is added to rubber to reinforce final products and is also used as a pigment for printing ink, paints and toners. Other carbonaceous nanomaterials, such as fullerenes and carbon nanotubes, have been developed recently and supplied to markets.

Kroto et al. (1985) determined the atomic structure of C_{60} fullerene having the same geometry as soccer ball, and since then there have been many studies about fullerene derivatives in the fields of chemistry and pharmacology. C_{60} fullerene is soluble in organic solvents, such as toluene and tetrahydrofuran, but insoluble in water. Purified C_{60} fullerene forms a dense molecular crystal structure (brown powder), not a random-shaped agglomerate of the single molecule of C_{60} fullerene.A sensational study on nano-risk reported that C_{60} fullerenes induced oxidative stress in the brain of juvenile largemouth bass, but later the authors admitted that the results were mainly affected by the tetrahydrofuran used as a dispersant of C_{60} fullerene (Oberdörster, 2004; Zhu et al., 2006).

Carbon nanotubes (CNTs) possess unique properties and have been the focus of extensive research originated by Japanese scientists (Endo, 1988; Iijima, 1991) during the last two decades. CNTs are fiber-shaped substances

---

[†] Received 24 May 2017; Accepted 7 June 2017
J-STAGE Advance published online 31 Augest 2017

[1] 1-1, Iseigaoka, Yahatanishi-ku Kitakyushu-shi, Fukuoka, 807-0804, Japan
[2] 6-21-1, Nagao, Kawasaki, Kanagawa, 214-8585, Japan
[*] Corresponding author: Toshihiko Myojo;
E-mail: tmyojo@med.uoeh-u.ac.jp
TEL: +81-93-691-7459 FAX: +81-93-602-1782

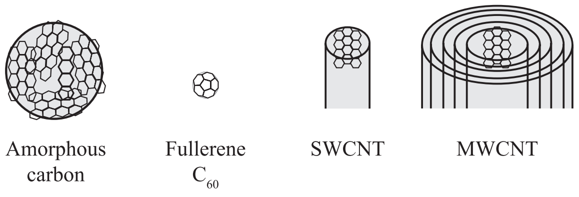

Fig. 1 Carbonaceous nanomaterial in this review.

that consist of graphite hexagonal-mesh planes (graphene sheets) that present as a single-layer or in multiple layers. Tubes with single-wall structures are called single-wall carbon nanotubes (SWCNTs), and those with multi-wall structures are called multi-walled carbon nanotubes (MWCNTs). The physical properties of SWCNTs and MWCNTs, including high tensile strength and conductivity, make them increasingly desirable for manufacturing and medical applications (Maynard, 2007). Carbon nanofiber (CNF) is also used as a general term of the products, such as VGCNF (Vapor Grown Carbon Nanofiber). Carbon nanofibers with graphene layers wrapped into perfect cylinders are called CNTs.

Hazard assessment and exposure assessment are essential elements in the risk-assessment and risk-management of nanomaterial production. Occupational exposure limits (OELs), key issues in hazard assessment, are determined by toxicological studies using laboratory animals, such as rats and mice, if epidemiological data are not available especially for nanomaterials. The Japan Society for Occupational Health (JSOH, 2015) defined "Occupational Exposure Limit-Mean (OEL-M) for mean concentration of a chemical substance is defined as the reference value to the mean exposure concentration at or below which adverse health effects caused by the substance do not appear in most workers working for 8 hours a day, 40 hours a week under a moderate work-load". The mean exposure concentration can be determined as the 8-hour time-weighted average (TWA) concentration of target materials.

For exposure assessment, we need analytical techniques for monitoring the concentrations of target nanomaterials in the ambient contaminants. Frequently, we have not suitable OELs or the monitoring techniques ranged from 1/10 level of OELs for the nanomaterials.

2. Health effects of carbonaceous nanomaterials

2.1 Carbon black

CB was the most examined nanomaterial in the past. Several studies have shown that inhaled CB particles induce lung tumors in rats when they are administered at doses that cause particle overload in the lungs, as well as chronic inflammation and epithelial hyperplasia. The International Agency for Research on Cancer (IARC) has classified CB as possibly carcinogenic to humans (Group 2B; IARC, 1996; 2010). Elder et al. (2005) reported that this evaluation was based on inadequate evidence in humans, but sufficient evidence in experimental animals. In the case of human epidemiological evidence, U.S. studies on cancer in carbon black workers showed no excess of lung cancer. Rats, mice, and hamsters were exposed for 13 weeks to inhaled CB, and, based on the results, a subchronic No-observable-adverse-effect-level (NOAEL) of 1 mg/m^3 respirable CB (Printex 90) can be assigned to female rats, mice, and hamsters.

Sager et al. (2009) reported that pulmonary responses to the instillation of ultrafine CB (Printex 90) to rats were comparable to equivalent particle surface area doses of ultrafine titanium dioxide, concluding that ultrafine titanium dioxide appears to be more bioactive than ultrafine CB on an equivalent surface area of particles on the delivered basis.

A short-term (5 consecutive days) inhalation study using rats (Ma Hock et al., 2013) was conducted to compare the effects of different carbon-based materials with different structures. No relevant toxicity was observed for CB (larger size than Printex 90) of 10 mg/m^3, but MWCNT of 0.5 mg/m^3 induced lung toxicity.

At present, the Japan Society of Occupational Health recommends that the OEL of CB should be 1mg/m^3 as the respirable fraction (JSOH, 2015).

2.2 Fullerene

The first assessment of the toxicity resulting from inhalation exposures to C_{60} fullerene nanoparticles and microparticles found minimal changes in the toxicological endpoints examined (Baker et al., 2008).

In a project (P06041, Risk assessment of manufactured nanomaterials) of Japanese New Energy and Industrial Technology Development Organization (NEDO), intratracheal instillation (IT) and inhalation (IH) studies on rats exposed to C_{60} suggested that well-dispersed fullerenes do not have a strong potential of neutrophil inflammation (Morimoto et al., 2010), and the pulmonary inflammation pattern after exposure to C_{60} was slight and transient in the pathological features of rat lungs. (Ogami et al., 2011) The half-life of intratracheally instilled C_{60} (0.1 to 1 mg/rat) was 15–28 days; a short period compared with other nanomaterials (Shinohara et al., 2010). An OEL of 0.39 mg/m^3 was adopted for fullerenes in a report by the NEDO project (Nakanishi, 2011).

2.3 Carbon nanotubes

The continuing increase in CNT production will lead to heightened risks of occupational exposure, raising concern that CNT exposure via inhalation, ingestion or dermal contact will lead to harmful effects (Donaldson et al., 2006). Many in vivo experimental studies have been conducted to assess the potential effects of MWCNTs.

In the NEDO project, MWCNTs and SWCNTs were evaluated in IH tests and/or IT tests using rats (Nakanishi, 2011), and the biological results from the project were published by Kobayashi et al. (2010) and Morimoto et al. (2012). In one specific result of the project, Lee et al. (2013) analyzed the data of rat lungs administered two samples of MWCNTs (Nikkiso) with different average lengths derived from one bulk sample (44 nm in diameter) by IT and found that, based on histopathological changes, the pulmonary surfactants and inflammation scores of the lungs were significantly higher by MWCNT-Long (3.4 µm in mean length) than by MWCNT-Short (0.94 µm in mean length) exposure. Nakanishi et al. (2015) analyzed the relationship between the specific surface area of CNTs and the rate of increase of Polymorphonuclea leucocytes (PMNs) in Bronchoalveolar-lavage-fluid (BALF) and reported that the larger the specific surface area, the larger the rate of increase. The authors concluded that there was only a common relationship between the specific surface area and the increased rate of PMNs, regardless of SWCNTs or MWCNTs. The surface energy or surface activity of the CNTs was assumed to be the real reason for this difference, and the surface area reflects this indirectly. Generally, a larger specific surface area of CNTs means a smaller fiber diameter. An OEL of 0.03 mg/m^3 was adopted for SWCNTs, DWCNTs, and MWCNTs as a common criterion in a report by the NEDO project (Nakanishi, 2011), based on the integration of IT and IH tests. Considering the uncertainties in the data processing, they proposed limiting the period of application of the OEL to 15 years on the assumption that the values will be reviewed whenever new data are obtained.

One of the earliest OELs for CNTs was proposed by the British Standards Institution (2007); they proposed a “benchmark exposure limit” of 0.1 fiber/cm^3. Other OELs, however, were based on mass concentrations of CNT particles as a metric.

The U.S. NIOSH reviewed animal and other toxicological data relevant to assessing the potential non-malignant adverse respiratory effects of CNTs and CNFs, provided a quantitative risk assessment based on animal dose-response data, and proposed a recommended exposure limit (REL) of 0.001 mg/m^3 (1 µg/m^3) for elemental carbon (EC) as a respirable mass 8-hour time-weighted average (TWA) concentration in the NIOSH Current Intelligence Bulletin 65 (2013). Irrespective of many reports on MWCNT toxicity studies from the US NIOSH, the recommended OEL for CNTs was based on the limit of quantification of Method 5040 (NIOSH, 2003), a thermal-optical carbon analysis method for determining airborne exposure to respirable CNTs.

Pauluhn (2010) selected 0.1 mg/m^3 as the NOAEL in a rat 13-week inhalation study to derive a human-equivalent concentration, and proposed 0.05 mg/m^3 (8-h TWA) as the OEL for a specific MWCNT (Baytubes).

Ma-Hock et al. (2009) conducted a MWCNT inhalation test in which rats were head-nose exposed for 13 weeks to concentrations of 0.1, 0.5, or 2.5 mg/m^3. At 0.1 mg/m^3, there was still minimal granulomatous inflammation in the lung and in lung-associated lymph nodes, while there was no substance-related systemic toxicity at 2.5 mg/m^3. They did not select a NOAEL for MWCNT (Nanocyl NC 7000) from their study.

The Japan Bioassay Research Center conducted a rat 2-year inhalation study of MWCNT (MWNT-7) at concentrations of 0.02, 0.2, and 2 mg/m^3. Adenoma and adenocarcinoma in rat lungs were observed dose-dependently in male rats. Inflammatory responses were observed from 0.02 mg/m^3 (Kasai et al., 2016). Before publication of the study, IARC (Kuempel et al., 2017) classified MWCNT-7 as possibly carcinogenic to humans (Group 2B); and SWCNTs and MWCNTs excluding MWCNT-7 were categorized as not classifiable as to their carcinogenicity to humans (Group 3). These categories of CNTs may be changed in the future along with the progress of toxicological studies.

3. Workplace handling of carbonaceous nanomaterials

Aerosol concentrations of carbonaceous nanomaterials in work environments are usually measured by *online* instruments, such as a scanning mobility particle sizer (SMPS), and *offline* measurement, such as Transmission Electron Microscopy (TEM), Scanning Electron Microscopy (SEM) and carbon analysis. *Online* measurement of particle size, number, and surface area is convenient, but the instruments used for these measurements respond to all particles, not just carbonaceous nanomaterials, and do not show information on shape/morphology and chemical composition.

Carbon is a common element on the earth and it is not easy to distinguish the sources of EC in ambient particles, such as carbonaceous nanomaterials and ambient particulate matter (APM) (see **Fig. 2**), but it has the merit that carbon analysis for the mass concentration of EC is a relatively sensitive and quick procedure from sampling to analysis.

Kuhlbusch et al. (2006) studied the particle characteristics in reactor and pelletizing areas of CB production. Filters that collected PM2.5 and PM10 at worksites and outdoor sites within the same production facilities were analyzed for EC and organic carbon (OC) to assess and

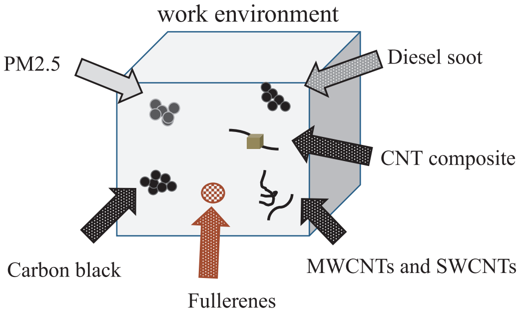

Fig. 2 Many sources of elemental carbon in work environment atmosphere.

quantify the magnitude and proportion of the carbon fractions in the total particulate matter in the work areas. The particle number and mass concentrations in the reactor and pelletizing areas of the CB production plants appeared to fall within the range of ambient air values, but the pelletizing areas for CB showed high ratios of EC to PM10: 60–74 %, compared with 9–16 % for APM.

Fujitani et al. (2008) reported on a work environment in a C_{60} production facility in Japan. They used SMPS and optical particle counter (OPC) for *online* measurement, and filter sampling and SEM observation for *offline* analysis. The particle volume concentration in the coarse size range (> 2 μm) was higher during the removal of fullerenes from the storage tank and/or weighing. The presence of fullerenes in the filter samples was confirmed by SEM observation of the morphology of microparticles collected during the bagging operation.

Takaya et al. (2010) carried out aerosol monitoring in two types of packing facilities of MWCNTs, where one of the packing facilities was manually operated and the other was automated, and found that the personal exposures were 2.39/0.39 (total/respirable) mg/m^3 and 0.29/0.08 (total/respirable) mg/m^3, respectively. The task, however, was related to nanoscale particle release and was not observed by real-time aerosol monitors. In further research by Takaya et al. (2012), micron-size particles containing MWCNTs were released into the air in a weaving process of MWCNT-coated yarn. The mass concentrations of total/respirable dust collected by personal sampling were 0.159/0.093 mg/m^3 (total/respirable). The concentrations of EC in the respirable mass ranged from 1 to 5 μg C/m^3.

Hedmer et al. (2014) quantified the occupational exposures and emissions during arc discharge production, purification, and functionalization of MWCNTs in a laboratory-scale worksite. In the personal exposure measurements, respirable dust ranged between detection limit and 93 μg/m^3, and EC ranged between detection limit and 7.4 μg C/m^3.

Dahm et al. (2015) assessed exposures to CNT (13 sites) and CNF (1 site). Personal breathing zone (PBZ) and area samples were collected for both the inhalable and respirable mass concentration of EC, using the NIOSH Method 5040. The respirable EC PBZ concentrations ranged from 0.02 to 2.94 μg/m^3, with a geometric mean of 0.34 μg/m^3 and an 8-h TWA of 0.16 μg/m^3.

Kuijpers et al. (2016) assessed personal exposure to MWCNTs during the synthesis and handling of MWCNTs in a commercial production facility and linked these exposure levels to specific activities. The exposure levels of the MWCNTs observed in the production area during the full scale synthesis of MWCNTs ($N = 23$) were comparable to levels observed during further handling of MWCNTs ($N = 19$); 41 μg/m^3 and 43 μg/m^3, respectively. Carbon analysis has also been used to determine the mass concentration of SWCNT aerosols generated (Maynard et al., 2004), the concentration of MWCNT aerosols in a laboratory (Han et al., 2008), and the concentration of carbon nanofibers and MWCNTs in factories (Methner et al., 2010; Birch et al., 2002).

There have been other studies to determine the number concentration of CNTs as asbestos fibers. We think that morphological observation by SEM and/or TEM can yield important data to confirm the presence of CNTs, but that the counting of CNT fibers is not a good way to determine the exposure assessment because the toxicological studies mentioned above were based on mass concentration and did not observe any clear toxicological similarity between CNTs and asbestos fibers. In addition, most CNT particles observed in work environments are large (micron size) agglomerates, which should be omitted according to the rules of asbestos counting.

4. Analysis of airborne carbonaceous nanomaterials

In the case of carbonaceous nanomaterials, carbon analysis has been used to determine the aerosol concentrations mentioned above. The U.S. NIOSH recommended applying Method 5040, a thermal-optical carbon analysis method, to determine airborne exposure to respirable CNT (Birch and Cary, 1996). Method 5040 was originally developed to measure EC concentration to estimate diesel particulates in work-environments. A similar carbon analysis method that determines the EC concentration in APM was also published by Chow et al. (1993). Both methods were originally intended to determine the EC mass generated by combustion processes and focused on the separation of organic carbon and elemental carbon in the particulates. The concentrations of EC in APM measured in urban areas of Japan were usually more than 1 μg/m^3 (Ono-Ogasawara et al., 2009; Kim et al., 2011; Kudo et al., 2011), which value is similar to the level proposed by the US NIOSH as the OEL for CNT: 1 μg/m^3 as EC.

In our pilot study, we obtained samples from quartz fiber filters at a factory for CNT production. The color of the obtained samples was almost black, and the automatic function of thermal optical split of OC and EC by the carbon analyzer did not work. The samples were also resistant to high temperatures (850 degree C) and remained after the carbon analysis because the CNT had a graphite structure and annealed in the inert gas atmosphere. We decided to stop using the Method 5040, based on the optical split of OC and EC, and adopted a modified IMPROVE protocol by Chow et al. (1993). We used the modified IMPROVE protocol at each temperature stage, defined as OC1–OC4 and EC1–EC3, as shown in **Table 1** (Ono-Ogasawara and Myojo, 2013). This protocol was adopted for the analysis of CNTs in the reports by Takaya et al. (2010, 2012).

Airborne particle samples on the quartz fiber filters in the impaction stages of a Sioutas cascade impactor (SCI; SKC Inc., Eighty Four, PA, USA) were observed by SEM. **Fig. 3** shows particles collected on the filter fibers of the stage (> 2.5 µm). The fine and tangled fibers in the debris must be carbon nanotubes. We assumed that CNTs, in particular MWCNTs, decomposed at a higher temperature than APM and behaved as micron-size agglomerates irrespective of the nano-size diameter. In our method, at first, size-segregated particles are collected using an impactor, and then the EC concentrations of the collected particles of each size fraction are measured by carbon analysis without optical correction. The presence of MWCNTs is evaluated using factors of both size and the oxidation temperature in the measured data. Airborne particles were collected using a SCI, and the EC in the particles was analyzed using a carbon monitor. A schematic diagram of this procedure is shown in **Fig. 4** (Ono-Ogasawara and Myojo, 2011). The SCI is designed to collect size-segregated particles in six stages of > 6.6 µm, > 2.5 µm, > 1.0 µm, > 0.5 µm, > 0.25 µm, and smaller than 0.25 µm at a flow rate of 9 L/min. The middle four stages are called stages A to D, and the final stage is a back-up filter. A quartz fiber filter (2500QAT-UP, PALL, Port Washington, NY, USA) was used to collect particles, as shown in **Fig. 4**.

Typical cases of simulated MWCNT aerosols and APM are shown in **Fig. 5**. The EC of the MWCNTs is localized at stage A as EC3, and the EC of APM is localized at backup filter F as EC2. We analyzed several samples from the maintenance work of instruments for heat treatment of MWCNTs: automated packing during and not during work; and outside of the factory at 5 m from the air inlet to the factory. These real airborne particle samples at CNT production facilities showed tendencies somewhere between the MW1 and APM shown in **Fig. 5**. The details were shown in our previous paper (Ono-Ogasawara and Myojo, 2013).

Table 1 IMPROVE protocol for carbon aerosol analyzer.

	Time* (s)	Temperature (˚C)	Atmospheric gas
OC1	180	120	He
OC2	180	250	He
OC3	300	450	He
OC4	300	550	He
EC1	360	550	2% O_2/He
EC2	600	700	2% O_2/He
EC3	360	920	2% O_2/He

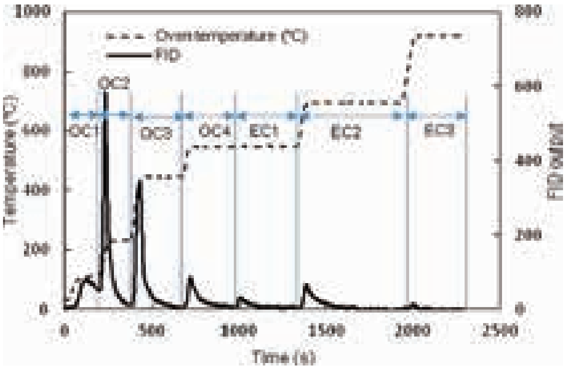

*: Time of each step was adjusted for non-MWCNT samples. Inset shows a thermogram of an aerosol sample (Ono-Ogasawara and Myojo, 2013).

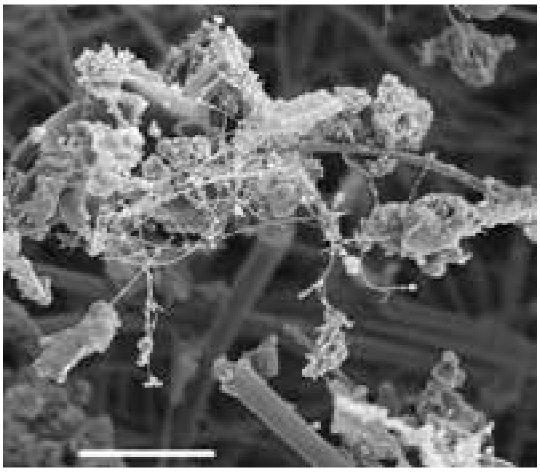

Fig. 3 Scanning electron microscopy of MWCNTs suspended in a workplace air. The bold fibers in the image are fibers of quartz filter. The white bar in the photo shows 10 µm.

Based on our data, a schematic diagram of the size and EC amounts that evolved at different oven temperatures could be depicted as shown in **Fig. 6** (Ono-Ogasawara and Myojo, 2013). Fullerene (C_{60}) decomposed easily at a low temperature (Myojo et al., 2011). SWCNTs and thin MWCNTs also oxidized at 700 degree C, and the main proportion was EC2. The MWCNTs oxidized as EC2, as indicated by the presence of thinner MWCNTs, then EC3 must be an indication of the presence of thick MWCNTs. Well-produced carbon black (CB) is stable at high temperatures, and EC3 was a main constituent. **Fig. 6** shows

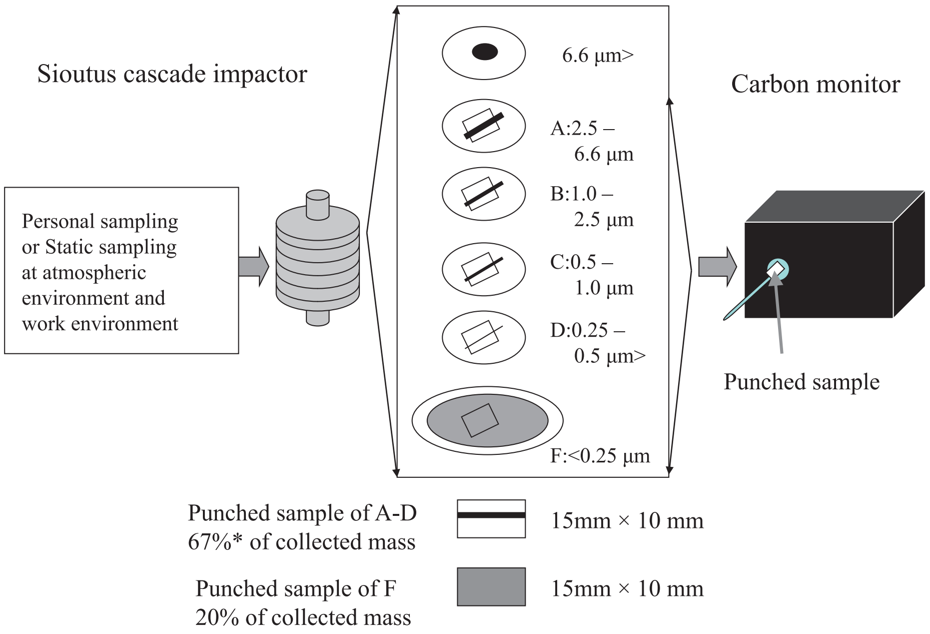

Fig. 4 Schematic diagram of sampling and analysis of ambient MWCNT particles.
* Determined by measured data (Ono-Ogasawara and Myojo, 2011). Nominally 75 % (= 15 mm/20 mm).

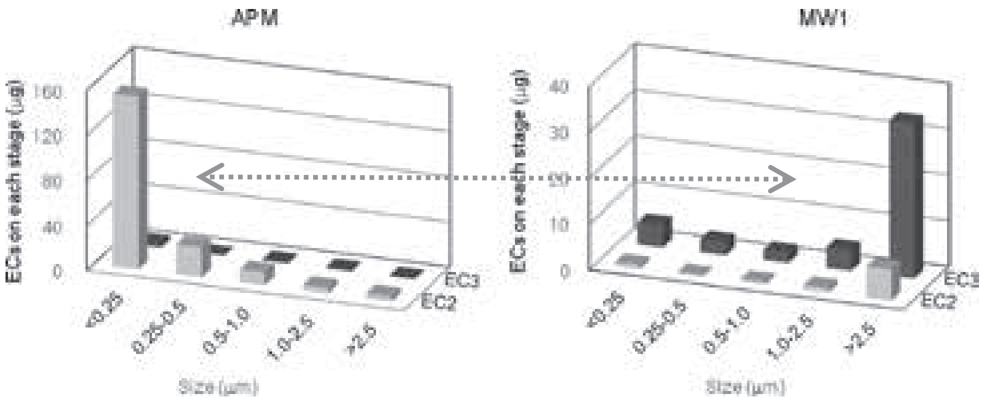

Fig. 5 Typical size effects on EC2 and EC3 of carbon analysis for typical samples of APM and MW1 (a sample of MWCNTs). Agglomerates of MWCNTs were detected at large fractions (> 2.5 µm and EC3). EC in a sample of ambient particulate matters were detected at small fractions (< 0.25 µm and EC2). Real samples were mixtures of the both graphs. (Ono-Ogasawara and Myojo, 2013)

a general tendency of the appearance of different types of carbon from carbonaceous nanomaterials in a carbon analysis. This tendency depends not only on the graphitization but also on the impurities in each sample, such as catalytic metals. To apply this method to the workplace, it is important to know the properties of the target materials used in each workplace. For measurements using a carbon monitor, the limit of quantitation is around 1 µg EC on a punched filter. This means stages A to D need to be more than 1.5 µg EC at each stage. The quantitation limit for the backup filter is expected to be 5.3 µg on the filter, and the expected minimum concentration of 2 hours sampling by SCI should be 1 µg EC/m^3.

5. Conclusion

The lifecycle of carbonaceous nanomaterials can be categorized into the following six stages: manufacturing or synthesizing; manufacturing of interim products (master batches and dispersed solutions); manufacturing of products (composite, papers or fibers); processing of the products (cutting or sanding); use of the products; and disposal/recycling (Ono-Ogasawara et al. 2015). In these phases of the life cycle, the isolated nanoparticles or nanofibers discussed above may exist only in the first two phases and the last phase. The binding strength between nanomaterials and base materials of the composite ranges from weak surface adhesion to chemical bonding. The

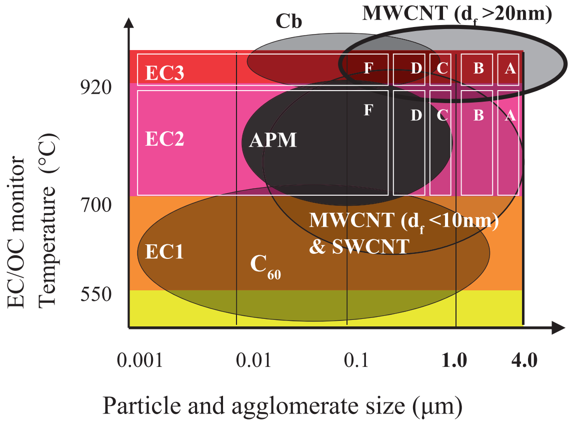

Fig. 6 Estimated 2 dimensional map of size and EC1 to EC3 by our carbon analysis for MWCNT and other carbonaceous materials. CB: carbon black, APM: ambient particulate matter, d_f: diameter of MWCNTs. A to D and F are samples on the stages of SCI. (Ono-Ogasawara and Myojo, 2013)

exposure assessment and risk assessment of nanomaterials should be anticipated at all these stages. The thermal carbon analysis method with size-segregation of airborne particles is applicable to the measurement of exposure to carbonaceous nanomaterials at any stage of the life cycle. Further validation of the method and examples of its application are needed, however, in order to reach consensus regarding exposure measurements of carbonaceous nanomaterials.

This review is not a systematic review and mainly focused on reports on the risk assessment of carbonaceous nanomaterials as conducted by the authors and their co-workers or related work by others.

Acknowledgements

Table 1 and **Fig. 5** and **6** in this article are reprinted from "Characteristics of multi-walled carbon nanotubes and background aerosols by carbon analysis; particle size and oxidation temperature. Advanced Powder Technol. (2013) 24(1): 263–69 by Ono-Ogasawara, M. and Myojo, T." with permission from Elsevier.

Fig. 4 in this article is reprinted from "A proposal of method for evaluating airborne MWCNT concentration. Ind Health. (2011) 49(6): 726–34 by Ono-Ogasawara, M. and Myojo, T." with permission from Industrial Health.

References

Baker G.L., Gupta A., Clark M.L., Valenzuela B.R., Staska L.M., Harbo S.J., Pierce J.T., Dill J.A., Inhalation toxicity and lung toxicokinetics of C_{60} fullerene nanoparticles and microparticles, Toxicological Sciences, 101 (2008) 122–131.

Birch M.E., Cary R.A., Elemental carbon-based method for monitoring occupational exposures to particulate diesel exhaust, Aerosol Science and Technology, 25 (1996) 221–241.

Birch M.E., Occupational monitoring of particulate diesel exhaust by NIOSH method 5040, Applied Occupational and Environmental Hygiene, 17 (2002) 400–405.

British Standards Institution, Nanotechnologies—Part 2: Guide to safe handling and disposal of manufactured nanomaterials, (2007) PD 6699-2:2007.

Chow J.C., Watson J.G., Pritchett L.C., Pierson W.R., Frazier C.A., Purcell R.G., The DRI thermal/optical reflectance carbon analysis system: description, evaluation and applications in U.S. Air quality studies, Atmospheric Environment Part A General Topics, 27 (1993) 1185–1201.

Dahm M.M., Schubauer-Berigan M.K., Evans D.E., Birch M.E., Fernback J.E., Deddens J.A., Carbon nanotube and nanofiber exposure assessments: an analysis of 14 site visits, The Annals of Occupational Hygiene, 59 (2015) 705–723.

Donaldson K., Aitken R., Tran L., Stone V., Duffin R., Forrest G., Alexander A., Carbon nanotubes: a review of their properties in relation to pulmonary toxicology and workplace safety, Toxicological Sciences, 92 (2006) 5–22.

Elder A., Gelein R., Finkelstein J.N., Driscoll K.E., Harkema J., Oberdörster G., Effects of subchronically inhaled carbon black in three species. I. Retention kinetics, lung inflammation, and histopathology, Toxicological Sciences, 88 (2005) 614–629.

Endo M., Grow carbon fibers in the vapor phase, CHEMTECH, 18 (1988) 568–576.

Fujitani Y., Kobayashi T., Arashidani K., Kunugita N., Suemura K., Measurement of the physical properties of aerosols in a fullerene factory for inhalation exposure assessment, Journal of Occupational and Environmental Hygiene, 5 (2008) 380–389.

Han J.H., Lee E.J., Lee J.H., So K.P., Lee Y.H., Bae G.N., Lee S.-B., Ji J.H., Cho M.H., Yu I.J., Monitoring multiwalled carbon nanotube exposure in carbon nanotube research facility, Inhalation Toxicology, 20 (2008) 741–749.

Hedmer M., Isaxon C., Nilsson P.T., Ludvigsson L., Messing M.E., Genberg J., Skaug V., Bohgard M., Tinnerberg H., Pagels J.H., Exposure and emission measurements during production, purification, and functionalization of arc-discharge-produced multi-walled carbon nanotubes, The Annals of Occupational Hygiene, 58 (2014) 355–379.

IARC Monographs on the Evaluation of Carcinogenic Risks to Humans, Eds., volume 65, Printing processes and printing inks, carbon black and some nitro compounds, Lyon, France, 1996, pp. 149–262.

IARC Monographs on the Evaluation of Carcinogenic Risks to Humans, Eds., volume 93, Carbon Black, Titanium Dioxide, and Talc, Lyon, France, 2010, pp. 1–413.

Iijima S., Helical microtubules of graphitic carbon, Nature, 354 (1991) 56–58.

JSOH (the Japan Society for Occupational Health), Recommendation of occupational exposure limits (2015–2016), Journal of Occupational Health, 57 (2015) 394–417.

Kasai T., Umeda Y., Ohnishi M., Mine T., Kondo H., Takeuchi T., Matsumoto M., Fukushima S., Lung carcinogenicity of inhaled multi-walled carbon nanotube in rats, Particle and Fibre Toxicology, 13 (2016) 53.

Kim K.H., Sekiguchi K., Kudo S., Sakamoto K., Characteristics of atmospheric elemental carbon (char and soot) in ultrafine and fine particles in a roadside environment, Japan, Aerosol and Air Quality Research, 11 (2011) 1–12.

Kobayashi N., Naya M., Ema M., Endoh S., Maru J., Mizuno K., Nakanishi J., Biological response and morphological assessment of individually dispersed multi-wall carbon nanotubes in the lung after intratracheal instillation in rats, Toxicology, 276 (2010) 143–153.

Kroto H.W., Heath J.R., O'Brien S.C., Curl R.F., Smalley R.E., C_{60}: Buckminsterfullerene, Nature, 318 (1985) 162–163.

Kudo S., Sekiguchi K., Kim K.H., Sakamoto K., Spatial distributions of ultrafine particles and their behavior and chemical composition in relation to roadside sources, Atmospheric Environment, 45 (2011) 6403–6413.

Kuempel E.D., Jaurand M.-C., Møller P., Morimoto Y., Kobayashi N., Pinkerton K.E., Sargent L.M., Vermeulen R.C.H., Fubini B., Kane A.B., Evaluating the mechanistic evidence and key data gaps in assessing the potential carcinogenicity of carbon nanotubes and nanofibers in humans, Critical Reviews in Toxicology, 47 (2017) 1–58.

Kuhlbusch T.A.J., Fissan H., Particle characteristics in the reactor and pelletizing areas of carbon black production, Journal of Occupational and Environmental Hygiene, 3 (2006) 558–567.

Kuijpers E., Bekker C., Fransman W., Brouwer D., Tromp P., Vlaanderen J., Godderis L., Hoet P., Lan Q., Silverman D., Vermeulen R., Pronk A., Occupational exposure to multi-walled carbon nanotubes during commercial production synthesis and handling, The Annals of Occupational Hygiene, 60 (2016) 305–317.

Lee B.-W., Kadoya C., Horie M., Mizuguchi Y., Hashiba M., Kambara T., Okada T., Myojo T., Oyabu T., Ogami A., Morimoto Y., Tanaka I., Uchida K., Endoh S., Nakanishi J., Analysis of pulmonary surfactant in rat lungs after intratracheal instillation of short and long multi-walled carbon nanotubes, Inhalation Toxicology, 25 (2013) 609–620.

Ma-Hock L., Strauss V., Treumann S., Küttler K., Wohlleben W., Hofmann T., Gröters S., Wiench K., van Ravenzwaay B., Landsiedel R., Comparative inhalation toxicity of multi-wall carbon nanotubes, graphene, graphite nanoplatelets and low surface carbon black, Particle and Fibre Toxicology, 10 (2013) 23.

Ma-Hock L., Treumann S., Strauss V., Brill S., Luizi F., Mertler M., Wiench K., Gamer A.O., van Ravenzwaay B., Landsiedel R., Inhalation toxicity of multiwall carbon nanotubes in rats exposed for 3 months, Toxicological Sciences, 112 (2009) 468–481.

Maynard A.D., Baron P.A., Foley M., Shvedova A.A., Kisin E.R., Castranova V., Exposure to carbon nanotube material: aerosol release during the handling of unrefined single-walled carbon nanotube material, Journal of Toxicology and Environmental Health, Part A, 67 (2004) 87–107.

Maynard A.D., Nanotechnology: The next big thing, or much ado about nothing?, The Annals of Occupational Hygiene, 51 (2007) 1–12.

Methner M., Hodson L., Geraci C., Nanoparticle emission assessment technique (NEAT) for the identification and measurement of potential inhalation exposure to engineered nanomaterials—Part A, Journal of Occupational and Environmental Hygiene, 7 (2010) 127–132.

Morimoto Y., Hirohashi M., Ogami A., Oyabu T., Myojo T., Nishi K.-i., Kadoya C., Todoroki M., Yamamoto M., Murakami M., Shimada M., Wang W.-N., Yamamoto K., Fujita K., Endoh S., Uchida K., Shinohara N., Nakanishi J., Tanaka I., Inflammogenic effect of well-characterized fullerenes in inhalation and intratracheal instillation studies, Particle and Fibre Toxicology, 7 (2010) 4. DOI: 10.1186/1743-8977-7-4

Morimoto Y., Hirohashi M., Ogami A., Oyabu T., Myojo T., Todoroki M., Yamamoto M., Hashiba M., Mizuguchi Y., Lee B.W., Kuroda E., Shimada M., Wang W.-N., Yamamoto K., Fujita K., Endoh S., Uchida K., Kobayashi N., Mizuno K., Inada M., Tao H., Nakazato T., Nakanishi J., Tanaka I., Pulmonary toxicity of well-dispersed multi-wall carbon nanotubes following inhalation and intratracheal instillation, Nanotoxicology, 6 (2012) 587–599.

Myojo T., Oyabu T., Nishi K., Kadoya C., Tanaka I., Ono-Ogasawara M., Sakae H., Shirai T., Aerosol generation and measurement of multi-wall carbon nanotubes, Journal of Nanoparticle Research, 11 (2009) 91–99.

Myojo T., Oyabu T., Ogami A., Hirohashi M., Murakami M., Yamamoto M., Todoroki M., Kadoya C., Nishi K., Yamasaki S., Morimoto Y., Tanaka I., Shimada M., Endoh S., Monitoring of C_{60} aerosol concentrations during 4-week inhalation study using a carbon aerosol analyzer with adjusted analytical protocol, Journal of Nanoparticle Research, 13 (2011) 2063–2071.

Nakanishi J, Risk Assessment of Manufactured Nanomaterials: "Approaches"—Overview of Approaches and Results—Final Report Issued on August 17, 2011. NEDO Project (P06041) Research and development of Nanoparticle characterization method, Tokyo, 2011, <www.aist-riss.jp/projects/nedo-nanorisk/index_e.html> accessed 08.06.2017.

Nakanishi J., Morimoto Y., Ogura I., Kobayashi N., Naya M., Ema M., Endoh S., Shimada M., Ogami A., Myojyo T., Oyabu T., Gamo M., Kishimoto A., Igarashi T., Hanai S., Risk assessment of the carbon nanotube group, Risk Analysis, 35 (2015) 1940–1956.

NIOSH (National Institute for Occupational Safety and Health), Current Intelligence Bulletin 65, Occupational Exposure to Carbon Nanotubes and Nanofibers, Ohio, 2013, <www.cdc.gov/niosh/docs/2013-145/pdfs/2013-145.pdf> accessed 08.06.2017.

NIOSH Manual of Analytical Methods (NMAM), in: PC. Schlecht, PF. O'Connor (Eds.), Method 5040 update DHHS (NIOSH) Publication No. 2003-154, Third Supplement to NMAM, fourth ed., National Institute for Occupational Safety and Health, Cincinnati, OH, USA, 2003.

Oberdörster E., Manufactured nanomaterials (fullerenes, C(60)) induce oxidative stress in the brain of juvenile largemouth bass, Environmental health perspectives, 112 (2004) 1058–

1062.

Ogami A., Yamamoto K., Morimoto Y., Fujita K., Hirohashi M., Oyabu T., Myojo T., Nishi K., Kadoya C., Todoroki M., Yamamoto M., Murakami M., Shimada M., Wang W.-N., Shinohara N., Endoh S., Uchida K., Nakanishi J., Tanaka I., Pathological features of rat lung following inhalation and intratracheal instillation of C_{60} fullerene, Inhalation Toxicology, 23 (2011) 407–416.

Ono-Ogasawara M., Myojo T., Kobayashi S., A nanoparticle sampler incorporating differential mobility analyzers and its application at a road-side near heavy traffic in Kawasaki, Japan, Aerosol and Air Quality Research, 9 (2009) 290–304.

Ono-Ogasawara M., Myojo T., A proposal of method for evaluating airborne MWCNT concentration, Industrial Health, 49 (2011) 726–734.

Ono-Ogasawara M., Myojo T., Characteristics of multi-walled carbon nanotubes and background aerosols by carbon analysis; particle size and oxidation temperature, Advanced Powder Technology, 24 (2013) 263–269.

Ono-Ogasawara M., Takaya M., Yamada M., Exposure assessment of MWCNTs in their life cycle, Journal of Physics: Conference Series, 617 (2015) 012009.

Pauluhn J., Subchronic 13-week inhalation exposure of rats to multiwalled carbon nanotubes: toxic effects are determined by density of agglomerate structures, not fibrillar structures, Toxicological Sciences, 113 (2010) 226–242.

Sager T.M., Castranova V., Surface area of particle administered versus mass in determining the pulmonary toxicity of ultrafine and fine carbon black: comparison to ultrafine titanium dioxide, Particle and Fibre Toxicology, 6 (2009) 15.

Shinohara N., Nakazato T., Tamura M., Endoh S., Fukui H., Morimoto Y., Myojo T., Shimada M., Yamamoto K., Tao H., Yoshida Y., Nakanishi J., Clearance kinetics of fullerene C_{60} nanoparticles from rat lungs after intratracheal C_{60} instillation and inhalation C_{60} exposure, Toxicological Sciences, 118 (2010) 564–573.

Takaya M., Ono-Ogasawara M., Shinohara Y., Kubota H., Tsuruoka S., Koda S., Evaluation of exposure risk in the weaving process of MWCNT-coated yarn with real-time particle concentration measurements and characterization of dust particles, Industrial Health, 50 (2012) 147–155.

Takaya M., Serita F., Ono-Ogasawara M., Shinohara Y., Saito H., Koda S., Airborne particles in a multi-wall carbon nanotube production plant: observation of particle emission and personal exposure 1: Measurement in the packing process, Sangyo Eiseigaku Zasshi, 52 (2010) 182–188.

Zhu S., Oberdörster E., Haasch M.L., Toxicity of an engineered nanoparticle (fullerene, C_{60}) in two aquatic species, Daphnia and fathead minnow, Marine Environmental Research, 62 (2006) S5–S9.

Author's short biography

Toshihiko Myojo

His research interests are the sampling and analysis of airborne particles at workplaces and biological effects after inhalation of the particles based on *in vivo* studies.

He was educated at Kanazawa University, B.S. and M.S. in Chemical Engineering. He got Ph.D. degree (1991) from Kanazawa University. He worked as a researcher at National Institute of Industrial Health, Ministry of Labour, Japan (1979–2006). He was appointed to Associate Professor, University of Occupational and Environmental Health, Japan (2006–2010) and then promoted Professor in 2010.

Mariko Ono-Ogasawara

Her research interest is the exposure assessment of hazardous vapors and particles, especially carbon nanotubes and carbonaceous nanomaterials, in workplaces.

She was educated at Saitama University, B.S. and M.S. in Environmental Chemistry. She got the Ph.D. degree (2011) from Saitama University. She has been working for National Institute of Occupational Safety and Health, Japan (JNIOSH), former National Institute of Industrial Health, Ministry of Labour, as a researcher since 1987. She was appointed to Director of Work Environment Research group, JNIOSH in 2015.

KONA Powder and Particle Journal No. 35 (2018) 89–111/Doi:10.14356/kona.2018015 Review Paper

Nanoparticles Carrying Biological Molecules: Recent Advances and Applications [†]

Suryani Saallah [1,2] **and I. Wuled Lenggoro** [1,3*]

[1] *Graduate School of Bio-Applications and Systems Engineering, Tokyo University of Agriculture and Technology, Japan*
[2] *Biotechnology Research Institute, Universiti Malaysia Sabah, Malaysia*
[3] *Department of Chemical Engineering, Tokyo University of Agriculture and Technology, Japan*

Abstract

In the past few decades, enormous advances have been achieved in the field of particle technology and the trend has been shifted from macro to micro and recently to the nanoscale. Integration of nanotechnology and biotechnology has paved the way to the development of biological nanoparticles, derived from biomolecules, and biomolecule-nanoparticle conjugates for numerous applications. This review provides an overview of various types of biological nanoparticles and the methods of their fabrication with primary emphasis on the drying methods, particularly on the newly emerging technique, the electrospraying. Recent advances in the integration of biomolecules with nanoparticles in the past five years to present are also discussed. Finally, the application of the biomolecule-nanoparticle conjugates in various fields including medicals and pharmaceuticals, biosensors and bioelectronics, foods, and agricultures are also highlighted.

Keywords: powder, particle, electrospray, biomaterial, enzyme

1. Introduction

Nanotechnology is a rapidly growing field that deals with the processing of materials with size less than 1000 nm, from the production to its applications (Jaworek A. and Sobczyk A.T., 2008). Owing to its large surface area to volume ratio, the reduction of particle size to nanoscale offers remarkable improvement in the physical, mechanical, electrical, and optical properties, that is not seen in the bulk materials (Yurteri C.U. et al., 2010). Breakthroughs in nanomaterial synthesis increased diverse nanomaterials production and subsequently their applications.

Nature had provided various types of biomolecules such as proteins, nucleic acids, lipids, and polysaccharides, which have their own unique properties that can be utilised for the development of nanoparticles (Sperling R.A. and Parak W.J., 2010). These organic based nanoparticles received little attention in the past; in comparison with inorganic based such as metals, metal oxides, ceramics and quantum dots where enormous researches and technological advancements have been made (Kumar R. and Lal S., 2014). However, in recent years, considerable interest has been shown in the utilisation of biological nanoparticles, derived from biomolecules as an alternative to the chemically synthesised nanoparticles. This is due to the need for developing biocompatible and biodegradable nanoparticles in addition to the other advantages offered including ease of availability and non-immunogenic (Sundar S. et al., 2010).

Biomolecules can also be engineered to possess unique compositions and functionalities and can be conjugated with various types of nanoparticles such as metals and metal oxides, to complement the unique properties of nanoparticles with intrinsic features of biomolecules, to yield novel biomolecule-nanoparticle hybrid. To date, many review papers are available in the literature that highlights the development and application of nanoparticles in various sectors (De M. et al., 2008, Salata O.V., 2004, Wang E.C. and Wang A.Z., 2014). However, limited reviews are available for biological nanoparticles and the integration of nanoparticles with biomolecules. Therefore, up to date information on the technology and current trend in the field is required. The present review details the types of biological nanoparticles, their methods of synthesis, the recent advances in the integration of biomolecules with nanoparticles, and the application of biomolecule-nanoparticle conjugates in medicals and

---

[†] Received 12 April 2017; Accepted 4 August 2017
J-STAGE Advance published online 30 September 2017
[1] 2-24-16 Nakacho, Koganei, Tokyo 184-8588, Japan
[2] 88400, Kota Kinabalu, Sabah, Malaysia
[3] 2-24-16 Nakacho, Koganei, Tokyo 184-8588, Japan
* Corresponding author: I. Wuled Lenggoro
E-mail: wuled@cc.tuat.ac.jp
TEL/FAX: +81-42-388-7987

pharmaceuticals, biosensors and bioelectronics, foods, and agricultures. For the context of this review, only nanoparticles derived or conjugated with biomolecules were discussed.

2. Types of biological nanoparticles

Biological nanoparticles are particles with size ranging from 10 nm to 1 μm, derived from biomolecules or organic compounds. They can be divided into four major categories which are proteins, nucleic acids, lipids and polysaccharides based (Kumar R. and Lal S., 2014).

Protein is the predecessor of the naturally occurring material used for the preparation of nanoparticle, attributed to their unique functionalities and defined primary structure. These features enable various possibilities for surface modifications and attachment of other compounds such as drugs and therapeutics (Bhunchu S. and Rojsitthisak P., 2014; Jahanshahi M. and Babaei Z., 2008). Additionally, they can be processed in the form of gels, emulsions and dried particles, have greater stability in vivo and during storage, and relatively easy to synthesise with controllable size distribution (Sundar S. et al., 2010), which allows them to be an ideal material for nanoparticles preparations. To date, wide varieties of proteins have been used for nanoparticle formulations including albumin, gelatine, elastin, collagen, gliadin, zein, ferritin (Nitta S.K. and Numata K., 2013) and silk proteins such as sericin and fibroin (Hazeri N. et al., 2012; Zhao Z. et al., 2015).

Nanoparticles can also be formulated from nucleic acids strands of DNA and RNA. These biomolecules can be engineered to form 3-dimensional nano-scaffolds due to the simplicity of their primary structure. Furthermore, nucleic acids have a unique ability to self-assemble into compact and stable structures with precise control over the nanoparticle size, geometry, and composition (Panigaj M. and Reiser J., 2016). The current research in the development of bio-based nanoparticles have shown that the DNA and RNA nanoparticles can be utilised as scaffolds and can be tagged with various types of biological and therapeutic compounds such as aptamers, fluorophores, and oligonucleotides to carry its desired function (Friedman A.D. et al., 2013; Panigaj M. and Reiser J., 2016).

Lipid based nanoparticles which include liposomes, nanoemulsions, solid lipid nanoparticles (SLN) and nanostructured lipid carriers (NLC) have emerged as a potential nanoparticulate system and have been recognised among the most promising encapsulant in the nanobiotechnology field (Tamjidi F. et al., 2013). In addition to their high encapsulation efficiency, lipid nanoparticles demonstrated longer shelf life and storage stability, hassle-free scaling up from lab to industrial scale, and ability to target and entrap compound with different solubility (Weiss J. et al., 2008).

Polysaccharides are naturally occurring carbohydrate polymers that are linked together by glycosidic bonds. They can be obtained from plants (e.g. pectin, insulin), animals (e.g. chitosan), and algae (alginates) and also from a microorganism such as a dextran. Among various types of polysaccharides, chitosan is one of the most valued polysaccharides probably due to its permeability enhancing properties. Chitosan, a cationic polyaminosaccharide, have high-density amino groups and mucoadhesive properties, allowing facile chemical modification and complexation with negatively charged molecules (Sahdev P. et al., 2014). By exploiting the charge mediated ionic interactions, a wide variety of biomolecules such as proteins (Mattu C. et al., 2013), plasmid DNA and antigens as well as bioflavonoids (Ha H.-K. et al., 2013; Hosseini S.F. et al., 2013) have been successfully incorporated into chitosan nanoparticles. The nanoparticles are commonly fabricated through ionotropic gelation and self-assembly of polyelectrolytes, a relatively simple procedure that does not require the use of organic solvents and operated in mild temperature and pressure condition (Rampino A. et al., 2013; Sahdev P. et al., 2014).

3. Methods to synthesise biological nanoparticles

Synthesis of nanoparticles derived from inorganic compounds such as metal, metal oxides and polymeric materials have been discussed deeply in a number of review papers. However, only a few reviews are available for the synthesis of biological nanoparticles. Design and synthesis of biological nanoparticles with desired properties is an important field of research in nanotechnology to allow applications of such materials in various fields which consequently give a positive impact to nature and human being. Recently, different strategies for production of nanosized materials exist and new techniques are constantly developed (**Table 1**). In biotechnology context, several criteria have to be taken into account for the selection of techniques to produce particles with controlled characteristics such as uniform size distribution, morphology, high purity, and composition. Additionally, the method should be simple, inexpensive, and have high throughput (Peltonen L. et al., 2010). In this section, general overviews of the methods to synthesise biological nanoparticles which include two steps procedures based on emulsification, a one-step procedure involving nanoprecipitation, desolvation, and gelation, and through drying methods are presented, with primary emphasis on the preparation by drying process.

Table 1 Summary of various types and methods to synthesise biological nanoparticles.

Material	Fabrication method	Particle size and characteristics	Application	Reference
BSA	Dynamic aggregation, radiation-induced cross-linking	20–40 nm	Drug carrier	Achilli E. et al. (2015)
Cruciferin	Cold gelation	~200 nm spherical, polydispersity index (PDI) of 0.2–0.3	Delivery of bioactive food components	Akbari A. and Wu J. (2016)
Chimeric polypeptide	Genetically encoded synthesis in E. Coli	60 nm, nearly monodisperse	Treatment of cancer Conjugated drug: paclitaxel	Bhattacharyya J. et al. (2015)
Fibronectin	Electrospraying	28.2–31.52 nm	Functionally active protein for tissue engineering	Fornari E. et al. (2015)
Zein	Electrospraying	175–900 nm	Encapsulant for food coloring and ingredients	Gomez-Estaca J. et al. (2012)
Fluorescent proteins	Liquid nanodispensing (NADIS)	50 nm–microns	Nanodevice (Scanning probe lithography)	Fabie L. et al. (2015)
Fibroin	Electrospraying	80 nm	Wound dressing and tissue engineering	Gholami A. et al. (2010)
Whey protein isolate (WPI)	Homogenisation-evaporation	90 nm	Delivery vehicle for beta-carotene to intestine	Yi J. et al. (2015)
Soybean protein isolate (SPI)	Homogenisation-evaporation	370 nm	Delivery vehicle for beta-carotene to intestine	Yi J. et al. (2015)
Chitosan oligosaccharide/ β-lactoglobulin	Ionic gelation	150–30 nm, spherical	Delivery of hydrophobic bioactive compounds into aqueous foods	Ha H.-K. et al. (2013)
Bioactive peptides/chitosan	Ionic gelation	150 ± 4.3 nm, PDI = 0.05 to 0.14	Encapsulant of epigallocatechin-3-gallate (EGCG) for nanochemoprevention	Hu B. et al. (2012)
Chitosan	Ionic gelation	550–850 nm, spherical with some irregular shape particles	Protein carriers in tissue engineering	Mattu C. et al. (2013)

3.1 Two steps procedure based on emulsifications

Methods for the preparation of biological nanoparticles based on emulsification strategies have been evolved in the past decades due to the advancement in the technology and emulsification devices (Kumar R. and Lal S., 2014). The emulsion system can be in the form of oil in water (o/w), water in oil (w/o) and oil in oil (o/o), depending on the type of the dispersed phase and dispersion medium. A more complex system based on a combination of multiple emulsions has also been synthesised such as water in oil in water (w/o/w), oil in water in oil (o/w/o) and water in oil in oil (w/o/o). After generation of the emulsion nanodroplets, nanoparticles can be produced through precipitation induced by various solvent extractions mechanisms such as solvent evaporation, solvent diffusion or salting-out. Other techniques such as gelation and polymerisation can also be used for converting the emulsions to nanoparticles (Bilati U. et al., 2005; Kumar R. and Lal S., 2014).

Emulsification method offers high encapsulation efficiency and high batch-to-batch reproducibility. Furthermore, nanoparticles obtained through this method usually have narrow size distribution (Chaturvedi S.P. and Kumar V., 2012; Pal S.L. et al., 2011). The avoidance of heat treatment during the preparation step has made this method as a useful strategy for encapsulation of highly thermolabile compounds. However, the presence of residual solvent in the final dispersion is undesirable due to regulatory concern. Therefore, intensive washing procedures are required to eliminate the solvent residue (Chaturvedi S.P. and Kumar V., 2012). Moreover, the application of this method is mainly limited to lipophilic molecules. Compounds which have limited solubility in organic solvent require a subsequent addition of excess water, resulted in dilute dispersion that needs to be concentrated by means of another operation such as filtration and evaporation (Das S. and Chaudhury A., 2011). The particles generation through emulsification have been reviewed extensively by Anton and co-workers (2008) and will not be discussed in details.

3.2 One step procedures

Nano-precipitation is a method to synthesise nanoparticles based on the interfacial deposition of polymer after displacement of a semi polar solvent (miscible with water) from a lipophilic solution. Therefore, nano-precipitation is also termed as interfacial deposition or solvent displacement methods. This method was developed by Fessi et al. in the late 1980s (Kumar R. and Lal S., 2014). Nanoparticles are formed through a quick diffusion of the polymer solvent such as acetone in the non-solvent or aqueous phase. The reduction in the interfacial tension between the two phases resulted in the increase of the surface area and momentary precipitation of nanoparticles. The process can occur in the absence or presence of mechanical stirring. This method provides a simple and rapid route for the fabrication of biological nanoparticles from natural polymers and peptides with high reproducibility, even at low concentration. However, the use of nanoprecipitation approach is often hampered by the low nanoparticle recovery yields due to the low concentration of polymer required and low entrapment efficiency for water-soluble molecules such as drugs (Bilati U. et al., 2005; Kumar R. and Lal S., 2014).

Desolvation or also known as coacervation, a technique designed by Marty et al. in 1978 is a thermodynamically driven self-assembly of proteins that occur based on the addition of desolvating agents such as salts, alcohol or solvents (e.g. acetone) in a solution of biomolecules, which separates and coacervates the molecules in the aqueous phase. In this process, electrostatic interaction plays a vital role to promote self-assembly of protein (Sundar S. et al., 2010). Variety types of proteins such as albumins (human serum albumin and bovine serum albumin), gliadin and gelatine, polysaccharide particles such as chitosan, DNA and oligonucleotides have been fabricated through this method (Allouche J., 2013). To improve the stability of the nanoparticles and prevent dissolution in water, crosslinking reaction with glutaraldehyde and carbodiimide was usually performed (Sundar S. et al., 2010).

Many proteins have gel forming properties at particular conditions of pH and temperature. These properties enable the proteins to form heat-induced gels through thermal gelation process, attributed to the protein structures (primary, secondary, tertiary and quaternary) and the surrounding conditions. Under suitable conditions, the protein molecules will denature and unfold followed by the rearrangement and aggregation into a 3-dimensional structure that finds numerous applications in food industry. For charged biomolecules such as chitosan and alginate, gelation can occur through interactions with small ions of opposite charges to form nanoclusters that can be stabilised further with the addition of oppositely charged polyelectrolytes (Allouche J., 2013; Nitta S.K. and Numata K., 2013).

3.3 Preparation by drying process

Environmental considerations have motivated researchers to find alternative methods for synthesis of nanoparticles with the elimination of the use of organic solvents (Allouche J., 2013). To achieve this goal, preparation of biological nanoparticles through drying method has been seen as a promising alternative to the conventional methods discussed above. Furthermore, dry formulation of biological nanoparticles offers further stabilisation against degradation, improves shelf life and ease of handling that often difficult to achieve in liquid formulation due to the complexity of the biological molecules (Haggag Y.A. and Faheem A.M., 2015).

Besides, nanosuspensions often need to be dried for further processing and formulation for example in the form of tablets or capsules. In this regard, drying based techniques provide a convenient and straightforward method, as dried nanoparticles can be produced directly in a single step without the need for further drying steps, and the dried particles still preserved the unique properties of the original suspension (Peltonen L. et al., 2010). There are three main strategies to produce biological nanoparticles through drying methods which are supercritical drying, spray drying and the newly emerging technique, the electrospraying method which will be discussed in details.

3.3.1 Supercritical drying

Supercritical drying involves utilisation of supercritical fluid (SCF) as a drying medium (antisolvent) which offers unique property of having the density and solvating power of a liquid but with gas-like transport properties (with respect to its viscosity and diffusivity). In most supercritical fluid processing, carbon dioxide (CO_2) is used, attributed to its low critical temperature and pressure, nontoxic, non-flammable and environmentally friendly characteristics as well as availability at low prices (Sellers S.P. et al., 2001). A number of supercritical techniques are currently available for production of submicrometer-sized and nano-sized particles.

The rapid expansion of a supercritical solution (RESS) typically uses supercritical CO_2 to form finely divided dry thermolabile drugs and pharmaceutical powders. In this technique, biological constituents are solubilised in supercritical CO_2 which subsequently decompress through a nozzle into an ambient air. This process created high supersaturation conditions that promote homogeneous nucleation and precipitation of the biological solutes into well-dispersed particles. Despite the ability to generate nano-sized particles, the coalescence mechanism involved in the free jet promotes particle aggregation into micro-sized. Besides that, although the process can be conducted in a solvent free environment, the solubility of many pharmaceutical constituents in supercritical CO_2 is very low (Allouche J., 2013). Therefore, another supercritical technology such as solution enhanced dispersion by supercritical solution (SEDS) has been developed. In this system, co-solvents have been used to improve the solubility of the pharmaceutical compounds in CO_2 (Zhao Z. et al., 2015). This method has been used for precipitation of protein nanoparticles such as lysozyme, insulin, and rhDNase from their aqueous solution with the use of ethanol as co-solvent, yielding nanoparticles with size ranging from 100–500 nm (Chan H.K. and Kwok P.C.L., 2011; Sellers S.P. et al., 2001). Alternatively, supercritical fluid antisolvent (SAS) strategy can be applied to exploit the low solubilities of the solute compounds in supercritical CO_2 by mixing the solution with compressed CO_2 to promote crystallisation or by spraying into the compressed CO_2. Organic non-aqueous solvents such as dimethylsulfoxide that have been normally used in the SAS technique to enhance miscibility of solute with CO_2 at its recrystallisation temperature and pressure, however, compromised the environmental friendly nature of the CO_2. Thus, this method may not be favourable for biomolecules processing as it may cause conformational changes to their native structure (Tabernero A. et al., 2012; Zhao Z. et al., 2015).

3.3.2 Spray drying

Spray drying has been used since the 1980s as an alternative means of fine particles or powders production. The utilisation of this method for drying of biological compounds was started in the early 1990s when the potential of therapeutic proteins or drugs delivery through pulmonary route was discovered (Chan H.K. and Kwok P.C.L., 2011). In spray drying, a solution containing biomolecules is atomised into a plume of fine droplets which subsequently dried in a hot air to form solid particles. The dried particles are finally collected via a cyclone. The spray drying technology has been evolved in the past years and many types of biological solution have been processed into nanoparticles or nanopowder through this technology particularly for food and pharmaceutical application. However, the collection yield of particles generated through the conventional spray drying method is very low, resulted from the very small size of the nanoparticles. Recently, a nano-spray dryer has been developed by BÜCHI Labortechnik AG to increase the particle recovery. In this system, tiny droplets with size much smaller than the conventional spray dryer were generated by using piezoelectric actuator. The actuator is driven at an ultrasonic frequency to provide vibrating energy to a membrane, which causes ejection of millions of nanodroplets per second. The size of the particles collected depends on various factors such as the solution properties (e.g. concentration), operating conditions (e.g. feed rate, drying temperature) and the presence or absence of surfactant (Haggag Y.A. and Faheem A.M., 2015; Lee S.H. et al., 2011). By using this innovative approach, spherical shape BSA nanoparticles with smooth surface have been successfully produced by Lee S.H. et al. (2011) from BSA solution in the presence of surfactant (Tween-80). Despite the technological advancement in the spray drying system, the applicability of such system to produce biologically active particles remains a hot debate. This is mainly due to the fragile nature of biomolecules when subjected to hot drying air during the process which may lead to aggregation and loss of biological activity (Mehta P. et al., 2016). The inclusion of surfactant or disaccharide to the heat-sensitive materials such as proteins, peptides and enzymes can help to minimise these effects (Lee S.H. et al., 2011).

3.3.3 Electrospraying

Electrospraying is an electrohydrodynamic atomisation of liquid into uniform sized droplets under the influenced of electrical forces. The phenomenon of the interaction of liquid with electric field was first reported by William Gilbert in the sixteenth century who discovered that a water droplet transformed into conical shape when a piece of amber was held close to it (Yurteri C.U. et al., 2010). The first attempt to use electrospraying for the production of protein nanoparticles was demonstrated by Gomez A. et al. (1998). Insulin was used as a model protein to study the feasibility of electrospraying to produce monodispersed protein particles with preserved biological activity. In their work, the electrospraying was conducted in Taylor cone jet mode with controlled current and flowrate of 64–100 nA and 0.17–0.38 μL/min, respectively. The size of the produced insulin particles was in the range of 98–117 nm with a doughnut shape. The analysis of receptor binding properties of the electrosprayed insulin and the control insulin showed identical results, which proved that biological activity of insulin is preserved upon electrospraying. With these findings, researches involving the generation of active particles of biomolecules using the electrospraying method have emerged rapidly, especially for drug delivery application.

Besides the ability to preserve the bioactive properties of the biomolecules, the emerging utilisation of the electrospraying method is also attributed to the other unique advantages offered; the production of monodisperse particles in cone-jet mode which is often difficult to be achieved by the other particle synthesis methods, a reduction in the number of molecular aggregates due to the coalescences of droplets with the same polarity, a reduction in the risk of product contamination, can be operated in ambient conditions, cost effectiveness and simple operation. In view of these advantages, a few types of biologically active substances including DNA (Lee Y.-H. et al., 2011), proteins such as sericin (Hazeri N. et al., 2012), fibroin (Gholami A. et al., 2010), cytochrome c (Mortensen D.N. and Williams E.R., 2015), and α-lactalbumin (α-LA) (Uematsu I. et al., 2004), enzymes such as alkaline phosphatase (ALP) (Avseenko N.V. et al., 2001) and peptide such as α-cyano-4-hydroxycinnamic acid (Wei H. et al., 2004) have been successfully electrosprayed with preserved biological activity.

Basic electrospraying setup, which consists of a high voltage supply, metal capillary, and grounded collector, and the mechanism of particle generation, is shown in **Fig. 1**. The four major processes involved in electrospraying are; 1) generation of charged droplets, 2) shrinkage of the droplets due to removal or evaporation of solvent, 3) continual disintegration of the droplets to form dry particles, and finally, 4) collection or deposition of the particles (Lenggoro I.W. et al., 2002; Naim M.N. et al., 2010).

In electrospraying, the particle size and shape can be controlled by controlling the solution properties such as conductivity and surface tension and also the electrospraying parameters which include spraying voltage, flowrate and distance of the needle tip to the collector. In our group, the electrospraying technique was used to produce cyclodextrin glucanotransferase (CGTase) nanoparticles from its aqueous suspension. It was found that by conducting the electrospraying in cone jet mode and changing the needle tip to collector distance from 10 to 25 cm, nanoparticles with narrow size distribution can be obtained and the average particle size was reduced significantly from 201 to 75 nm. The reduction in the particle size has been shown to improve the CGTase catalytic performance (Saallah S. et al., 2014).

4. Integrated biomolecule-nanoparticle systems

Biomolecules exhibit nanoscale dimensions comparable to the dimensions of nanoparticles (**Fig. 2**). Revolutionary of nanotechnology and biotechnology have paved the way to complement these size similarities and intrinsic features of biomolecules with unique properties of nanoparticles to yield novel biomolecule-nanoparticle hybrid of synergistic characteristics and functions (Sperling R.A. and Parak W.J., 2010). Biomolecules also display several fundamental features that can be utilised as future building blocks for nanoparticle architecture. For example, the nature-evolved multiple binding sites of biomolecules in addition with its catalytic properties could facilitate the development of multifunctional nanoparticles (Katz E. and Willner I., 2004). Recently, substantial research efforts were directed towards developing and extending the applications of biomolecules by integrating the biomolecules with biological nanoparticles such as polysaccharides and lipids (Liao W. et al., 2016; Rassu G. et al., 2015) and other types of nanoparticles including metals (Chinen A.B. et al., 2015; Politi J. et al., 2015), metal oxides (Cao Y. et al., 2016; Shahrestani H. et al., 2016) and polymers (Cavalli R. et al., 2011; Lin T.-T. et al., 2016) through various conjugation strategies (**Table 2**).

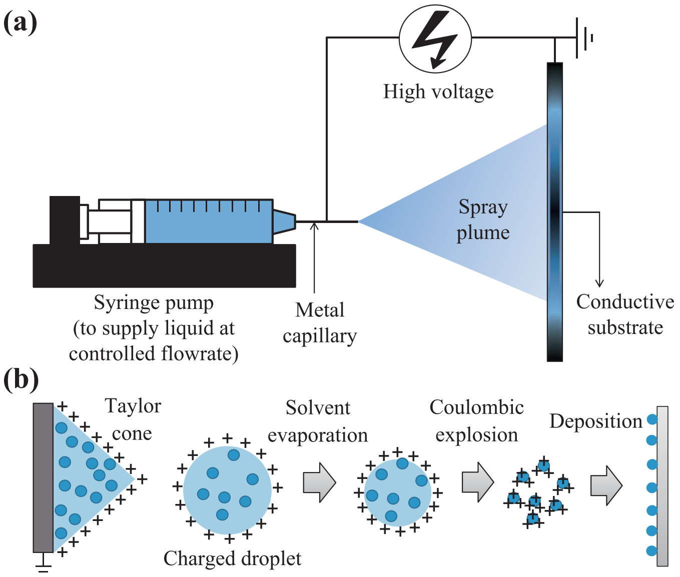

Fig. 1 (**a**) Basic electrospraying setup and (**b**) Electrospraying mechanism.

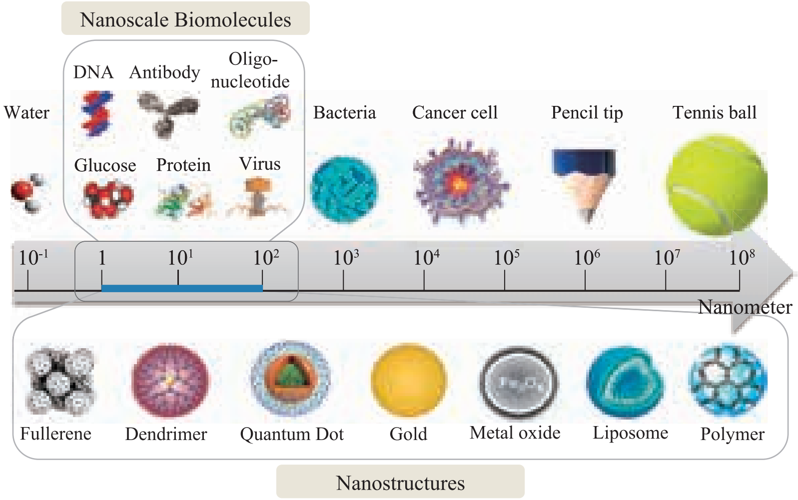

Fig. 2 Nanoscale integration of nanoparticles and biomolecules.

4.1 Strategies for the development of biomolecule-nanoparticle conjugates

4.1.1 Functionalisation of nanoparticles with biomolecules through non-covalent interactions

Non-covalent biofunctionalisation is a physical conjugation strategy that can be realised through electrostatic, hydrophobic and affinity interactions (**Fig. 3**) (Yu M.K. et al., 2012). Electrostatic adsorption is useful for the assembly of biomolecules to nanoparticles that are stabilised by anionic ligands such as lipoic acid and citrate in which the interaction of nanoparticles and the biomolecules rely on the opposite charged of both materials (Niemeyer C.M., 2001). Biological nanoparticles can be engineered to have a specific charge to enable interaction with biomolecules. The recent example is the utilisation of cationic lipid nanoparticles modified with a supercharged coiled-coil protein having positively charged arginine residues to facilitate interaction with the negatively charged SiRNA (Rabbani P.S. et al., 2017). Another example is the development of a self-assembled nanocomplex based on fucoidan, a sulphated marine polysaccharide and protamine, a strongly basic protein by utilising the electrostatic interaction between the oppositely charged polysaccharide and protein (Lu K.Y. et al., 2017). The non-covalent electrostatic complexes between proteins and polysaccharides can potentially enhance the functional properties by the synergistic combination of functional properties of both materials, compared to the single biological nanoparticle system (Hosseini S.M.H. et al., 2015).

In some cases, the strong electrostatic interaction between the charged biomolecules and its host is not always preferred. As observed by Lebre F. et al. (2016), the strong binding between positively charged chitosan and negatively charged DNA resulted in low transfection efficiency in vivo. To encounter this issue, the electrostatic interactions between the cationic chitosan nanoparticles with the anionic DNA were modified by attaching anionic human serum albumin onto the chitosan nanoparticles surface. This system enabled the intracellular release of DNA, thus enhancing the transfection efficiency.

The role of electrostatic interactions in adsorption of protein onto inorganic nanoparticles such as silica and metal oxides has been well described in many studies (Meissner J. et al., 2015). For instance, immobilisation of lysozyme and β-lactoglobulin, a globular protein onto negatively charged silica nanoparticles and binding of bovine serum albumin and β-lactoglobulin to cationic gold nanoparticle functionalised with 3,6,9,12-tetraoxatricosan1-1-aminium, 23-mercapto-*N*,*N*,*N*-trimethyl, under different pH and ionic conditions (Chen K. et al., 2011; Meissner J. et al., 2015). Generally, the maximum adsorption occurs at the protein isoelectric point. This is due to the minimum repulsion between the adsorbed protein molecules at its isoelectric point which allow them to make a closer packing at the particle surface.

Although extensive investigation on the interactions of biomolecules such as amino acids, proteins, and peptides with silica nanoparticles have shown that binding of biomolecules to silica nanoparticle is mainly driven by electrostatic interaction, Puddu V. and Perry C.C. (2012) found that hydrophobic interactions were responsible for the recognition and adsorption of peptide sequence of different charge on silica at various pH conditions. They also showed that it is possible to modulate the uptake of biomolecules on nanoparticles by tuning the surface properties and binding environments such as the biomolecules bulk concentration and pH. Bioconjugation of silica with peptide sequence having hydrophobic character is favoured when the surface charge of silica is close to its point of zero charge (more hydrophobic) (Puddu V. and Perry C.C.,

Table 2 Summary of integrated biomolecule-nanoparticle systems.

Biomolecule	Nanoparticle	Fabrication method	Conjugation strategy	Application	References
(i) Organic-organic nanoparticle conjugates					
BSA	Tripolyphosphate-crosslinked chitosan	Ionic gelation	Electrostatic interaction, encapsulation	Sustained release of protein	Mattu C. et al. (2013)
Propolis	Lipid	High shear homogenisation	Entrapment	Nasal drug delivery	Rassu G. et al. (2015)
D. indusiata polysaccharide	Selenium	Redox reaction	Encapsulation	Anticancer treatment	Liao W. et al. (2016)
Curcumin	O-carboxymethyl chitosan/fucoidan	Ionic gelation	Crosslinking	Oral delivery system	Huang Y.C. and Kuo T.H. (2014)
Quercetin	Chitosan oligosaccharide/ β-lactoglobulin	Ionic gelation	Covalent	Encapsulation of bioactives	Ha H.-K. et al. (2013)
Curcumin	Zein–pectin/ alginate	Electrostatic deposition	Electrostatic interaction, encapsulation	Functional foods and beverages	Hu K. et al. (2015)
Beta-carotene	Whey protein concentrate	Electrospraying	Encapsulation	Encapsulation of bioactives	López-Rubio A. and Lagaron J.M. (2012)
Anthocyanin-rich extract	Whey protein isolate/beet pectin	Thermal processing	Electrostatic complexation	Encapsulation of natural colorants and food nutraceuticals	Arroyo-Maya I.J. and McClements D.J. (2015)
(–)-epigallocatechin-3-gallate	Peptide/chitosan	Ionic interaction, hydrophobic association	Encapsulation	Nano-chemoprevention	Hu B. et al. (2012)
(ii) Biomolecule-polymeric nanoparticle conjugates					
BSA	PLGA	Co-axial electrospraying	Encapsulation	Drug delivery	Zamani M. et al. (2014)
BSA	HPMA/Ac-DAP-Boc	One-pot synthesis	Encapsulation	Delivery of platinum drugs into cancerous cells	Dag A. et al. (2015)
Cholestrol	Polyamidoamines	Electrospraying	Covalent	Tamoxifen delivery	Cavalli R. et al. (2011)
Chitosan	Polylactic acid/ nifedipine	Emulsion	Encapsulation	Treatment of angina pectorice and hypertension	Chinh N.T. et al. (2016)
Serum albumin	PCL/PLGA	Electrospraying	Encapsulation	Delivery of therapeutics	Bock N. et al. (2014)
Sorafenib	PEG-PLGA/PLGA co-polymer	O/W emulsion	Encapsulation	Systemic treatment of liver fibrosis	Huang X. et al. (2016)
Cisplatin	PCL-block-PEG-diblock copolymer	Dialysis, lyophilisation	Encapsulation	Treatment of glutathione over-expressed breast cancer cells	Surnar B. et al. (2015)
(iii) Organic-inorganic nanoparticle conjugates					
Lysozyme and β-lactoglobulin	Silica	—	Electrostatic interaction	Not specifically mentioned	Meissner J. et al. (2015)
Hydrophobin Vmh2	AuNP	One pot synthesis	Covalent	Biomedical	Politi J. et al. (2015)

Table 2 Summary of integrated biomolecule-nanoparticle systems (contd.).

Biomolecule	Nanoparticle	Fabrication method	Conjugation strategy	Application	References
Chitosan/Collagen	Bioactive glass	Sol-gel/freeze drying	Non-covalent	Injectable scaffolds in bone and cartilage repair	Moreira C.D.F. et al. (2016)
Spherical nucleic acid	AuNP	—	Covalent	Cellular uptake	Chinen A.B. et al. (2015)
DNA	Magnesium phosphate	Water-in-oil emulsion	Entrapment	DNA vaccine formulation	Bhakta G. et al. (2014)
Mussel adhesive proteins	Iron(III)–3,4-dihydroxyphenylalanine (DOPA)	Electrospraying	Crosslinking	pH-responsive drug delivery Model drug: Doxorubicin	Kim B.J. et al. (2015)
Plasmid DNA	Calcium phosphate	Precipitation	Encapsulation	Stem cell uptake and gene transfer	Cao X. et al. (2011)
Pepsin	AuNP	Chemical reduction	Covalent-amide coupling	Analytical sample preparation	Höldrich M. et al. (2016)
α-amylase, pectinase, cellulose	Fe_3O_4	Co-precipitation	GA crosslinking	Clarification of fruit juices	Sojitra U.V. et al. (2016)
(iv) Biomolecule-hybrid nanoparticle conjugates					
BSA	Ampiphilic polymer coated hydrophobic silver nanoparticle	Chemical precipitation	Physisorption	To study protein-nanoparticle interaction	Guo J. et al. (2015)
Lipase	Hydroxyapatite-encapsulated-c-Fe_2O_3	Chemical precipitation	EncapsulationCovalent	Interesterification of soybean oil	Xie W. and Zang X. (2016)
Curcumin	Albumin–polycaprolactone	Ring opening polymerisation	Covalent	Drug delivery system for prostate carcinoma therapeutics	Jiang Y. et al. (2016)
Xylanase	Fe_3O_4/SiO_2	Co-precipitation	Covalent	Enzymatic clarification of fruit juices	Shahrestani H. et al. (2016)
Organic fluorescent dye	$PVP/SiO_2/Fe_3O_4$	Co-precipitation, polymerization, sol–gel	Encapsulation Electrostatic interaction	Biomedical, analytical and catalytic application	Viswanathan K. (2011)
Glucose oxidase	Fe_3O_4/Polypyrrol	Co-precipitation	Encapsulation	Potentiomeric glucose biosensor	Yang Z. et al. (2014)
Trypsin	AuNP/Fe_3O_4	Solvothermal reaction	Covalent	Enzymatic digestion of proteins to peptides	Cao Y. et al. (2016)
Aptamers	AgNP/Fe_3O_4	Redox reaction	Streptavidin-biotin affinity binding	Detection of *Staphylococcus aureus*	Abbaspour A. et al. (2015)
v) Self-assembled biomolecule-nanoparticle hybrid					
BSA	Copper(II) phosphate	Self-assembly	—	Decomposition of organic dyes in wastewater treatment	Huang Y. et al. (2015)
α-lactalbumin, laccase, carbonic anhydrase and lipase	Copper(II) phosphate	Self-assembly	—	Bionsensors	Ge J. et al. (2012)
Sericin	Copper(II) phosphate	Self-assembly	—	Adsorption of heavy metal ions	Koley P. et al. (2016)

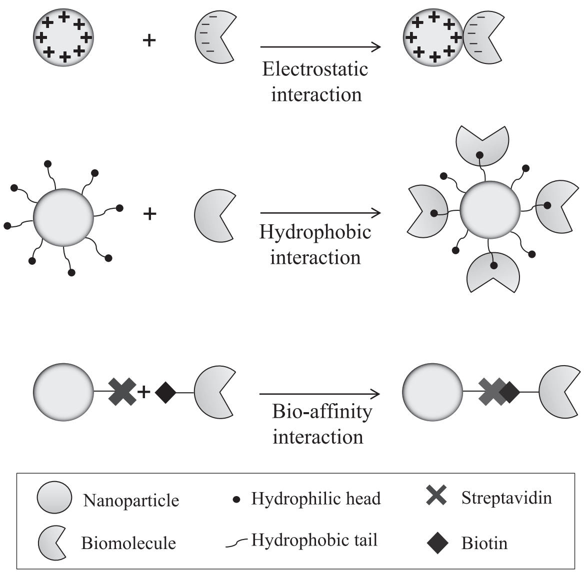

Fig. 3 Non-covalent functionalisation of nanoparticles with biomolecules.

2012). Hydrophobic interaction can also be utilised to allow binding of biomolecules with protein nanoparticles having hydrophobic properties such as gliadin as reported by Joye I.J. et al. (2015). Through fluorescence quenching and thermodynamic analysis, they found that binding of gliadin nanoparticles and resveratrol, a polyphenol extracted from a grape skin is predominantly mediated by hydrophobic interactions rather than hydrogen bonding.

Both of the electrostatic and hydrophobic interactions requires fewer modification steps, thus provide a simple and rapid route for Biofunctionalisation of nanoparticles. However, molecular orientations of the physically bound biomolecules are difficult to control. By introducing specific functional groups on the nanoparticles such as avidin, biomolecules can bound onto the nanoparticles more effectively through affinity interactions (Zhang Y. et al., 2012). Avidin is a glycoprotein composed of four identical subunits which have high specificity and affinity towards biotin, resulted in a strong affinity interaction. Despite these advantages, avidin possesses several drawbacks including a high degree of non-specific binding in vivo attributed to its basic isoelectric point and glycosylation, and the high possibility of immunogenicity. Moreover, the strong avidin-biotin interaction might hinder the release of tagged biomolecules from the biotin or avidin. To overcome these issues, extensive research effort has been devoted to develop new variants of avidin from different sources or through genetic modification (Jain A. and Cheng K., 2017).

Streptavidin, a non-glycosylated tetrameric protein, is the most widely used avidin analogue. Biotinylated proteins such as immunoglobulins and bovine serum albumin, oligonucleotides and single strand DNA have been bound onto streptavidin functionalised nanoparticles such as silver and gold (Tauran Y. et al., 2013). By utilising an electric-field-directed self-assembly method, Hsiao A.P. and Heller M.J. (2012) have successfully developed a multilayer structures glucose sensor composed of glucose oxidase, horseradish peroxidase and alkaline phosphatase enzymes conjugated with streptavidin/avidin-biotin nanoparticles through affinity interaction. The catalytic activity of the enzymes was preserved after the assembly, suggesting that the process employed did not have an adverse effect on the enzyme. Affinity interactions can also be achieved through antibody-antigen binding to allow assembly of NP-antibody conjugate with its respective antigen which is beneficial to increase the NP-antibody-antigen association constant, with respect to the free antibody (Katz E. and Willner I., 2004).

4.1.2 Functionalisation of nanoparticles with biomolecules through covalent interactions

Conjugation of biomolecules with nanoparticles via covalent interactions can be achieved by means of chemisorption of the biomolecules on the particle surface or through the use of a bifunctional linker (De M. et al., 2008). Chemisorption is a simple chemical reaction that occurs between thiol group of biomolecules and the nanoparticles through cysteine residues that are present on the surface of the biomolecules (**Fig. 4a**). If no thiolated residues available in the native biomolecules, the thiol group can be introduced chemically onto the outer part of biomolecules using Traut`s reagent (2-aminothiolane) to allow biomolecules-NP interaction (**Fig. 4b**) (De M. et al., 2008; Zhang Y. et al., 2012). The noble metal nanoparticle, particularly gold (Au) nanoparticle is highly reactive toward thiol group, thus forming a superior Au-S bond. The strong binding affinity of Au towards thiols has been exploited for conjugation of biomolecules such as DNA, peptides, antibodies, and proteins onto the nanoparticle surface (Katz E. and Willner I., 2004; Spampinato V. et al., 2016; Yu M.K. et al., 2012). Conjugation of maltose binding protein (MBP) to gold nanoparticles funtionalised with thiol-modified glucose (TG) self-assembled monolayers has been studied by Spampinato V. et al. (2016).

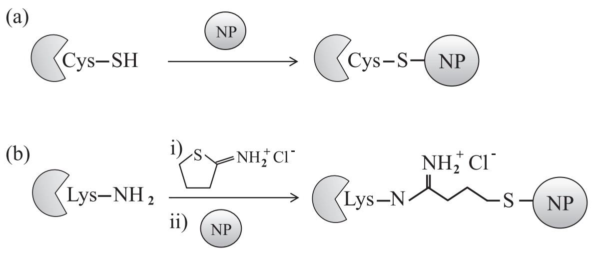

Fig. 4 Covalent functionalisation of nanoparticles through **a**) Cysteine residue; **b**) Addition of Traut’s reagent.

Surface chemistry analysis of the gold nanoparticles before and after functionalisation and interaction with TG and MBP revealed that the reaction of the thiolated gold nanoparticles with MBP occurred with specific amino acid residues exist in the protein binding pocket. In another study, Mejias S.H. et al. (2016) have demonstrated the successful assembly of an idealised protein building block, the consensus tetratricopeptide repeat (CTPR) into the nanoparticle surface through thiol chemisorption of the protein cysteine residues. As a comparison, adsorption of CTPR without cysteine residues on the gold surface was also carried out. They found that direct adsorption of CTPR having cysteine residues occurs through a single-point interaction of the thiol-derivative protein on the gold surface while the adsorption of CTPR with no cysteine residues proceeds through unspecific multipoint attachment of the protein.

Covalent binding through bifunctional linkers provide a versatile means for biomolecules conjugation. Low molecular weight bifunctional linkers which have anchor groups such as thiols, disulfides and phosphine ligands containing terminal carboxy, amino or maleimide groups are commonly used to bind biomolecules to the nanoparticles such as Au, CdS, ZnS, CdSe/ZnS and Ag. These anchor groups can be utilised to replace weakly adsorbed molecules for the nanoparticles stabilisation. Besides, during the synthesis stage of the nanoparticles, the anchor groups can be introduced to functionalise the nanoparticles surface for further reactions. Coupling of biological components to the ligands occur via carbodiimide-mediated amidation and esterification, or through reaction with thiol groups (De M. et al., 2008; Niemeyer C.M., 2001). For the oxide nanoparticles such as SiO_2, alkoxy- or halosilane groups are commonly used to covalently bind the linkers to the nanoparticles (Katz E. and Willner I., 2004). In other research done by Mejias S.H. et al. (2016), gold nanoparticles were attached to the immobilised CTPR having cysteine residues via the formation of a covalent amide linkage between the terminal amine of the protein and the carboxylate groups of the gold nanoparticles, resulting in the formation of an ordered monolayer of CTRP that can be applied in the controlled patterning of gold nanoparticles.

4.1.3 Encapsulation of biomolecules in polymeric materials

Polymeric nanoparticles are solid particles that have been used extensively as carriers for biomolecules attributed to their unique properties such as can be copolymerised, easy to synthesise and the polymer surface can be modified for biomolecules conjugation (Menon J.U. et al., 2014).. They can be fabricated in the form of nanospheres and nanocapsules (**Fig. 5**). The entire mass of the nanospheres composed of a solid polymer and the biomolecules can be attached to the surface or encapsulated within the particle while the nanocapsules are designed in such a way that the biomolecules are confined inside a core-shell structure (Rao J.P. and Geckeler K.E., 2011; Wang E.C. and Wang A.Z., 2014). In some cases, the bioactive substances can also be adsorbed on the surface of the capsule (Jawahar N. and Meyyanathan S., 2012).

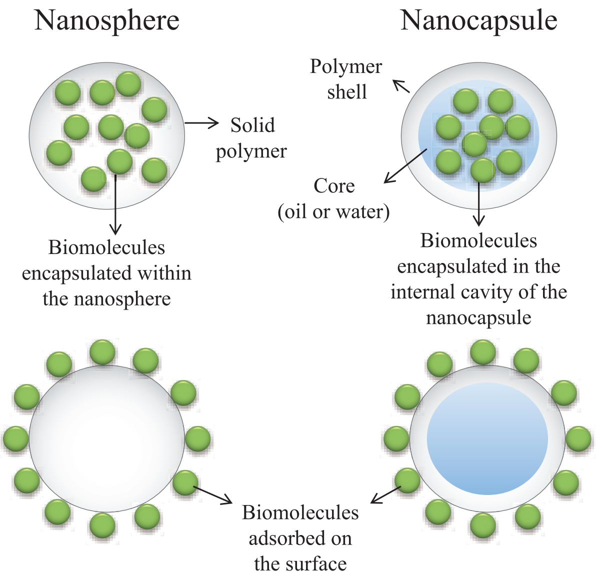

Fig. 5 Different modes of interaction of biomolecules with polymeric nanosphere and nanocapsule.

Encapsulation is a rapidly growing technology with diverse potential applications particularly in pharmaceutical and food industries. The major advantage of the encapsulation strategy is the protection of biomolecules against denaturing environment which might cause undesirable conformational changes to the biomolecules native structure and function. Moreover, encapsulation allows controlled release of biomolecules at the targeted sites. Techniques for nanoencapsulation of food and bioactive compounds have been reviewed comprehensively by Ezhilarasi P.N. et al. (2013).

4.2 Recent advances in the integration of biomolecules with nanoparticles

4.2.1 Organic-organic nanoparticle conjugates

Biological nanoparticles form part of many industrial products, particularly in food, pharmaceutical, and cosmetic industries. One of the most important features of biological nanoparticles is that they offer relatively simple means for encapsulation of biomolecules, resulting in the formation of organic-organic nanoparticle complexes. For instance, encapsulation of β-carotene into whey protein concentrate (WPC) was achieved by means of electrospraying from aqueous solutions of β-carotene/WPC mixture at various pH conditions, resulting in a formation of nanocapsule with high encapsulation efficiency and stability against photo-oxidation (López-Rubio A. and Lagaron J.M., 2012).

Biological nanoparticles derived from a single component of biomolecule have been widely used as cancer chemo-preventive and therapeutic agents. However, the single component biological nanoparticle system might possess a lack of stability and potential toxicity in a cellular system. These challenges can be potentially solved by conjugation of biomolecules with biological nanoparticle through strategic functionalisation. Liao W. et al. (2016) reported that selenium nanoparticles functionalised with a *Dictyophora indusiata* polysaccharide formed monodispersed nanoparticles with high stability attributed to the high electrostatic repulsion between hydrophilic moieties on the surface of the polysaccharide in comparison with the bare selenium. Moreover, the nanoparticle conjugate exhibited enhanced selectivity and antiproliferative activity by inducing cell apoptosis.

Strategies of mixing of two or more biological components to yield hybrid biological nanoparticles have also been reported by several researchers for encapsulation of biomolecules and bioactives such as curcumin (Huang Y.C. and Kuo T.H., 2014), quercetin (Ha H.-K. et al., 2013) and (–)-epigallocatechin-3-gallate (Hu B. et al., 2012) into chitosan based nanoparticles. This is due to the fact that nanoparticles formulated from bare chitosan are unstable and can be easily dissociated at low pH which potentially leads to the release of the encapsulated biomolecules. By mixing the chitosan with other biological compounds such as fucoidan, β-lactoglobulin, and peptide, hybrid nanoparticles with remarkable improvement in stability, encapsulation efficiency and functional properties were obtained (Ha H.-K. et al., 2013; Hu B. et al., 2012; Huang Y.C. and Kuo T.H., 2014).

Recently, considerable interests have been shown to utilise hydrophobic protein nanoparticles such as zein for encapsulation of lipophilic compounds such as curcumin. However, zein nanoparticles have poor stability against the changes in environmental conditions such as pH and temperature. Coating the protein nanoparticle with polysaccharide molecules allow the modulation of an electrostatic interaction and steric repulsion between the particles, thus improving the nanoparticle stability. The recent example is the development of zein-pectin/alginate nanoparticle for encapsulation of curcumin as reported by Huang X. et al. (2016). The curcumin loaded core-shell nanoparticles show enhanced water dispersibility and antioxidant activity.

4.2.2 Biomolecule-polymer nanoparticle conjugates

A great deal of effort has now been focused on designing biomolecule-polymer nanoparticle conjugates with unprecedented properties, driven by the vast development of novel bio-conjugation and polymerisation techniques. Various type of polymeric materials have been investigated either as support or carrier matrix for biological compounds which include poly (ethylene glycol) (PEG), poly (lactic acid) (PLA), polyglycolides (PGA), poly (lactide-co-glycolides) (PLGA), polycaprolactone (PCL) and poly(hydroxy butyrate) (PHB) (Panta P. et al., 2014; Sapsford K.E. et al., 2013). These polymers are mostly biocompatible and biodegradable and may have other useful properties such as stimulus-responsive function and good mechanical strength that can be utilised for fabrication of various types of biomolecule-polymer conjugates (Wang E.C. and Wang A.Z., 2014).

Conjugation of polymer with protein such as albumin has been widely explored for drug delivery applications. The resulting nanoparticles usually have a biocompatible and bioactive albumin shell while the core is rich in a hydrophobic polymer that can entrap drugs. This strategy can aid the delivery of drugs and targeting the cancer cells. Protein-polymer nanoparticles conjugate consisted of FDA approved thermoplastic hydrophobic polymer of poly-methyl methacrylate (PMMA) and bovine serum albumin (BSA) have been successfully synthesised by Ge J. et al. (2011) for application in drug delivery. This hybrid nanoparticle with spherical structure and an average size of 100 nm was fabricated by using nanoprecipitation method. The size and surface charge can be tuned by controlling the weight ratio and concentration of both the BSA and PMMA. Encapsulation of hydrophobic drug, a camptothecin in the BSA-PMMA nanoparticles showed efficient cell uptake and enhanced antitumor activity. Since PMMA is a nondegradable polymer, Jiang Y. et al. (2016) prepared a curcumin loaded albumin-polymer nanoparticle from a biodegradable polymer of polycaprolactone (PCL) and the performance of this nanoparticle was compared with PMMA for prostate carcinoma therapy. The fully degradable PCL-based nanoparticles can deliver the drug more efficiently in comparison with the PMMA-based nanoparticles and effectively limits the tumor growth.

Other work on the synthesis of a protein-polymer hybrid was done by Dag A. et al. (2015) to enhance the delivery of macromolecular platinum drugs into cancer cells. The polymer was prepared by copolymerization of N-(2-hydroxypropyl) methacrylamide (HPMA) and Boc protected 1,3-diaminopropan-2-yl acrylate (Ac-DAP-Boc), yielded a P(HPMA 14-co-(Ac-DAP-Boc), which was used as a macromolecular ligand for the conjugation of the platinum drug. After activation, the polymer-drug was further conjugated with albumin by exploiting the Cys34 functionality. This albumin-coated nanoparticle shows superior toxicity to the cancer cell in comparison with the polymer nanoparticles without protein coating.

A special form of polymeric nanomaterial, a dendrimer, is a cationic polymer with well-defined molecular shape and unique architecture. This type of polymer has high water solubility and a large number of surface groups which make them as a versatile nanostructure. Conjugation of protein to dendrimer has been reported by Chanphai P. et al. (2016). Polyamidoamines (PAMAM) dendrimers were conjugated with trypsin from bovine pancreas and trypsin inhibitor from glycine. Stable bindings of the PAMAM dendrimers with both proteins occur through hydrophilic and hydrogen bonding as well as Van der Waals interaction, suggesting that this hybrid system could be used further enzymatic catalysis study. Besides that, the PAMAM dendrimers have been studied previously by Menjoge A.R. et al. (2011) for the delivery of drug to pregnant women, without affecting the fetus by intercepting the drug so that it cannot pass through the fetal membrane.

4.2.3 Organic-inorganic nanoparticle conjugates

Considering the versatile physicochemical properties of inorganic nanoparticles including wide availability and rich functionality, in combination with their unique optical, electronic, and catalytic properties, conjugation of biological molecules and inorganic nanoparticles have opened a new route in the development of advanced functional materials with significantly enhanced features and broad applications. Various inorganic nanoparticles including metals, metal oxides, and quantum dots have been prepared by various synthetic procedures and hybridised or immobilised with biomolecules such as DNA, enzymes, and antibodies either through covalent or non-covalent interactions that have been discussed previously.

Gold nanoparticles (AuNPs) represent one type of metal nanoparticles that found numerous applications in imaging, sensing, and nanomedicine. The utilisation of biomolecules to tune the surface chemistry and the assembly of AuNPs is a very attractive approach for the development of next generation nanometric complexes. Politi J. et al. (2015) have shown that hybridisation of a fungal protein, namely hyrophobin (HFB) Vmh2 with AuNPs can be achieved via a simple one step chemical reduction process, yielding a highly stable HFB-AuNPs that can interact well with a model protein of BSA and immunoglobulins. The addition of dicarboxylic acid-terminated polyethylene-glycol (PEG) during the synthesis process produced hybrid complexes with outer surface rich in functional chemical groups that can be tailored for attachments of various compounds.

Integration of enzymes with inorganic nanoparticles has shown to have a remarkable effect on the enzyme catalytic performance. This is attributed to the extremely small size of the nano scale material and their unique surface chemistry (Ding S. et al., 2015). For example, covalently bound pepsin on gold nanoparticles via amide coupling has produced efficient biocatalyst with sufficiently high stability for application in analysis of therapeutic proteins and peptides (Höldrich M. et al., 2016).

Recently, multi-enzyme catalysis was developed by Sojitra U.V. et al. (2016) by covalently bind three types of enzymes (alpha-amylase, pectinase and cellulase) on amino functionalised magnetic nanoparticles for clarification of fruit juices. The tri-enzyme magnetic nanobiocatalyst allows rapid reduction of the fruit juices turbidity, in comparison with the individual enzyme system. Another multienzyme-nanoparticle complex was constructed by Honda T. et al. (2015) by using magnetosome display system to prepare a system that can mimick natural cellulosomes on magnetic nanoparticle. As a proof of concept, two types of fluorescent proteins which are the green fluorescent and mCherry were initially immobilised on the MNPs. These proteins showed a close proximity on the magnetic nanoparticles. Later, endoglucanase (EG) and β-glucosidase (BG) were immobilised on the magnetic nanoparticles to promote rapid hydrolysis of carboxymethyl cellulose.

4.2.4 Biomolecule-hybrid nanoparticle conjugates

Hybrid nanocarrier can be prepared by mixing two or more components such as magnetic and metal nanoparticles. By using this strategy, properties of both materials can be merged and enhanced. As recently being reported by Cao Y. et al. (2016), a magnetic iron oxide nanoparticles were coated with a layer of gold nanoparticles and used for trypsin immobilisation. This system provides a robust carrier for the enzyme. Moreover, the magnetic feature facilitated separation from the reaction media and enabled repeated usage of the enzyme. Magnetic nanoparticles can also be designed in a form of core-shell structure by conjugation with other materials such as hydroxyapatite (Xie W. and Zang X., 2016), silica (Shahrestani H. et al., 2016) and polypyrrol (Yang Z. et al., 2014) for the development of novel composites support for enzyme immobilisation.

A sandwich hybrid nanoparticle has been designed by Abbaspour A. et al. (2015) by immobilising a biotinylated primary aptamer on capture probe of a streptavidin coated magnetic nanoparticle. A secondary aptamer was coupled to a silver nanoparticle (AgNP) for the target detection. In the presence of target bacterium (*S. aureus*), a sandwich complex of Apt/*S.aureus*/Apt-AgNP is formed on the magnetic nanoparticle surface, giving an electrochemical signal. This sandwich system combined the unique features of magnetic nanoparticles as a carrier of affinity ligands for solution-phase recognition, a hassle free magnetic separation and highly sensitive signal amplification by AgNP.

Hybrid nanoparticles based on polymeric materials conjugated with protein have also been reported. In the study done by Jiang Y. et al. (2016), bovine serum albumin (BSA) was utilised as a hydrophilic moiety of the hydrophobic maleimide-terminated polycaprolactone nanoparticles to improve the biodegradability and biocompatibility of the polymer nanoparticle for encapsulation of curcumin.

4.2.5 Self-assembled biomolecule-nanoparticle conjugates

Self-assembly is an advanced technology that is capable of integrating different components together spontaneously for the fabrication of the desired hybrid materials. Proteins can be incorporated into nanostructures during the growth phase of the inorganic material and a unique flower-like structure was obtained as shown in the study done by Ge J. et al. (2012). The formation of hybrid nanoflowers is believed due to the protein-induced nucleation of copper phosphate crystal during the self-assembly process, which binds the nanocrystal petals together. Incorporation of laccase into the protein-inorganic nanoflowers resulted in enhanced laccase activity and stability, in comparison with the free enzyme.

Huang Y. et al. (2015) extended this work to explore the potential applications of the inorganic copper-phosphate framework of the hybrid nanoflowers by introducing BSA as the model protein. This copper-phosphate framework has an intrinsic peroxidise-like activity that promotes the development of a hybrid material with superior durability and stability. Moreover, the nanostructure morphology can be preserved during catalytic reaction, even at high temperature. The system also has been tested by using glucose oxidase (GOx) to replace BSA as the protein component to study the communication between artificial and natural enzyme. Interestingly, they found that a self-activated cascade reaction could be achieved through in one integrated system whereby the artificial enzymatic cascade could mimic the natural ones. Through this newly developed technology, deep understanding of the complex enzymatic reactions could be achieved. They also proposed that this hybrid nanoflowers have potential to be applied in the decomposition of organic dyes and waste water treatment.

Most recently, the fabrication of hybrid nanoflowers with abundant surface porosity has been reported by Koley P. et al. (2016). Sericin, a silk protein, was used as the organic component and copper-phosphate as the inorganic counterpart. By tuning the protein concentration, various morphological structures of the nanoflowers were observed. Similar with the BSA-copper phosphate nanoflowers synthesized by Huang Y. et al. (2015), this sericin hybrid nanoflowers exhibited excellent thermal stability even after calcination. The calcination process resulted in the complete evaporation of the sericin molecules which eventually increase the nanoflowers porosity, thus significantly increased their surface area for adsorption of heavy metal ions from wastewater.

5. Applications of biomolecule-nanoparticle conjugates

5.1 Medical and pharmaceutical

The recent development in the field of nanomedicine particularly in the drug delivery application has led to the discovery of nanoparticle-based therapeutics for diagnosis and treatment of diseases such as cancer, diabetes, and allergy. The fundamental characteristics of nanoscale materials such as greater solubility and diffusivity have been shown to improve drug release characteristic and blood circulation half-life (Valo H., 2012). Furthermore, the nanoparticle-based drug delivery system allows better control of drug release to the targeted area which consequently lowers the administration frequency and minimises the possibilities of systemic side effects (Mahapatro A. and Singh D.K., 2011).

Several studies have been attempted to develop biomolecule-nanoparticle conjugates for cancer therapies. By mimicking the ability of *Salmonella enterica* serotype Typhimurium pathogen to reverse multidrug resistance, a semi-synthetic 'Salmonella nanoparticle mimic' based on gold nanoparticle packaged with effector protein (SipA) has been constructed by Mercado-Lubo R. et al. (2016). The system could suppress the growth of tumour by reducing the P-glycoprotein, a multidrug resistance transporter, at a SipA dose significantly lower than the free SipA and increases tumour sensitivity to conventional chemotherapeutics. In another study, conjugation of prostate-specific antigen (PSA) to gold nanoparticles has enhanced the efficacy and sensitivity of the PSA for diagnosis of prostate cancer based on localised surface plasmon resonance (Jazayeri M.H. et al., 2016). Enzyme prodrug therapy based on horseradish peroxidase (HRP) immobilised onto mesoporous silica nanoparticles converts a prodrug (indole-3-acetic acid (IAA)) into cytotoxic radicals, which caused apoptotic tumor cell death in human colon carcinoma cells as reported by Hung B.-Y. et al. (2015).

Integration of nanoparticle with biomolecule also allows the development of three-dimensional scaffolds based on gelatin-hydroxyapatite hybrid nanoparticles with uniformly distributed nano-topologies for application in osteogenesis (Yang G. et al., 2017). Interestingly, the particle morphology has shown to have a remarkable effect on bone formation in which the spherical nanoparticles show the strongest bone formation capacity in comparison to the nanoparticles with a different shape.

For minimising carrier-induced undesirable cytotoxicity, nanoparticle which are derived from proteins and polysaccharides are promising vehicles in nanoparticle-mediated delivery systems (Gan Q. et al., 2005; Hu B. et al., 2012; Nitta S.K. and Numata K., 2013). Encapsulation of dietary phytochemicals, (–) epigallocatechin-3-gallate (EGCG) with highly biocompatible nanoparticles derived from bioactive peptide/chitosan is able to enhance bioavailability of the EGCG (Hu B. et al., 2012). The EGCG loaded-peptide/chitosan nanoparticle could serve as an effective nanochemoprevention in cancer management and prevention.The use of protein nanoparticles as a carrier for various types of drugs allows the drugs to be transported across the blood-brain barrier (Sundar S. et al., 2010). Binding of drugs to polysaccharide nanoparticles such as albumin and gelatine could enhance the antitumour function of the drugs (Huang Y.C. and Kuo T.H., 2014; Jiang Y. et al., 2016; Kobayashi K. et al., 2014). In an advanced drug delivery system, more types of drugs could be delivered simultaneously to generate synergistic therapies of diseases.

One of the major challenges in the intracellular delivery of anti-cancer drugs to a cancer cell is the rapid changes in pH due to the acidification that occurs in the endosomal compartments. In this viewpoint, a novel strategy has been designed by Kim B.J. et al. (2015) for the synthesis of pH-responsive drug delivery system by using mussel adhesive proteins (MAPs)-based iron(III)–3,4-dihydroxyphenylalanine (DOPA) nanoparticles. The pH-responsive release of drugs was achieved by exploiting the pH-dependent changes in the coordination stoichiometry of the DOPA complexes. This newly developed system has shown effective cytotoxicity towards cancer cells and therefore, can be applied further for the diverse controlled-drug delivery application.

With the significant advantages of the nanoscale materials and the advancement made in the drug delivery, several types of the drug-bound biological nanoparticles are currently under clinical trial and a few are already commercialised such as albumin-bound paclitaxel, which is marketed as Abraxane, for use in metatstatic breast cancer treatment. Most recently, Bhattacharyya J. et al. (2015) have successfully designed a new drug delivery system for paclitaxel that outperforms the readily commercialised Abraxane with 2 times greater systemic exposure and tumor uptake. The system was prepared with a chimeric polypeptide that could self-assemble spontaneously, producing monodispersed nanoparticle of 60 nm in size. The chimeric polypeptide-paclitaxel conjugate has shown near complete tumor regression in breast and prostate cancer tumor models after single dose injection. These outstanding performances are attributed to the improvement of the aqueous solubility, plasma-half life, tumor uptake and therapeutic potential of the self-assembled chimeric polypeptide nanoparticle.

5.2 Biosensors and bioelectronics

Nanotechnology has broadened the opportunities and added a new dimension in designing powerful biosensor and bioelectronic devices for diagnostic of diseases and detection of contaminants in medical, food and agricultural sector. Substantial research efforts are currently being directed towards the utilisation of biological molecules hybridised with nanoparticles for the development of novel biosensor and bioelectronic system (Willner I. et al., 2007).

Ulltrasensitive biosensor for detection of epithelial tumor marker has been developed by Hu R. et al. (2014) through the immobilisation of hairpin oligonucleotide (HO) and horseradish peroxidase (HRP) on AuNPs. The HO-AuNP-HRP conjugate provides multiple signal amplification strategy that could enable rapid detection and enhanced the detection sensitivity in a wide linear range. This strategy was achieved by modification of the biosensor surface by carbon nanotubes for accelerating the electron transfer while the HO-AuNPs-HRP enzyme acts as a tracing tag for the electrochemical detection. This newly developed electrochemical method can be applied for diagnostic and detection of diseases.

Besides for cancer detection, a biosensor based on immobilised enzyme-nanoparticles has also been applied for neurobiology for detection of glutamate, important excitatory signaling molecules that are responsible for carrying out various brain functions. Özel R.E. et al. (2014) used nanocomposite based on ceria and titania nanoparticles, dispersed in a semi-permeable membrane made up from chitosan, that was co-immobilised with glutamate oxidase (GmOX) on the platinum electrode for fabrication of glutamate biosensor. Conjugation of the ceria and titania nanoparticles provide ‘oxygen rich’ environment for the biosensor to detect glutamate in hypoxic conditions while the immobilisation of this nanoparticle conjugate in a biocompatible chitosan membrane facilitate the enzyme stabilisation.

Enzymes-based biosensors are now gaining more popularity for a rapid detection and on-line and *in situ* monitoring of specific compounds in medical, environmental and food industries. For example, a novel potentiometric glucose biosensor has been fabricated by Yang Z. et al. (2014) by immobilising core-shell hybrid nanoparticles of iron oxide, glucose oxidase (GOx) and polypyrrole to the surface of magnetic glassy carbon electrode. This biosensor enabled fast detection and highly-selective glucose monitoring with low detection limit and wider linear range. Enzymes-based biosensors have also been used for detection of phenolic compounds by using various types of enzymes such as tyrosinase, horseradish peroxidise and laccase (Rodríguez-Delgado M.M. et al., 2015).

Recently, many researchers discovered the unique and programmable molecular recognition of DNA for the development of artificial, machine-like devices. DNAzymes, an important functional nucleotide acid have been recognised as important building blocks for the construction of nanodevices. The development of a walking system based on DNAzymes that are moving along a DNA track has been reported. The motion is driven by the chemical energy that has been supplied by the DNAzyme substrate. This concept was used by Liu and co-workers (2013) to design DNA hemin-G-quadruplex-DNAzyme-based walkers which allow the chemiluminescence, chemiluminescence resonance energy transfer (CRET), electrochemical, or photoelectrochemical transduction of the switchable states of the different DNA machines. Besides that, the DNA exhibited a unique feature of being easy to code which enables them to be used in the computational operation and logic gates (Gong L. et al., 2015).

Development of nanoscale memory devices is another interesting application of biomolecule-nanoparticle conjugates. Hybrid nanoparticle composed of recombinant azurin, a well-characterised redox protein and a quantum dot (CdSe-ZnS) have been developed by Yagati A.K. et al. (2017). By introducing a site specific amino acid sequences in azurin, the CdSe-ZnS nanoparticle can bind with the protein, thus forming resistive random access memory (ReRAM) device with reversible voltage driven-switching function and repeatable writing-reading processes.

5.3 Foods

Despite the explosion of nanotechnology in diverse fields, particularly in medical and pharmaceutical, the application of nanotechnology in the food sector is considered still in infancy stage due to the public perception and preference on the so called ‘natural’ food products, which limit the development of new food technologies (Duncan T.V., 2011). However, as the nanotechnology has been revolutionised in the past few years, the potential uses of nanotechnology in food industries have already been recognised in every chain of food products development, ranging from the processing to packaging and storage (Berekaa M.M., 2015).

Nanoparticles have been used as nanocarrier which is known as ‘nutrition delivery system’. The nanoscale delivery system plays an important role in improving food or nutrients absorption in the human body, particularly for those who suffer from the gastroinstestinal disease. Nanoparticles are also useful for enhancing bioavailability of poorly soluble bioactive compounds and improving food properties such as stability and texture.

The main criterion for the application of nanoparticles in food products is the particles which must be developed from food grade materials. In this regard, nanoparticles from biomolecules origin are the most suited for that purpose (Ha H.-K. et al., 2013). Chitosan and whey protein have been widely used as encapsulant of neutraceuticals, food ingredients, probiotics and enzymes due to their ease of availability in large quantity in combination with their good physical and mechanical properties. Ha and co-workers (2013) used linoleic acid modified chitosan/β-lactoglobulin for encapsulation of quercetin, a hydrophobic bioactive compound with good anticancer, antiviral and antioxidant properties. Findings by Yi J. et al. (2015) have shown that whey protein isolate was more effective for encapsulating beta-carotene than other type of protein such as soybean protein with great improvement in radical scavenging and cellular antioxidant activities. Recently, calcium induced cruciferin nanoparticles from canola protein prepared by cold gelation method have been utilised as a protecting agent for β-carotene to increase its bioavailability (Akbari A. and Wu J., 2016). The main driving forces for the formation of the nanoparticles were hydrophobic interaction and electrostatic forces. Another study done by Marelli B. et al. (2016) shows that coating of food ingredients with protein nanoparticles such as silk fibroin has a positive effect on improving food shelf-life.

Besides used in the development of food products, nanotechnology also plays a crucial role in food packaging sector. Incorporation of nanoparticles in food packaging materials could provide efficient food preservation system by improving barrier protection by scavenging oxygen and other spoilage causing constituents and improve antimicrobial properties. For example, packaging film made up from whey protein-montmorillonite nanoparticle activated with lycopene could improve the film barrier property against water vapour and at the same time provide antioxidant activity and UV-light protection (Pereira R.C. et al., 2016).

5.4 Agricultures

The role of nanotechnology in agricultural sectors covers the conversion of agricultural waste into energy or other useful byproducts, detection and prevention of crops diseases, treatment of plants using various types of nanocides and delivery of agrochemicals such as pesticides, fertilizers, genetic materials and growth hormone (Nair R. et al., 2010; Nuruzzaman M. et al., 2016). With respects to the delivery of agrochemicals, nanoscale materials have novel characteristics that can improve bioactivity and agrochemicals efficiency through the development of a smart delivery system. In the smart delivery system, nanoscale carriers are utilised with the aim to enhance controlled-release properties of the agrochemicals, increase the active ingredients solubility, and improve the stability of pesticides as well as for preventing premature degradation of crops.

Silica nanoparticles have been explored as a control agent for agricultural pesticides. Conjugation of terpenes (α-pinene and linalool) onto the silica nanoparticles surface resulted in enhanced bioavailability of the compounds and improved the antifeedant potential of the individual terpenes against insects which consequently prolonged shelf-life of the terpenes (Usha Rani P. et al., 2014).

Nowadays, growing interest has been shown in the utilisation of biodegradable and biocompatible materials derived from natural materials particularly chitosan-based for the development of the agriculture nanocarriers. Chitosan is a versatile polymer which is well known to serve two major functions in agriculture; preventing the spread of pathogens with its wide-spectrum of antimicrobial properties and enhancing immunity defenses of the plant (Xing K. et al., 2016).

The presence of phytopathogenic fungi and viruses has resulted in severe damages to many crops around the globe. The control of diseases caused by these microorganisms is a problem that remains unsolved (Cota-Arriola O. et al., 2013). To protect crops from fungal pathogens, the growth of the fungi can be inhibited by using protein-chitosan nanoparticle conjugate as demonstrated by Sathiyabama M. and Parthasarathy R. (2016). The chitosan nanoparticle was prepared through the biological method by the addition of anionic proteins to the chitosan solution. They found that this protein-chitosan nanoparticle conjugate has high antifungal activities which inhibit the growth of the phytopathogenic fungi tested. Additionally, treatment of the chitosan nanoparticle with chickpea seeds allows the nanoparticle to be used as a growth promoter. Chitosan-based nanoparticles have also been prepared by Xing K. et al. (2016) for controlling pathogenic fungi in agriculture. The antifungal nanoparticle was prepared by grafting oleoyl onto the chitosan molecules, yielding an oleoyl-chitosan nanoparticle hybrid with size around 297 nm. Improvement in the antifungal index was observed as the concentration of the nanoparticle increased.

6. Conclusions and future prospects

In this review, various types of biological nanoparticles and the synthesis methods have been discussed. Fabrication of biological nanoparticles through drying methods, particularly electrospraying is highlighted mainly due to the ability of the method to generate nanoparticles with a narrow size distribution that often could not be achieved by the other nanoparticulate fabrication techniques. In order to broaden the application of biological nanoparticles, integration of biomolecules with other types of nanoparticles such as inorganic and polymeric through numerous biofunctionalisation strategies have been established. However, much remains to be discovered in this newly emerging field. With the recent technological advancements and innovations, next generation of biological nanoparticles that has multiple functionalities will be developed which could improve the characteristics of the biological nanoparticles and extend its application to diverse fields.

References

Abbaspour A., Norouz-Sarvestani F., Noori A., Soltani N., Aptamer-conjugated silver nanoparticles for electrochemical dual-aptamer-based sandwich detection of staphylococcus aureus, Biosensors and Bioelectronics, 68 (2015) 149–155.

Achilli E., Casajus G., Siri M., Flores C., Kadlubowski S., Alonso S.d.V., Grasselli M., Preparation of protein nanoparticle by dynamic aggregation and ionizing-induced crosslinking, Colloids and Surfaces A: Physicochemical and Engineering Aspects, 486 (2015) 161–171.

Akbari A., Wu J., Cruciferin nanoparticles: Preparation, characterization and their potential application in delivery of bioactive compounds, Food Hydrocolloids, 54 (2016) 107–118.

Allouche J., Synthesis of Organic and Bioorganic Nanoparticles: An overview of the preparation methods, in: Brayner R. (Ed.), Springer-Verlag, London, 2013, pp. 27–74.

Anton N., Benoit J.-P., Saulnier P., Design and production of nanoparticles formulated from nano-emulsion templates—A review, 128 (2008) 185–199.

Arroyo-Maya I.J., McClements D.J., Biopolymer nanoparticles as potential delivery systems for anthocyanins: Fabrication and properties, Food Research International, 69 (2015) 1–8.

Avseenko N.V., Morozova T.Y., Ataullakhanov F.I., Morozov V.N., Immobilization of proteins in immunochemical microarrays fabricated by electrospray deposition, Analytical chemistry, 73 (2001) 6047–6052.

Berekaa M.M., Nanotechnology in food industry; Advances in food processing, packaging and food safety, International Journal of Current Microbiology and Applied Sciences, 4 (2015) 345–357.

Bhakta G., Nurcombe V., Maitra A., Shrivastava A., DNA-encapsulated magnesium phosphate nanoparticles elicit both humoral and cellular immune responses in mice, Results in Immunology, 4 (2014) 46–53.

Bhattacharyya J., Bellucci J.J., Weitzhandler I., McDaniel J.R., Spasojevic I., Li X., Lin C.-C., Chi J.-T.A., Chilkoti A., A paclitaxel-loaded recombinant polypeptide nanoparticle outperforms Abraxane in multiple murine cancer models, Nature Communications, 6 (2015) 7939 (12pp). http://doi.org/10.1038/ncomms8939

Bhunchu S., Rojsitthisak P., Biopolymeric alginate-chitosan nanoparticles as drug delivery carriers for cancer therapy, Pharmazie, 69 (2014) 563–570.

Bilati U., Allémann E., Doelker E., Nanoprecipitation versus emulsion-based techniques for the encapsulation of proteins into biodegradable nanoparticles and process-related stability issues, AAPS PharmSciTech, 6 (2005) E594–E604.

Bock N., Dargaville T.R., Woodruff M.A., Controlling microencapsulation and release of micronized proteins using poly(ethylene glycol) and electrospraying, European Journal of Pharmaceutics and Biopharmaceutics, 87 (2014) 366–377.

Cao X., Deng W., Wei Y., Su W., Yang Y., Wei Y., Yu J., Xu X., Encapsulation of plasmid DNA in calcium phosphate nanoparticles: stem cell uptake and gene transfer efficiency, International Journal of Nanomedicine, 6 (2011) 3335–3349.

Cao Y., Wen L., Svec F., Tan T., Lv Y., Magnetic AuNP@Fe_3O_4 nanoparticles as reusable carriers for reversible enzyme immobilization, Chemical Engineering Journal, 286 (2016) 272–281.

Cavalli R., Bisazza A., Bussano R., Trotta M., Civra A., Lembo D., Ranucci E., Ferruti P., Poly(amidoamine)-cholesterol conjugate nanoparticles obtained by electrospraying as novel tamoxifen delivery system, Journal of Drug Delivery, 2011 (2011) 587604 (9pp). http://doi.org/10.1155/2011/587604

Chan H.K., Kwok P.C.L., Production methods for nanodrug particles using the bottom-up approach, Advanced Drug Delivery Reviews, 63 (2011) 406–416.

Chanphai P., Thomas T.J., Tajmir-Riahi H.A., Conjugation of biogenic and synthetic polyamines with trypsin and trypsin inhibitor, RSC Advances, 6 (2016) 53690–53697.

Chaturvedi S.P., Kumar V., Production techniques of lipid nanoparticles: A review, Research Journal of Pharmaceutical, Biological and Chemical Sciences, 3 (2012) 525–541.

Chen K., Xu Y., Rana S., Miranda O.R., Dubin P.L., Rotello V.M., Sun L., Guo X., Electrostatic selectivity in protein-nanoparticle interactions, Biomacromolecules, 12 (2011) 2552–2561.

Chinen A.B., Guan C.M., Mirkin C.A., Spherical nucleic acid nanoparticle conjugates enhance G-quadruplex formation and increase serum protein interactions, Angewandte Chemie International Edition, 54 (2015) 527–531.

Chinh N.T., Trang N.T.T., Giang N.V., Thanh D.T.M., Hang T. T.X., Tung N.Q., Truyen C.Q., Quan P.M., Long P.Q., Hoang T., In vitro nifedipine release from poly(lactic acid)/chitosan nanoparticles loaded with nifedipine, Journal of Applied Polymer Science, 43330 (2016) 1–8.

Cota-Arriola O., Onofre Cortez-Rocha M., Burgos-Hernandez A., Marina Ezquerra-Brauer J., Plascencia-Jatomea M., Controlled release matrices and micro/nanoparticles of chitosan with antimicrobial potential: Development of new strategies for microbial control in agriculture, Journal of the Science of Food and Agriculture, 93 (2013) 1525–1536.

Dag A., Jiang Y., Karim K.J.A., Hart-Smith G., Scarano W., Stenzel M.H., Polymer-albumin conjugate for the facilitated delivery of macromolecular platinum drugs, Macromolecular Rapid Communications, 36 (2015) 890–897.

Das S., Chaudhury A., Recent advances in lipid nanoparticle formulations with solid matrix for oral drug delivery, AAPS PharmSciTech, 12 (2011) 62–76.

De M., Ghosh P.S., Rotello V.M., Applications of nanoparticles in biology, Advanced Materials, 01003 (2008) 4225–4241.

Ding S., Cargill A.A., Medintz I.L., Claussen J.C., Increasing the activity of immobilized enzymes with nanoparticle conjugation, Current Opinion in Biotechnology, 34 (2015) 242–250.

Duncan T.V., Applications of nanotechnology in food packaging and food safety: Barrier materials, antimicrobials and sensors, Journal of Colloid and Interface Science, 363 (2011) 1–24.

Ezhilarasi P.N., Karthik P., Chhanwal N., Anandharamakrishnan C., Nanoencapsulation techniques for food bioactive components: A review, Food and Bioprocess Technology, 6 (2013) 628–647.

Fabie L., Agostini P., Stopel M., Blum C., Lassagne B., Subramaniam V., Ondarcuhu T., Direct patterning of nanoparticles and biomolecules by liquid nanodispensing, Nanoscale, 7 (2015) 4497–4504.

Fessi H., Puisieux F., Devissaguet J.P., Ammoury N., Benita S., Nanocapsule formation by interfacial polymer deposition following solvent displacement, International Journal of Pharmaceutics, 55 (1989) 1–4.

Fornari E., Roberts C.J., Temperton R.H., O'Shea J.N., Electrospray deposition in vacuum as method to create functionally active protein immobilization on polymeric substrates, Journal of Colloid and Interface Science, 453 (2015) 252–259.

Friedman A.D., Claypool S.E., Liu R., The smart targeting of nanoparticles, Current Pharmaceutical Design, 19 (2013) 6315–6329.

Gan Q., Wang T., Cochrane C., McCarron P., Modulation of surface charge, particle size and morphological properties of chitosan-TPP nanoparticles intended for gene delivery, Colloids and Surfaces B: Biointerfaces, 44 (2005) 65–73.

Ge J., Lei J., Zare R.N., Bovine serum albumin–poly(methyl methacrylate) nanoparticles: An example of frustrated phase separation, Nano Letters, 11 (2011) 2551–2554.

Ge J., Lei J., Zare R.N., Protein–inorganic hybrid nanoflowers, Nature Nanotechnology, 7 (2012) 428–432.

Gholami A., Tavanai H., Moradi A.R., Production of fibroin nanopowder through electrospraying, Journal of Nanoparticle Research, 13 (2010) 2089–2098.

Gilbert W., De Magnete, Anno MDC, Londini, Anno MDC, 1600.

Gomez-Estaca J., Balaguer M.P., Gavara R., Hernandez-Munoz P., Formation of zein nanoparticles by electrohydrodynamic atomization: Effect of the main processing variables and suitability for encapsulating the food coloring and active ingredient curcumin, Food Hydrocolloids, 28 (2012) 82–91.

Gomez A., Bingham D., De Juan L., Tang K., Production of protein nanoparticles by electrospray drying, Journal of Aerosol Science, 29 (1998) 561–574.

Gong L., Zhao Z., Lv Y.-F., Huan S.-Y., Fu T., Zhang X.-b., Shen G.-L., Yu R.-Q., DNAzyme-based biosensors and nanodevices, Chemical Communications, 51 (2015) 979–995.

Guo J., Zhong R., Li W., Liu Y., Bai Z., Yin J., Liu J., Gong P., Zhao X., Zhang F., Interaction study on bovine serum albumin physically binding to silver nanoparticles: Evolution from discrete conjugates to protein coronas, Applied Surface Science, 359 (2015) 82–88.

Ha H.-K., Wook J., Lee M.-R., Lee W.-J., Formation and characterization of quercetin-loaded chitosan oligosaccharide/β-lactoglobulin nanoparticle, Food Research International, 52 (2013) 82–90.

Haggag Y.A., Faheem A.M., Evaluation of nano spray drying as a method for drying and formulation of therapeutic peptides and proteins, Frontiers in Pharmacology, 6 (2015) 1–5.

Hazeri N., Tavanai H., Moradi A.R., Production and properties of electrosprayed sericin nanopowder, Science and Technology of Advanced Materials, 13 (2012) 035010 (7pp). http://dx.doi.org/10.1088/1468-6996/13/3/035010

Höldrich M., Sievers-Engler A., Lämmerhofer M., Gold nanoparticle-conjugated pepsin for efficient solution-like heterogeneous biocatalysis in analytical sample preparation protocols, Analytical and Bioanalytical Chemistry, 408 (2016) 5415–5427.

Honda T., Tanaka T., Yoshino T., Stoichiometrically controlled immobilization of multiple enzymes on magnetic nanoparticles by the magnetosome display system for efficient cellulose hydrolysis, Biomacromolecules, 16 (2015) 3863–3868.

Hosseini S.F., Zandi M., Rezaei M., Farahmandghavi F., Two-step method for encapsulation of oregano essential oil in chitosan nanoparticles: Preparation, characterization and in vitro release study, Carbohydrate Polymers, 95 (2013) 50–56.

Hosseini S.M.H., Emam-Djomeh Z., Sabatino P., Van der Meeren P., Nanocomplexes arising from protein-polysaccharide electrostatic interaction as a promising carrier for nutraceutical compounds, Food Hydrocolloids, 50 (2015) 16–26.

Hsiao A.P., Heller M.J., Electric-field-directed self-assembly of active enzyme-nanoparticle structures, Journal of Biomedicine & Biotechnology, 2012 (2012) 178487 (9pp). http://dx.doi.org/10.1155/2012/178487

Hu B., Ting Y., Yang X., Tang W., Zeng X., Huang Q., Nanochemoprevention by encapsulation of (–)-epigallocatechin-3-gallate with bioactive peptides/chitosan nanoparticles for enhancement of its bioavailability, Chemical Communications, 48 (2012) 2421 (4pp). http://www.rsc.org/suppdata/cc/c2/c2cc17295j/c2cc17295j.pdf.

Hu K., Huang X., Gao Y., Huang X., Xiao H., McClements D.J., Core-shell biopolymer nanoparticle delivery systems: Synthesis and characterization of curcumin fortified zein-pectin nanoparticles, Food Chemistry, 182 (2015) 275–281.

Hu R., Wen W., Wang Q., Xiong H., Zhang X., Gu H., Wang S., Novel electrochemical aptamer biosensor based on an enzyme–gold nanoparticle dual label for the ultrasensitive detection of epithelial tumour marker MUC1, Biosensors and Bioelectronics, 53 (2014) 384–389.

Huang X., Huang X., Gong Y., Xiao H., McClements D.J., Hu K., Enhancement of curcumin water dispersibility and antioxidant activity using core-shell protein-polysaccharide nanoparticles, Food Research International, 87 (2016) 1–9.

Huang Y., Ran X., Lin Y., Ren J., Qu X., Self-assembly of an organic–inorganic hybrid nanoflower as an efficient biomimetic catalyst for self-activated tandem reactions, Chemical Communications, 51 (2015) 4386–4389.

Huang Y.C., Kuo T.H., O-carboxymethyl chitosan/fucoidan nanoparticles increase cellular curcumin uptake, Food Hydrocolloids, 53 (2014) 261–269.

Hung B.-Y., Kuthati Y., Kankala R., Kankala S., Deng J.-P., Liu C.-L., Lee C.-H., Utilization of enzyme-immobilized mesoporous silica nanocontainers (IBN-4) in prodrug-activated cancer theranostics, Nanomaterials, 5 (2015) 2169–2191.

Jahanshahi M., Babaei Z., Protein nanoparticle : A unique system as drug delivery vehicles, Journal of Biotechnology, 7 (2008) 4926–4934.

Jain A., Cheng K., The principles and applications of avidin-based nanoparticles in drug delivery and diagnosis, Journal of Controlled Release, 245 (2017) 27–40.

Jawahar N., Meyyanathan S., Polymeric nanoparticles for drug delivery and targeting: A comprehensive review, International Journal of Health & Allied Sciences, 1 (2012) 217–223.

Jaworek A., Sobczyk A.T., Electrospraying route to nanotechnology: An overview, Journal of Electrostatics, 66 (2008) 197–219.

Jazayeri M.H., Amani H., Pourfatollah A.A., Avan A., Ferns G.A., Pazoki-Toroudi H., Enhanced detection sensitivity of prostate-specific antigen via PSA-conjugated gold nanoparticles based on localized surface plasmon resonance: GNP-coated anti-PSA/LSPR as a novel approach for the identification of prostate anomalies, Cancer Gene Therapy, 23 (2016) 365–369.

Jiang Y., Lu H., Dag A., Hart-Smith G., Stenzel M.H., Albumin–polymer conjugate nanoparticles and their interactions with prostate cancer cells in 2D and 3D culture: comparison between PMMA and PCL, Journal of Materials Chemistry B, 4 (2016) 2017–2027.

Joye I.J., Davidov-Pardo G., Ludescher R.D., McClements D.J., Fluorescence quenching study of resveratrol binding to zein and gliadin: Towards a more rational approach to resveratrol encapsulation using water-insoluble proteins, Food Chemistry, 185 (2015) 261–267.

Katz E., Willner I., Integrated nanoparticle-biomolecule hybrid systems: Synthesis, properties, and applications, Angewandte Chemie International Edition, 43 (2004) 6042–6108.

Kim B.J., Cheong H., Hwang B.H., Cha H.J., Mussel-inspired protein nanoparticles containing iron(III)-DOPA complexes for ph-responsive drug delivery, Angewandte Chemie International Edition, 54 (2015) 7318–7322.

Kobayashi K., Wei J., Iida R., Ijiro K., Niikura K., Surface engineering of nanoparticles for therapeutic applications, Polymer Journal, 46 (2014) 460–468.

Koley P., Sakurai M., Aono M., Controlled fabrication of silk protein sericin mediated hierarchical hybrid flowers and their excellent adsorption capability of heavy metal ions of Pb(II), Cd(II) and Hg(II), ACS Applied Materials and Interfaces, 8 (2016) 2380–2392.

Kumar R., Lal S., Synthesis of organic nanoparticles and their applications in drug delivery and food nanotechnology: A Review, Journal of Nanomaterials & Molecular Nanotechnology, 03 (2014).

Lebre F., Borchard G., Faneca H., Pedroso de Lima M.C., Borges O., Intranasal administration of novel chitosan nanoparticle/DNA complexes induces antibody response to hepatitis B surface antigen in mice, Molecular Pharmaceutics, 13 (2016) 472–482.

Lee S.H., Heng D., Ng W.K., Chan H.K., Tan R.B.H., Nano spray drying: A novel method for preparing protein nanoparticles for protein therapy, International Journal of Pharmaceutics, 403 (2011) 192–200.

Lee Y.-H., Wu B., Zhuang W.-Q., Chen D.-R., Tang Y.J., Nanoparticles facilitate gene delivery to microorganisms via an electrospray process, Journal of Microbiological methods, 84 (2011) 228–233.

Lenggoro I.W., Xia B., Okuyama K., de la Mora J.F., Sizing of colloidal nanoparticles by electrospray and differential mobility analyzer methods, Langmuir, 18 (2002) 4584–4591.

Liao W., Yu Z., Lin Z., Lei Z., Ning Z., Regenstein J.M., Yang J., Ren J., Biofunctionalization of selenium nanoparticle with dictyophora indusiata polysaccharide and its antiproliferative activity through death-receptor and mitochondria-mediated apoptotic pathways, Scientific Reports, 5 (2016) 18629 (13pp). http://doi.org/10.1038/srep18629

Lin T.-T., Gao D.-Y., Liu Y.-C., Sung Y.-C., Wan D., Liu J.-Y., Chiang T., Wang L., Chen Y., Development and characterization of sorafenib-loaded PLGA nanoparticles for the systemic treatment of liver fibrosis, Journal of Controlled Release, 221 (2016) 62–70.

Liu X., Niazov-Elkan A., Wang F., Willner I., Switching photonic and electrochemical functions of a DNAzyme by DNA machines, Nano Letters, 13 (2013) 219–225.

López-Rubio A., Lagaron J.M., Whey protein capsules obtained through electrospraying for the encapsulation of bioactives, Innovative Food Science and Emerging Technologies, 13 (2012) 200–206.

Lu K.Y., Li R., Hsu C.H., Lin C.W., Chou S.C., Tsai M.L., Mi F.L., Development of a new type of multifunctional fucoidan-based nanoparticles for anticancer drug delivery, Carbohydrate Polymers, 165 (2017) 410–420.

Mahapatro A., Singh D.K., Biodegradable nanoparticles are excellent vehicle for site directed in-vivo delivery of drugs and vaccines, Journal of Nanobiotechnology, 9 (2011) 55 (11pp). https://doi.org/10.1186/1477-3155-9-55

Marelli B., Brenckle M.A., Kaplan D.L., Omenetto F.G., Silk fibroin as edible coating for perishable food preservation, Scientific Reports, 6 (2016) 25263 (11pp). http://doi.org/10.1038/srep25263

Marty J.J., Oppenheim R.C., Speiser P., Nanoparticles—a new colloidal drug delivery system, Pharmaceutica acta Helvetiae, 53 (1978) 17–23.

Mattu C., Li R., Ciardelli G., Chitosan nanoparticles as therapeutic protein nanocarriers : the effect of ph on particle formation and encapsulation efficiency, Polymer Composites, (2013) 1538–1545.

Mehta P., Haj-Ahmad R., Rasekh M., Arshad M.S., Smith A., van der Merwe S.M., Li X., Chang M.-W., Ahmad Z., Pharmaceutical and biomaterial engineering via electrohydrodynamic atomization technologies, Drug Discovery Today, 00 (2016) 1–9.

Meissner J., Prause A., Bharti B., Findenegg G.H., Characterization of protein adsorption onto silica nanoparticles: influence of pH and ionic strength, Colloid and Polymer Science, 293 (2015) 3381–3391.

Mejias S.H., Couleaud P., Casado S., Granados D., Garcia M.A., Abad J.M., Cortajarena A.L., Assembly of designed protein scaffolds into monolayers for nanoparticle patterning, Colloids and Surfaces B: Biointerfaces, 141 (2016) 93–101.

Menjoge A.R., Rinderknecht A.L., Navath R.S., Faridnia M., Kim C.J., Romero R., Miller R.K., Kannan R.M., Transfer of PAMAM dendrimers across human placenta: Prospects of its use as drug carrier during pregnancy, Journal of Controlled Release, 150 (2011) 326–338.

Menon J.U., Ravikumar P., Pise A., Gyawali D., Hsia C.C.W., Nguyen K.T., Polymeric nanoparticles for pulmonary protein and DNA delivery, Acta Biomaterialia, 10 (2014) 2643–2652.

Mercado-Lubo R., Zhang Y., Zhao L., Rossi K., Wu X., Zou Y., Castillo A., Leonard J., Bortell R., Greiner D.L., Shultz L.D., Han G., McCormick B.A., A Salmonella nanoparticle mimic overcomes multidrug resistance in tumours, Nature Communications, 7 (2016) 12225 (13pp). http://doi.org/10.1038/ncomms12225

Moreira C.D.F., Carvalho S.M., Mansur H.S., Pereira M.M., Thermogelling chitosan-collagen-bioactive glass nanoparticle hybrids as potential injectable systems for tissue engineering, Materials Science and Engineering C, 58 (2016) 1207–1216.

Mortensen D.N., Williams E.R., Investigating protein folding and unfolding in electrospray nanodrops upon rapid mixing using theta-glass emitters, Analytical Chemistry, 87 (2015) 1281–1287.

Naim M.N., Abu Bakar N.F., Iijima M., Kamiya H., Lenggoro I.W., Electrostatic deposition of aerosol particles generated from an aqueous nanopowder suspension on a chemically treated substrate, Japanese Journal of Applied Physics, 49 (2010) 06GH17 (6pp). http://stacks.iop.org/1347-4065/49/i=6S/a=06GH17

Nair R., Varghese S.H., Nair B.G., Maekawa T., Yoshida Y., Kumar D.S., Nanoparticulate material delivery to plants, Plant Science, 179 (2010) 154–163.

Niemeyer C.M., Biotechnology meets materials science, Angewandte Chemie International Edition, 40 (2001) 4128–4158.

Nitta S.K., Numata K., Biopolymer-based nanoparticles for drug/gene delivery and tissue engineering, International Journal of Molecular Sciences, 14 (2013) 1629–1654.

Nuruzzaman M., Rahman M.M., Liu Y., Naidu R., Nanoencapsulation, nano-guard for pesticides: A new window for safe application, Journal of Agricultural and Food Chemistry, 64 (2016) 1447–1483.

Özel R.E., Ispas C., Ganesana M., Leiter J.C., Andreescu S., Glutamate oxidase biosensor based on mixed ceria and titania nanoparticles for the detection of glutamate in hypoxic environments, Biosensors & Bioelectronics, 52 (2014) 397–402.

Pal S.L., Jana U., Manna P.K., Mohanta G.P., Manavalan R., Nanoparticles–an overview of preparation and characterization, Journal of Applied Pharmaceutical Science, 1 (2011)

228–234.

Panigaj M., Reiser J., Aptamer guided delivery of nucleic acid-based nanoparticles, DNA and RNA Nanotechnology, 2 (2016) 42–52.

Panta P., Kim D.Y., Kwon J.S., Son A.R., Lee K.W., Kim S., Protein drug-loaded polymeric nanoparticles, Journal of Biomedical Science and Engineering, 7 (2014) 825–832.

Peltonen L., Valo H., Kolakovic R., Laaksonen T., Hirvonen J., Electrospraying, spray drying and related techniques for production and formulation of drug nanoparticles, Expert Opinion on Drug Delivery, 7 (2010) 705–719.

Pereira R.C., de Deus Souza Carneiro J., Borges S.V., Assis O.B.G., Alvarenga G.L., Preparation and characterization of nanocomposites from whey protein concentrate activated with lycopene, Journal of Food Science, 81 (2016) E637–E642.

Politi J., De Stefano L., Longobardi S., Giardina P., Rea I., Methivier C., Pradier C.M., Casale S., Spadavecchia J., The amphiphilic hydrophobin Vmh2 plays a key role in one step synthesis of hybrid protein-gold nanoparticles, Colloids and Surfaces B: Biointerfaces, 136 (2015) 214–221.

Puddu V., Perry C.C., Peptide adsorption on silica nanoparticles: Evidence of hydrophobic interactions, ACS Nano, 6 (2012) 6356–6363.

Rabbani P.S., Zhou A., Borab Z.M., Frezzo J.A., Srivastava N., More H.T., Rifkin W.J., David J.A., Berens S.J., Chen R., Hameedi S., Junejo M.H., Kim C., Sartor R.A., Liu C.F., Saadeh P.B., Montclare J.K., Ceradini D.J., Novel lipoproteoplex delivers Keap1 siRNA based gene therapy to accelerate diabetic wound healing, Biomaterials, 132 (2017) 1–15.

Rampino A., Borgogna M., Blasi P., Bellich B., Cesàro A., Chitosan nanoparticles: Preparation, size evolution and stability, International Journal of Pharmaceutics, 455 (2013) 219–228.

Rao J.P., Geckeler K.E., Progress in Polymer Science Polymer nanoparticles : Preparation techniques and size-control parameters, Progress in Polymer Science, 36 (2011) 887–913.

Rassu G., Cossu M., Langasco R., Carta A., Cavalli R., Giunchedi P., Gavini E., Propolis as lipid bioactive nano-carrier for topical nasal drug delivery, Colloids and Surfaces B: Biointerfaces, 136 (2015) 908–917.

Rodríguez-Delgado M.M., Alemán-Nava G.S., Rodríguez-Delgado J.M., Dieck-Assad G., Martínez-Chapa S.O., Barceló D., Parra R., Laccase-based biosensors for detection of phenolic compounds, TrAC Trends in Analytical Chemistry, 74 (2015) 21–45.

Saallah S., Naim N.N., Mokhtar M.N., Abu Bakar N.F., Gen M., Lenggoro W.W., Transformation of cyclodextrin glucanotransferase (CGTase) from aqueous suspension to fine solid particles via electrospraying, Enzyme and Microbial Technology, 64–65 (2014) 52–59.

Sahdev P., Ochyl L.J., Moon J.J., Biomaterials for nanoparticle vaccine delivery systems, Pharmaceutical Research, 31 (2014) 2563–2582.

Salata O.V., Applications of nanoparticles in biology and medicine, Journal of Nanobiotechnology, 2 (2004) 3 (6pp). https://doi.org/10.1186/1477-3155-2-3

Sapsford K.E., Algar W.R., Berti L., Gemmill K.B., Casey B.J., Oh E., Stewart M.H., Medintz I.L., Functionalizing nanoparticles with biological molecules: Developing chemistries that facilitate nanotechnology, Chemical Reviews, 113 (2013) 1904–2074.

Sathiyabama M., Parthasarathy R., Biological preparation of chitosan nanoparticles and its in vitro antifungal efficacy against some phytopathogenic fungi, Carbohydrate Polymers, 151 (2016) 321–325.

Sellers S.P., Clark G.S., Sievers R.E., Carpenter J.F., Dry powders of stable protein formulations from aqueous solutions prepared using supercritical CO_2-assisted aerosolization, Journal of Pharmaceutical Sciences, 90 (2001) 785–797.

Shahrestani H., Taheri-Kafrani A., Soozanipour A., Tavakoli O., Enzymatic clarification of fruit juices using xylanase immobilized on 1,3,5-triazine-functionalized silica-encapsulated magnetic nanoparticles, Biochemical Engineering Journal, 109 (2016) 51–58.

Sojitra U.V., Nadar S.S., Rathod V.K., A magnetic tri-enzyme nanobiocatalyst for fruit juice clarification, Food Chemistry, 213 (2016) 296–305.

Spampinato V., Parracino M.A., La Spina R., Rossi F., Ceccone G., Surface analysis of gold nanoparticles functionalized with thiol-modified glucose SAMs for biosensor applications, Frontiers in Chemistry, 4 (2016) 1–12.

Sperling R.A., Parak W.J., Surface modification, functionalization and bioconjugation of colloidal inorganic nanoparticles, Philosophical transactions Series A, Mathematical, physical, and engineering sciences, 368 (2010) 1333–1383.

Sundar S., Kundu J., Kundu S.C., Biopolymeric nanoparticles, Science and Technology of Advanced Materials, 11 (2010) 014104 (13pp). http://dx.doi.org/10.1088/1468-6996/11/1/014104

Surnar B., Sharma K., Jayakannan M., Core–shell polymer nanoparticles for prevention of GSH drug detoxification and cisplatin delivery to breast cancer cells, Nanoscale, 7 (2015) 17964–17979.

Tabernero A., Martín Del Valle E.M., Galán M.A., Supercritical fluids for pharmaceutical particle engineering: Methods, basic fundamentals and modelling, Chemical Engineering & Processing: Process Intensification, 60 (2012) 9–25.

Tamjidi F., Shahedi M., Varshosaz J., Nasirpour A., Nanostructured lipid carriers (NLC): A potential delivery system for bioactive food molecules, Innovative Food Science and Emerging Technologies, 19 (2013) 29–43.

Tauran Y., Brioude A., Coleman A.W., Rhimi M., Kim B., Molecular recognition by gold, silver and copper nanoparticles, World Journal of Biological Chemistry, 4 (2013) 35–63.

Uematsu I., Matsumoto H., Morota K., Minagawa M., Tanioka A., Yamagata Y., Inoue K., Surface morphology and biological activity of protein thin films produced by electrospray deposition, Journal of Colloid and Interface Science, 269 (2004) 336–340.

Usha Rani P., Madhusudhanamurthy J., Sreedhar B., Dynamic adsorption of α-pinene and linalool on silica nanoparticles for enhanced antifeedant activity against agricultural pests, Journal of Pest Science, 87 (2014) 191–200.

Valo H., Biopolymer-Based Nanoparticles for Drug Delivery, Helsinki University Printing House, Helsinki, 2012.

Viswanathan K., Preparation and characterization of fluorescent silica coated magnetic hybrid nanoparticles, Colloids and Surfaces A: Physicochemical and Engineering Aspects, 386 (2011) 11–15.

Wang E.C., Wang A.Z., Nanoparticles and their applications in cell and molecular biology, Integrative Biology, 6 (2014) 9–26.

Wei H., Nolkrantz K., Powell D.H., Woods J.H., Ko M.-C., Kennedy R.T., Electrospray sample deposition for matrix-assisted laser desorption/ionization (MALDI) and atmospheric pressure MALDI mass spectrometry with attomole detection limits, Rapid Communications in Mass Spectrometry: RCM, 18 (2004) 1193–1200.

Weiss J., Decker E.A., McClements D.J., Kristbergsson K., Helgason T., Awad T., Solid lipid nanoparticles as delivery systems for bioactive food components, Food Biophysics, 3 (2008) 146–154.

Willner I., Willner B., Katz E., Biomolecule–nanoparticle hybrid systems for bioelectronic applications, Bioelectrochemistry, 70 (2007) 2–11.

Xie W., Zang X., Covalent immobilization of lipase onto aminopropyl-functionalized hydroxyapatite-encapsulated-γ-Fe_2O_3 nanoparticles: A magnetic biocatalyst for interesterification of soybean oil, Food Chemistry, 194 (2016) 1283–1292.

Xing K., Shen X., Zhu X., Ju X., Miao X., Tian J., Feng Z., Peng X., Jiang J., Qin S., Synthesis and in vitro antifungal efficacy of oleoyl-chitosan nanoparticles against plant pathogenic fungi, International Journal of Biological Macromolecules, 82 (2016) 830–836.

Yagati A.K., Kim S.U., Lee T., Min J., Choi J.W., Recombinant azurin-CdSe/ZnS hybrid structures for nanoscale resistive random access memory device, Biosensors & Bioelectronics, 90 (2017) 23–30.

Yang G., Liu H., Hu X., Chen Z., Friis T.E., Wang J., Xiao Y., Zhang S., Bio-inspired hybrid nanoparticles promote vascularized bone regeneration in a morphology-dependent manner, Nanoscale, 9 (2017) 5794–5805.

Yang Z., Zhang C., Zhang J., Bai W., Potentiometric glucose biosensor based on core-shell Fe_3O_4-enzyme-polypyrrole nanoparticles, Biosensors and Bioelectronics, 51 (2014) 268–273.

Yi J., Lam T.I., Yokoyama W., Cheng L.W., Zhong F., Beta-carotene encapsulated in food protein nanoparticles reduces peroxyl radical oxidation in Caco-2 cells, Food Hydrocolloids, 43 (2015) 31–40.

Yu M.K., Park J., Jon S., Targeting strategies for multifunctional nanoparticles in cancer imaging and therapy, Theranostics, 2 (2012) 3–44.

Yurteri C.U., Hartman R.P.A., Marijnissen J.C.M., Producing pharmaceutical particles via electrospraying with an emphasis on nano and nano structured particles—A review, KONA Powder and Particle Journal, 28 (2010) 91–115.

Zamani M., Prabhakaran M.P., Thian E.S., Ramakrishna S., Protein encapsulated core-shell structured particles prepared by coaxial electrospraying: Investigation on material and processing variables, International Journal of Pharmaceutics, 473 (2014) 134–143.

Zhang Y., Huang R., Zhu X., Wang L., Wu C., Synthesis, properties, and optical applications of noble metal nanoparticle-biomolecule conjugates, Chinese Science Bulletin, 57 (2012) 238–246.

Zhao Z., Li Y., Xie M.B., Silk fibroin-based nanoparticles for drug delivery, International Journal of Molecular Sciences, 16 (2015) 4880–4903.

Author's short biography

Suryani Saallah

Suryani Saallah is currently a PhD student at Graduate School of Bio-Application and Systems Engineering, Tokyo University of Agriculture and Technology (TUAT). She also served as a Lecturer at Biotechnology Research Institute, Universiti Malaysia Sabah (UMS) with a specialization in Bioprocess Engineering. She earned her B. Eng (Chemical-Bioprocess) from Universiti Teknologi Malaysia (UTM) and Master Degree from Universiti Putra Malaysia. Her research is mainly focused on synthesis of nanomaterials including nanoparticles and nanofibers and its application in bioprocessing.

I. Wuled Lenggoro

Dr. Wuled Lenggoro is a faculty member at TUAT. He holds a doctoral degree and faculty position at Hiroshima Univ., followed by visiting positions in RIKEN (Institute of Physical and Chemical Research) and Yale Univ. In 2007, he established a research group under JST/TUAT "Tenure-track" program. At TUAT, he has supervised more than 10 doctoral-, 20 master's degree students, and more than 30 undergraduates. He was a Regional Editor of Journal of Nanoparticle Research (Springer). He was awarded "Asian Young Aerosol Scientist Award" (2007), "Chemical Engineering Science's Most Cited Paper 2003–2006 Award" (Elsevier), "Iinoya Award" (2005), "Takahashi Award" (2013), and "Measurement Award" (2016) from Japan Association of Aerosol Science and Technology.

KONA Powder and Particle Journal No. 35 (2018) 112–121/Doi:10.14356/kona.2018018 Review Paper

Leading Edge of Coal Utilization Technologies for Gasification and Cokemaking †

Kenji Kato [1*] **and Keiji Matsueda** [2]

[1] *Engineering R&D Institute, Nippon Steel & Sumikin Engineering Co., Ltd., Japan*
[2] *Head Office, Nippon Steel & Sumitomo Metal Corp., Japan*

Abstract

Coal is a very important resource for power generation and cokemaking. Moreover, coal is a very useful resource for producing city gas and chemical materials by gasification technology. Low grade coals are suitable for the coal gasification resources because they are easily decomposed and converted to generate gas in the gasifier. On the other hand, high quality coals such as good quality bituminous coals are required for producing metallurgical coke. Recently, the amount of high quality coals has been decreasing. The expansion of raw coal brands for producing metallurgical coke is very important. In this paper, the development of high energy efficiency gasification technology, ECORO®, and new cokemaking technologies such as the DAPS and the SCOPE21 enabling the expansion of coal resources are introduced. These technologies are contributed to the expansion of coal resources and energy savings.

Keywords: coal, low rank coal, gasification, cokemaking, SCOPE21

1. Introduction

Coal is a very important resource for power generation and cokemaking. Moreover, coal is a very useful resource for producing city gas and chemical materials by gasification technology. Low grade coal is suitable as coal gasification resources because they are easily decomposed and converted to generate gas in the gasifier.

On the other hand, high quality coals such as good quality bituminous coals are required for producing metallurgical coke. **Fig. 1** shows the coal band and the expansion target of coal resources for producing metallurgical coke (Kato, 2008). In the conventional cokemaking process, only high quality bituminous coals can be used as raw coals. Recently, the amount of high quality coals has been decreasing. The expansion of raw coal brands for producing metallurgical coke is very important. In Japan, improvement of coke quality is strongly demanded to smoothly operate large inner volume blast furnaces. Therefore, the effective coal utilization technologies involving the dry coal charging process and the new cokemaking process were developed.

In this paper, the trend of gasification technologies and new cokemaking processes enabling the expansion of coal resources are introduced.

2. Coal gasification technology

2.1 Trend of coal gasification technology

Coal gasification is the technology to convert coal into gas such as hydrogen (H_2), carbon monoxide (CO) and methane (CH_4) at high temperature using air or oxygen and steam as the gasifying agent. The main coal gasification reactions are shown in equation (1) to (8). The generated gas is used as the clean gas for raw materials to produce city gas, chemical products etc.

1) Pyrolysis;

Coal to gas component, tar, heavy oil, char(C)

2) Reaction with oxygen;

$$C + O_2 = CO_2 + 393\ \text{kJ/mol} \tag{1}$$

$$C + 1/2O_2 = CO + 111\ \text{kJ/mol} \tag{2}$$

$$C + CO_2 = 2CO - 171\ \text{kJ/mol} \tag{3}$$

3) Reaction with steam

$$C + H_2O = CO_2 + H_2 - 131\ \text{kJ/mol} \tag{4}$$

$$C + 2H_2O = CO_2 + 2H_2 - 76\ \text{kJ/mol} \tag{5}$$

---

† Received 27 June 2017; Accepted 21 August 2017

[1] 10-12, Koyocho, Wakamatsu-ku, Kitakyushu-city, Fukuoka 808-0002, Japan
[2] 2-6-1, Marunouchi, Chiyoda-ku, Tokyo 100-8071, Japan
* Corresponding author: Kenji Kato
E-mail: katoh.kenji.e2q@eng.nssmc.com
TEL: +81-93-751-0780 FAX: +81-93-752-3159

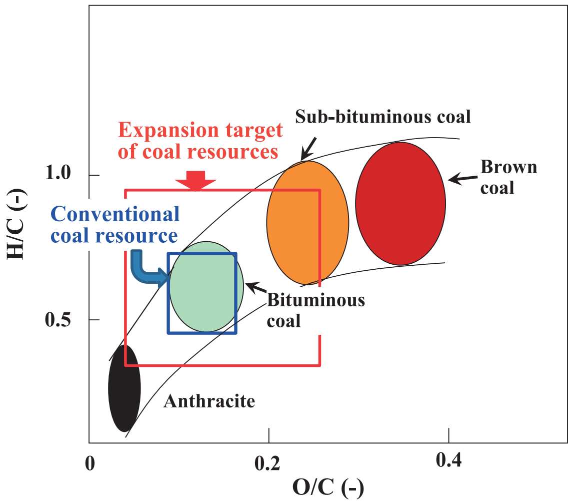

Fig. 1 Coal band.

$$CO + H_2O = CO_2 + H_2 + 41 \text{ kJ/mol} \quad (6)$$

4) Reaction with hydrogen

$$C + 2H_2 = CH_4 + 75 \text{ kJ/mol} \quad (7)$$

$$CO + 3H_2 = CH_4 + H_2O + 206 \text{ kJ/mol} \quad (8)$$

Fig. 2 shows the history of the coal gasification technology (Gräbner M., 2014). The history of coal gasification is divided into three generations. The first generation of industrial gasification arose from the idea of supplying a chemical synthesis produced from coal. A typical example is the Winkler fluidized bed gasifier, which found its first commercial application in 1926 in Germany. Among the first generation of gasification technologies, the Lurgi fixed bed dry bottom technology was developed.

Besides minor industrial factors, the oil crises relaunched interest in coal gasification again leading to the development of a second generation of coal gasification processes from 1970s until the early 1990s.

For fluidized bed and entrained bed processes, the gasification pressure should be raised from atmospheric to 2–6 MPa. For fluidized bed and fixed bed processes, the performance was enhanced in the points of high carbon conversion rate and high energy efficiency. Another focus was on the integration of heat recovery from syngas by steam generation if gasification is employed for power generation.

However, after a decade of relative silence surrounding coal gasification, beginning around 2000s, the following general trends have renewed interest in the technology.

(1) Substitution of crude oil by other energy carriers, such as biomass or coal targeting supply security and local energy price stabilization

(2) Increasing interest in the use of low grade coals with high ash or moisture contents in emerging nations

The Lurgi process uses the pressurized fixed bed gasifier. The Winkler process uses the fluidized bed type gasifier developed in German, and the Koppers-Totzek process uses the entrained bed gasifier developed in Germany in 1952.

After the first oil crisis of the 1970s, coal was reviewed as the industrial raw materials. Various types of gasification process were developed and the energy efficiency was improved. The feature of the Texaco and the GE process is a coal-water slurry type, and the Shell furnace is a dry process.

One of the coal gasification technologies developed in Japan is the ECOPRO®. This technology has the feature of two stage coal gasification.

2.2 ECOPRO® gasification technology

ECOPRO® is the gasification technology with an entrained bed type gasifier with two stages (Kosuge et al., 2014). Generally, an entrained bed type gasifier can take high carbon conversion and high energy efficiency. Furthermore, the energy efficiency of the ECOPRO® process is higher than that of a conventional entrained bed gasifier

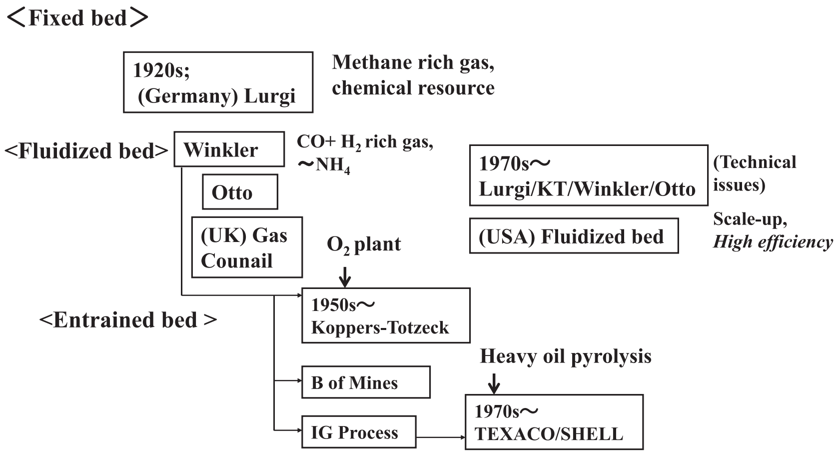

Fig. 2 Trend of coal gasification technologies.

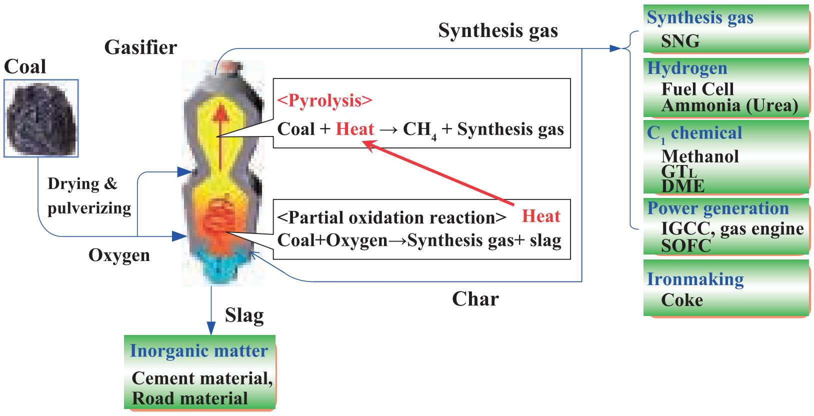

Fig. 3 Process flow of the ECOPRO®.

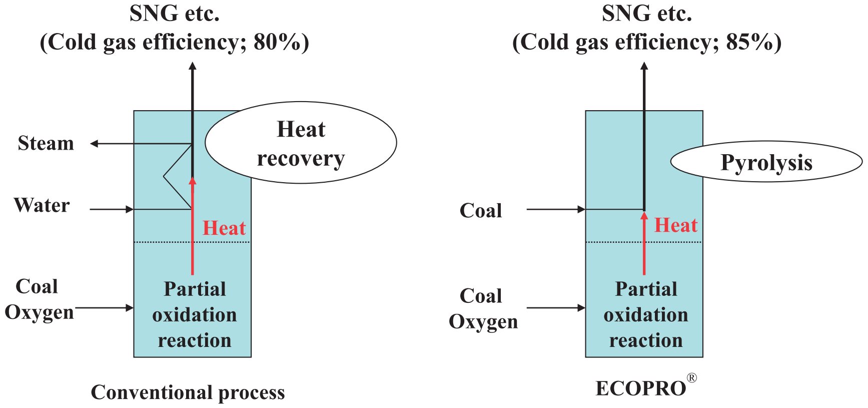

Fig. 4 Comparison of energy efficiency involving the ECOPRO® and conventional gasification process.

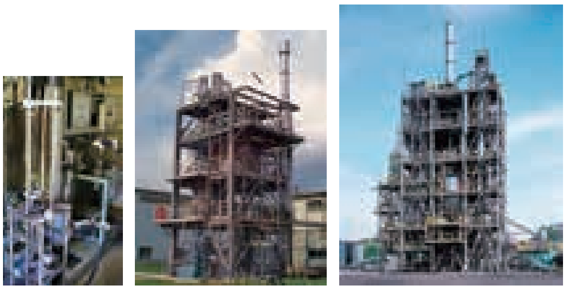
Bench scale (1 kg/d)

PDU(1 t/d)

Pilot plant (20 t/d)

Fig. 5 Experimental apparatuses of the ECOPRO®.

because it has two stage reactors. **Fig. 3** shows the outline of the ECOPRO® process. First, coal is crushed and dried to prepare pulverized coal for gasification. Pulverized coal is introduced into both of the chambers of the gasifier with the career gas, and quickly converted to the syngas. In the lower chamber, coal is reacted with oxygen and steam. Partial oxidation reaction occurs, and syngas is generated from 1300 °C to 1400 °C. The generated syngas is introduced into the upper part of the reactor. In the upper chamber, the coal pyrolysis reaction is occurred by the sensible heat of the high temperature syngas introduced from the lower chamber. Syngas including methane and char is generated at 1100 °C in the upper chamber.

Fig. 4 shows the unique feature of the ECOPRO® process. In the ECOPRO® process, the sensible heat generated during coal partial combustion at the lower chamber can be used for coal pyrolysis at the upper chamber. Therefore, total energy efficiency of the process increases by 5 % compared with other conventional gasification processes.

In other gasification processes, the sensible heat from the high temperature syngas obtained by coal gasification is recovered as steam by the boiler. Therefore, the maximum energy efficiency of these processes is 80 % (DOE/NETL, 2011). In the ECOPRO® process, part of the sensible heat from the high temperature syngas generated at the lower chamber is used for coal pyrolysis in the upper part of gasifier. As a result, the ECOPRO® provides 85 % energy efficiency (Kosuge et al., 2014).

Fig. 5 shows the experimental apparatuses of ECOPRO®. Since the early 1990s, Nippon Steel & Sumikin Engineering has been developing coal gasification technologies and has developed the ECOPRO® process. Based on the basic research with 1 kg/d-scale experimental apparatus (1992–1996) and bench scale tests with 1 t/d

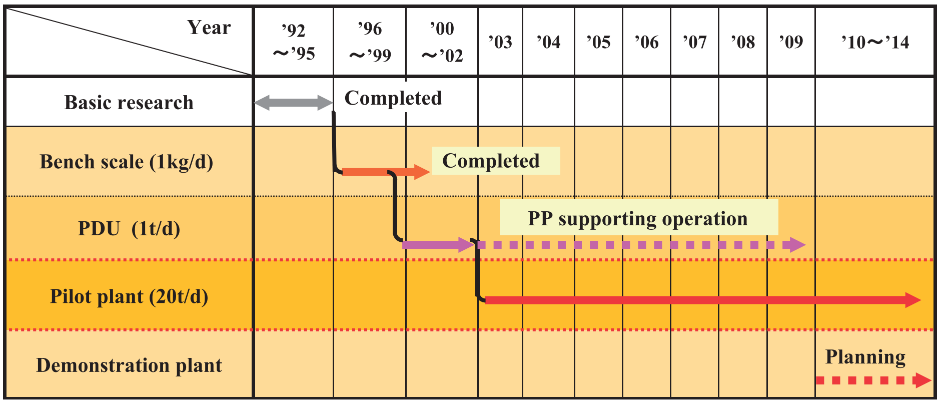

Fig. 6 Development schedule of the ECOPRO® process.

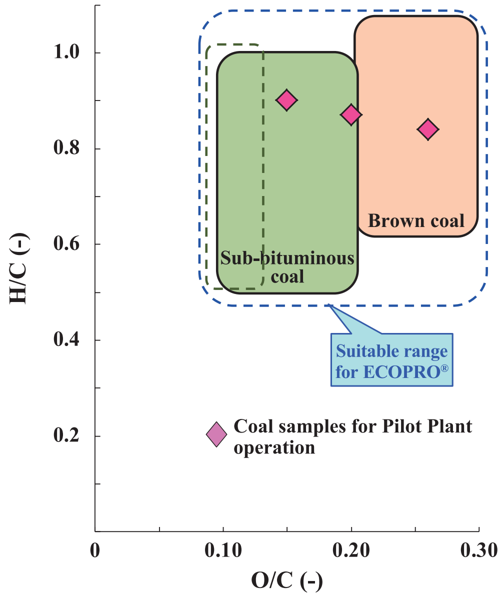

Fig. 7 Coal map suitable for gasification technology.

scale unit, pilot plant scale tests with 20 t/d started in 2003 (**Fig. 6**) (Kosuge et al., 2014).

The pilot plant operation with three different types of coal samples of brown coals and sub-bituminous coals had been conducted for 3101 h in total. **Fig. 7** shows the coal characteristics used for the pilot plant operation. It was clarified that the ECOPRO® process is suitable for a wide range of coal resources such as sub-bituminous coals and brown coals.

3. Cokemaking technology

3.1 Conventional cokemaking technology

Coke is mainly used for producing pig iron using the blast furnace method. More than 90 % of coke produced in Japan is used for blast furnace (**Fig. 8**). The role of coke is mainly as follows, iron ore reducing agent, heating material and permeability maintaining spacer that sustains the flow passes in the blast furnace (**Fig. 9**). Coke is

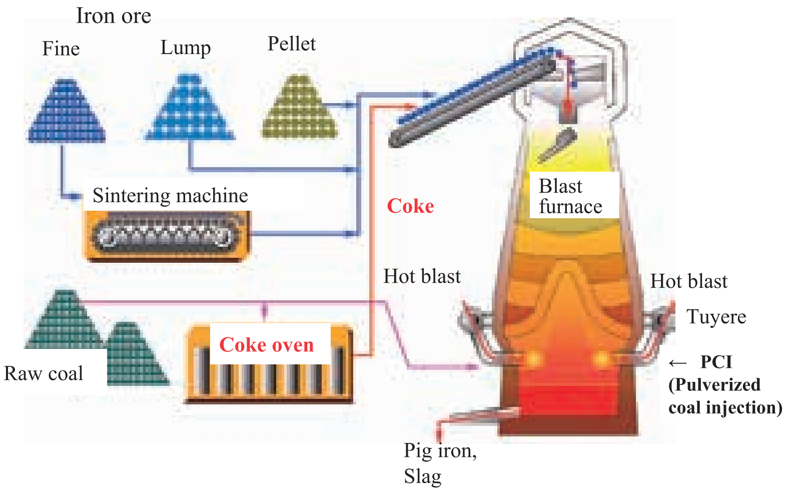

Fig. 8 Schematic diagram of ironmaking process flow.

very important because no alternative of coke is available in the blast furnace process.

Fig. 10 shows the conventional cokemaking process flow. First, several brands of raw coals are blended and crushed by a coal crusher. Blended raw coals are charged into coke ovens for producing metallurgical coke. **Fig. 11** shows the appearance of a coke oven battery. The carbonization time is from 19 to 24 h and the raw coals are carbonized in the coke oven. The carbonization temperature is around 1,000 °C.

3.2 Dry coal charging process for improving coke quality

Dry coal charging processes such as coal moisture control (CMC) process and dry-cleaned and agglomerated precompaction system (DAPS) were successfully developed by Nippon Steel & Sumitomo Metal Corp (Kato, 2004; Kato et al., 2006).

The first CMC process using indirect heating in a rotary dryer was operated in 1983. Coal moisture of raw coal charged into a coke oven is reduced from 10 mass% to 5–6 mass% with the CMC process. The use of the CMC process has been spreading because this technology saves energy, permits the increased use of non- or slightly-caking coals, stabilizes the operation of cokemaking process by keeping the moisture content of coal charges constant.

To increase the blending ratio of non- or slightly-caking coals in coal charges, the new pretreating technology for the coal charge, DAPS was developed and came on stream at Nippon Steel & Sumitomo Metal Oita works in 1992 (Kato, 2004).

At first, to evaluate the dust occurrence during the coal transportation from a coal dryer to coke oven, the rela-

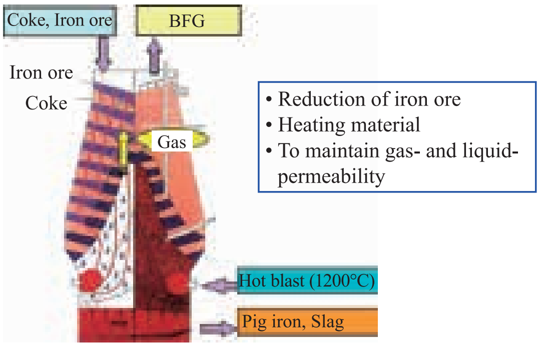

- Reduction of iron ore
- Heating material
- To maintain gas- and liquid-permeability

Fig. 9 Role of coke on blast furnace operation.

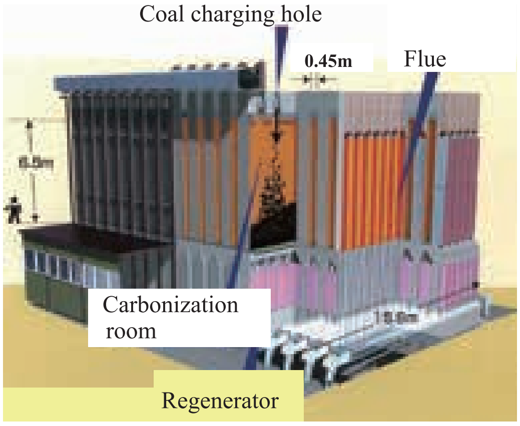

Fig. 11 Appearance of coke oven battery.

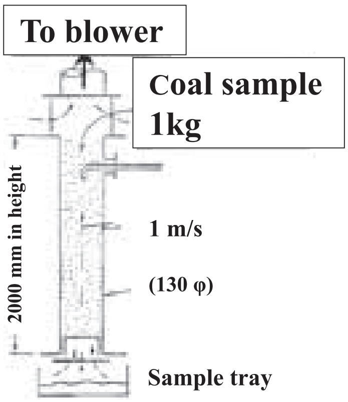

Fig. 12 Experimental apparatus for dust occurrence measurement. Reprinted with permission from Ref. (Kato, 2004). Copyright: (2004) The Iron and Steel Institute of Japan.

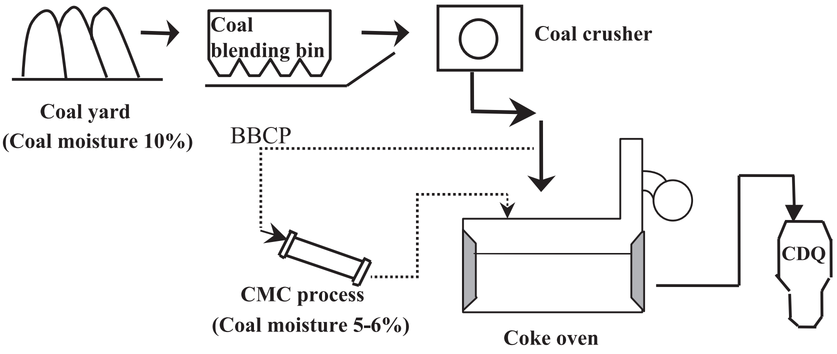

Fig. 10 Conventional cokemaking process flow.

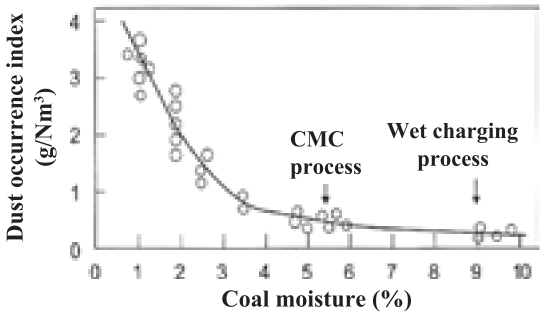

Fig. 13 Relationship between dust occurrence index and coal moisture. Reprinted with permission from Ref. (Kato, 2004). Copyright: (2004) The Iron and Steel Institute of Japan.

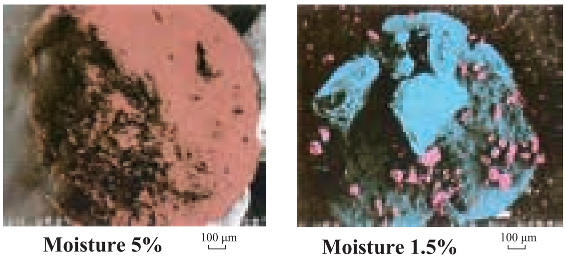

Moisture 5% Moisture 1.5%

Fig. 14 Coal particles in charging coal (SEM). Reprinted with permission from Ref. (Kato, 2004). Copyright: (2004) The Iron and Steel Institute of Japan.

tionship between the coal moisture and dust occurrence was investigated using a dust occurrence tester. **Fig. 12** schematically illustrates the experimental apparatus (Kato, 2004).

Sample coal 1 kg in weight was put into the experimental apparatus from the top; the coal particles floating inside the tube were sucked by a blower until the tube inside became visually clear of the particles, and the quantity of the particles collected was measured.

Fig. 13 shows the results (Kato, 2004). The dust occurrence increased as the moisture of coal decreased. **Fig. 14** shows the photomicrographs of coal grains with different moisture contents (Kato, 2004). With the high moisture content, fine particles either adhere to coarse grains or cohere with each other to form pseudo-particles with water serving as a binder and the dust occurrence is low. On the other hand, when the coal is dried for pretreatment, the pseudo-particles disintegrate into fine particles and the dust occurrence increases.

Fig. 15 shows the relation between the fractions of fines that are 74 µm or less in size in the feedstock coal and dust occurrence (Kato, 2004). As a result, it was presumed that the coal particles that are 74 µm or less in size were mainly responsible for the dust occurrence.

From the above, it was clarified that agglomeration of fine coals was important to reduce the dust occurrence and stabilize the dry coal charging process.

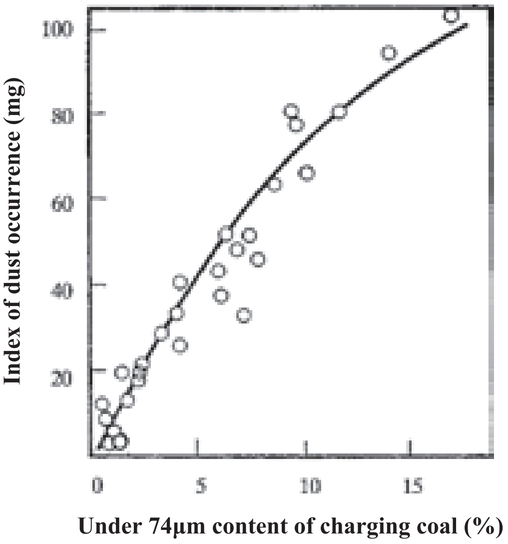

Fig. 15 Relation between dust occurrence and the content of under 74 µm of coal charge. Reprinted with permission from Ref. (Kato, 2004). Copyright: (2004) The Iron and Steel Institute of Japan.

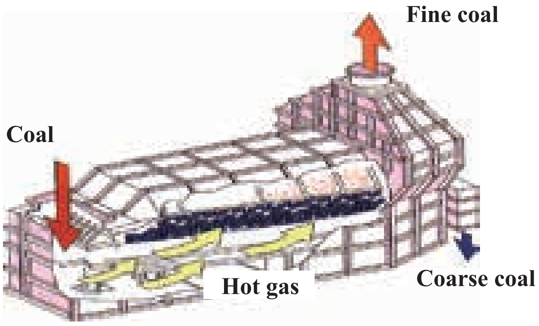

Fig. 16 Outline of fluidized bed dryer. Reprinted with permission from Ref. (Kato, 2004). Copyright: (2004) The Iron and Steel Institute of Japan.

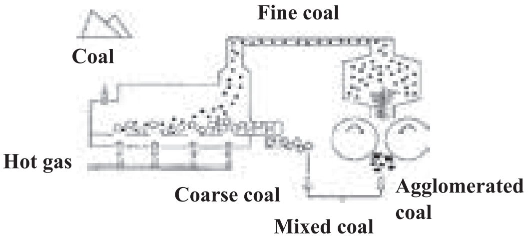

Fig. 17 Process flow of DAPS. Reprinted with permission from Ref. (Kato, 2004). Copyright: (2004) The Iron and Steel Institute of Japan.

The application of the fluidized bed method for drying and classification of fine coal in the cokemaking process was studied as the first case in the world. Moreover, a fluidized bed coal dryer was developed that is capable of efficiently drying and classifying roughly 6,800 t/d of coal (**Fig. 16**) (Kato, 2004).

Fig. 17 shows the process flow of DAPS (Kato, 2004). In the process, the coal is dried in the fluidized bed dryer

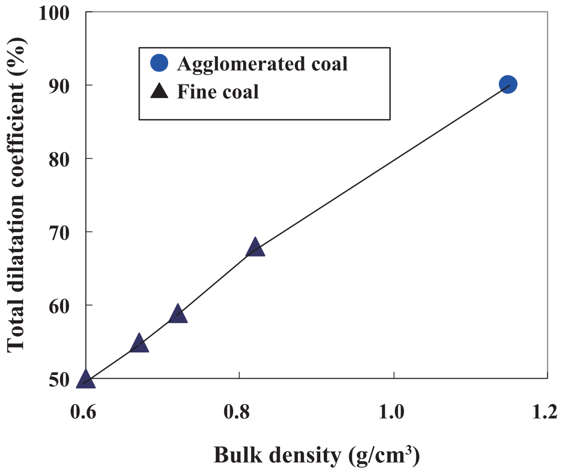

Fig. 18 Relation between bulk density and total dilatation coefficient of fine coal. Reprinted with permission from Ref. (Kato, 2004). Copyright: (2004) The Iron and Steel Institute of Japan.

and fine coal is separated from coarser grains by the gas flow, collected by a cyclone separator, and formed into agglomerated by a roll compactor. The ratio of fine coal is about 30 mass% of the coal charge. The agglomerated fine coal is added to the coarse coal and charged into coke ovens.

The relation between the bulk density of coal charge and total dilatation coefficient of fine coal was investigated. The result is shown in **Fig. 18** (Kato, 2004). The dilatation of fine coal increases when the bulk density is increased. From the result, it is apparent that the agglomeration of fine coal not only suppresses the generation of dust but also improves the dilatation of fine coal.

The coke strength from the DAPS process was compared the one from the CMC process under the same coal blending conditions. As a result, the coke quality in the DAPS was improved. The coke quality is thought to be improved in the DAPS process owing to the increase in the bulk density of coal charge, which is caused by a decrease in the moisture of coal charge (Nomura et al., 2004), and the improvement in coal dilatation, which is caused by the agglomeration of fine coal.

Fig. 19 shows the comparison of non- or slightly-caking coal ratio in each process without deteriorating coke strength (Kato, 2004). By the application of the DAPS process to the cokemaking plant, it was found that the ratio of non- or slightly-caking coal in coal charge is increased by 20 mass% compared with the CMC process without deteriorating coke strength.

As a result, it was found that coke strength was improved in the DAPS process owing to increase in the bulk density of coal charge, due to decrease in the moisture of coal charge. So, it was clarified that the DAPS process was suitable for expansion of coal resources.

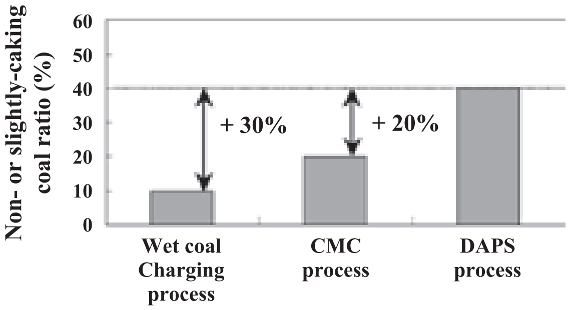

Fig. 19 Comparison of non- or slightly caking coal ratio in coal charge. Reprinted with permission from Ref. (Kato, 2004). Copyright: (2004) The Iron and Steel Institute of Japan.

3.3 SCOPE21 process

Research and development of a new cokemaking process —super coke oven for productivity and environmental enhancement toward the 21st century (SCOPE21)— was conducted in Japan from 1994 to 2003 by the Japan Iron and Steel Federation (JISF) (Nishioka et al., 2004).

Fig. 20 shows the SCOPE21 process flow (Kato, 2010). The SCOPE21 process mainly consists of three units. First is coal rapid preheating unit, second is coal carbonization unit and third is coke quality upgrading and quenching unit by coke dry quenching equipment. The aim for dividing the whole process into three is to make full use of the function of each process in order to maximize the total process efficiency.

Preheating the charging coal heated up from 330 °C–400 °C in the coal pretreatment facility has the effect of reducing carbonization time (**Fig. 21**) (Kato, 2010).

The pilot plant had a coal pretreatment facility, which was the scale-up version of the bench scale plant and a coke oven (**Fig. 22**) (Kato, 2010). The coal pretreatment facility was designed to have a 6 t/h coal throughput, and the basic specifications were determined from the bench scale plant data. One coke oven was constructed. The coke oven chamber was 8 m in length, which was almost half of the length of the commercial plant, 7.5 m in height, and 450 mm in width.

In the coal rapid preheating test, the coal was heated slowly to 300 °C in a fluidized bed dryer, and then heated rapidly to 380 °C in a pneumatic preheater, and carbonized in the coke oven (Matsuura et al, 2004; Kato et al., 2004, Matsuura et al., 2005). The quality of the obtained coke was measured by the JIS drum strength index (DI^{150}_{15}) (DI: Drum Index). (Kubota et al., 2004). Non- or slightly-caking coal was blended 50 mass% in the coal charge. As a result, coke strength (DI^{150}_{15}) became about 2.5points higher than the conventional level by virtue of the rapid preheating effect and the increased bulk density (**Fig. 23**) (Kato, 2010). Pilot plant scale test of the SCOPE21

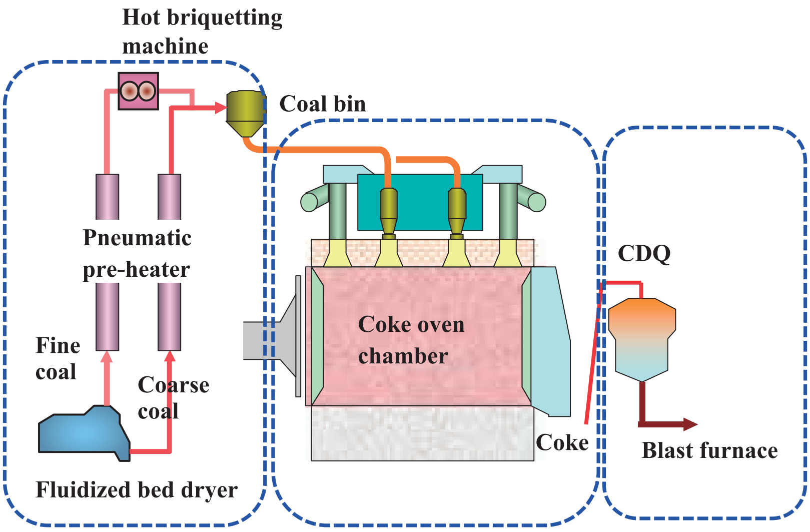

Fig. 20 Schematic diagram of the SCOPE21 process flow. Reprinted with permission from Ref. (Kato, 2010). Copyright: (2010) The Iron and Steel Institute of Japan.

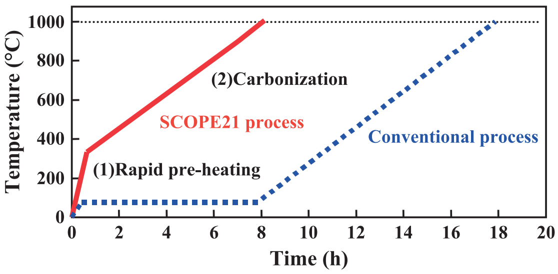

Fig. 21 Comparison of carbonization time between SCOPE21 and conventional process. Reprinted with permission from Ref. (Kato, 2010). Copyright: (2010) The Iron and Steel Institute of Japan.

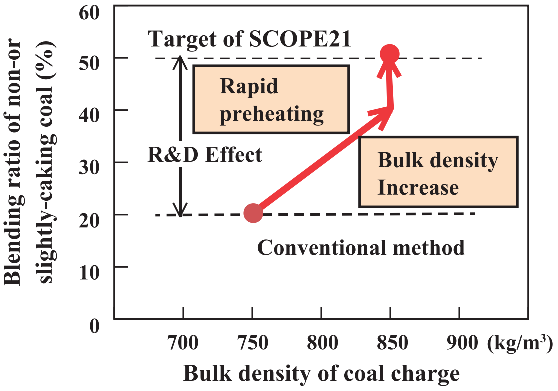

Fig. 23 Technologies for improving coke quality. Reprinted with permission from Ref. (Kato, 2010). Copyright: (2010) The Iron and Steel Institute of Japan.

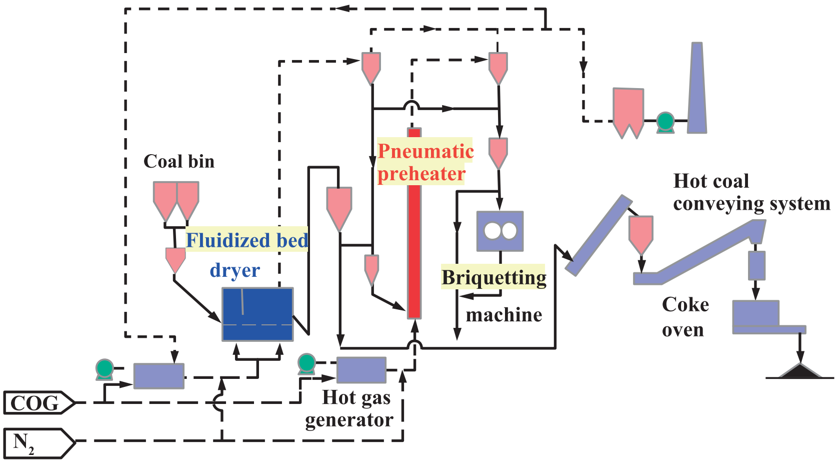

Fig. 22 Process flow of SCOPE21 pilot plant. Reprinted with permission from Ref. (Kato, 2010). Copyright: (2010) The Iron and Steel Institute of Japan.

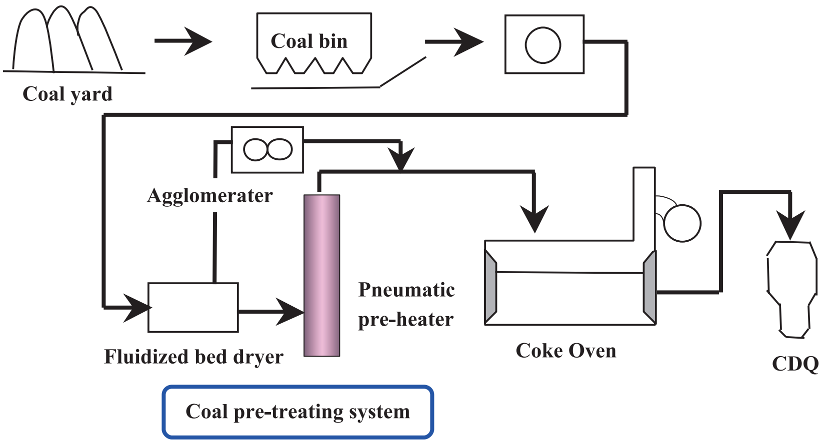

Fig. 24 Process flow of Oita No. 5 coke oven battery. Reprinted with permission from Ref. (Kato, 2010). Copyright: (2010) The Iron and Steel Institute of Japan.

Table 1 Specification of Oita No. 5 coke oven battery. Reprinted with permission from Ref. (Kato, 2010). Copyright: (2010) The Iron and Steel Institute of Japan.

Equipment		Specification (Capacity)
Coal pre-treating	Fluidized bed dryer	155 dry-t/h
	Pneumatic pre-heater	106 dry-t/h
	Agglomerater	34 dry-t/h ~2
Coke oven CDQ	Coke oven chamber	64 ovens, 6.7 mH * 0.45 mW * 16.6 mL
		120 t/h

process was conducted successfully and targets of the project were confirmed by the pilot plant test (Sugiyama et al., 2005) .

The SCOPE21-type new coke oven battery was constructed at Nippon Steel & Sumitomo Metal Oita works from 2006 to 2008 and the operation of the new coke plant was started in 2008. The coke production capacity is 1 million ton per year. **Fig. 24** shows the process flow of the new coke plant and **Table 1** shows the main specification of Oita No. 5 coke oven battery (Kato, 2010). The coal is dried in a fluidized bed dryer and fine coal is separated, and then agglomerated by an agglomerater. Next, the agglomerated fine coal is added to the coarse coal, and charged into coke ovens. The coal is pre-heated rapidly to 350 °C in a pneumatic pre-heater, and carbonized in the coke oven.

The 2nd SCOPE21-type new coke plant was constructed at Nippon Steel & Sumitomo Metal Nagoya works and the operation of the plant started in 2013 (Kato et al., 2013).

These two plants have been operated very smoothly with high productivity and high non- or slightly-caking coal ratio in coal charge.

4. Conclusion

Coal is a very important resource for power generation, cokemaking, gasification, etc. R & D of effective coal utilization technologies has been conducted. In this paper, the trend of the coal gasification technology and new coal gasification technology, ECOPRO®, are introduced. Furthermore, new cokemaking technologies are discussed. They are summarized as follows.

(1) New gasification technology the ECOPRO® has been developing. ECOPRO® is a suitable process for low rank coals gasification with high energy efficiency.
(2) To expand the coal resources for metallurgical coke making process, dry coal charging process DAPS was developed. Coke strength was improved in the DAPS process owing to increase in the bulk density of coal charge, due to decrease in the moisture of coal charge. So, it was clarified that the DAPS process was suitable for expansion of coal resources.
(3) Furthermore, new cokemaking technology SCOPE21 for improving coke quality was developed. New coke plants of the SCOPE21-type were constructed at Nippon Steel & Sumitomo Metal Oita and Nagoya works. The new coke plants have been operated very smoothly.

References

DOE/NETL (Department of Energy / National Energy Technology Laboratory), Cost and Performance Baseline for Fossil Energy Plants; Volume 3a: Low Rank Coal to Electricity: IGCC Cases, (2011) 99–101.

Gräbner M., Ed., Coal gasification in a global context, in: Industrial Coal Gasification Technologies Covering Baseline and High-Ash Coal, Wiley-VCH Verlag GmbH & Co. KGaA, Weinheim, Germany, 2014, pp. 3–9. doi: 10.1002/9783527336913.ch02

Kato K., Development of dry-cleaned and agglomerated precompaction system (DAPS) for metallurgical coke-making, Ferrum, 9 (11) (2004) 810–815.

Kato K., Matsuura M., Sasaki M., Sakawa M., Komaki I., Effect of rapid preheating treatment on coal thermoplasticity and its evaluation method, Journal of the Japan Institute of Energy, 83 (2004) 868–874.

Kato K., Nakashima Y., Yamamura Y., Development of dry-cleaned and agglomerated precompaction system (DAPS) for metallurgical cokemaking, SHINNITTETSU GIHO, 94 (2006) 42–46. http://www.nssmc.com/en/tech/report/nsc/pdf/n9407.pdf

Kato K., Expansion of coal resources for cokemaking, Journal of the Japan Institute of Energy, 87 (2008) 344–352.

Kato K., Development of new cokemaking technology (SCOPE21), Tetsu-to-Hagane, 96 (2010) 196–200.

Kato K., Suzuki Y., Development of coal utilization technologies and future tasks in cokemaking process, Journal of the Japan Institute of Energy, 92 (2013) 985–993.

Kosuge K., Takeda S., Mizuno M. and Kato K., Development of coal gasification technology (ECOPRO® process) for brown coals, Journal of the Japan Institute of Energy, 93 (2014) 1106–1114.

Kubota Y., Arima T., Kato K., Matsuura M., Nakai H., Sasaki M., Sugiyama I., Evaluation of coke strength and coke size in the SCOPE21 process, Tetsu-to-Hagane, 90 (2004) 686–693.

Matsuura M., Sasaki M., Kato K., Nakashima Y., Effects of Coal Blend Type and Preheating Temperature in Coal Rapid Preheating Process on Coke Strength, Tetsu-to-Hagane, 90 (2004) 656–660.

Matsuura M., Kato K., The structural analysis of rapid preheated coal using ESR spectroscopy, Journal of the Japan Institute of Energy, 84 (2005) 426–430.

Nishioka K., Oshima H., Sugiyama I., Fujikawa H., Development of the Innovative Cokemaking Process (SCOPE21) for the 21st Century, Tetsu-to-Hagane, 90 (2004) 614–619.

Nomura S., Arima T., Kato K., Coal blending theory for dry coal charging process, Fuel, 83 (2004) 1771–1776.

Sugiyama I., Kato K., Nishioka K., Oshima H., Fujikawa H., Development of innovative cokemaking process SCOPE21, The 5th European Coke and Ironmaking Congress(5th ECIC), 2005, Stockholm, We 6:4.1.

Author’s short biography

Kenji Kato

Kenji Kato is a general manager of R & D institute, Nippon Steel & Sumikin Engineering Co. Ltd. since 2013. He graduated Chiba University and entered Nippon Steel Corporation in 1981. He was a general manger (2009-2012) of Nippon Steel Corporation, a general manager (2012–2013) of Nippon Steel & Sumitomo Metal Corporation. He received his doctoral degree from Tohoku University (Environmental Science) in 2005. His research area ranges over cokemaking, low rank coal utilization technologies and environmental technologies.

Keiji Matsueda

Keiji Matsueda is a general manager of head office, Nippon Steel & Sumitomo Metal Corporation. He received his master degree from Nagaoka Universiyty of Technology and entered Nippon Steel Corporation in 1991. His research covers metallurgical cokemaking technology.

KONA Powder and Particle Journal No. 35 (2018) 122–138/Doi:10.14356/kona.2018020 Review Paper

Powder Particles and Technologies for Medicine Delivery to the Respiratory System: Challenges and Opportunities [†]

Tomasz R. Sosnowski

[1] *Faculty of Chemical and Process Engineering, Warsaw University of Technology, Poland*

Abstract

The paper discusses essential engineering challenges related to the application of powder medicines for pulmonary delivery as inhaled aerosol. Starting from a physically based description of the complexity of aerosol dynamics inside the respiratory system, the paper discusses several technical factors responsible for efficient drug delivery to the lungs: (i) interparticle interactions—which can be tuned by selection and control of powder manufacturing methods, (ii) inhaler design—as a determinant of flow dynamics through the inhaling device and degree of powder dispersion, (iii) the dynamics of inhalation in a given inhaler—which is related to patient-device interaction. Basic information on the standard (compendial) methods of the quantitative evaluation of dry powder inhalers (DPIs) are presented with a special focus on the correct data interpretation and the consequences for in vivo-in vitro correlation (IVIVC) problems. Some issues regarding the development of inhalation products (including generics) are also briefly highlighted. Finally, possible strategies of powder particle functionalization to obtain the required bioavailability are outlined on the basis of knowledge on the physicochemical interactions of inhaled particles with the lung fluids.

Keywords: inhalation, lung deposition, DPI, flow dynamics, mucus, pulmonary surfactant

1. Introduction

The idea of using aerosol particles as drug carriers comes from the ancient times when the inhalation of smoke and fumes from burned plants appeared to induce favorable health effects (Sanders M., 2011; Stein S.W. and Thiel C.G., 2017). In modern times, it has been realized that the atomization of medicinal liquids to very small droplets helps to transfer them to the respiratory system beyond the upper airways (mouth and throat). Such a possibility of drug targeting to specific lung regions provided the opportunity to treat pulmonary diseases locally with low overall drug mass and minimized side effects. It also became clear that aerosolized drugs need not necessarily be a liquid, but can also be in the form of fine particles of solids.

The technical possibility of using dry powders as vehicles of drugs carried into the respiratory system is the topic of this paper. This apparently simple idea of drug delivery covers non-trivial challenges and many physical limitations which need to be overcome if a reproducible drug dose is to be delivered from a portable and inexpensive inhaling device.

This analysis starts with the overall characteristics of physical phenomena related to aerosol inhalation and particle deposition in the lungs. Next, the major challenges of aerosol formation in inhaling devices are discussed with the main focus on the proper design of dry powder inhalers (DPIs) and on the properties of powders as precursors of inhalable aerosols. The dynamic aspects of the above-mentioned problems are highlighted because very often they are ignored in the analysis of particle deposition in the lungs and powder inhaler performance. Some essential information on aerosol evaluation using the compendial (pharmacopeial) methods is also presented, indicating their limitations which can lead to the inaccurate interpretation of data. Finally, some facts regarding physical aspects of interactions between deposited particles and the lung surface are discussed to show the relationships between particle properties and drug bioavailability. All presented data make it possible to highlight potential new opportunities of inhalation therapy with the use of powder particles.

[†] Received 7 June 2017; Accepted 9 August 2017

[1] Waryńskiego 1, 00-645 Warsaw, Poland
E-mail: tomasz.sosnowski@pw.edu.pl
TEL: +48-22-234-6278 FAX: +48-22-825-1440

Table 1 Main benefits and drawbacks of drug delivery by aerosol inhalation.

Benefits	Drawbacks/limitations
1. Drug delivered directly to the expected site of action in the respiratory system: the dose can be minimized, low side effects	1. Uncertainty of dose delivered locally to the target area
2. Low enzymatic drug deactivation in the lungs: the dose can be minimized	2. Technical challenges related to drug formulation, dosing and aerosolization
3. Non-invasive, pain-free and easy-to-use method of drug delivery	3. Patient-dependent efficiency of drug delivery

2. Basic concepts and the physics of inhalation drug delivery

2.1 Drug inhalation as a unique method of pharmacotherapy

Drug delivery by the inhalation of aerosolized medicines is a therapeutic method which has several advantages but also some essential drawbacks (**Table 1**).

The main benefit is related to minimization of the dose which needs to be introduced to the organism to produce the expected concentration in the target site (i.e. on the surface of the respiratory system). For inhalation devices (inhalers), it is often enough to deliver only several micrograms of the active pharmaceutical ingredient (API) to result in the local lung dose comparable to almost one hundred milligrams delivered by injection or tablets (Alangari A.A., 2014). With a natural and painless application mode, inhalation therefore presents a safe and convenient method of pharmacotherapy. On the other hand, unlike other drug delivery systems (tablets, pills, injections), the inhalation of aerosolized medicine does not guarantee precise dosing. The reason is that none of the sequential processes of aerosol generation, aerosol evacuation from the inhaler and regional deposition in the respiratory system is 100 % efficient, which means that only a fraction of the drug initially loaded to the inhaler can be transferred to the target area, **Fig. 1**. Moreover, this number is noticeably variable since it depends both on the performance of the inhaling device and on the patient's individual capabilities to use it correctly, **Fig. 2**. As stated earlier, there is a long list of technical problems which need to be solved to achieve a reliable and reproducible drug delivery system based on powder inhalation, and they will be addressed herein.

It is obvious that not all aerosol particles can be used as effective drug carriers. To play that role, particles must be inhalable, i.e. small enough to be drawn with air into the mouth or nose. Moreover, they must be capable of penetrating beyond the naso-oro-pharynx and the upper bronchial tree so they can reach the lower respiratory system and settle there.

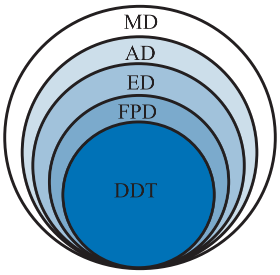

Fig. 1 General relationship between the nominal (metered) dose–MD, aerosolized dose–AD, emitted dose–ED, fine particles dose–FPD and dose deposited at the target–DDT.

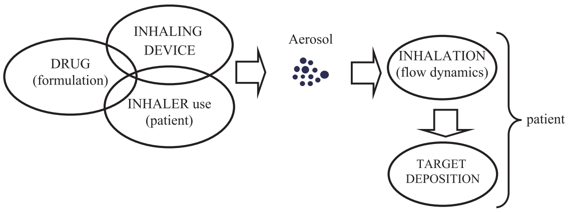

Fig. 2 Schematic path from the drug to target deposition.

Interestingly, the preferred deposition region may be different for various types of inhaled drug, since the occurrence and surface density of cellular receptors for drug binding/stimulation differs along the walls of the bronchial and pulmonary airways (Howarth P.H., 2001; Barnes P.J., 2004; Usmani O.S. et al., 2005; Pirożyński M. and Sosnowski T.R., 2016). For instance, muscarinic receptors (e.g. M3) are located mainly in the central airways, so the relevant drugs (bronchodilating cholinergic antagonists) should be preferentially delivered to these lung regions. The distribution of the receptors for beta2-mimetics requires the deposition of such drugs both in the central and distal respiratory tract, although the alveolar region can be omitted since no bronchodilating effect is expected there. Glucocorticoid receptors (GRs) are distributed all over the lower respiratory system, but steroids should not penetrate in large amounts into the lung periphery since we want to avoid their undesired absorption into the circulation from alveoli. It is therefore clear that different aerosol drugs can be formulated differently to obtain the most desired therapeutic effects.

2.2 Physics of aerosol particle flow and deposition in the respiratory tract

The whole respiratory tract acts as a filter for inhaled aerosols where particle flow, penetration and deposition in the respiratory system are governed by general physical

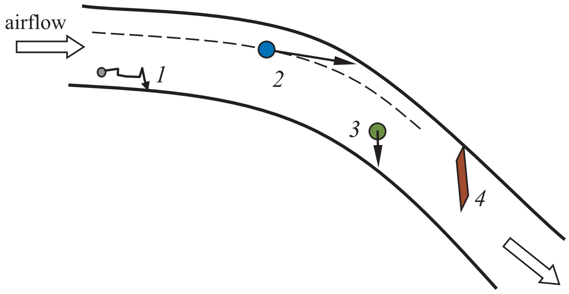

Fig. 3 Basic deposition mechanism of airborne particles in the respiratory airways: 1 - diffusion, 2 - inertial impaction, 3 - sedimentation, 4 - interception.

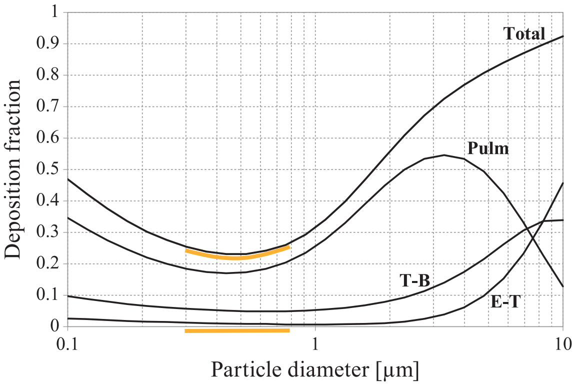

Fig. 4 Regional and total particle deposition in the respiratory system as a function of particle size—calculations based on the ICRP model and Multi-Path Particle Dosimetry software (MPPD, 2015) for deep and slow oral inhalation (TV = 1500 ml, breathing cycle time = 12 s). Lung regions: Pulm = pulmonary (alveolar), T-B = tracheobronchial, E-T = extra-thoracic (airways of head and neck). The particle size range with the lowest deposition is highlighted.

laws (Heyder J. and Svartengren M.U., 2002; Darquenne C., 2012; Tsuda A. et al., 2013; Cheng Y.S, 2014). Obviously, particle 'filtration' in the respiratory system is sequential, i.e. only those particles which have avoided elimination in the previous generations of the bronchial tree can penetrate and deposit in the next ones. This factor must be considered if we try to target any specific region with inhaled aerosol medicine (Zanen P., 2003; Kleinstreuer C. et al., 2008). **Fig. 3** shows all particle deposition mechanisms which are believed to predominate in respiratory airways.

Particles with a high momentum (mass × velocity) hit the walls of the air ducts due to inertial impaction, mostly when the airflow rapidly turns. It takes place, e.g. in the mouth (hard and soft palate), throat and at bifurcations of large bronchi (Moskal A. and Gradoń L., 2002; Sosnowski T.R. et al., 2007). Particles which are able to penetrate these regions but have a relatively high mass can still fall gravitationally at an appreciable rate. Therefore, the chance of their penetration beyond the small bronchi, where aerosol residence time is extended due to a decrease of the average flow velocity, is minute. Moreover, the diameter of the airways in this region is reduced so the gravitational settling becomes effective. Submicron particles, which have a low inertia and also a negligible sedimentation rate, penetrate to the lung periphery to a greater extent. They can reach the airway walls of that region by Brownian diffusion.

Presented facts allow the development of quantitative methods for predicting particle deposition in various lung regions (Longest P.W. and Holbrook L.T., 2012; Tu J. et al., 2013). Different approaches to that problem are presented in the next section.

2.3 Quantitative models of deposition of inhaled particles

The deposition of inhaled drug particles can be quantitatively predicted by adaptation of the models which have been originally elaborated in the field of inhalation toxicology. Such semi-empirical models are often based on the experimental data fitted by relatively simple mathematical formulae which can estimate the deposition of particles with different sizes and for variable breathing regimes. Such models (e.g. ICRP (Annals of the ICRP, 1994)) calculate only the regional deposition efficiencies (in the upper airways, tracheo-bronchial region, small bronchi or alveolar zone) which, by summing up, give also the total deposition in the whole respiratory system (**Fig. 4**).

Regional deposition can be derived also from other models which consider more precisely the predominating deposition mechanisms in various regions of the respiratory system. For instance, Finlay W.H. and Martin A.R. (2008) proposed mathematical formulae for the oropharyngeal region and the lower respiratory tract deposition, taking into account the residence time and the average local particle aerodynamics. In this model, the average Reynolds (*Re*) and Stokes (*Stk*) numbers are used to generalize air and particle flow in the respiratory system.

A more detailed approach to the quantitative description of particle deposition is based on particle tracking during their flight through the respiratory airways. Reliable quantitative data regarding bronchial tree geometry (airway lengths, diameters and branching angles) are needed to predict the average airflow rates and particle behavior in each generation. Symmetrical or asymmetrical lung geometry can be used (Yeh H.C. and Schum G.M., 1980) where the first leads to a single path while the second leads to multipath trajectories of aerosol particle transport (Asgharian B. et al., 2001). In the multipath transport, a random choice of geometry is assumed resulting in a so-called stochastic lung deposition model (Koblinger L. and Hofmann W., 1990).

In these models, the fractional deposition in each generation of the bronchial tree can be calculated which gives more detailed information on drug distribution in the lungs.

It may be mentioned that some of the above-discussed models are accessible in the user-friendly calculators which are freely available on the Internet (MPPD, 2015; ARLA, 2008).

The most precise predictions of local particle dynamics and deposition can be obtained from detailed calculations of the particle trajectory within the numerically reconstructed geometry of the selected fragments of the respiratory system. It can be conveniently done applying computational fluid dynamics (CFD) methodology (Tu J. et al., 2013). Commercial packages help to predict the actual three-dimensional airflow field in the defined airway geometry by numerically solving the Navier-Stokes equation within the domain decomposed into finite volume elements. Even with the use of a commercial computational package, the task itself is not trivial and requires correct construction and optimized resolution of the numerical mesh followed by the application of a suitable solver with appropriate boundary conditions. Tracking of each particle in the airflow field is done by the Lagrangian approach, i.e. solving the mass balance of a single particle. The most general description combines both deterministic and stochastic forces acting on particles, the latter being associated with Brownian diffusion, i.e. particle motion caused by random collisions with air molecules. The Langevin equation which describes particle acceleration under such conditions takes the form (Moskal A., 2011):

$$\frac{\mathrm{d}u_\mathrm{p}}{\mathrm{d}t} = -\frac{18\mu}{\rho_\mathrm{p} {d_\mathrm{p}}^2}\left(u_\mathrm{p} - u\right) + \frac{6}{\pi\rho_\mathrm{p} {d_\mathrm{p}}^3} F_\mathrm{ext} + \frac{6}{\pi\rho_\mathrm{p} {d_\mathrm{p}}^3} F_\mathrm{B} \tag{1}$$

where u_p and u denote the velocity of particle and air, respectively, d_p – particle diameter, ρ_p – particle density, μ – air viscosity, F_ext – external forces affecting the particle trajectory (gravity, electrostatic or magnetic interactions, etc.) and F_B – the Brownian force which plays a role mainly for submicrometer-size particles. For a spherical aerosol particle suspended in the air, the Brownian force is given by:

$$F_\mathrm{B} = m_\mathrm{p} \alpha_\mathrm{B} \boldsymbol{Z} \tag{2}$$

where α_B is the characteristic magnitude of acceleration due to thermal excitation, and can be expressed as:

$$\alpha_\mathrm{B} = \sqrt{\frac{2\pi S_0}{\Delta t}} \tag{3}$$

S_0 is a spectral intensity of a white noise which can be conveniently used to model the stochastic Brownian effects:

$$S_0 = \frac{216\mu_\mathrm{f} k_\mathrm{B} T}{\pi^2 d_\mathrm{p}^5 \rho_\mathrm{p}^2 C_\mathrm{s}} \tag{4}$$

where T is the absolute temperature, k_B is the Boltzmann constant, and C_s the Cunningham slip correction factor. $\boldsymbol{Z}$ in eq. (2) is the dimensionless vector with random direction and Δt denotes the time step of numerical integration of the trajectory equation. It can be noted that the Brownian force acts on aerosol particles all the time but its direction and magnitude are randomly changed (through the random updating of value of $\boldsymbol{Z}$) at the end of every time step Δt. The presented method of numerical computations can be used to analyse particle motion in a human breathing system also at realistic non-steady-state flow conditions (Moskal A. and Gradoń L., 2002). Numerical solutions allow finding the trajectory of any particle of the defined size and properties, and eventually finding the place of particle deposition on the airway wall. If the computations are repeated many times for thousands of particles with various sizes, the results of particle deposition probability (i.e. deposition efficiency) in the analysed region is obtained as a function of the particle size.

As in any type of particle separation process (e.g. conventional air filtration), a certain particle size range exists where none of the previously mentioned mechanisms is sufficiently effective. Such particles (typically 0.3–0.8 μm) can be exhaled without significant previous deposition in the respiratory system. In the example of the relationships of regional deposition efficiency vs. particle size shown in **Fig. 4**, the minimum of total deposition in the size range referred to above is clearly seen. Interestingly, some systems dedicated to aerosol delivery to the lungs may take advantage of a non-optimal deposition. For instance, e-cigarettes are designed in a way which allow a visible mist (typically composed of fine droplets of glycerine and propylene glycol) to be exhaled since this mimics the use of classic (i.e. tobacco) products. All droplets released from e-cigarettes are smaller than 2 μm (mass median diameter ~0.4 μm), for which the predicted deposition in the respiratory system is less than 50 %, independent of the breathing maneuver (Sosnowski T.R. and Kramek-Romanowska K., 2016).

2.4 Aerosol dynamics and other factors influencing particle deposition during inhalation

It is commonly agreed that the aerodynamic particle diameter d_a is the most suitable measure of the particle ability to penetrate and deposit within the respiratory system. The aerodynamic diameter is defined as:

$$d_\mathrm{a} = d_\mathrm{p}\left(\frac{1}{\chi}\frac{\rho_\mathrm{p}}{\rho_\mathrm{w}}\right)^{0.5} \tag{5}$$

where ρ_w denotes density of water, and χ the dynamic shape factor of the particle. Only particles with $d_\mathrm{a} < 5$ μm are expected to be inhaled deeply to the bronchial tree where they eventually settle. Aerosol particle size distribution based on the aerodynamic diameter is typically assessed by standard compendial methodology using multi-stage (cascade) impaction separators: NGI (Next Generation Impactor), Andersen, Marple-Miller or impinging jet impactors (USP, 2008; European Pharmacopoeia, 2013). This type of determination of the aerosol particle size distribution is an indispensable step in the pharmaceutical development and validation of orally inhaled medical products (CHMP, 2009), and some details of such characterizations of aerosol drug particles will be discussed in section 3.3.

The aerodynamic diameter is a disputable criterion of particle behavior in the lungs if the particles are noncompact in shape, e.g. plate-like or needle-like, when interception can become the predominant deposition mechanism (**Fig. 3**). Moreover, the aerodynamic size properly describes the particle settling time under gravity or inertial forces, assuming that a particle is carried with air at constant velocity. In reality, it is obviously not true. Inhalation is a dynamic (time-dependent) process in which a certain volume of air is pumped through the airways at variable acceleration and deceleration. Therefore, the aerodynamic size has a different influence on particle behavior depending on the time-instant during inhalation. This complicates analysis of the processes of aerosol penetration and deposition in the respiratory system. In many theoretical and experimental analyses of aerosol inhalation and deposition, the constant flow rate is assumed (such as the mean flow of the inspiration, e.g. Matida E.Z. et al., 2004; Zhang Z. et al., 2005; Farkas A. and Balazhazy I., 2008; Ma B. and Lutchen K.R., 2009), which is an inaccurate simplification. Some studies show that particles in the realistic non-steady inhalation flow show dissimilar dynamics as compared to the constant flow conditions, and this leads to a different spatial distribution of particle deposition (Moskal A. and Gradoń L., 2002; Sosnowski T.R. et al., 2007). The influence of flow dynamics on particle deposition can be demonstrated by a simple example. **Fig. 5** schematically shows the dynamics of the inhalation phase and the relationship between the temporal volumetric flow rate $Q(t)$ and two characteristic values—the mean flow:

$$\hat{Q} = \frac{1}{t_{\text{inh}}} \int_0^{t_{\text{inh}}} Q(t)\,\mathrm{d}t \tag{6}$$

and the maximum flow value, $Q_{\max}$ = PIFR (peak inspiratory flow rate). It is important to note that the flow value equal to $\hat{Q}$ occurs in reality only at two instants of time (t_1 and t_2) during the whole inspiration.

The temporal dimensionless Stokes number, being an indicator of inertial deposition (impaction), is defined as:

$$Stk = \frac{\rho_{\text{p}} u d_{\text{p}}^{\,2}}{\mu L_0} \tag{7}$$

where—in addition to already defined variables—L_0 denotes the characteristic local dimension of the airways. It can be easily seen that the same local value of the Stokes number is obtained if:

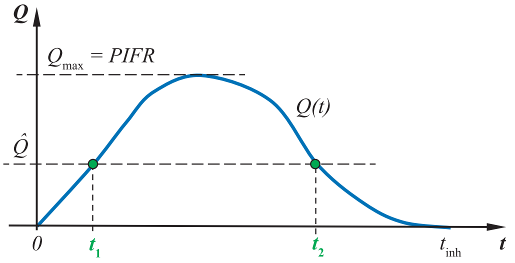

Fig. 5 Relationships between real flow dynamics $Q(t)$, average flow rate $\hat{Q}$ and the peak inspiratory flow rate (PIFR).

$$u d_{\text{p}}^{\,2} = const. \tag{8}$$

Consequently, for a variable airflow rate during inhalation, a particle with d_{p} = 10 µm which moves at a velocity equal to the air velocity u_1 will be locally (L_0 = const) deposited by impaction with the similar efficiency as a 5-µm particle at the velocity $4u_1$. The analogous analyses can be done also for other deposition mechanisms and they will show that at variable airflow, one cannot unambiguously link the regional deposition efficiency with the aerodynamic (or geometric) particle size.

The complexity of the description of dynamic behavior of inhaled powder particles in the lungs is additionally caused by other issues:

- in general, particles of medical aerosols are polydisperse;
- quite often powder particles are hygroscopic, so their actual size in the respiratory system will increase and their density will also be changed (Schum G.M. and Phalen R.F., 1997; Asgharian B., 2004; Winkler-Heil R. et al., 2014).
- particles at high concentrations may coagulate or move collectively in a so-called ‘cloud motion’ (Broday D.M. and Robinson R., 2003);
- bronchi and bronchioles are short-tubes, so inlet effects have an influence on the flow pattern—e.g. the secondary flows are formed (Zhang Z. and Kleinstreuer C., 2002; Fresconi F.E. and Prasad A.K., 2007);
- due to flow periodicity, the analysis based on the local flow regime (laminar/turbulent) according to the Reynolds number as a basic criterion is inadequate;
- in DPIs, particles can appear in different phases of inhalation which has an influence on their transport in the respiratory system (see section 3.2).

Flow dynamics influences not only the behavior of particles in the respiratory system but also the performance of inhaling devices (aerosol formation and emission). This problem will be discussed in section 3.

3. Technical problems of effective powder drug delivery by inhalation

Several books, book chapters and review papers are focused on a variety of technical solutions required for drug delivery of aerosolized powders via inhalation (e.g. Dunbar C.A. et al., 1998; Zeng X.M. et al., 2000; Borgström L. et al., 2002; Vanbever R., 2003; Newman S. and Peart J., 2009; Hoppentocht M. et al., 2014; Berkenfeld K. et al., 2015; Carvalho S.R. et al., 2015; de Boer A.H. et al., 2017). Here we will highlight the critical issues. Assuming that aerosol particles within a certain size-range are required for effective lung treatment by inhalation, the following technical problems must be identified:

- raw powders with the required particle size and surface properties must be prepared. Fine aerosol particles cannot be obtained from a powder composed of large grains;
- in addition, the surface properties of powders must assure that particles are not too cohesive so that their flow, fluidization and de-agglomeration are easily obtainable in a given inhaling device (Zeng X.M. et al., 2000);
- such powders must allow the formation of reproducible inhalable API doses in the range of several to some hundreds of micrograms. This frequently requires blending the API grains with additional powder. Anhydrous lactose or lactose monohydrate particles are typically used as the excipient, and it must have an optimized particle size and surface properties to ensure flowability and the required de-agglomeration of the blend upon aerosolization (Pilcer G. et al., 2012);
- optionally, the suitable API powder can be prepared without the excipient (Healy A.M. et al., 2014). In that case, the powder should possess special properties which can be obtained by particle engineering methods (Kaialy W. and Nokhodchi A., 2015)—see section 3.1;
- powder properties must be stable during the typical shelf lifetime of pharmaceutical products (typically 3 years);
- the medical powder must be packed in capsules or blisters with suitable properties to guarantee their efficient emptying during inhalation (Martinelli F. et al., 2015). Another choice is the use of reservoir-type inhaling devices, when the powder dose is metered immediately prior to the inhalation (Islam N. and Gladki E., 2008);
- the inhaling device itself must be optimized in a way to ensure reproducible powder metering and aerosolization (emitted dose: ED, fine particle dose: FPD). At the same time, the device should be easy to use, ergonomic, mechanically resistant and inexpensive in production. Certain conditions must be met regarding the internal aerodynamic resistance of the inhaler (the airflow through the device must match the inhaling force of the patients) (Hoppentocht M. et al., 2014)—see section 3.2.

3.1 Essential properties of powders used in drug delivery by inhalation

To be effective vehicles for inhaled drugs, powder particles must be de-agglomerated in the airflow to form micrometer-size particles as schematically shown in **Fig. 6** The outcome of this process depends on inhaler design, applied flow rate and powder properties. This is why the pharmaceutical powder has to be properly prepared before it can be used as a drug carrier. The main cohesive interactions which act against powder redispersion are caused by van der Waals forces, electrostatic and capillary forces, by hydrogen bonds and mechanical interlocking due to surface roughness (Zeng X.M. et al., 2000; Ramachandran V. et al., 2015). These interactions depend not only on the particle properties and their preparation method, but also on the ambient conditions such as air humidity.

Strategies which are used to prepare powder particles with the properties that facilitate their de-agglomeration include: (i) controlling the surface smoothness of the particles (Chew N.Y.K. and Chan H.-K., 2001; Geller D.E. et al., 2011), (ii) increasing interparticle distance, e.g. by adding nanoparticles (Begat P. et al., 2005), (iii) changing the properties of the particle surface, e.g. by coating with, e.g. leucine, magnesium stearate or surfactants as force-control agents (Begat P. et al., 2009; Sosnowski T.R. and Gradoń L., 2010). It can be also be beneficial to use micrometer-size nanostructured (partly porous) particles instead of compact ones with the same size (Tsapis N. et al., 2002; Jabłczyńska K. et al., 2015). All these strategies can be used both for drugs prepared as interactive mixtures (API-excipient) and for excipient-free formulations. Inhalable particles can also be developed with API embedded in a polymer matrix with PLGA (poly(lactic-co-glycolide) acid) being the most common matrix builder (Liang Z. et al., 2014). This drug delivery system has the additional advantage of sustained drug release in the target area. We should also mention a novel concept of inhalation powders based on the application of solid lipid nanoparticles (SLN) and nanostructured lipid carriers (NLC) forming a dry lipid matrix which can be loaded with the API and transferred to the lungs from DPIs without additional excipients (Weber S. et al., 2014; Li Y.Z. et al., 2010).

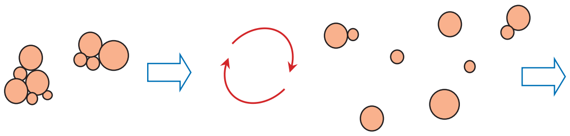

Fig. 6 De-agglomeration of powder drug in the airflow.

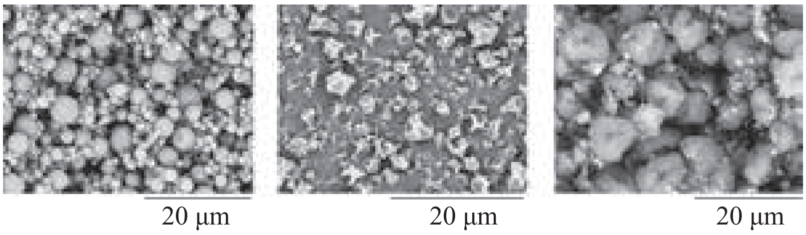

Fig. 7 Examples of different shape and structure of powder particles obtained by the controlled spray-drying of various precursors (unpublished SEM images from author's laboratory).

Spray drying, spray-freeze drying and enhanced crystallization/precipitation (ultrasonic-assisted or utilizing the supercritical fluid technology) are applied to obtain engineered powder particles. We will skip the detailed characteristics of these methods as their thorough description can be found elsewhere (Gradoń L. and Sosnowski T.R., 2014; Kaialy W. and Nokhodchi A., 2015). Due to the technological feasibility and easy scale-up, spray drying is probably the most convenient method of producing inhalable powders. It also allows control of the particle structure, size and aerosolization properties (Vehring R., 2008; Weers J.G. and Miller D.P., 2015). Correct selection of the composition and concentration of the precursor (i.e. liquid solution or suspension), as well as of the drying parameters are decisive in obtaining powders with the desired particle size and shape (Nandiyanto A.B.D. and Okuyama K., 2011; Kramek-Romanowska K. et al., 2011). **Fig. 7** shows some examples of different powder structures which can be obtained by tuning the parameters of the spray-drying process into a conventional laboratory-scale device with pneumatic atomization of liquid precursors.

3.2 Inhaler design and performance

In all powder inhaler devices, aerodynamic stresses are used to fluidize the powder and de-agglomerate particle clusters to maximize the number of individual fine particles. The majority of DPIs currently available in the market belong to so-called 'passive' devices (Islam N. and Gladki E., 2008), where the aerosol is formed solely due to powder interaction with the flow generated by the patient's inhalation. In all such devices it is necessary to maximize the transfer of airflow energy to the powder, possibly without useless dissipation. This can be effectively done by the creation—in a logical way—of local turbulence or other effects such as flow focusing or fluctuations (Gac J. et al., 2008; Sosnowski T.R. et al., 2014). However, flow arrangements of this type always increase the aerodynamic resistance (the pressure drop) in the inhaler, so the final design of a DPI must be optimized. It is important to note that erroneous concepts of aerosolization chambers can result in completely inefficient powder redispersion. This obvious rule is shown schematically in **Fig. 8** by presenting two hypothetical inhaler chambers of identical design and aerodynamic resistance, but with totally different performance regarding the aerosol emission.

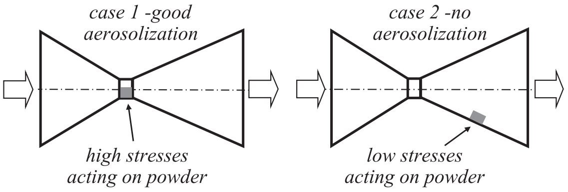

Fig. 8 Comparison of two hypothetical aerosolization systems with the same aerodynamic resistance but disparate dispersion efficiencies due to a different location of the powder layer (grey rectangle).

Aerodynamic resistance of the inhaler is a very important issue which needs to be well understood since it often leads to ambiguities. The intrinsic inhaler resistance is defined by the equation (Clark A.R. and Hollingworth A.M., 1993):

$$R_{\mathrm{D}} = \frac{\sqrt{\Delta P}}{Q} \tag{9}$$

where ΔP denotes the pressure drop (typically in hPa) and Q the volumetric airflow rate (typically in liters per minute, L/min).

Eq. (9) can be derived from the well-known relationship describing the local pressure drop:

$$\Delta P = \gamma \frac{\rho u^2}{2} \tag{10}$$

where γ denotes the local resistance coefficient, which can be assumed independent of the airflow rate in the range relevant to inhalation (30–120 L/min). This equation can be rewritten as:

$$\Delta P = \frac{\gamma\rho}{2}\left(\frac{Q}{A}\right)^2 \tag{11}$$

where A denotes the cross-sectional area for the airflow. After substituting:

$$R_D{}^2 = \frac{\gamma\rho}{2A^2} \tag{12}$$

Eq. (9) is obtained directly.

Passive DPIs have different degrees of aerodynamic resistance, typically in the range of 0.05–0.2 $\text{hPa}^{0.5}\text{min/L}$ (or: 30–120 $\text{Pa}^{0.5}\text{s/L}$). At the given inspiratory effort, low-resistant (L-R) DPIs allow high flow rates to be obtained at which good aerosolization is achieved. In the case of high-resistant (H-R) DPIs, similar efforts will produce lower flow rates, however, the flow restriction obtained in such inhalers should cause strong aerodynamic effects and a similar powder deaggreation as in the low-resistant devices at higher flows. This is why DPIs need to be tested at the fixed pressure drop (the standard value is 4 kPa (USP, 2008; European Pharmacopoeia, 2013) not at a fixed flow rate.

A frequent mistake is the comparison of different DPIs based on the criterion of the optimum volumetric flow rate (Q_{opt} needed to get aerosol with maximized FPD). It is often believed that a low Q_{opt} is always equivalent to a better performance of the DPI. But a low Q_{opt} actually means a high resistance of the inhaler, which may limit correct operation by all groups of patients due to the demands of high inspiratory efforts. It is easier to obtain high flow rates in L-R DPIs, so even if they work suboptimally at $Q < Q_{\text{opt}}$, they can be used with some success by patients who may be not able to use H-R DPIs. The problem of L-R inhalers is that they are typically flow-dependent, i.e. the mass and particle size distribution of the aerosol they release are significantly improved when flow increases (Weuthen T. et al., 2002; Azouz W. et al., 2015). Powder de-agglomeration is better at high airflow rates but at the same time the aerosol velocity at the inlet to the mouth becomes higher, which increases undesired drug deposition in the oro-pharynx. For H-R DPIs, the airflow through the device is limited, and dependence of their performance on the flow rate is lower. Concluding this analysis, it may be stated that there should be an optimum of flow resistance in DPIs. The flow must be restricted to produce the high aerodynamic stresses required for good aerosolization of the powder, however, if the overall resistance of the device is too high, it can exclude a large group of patients from proper use of such device. Elimination of the problem of DPIs flow-dependence is achieved in 'active' DPIs which utilize, for instance, the compressed gas to facilitate powder de-agglomeration to fine particles. More than a decade ago, Exubera® was developed as an active DPI for insulin delivery, however—due to various reasons—it was withdrawn from the market in 2007 (Heinemann L., 2008). Another active DPI—Spiromax®—has emerged recently for the delivery of drugs for asthma and COPD patients (Canonica G.W. et al., 2015).

Similarly to particle deposition in the lungs, drug inhalation from passive DPIs is a dynamic process. The aerosol is formed and released from the device during the given (rather short) period of the inhalation. Let us recall the flow curve already shown in **Fig. 5** to analyse this process. Two different situations are depicted in **Fig. 9**. Assuming that the two DPIs denoted as *1* and *2* have a similar aerodynamic resistance but a different principle of powder release, we can see that the aerosol is emitted from inhaler *1* during time period $t_1 \div t_1'$, but from inhaler *2* during time period $t_2 \div t_2'$. **Fig. 9a** shows the corresponding flow rate, i.e. inhalation curve, while **Fig. 9b** shows the corresponding volume of air aspirated to the lungs.

Let us note that aerosol is emitted from inhaler *1* during a short period which is finished at t_1', i.e. before the maximum flow rate Q_{max} is achieved. In contrast, inhaler *2* is activated later (at t_2) by the flow rate close to Q_{max} and the release time is longer, so the aerosol is introduced to the air stream until t_2', which is not far from the end of inhalation, t_{inh}. It can be expected that the quality (size distribution) of aerosol produced at higher flow rates, i.e. in case *2,* will be more favorable than in case *1.*

The graph of inhaled volume (**Fig. 9b**) shows that when the aerosol is totally emitted from inhaler *1*, the remaining volume of air to be inhaled is still large (V_{r1}), which means that the released particles can be carried even to the lung periphery. In contrast, after the entire dose of aerosol is released from inhaler *2* (at t_2'), a small volume of air V_{r2} remained for inhalation, so probably these particles can penetrate only the very first generations of the bronchial tree before the exhalation will begin.

The presented example shows another, often overlooked, factor which should be considered for the rational

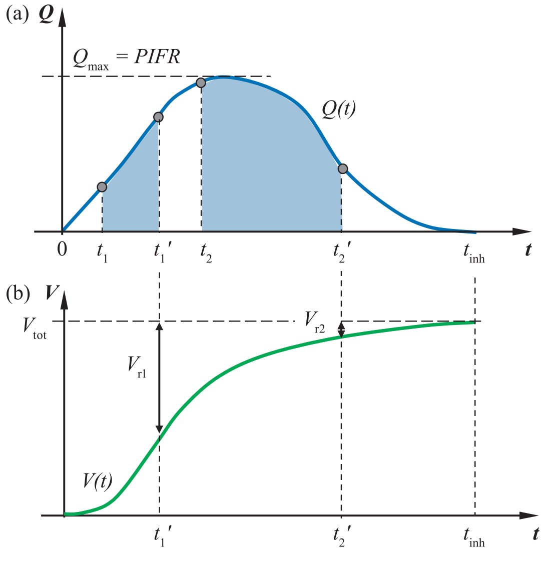

Fig. 9 (a) Inhalation curve *Q(t)* and periods of aerosol release (gray fields) for two DPIs; (b) the corresponding inhaled volume curve $V(t) = \int Q(t)\text{d}t$ and indicated remaining volumes of air inhaled after complete release of aerosol from both DPIs (V_{r1} or V_{r2}).

design of inhalation systems based on powder redispersion.

3.3 Understanding the compendial methods of aerosol characterization

Aerosol particles of medicines intended for inhalation must be evaluated by specialized methods to confirm that they have the proper size characteristics and reproducibility (USP, 2008; European Pharmacopoeia, 2013). Use of impactors instead of other measuring techniques is necessary because the majority of formulations contain particles with different chemical composition, e.g. in DPIs based on API-lactose blends or in combined products (two or more drugs delivered in one inhalation). In such cases, optical methods which are typically used for aerosol assessment (e.g. time-of-flight or light scattering/light diffraction) cannot be used because they do not distinguish particles that carry different chemicals. Since only the mass of API is of interest from the therapeutic perspective, all other particles should be ignored in such analyses. Cascade impactors can sort particles into several (typically 5–8) size classes based on their inertial deposition which is caused by flow acceleration at the consecutive separation stages. In the testing of DPIs, the aerosolized drug is drawn to the impactor via the inlet and the additional vessel (preseparator) capable of capturing large grains of the excipient which usually also contains some API is attached. Impactor inlet and preseparator are believed to mimic the upper airways (mouth and throat), however, the particle separation efficiency of these impactor elements is not strictly defined. Material collected at each stage of the impactor is then quantified by sensitive chemical assays – typically high-performance liquid chromatography (HPLC) – against the pharmacopeial standard of the API under test. Chromatographic analysis ensures that the API concentration is evaluated selectively and assigned to the given size class of particles captured at each separation stage. Thanks to this technique, the size distribution based on drug mass is obtained, which allows finding the most important indicators of the quality of medical aerosol: fine particle dose (FPD), fine particle fraction (FPF) and mass median aerodynamic diameter (MMAD). Due to their principle of operation, all impactors classify particles based on their aerodynamic size d_{a} defined by equation (5). Assuming a quasi-spherical particle shape and density in the range of 800–1200 kg/m^3, the aerodynamic particle diameter is almost the same (± 10 %) as the geometric diameter, d_{p}. However, these two diameters can be very different in the case of, e.g. porous particles with an effective density in the range of hundreds of kg/m^3. In such cases, large particles (larger than 10 μm) may still be effective as drug carriers for inhalation since their aerodynamic behavior and inertial deposition is equivalent to smaller particles with a typical density.

There are two major drawbacks to impactor particle size analysis:

– the size resolution is limited to only 8 classes which are variable if the flow imposed during different assays is not the same;
– the measurements are time-consuming, expensive and sensitive to human factors. Errors can easily be made due to an extensive number of manual operations (assembly/disassembly of the impactor, pipetting, labware handling, impactor cleaning, etc.)

Until the Next Generation Impactor (NGI) was developed, inhalers could be tested only at several standard airflow rates (e.g. 28.3, 60 and 90 L/min in the Andresen cascade impactor) due to a lack of certified calibration for other flows. The NGI allows characterization of the aerosol particle size at any flow rate in the range of 30–100 L/min, but also at lower values (down to 15 L/min). The aerodynamic cut-off size, d_{ci}, at each stage i depends on the applied flow rate and for 30–100 L/min, they can be calculated from the equation:

$$d_{\mathrm{ci}\,at\,Q} = d_{\mathrm{ci}\,at\,60\mathrm{LPM}} \left(\frac{Q}{60} \right)^{xi} \qquad (13)$$

where xi is the unique exponent for the given separation stage (MSP Corporation, 2008). A slightly modified correlation is valid for flow rates in the range 15–30 L/min. Cut-off sizes for selected airflow rates are listed in **Table 2**.

As seen from **Table 2**, the NGI cannot determine the size of particles larger than those captured at stage no. 1, and this maximum diameter depends on the flow rate applied during DPI testing. According to the standard, the mass median aerodynamic diameter (MMAD), which is often considered the important parameter in comparing different inhalation products, is calculated only taking into account the drug particles within the range of cut-off sizes specified for the numbered stages, thus ignoring the API mass collected inside the inlet port and preseparator. This leads to a risk of misinterpretation of the experimen-

Table 2 Nominal cut-off sizes [μm] for NGI impactor at selected airflow rates [L/min].

Stage no.	15 L/min	30 L/min	60 L/min	90 L/min
1	14.1	11.7	8.06	6.12
2	8.61	6.40	4.46	3.42
3	5.39	3.99	2.82	2.18
4	3.30	2.30	1.66	1.31
5	2.08	1.36	0.94	0.72
6	1.36	0.83	0.55	0.40
7	0.98	0.54	0.34	0.24

tal data. Since the range of particle sizes used for calculation of the MMAD depends on the applied flow (**Table 2**), it will be incorrect to compare the MMAD obtained for DPIs characterized by different resistance, R_D. According to the standard, they must be compared at the same pressure drop (4 kPa), hence at different flow rates. As particles eliminated before stage no. 1 are not considered in the mass balance, then it is possible to achieve a low MMAD (apparently a good value) even if a large amount of aerosol drug is contained in big particles deposited in the impactor inlet port and preseparator, as shown in **Fig. 10**. Therefore, the MMAD should be considered rather as a quality parameter which allows verification if different batches of a given inhalation product (i.e. with a given DPI) deliver—at the fixed airflow rate—the aerosol with a similar particle size distribution. According to the presented discussion, it is incorrect to use MMAD as a criterion of comparison of different DPIs and drugs.

The troublesome aerosol particle sizing by cascade impactors can sometimes be replaced by fast and accurate optical on-line measuring techniques such as laser diffraction, however, only under certain conditions. These methods can be used, e.g. in carrier-free DPIs which aerosolize only a single API. It is also reasonable to apply optical methods for pMDIs (pressurized metered dose inhalers), SMIs (soft mist inhalers) and nebulizers, assuming that all particles/droplets have a statistically identical composition. In such cases, they contain the API mass which is proportional to the cube of the particle diameter. For aqueous droplets $\rho_p \approx \rho_w$, according to eq. (5), we will directly obtain the aerodynamic diameter. For other materials, the geometric diameters d_p can be easily recalculated to d_a if the material density is known. Although optical methods are not compendial, for some inhalers (e.g. nebulizers), they have been demonstrated to be equivalent to pharmacopeial impactors (Kwong W.T.J et al., 2000; Ziegler J. and Wachtel H., 2005; Mao L. et al., 2010).

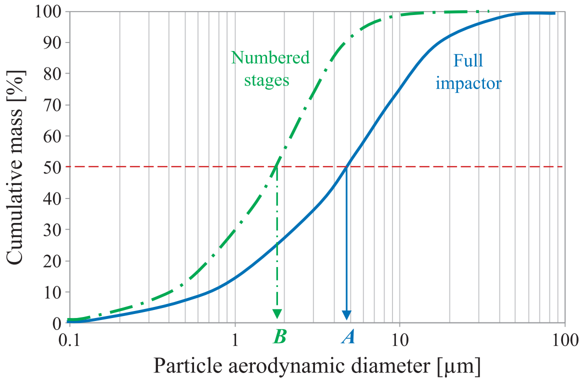

Fig. 10 Comparison of the real MMAD (A) of the aerosol and the MMAD calculated only on the basis of particles in the range limited to 0–11.70 µm, i.e. the sizes classified inside the NGI at 60 L/min (B).

3.4 In vitro-in vivo correlation (IVIVC) problem in aerosol inhalation

The aerodynamic size of drug particles is needed not only to verify the reproducibility of the inhalation product (quality assurance) but also to confirm that the drug can be expected to effectively penetrate to the target region in the respiratory system. FPD ($d_a < 5$ µm) informs about the dose which has the best chance to reach the lower airways (USP, 2008; European Pharmacopeia, 2013). However, the applicability of this criterion is still discussed within the issue of IVIVC, i.e. in vitro-in vivo correlation (Clark A.R. and Borgström L., 2002; Newman S.P. and Chan H.-K., 2008). This problem tries to find a possibly precise link between the particle size of inhaled drugs and the expected health benefit and must, in fact, acknowledge the complexity of particle deposition discussed in section 2. Some researchers claim that the mass of extra-fine particles (1–3 µm) is more relevant to the real deposition and health effects (de Boer A.H. et al., 2015). However, as shown in **Fig. 4**, it is difficult to unequivocally indicate the optimum particle size, in particular considering inter-subject variability in inhalation flow dynamics and airway geometry where both can be additionally altered in lung disease. Mitchell J. et al. (2007) additionally pointed out that the clinical response (the real in-vivo effect) will depend not only on the actual deposition of drug particles but also on the drug potency and the severity of lung disorder. These authors also discussed other limitations of application of the results of aerodynamic particle sizing to predict the regional aerosol deposition in the respiratory system. Cascade impactors are the technical devices which operate at ambient temperature and at a constant flow rate, which is a completely different situation compared to real aerosol inhalation. Laboratory testing conditions may influence the particle size distribution, e.g. due to evaporation of nebulized droplets (Zhou Y. et al., 2005) or additional deagglomeration of powders (Sosnowski T.R., 2008), which make such aerosols incomparable with the ones entering the lungs during drug inhalation. Although some additional technical improvements of cascade impactors have been proposed such as a more realistic mouth-throat model instead of the standard inlet (Copley M. et al., 2011), the problem of a direct conversion of the measured particle size to the real in-vivo drug delivery and efficacy still remains unsolved (Clark A.R. and Borgström L., 2002; Mitchell J. et al., 2007).

3.5 Innovative and generic drugs development

At the end of the discussion of challenges and opportunities in using inhalable powders for drug delivery, we should take a short look at the problems of development of inhalable medical products. Completely new inhalation concepts (i.e. the new molecules with new inhalers) require strictly defined, demanding and expensive procedures to become a candidate for the medial product. In addition to precisely documented development steps, clinical studies to confirm the efficacy and safety are always required. Since many patents for therapeutic molecules are expiring, there is a trend to develop the generic products as cheaper substitutes of drugs originally developed some years ago. The procedure required to introduce a generic inhalation product to the market is simplified, and—according to some regulations (e.g. in Europe)—clinical studies are not required if therapeutic equivalence is convincingly demonstrated (CHMP, 2009). Accordingly, the whole procedure is cheaper and faster, although there is concern whether such an approach is fully justified. It should also be noted that the legislation regarding generic inhalation products is different worldwide (Pirożyński M., and Sosnowski T.R., 2016). In any case, an important issue is the quality of the powder drug and the inhaling device, and both have to match the original product closely regarding the aerodynamic performance (e.g. DPI resistance) and the API aerosol size distribution obtained at different flow rates through the inhaler (CHMP, 2009).

Consequently, all key problems highlighted in the previous sections should be taken into account when the development of innovative or generic powder inhalation products is considered.

4. Interactions of inhaled powders with lung surface—towards functional particles

Powder properties should also be optimized regarding the bioavailability of the drug they carry into the lungs. Inhaled particles land on the wet surface of bronchi, bronchioles or alveoli, so they directly interact with the fluid layers of the lungs. In conducting airways, particles come into contact with mucus and the drug molecules eventually reach the epithelium after penetrating across the layer of this complex viscoelastic liquid. Deposited particles can be simultaneously transported along the airways due to the action of 'mucociliary escalator', i.e. the longitudinal flow propelled by beating cellular cilia (Smith D.J. et al., 2007). Since the underlying epithelium is the main target for inhaled bronchodilating and anti-inflammatory drugs, it is important to prepare the aerosol drug carriers in a way which facilitates API penetration through the mucus blanket. In diseased lungs, the mucus is abundant and more viscous (Cone R.A., 2009), so less permeable for inhaled drugs. In such a situation, inhalable powders with a specific composition and properties can be useful. According to a recent idea (Odziomek M. et al., 2012), the excipient particles might contain a mucolytic agent such as N-acetylcysteine together with the stabilizing additive (e.g. dextran). Deposited particles of the drug bonded to such a carrier (in a similar way as in typical API-lactose blends) are capable of rheologically thinning the mucus due to interactions with the mucolytic agent which is released locally. This allows the drug to penetrate faster through the mucus layer (Odziomek M. et al., 2015). In the alternative concept, multicomponent powders combining both the mucolytic agent and the drug in a single particle were proposed (Gradoń L. et al., 2009). The described functional particles can be effectively prepared by spray-drying through the adjustment of process conditions to obtain powders with good aerosolization properties. Mucus rheology and mass transfer phenomena in raw or modified mucus can be analysed by selected physicochemical methods (Schuster B.S. et al., 2013; Odziomek M. et al., 2017).

Particles deposited in the respiratory (alveolar) region interact not with the mucus but with the pulmonary surfactant (PS). The PS produced by type II alveolar cells contains lipids (mainly lecithins) and some unique proteins (Parra E. and Perez-Gil J., 2015). True to its name, the PS demonstrates strong surface-active properties. They have important consequences for lung physiology, due to:

– reduction of the work of breathing, i.e. the energy input required to expand during inspiration a large surface of the lungs (~100 m^2),
– several functions related to the lung clearance and improvement of other mass transfer processes in the pulmonary region (Sosnowski T.R., 2016).

It is important to note that PS is highly surface-active under the dynamic conditions of breathing, i.e. during oscillatory variations of the air/liquid interfacial area. Both temporal and spatial fluctuations of the surface tension along the interface take place due to surfactant mass exchange between the bulk liquid and the free interface, but also due to flow and diffusion at the interfacial boundary. Marangoni effects are generated due to the surface tension gradients providing the driving force for the hydrodynamic clearance of deposited particulates from the alveolar zone (Gradoń L. and Podgórski A., 1989; Gradoń L. et al., 1996) - **Fig. 11**.

Such behavior of the air-liquid interface can be reproduced in the laboratory using specialized measuring devices, e.g. Langmuir-Wilhelmy balance, oscillating bubble or oscillating drop tensiometers (e.g. Sosnowski T.R. et al., 2017; Kondej D. and Sosnowski T.R., 2013; Kondej D. and Sosnowski T.R., 2016; Wüstneck R. et al., 2002). These experimental systems allow determination of the dynamic surface tension variations during the breathing-like compression and expansion of the interface with the PS. Experimental measurements can also directly demonstrate the occurrence of the Marangoni flows in-

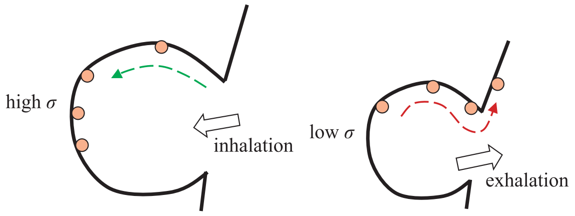

Fig. 11 Dynamic surface tension in alveolar region. Marangoni flows and particle transport are due to dynamic surface tension gradients $\nabla\sigma$ (t).

duced by the variations of interfacial area. For some types of inhaled medicinal aerosols (e.g. drugs with the desired systemic absorption), it may be beneficial to extend their residence time in the alveolar region, so this kind of fast transport would be undesired. Tuning the surface properties of particles (e.g. total surface area, porosity, wettability) may influence their interactions with the surfactant which can extend the residence time and improve the local bioavailability of inhaled drugs (Sosnowski T.R. et al., 2003).

The results shown in **Fig. 12** confirm that local disturbance of the air/liquid interface with a model PS generates the surface tension gradient $\nabla\sigma$ and, as a consequence, the superficial flows. In **Fig. 12**, the surface tension gradient is produced by the unidirectional compression of the interface, and the superficial flow is illustrated by a lateral displacement of tracer particles.

Similar flows can contribute to alveolar clearance in vivo, i.e. to the effective removal of deposited particles (or particles already captured by alveolar macrophages) from alveoli as shown in **Fig. 11**.

Surface tension hysteresis measured in vitro for PS shown in **Fig. 13** is another characteristic dynamic feature of the pulmonary surfactant, and it can be used to trace alterations in the dynamic surface tension of the PS caused by deposited particles (Kondej D. and Sosnowski T.R., 2013). In this way, physicochemical methods help to assess potential disturbance of the alveolar mass transfer caused by inhaled particles, including powder drugs (Kramek-Romanowska K. et al., 2015). The results may indicate which properties of the inhaled powders are required for the best drug bioavailability. These specific powder properties can be obtained during their production by particle engineering methods highlighted in section 3.1.

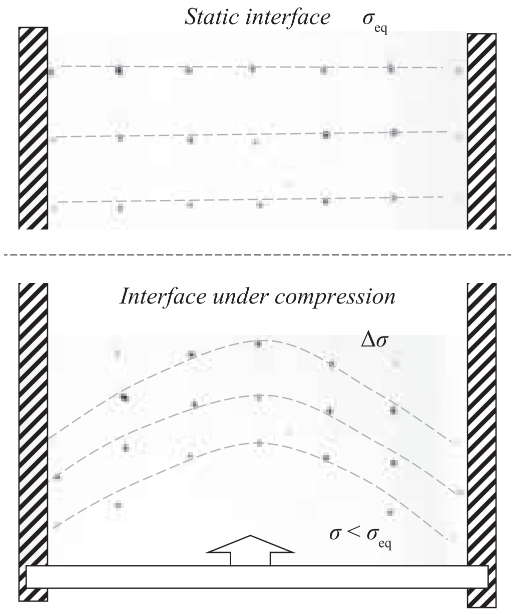

Fig. 12 Experimental results (top view of the Langmuir-Wilhelmy balance) showing the flow of tracer particles at the air-water surface with the phospholipid monolayer (as the model of PS) during unidirectional surface compression.

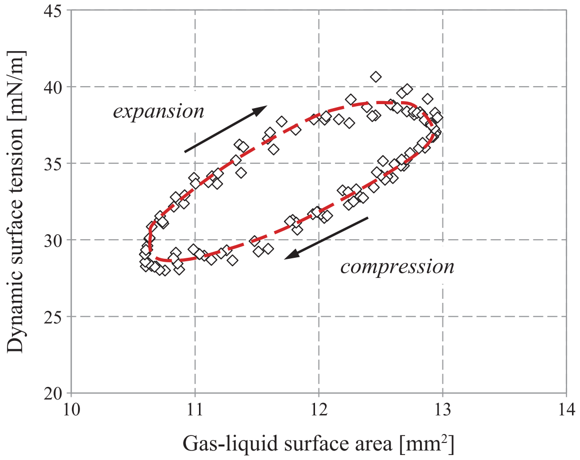

Fig. 13 Example of surface tension hysteresis recorded in the PS during oscillation of the air/liquid surface at a physiological rate and temperature (results obtained with PAT-1M device, Sinterface, Germany).

5. Conclusions

The main intention of this paper was to indicate important technical issues of the use of aerosolized powder particles as vehicles of drugs delivered to the lungs. Starting from the overall physical overview of the aerodynamic particle transport in the respiratory system, the importance of dynamic effects related to the non-steady airflow during breathing was pointed out. Other difficulties and uncertainties in predicting particle flow and deposition in the respiratory tract are related to the specific phenomena (e.g. particle coagulation, hygroscopic growth) which can influence the dynamic behavior of particles in the lungs. The properties of powders and the selected issues related to their preparation for inhalation purposes were briefly presented to indicate the key factors in optimizing the inhalation product. The proper design of powder inhaling devices, i.e. DPIs, is another vital condition of successful drug delivery. Again, special attention was given here to the dynamic processes of aerosol formation and entrance into the organism. This allowed demonstration of the fact that for particles which are not drawn in sufficiently early during the inhalation phase of the breathing cycle, their deep penetration to distal lung regions will not be possible. Discussion of the unique methods of the characterization of aerosols produced in the inhalers (including DPIs) was used to indicate common misinterpretations of certain experimental data. Finally, the possibility of designing powder particles with a better pharmaceutical outcome was highlighted on the basis of a brief description of physicochemical interactions between deposited particles and lung fluids (mucus and pulmonary surfactant).

It should be realized that the physics of all processes of powder aerosolization, penetration through the respiratory system, deposition and interaction with the lung surface are so complex that we are still lacking their complete quantitative description. Classic considerations which are often based on strong simplifications overlook some key features of these processes and can lead to erroneous conclusions. It may have certain consequences in choosing the appropriate steps in product development by the pharmaceuticals industry, but also in non-optimal therapeutic decisions made by physicians. It is therefore always important to take into account the latest achievements in understanding aerosol generation from powders and their deposition in the lungs.

Acknowledgements

This scientific work was partly supported by the budget for sciences in the years 2015–2018 as Research Project No. 2014/13/B/ST8/00808. The author thanks Katarzyna Jabłczyńska, M.Sc., for preparation of the spray-dried powders and their SEM images used in this paper.

Nomenclature

AD	Aerosolized Dose
API	Active Pharmaceutical Ingredient
CFD	Computational Fluid Dynamics
COPD	Chronic Obstructive Pulmonary Disease
DDT	Dose Delivered to Target
DPI	Dry Powder Inhaler
ED	Emitted Dose
E-T	Extra-Thoracic (deposition)
FPD	Fine Particle Dose
H-R	High-Resistant (inhaler)
ICRP	International Committee for Radiological Protection
L-R	Low-Resistant (inhaler)
MD	Metered Dose
MMAD	Mass Median Aerodynamic Diameter
MPPD	Multi-Path Particle Deposition (model)
NGI	Next Generation Impactor
PIFR	Peak Inspiratory Flow Rate
pMDI	Pressurized Metered Dose Inhaler
PS	Pulmonary Surfactant
SMI	Soft Mist Inhaler
T-B	Tracheo-Bronchial
TV	Tidal Volume
A	cross-sectional area (m^2)
C_s	Cunningham slip correction factor (–)
d_a	particle aerodynamic diameter (μm)
d_{ci}	cut-off diameter of stage i (μm)
d_p	particle diameter (μm)
F_B	Brownian force (N)
F_ext	external forces (N)
k_B	Boltzmann constant ($\mathrm{J\ K^{-1}}$)
L_0	characteristic length (m)
m	mass (kg)
ΔP	pressure drop (Pa)
Q	airflow rate ($\mathrm{m^3 s^{-1}}$)
Q_max	maximum airflow rate ($\mathrm{m^3 s^{-1}}$)
Q_opt	optimum airflow rate ($\mathrm{m^3 s^{-1}}$)
$\hat{Q}$	mean airflow rate ($\mathrm{m^3 s^{-1}}$)
R_D	intrinsic aerodynamic resistance of a DPI ($\mathrm{hPa^{0.5} min\ L^{-1}}$)
Re	Reynolds number (–)
S_0	spectral intensity of fluctuations ($\mathrm{m^2 s^{-3}}$)
Stk	Stokes number (–)
t	time (s)
t_inh	time of inhalation (s)
Δt	time step of numerical integration (s)
T	temperature (K)
u	air velocity ($\mathrm{m\ s^{-1}}$)
u_p	particle velocity ($\mathrm{m\ s^{-1}}$)
V	inhaled volume (L)

xi	exponent of the correlation in NGI (–)
$\boldsymbol{Z}$	dimensionless vector (–)
α_B	magnitude of the acceleration of thermal excitations (m s^{-2})
γ	local resistance coefficient (–)
μ	air viscosity (Pa s)
ρ_p	air density (kg m^{-3})
ρ_w	water density (kg m^{-3})
σ	surface tension (N m^{-1})
σ_{eq}	equilibrium surface tension (N m^{-1})
χ	dynamic shape factor (–)

References

Asgharian B., A model of deposition of hygroscopic particles in the human lung, Aerosol Science and Technology, 38 (2004) 938–947.

Asgharian B., Hofmann W., Bergmann R., Particle deposition in a multiple-path model of the human lung, Aerosol Science and Technology, 34 (2001) 332–339.

Alangari A.A., Corticosteroids in the treatment of acute asthma. Annals of Thoracic Medicine 9 (2014) 187–192.

Annals of the ICRP 24. International Commission on Radiological Protection (ICRP) Publication 66, Human respiratory tract model for radiological protection. Oxford: Elsevier Science; 1994.

ARLA. The Aerosol Research Lab of Alberta Respiratory Deposition Calculator (2008) <www.mece.ualberta.ca/arla/deposition_ calculator.html> accessed 10.05.2017.

Azouz W., Chetcuti P., Hosker H.S., Saralaya D., Stephenson J., Crystyn H., The inhalation characteristics of patients when they use different dry powder inhalers. Journal of Aerosol Medicine and Pulmonary Drug Delivery, 28 (2015) 35–42.

Barnes P.J., Distribution of receptor targets in the lung, Proceedings of American Thoracic Society, 1 (2004) 345–351.

Begat P., Morton D.A., Shur J., Kippax P., Staniforth J.N., Price R., The role of force control agents in high-dose dry powder inhaler formulations, Journal of Pharmaceutical Sciences, 98 (2009) 2770–2783.

Begat P., Price R., Harris H., Morton D.A.V., Staniforth J.N., The influence of force control agents on the cohesive-adhesive balance in dry powder inhaler formulations, KONA Powder and Particle Journal, 23 (2005)109–121.

Berkenfeld K., Lamprecht A., McConville J.T., Devices for dry powder drug delivery to the lung, AAPS Pharmaceutical Science and Technology, 16 (2015) 479–490.

Borgström L., Bisgaard H., O'Callaghan C, Pedersen S., Dry-powder inhalers, in: Bisgaard H., O'Callaghan C., Smaldone G.C. (Eds.), Drug Delivery to the Lung (Lung Biology in Health and Disease), Marcel Dekker, Inc., New York-Basel, 2002, pp. 421–448.

Broday D.M., Robinson R., Application of cloud dynamics to dosimetry of cigarette smoke particles in the lungs. Aerosol Science and Technology, 37 (2003) 510–527.

Canonica G.W., Arp J., Keegstra J.R., Chrystyn H., Spiromax, a new dry powder inhaler: dose consistency under simulated real-world conditions. Journal of Aerosol Medicine and Pulmonary Drug Delivery, 28 (2015) 309–319.

Carvalho S.R., Watts A.B., Peters J.I., Williams III R.O., Dry powder inhalation for pulmonary delivery: recent advances and continuing challenges, in: Nokhodhi A., Martin G.P. (Eds.), Pulmonary Drug Delivery. Advances and Challenges (Advances in Pharmaceutical Technology), John Wiley & Sons, Chichester, UK, 2015, pp. 35–62.

Cheng Y.S., Mechanisms of pharmaceutical aerosol deposition in the respiratory tract, AAPS Pharmaceutical Science and Technology, 15 (2014) 630–640.

Chew N.Y.K., Chan H.-K., Use of solid corrugated particles to enhance powder aerosol performance, Pharmaceutical Research, 18 (2001) 1570–1577.

CHMP (Committee for Human Medical Products), Guideline on the requirements for clinical documentation for orally inhaled products (OIP) including the requirements for demonstration of therapeutic equivalence between two inhaled products for use in the treatment of asthma and chronic obstructive pulmonary disease (COPD) in adults and for use in the treatment of asthma in children and adolescents, London: European Medicinal Agency, 2009.

Clark A.R., Borgström L., In vitro testing of pharmaceutical aerosols and predicting lung deposition from in vitro measurements, in: Bisgaard K., O'Callaghan C., Smaldone G.C. (Eds.), Drug Delivery to the Lung, Marcel Dekker, New York, 2002, pp. 105–142.

Clark A.R., Hollingworth A.M, The relationship between powder inhaler resistance and peak inspiratory conditions in healthy volunteers-implications for in vitro testing, Journal of Aerosol Medicine, 6 (1993) 99–110.

Cone R.A., Barrier properties of mucus, Advanced Drug Delivery Reviews, 61 (2009) 75–85.

Copley M., Mitchell J., Solomon D., Evaluating of the Alberta throat: an innovation to support the acquisition of more clinically applicable aerosol aerodynamic particle sized distribution (ASPD) data in oral inhaled product (OIP) development, Inhalation, 5 (2011), 12–16.

Darquenne C., Aerosol deposition in health and disease, Journal of Aerosol Medicine and Pulmonary Drug Delivery, 25 (2012) 140–147.

de Boer A.H., Gjaltema D., Hagedoorn P., Frijlink H.W., Can 'extrafine' dry powder aerosols improve lung deposition?, European Journal of Pharmaceutics and Biopharmaceutics, 96 (2015) 143–151.

de Boer A.H., Hagedoorn P., Hoppentocht M., Buttini F., Grasmeijer F., Frijlink H.W., Dry powder inhalation: past, present and future, Expert Opinion on Drug Delivery, 14 (2017) 499–512.

Dunbar C.A., Hickey A.J., Holzner P., Dispersion and characterization of pharmaceutical dry powder aerosols, KONA Powder and Particle Journal, 16 (1998) 7–45.

European Pharmacopoeia, 8th ed., Council of Europe, Strassbourg, 2013.

Farkas A., Balashazy I., Quantification of particle deposition in asymmetrical tracheobronchial model geometry, Computers in Biology and Medicine, 38 (2008) 508–518.

Finlay W.H., Martin A.R., Recent advances in predictive understanding of respiratory tract deposition, Journal of Aerosol Medicine and Pulmonary Drug Delivery, 21 (2008) 189–206.

Fresconi F.E., Prasad A.K., Secondary velocity fields in the conducting airways of the human lung, Journal of Biomechanical Engineering, 129 (2007) 722–732.

Gac J., Sosnowski T.R., Gradoń L., Turbulent flow energy for aerosolization of powder particles, Journal of Aerosol Science, 39 (2008) 113–126.

Geller D.E., Weers J., Heuerding S., Development of an Inhaled Dry-Powder Formulation of Tobramycin Using PulmoSphere™ Technology, Journal of Aerosol Medicine and Pulmonary Drug Delivery, 24 (2011) 175–182.

Gradoń L., Podgórski A., Hydrodynamical model of pulmonary clearance, Chemical Engineering Science, 44 (1989) 741–749.

Gradoń L., Podgórski A., Sosnowski T.R., Experimental and theoretical investigations of transport properties of DPPC monolayer, Journal of Aerosol Medicine, 9 (1996) 357–367.

Gradoń L., Sosnowski T.R., Formation of particles for dry powder inhalers, Advanced Powder Technology 25 (2014) 43–55.

Gradoń L., Sosnowski TR, Pirożyński M, Han S., European Patent Application, (2009) EP 2340817A1Stein S.W., Thiel C.G., The history of therapeutic aerosols: a chronological review, Journal of Aerosol Medicine and Pulmonary Drug Delivery, 30 (2017) 20–41.

Healy A.M., Amaro M.I., Paluch K.J., Tajber L., Dry powders for oral inhalation free of lactose carrier particles. Advanced Drug Delivery Review 75 (2014) 32–52.

Heinemann L., The failure of Exubera: are we beating a dead horse?, Journal of Diabetes Science and Technology, 2 (2008) 518–529.

Heyder J., Svartengren M.U., Basic principles of particle behavior in the human respiratory tract, in: Bisgaard H., O'Callaghan C., Smaldone G.C. (Eds.), Drug Delivery to the Lung (Lung Biology in Health and Disease), Marcel Dekker, Inc., New York-Basel, 2002, pp. 21–45.

Hoppentocht, M., Hagedoorn, P., Frijlink, H.W., de Boer, A.H., Technological and practical challenges of dry powder inhalers and formulations, Advanced Drug Delivery Review, 75 (2014) 18–31.

Howarth P.H., Why particle size should affect clinical response to inhaled therapy, Journal of Aerosol Medicine, 14S1 (2001) S27–S34.

Islam N., Gladki E., Dry powder inhalers (DPIs)—a review of device reliability and innovation, International Journal of Pharmaceutics, 360 (2008) 1–11.

Jabłczyńska K., Janczewska M., Kulikowska A., Sosnowski T.R., Preparation and characterization of biocompatible polymer particles as potential nanocarriers for inhalation therapy, International Journal of Polymer Science, 2015 (2015) 763020 (8 pages), DOI:10.1155/2015/763020

Kaialy W., Nokhodchi A., Particle engineering for improved pulmonary drug delivery through dry powder inhalers, in: Nokhodhi A., Martin G.P. (Eds.), Pulmonary Drug Delivery. Advances and Challenges (Advances in Pharmaceutical Technology), John Wiley & Sons, Chichester, UK, 2015, pp. 171–197.

Kleinstreuer C., Zhang Z., Donohue J.F., Targeted drug-aerosol delivery in the human respiratory system, Annual Reviews in Biomedical Engineering 10 (2008) 195–220.

Koblinger L., Hofmann W., Monte Carlo modeling of aerosol deposition in human lungs: Part I: Simulation of particle transport in a stochastic lung structure, Journal of Aerosol Science, 21 (1990) 661–674.

Kondej D., Sosnowski T.R., Alteration of biophysical activity of pulmonary surfactant by aluminosilicate nanoparticles. Inhalation Toxicology 25 (2013) 77–83.

Kondej D., Sosnowski T.R., Effect of clay nanoparticles on model lung surfactant: a potential marker of hazard from nanoaerosol inhalation. Environmental Science and Pollution Research, 23 (2016) 4660–4669.

Kramek-Romanowska K., Odziomek M., Sosnowski T.R., Dynamic tensiometry studies on interactions of novel therapeutic inhalable powders with model pulmonary surfactant at the air–water interface, Colloids Surfaces A: Physicochemical and Engineering Aspects, 480 (2015) 149–158.

Kramek-Romanowska K., Odziomek M., Sosnowski T.R., Gradoń L., Effects of process variables on the properties of spray-dried mannitol and mannitol/disodium cromoglycate powders suitable for drug delivery by inhalation, Industrial and Engineering Chemistry Research, 50 (2011) 13922–13931.

Kwong W.T.J., Ho S.L., Coates A.L., Comparison of nebulized particle size distribution with Malvern diffraction analyzer versus Andersen Cascade Impactor and Marple Personal Cascade Impactor, Journal of Aerosol Medicine, 13 (2000) 303–314.

Li Y.Z., Sun X., Gong T., Liu J., Zuo J., Zhang Z.R., Inhalable microparticles as carriers for pulmonary delivery of thymopentin-loaded solid lipid nanoparticles, Pharmaceutical Research, 27 (2010) 1977–1986.

Liang Z., Ni R., Zhou J., Mao S., Recent advances in controlled pulmonary drug delivery, Drug Discovery Today, 20 (2014) 380–389.

Longest P.W., Holbrook L.T., In silico models of aerosol delivery to the respiratory tract - development and applications, Advanced Drug Delivery Review, 64 (2012) 296–311.

Ma B., Lutchen K.R, CFD Simulation of aerosol deposition in an anatomically based human large–medium airway model. Annals of Biomedical Engineering, 37 (2009) 271–285.

Mao L., Wilcox D., Kippax P., Laser diffraction particle size analysis: a powerful tool for rapidly screening nebulizer formulations, Drug Delivery Technology, 10 (2010) 64–67.

Martinelli F., Balducci A.G., Rossi A., Sonvico F., Colombo P., Buttini F., "Pierce and inhale" design in capsule based dry powder inhalers: Effect of capsule piercing and motion on aerodynamic performance of drugs, International Journal of Pharmaceutics, 487 (2015), 197–204.

Matida E.A., Finlay W.H., Lange C.F., Grgic B., Improved numerical simulation of aerosol deposition in an idealized mouth–throat. Journal of Aerosol Science, 35 (2004) 1–19.

Mitchell J., Newman S., Chan H.-K., In vitro and in vivo aspects of cascade impactor tests and inhaler performance: a review, AAPS Pharmaceutical Science and Technology, 8 (2007) 237–248.

Moskal A., On Transport and Deposition of Aerosol Particles in the Human Breathing System—Selected Problems, Publishing House of Warsaw University of Technology, Poland, 2011.

Moskal A., Gradoń L., Temporary and spatial deposition of aerosol particles in the upper human airways during breathing cycle. Journal of Aerosol Science, 33 (2002) 1525–1539.

MPPD, Multiple-Path Particle Dosimetry Model v.3.04 (2015). <www.ara.com/products/multiple-path-particle-dosimetry-model-mppd-v-304> accessed 10.05.2017

MSP Corporation, The Next Generation Pharmaceutical Impactor (NGI) User Guide, Shoreview, MN, USA (2008).

Nandiyanto A.B.D., Okuyama K., Progress in developing spray-drying methods for the production of controlled morphology particles: from the nanometer to submicrometer size ranges, Advanced Powder Technology, 22 (2011) 1–19.

Newman S.P., Chan H.-K., In vitro/in vivo comparisons in pulmonary drug delivery. Journal of Aerosol Medicine and Pulmonary Drug Delivery 21 (2008) 77–84.

Newman S., Peart J., Dry powder inhalers, in: Newman S. (Ed.), Respiratory Drug Delivery. Essential Theory and Practice, RDD Online/VCU, Richmond, VA, USA, 2009, pp. 257–307.

Odziomek M., Kalinowska M., Płuzińska, A., Rożeń A., Sosnowski T.R., Bronchial mucus as a complex fluid: molecular interactions and influence of nanostructured particles on rheological and transport properties. Chemical and Process Engineering 38 (2017) 217–229.

Odziomek M., Sosnowski T.R., Gradoń L., Conception, preparation and properties of functional carrier particles for pulmonary drug delivery, International Journal of Pharmaceutics, 433 (2012) 51–59.

Odziomek M., Sosnowski T.R., Gradoń L., The influence of Functional Carrier Particles (FCPs) on the molecular transport rate through the reconstructed bronchial mucus - in vitro studies, Transport in Porous Media, 106 (2015) 439–454.

Parra E., Pérez-Gil J., Composition, structure and mechanical properties define performance of pulmonary surfactant membranes and films, Chemistry and Physics of Lipids, 185 (2015) 153–175.

Pilcer G., Wauthoz N., Amighi K., Lactose characteristics and the generation of the aerosol, Advanced Drug Delivery Reviews, 64 (2012) 233–256.

Pirożyński M., Sosnowski T.R., Inhalation devices: from basic science to practical use, innovative vs generic products, Expert Opinion on Drug Delivery, 13 (2016) 1559–1571.

Ramachandran V., Murnane D., Hammond R.B., Pickering J., Roberts K.J., Soufian M., Forbes B., Jaffari S., Martin G.P., Collins E., Pencheva K., Formulation pre-screening of inhalation powders using computational atom–atom systematic search method, Molecular Pharmaceutics, 12 (2015) 18–33.

Sanders M., Pulmonary drug delivery: an historical overview, in: Smyth H.D.C., Hickey A.J. (Eds.), Controlled Pulmonary Drug Delivery (Advances in Delivery Science and Technology), Springer, NY-Dordrecht-Heildeberg-London, 2011, pp. 51–73.

Schuster B.S., Suk J.S., Woodworth G.F., Hanes J., Nanoparticle diffusion in respiratory mucus from humans without lung disease, Biomaterials, 34 (2013) 3439–3446.

Schum G.M., Phalen R.F., Modelling hygroscopic particle growth in human lung airways, Annals of Occupational Hygiene, 41 (1997) 60–64.

Smith D.J., Gaffney E.A., Blake J.R., A viscoelastic traction layer model of mucociliary transport, Bulletin of Mathematical Biology, 69 (2007) 289–327.

Sosnowski T.R., Powder de-aggregation in the cascade impactor, Abstracts of European Aerosol Conference, Thessaloniki, 24–29.08.2008, paper T09A035P.

Sosnowski T.R., Selected engineering and physicochemical aspects of systemic drug delivery by inhalation, Current Pharmaceutical Design, 22 (2016) 2453–2462.

Sosnowski T.R., Giżyńska K., Żywczyk Ł., Fluidization and break-up of powder particle aggregates during constant and pulsating flow in converging nozzles, Colloids Surfaces A: Physicochemical and Engineering Aspects, 441 (2014) 905–911.

Sosnowski T.R., Gradoń L., Modification of inhalable powders by pulmonary surfactant components adsorbed on droplets during spray-drying process, Colloids Surfaces A: Physicochemical and Engineering Aspects, 365 (2010) 56–61.

Sosnowski T.R., Gradoń L., Iskandar, F., Okuyama K., Interaction of deposited aerosol particles with the alveolar liquid layer, in: Gradoń L., Marijnissen J. (Eds.), Optimization of Aerosol Drug Delivery, Kluwer Academic Publishers, Dordrecht, 2003, pp. 205–216.

Sosnowski T.R., Kramek-Romanowska K., Predicted deposition of e-cigarette aerosol in the human lungs, Journal of Aerosol Medicine and Pulmonary Drug Delivery, 29 (2016) 299–309.

Sosnowski T.R., Kubski P., Wojciechowski K., New experimental model of pulmonary surfactant for biophysical studies, Colloids and Surfaces A: Physicochemical and Engineering Aspects, 519 (2017) 27–33.

Sosnowski T.R., Moskal A., Gradoń L., Mechanisms of aerosol particle deposition in the oro-pharynx under non-steady airflow, Annals of Occupational Hygiene, 51 (2007) 19–25.

Stein S.W, Thiel C.G., The history of therapeutic aerosols: a chronological review, Journal of Aerosol Medicine and Pulmonary Drug Delivery, 30 (2017) 20–41.

Tsapis N., Bennett D., Jackson B., Weitz D.A., Edwards D.A., Trojan particles: large porous carriers of nanoparticles for drug delivery, Proceedings of the National Academy of Sciences of the USA 99 (2002) 12001–12005.

Tsuda A., Henry F.S., Butler J.P., Particle transport and deposition: basic physics of particle kinetics, Comprehensive Physiology, 3 (2013), 1437–1471.

Tu J., Inthavong K., Ahmadi G.S., Computational Fluid and Particle Dynamics in The Human Respiratory System, Springer, Dordrecht, 2013.

Usmani O.S., Biddiscombe M.F., Barnes P.J., Regional lung deposition and bronchodilator response as a function of beta2-agonist particle size, American Journal of Respiratory and Critical Care Medicine 172 (2005) 1497–1504.

USP (United States Pharmacopeia). Aerosols, nasal sprays, metered dose inhalers and dry powder inhalers, US Pharmacopeial Convention, Rockville, 2008.

Vanbever R., Optimization of dry powder aersosols for systemic drug delivery, in: Gradoń L., Marijnissen J. (Eds.), Optimization of Aerosol Drug Delivery, Kluwer Academic Publishers, Dordrecht, 2003, pp. 91–103.

Vehring R., Expert review: pharmaceutical particle engineering via spray drying, Pharmaceutical Research, 25 (2008) 999–1022.

Weber S., Zimmer A., Pardeike J., Solid Lipid Nanoparticles (SLN) and Nanostructured Lipid Carriers (NLC) for pulmonary application: A review of the state of the art, European Journal of Pharmaceutics and Biopharmaceutics, 86 (2014) 7–22.

Weers J.G., Miller D.P., Formulation design of dry powders for inhalation, Journal of Pharmaceutical Sciences, 104 (2015) 3259–3288.

Weuthen T., Roeder S., Brand P., Mullinger B., Scheuch G., In vitro testing of two formoterol dry powder inhalers at different flow rates, Journal of Aerosol Medicine, 15 (2002) 297–303.

Winkler-Heil R., Ferron G., Hofmann W., Calculation of hygroscopic particle deposition in the human lung, Inhalation Toxicology, 26 (2014) 193–206.

Wüstneck R., Wüstneck N., Moser B., Karageorgieva V., Pison U., Surface dilatational behavior of pulmonary surfactant components spread on the surface of a pendant drop. 1. Dipalmitoyl phosphatidylcholine and surfactant protein C, Langmuir, 18 (2002) 1119–1124.

Yeh H.C., Schum G.M., Models of human lung airways and their application to inhaled particle deposition, Bulletin of Mathematical Biology 42 (1980) 461–480.

Zanen P., Targetting aerosols to disease area, in: Gradoń L., Marijnissen J. (Eds.), Optimization of Aerosol Drug Delivery, Kluwer Academic Publishers, Dordrecht, 2003, pp. 243–276.

Zeng X.M., Martin G.P., Marriott C., Particulate Interactions in Dry Powder Formulations for Inhalation, CRC Press, London, 2000.

Zhang Z., Kleinstreuer C., Transient airflow structures and particle transport in a sequentially branching lung airway model, Physics of Fluids, 14 (2002) 862–880.

Zhang Z., Kleinstreuer C., Donohue J.F., Kim C.S., Comparison of micro- and nano-size particle depositions in a human upper airway model. Journal of Aerosol Science, 36 (2005) 211–233.

Zhou Y., Ahuja A., Irvin C.M., Kracko D.A., McDonald J.D., Cheng Y.S., Medical nebulizer performance: effects of cascade impactor temperature, Respiratory Care, 50 (2005) 1077–1082.

Ziegler J., Wachtel H., Comparison of cascade impaction and laser diffraction for particle size distribution measurements, Journal of Aerosol Medicine, 18 (2005) 311–324.

Author’s short biography

Tomasz R. Sosnowski

Tomasz R. Sosnowski received his PhD (1997) and DSc (habilitation - 2006) in chemical engineering from Warsaw University of Technology (WUT), Poland. In 1999–2000 he was a post-doc fellow at Lovelace Respiratory Research Institute in Albuquerque, USA. Currently he is a full professor at the Faculty of Chemical and Process Engineering WUT. His main scientific interests are: (i) interfacial phenomena in human lungs, including the role of the pulmonary surfactant, (ii) technical aspects of aerosol systems used in drug delivery by inhalation. He is a co-author of more than 70 scientific papers, several books and chapters, 2 granted patents and 6 patent applications.

KONA Powder and Particle Journal No. 35 (2018) 139–149/Doi:10.14356/kona.2018021 Review Paper

Development Tendency and Prospect of High Performance Coal Utilization Power Generation System for Low Carbon Society †

Kenji Tanno * and Hisao Makino

[1] *Energy Engineering Research Laboratory, Central Research Institute of Electric Power Industry (CRIEPI), Japan*

Abstract

Coal is an important energy resource for meeting future demands for electricity, as coal reserves are much more abundant than those of other fossil fuels. However, coal utilization technologies exhaust carbon dioxide more than other fossil fuels, because of the higher carbon content of coal. To control of global warming, development of new technologies for the reduction of carbon dioxide emission from a coal-utilized power station are thus required. For reduction of carbon dioxide emission, it is very important to utilize low carbon content fuel such as sub-bituminous coal and lignite, as well as carbon neutral biomass, and develop new technologies needed for a high efficiency power generation system. For the further reduction of carbon dioxide, effective removal and storage technologies are also necessary. In this paper, the utilization technology of low carbonized sub-bituminous coal and carbon neutral biomass in pulverized coal combustion is at first introduced. The development situation of a high efficiency coal-fired power generation technique including an integrated coal gasification combined cycle system (IGCC) and an integrated coal gasification fuel cell combined cycle system (IGFC) are overviewed, and carbon dioxide removal technologies in a thermal power station are investigated. Finally, the high efficiency power generation oxy-fuel IGCC system with CO_2 removal is presented, and the characteristics of this system are examined.

Keywords: coal utilization, carbon dioxide, biomass, low rank coal, high efficiency power generation

---

1. Introduction

Coal is an important energy resource for meeting the future demands for electricity. Coal reserves are much more abundant than those of other fossil fuels. However, the higher carbon content of coal exhausts carbon dioxide in the coal utilization process more than in other fossil fuel utilization processes. To prevent global warming, it is required to develop new technologies for the reduction of carbon dioxide emission from coal-fired power stations.

To reduce carbon dioxide emission, it is essential to develop a high efficiency power generation system, with the technology for utilization of low carbonized coal or carbon neutral biomass. Carbon dioxide removal technology is one option but it involves high power consumption and cost.

In this paper, the utilization technology of low rank coal, characterized by a low carbon content, and the utilization technology of biomass based fuels in pulverized coal power plants are firstly presented. Furthermore, the development situation of a high efficiency power generation system including an Integrated Coal Gasification Combined Cycle and an Integrated Coal Gasification Fuel Cell Combined Cycle, as well as power generation systems combined with carbon dioxide removal technology are introduced. Finally, a new high-efficiency power generation system for CO_2 removal using an O_2-CO_2 blown gasifier is introduced.

2. Overview of reduction technology of CO_2 emission

2.1 Reduction of CO_2 emission by utilization of low carbon fuel

As low carbonized coal such as sub-bituminous coal or lignite is lower in carbon content than bituminous coal, the utilization of low carbonized coal has the possibility of reducing CO_2 emission. Especially, the mineable reserves of sub-bituminous coal are more than 30 % that of bituminous coal, so the utilization of sub-bituminous coal

---

† Received 14 June 2017; Accepted 28 August 2017
J-STAGE Advance published online 30 September 2017

[1] 2-6-1 Nagasaka, Yokosuka, Kanagawa 240-0196, Japan
* Corresponding author: Kenji Tanno
E-mail: k-tanno@criepi.denken.or.jp
TEL: +81-46-856-2121

in a coal fired power plant has progressed in Japan. In a coal-fired power plant, coal is pulverized to particles of 40 µm median diameter size and then the pulverized coal is fired in a boiler. The properties of sub-bituminous coal are different from those of bituminous coal. For the reduction of CO_2 emission by using sub-bituminous coal, it is important to retain the same power generation efficiency as produced with bituminous coal.

Fig. 1 indicates the difference in the oxygen concentration distribution in the test furnace (Ikeda, et al., 2002). **Fig. 1(a)** shows the oxygen concentration distribution on bituminous coal combustion and **Fig. 1(b)** shows that on sub-bituminous coal combustion. Oxygen consumption in the furnace is affected by the combustion situation, so this contour indicates the profile of the combustion flame. The oxygen consumption rate near the burner exit in sub-bituminous coal combustion is lower than that on bituminous coal combustion, as an evaporation period for moisture is necessary in sub-bituminous coal before combustion. So, the ignition of sub-bituminous coal takes place later as compared with bituminous coal. Also, after ignition, sub-bituminous coal combustion flame is diffused rapidly to the outer side of the furnace. This phenomenon is caused by the diffusion of pulverized coal particles. As sub-bituminous coal contains a high moisture content, the particles of sub-bituminous coal become porous or burst into fine particles by the rapid evaporation of moisture from the pore. Small coal particles or porous coal particles possess weak inertia, so these particles can be easily diffused by the swirl force of combustion air.

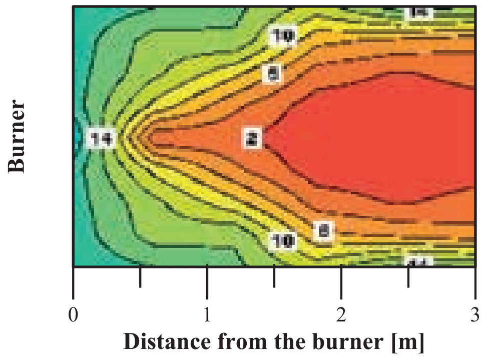

(a) Bituminous coal

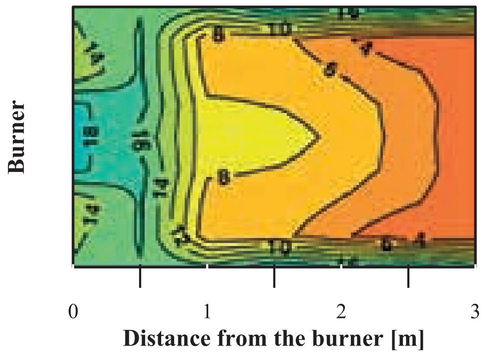

(b) Sub-bituminous coal

Fig. 1 Comparison of oxygen concentration distribution in the furnace. Reprinted with permission from Ikeda et al. 2002. Copyright: (2002) The Japan Society of Mechanical Engineers.

As a solution to this problem, it is effective to reduce the flow rate of primary air and the swirl force of secondary air. The reduction of primary air velocity can move the ignition point closer to the burner exit and the reduction of swirl force can reduce the diffusion of coal particles to the outer side of the furnace. **Fig. 2** indicates the oxygen concentration of the flame on sub-bituminous coal combustion after this modification. The flame shape in this condition is similar to the flame shape for bituminous coal combustion, as shown in **Fig. 1(a)**. The power generation efficiency using sub-bituminous coal in a pulverized coal combustion plant can maintain almost the same as the power generation efficiency using bituminous coal by optimizing the burner operation condition.

Biomass is defined as carbon neutral since biomass is renewable. However, as there are many kinds of biomass, such as woodchips, wood pellets, and sewage sludge, the pulverizing and combustion characteristics of these species are different from each other. For utilization of biomass, the main problem is the high moisture content and the difficulty in pulverizing. Although many kinds of technology for biomass upgrading have been developed, the drying and carbonizing technologies are the most important. For high performance removal of moisture, the methods using evaporation are effective. However, these methods require higher power consumption because of increase in coal temperature. In CRIEPI, the extraction method using DME (di-methyl-ether) has been investigated. **Fig. 3** shows the concept of the method (Kanda, et al., 2008). Although DME is in the gas phase in ambient pressure and temperature, it becomes liquid after pressurization in ambient temperature. The liquefied DME can include moisture. In this system, the liquefied DME is

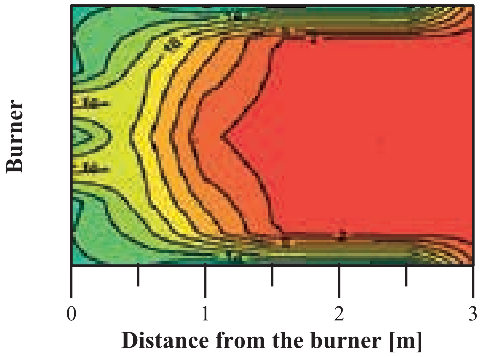

Fig. 2 Oxygen concentration distribution for sub-bituminous coal under the modified condition. Reprinted with permission from Ikeda et al. 2002. Copyright: (2002) The Japan Society of Mechanical Engineers.

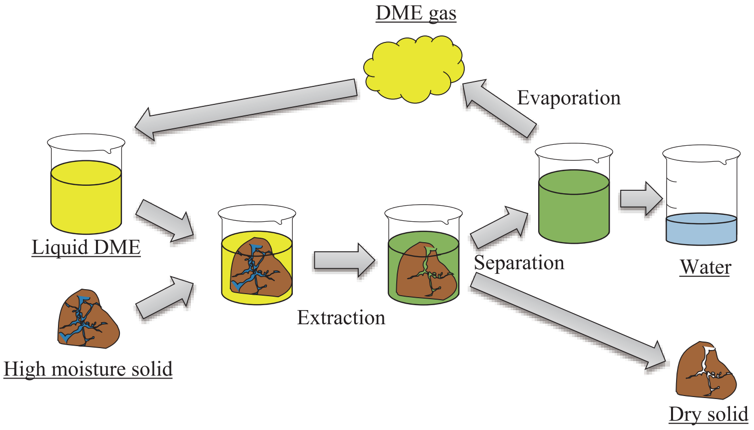

Fig. 3 Concept of the moisture extraction method using DME.

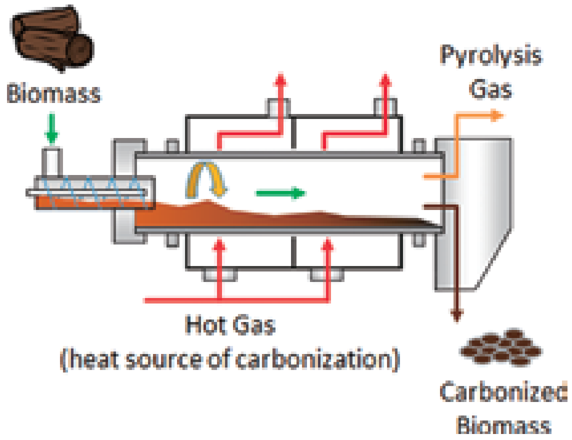

Fig. 4 Schematic of a typical carbonizing system.

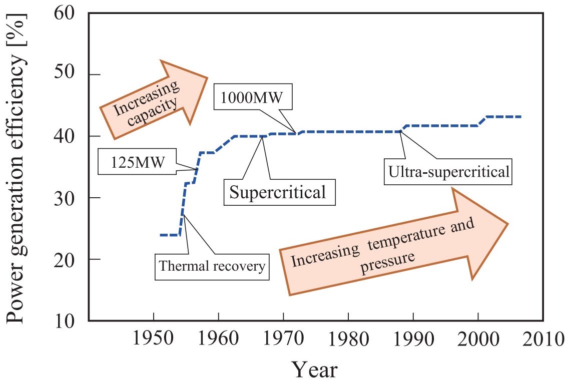

Fig. 5 Improvement of power generation efficiency in Japan.

mixed with the biomass, and DME extracts the moisture. After separation of the liquefied DME including moisture extracted from the law biomass, DME is converted to gas phase by decompression. The gaseous DME is then separated with liquid water. The gaseous DME can be converted to liquid phase by pressurization, and the DME is used again by recycling. This method can reduce the power consumption required for the drying of biomass and be applied to biomass drying.

For utilization of biomass (especially woody biomass), mixing with coal, as a blended fuel, in pulverized coal combustion power plants is a major technique. The pulverizing characteristics of biomass are important topic in blend combustion. The power consumption of a typical mill for coal is increased in the case of mixing biomass. To control the pulverizing characteristics of woody biomass, the carbonization of biomass is an effective technology. A typical carbonizing system is shown in **Fig. 4**. The woody biomass is carbonized in high temperature condition (600 K–1,000 K). The grindability and heat value of the carbonized biomass is increased which consequently enables the utilization of the biomass in a higher blend ratio. Tar produced in a carbonizing process is combusted and the generated heat is used as a heat source of carbonization.

2.2 High efficiency power generation system

A high efficiency power generation system can reduce CO_2 emission while producing the required electric power. In Japan, the ultra-super critical (USC) boiler has been introduced into operation and the steam condition has been gradually improved (**Fig. 5**). For the greater improvement of power generation efficiency, the development of the integrated coal gasification combined cycle (IGCC) and the integrated coal gasification and fuel cell combined cycle (IGFC) are being promoted.

Fig. 6 indicates the system flow of the IGCC process. In Japan, the demonstration plant of IGCC has been operated since 2007. This plant has succeeded in a continuous run of 5,000 hours and is now used commercially. In the IGCC system, coal is pulverized to particles of about 40 μm median diameter size and the pulverized coal is then converted to gaseous phase fuel. The coal derived gas is purified by gas cleaning equipment and fired in a gas turbine combustor. Usually, IGCC plants use a wet gas cleaning system. For more power generation efficiency, the development of hot gas cleaning system and

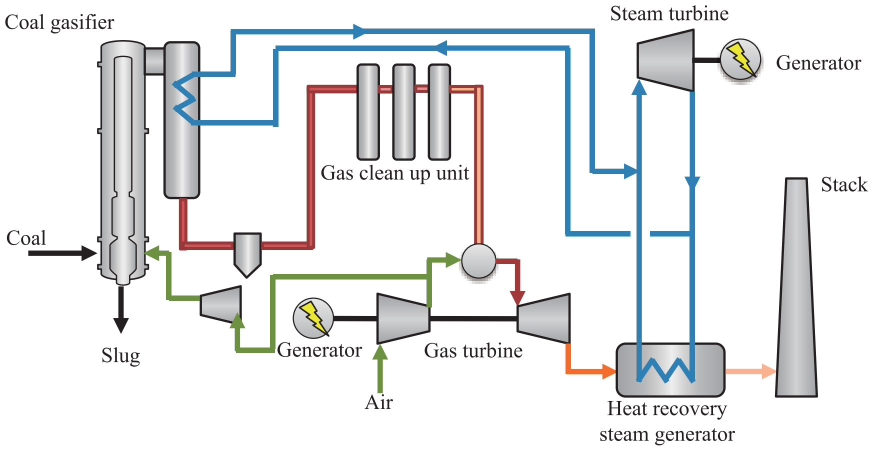

Fig. 6 System flow of IGCC process.

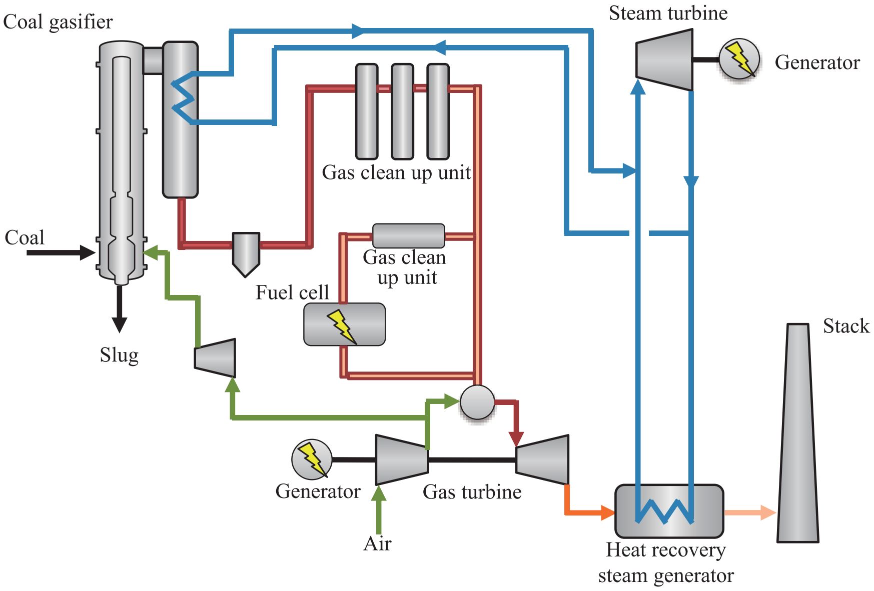

Fig. 7 System flow of IGFC using MCFC.

utilization of a high temperature gas turbine are important. In the future, the power generation efficiency of IGCC may be improved by the application of a hot gas cleaning system and high temperature gas turbine system.

The high temperature fuel cell can maintain high power generation efficiency. IGFC can reduce CO_2 emission more than IGCC. As a high temperature fuel cell, the molten carbonate fuel cell (MCFC) and the solid oxide fuel cell (SOFC) have been investigated.

Fig. 7 shows the system flow of IGFC. Pulverized coal is converted to gaseous fuel as in a usual IGCC system. Part of the gaseous fuel is introduced into a fuel cell and injected into a gas turbine combustor after generating electricity in the fuel cell, whereas in usual IGCC all of the gaseous fuel is introduced into a gas turbine combustor. Consequently, thermal power generation efficiency of IGFC surpasses that of IGCC. The major issues in the utilization of fuel cell are improvement in the durability of cell performance and the cost.

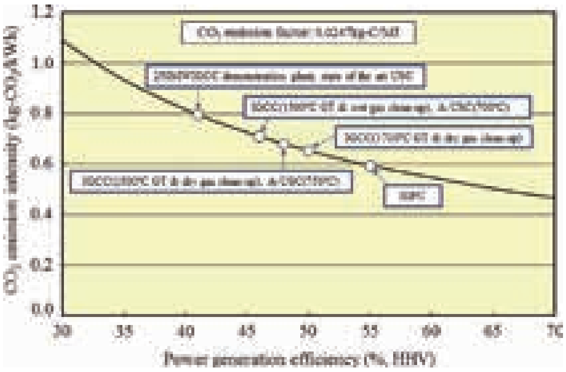

Fig. 8 Comparisons of power generation efficiency and CO_2 emission rate.

Fig. 8 shows the power generation efficiency and CO_2 emission rate of these high efficiency power generation

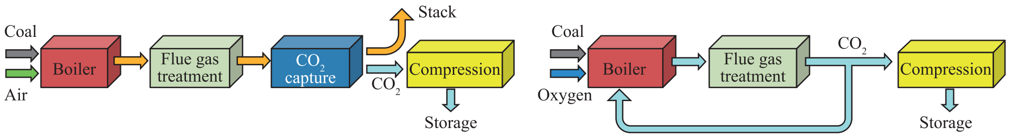

(a) Post combustion

(b) Oxy-fuel combustion

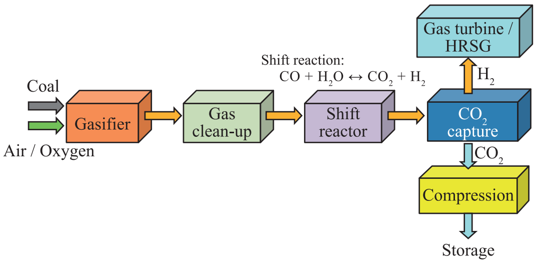

(c) Pre-combustion

Fig. 9 System flow of thermal power plant with CO_2 removal.

systems. Consistent with the improvement in power generation efficiency, the CO_2 emission rate is reduced.

2.3 CO_2 removal technology

To reduce CO_2 emission to a great extent, the CO_2 capture and storage (CCS) system is one of the foremost techniques. However, emission of CO_2 from a thermal power plant is of a large amount, therefore the CO_2 removal method requires a high consumption of power and thus a reduction in power generation efficiency. As a consequence, this method causes an extreme increase in power generation cost. **Fig. 9** shows some examples of a power generation system with CO_2 removal (Minchener et al., 2007). Post combustion and oxy-fuel combustion processes are for conventional coal-fired boilers, and pre-combustion process is for IGCC. The post combustion process captures CO_2 in the exhaust gases after the coal has been fully burned out. The oxy-fuel process consists of oxygen combustion with recycled exhaust gases, where the exhaust gasses are mainly composed of CO_2 and moisture. The generated as particles are collected in an electrostatic precipitator in the post combustion and oxy-fuel combustion system. The pre-combustion process captures CO_2 in a synthesis gas after conversion of CO into CO_2 by using the shift reactor. Generated ash particles are collected by a ceramic filter in the pre combustion system.

There are some ways of capturing CO_2 from flue gas such as separation with chemical/physical solvents (absorption), adsorption, separation with membranes and cryogenic separation. At any rate, capturing CO_2 from flue gas needs a huge amount of energy and decreases power generation efficiency. **Fig. 10** indicates the comparison of estimation result of power generation efficiency with and without CO_2 removal (Makino and Noda, 2011).

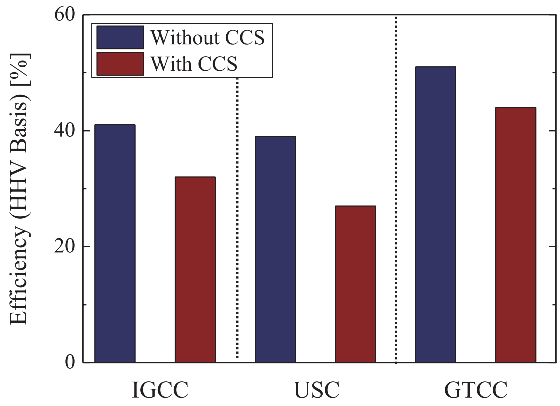

Fig. 10 Power generation efficiency with and without CO_2 removal. (Makino and Noda, 2011)

In general, the power generation efficiency of a thermal power plant with CO_2 removal is about 30 % lower as compared to that of a power generation plant without CO_2 removal. In these CO_2 removal systems, the CO_2 removal technology in the IGCC system is better than the CO_2 removal technology in the pulverized coal combustion power plant. For greater improvement of power generation efficiency of IGCC system with CO_2 removal, the development of high performance CO_2 separation technology is important.

3. Development of the oxy-fuel IGCC system

3.1 Outline of the system

As mentioned in a previous chapter, the consumption of a huge amount of energy has been a severe problem in installing the CO_2 capturing system in thermal power plants.

The pre-combustion system (**Fig. 9(c)**) converts syngas to a mixed gas of CO_2 and H_2 using a shift reactor and then separates CO_2 using a capture unit. The remaining H_2 is injected into gas turbine combustors as fuel. However, a shift reactor requires large amount of steam which is extracted from the steam turbine system; as a result, thermal efficiency becomes lower than in a conventional IGCC without CO_2 capturing.

Recently, a new concept of IGCC, namely the oxy-fuel IGCC system, which retains high efficiency while capturing $CO_{2,}$ has been proposed. The system applies the concept of the oxy-fuel combustion system (**Fig. 9(b)**) to IGCC. **Fig. 11** shows the system flow of the oxy-fuel IGCC system. Pulverized coal is fed into a gasifier with recirculated exhaust gas (mostly composed of CO_2) and added oxygen, and converted to syngas in a gasifier. Syngas is injected into gas turbine combustors as fuel in the downstream of dry type gas clean-up unit. The exhaust gas from the gas turbine is supplied to a regenerative heat exchanger and the heat exchanger heats up the gas at the combustor inlet using the heat of GT exhaust gas. As specific heat of CO_2 is 1.6 times larger than that of N_2, it is hard to utilize the heat in the gas turbine. Therefore, the regenerative heat exchanger plays an important role in the system. In contrast to a pre-combustion system, this system does not require a shift converter and a CO_2 capture unit because of the high CO_2 concentration in the flue gas. Therefore, the system can retain high efficiency (more than 42 % HHV) while capturing CO_2.

The other merit of the system is derived from the recycled CO_2 injection into a gasifier. A conventional gasifier works with a mixed gas of O_2 and N_2. Although N_2 is neutral in a coal gasification reaction, CO_2 can work as a gasifying agent in coal gasification. Therefore, the performance of a coal gasifier is expected to increase under the oxy-fuel IGCC condition.

From 2008, the authors have developed the proposed system with the support of New Energy and Industrial Technology Development Organization (NEDO) in Japan.

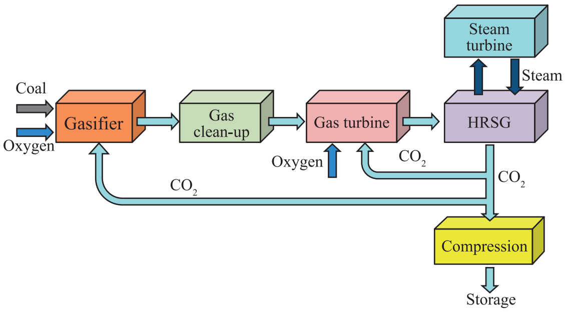

Fig. 11 System flow of the oxy-fuel IGCC system.

3.2 Development status of O_2-CO_2 blown coal gasifier

The O_2-CO_2 blown coal gasifier is a key component of the oxy-fuel IGCC system; hence it is of importance in evaluating the effect of CO_2 concentration on coalgasification reaction. The CO_2 effect in a coal gasifier and validity of the O_2-CO_2 blown coal gasifier have been experimentally investigated (Hamada et al., 2016). **Fig. 12** shows the schematic of coal gasifier used in their work. The lower chamber is called a “combustor” and the upper one is called a “reductor”. Two coal burner and two char burners were installed in the combustor, and two coal burners were installed in the reductor. The coal gasifier was a two-stage entrained flow type. The operating pressure was 2.0 MPa and the coal feeding rate was about 100 kg/h. Char discharged from the gasifier was collected by cyclone separator installed in the downstream of gasifier and recycled into the combustor as fuel. The coal ash was melted in the combustor and the melted ash, called “slag”, was dropped into an ash hopper installed under the gasifier. Coal gasification experiments were performed under the CO_2 enriched condition. **Fig. 13** shows the relationship between CO_2 concentration and gasifier carbon conversion efficiency (CCE) (Oki et al., 2014). Here, CCE is defined as (carbon in product gas)/(carbon in coal and char fed into gasifier). For almost all types of coal, CCE increases with CO_2 enrichment. The results show that CO_2 enrichment promotes the char gasification reaction and increases the coal gasifier performance. Present results were under the condition where CO_2 concentration was less than 30 % on account of the restrictions of the gas supplying system. However, CO_2 concentration in the actual oxy-fuel IGCC condition is expected to be

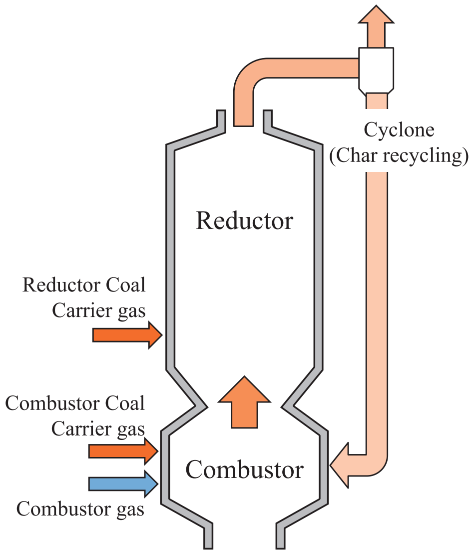

Fig. 12 Schematic of coal gasifier.

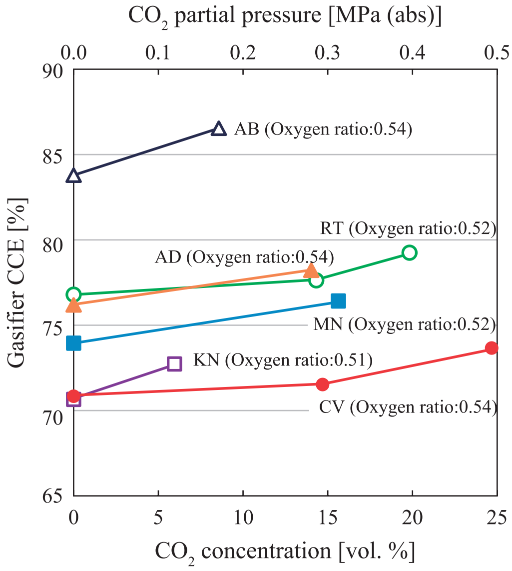

Fig. 13 Relationship between CO_2 concentration and coal gasifier performance. (Oki et al., 2014)

much higher. For our next step, it is planned to modify the gas supplying system to increase CO_2 concentration to as high as in the actual oxy-fuel IGCC condition.

4. Numerical analysis of O_2-CO_2 blown coal gasifier

In a previous chapter, current experimental results obtained in an O_2-CO_2 blown condition were introduced. As mentioned, CO_2 concentration was much higher than in the current experimental condition. Also, the size of the coal gasifier was much larger. In the early stages of system development, experimental studies using actual size equipment are quite difficult. Therefore, the authors have been developing numerical tools by which to estimate the validity of the system and performance of the O_2-CO_2 blown coal gasifier. The numerical method is based on CFD code coupled with chemical reactions such as the coal gasification reaction. The details of the numerical method are addressed in the author's previous paper (Watanabe et al., 2015).

The char particle reaction is the most important point in the modeling of the coal gasifier. Therefore, an appropriate particle reaction model was employed in the study (Umemoto et al., 2013).

The numerical simulation for the 100 kg/h class coal gasifier that Hamada et al. used was first validated comparing with experimental results. **Table 1** shows the calculation condition of the 100 kg/h class coal gasifier. Case 1 is the typical condition for air-blown IGCC system whereas in cases 2 and 3, 15 % and 25 % N_2 have been replaced by CO_2, respectively.

Table 1 Numerical condition of 100 kg/h scale coal gasifier.

Items		Case 1	Case 2	Case 3
Coal feeding rate	kg/h	100	100	100
Oxygen ratio	—	0.52	0.55	0.54
Composition of gasifying agent				
O_2	vol%	25	25	25
CO_2	vol%	0	15	25
N_2	vol%	75	60	50

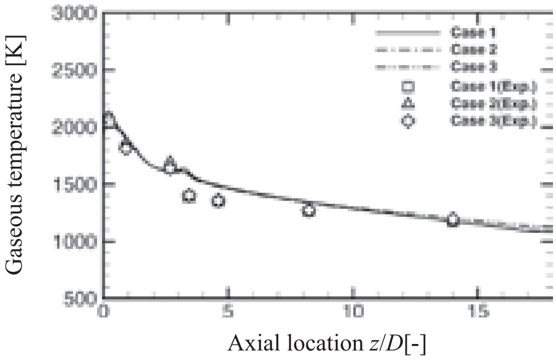

Fig. 14 Comparison of gaseous temperature distribution. Reprinted with permission from Tanno et al. 2015. Copyright: (2015) The Japan Institute of Energy.

Fig. 14 shows the comparisons of gaseous temperature distribution (Tanno et al., 2015). Axial location is normalized by gasifier diameter. Numerical results are in quite good agreement with experimental data for all cases. The burner in the combustor is located around $z/D = 0.5$ and the burner in the reductor is located $z/D = 3.0$. Gaseous temperature has a peak around the coal burner and rapidly decreases when getting closer to the reductor by reason of the endothermic coal gasification reaction. Gaseous temperature gradually decreases as a result of the heat release form the wall in the downstream of the reductor burner. **Fig. 15** shows the comparisons of product gas composition (Tanno et al., 2015). The major product gases are H_2, CO, CO_2 and H_2O. CO and CO_2 concentrations increase and H_2 decreases with increasing injected CO_2 concentration. This is due to the coal gasification reaction and water gas shift reaction. Numerical results also reflect the change in product gas composition.

From these results, the accuracy of the numerical results was validated. Subsequently, the numerical simulation for an actual size coal gasifier was performed. **Fig. 16** shows the schematic of the actual scale coal gasifier. The gasifier is two-stage entrained flow type. Four coal burners and four char burners are installed in the combustor and four coal burners are installed in the reductor. The operating and the coal feeding rate is 70 ton/h. **Table 2** shows the numerical conditions. A-25 case shows the typical conditions in an air-blown IGCC system whereas C25, C35 and C45 are the oxy-fuel IGCC conditions. 25, 35, and 45 denote oxygen concentration.

Fig. 17 shows the comparison of velocity vectors on horizontal planes. A25, the air-blown condition, shows an almost axisymmetric distribution and the strong swirling flow is formed by the jet from the four burners. Almost the same flow behavior is found in C25. The magnitude of the swirling flow decreases with increasing O_2 concentration (C35 and C45). This is due to the fact that the flow rate is reduced to maintain the same oxygen amount with increasing O_2 concentration. **Fig. 18** shows the gaseous temperature distribution around the combustor. For all cases, the high temperature region is located near the coal burners, and gaseous temperature rapidly decreases as the gases pass through the throat section to the reductor. This is due to the fact that the exothermic reaction (combustion) dominant in the combustor changes to the endothermic reaction (gasification) in the reductor, namely, a chemical quenching. The same tendency is also observed in C25, C35 and C45. It is also seen that gaseous temperature significantly decreases when N_2 in the gasifying agents is replaced by CO_2 with the same O_2 concentration (A25 to C25).

This is due to the difference in specific heat between N_2 and CO_2. On the other hand, gaseous temperature recovers with increasing O_2 concentration in the gasifying agent and almost the same level and distribution of tem-

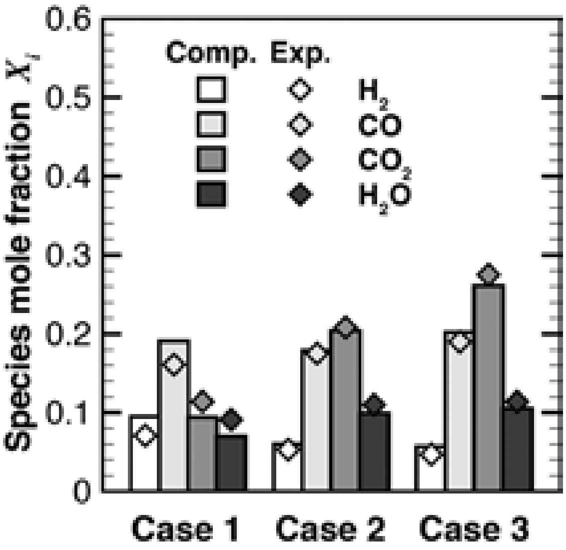

Fig. 15 Comparison of product gas composition. Reprinted with permission from Tanno et al. 2015. Copyright: (2015) The Japan Institute of Energy.

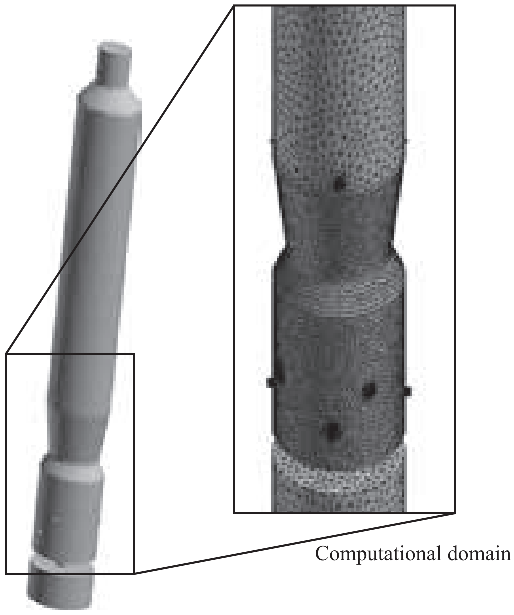

Fig. 16 Schematic of the actual scale coal gasifier.

Table 2 Numerical condition of actual scale coal gasifier.

Items		A25	C25	C35	C45
Coal feeding rate	t/h	70	70	70	70
Oxygen ratio	—	0.45	0.45	0.45	0.45
Composition of gasifying agent					
O_2	vol%	25	25	35	45
CO_2	vol%	0	75	65	55
N_2	vol%	75	0	0	0

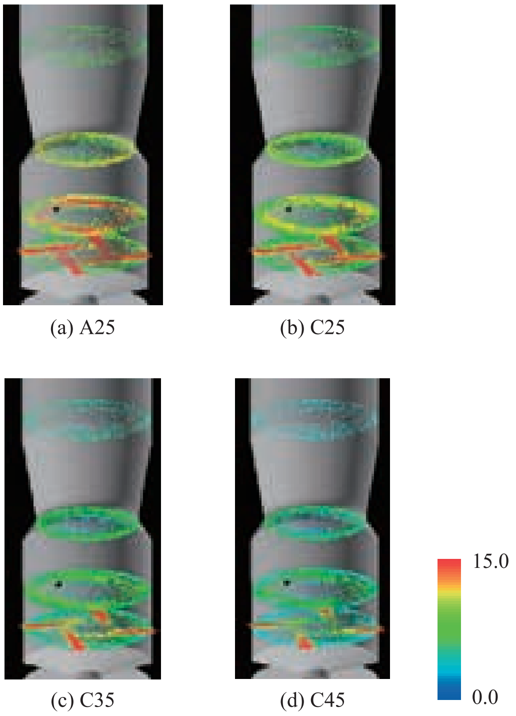

(a) A25 (b) C25

(c) C35 (d) C45

Fig. 17 Velocity vector on horizontal plane. Reprinted with permission from Tanno et al. 2015. Copyright: (2015) The Japan Institute of Energy.

perature as with A25 is observed, when the O_2 concentration is 35 % (C35). For a much higher O_2 concentration condition (C45), the gaseous temperature increases to that of A25. The temperature trend can be clearly seen in **Fig. 19** which shows the axial distributions of gaseous temperature. From the results, it is seen that even though gaseous temperature decreases as a result of replacing N_2 by CO_2 on account of the difference in specific heat, it can be recovered by optimizing the oxygen concentration.

Fig. 20 shows the axial distributions of the concentration of the major product gas. Just by replacing N_2 by CO_2 (A25 to C25) does not increase CO concentration very much, although the CO_2 concentration is very high. This is due to decrease in gaseous temperature in C25 sup-

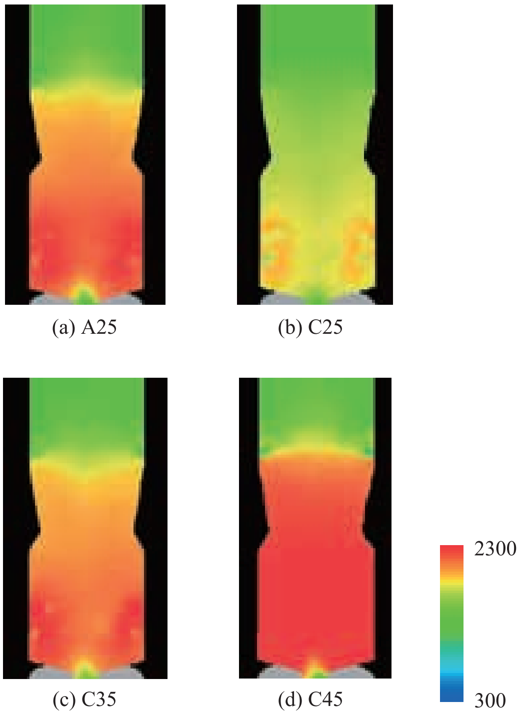

(a) A25 (b) C25

(c) C35 (d) C45

Fig. 18 Gaseous temperature distributions.

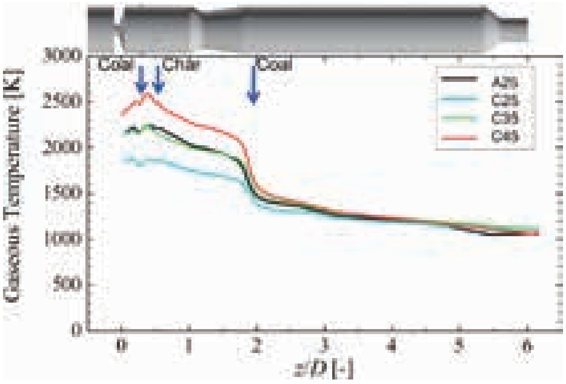

Fig. 19 Axial distributions of gaseous temperature. Reprinted with permission from Tanno et al. 2015. Copyright: (2015) The Japan Institute of Energy.

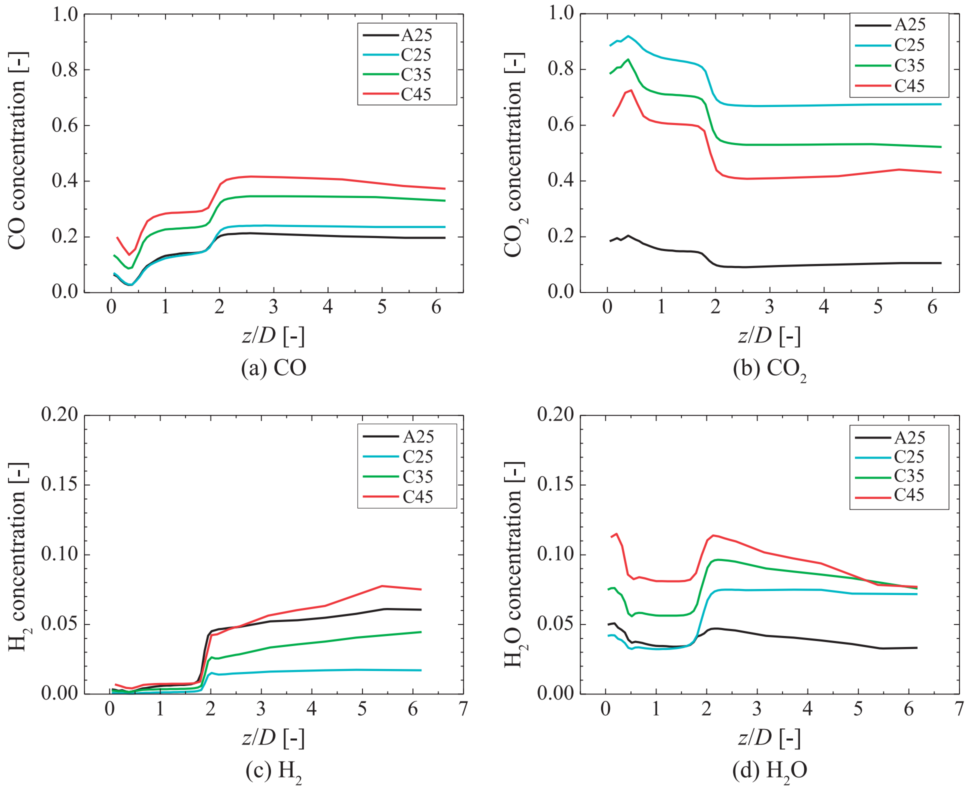

(a) CO (b) CO_2

(c) H_2 (d) H_2O

Fig. 20 Axial distributions of major product gas. Reprinted with permission from Tanno et al. 2015. Copyright: (2015) The Japan Institute of Energy.

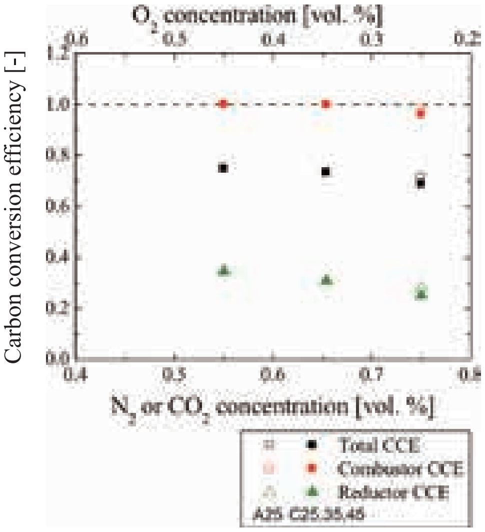

Fig. 21 Comparisons of carbon conversion efficiency. Reprinted with permission from Tanno et al. 2015. Copyright: (2015) The Japan Institute of Energy.

pressing CO production in the coal gasification. When O_2 concentration increases and consequently gaseous temperature increases for C35 and C45, CO concentration significantly increases. From these results, maintaining a high temperature in the combustor is found to be important in order to take advantage of the oxy-fuel IGCC condition.

Fig. 21 shows the comparisons of carbon conversion efficiency (CCE). Here, combustor CCE is the carbon conversion efficiency of the coal fed into the combustor, reductor CCE is that fed into the reductor and total CCE is that introduced into the gasifier. Combustor CCE reaches almost 100 % in all cases; the difference in total CCE is thus due to the reductor CCE. Replacing N_2 with CO_2 (between A25 and C25) slightly suppresses total CCE. This is due to the decrease in gaseous temperature seen in **Figs. 18** and **19**. However, total CCE for C35 exceeds that for A25 in spite of the same level of gaseous temperature. This is due to the high CO_2 concentration; the advantages of the oxy-fuel IGCC are therefore numerically indicated.

5. Conclusion

Coal is an important energy resource for meeting the future demands for electricity, as coal reserves are much more abundant than those of other fossil fuels. For future coal utilization, it is necessary to reduce CO_2 emission. It is thus very important to utilize low carbonized coal and carbon neutral biomass and develop new technologies for a high efficiency power generation system. For the further reduction of CO_2 emission, CO_2 removal technology is also effective, but requires high power consumption and cost. Recently, a new type of thermal power generation system which maintains high efficiency while capturing CO_2 has been proposed. The O_2-CO_2 blown coal gasifier is a key component of the system, therefore feasibility of the O_2-CO_2 blown gasifier and gasification characteristics were experimentally and numerically investigated in this paper.

(1) For the utilization of low rank coal and biomass in the pulverized coal combustion power plant, it is important to maintain the combustion profile of the sub-bituminous coal similar to bituminous coal combustion and develop drying or carbonizing technologies of biomass to improve the calorific value and pulverizing characteristics.
(2) The integrated coal gasification combined cycle system (IGCC) and the integrated coal gasification fuel cell combined cycle system (IGFC) can reduce CO_2 emission because of their high efficiency power generation characteristics.
(3) To reduce carbon dioxide emission to an extreme amount, CO_2 removal technology is very effective, but usual CO_2 removal technologies require high power consumption and cost. As a high performance power generation system with CO_2 removal, the oxy-fuel IGCC system is promising.
(4) The coal gasifier performance under the oxy-fuel IGCC condition was numerically investigated and the feasibility of the gasifier in the system was validated. Furthermore, the oxy-fuel IGCC condition has the possibility to increase coal gasifier performance compared with the conventional IGCC.

Acknowledgements

This work was in part supported financially by the New Energy and Industrial Technology Development Organization (NEDO) program “Innovative Zero-emission Coal Gasification Power Generation Project”, P08020.

Nomenclature

CCE	Carbon conversion efficiency
D	Diameter of gasifier
X_i	Species mass fraction
z	Axial location of gasifier

References

Hamada H., Evaluation of CO_2-enriched gasification characteristics using small coal research gasifier, Proceedings of

Annual conference of JSME (2016)

Ikeda M., Kozai Y., Makino H., Emission characteristics of NOx and unburned carbon in fly ash of sub-bituminous coal combustion, JSME International Journal Series B Fluids and Thermal Engineering, 45 (2002) 506–511.

Kanda H., Makino H., Miyahara M., Energy-saving drying technology for porous media using liquefied DME gas, Adsorption, 14 (2008) 467–473.

Makino H., Noda N., Reduction technology of carbon dioxide emission from a coal utilized power generation system, WIT Transactions on Ecology and the Environment, 154 (2011) 83–92.

Minchener A.J., McMullan J.T., Sustainable clean coal power generation within a European context – The view in 2006, Fuel, 86 (2007) 2124–2133.

Oki Y., Hara S., Umemoto S., Kidoguchi K., Hamada H., Kobayashi M., Nakao Y., Development of High-efficiency Oxy-fuel IGCC System, Energy Procedia, 63 (2014) 471–475.

Tanno K., Watanabe H., Makino H., Numerical simulation of coal gasifier for oxy-fuel IGCC system, Journal of the Japan Institute of Energy, 94 (2015) 403–412.

Umemoto S., Kajitani S., Hara S., Modeling of coal char gasification in coexistence of CO_2 and H_2O considering sharing of active sites, Fuel 103 (2013) 14–21.

Watanabe H., Tanno K., Umetsu H., Umemoto S., Modeling and simulation of coal gasification on an entrained flow coal gasifier with a recycled CO2 injection, Fuel, 142 (2015) 250–259.

Watanabe H., Ahn S., Tanno K., Numerical investigation of effects of CO_2 recirculation in an oxy-fuel IGCC on gasification characteristics of a two-stage entrained flow coal gasifier, Energy, 118 (2017) 181–189.

Author’s short biography

Kenji Tanno

Dr. Kenji Tanno is a senior research scientist of CRIEPI (Central Research Institute of Electric Power Industry) in Japan. He received his doctoral degree in 2007 in Mechanical Engineering at Kyoto University. He was employed at CRIEPI in 2007 as a research scientist in coal combustion group. His research covers numerical simulation of coal combustion and gasification, flue gas treatment technology and non-contact laser applied measurement for multiphase combustion.

Hisao Makino

Dr. Hisao Makino is an executive research scientist of CRIEPI (Central Research Institute of Electric Power Industry) in Japan. He graduated from Kyoto University in 1977 and received M.E. degree in Chemical Engineering from Kyoto University in 1979 and a Ph.D. in Chemical Engineering from Kyoto University in 1995. He was employed at CRIEPI in 1979 as a Research Associate in combustion research section. His research interests are powder technology, coal utilization technology for the energy supply and environmental protection. Current main subjects are an advanced combustion technology for pulverized coal, upgrading technology for low rank coal and flue gas treatment technology.

KONA Powder and Particle Journal No. 35 (2018) 150–159/Doi:10.14356/kona.2018010 Special Contribution

Historical Review of Pneumatic Conveying[†]

George E. Klinzing

[1] *Swanson School of Engineering, University of Pittsburgh, USA*

Abstract

This document attempts to cover the development of pneumatic conveying over the past 100 years or so. The individual researchers who worked in the field are highlighted along with their photograph which is included at the end of the document. As time progressed in the scientific and engineering developments of these years one see a transition from a purely experimental approach with considerable empiricism to adapt to the development of numerical procedures in attempt to predict the flow characteristics. The basic physics of the phenomena of pneumatic still is not completely understood and new and novel experimental techniques are always welcome in the field.

Keywords: pneumatic conveying, dilute phase, dense phase, measurements, numerical

1. Introduction

Pneumatic conveying appears to have been in existence for well over 100 years. The literature indicates that grain was being unloaded from ships from 1856 to 1876 in the ports of London, Rotterdam, Hamburg and Leningrad. **Fig. 1** shows this operation of a Russian ship loading of grain in 1882. Possibly other applications did exist before this but this is the only one found to date. The Russian literature most likely exists but is difficult to discover.

2. Air movers

It is said that pneumatic conveying took off with the invention of the Roots Blower by the Roots brothers, Philander and Francis, in Indiana in 1859, Roll (1931). At that time the blowers were used in supercharging the internal combustion engine and first being employed in blast furnaces to help with the melting of iron. Undoubtedly compressors did exist before this so that high pressure air could be obtained to utilize in the pneumatic conveying operations. Vacuum conveying was also possible about the same time frame.

The vacuum pump is attributed to the Romans and later in the 13th century the Arabs were using suction pumps. The pumps surfaced in Europe in the 15th century. The first vacuum pump is attributed to Otto von Guericke in 1654.

Compressors have their early beginning in 1762 with John Smeaton followed by a compressor producing about 15 psi. Improvements were made in 1872 with a compound air compressor.

Thus one sees that the vacuum pumps and the air compressors pre-dates the air blowers so pneumatic conveying could have taken place in very early times. We have no record or mention of pneumatic conveying previous to the Russian grain unloading citation.

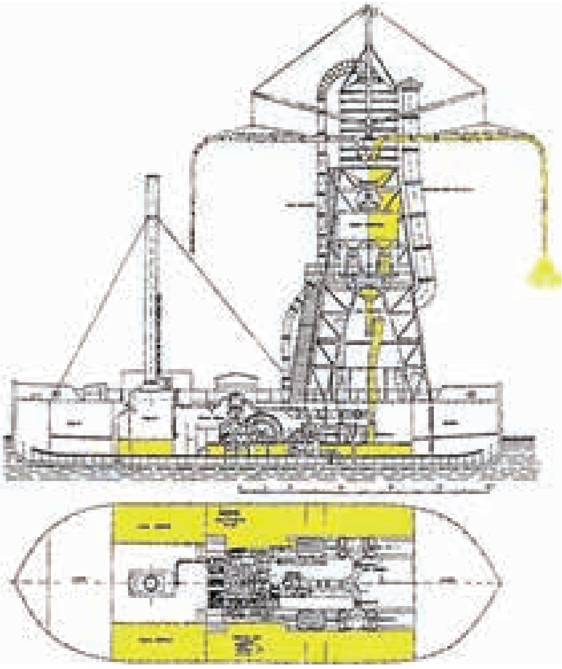

Fig. 1 Grain Unloading in 1882.

[†] Received 23 February 2017; Accepted 13 June 2017
J-STAGE Advance published online 30 July 2017

[1] Benedum Hall 700 O'Hara Street | Pittsburgh, PA 15261, USA
E-mail : Klinzing@pitt.edu
TEL : +1-412-624-4604 FAX: +1-412-624-4618

3. Earlier pneumatic conveying studies

The earliest technical exploration into pneumatic conveying occurred in Germany by Gasterstadt (1924) at the Technische Hochschule Dresden. The work is reported in the German Engineering Journal, VDI. The work reported a linear behavior of the pressure drop in a straight section of pipe with the solids flow rate. The flow was dilute in nature. This concept was used by Cabrejos and Klinzing (1992) to develop a flow meter for measuring the solids flow rates with a system of transducers and valve to explore the full range of experimental conditions. Using the data from a large conveying system the linearity of the system pressure drop with the solids flow rate (**Fig. 2**) was constructed by Baker (1997).

Following this work the field seemed to be quiet with publications until after the Second World War when activity at Karlsruhe University began. The Karlsruhe group flourished under Rumpf, (Students-Leschonski, Molerus, Schwedes, Sommer, Werther), working in Process Technology. Teamed with Barth, (Students-Reh, Muschelknautz, Leineweber, Moller, Bohnet, Weber, Rizk), who worked in Conveying Flow Technology, to address all aspects of solids processing. Barth developed a solids friction factor term, λ_z which has been used extensively in the literature.

$$\text{Solids Friction} = \lambda_z\ (\text{velocity of the particle})^2/2D \qquad (1)$$

Rizk (1973) through his dissertation work with Barth developed the first equation for the saltation velocity of polymer particles and explore the material of construction of the pipe to ascertain the frictional terms developed by the interaction of the particles with the wall. About the same time Zenz and Othmer published a book of Fluidization and Fluid-Particle Systems (1960). This work contained the first known experiments which Zenz performed in pneumatic conveying which according to legend were performed in his garage with a vacuum cleaner as an air source. Zenz was able to develop a phase diagram which is used extensively in the analysis of pneumatic conveying. See **Fig. 3**. In Japan pneumatic conveying blossomed under the direction of Morikawa who mentored such noted researchers as Tsuji and Tomita. Tomita began his contributions to pneumatic in 1971 and had a long and successful career at Kyushu Institute of Technology. His work was mostly experimental but he did delve into numerical simulation later in his career. He also addressed the issue of introducing swirl into the initial part of the pipe in order to enhance the transfer of particulate solids.

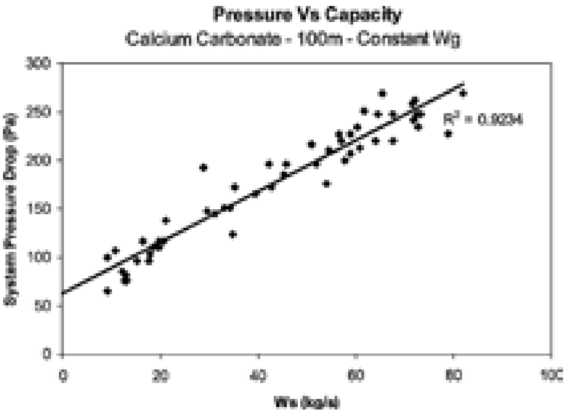

Fig. 2 System Pressure Drop as a function of the solids flow rate. (With permission of the author.)

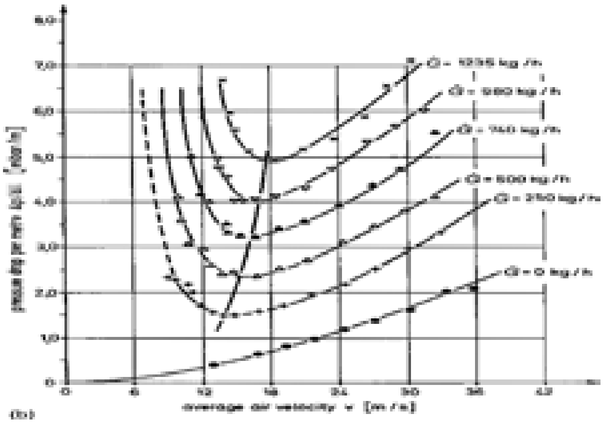

Fig. 3 Zenz diagram from pressure loss versus the conveying velocity at various flow rates, Rizk (1973) (With Permission of the author).

4. Germany

As noted above, before the 1950's Gasterstadt (1924) did some very basic studies in pneumatic conveying. His results of the pressure drop linearity with flow rate for dilute solid flow was the first flow meter of its kind. In addition he performed pneumatic conveying studies on a 100 m long horizontal pipe.

As noted above, in Germany the solids processing concept and its study began in earnest with Rumpf of Karlsruhe University along with other senior colleagues especially Barth who concentrated his studies in pneumatic conveying providing a rich source of students in solid processing. Almost all of the researchers in Germany in this solids processing through 1960's to 1990's came out of Karlsruhe. Many of the existing researchers can also trace their academic lineage back to Karlsruhe.

Professor Barth's untimely death did not stop the research machine from going. Some of the notables from Karlsruhe who populated Europe's elite of solids processing were Leschonski, de Silva, Schoenert, Loeffler, Molerus, and Schwedes. The Karlsruhe group spread throughout Europe taking professorships or senior re-

Table 1 Researcher from the Karlsruhe Group.

Last name	Affiliation
Leschonski	Clausthal Technical University
de Silva	Tel-Tek in Porsgrunn, Norway
Molerus	University of Erlangen
Rizk	BASF
Sommer	BASF—Technical University of Munich
Muschelknautz	Bayer—University of Stuttgart
Weber	Karlsruhe University
Bohnet	BASF—Technical University of Braunschweig

search positions in industry. Many started in industry and then moved on to universities.

Krambrock (1979–2004) is another German pneumatic conveying practitioner who has been prolific in the development of patents in pneumatic conveying and solids processing. He worked initially with Bayer collaborated with Muschelknautz who was also at the same firm at that time. He then joined Waeschle and from there formed his own firm eventually cooperating with Zeppelin and Wilms. Muschelknautz (1969, 1985) after the University of Karlsruhe started his industrial career with Bayer and then joined the University of Stuttgart.

Sommer (2009, 2011) from the Technical University of Munich and his students developed a clever way of measuring the wall stress in dense phase flow as well as exploring the structure of dense phase flow with two-dimensional tomographics. These results showed that the voidage is not uniform across the pipe cross-section.

Bohnet after working for BASF joined the faculty at the Technical University of Braunschweig and studied long distance conveying and cyclone operation in solids processing. He and his colleagues, Gottschalk and Morweiser (1997) produced a work on modern design of cyclones.

Molerus (1993) of the Technical University of Erlangen who also was Karlsruhe and Rumpf educated concentrated mostly on developing theories for solids processing operations including pneumatic conveying.

5. Japan

In Japan Iinoya at Nagoya and Kyoto Universities assembled a team of students to begin to address the challenging area of solids processing from all levels. His lab produced many of the researchers in this field throughout Japan for the next 20 years or more. In fact it was challenging for other Japanese researcher who did not have the Nagoya or Kyoto stamp to advance. In pneumatic conveying Morikawa of Osaka University began to research pneumatic conveying and added a well-known student to his research team; Tsuji. Morikawa (1982) and Tsuji did many projects together mostly experimental before branching out to numerical simulations.

Tsuji followed Morikawa as the Principal Professor at Osaka University and since has retired being followed by Tanaka, his student. They have produced a large volume of students who are world renown in the modeling and simulations area of solid processing and pneumatic conveying. After retirement from Osaka, Tsuji became the technical director of the Hosokawa Research Foundation. He still participates in symposium on numerical simulations although not formally attached in any entity.

In Japan there were a few other hot spots of pneumatic conveying research. Tomita of Kyushu Institute of Technology (1971) contributed extensively to the literature covering a wide spectrum of solids transport from pneumatic to hydraulic to capsule. As noted above he studied induced rotational flows to numerical simulations in dense phase flows. Tashiro was a student of his and he now at Kurume Technical University. Tashiro has done some fascinating work on the rotational motion of particle in dense phase flow.

At the large Nihon University Ochi has done pneumatic conveying research mostly in the dilute phase regime although he has also explored some dense phase work

At Kyoto University Masuda (2003) concentrated on trying to understand the electrostatic phenomena that occurs in pneumatic conveying. He performed some very basic work and also has explored measurement devices and flow measurement in pneumatic conveying. These are really fundamental in all electrostatic interactions.

6. United states

Much of the U.S. pneumatic conveying work did not come out of one font as was in Germany with Karlsruhe. With the importance of energy and coal, fluidizations studies were plentiful and many industrial companies and research organization developed extensive expertise in this field which is ancillary to pneumatic conveying. The work of Yang of Westinghouse and Knowlton at GRI and later PSRI are most noteworthy. Novel and creative experiments and devices were developed being placed almost immediately on the industrial scale. Expertise developed in the solids processing and fluidization area at Exxon, Texaco, Shell and others. Agrawal from Union Carbide was their resident expert in pneumatic conveying design with a specialty in dilute phase transport. Dow Chemical developed similar solids processing expertise under the leadership of Jacob and Dhodapkar. They fostered research in solids processing in the chemical industry making significant contributions to the state-of-the-art. At Dupont Bell spearheaded the pneumatic conveying activities in their solids processing team lead by Reg Davies. Bell explored many relevant industrial issues including the use of multiple bends in conveying systems and particle attrition.

The area of consulting engineering cannot be forgotten when it comes to pneumatic conveying. Solt after many years with Fuller Company carried out extensive testing on a wide variety of materials and designs. Presently he is teamed with Hilbert in having webinars through the magazine Bulk Solids Engineering. Solt's **"Point to Ponder"** in the same magazine is classic with series now being sold separately. Solt did extensive short course offerings with the Center for Professional Development, AICHE and the University of Wisconsin. Jenike and Johanson is now also offering consulting services in pneumatic conveying. In Great Britain Bates has been an active contributor to the consulting field in addition to providing articles on practical guidelines on solids processing.

As mentioned before the field of pneumatic conveying did not spring from a single source but had a variety of different researchers at universities approach the topic. Michaelides (1984) did some interesting work on the solids friction factors. Soo developed unique mathematical analyses for pneumatic conveying with a heavy emphasis of electrostatic generation. Sinclair-Curtis (2015) probed both simulation and modeling proficiencies as well as experimental verification in her work. Sinclair-Curtis contributed heavily to the numerical simulations in solids processing including pneumatic conveying. Work in the area of constitutive models for stress/viscosity is noteworthy. She also carried out fundamental studies using Laser Doppler Velocimetry for both dilute and dense phase conveying. Most recently she is addressing the issue of particle shape which has been a challenge in the field from the beginning.

Klinzing and his students carried out experimental work in a wide scope of topics related to pneumatic conveying; electrostatics, drag reduction, meter development, long distance conveying, dense phase resulting in a number patents and copyrights. In collaboration with Rizk, Marcus and Leung a comprehensive book on pneumatic conveying was produced and is in its 3rd edition (2010).

7. Great Britain

Early work in Great Britain began with Rose and Duckworth (1969) who did research in pneumatic conveying at Kings College, University of London and City University London. Later, in the early 1970s, Mason developed a strong pneumatic conveying facility and expertise at Thames Polytechnic in London. He attracted Mills as a student who later developed into a trusted colleague in pneumatic conveying Mills and Mason (1985). Mills has published widely and lectures often. Mills has had a close collaboration with Agarwal at IIT—Delhi in India in the transport of fly ash (1999, 2000). Reed also was part of the Thames group and took a real leadership role in research and administration later being part of Greenwich University. Mills initiate work with Mason on bend erosion started a long and productive career in pneumatic conveying provide a compendium of design procedures in the field developed from his many studies (1985). He focused on different feeders exploring the blow tank operation in considerable detail. He began his work at Thames Polytechnic and then at Glasgow Calendonian University and then private consultancy. Mills has work extensive with Agarwal of the Indian Institute of Technology in New Delhi on the transport of flyash. Extensive studies were performed under this partnership.

Bradley at the University of Greenwich has developed a large consultancy that goes under the name of the Wolfson Center (2008). While in Scotland, Mason with Jones and Mills attracted two researchers who developed some interesting basic concepts in measurements in pneumatic conveying: McGlinchey (1999), Pugh and Marjaovic. They continued to develop novel flow measurements devices and research in pneumatic conveying. During a sabbatical stay at Glasgow Calendonian University Levy collaborated strongly with David Mason and Marjanovic to produce three notable works in pneumatic conveying; Mason, Marjanovic (1998), Mason and Marjanovic (1998) and Mason and Levy (2001). In addition his work on a nozzles with Jones is also noteworthy; Levy, Jones and Das (1996).

At Cambridge University in Great Britain Nedderman supervised Konrad; Konrad, Harrison, Nedderson, and Davidson (1980), in theoretical and experimental analysis of dense phase conveying using the basic principles of soil mechanics. Their work is classic and the real beginning to the basic understanding of dense phase flow. Konrad had a brief stint at Virginia Tech to teach and then moved to Exxon changing fields somewhat. Lyndon Bates is a well-known consultant from Great Britain but his expertise is used widely around the world. He published review articles and guidelines often in the field of solids processing.

8. South Africa

South Africa came into the pneumatic conveying realm with a great force in moving large quantities of solids through large pipelines over long distances. Marcus began this effort through his dissertation work and continued on with a faculty position in Mechanical Engineering at Witwatersrand University. The mining industry and the coal conversion activities of Sasol supplied a rich variety of challenging problems in pneumatic conveying. Marcus supervised about a dozen students who went on to continue in the field making contributions to industry and academia. The most successful ones were Meijer with Bateman (ELB, CEO) and Sheer (1995) who now is on the faculty at Witwatersrand (Wits) after working for a gold mining company. Unusual applications of pneumatic conveying were seen in carrying ice into gold and diamond mines for cooling. Long distance conveying processes were explored by Marcus and his students having some of the longest examples of actual commercial systems. Presently there is some work going on at Wits and the University of Johannesburg.

9. Australia and New Zealand

Australia has been a hot bed for solids processing lead by their vast mineral industry. Their ability to design large scale systems is found by their large scale experimental facilities both at Newcastle and Wollongong. Roberts started the bulk solids work in Australia before moving to the University of Newcastle in 1974. Arnold, Roberts' first research student, continued the work at Arnold at University of Wollongong in close communication with Roberts of Newcastle University. Arnold specialized in bin and hopper design as well as mechanical transport with belt conveyors. Wypych who studied with Arnold moved the progress forward in large scale pneumatic conveying. He always obtained data on experimental facilities that were comparable to industry. Wypych has been able to explore pneumatic conveying with realistic size conveying lines in both distance and pipe diameters. He has modelled dense phase transport with a two layer flow theory. The minimum transport boundary was studied with flyash and cement. He studied dense phase transport of various materials and probed the frictional term in pneumatic conveying as well as scale-up procedures. Wypych is active in his interactions with industry through consultancies.

Wypych guided a number of very talented students in his laboratory; Mi and Pan come quickly to mind. Pan has returned to China and leading a larger effort in China at this time, (2013, 2014, 2016)

About 15 to 20 years ago Newcastle University was able to attract Jones to their research group at The University of Newcastle Research Associates (TUNRA). Jones left the Mason group at Caledonian University in Glasgow, Scotland. Jones (1987, 1990, 1994), has been successful in leading the pneumatic conveying group at Newcastle and has grown the group into a well-recognized team. Jones served as the advisor and mentor to Williams and Krull both who have become recognized for their innovative studies. The Newcastle team is active in most of the solids processing conveying conference world-wide.

Jones explored various topics in pneumatic conveying. He and his colleagues probed the performance of blow tanks; product classification in relationship to pneumatic conveying; the effect of gas density on pneumatic conveying; bench scale tests for assessment of pneumatic conveying; blending and segregation of coals for pneumatic conveying; suction nozzles; fly ash, sand and cement properties in conveying; dense phase conveying; Behera, Das (2000)

In New Zealand Davies and Tallon (2006, 2014, 2015) collaborative work yielded a number of contributions to the field in measurements. Many of these resulted in patents for new devices using tracers in the flow and acoustic pulsations did considerable work on developing flow meters which a variety of sensors mainly based on acoustics. Davies and Gunabalan (1998) attacked the difficult problem of assessing the effect of back-to-back bends in conveying system. These meters have been proven to work in pneumatic conveying operation and in other solids processing applications. Many of the devices developed where applied to other solid processing systems.

10. Israel

A little later in the time line researcher in Israel began to explore the intricacies of pneumatic conveying lead by Kalman (1998, 1999). There were other researchers in two phase flow system in Israel who approached the topic in a fundamental basic analysis such as Hetsroni at the Technion and Taitel at Tel-Aviv University. Kalman spurred research to attrition, wear and threshold velocities and produced a number of students who advances these topics. Kalman's work in pneumatic conveying spans a number of different aspect of the technology. Besides his leadership in the International Conveying and Handling of Particulate Solids conferences and procedures he began with studies on size reduction and attrition phenomena is pneumatic conveying. He has explored the behavior of particles under different shear and impact conditions as well as multiple impacts. He probed deeper into this phenomena and was able to show the behaviors of stresses in particles over a wider range of temperatures. He and his students addressed the pickup and saltation velocities of particle in pneumatic conveying systems producing a generalized approach which is applicable for both pneumatic and hydraulic conveying. Some recent work in particle velocities in conveying both in bends and feeders has led to some interesting observations.

Kalman also works closely with Levy (2011) expanding their work to modeling and simulation with wide applications in solids processing; Han, Levy and Kalman (2003).

Kalman has questioned the basic premises on which most of pneumatic conveying is built and examined previous data assiduously. Most notable of Kalman's students have been Rabinovich, Goder, Portnikov. Shaul and others. The research of Levy (2000) concentrated on numerical simulations of pneumatic conveying and other solids processing operations. The effect of a bend on the particle cross-section concentration and segregation in pneumatic conveying systems and finite-volume for conservations of mass and momentum are a few examples.

11. Norway

When de Silva came to Porsgrunn in Norway to head up the solids processing group at Tel-Tek he began to construct a laborator he termed an insulated tent housing the pneumatic conveying facilities. De Silva organized a series of conferences on reliability of solids flow terms REPOWFLO. Some fundamentals studies were carried out as well as testing of powders and bins and hopper design. He worked closely with Enstad on particle characterization and behaviors. De Silva was able to attract Datta to his group to concentrate on pneumatic conveying and then followed by Ratnayake who is active today.

12. Chile

In Chile Francisco Cabrejos has been a force in pneumatic conveying working for Jenike-Johanson and also teaching at the Universidad Tecnica Federico Santa Maria in Valparaiso, Chile. His work has been mainly in the mining industry often carrying out transport at high altitudes where the mines are located. He has written a book on pneumatic conveying in Spanish entitled “Transport Neumatico” by Editorial USM (2013).

13. Interaction of pneumatic conveying with other solids processing operations and designs

Pneumatic conveying developed initially quite separately from other operations in solids processing although determination of the properties of the materials conveyed were always recognized as being an important parameter. The size, shape, distribution of both, true densities and bulk densities were essential in the analysis and experimentation. With the classification of Geldart (1973) into his A, B, C, and D type powders interest began in earnest to utilize this classification in reference to the ability and modes of conveying. It was quickly recognized as it was in the fluidization field that A type powders were one of the easiest to be conveyed. The C—cohesive powder were a challenge with such materials as coal, flyash and cement being representative of these powders. The stresses that seen in dense phase conveying are similar to the analysis of bins and hoppers and Konrad (1980) under the direction of Nedderman recognized this and formulated the first attempt to understand dense phase conveying using first mechanistic principles. The feeder for pneumatic conveying systems vary from the simple to the very complex and their inter-relationship with bins and hoppers is imperative to understand. The same principles used in bins and hoppers and especially with outlet sizing is important to pneumatic conveying. In addition collection of the product at the end of the conveying lines requires knowledge of cyclone operation, filters and electrostatic separators depending on the size and characteristics of the solids being conveyed.

14. Modeling and simulation

Tsuji and Morikawa were the first to apply numerical techniques to the simulation of pneumatic conveying (1982). Since this beginning there has been a strong addition of more studies in the numerical simulation area which continues until today. Each investigator has refined the models that they employ and relaxed assumptions. In 2006 Tsuji gave a good summary of the status of modeling in pneumatic conveying and other solids processing operations. Theuerkauf in 2012 also presented a comprehensive survey of simulations and modeling in solids processing. Modelers have attempted to find experimental data with which to compare their findings with the work of Tsuji and Morikawa using LDV to measure the motion of particles in pneumatic conveying. Other researchers who explored the modeling and simulation from the sue of discrete element methods to numerical fluid dynamics modeling have been Yu (2008), Tomita, Sinclair-Curtis (2012, 2013a, 2013b), Sommerfeld, Levy and others.

Tsuji (2006) has given an excellent summary of computational activities related to solids processing including pneumatic conveying. He noted that these computations can be separated into four groups; 1. gas-particle multiphase flows, classification according to numerical analysis, 2. collision-dominated flow and Direct Simulation Monte Carlo methods (DSMC) and 3. the contact-dominated flow and 4. the Discrete Element Method (DEM).

Theuerkauf in his talk at Conveying, Handling of Particulate Solids-7 conference gave a good summary of modeling granular flows using the DEM. He also considered the DEM to be part of the modeling toolkit for design over the coming 10 years.

14.1 The need for further work

The reliable design of bulk solids storage systems was given a significant boost when Andrew Jenike and Jerry Johanson were able to develop a systematic design procedure based on bench scale bulk property testing. From a reasonable sized representative bulk sample of the material to be stored, material testing provides key parameters that can be used directly in an analytical design procedure. At present this is not possible in pneumatic conveying. Although many workers have attempted to classify bulk materials according to their pneumatic conveying mode of flow capability, none of the classifications can predict with certainty particularly around boundaries between categories of behavior. Neither can these classifications be used to establish the critical relationship between air flow rate, material flow rate and pressure gradient. This is an area of work that needs further development.

Many of the theoretical approaches that have been developed are empirically based. While this approach often yields good quality correlations for specific sets of circumstances it does little to further the real understanding of the mechanisms. The significant developments and reduction in cost of high quality instrumentation opens up many avenues for further investigation. An example of this is the miniaturization of technology which will allow the investigation of a much wider range of parameters in real time. An example of this is the work of Klinzing and Clarke (2012) in the development of the smart particle which will allow the direct measurement of particle acceleration. This will provide useful data to improve modelling and understanding of the mechanisms involved in pneumatic conveying.

15. Technical conferences related to pneumatic conveying

As noted previously, the literature in pneumatic conveying mostly like began in Germany with VDI and followed in the U.S. with the book on Fluidization and Fluid-Particle Systems by Zenz and Othmer (1960). Regular technical meetings began with Pneumotransport in 1972 lasting for about twelve years followed with Pneumatech lead by Stan Mason. Now-a-days the topic is regularly treated in most chemical and mechanical engineering journals along with specialized journals such as Powder Technology, Granular Matter, Multiphase Flow, Chemical Engineering Science and the American Institute of Chemical Engineers. The series of technical meetings lead by Kalman called Conveying and Handling of Particulate Solids (CHoPS) has provided a wide venue for researchers throughout the world. These conferences are held every three years and CHoPS now beginning its 9th conference in 2018.

16. Future

Predicting the future is always dangerous because unforeseen development can surface which can upset the whole apple cart. At the present time there will undoubted more and more simulations and modeling approaches which can handle more and more particles that are not only spherical in nature. We have to address the non-spherical systems and multi-distributions and cohesive behaviors which occur in nature. In order to obtain the proper information to input into the models more basic physics must be explored experimentally. The ultimate goal is to be able to model a new system with new properties and guarantee that the behavior is realistic. When this occurs, we will have programs that can operate in a reasonable amount of time to give designs that are true to the nature of the material and the system. In many respects pneumatic conveying has the same future that all solids processing systems will have. To set a time frame for this will be a wild estimation but in 30 to 40 years we should be on our way to achieve our objective.

References (Selected)

Agarwal V.K., Bharathi M.D., Mills D., The influence of particle size range on the pneumatic conveying of fly-ash, Powder Handling & Processing, 11 (1999) 197.

Agarwal V.K., Bharathi M.D., Mills D., The influence of material grade on pneumatic conveying system performance, Powder Handling & Processing, 12 (2000) 239–246.

Baker J.D., Performance analysis and control of dilute phase gas-solid systems employing neural networks and optimization techniques, Ph.D Dissertation, University of Pittsburgh, 1997.

Behera S., Das S., Desirable conveying characteristics for pneumatic transportation of flyash, sand, cement and crushed bath, Powder Handling & Processing, 12 (2000) 23–25.

Bohnet M., Gottschalk O., Morweiser M., Modern design of aerocyclones, Advanced Powder Technology, 8 (1997) 127–161.

Bunchatheeravate P., Fujii Y., Matsusaka S., Curtis J., Prediction of particle charging in a dilute pneumatic conveying system, AIChE Journal, 59 (2013) 2308–2316.

Cabrejos F.M., Transporte Neumatico, Editorial USM (2013).

Cabrejos F.M., Klinzing G.E., Solids mass flow rate measurements in pneumatic conveying, ASME Winter Annual Meeting, 92-WA/FE-3, Anaheim, CA. (1992).

Davies C., Gunabalan G., Effect of back to back bends on pressure loss in dilute phase pneumatic conveying, WCPT 3. (1998)

Davies C., Tallon S., X-ray measurement of voidage in a flat-bottom 2-D silo with central discharge, AIChE Meeting (ISBN: 978-0-8169-1086-1) (2014).

Davies C., Tallon S., Measurement of Flowrate of Particulate Solids, AIChE Meeting (ISBN: 978-0-8169-1094-6) (2015).

Deng T., Farnish R.J., Bradley M.S.A., Evaluation of particle degradation due to high-speed impacts in a pneumatic handling system, Particulate Science and Technology, 26 (2008) 438–450.

Fargette C., Jones M.G., Nussbaum G., Bench scale tests for the assessment of pneumatic conveying behaviour of powders, Powder Handling & Processing, 9 (1997) 103.

Gasterstadt J., Die experimentalle Untersuchung des pneumatischsen Fordervorganges, VDI, 68 (1924) 617–624.

Geldart D., Types of gas fluidization, Powder Tech, 7 (1973) 285–292.

Guo Y., Curtis, J., Discrete element method simulations for complex granular flows, Annual Review of Fluid Mechanics (2015) 21–46.

Guo Y., Wassgren C., Ketterhagen W., Hancock B., James B., Curtis J., A numerical study of granular shear flows of rod-like particles using the discrete element method, Journal of Fluid Mechanics, 713 (2012) 1–26.

Han T., Levy A., Kalman H., DEM simulation for attrition of salt during dilute-phase pneumatic conveying, Powder Tech, 129 (2003) 92–100.

Johnson P.A., Jones M.G., Mills D., Investigation into the influence of gas density on pneumatic conveying performance, Powder Handling & Processing, 6 (1994) 157.

Jones M.G., Mills D., Product classification for pneumatic conveying, Powder Handling & Processing, 2 (1990) 117.

Kalman H., Attrition Control by Pneumatic Conveying, Powder Technology, 104 (1999) 214–220.

Kalman H., Goder D., Design criteria for particle attrition, Advanced Powder Technology, 9 (1998) 153–167.

Kalman H., Levy A., Brosch T., DEM simulation of particle attrition in dilute phase pneumatic conveying, Granular Matter, 13 (2011) 175–181.

Klinzing G.E., Clark W.W., Zhang M., Pahk J.B., Exploratory development of a microprobe for pneumatic conveying measurements and analysis, ChoPS 7, Friedrichshafen, Germany (2012).

Klinzing G.E., Rizk F., Marcus R.D., Leung S.L., Pneumatic conveying of solids, 3rd edition, Springer (2010).

Konrad K., Harrison D., Nedderman R.M., Davidson J.F., Proc. of Pneumotransport 5. Paper D1, BHRA Fluid Engineering, Cranfield, Bedford, UK (1980) 225.

Krambrock W., Pneumatic conveying system, US Patent (1979) US4171925A.

Krambrock W., Paul Lubbehusen P., Method and apparatus for mixing loose material, US Patent (1980) US4194845A.

Krambrock W., Eberhard N., Device for pneumatic charging container-type balance, US Patent (1981) US4301880A.

Krambrock W., Device for closing a pipe branch, US Patent (1989) US4836250A.

Krambrock W., Rotary slide valve, US Patent (1991) US5072758A.

Krambrock W., Device for setting a prescribed gas quantity, US Patent (1995) US5397062A.

Krambrock W., Wilms H., Brar G.S., Loading apparatus for bulk materials, US Patent (1997) US5660215A.

Krambrock W., Elbow/countercurrent classifier, US Patent (1998) US5788083A.

Krambrock W., Wilms H., Method of blowing conveying conduits free of material after conveyance, US Patent (1998) US5704990A.

Krambrock W., Method for conveying a solid substance, US Patent (2005) US6971786B2.

Kuang S.B., Chu K.W., Yu A.B., Z. Zou S., Feng Y.Q., Computational investigation of horizontal slug flow in pneumatic conveying, Industrial & Engineering Chemistry Research, 47 (2008) 470–480.

Kuang S.B., LaMarche C.Q., Curtis J., Yu A.B., Discrete particle simulation of jet induced cratering of a granular bed, Powder Technology, 239 (2013) 319–336.

Lecreps I., Sommer K., Wolz K., Stress states and porosity within horizontal slug by dense-phase pneumatic conveying, Particulate Science and Tech, 27 (2009) 297–313.

Levy A., Two-fluid approach for plug flow simulations in horizontal pneumatic conveying, Powder Tech., 112 (2000) 263–272.

Levy A., Jones M.G., Das S., An investigation into the performance of a suction nozzle, Powder Handling & Processing, 8 (1996) 337.

Mallick S.S., Wypych P.W., Pan R., Modeling dense-phase pneumatic conveying of powders using suspension density, Particulate Science and Technology, 31 (2013) 340–347.

Mason D.J., Levy A., A model for non-suspension gas-solids flow of fine powders in pipes, Int. J. Multiphase Flow, 27 (2001) 415–435.

Mason D.J., Marjanovic P., Levy A., A simulation system for pneumatic conveying systems, Powder Technology, 95 (1998) 7–14.

Mason D.J., Marjanovic P., Levy A., The influence of bends on the performance of conveying systems, Advanced Powder Technology, 9 (1998) 197–206.

Matsusaka S., Masuda H., Electrostatics of particles, Advanced Powder Technology, 14 (2003) 143–166. DOI: 10.1163/156855203763593958

McGlinchey D., Jones M.G., Marjanovic P., Blending and segregation of coal for the U.K. industrial market, Bulk Solids Handling, 19 (1999–2001) 345.

Michaelides E.E., A model for the flow of solid particles in gases, Int. J. of Multiphase Flow, 10 (1984) 61.

Mills D., Mason J.S., Some aspects of bend erosion in pneumatic conveying system, Bulk Solids Handling, 5 (1985) 1085.

Mittal A., Mallick S.S., Wypych P.W., An Investigation into the transition of flow Mechanism during fluidized dense-phase pneumatic conveying of fine powders, Particulate Science and Technology, 34 (2016) 23–32.

Molerus O., Principles of flow in disperse systems, ISBN-13 9780412406300, CRC Monograph (1993).

Muschelknautz E., Werkstoffforschung und Verfahrenstechnik unter Weltraumbegingungen, Bundesministerium fur Forschung und Technologie, Vorhaben: SN/A-QV-543 (Reibungsverluste FPL 304/a) (1985).

Muschelknautz E., Krambrock W., Vereinfachte Berechnung horizontaler pneumatischer Forderleitungen bei hoher Gutbeladung mit feinkornigen Produkten, Chemie-Ing.-Techn, 41 (1969) 1164.

Nied C., Hauth D., Sommer K., Stress states and pressure loss in pneumatically conveyed spatially confined single plugs, ICBM, Newcastle, Australia DOI: 10.3850/978-981-07-2518-1_150. (2011).

Rizk F., Pneumatische Förderung von Kunststoffgranulaten in horizontalen Rohrleitungen unter Berücksichtigung des Gewichtseinflusses in Zusammenhang mit Guteigenschaften und Rohrwerkstoffeigenschaften, insbesondere im optimalen Förderbereich Ph.D. Dissertation, University of Karlsruhe, 1973.

Roll C., Indiana One Hundred and fifty years of American development, Vol. 3, The Lewis Publishing Company, 1931.

Rose H.E., Duckworth R.A., Transport of solid particles in liquids and gases, The Engineer, 227 (1969) 392–396.

Setia G., Mallick S.S., Wypych P.W., On improving solid friction factor modeling for fluidized dense-phase pneumatic conveying systems, Powder Tech., 257 (2014) 88–103.

Sheer T.J., Pneumatic conveying of ice particles through mine-shaft pipelines, Powder Tech., 5 (1995) 203.

Theuerkauf J., Application of discrete element method simulations industry, 7th International CHoPS, Friedrichshaven, Germany (2012).

Tomita Y., Solids velocities and pressure drops in a horizontal pneumatic conveying system, Proc. 1st Intl. Conference on Pneumatic Transport of Solids in Pipe, BHRA, B3 (1971) 99–108.

Tsuji Y., Proceedings of the 5th World Congress on Particle Technology, Orlando, FL, USA, World Congress of Particle Technology—AIChE—Plenary Lecture—Paper 109 (2006).

Tsuji Y., Morikawa Y., LDV measurements in an air-solid two phase flow in a horizontal pipe, J. Fluid Mech, 120 (1982) 385–409.

Wilson R.W., Sheer T.J., Erosion prediction in rotary regenerative boiler air preheaters. Proceedings of 2nd S. A Conference on Applied Mechanics, Cape Town, 1998.

Zenz F.A., Othmer D.F., Fluidization and Fluid Particle Systems, Reinhold (1960).

Author's short biography

George Klinzing

Dr. George Klinzing is a professor of Chemical Engineering and served as the Vice Provost for Research at the University of Pittsburgh. He has directed 50 MS and 25 PhD dissertations in chemical engineering over a 53-year period with a focus on solids transport, handling, processing, and mass transfer.

He has been a consultant to DOE, Goodyear, Mountain State Energy, Allen-Sherman-Hoff, Kimberly-Clark, Dow Chemical, Certain Teed, U.S. Steel, Falconbridge, and Sarnoff.

His experience includes co-inventing the LICADO coal-cleaning process and two gas-solid flow meters; developing four software packages for pneumatic design; solid-liquid separation processing, particularly coal filtration and dewatering with an emphasis on solids characterization and analysis; research into fundamentals of coal-liquid and coal-gas transport as related to flow behaviors and energy requirements; coal-water slurry stability studies; and mineral filtration and dewatering process research into fundamentals of cake structure.

George Klinzing was the Chair of the Organizing Committee for the World Congress of Powder Technology-2006, has developed several patents, authored more than 254 publications, and has authored/co-authored two books on pneumatic transport.

He received a BS in Chemical Engineering from the University of Pittsburgh and a M.S. and Ph.D. degree in Chemical Engineering from Carnegie-Mellon University.

Walter Barth—Courtesy of Lothar Reh former of ETH Zurich; www.thhz.ch

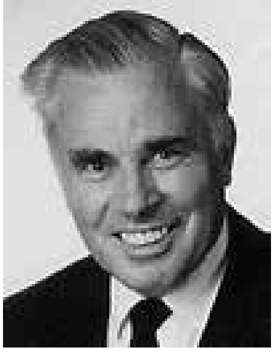

Edgar Muschelknautz—Website of University of Stuttgart; www.uni-stuttgart.de/en/

Karl Sommer—Website of Technical University of Munich; www.tum.de/en/homepage

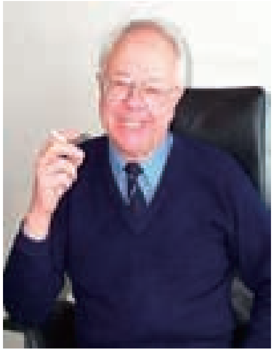

Otto Molerus—Courtesy of the staff of the University of Erlangen

Farid Rizk—Photo by Reinhard Wőhlblier from Bulk-online; https://www.bulk-online.com/faq

Yoshinobu Morikawa—Website of Osaka University; www.osaka-u.ac.jp

Yukata Tsuji—Website of Osaka University; www.osaka-u.ac.jp

S. L. Soo—Website of the University of Illinois; http://illinois.edu/

Paul Solt—Courtesy of Paul Solt

Peter Arnold—Website of University of Wollongong; www.uow.edu.au

Clive Davies—Website of Massey University; www.massey.ac.nz

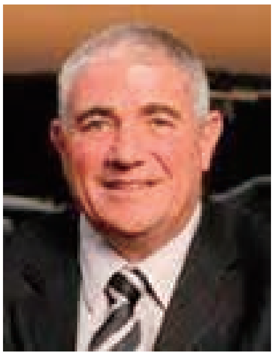

Roy Marcus—Website of the University of Johannesburg; www.uj.ac.za

KONA Powder and Particle Journal No. 35 (2018) 160–171/Doi:10.14356/kona.2018002 Original Research Paper

Analysis of the Periodic Motion in a Powder Rheometer and Development of a New Flowability Testing Method [†]

Ming Li, Mikel Leturia and Khashayar Saleh [*]

[1] *Chemical Engineering Department, Compiègne University of Technology, Sorbonne Universities, France*

Abstract

This study focuses on the periodic motion observed in the FT4 Powder Rheometer and aims to develop a new testing method to evaluate powder flowability. This new method is based on the autocorrelation analysis of the torque measurements. The test results of powders belonging to different Geldart's groups show that the torque measurements are periodic and that the cycle time (period) depends on the flowability. When the powder cohesiveness increases, the oscillations' amplitude and the cycle time increase. Conversely, a free-flowing powder exhibits a liquid-like behavior and shows almost no periodic motion.

Keywords: powder rheometer, flowability, periodic motion, autocorrelation

1. Introduction

Powders or bulk solids are widely used in the industries. A good powder flowability is of crucial importance since poor powder flow can lead to many problems during manufacturing such as inaccurate dosing and off-specification products (Valverde J.M., 2012). Especially during a number of processes such as filling small bags or tablet press dies, the powder materials are under very low stress conditions and their flow behavior is more difficult to predict (Zafar et al., 2015).

To replicate and characterize the powder flow at low stress conditions, a number of characterization techniques have been developed over the last 50 years (Jenike A.W., 1980; Prescott J.J. and Barnum R.A., 2000; Schwedes J., 2003; Zafar et al., 2015).

The shear cell test is most commonly used for the characterization of powder flowability. It gives the relationship between the shear stress (which leads to flow of the material) and the normal stress (Bek et al., 2016). The yield locus in the low stress region and the tensile strength are obtained indirectly by extrapolating to zero of the measured yield locus. However, the yield locus tends to curve downwards at low stresses for cohesive powders so that the results can be overestimated (Vasilenko et al., 2013).

Other techniques that allow powder flow characterization under low stress conditions are reported in the literature. The Sevilla Powder Tester (SPT) and the Raining Bed Method (RBM) are two similar test methods that can directly measure the tensile yield stress at low stress levels. Both methods use a controlled gas flow to introduce small stresses in the powder bed. The tensile yield stress is then calculated by measuring the pressure drop across the powder bed at failure (Formisani et al., 2002; Valverde et al., 2000).

Another recently developed test method, the ball indentation method (BIM), measures the resistance to plastic deformation of powder materials at very low stress to assess the flowability (Hassanpour and Ghadiri, 2007). However, this method was originally designed for continuum solids and the extension to the testing of cohesive powder beds has only recently been analyzed (Pasha et al., 2013).

Zafar et al. (2015) proposed a comparison of these four techniques (shear cell, SPT, RBM and BIM), and showed that:

- The powder flow characterization under low stress conditions is greatly influenced by the stress history. Consequently, the initialization procedure has to be well controlled in order to obtain reproducible data;
- Since the distribution of stresses in granular materials is highly heterogeneous, it is important to ensure the failure plane occurs at the proper location and in a reproducible way.

Quintanilla et al. (2006) studied the behavior of a series of granular materials of different cohesiveness in a half-filled and slowly rotating horizontal drum. The authors used a CCD camera and digital image processing to de-

---

[†] Received 15 May 2016; Accepted 19 September 2016
J-STAGE Advance published online 18 March 2017

[1] Lab. TIMR-EA 4297, 60200 Compiègne, France
[*] Corresponding author: Khashayar Saleh
E-mail: khashayar.saleh@utc.fr
TEL: +33 (0)3-4423-5274 FAX: +33 (0)3-4423-1980

tect and characterize the avalanches. By statistical analysis, they studied the periodicity of the signals as well as the probability distributions of the avalanche size and the maximum angle of stability. The results showed that the system cohesiveness was correlated to these probability distributions: the larger the cohesion, the larger the average size and maximum angle of stability of the avalanches.

More in-depth studies and new testing methods still need to be developed to better characterize powder flow properties under low stress conditions. This work aims to develop a new dynamic testing method to evaluate powder flowability under unconfined flow conditions. This new method is based on the autocorrelation analysis of the torque measurements obtained with the FT4 Powder Rheometer.

2. Materials

Six powders belonging to Geldart's groups A, B and C were used in this study. The properties of these six powders are summarized in **Table 1**. The particle size distributions were measured using a laser diffraction size analyzer (Mastersizer 2000, Malvern Instruments) and the particle density by a helium pycnometer Accupyc 1330 (Micromeritics). In addition, a liquid honey was used in this study as a reference material to simulate an "ideal" flow behavior. As it will be shown later in this paper, the liquid honey is viscous enough to obtain significant torque measurements. At the same time, these torque measurements are close to those corresponding to a "perfectly flowing" granular material. As a consequence, it will be considered as a "reference material" and will be used to simulate an "ideal" flow behavior.

3. Periodic motion during dynamic measurements

3.1 Standard dynamic test on the FT4 powder rheometer

Tests on the FT4 powder rheometer are based on a sophisticated twisted blade which passes through the powder bed along a predetermined helical path (**Fig. 1**). When the blade moves clockwise (conditioning cycle), the powder is lifted up and conditioned to obtain a uniform and reproducible state. When the blade moves anticlockwise (test cycle), it creates a compaction zone which is a local-

Fig. 1 Test cycle (left) and conditioning cycle (right) with the FT4 Powder Rheometer.

Table 1 Physical properties of the powders.

powder	$d[3, 2]$ (μm)	$d[4, 3]$ (μm)	$d[10]$ (μm)	$d[50]$ (μm)	$d[90]$ (μm)	span	ρ (kg/m^3)	shape	Geldart's classification
$CaCO_3$ (a)	3.4 ± 0.5	11.7 ± 1.7	1.2 ± 0.2	8.6 ± 1.4	26.1 ± 3.9	2.9	2750	angular	C
$CaCO_3$ (b)	4.0 ± 0.3	15.9 ± 1.4	1.5 ± 0.2	12.3 ± 1.1	35.2 ± 2.9	2.8	2750	angular	C
$CaCO_3$ (c)	8.4 ± 0.2	51.5 ± 1.2	4.9 ± 0.4	35.2 ± 0.3	104.6 ± 2.1	2.8	2750	angular	C
ZrO_2	23.7 ± 0.5	60.1 ± 0.5	12.8 ± 0.2	55.1 ± 0.4	113.0 ± 1.2	1.7	5790	angular	A
SiC	79.1 ± 0.7	66.0 ± 3.6	43.4 ± 0.9	73.7 ± 0.5	122.7 ± 0.4	1.1	3056	angular	A
sand	342.2 ± 15.7	287.1 ± 8.1	186.3 ± 6.6	306.3 ± 11.4	517.6 ± 20.6	1.1	2546	angular	B

Values after "±" indicate the 95 % confidence intervals;
span = $(d_{90} - d_{10})/d_{50}$

ized high-stress region in front of the blade and forces the powder to flow (Leturia M. et al., 2014).

The FT4 standard "dynamic test" measures the evolution of the torque and force for a downward flow pattern in a conditioned controlled volume of powder. The energy required to induce this movement is then calculated (by integration of the force and torque measurements) to evaluate the flow properties of the powder (Conesa C. et al., 2004). This test is divided into two main parts.

The first part, called "stability test", corresponds to seven identical complete cycles (conditioning + test cycles) at a constant blade tip speed of 100 mm/s. The objective is to detect any possible change in the powder flow properties after repeated tests (attrition, agglomeration, etc.). The stability test also allows a stable energy level to be achieved. The basic flow energy (BFE), as defined by Freeman Technology, corresponds to the stabilized flow energy. It represents the energy required to force a conditioned powder sample to flow during a downwards test:

$$BFE\ (\mathrm{mJ}) = Flow\,energy\ of\ test\ 7 \qquad (1)$$

Usually, fine powders have relatively high interparticulate forces compared to gravitational forces. As a consequence, they behave in a cohesive way: Agglomerates are formed and a large amount of air is trapped inside the bulk powder (Freeman R., 2007). In this case, particles forced to flow at the blade face can be accommodated by the voids that exist between the agglomerates (high compressibility). The resulting flow or stress transmission zone is relatively localized. Thus the displaced volume of powder is small and the measured BFE value is particularly low. Powders made of larger particles often behave in a non-cohesive manner due to the minimal effect of cohesive forces compared to gravitational forces. Less air is trapped in the bulk powder resulting in a relatively lower compressibility. The flow zone is transmitted far ahead of the blade (Freeman R., 2007). In this case, the displaced volume of powder is large and the measured flow energy is high.

The second part, called "variable flow rate test", corresponds to 4 complete cycles at decreasing blade tip speeds (100, 70, 40 and 10 mm/s). The objective is to evaluate the powder sensitivity to the flow rate. The flow rate index (FRI) corresponds to the ratio of the flow energy at 10 mm/s blade tip speed to the flow energy at 100 mm/s blade tip speed:

$$FRI = \frac{Flow\,energy\ of\ test\,11\ (10\ \mathrm{mm/s})}{Flow\,energy\ of\ test\,8\ (100\ \mathrm{mm/s})} \qquad (2)$$

Many factors can affect the value of the FRI index, e.g.:

- Cohesive powders are more sensitive to the flow rate and present a high FRI value (Freeman R., 2007);
- Angular particles generally have a high FRI value.

Although the combination of the values of the BFE and FRI helps to identify the powder flow properties, the standard dynamic test has many limitations for the classification of powder flowability.

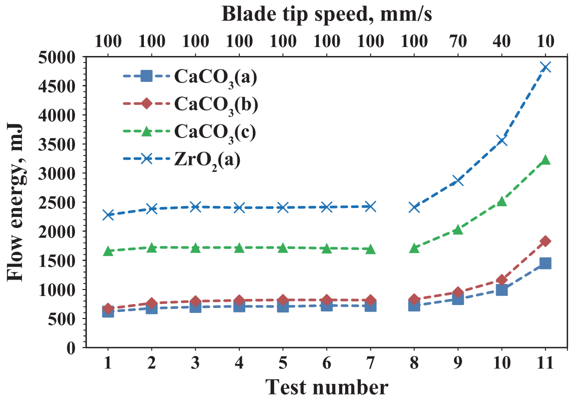

Fig. 2 Results of the FT4 standard dynamic test.

Table 2 Results of the FT4 standard dynamic test.

powder	BFE (mJ)	FRI
$CaCO_3$ (a)	715.4	2.0
$CaCO_3$ (b)	816.6	2.2
$CaCO_3$ (c)	1696.2	1.9
ZrO_2	2426.1	2.0

Fig. 2 and **Table 2** present the standard dynamic test results and the corresponding BFE and FRI values of four powder samples:

- $CaCO_3$ (a) has a slightly smaller BFE value than $CaCO_3$ (b), which generally means a lower flowability. On the other hand, $CaCO_3$ (a) has a smaller FRI value than $CaCO_3$ (b), which is generally associated with a better flowability;
- ZrO_2 has a much higher BFE value than $CaCO_3$ (c) and seems to have a better flowability. But ZrO_2 has a much higher bulk density, making it difficult to know whether the higher value of BFE is caused by the better flowability or the higher density. Meanwhile, ZrO_2 has a higher FRI value, which in contrast may indicate a poorer flowability.

In both cases, it is difficult to make a conclusion about which powder has better flowability. Therefore, the standard dynamic test on the FT4 cannot be used to compare two different powders and it can be difficult to distinguish between very similar materials.

3.2 Observation of a periodic motion

In order to optimize the FT4 standard procedures, the powder flow behavior during testing was closely observed (**Fig. 3**) and the resulting raw data were analyzed (normal force and torque measurements before integration for the

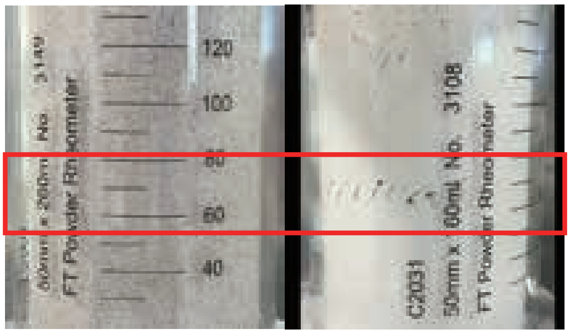

Fig. 3 Flow behavior of non-cohesive powders (sand, left) and cohesive powders ($CaCO_3$ (a), right).

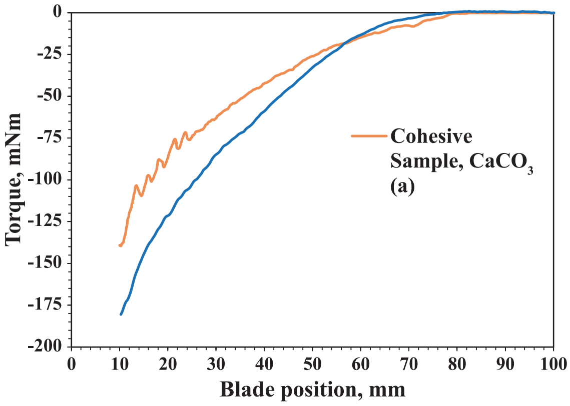

Fig. 4 Torque variation during a standard dynamic test (blade tip speed = 70 mm/s).

energy calculation). For cohesive powders, the blade leaves an empty space behind it when passing through the powder bed. This empty space grows in size as the blade moves forward and collapses when it reaches a maximum volume. It then grows in size and collapses again, following a cyclic pattern. It was also observed that this empty zone had a smaller maximum volume at a lower blade tip speed. For non-cohesive powders, the blade does not leave any significant empty space behind it and particles flow around the blade, almost like a liquid. The cyclic pattern is also reflected in the torque measurements where oscillations can be observed (**Fig. 4**). These oscillations are much more significant in a cohesive sample compared to a free-flowing powder.

A “verification test” was performed to reveal the causes of this cyclic pattern. In this test, only the surface of the powder bed was forced to flow so that the flow behavior could easily be observed. A 160-ml conditioned sample of $CaCO_3$ (a) was placed in the 50-mm ID cylinder vessel. The blade was moved just below the powder surface (70 mm from the bottom) and rotated for 60 seconds at 4 different blade tip speeds (100 mm/s, 70 mm/s, 40 mm/s and 10 mm/s). At the same time, a video camera recorded the powder motion around the blade. Since the blade stayed at the same height, there was no significant normal force. Under these conditions, the total energy needed to move the blade through the powder is proportional to the torque acting on the blade. The torque oscillations were evaluated through an autocorrelation analysis, which is a mathematical tool commonly used in signal processing and time-series analysis to investigate repeating patterns (Dunn and Patrick F., 2005)

In statistics, the autocorrelation function for a continuous-time process, X_t, is the correlation of the process with itself at a later time. It represents the similarity between observations as a function of the time lag (Box G.E.P. et al., 1994):

$$ACF(\tau) = \frac{E[(X_t - \mu)(X_{t+\tau} - \mu)]}{\sigma^2} \tag{3}$$

where “E” is the expected value operator. For a stationary process, the mean μ and the variance σ^2 are time-independent and the autocorrelation depends only on the time lag τ. In other words, the correlation depends only on the time distance between the two chosen values but not on their position on the time axis. Particularly, the autocorrelation function of a periodic function has the same period as the original function, which is the key to investigating the repeating patterns. The values of the autocorrelation function (ACF) should be in the range [–1, 1], with 1 indicating a perfect correlation (the signals exactly overlap when time is shifted by τ) and –1 indicating a perfect anti-correlation (Priestley M.B., 1982). For a discrete process with n observations such as the measured torque series in this test, an estimate of the autocorrelation may be obtained as (Chatfield C., 2004):

$$\widehat{ACF}(k) = \frac{1}{(n-k)\sigma^2}\sum_{t=1}^{n-k}(X_t - \mu)(X_{t+k} - \mu) \tag{4}$$

3.3 Analysis of the periodic motion

Fig. 5 presents the time evolution of the torque measurements and the corresponding autocorrelation functions (ACF) for the “verification test”. On the one hand, a series of oscillations in the torque measurements are observed and the autocorrelation function brings to light the existence of a cyclic pattern. At high blade tip speeds, the $CaCO_3$ (a) material has a period corresponding to one rotation of the blade. It should be noted that small peaks (small “events”) can be found at each half-rotation of the blade. As the blade tip speed decreases, it can be observed that:

- These small events become more significant and eventually reach the same value as the main peak. This means that the cycle time is halved;
- The maximum autocorrelation level decreases.

The test video was analyzed frame by frame. The im-

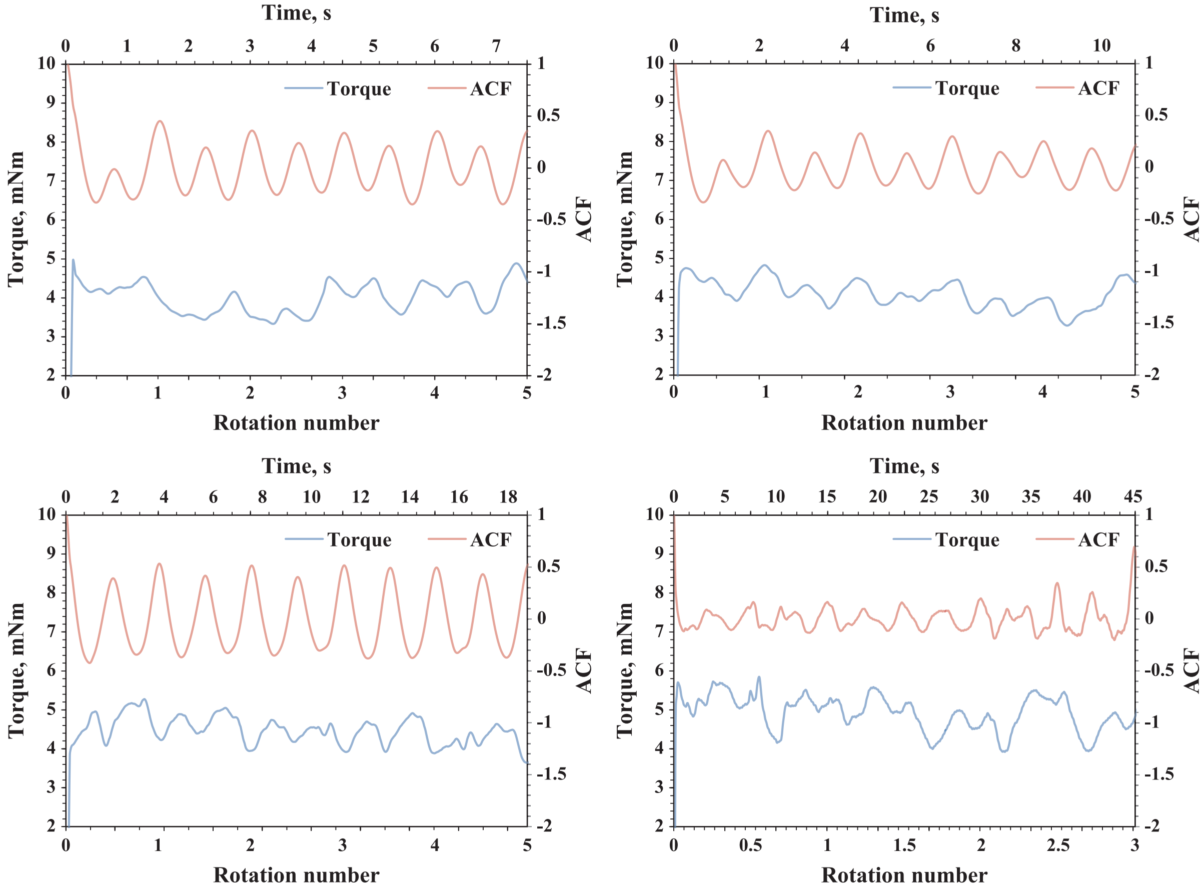

Fig. 5 Torque measurements and autocorrelation function (ACF) of $CaCO_3$ (a) for the verification test.

Fig. 6 Image of the verification test (the blade rotates in anti-clockwise direction).

ages clearly show (**Fig. 6**) that a “block” of powder moves in front of the blade while a large empty space is left behind it.

During the “verification test”, the “powder block” in front of the blade was observed in the form of several agglomerates (**Fig. 7**). Whenever some agglomerates fall off the blade (as the big one in the red frame in **Fig. 7-A**), a sudden drop is observed in the torque measurements (**Fig. 7-B**). The torque goes up again when this agglomerate is picked up by the other side of the blade in **Fig. 7-C, D**. Since the agglomerates are not exactly of the same size, the oscillations do not have the same amplitude. In **Fig. 7-E, F, G, H**, torque oscillations can also be observed as several small agglomerates fall off the blade one after another.

Indeed, while the blade pushes the powder to flow, an unstable “compacted powder zone” builds up in front of each side of the blade, forming two “powder blocks” and two empty spaces behind them. Since these powder blocks are unstable, they may eventually collapse to fill the empty spaces. The fallen agglomerates stay in the empty space for a short time and are picked up by the other side of the blade. The second powder block then increases in volume and becomes less stable. It will finally collapse like the first powder block and this flow pattern is repeated continuously.

The flow speed has an important impact on this periodic motion:

– When the blade moves slowly, this process is quite smooth and the flow pattern has a period corresponding to a 1/2 rotation of the blade;
– When the blade moves fast, the cycle time of the flow pattern becomes one rotation of the blade.

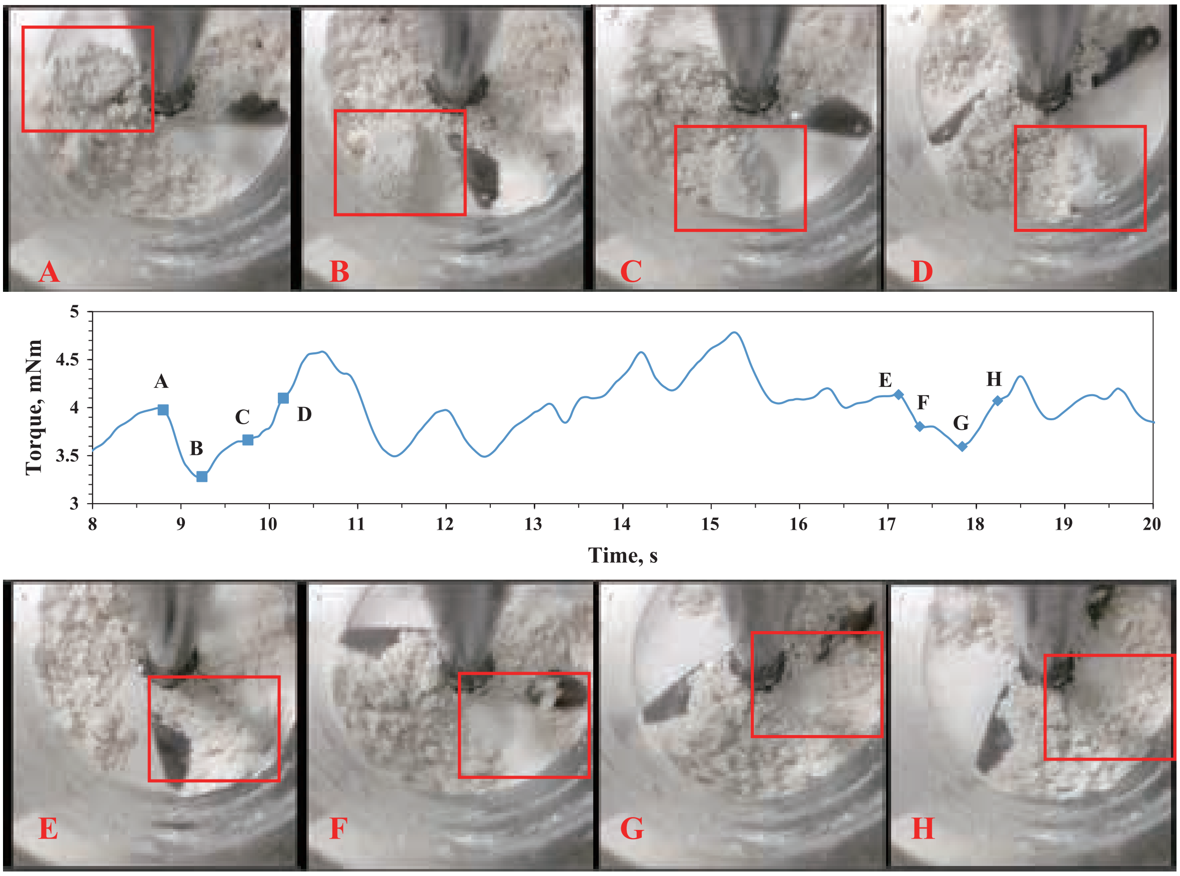

Fig. 7 Torque variation and agglomerates behavior (blade tip speed = 70 mm/s).

This behavior could be explained by the fact that the collapsing process is not immediate as a given powder has a certain response time to plastic flow deformation. As a consequence, there may be a critical flow speed above which the response time is longer than a 1/2 rotation, resulting in a cycle time of one complete rotation of the blade.

4. New powder rheometer testing method

A specific testing procedure was developed on the FT4 Powder Rheometer. First, a 160-ml conditioned sample was placed in the 50-mm ID cylinder vessel. Then the twisted blade was set to rotate in the powder bed at a height of 30 mm from the bottom with a blade tip speed of 100 mm/s for 200 seconds. The blade tip speed was then gradually decreased from 100 mm/s to 10 mm/s (by 10 mm/s steps for each speed reduction), and the rotation was repeated for 200 seconds at each step. A conditioning cycle was performed between each step.

The torque needed to induce flow was measured continuously. To ensure a stable powder flow (steady state), only the data measured during the last 50 seconds were analyzed for each step. The autocorrelation function was then used to determine the cycle time and correlation level. By this means, the periodic motion was characterized and the powders could then be classified depending on their behavior.

4.1 Results obtained with the proposed testing method

The liquid honey was first used to simulate a regular flow behavior (reference material). Indeed, it was viscous enough to obtain significant torque measurements while behaving like an ideal material under the testing conditions. **Fig. 8 (top)** presents the variations of the required torque to force the liquid honey to flow at different flow rates. The measured torque is very stable (small oscillations) and the corresponding ACF values (**Fig. 8 bottom**) are always close to 0. This means that the torque needed to force a viscous liquid to flow at a given speed is a constant and no periodic motion can be detected with the FT4. From this point of view, the liquid honey can be regarded as an “ideal” material (in this flow rate range). On the other hand, it can also be noted that the average torque (**Fig. 8, center**) is proportional to the flow speed. This corresponds to the flow behavior of a Newtonian fluid.

The $CaCO_3$ (a), SiC and sand powders were first char-

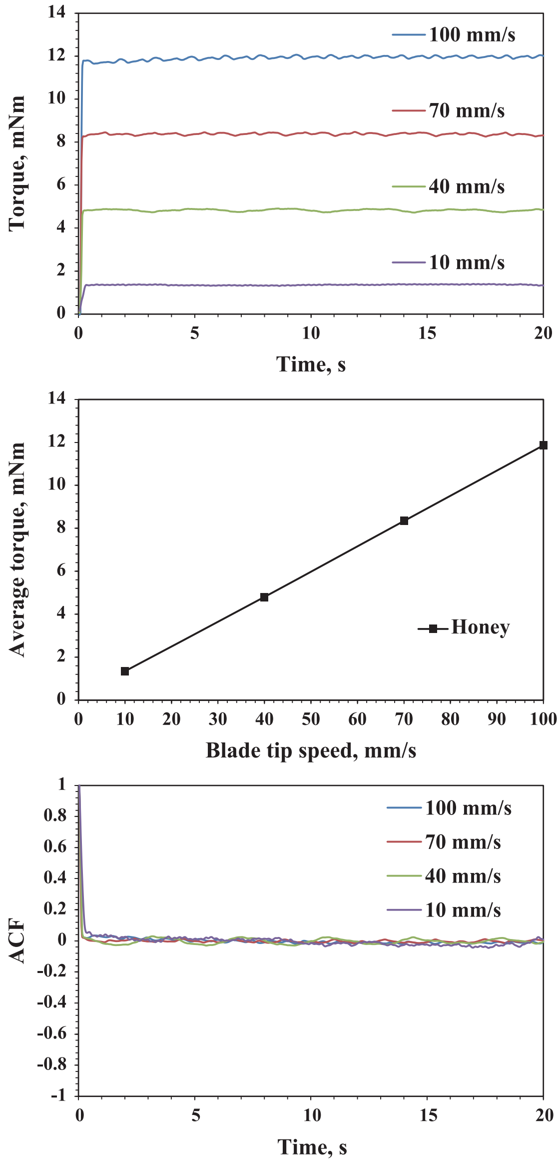

Fig. 8 Torque variation as a function of the blade tip speed for the liquid honey and autocorrelation analysis.

acterized by this method, since each of them belongs to a different Geldart's group. Visual observations during the tests showed that:

- For the $CaCO_3$ (a) powder (group C), the rotating blade left a large empty space behind it by passing through the powder bed and only a small part of the powder moved in front of the blade;
- In the SiC powder bed (group A), the particles flowed around the blade, a small empty space was left behind and the flowing zone extended above and in front of the blade;
- For the sand powder (group B), the particles flowed freely, almost like a liquid. No empty space was left behind the blade and the flowing zone extended even further above the blade up until the surface of the powder bed.

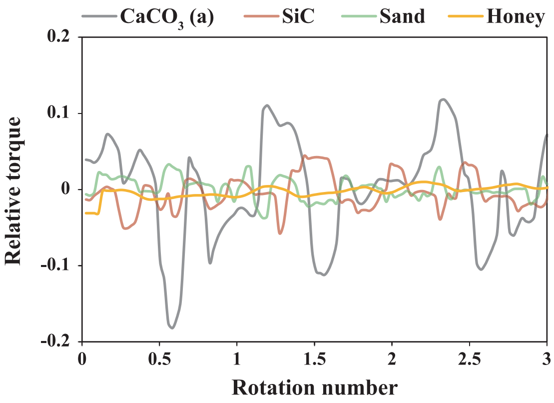

Fig. 9 Relative torque evolution ($(T-\overline{T})/\overline{T}$) at the blade tip speed = 100 mm/s.

- For all three specimens, the materials below the blade seemed to remain static.

Fig. 9 presents the relative torque measurements of the 3 powder specimens (+ honey) as a function of the number of rotations of the blade (at a blade tip speed of 100 mm/s). The relative torque is defined as:

$$Relativetorque = (T-\overline{T})/\overline{T} \tag{5}$$

where $\overline{T}$ is the mean torque value calculated within the 50-second measurements.

The results show that the torque measurements can be correlated to the system cohesiveness:

- A cohesive granular material like $CaCO_3$ (a) (group C) is characterized by large and slow torque oscillations. Because of the powder cohesiveness, the powder blocks formed in front of the blade can become large before they become unstable and collapse. The "build-up/collapse" process is repeated regularly as the blade rotates in the powder bed. This leads to a periodic behavior with large events (large oscillations) and a low frequency (slow oscillations). It can be said that the "response time" is slow when the powder bed is disturbed by the blade;
- For a less cohesive powder like SiC (group A), the powder blocks become unstable and collapse earlier compared to a group C powder. This still leads to a periodic "build-up/collapse" process, but with smaller and faster events;
- For a free-flowing powder (sand, group B), the gravitational forces are preponderant compared to cohesion forces. As a consequence, no stable powder block can be formed and the "build-up/collapse" process is almost instantaneous. This leads to a continuous flow of particles around the blade. The "response time" of a free-flowing powder is fast when the powder bed is disturbed by the blade. The corresponding torque signal is quite stable and there is no periodic pattern (relatively close to the honey torque signal).

These results can be related to those obtained by

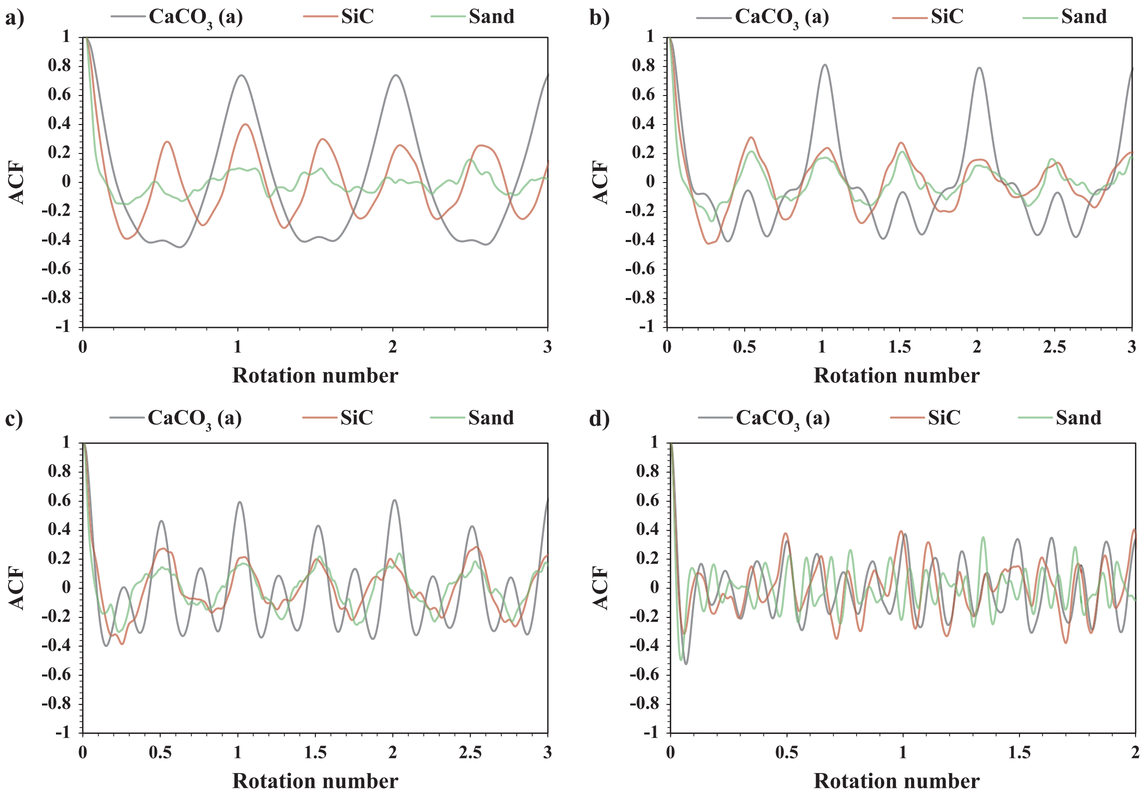

Fig. 10 Autocorrelation function at different blade tip speeds. **a)** blade tip speed = 100 mm/s; **b)** blade tip speed = 70 mm/s; **c)** blade tip speed = 40 mm/s; **d)** blade tip speed = 10 mm/s.

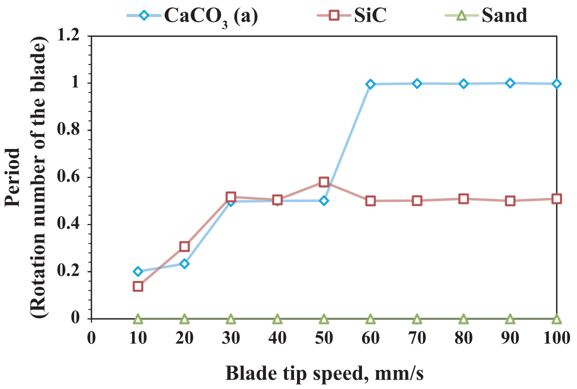

Fig. 11 Cycle time at different blade tip speeds.

Quintanilla et al. (2006), who used a half-filled and slowly rotating horizontal drum. Indeed, the collapse of the powder blocks can be assimilated to the avalanches in the rotating drum. In both cases, a periodic behavior is observed and the periodicity of the signals can be correlated to the system cohesiveness. Also, in both studies, it is shown that a higher cohesion leads to larger events (collapses or avalanches).

4.2 Periodic motion analysis and powder flowability classification

During the tests, the torque was recorded every 0.04 seconds and the 50-second measurements could then be treated as a discrete process with 1250 observations for the autocorrelation analysis. The autocorrelation functions of the three powders are presented in **Fig. 10**. These graphs indicate that the flow within the powder bed exhibits the same cyclic pattern as the flow on the surface (**Fig. 5**). However, the periodic motion on the surface shows a lower correlation level, which might be caused by the surface effects.

These ACF curves show that:

- At high flow speeds, the $CaCO_3$ (a) powder (group C) has a cycle time corresponding to one blade rotation and it is close to an "ideal" correlation (the maximum correlation level is close to 1). When the flow speed decreases, the cycle time of the $CaCO_3$ specimen is halved and the correlation level of the cyclic pattern decreases;
- The SiC powder (group A) always has a cycle time of 1/2 a rotation of the blade and a relatively lower correlation level.
- The sand powder (group B) has a low correlation level (ACF < 0.2), which means that no significant periodic motion can be detected in this case.

The cycle times (expressed in the number of rotations of the blade) of the three samples at different flow speeds are summarized in **Fig. 11**. Based on previous results, a threshold value of 0.2 was used to differentiate periodic

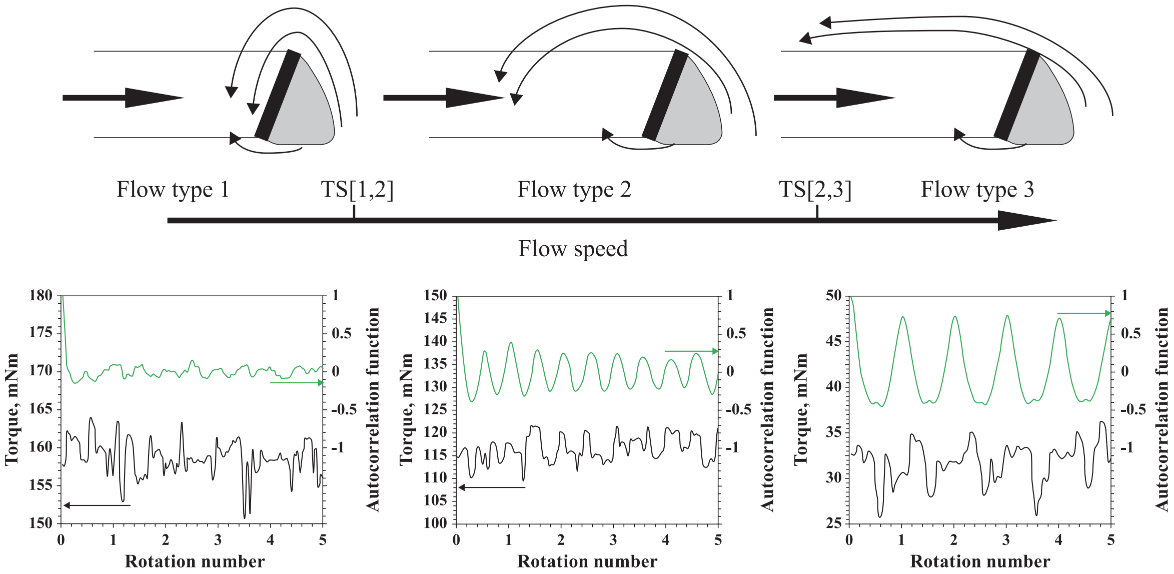

Fig. 12 Transition speeds and powder flow behaviors in the FT4 Powder Rheometer.

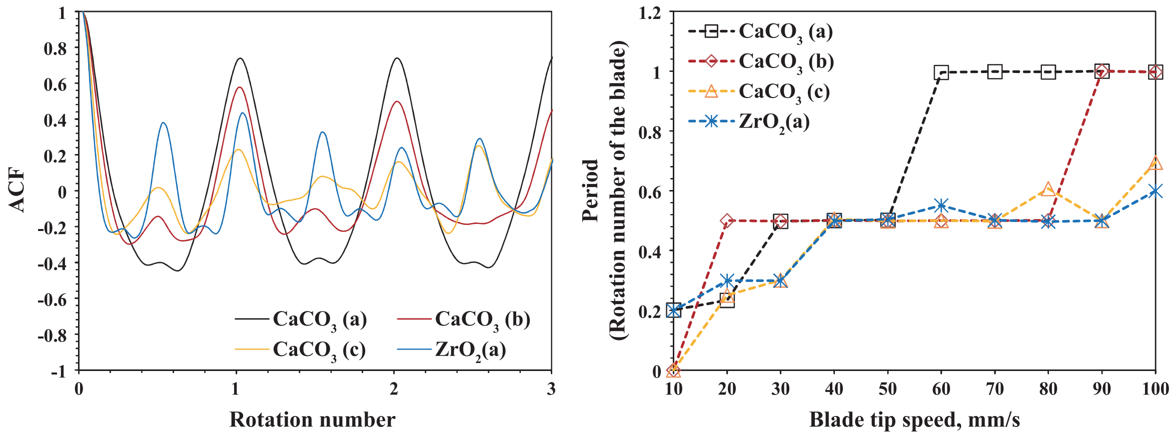

Fig. 13 Test results of the new testing method: autocorrelation function at 100 mm/s **(left)**; cycle time at different blade tip speeds **(right)**.

from non-periodic flow patterns. All the processes with a correlation level lower than 0.2 were ignored and considered as non-periodic flow patterns. For convenience, the cycle time of such processes was then considered as 0. The results of the autocorrelation analysis indicate that:

- The cycle time of a powder material increases as its cohesiveness increases;
- The cycle time doubles at a certain blade tip speed, which can be regarded as a "transition speed";
- Free-flowing powders have a very low correlation level (ACF < 0.2) and present almost no periodic flow pattern. These powders behave almost like the liquid honey ("ideal" flow)

These results suggest that for any powder material, there are three flow behaviors:

- Flow type 1 (**Fig. 12-left**): It is observed when the response time of the powder is significantly smaller than the time required for a 1/2 rotation of the blade. As a consequence, the particles flow freely and smoothly around the blade. The corresponding torque signal is quite stable and there are no periodic patterns. For this type of flow, the correlation level is less than 0.2 (the cycle time is set to 0);
- Flow type 2 (**Fig. 12-middle**): The response time of the powder is smaller but close to the time corresponding to a 1/2 rotation of the blade. In this case, the blade leaves a small unstable empty space behind it when passing through the powder bed. This empty space expands to a maximum volume and collapses before being reached by the other side of the blade. This type of flow corresponds to a cycle time of a 1/2 rotation of the blade and a moderate correlation level in the autocorrelation analysis (0.2 < ACF < 0.8);
- Flow type 3 (**Fig. 12-right**): The response time of the powder is larger than the time required for a 1/2 rotation of the blade. Thus the blade leaves a large empty

space behind it when passing through the powder bed. The other side of the blade reaches the empty space before it collapses. This type of powder flow corresponds to a cycle time of one complete rotation of the blade and a high correlation level (ACF > 0.8).

These results suggest the existence of two flow transition speeds (**Fig. 12**): TS[1, 2] is the transition speed from flow type 1 to flow type 2 and TS[2, 3] is the transition speed from flow type 2 to flow type 3. For a given powder, the values of TS[1, 2] and TS[2, 3] depend on its response time to plastic flow deformation. Therefore, the values of the two transition speeds can be used to identify the powder flow properties:

- Free-flowing powders such as the sand powder flow almost like a liquid and have a very short response time. The corresponding TS[1, 2] and TS[2, 3] values are very high. As a result, these powders exhibit the flow type 1 at any accessible flow speed with the FT4 Powder Rheometer;
- Cohesive powders such as the $CaCO_3$ powder on the contrary have a very long response time, which results in low TS[1, 2] and TS[2, 3] values. These powders then present all three flow types within the flow speeds accessible with the FT4 Powder Rheometer;
- The powders with moderate flowability such as the SiC powder have an intermediate response time, which means that they have intermediate TS[1, 2] values (accessible with the FT4 Powder Rheometer) and high TS[2, 3] values. As a consequence, these powders can exhibit flow type 1 or 2 depending on the flow speed.

Other tests were also performed to verify these conclusions. As explained in section 3.1, the standard dynamic test cannot discriminate the flowabilities between $CaCO_3$ (a), $CaCO_3$ (b), $CaCO_3$ (c) and ZrO_2. The results of the new testing method clearly show these differences (**Fig. 13**):

- $CaCO_3$ (a) has a poorer flowability than $CaCO_3$ (b) since it has a lower TS[2,3] and a higher correlation level;
- $CaCO_3$ (c) and ZrO_2 present similar flowabilities as they have similar cycle time variations. Still, $CaCO_3$ (c) flows a little more easily than ZrO_2, as it has a higher TS[1,2] and a lower correlation level.

5. Conclusion

In this study, a new flowability testing method is presented. This method is based on the FT4 standard dynamic test and quantifies the powder periodic motion under forced flow conditions. The test results prove that the dependence of the torque cycle time on the flow rate can be linked to the powder flow properties: when the powder cohesiveness increases, the autocorrelation level and cycle time increase; conversely, a free-flowing powder tends to act like a liquid and shows no periodic motion.

This work shows that this new method has a good capability to identify and classify powder flow properties. The flowabilities of different powders which cannot be discriminated with the standard dynamic method of the FT4 Powder Rheometer are easily identified with this new method

Further studies still need to be done to optimize this method such as the influence of the blade height (30 mm in this study), the variation of the periodic motion in a wider flow speed range, as well as the influence of the blade shape.

Nomenclature

BFE	Basic Flow Energy, [mJ]
$d[10]$	10 % of the population lies below the $d[10]$, [m]
$d[3, 2]$	Mean surface-volume diameter (Sauter mean diameter), [m]
$d[4, 3]$	Volume or mass moment mean (De Brouckere mean diameter), [m]
$d[50]$	Mass median diameter, [m]
$d[90]$	90 % of the population lies below the $d[90]$, [m]
E	Expected value operator
FRI	Flow Rate Index, [–]
k	Observation number in the discrete time process, [–]
n	Total observations of the discrete process
ACF	Autocorrelation function, [–]
$\widehat{ACF}$	Autocorrelation function of a discrete process, [–]
span	(d[90]-d[10])/d[50], [–]
t	Time, [s]
T	Torque, [mN m]
$\overline{T}$	Average torque, [mN m]
TS[1, 2]	Transition speed between flow type 1 and flow type 2, [mm/s]
TS[2, 3]	Transition speed between flow type 2 and flow type 3, [mm/s]
X	Signal of a continuous-time process
μ	Mean
ρ	Particle density, [kg/m^3]
σ	Standard deviation
τ	Time lag, [s]

References

Bek M., Gonzalez-Gutierrez J., Moreno Lopez J.A., Bregant D. and Emri I., Apparatus for measuring friction inside granular materials—Granular friction analyzer, Powder Technology, 288 (2016) 255–265.

Box G.E.P., Jenkin G.M. and Reinsel G.C., Time Series Analysis: Forecasting and Control, 3rd ed, Upper Saddle River, NJ: Prentice-Hall, 1994.

Chatfield C., The Analysis of Time Series: An Introduction. sixth ed., CRC Press Company, New York, 2004.

Conesa C., Saleh K., Thomas A., Guigon P. and Guillot N., Characterization of Flow Properties of Powder Coatings Used in the Automotive Industry, KONA Powder and Particle Journal, 22 (2004) 94–106.

Dunn and Patrick F., Measurement and Data Analysis for Engineering and Science, New York: McGraw-Hill, 2005.

Formisani B., Bernardo P., Girimonte R. and Minnicelli A., The bed support experiment in the analysis of the fluidization properties of fine solids. Paper presented at the Proceedings of the conference 4th World Congress on Particle Technology, 2002.

Freeman R., Measuring the flow properties of consolidated, conditioned and aerated powders. A comparative study using a powder rheometer and a rotational shear cell, Powder Technology, 174 (2007) 25–33.

Hassanpour A. and Ghadiri M., Characterisation of Flowability of Loosely Compacted Cohesive Powders by Indentation, Particle & Particle Systems Characterization, 24 (2007) 117–123.

Jenike A.W., Storage and flow of solids. Bull. No. 123, 20th Printing, 1980.

Leturia M., Benali M., Lagarde S., Ronga I. and Saleh K., Characterization of flow properties of cohesive powders: A comparative study of traditional and new testing methods, Powder Technology, 253 (2014) 406–423.

Pasha M., Hare C., Hassanpour A. and Ghadiri M., Analysis of ball indentation on cohesive powder beds using distinct element modelling, Powder Technology, 233 (2013) 80–90.

Prescott J.J. and Barnum R.A., On powder flowability, Pharm. Technol., 24 (2000) 60–84.

Priestley M.B., Spectral analysis and time series, Academic Press, London; New York, 1982.

Schwedes J., Review on testers for measuring flow properties of bulk solids, Granul. Matter, 5 (2003) 1–43.

Valverde J.M., Castellanos A., Ramos A., Pérez A.T., Morgan M.A. and Watson P., An automated apparatus for measuring the tensile strength and compressibility of fine cohesive powders, Rev. Sci. Instrum., 71 (2000) 2791.

Valverde J.M., Fluidization of Fine Powders: Cohesive Versus Dynamical Aggregation, Springer, 2012.

Vasilenko A., Koynov S., Glasser B.J. and Muzzio F.J., Role of consolidation state in the measurement of bulk density and cohesion, Powder Technology, 71 (2013) 2791.

Zafar U., Hare C., Calvert G., Ghadiri M., Girimonte R., Formisani B., Quintanilla M.A.S. and Valverde J.M., Comparison of cohesive powder flowability measured by Schulze Shear Cell, Raining Bed Method, Sevilla Powder Tester and new Ball Indentation Method, Powder Technology, 286 (2015) 807–816.

Author's short biography

Ming Li

Ming Li is a Ph.D. student in the Chemical Engineering Department at Compiègne University of Technology (Sorbonne Universities). His research is focused on the comparison of powder characterization methods and the improvement of testing protocols for a better evaluation of powder flow properties.

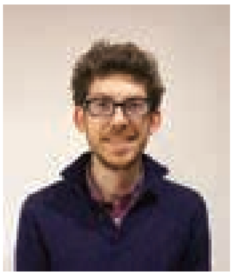

Mikel Leturia

Mikel Leturia is a chemical engineer from Compiègne University of Technology (2009). He prepared a Ph.D. thesis in the Chemical Engineering Department at Compiègne University of Technology on the experimental study and modeling of fluidized-bed reactors using cohesive powders (2013). He is currently associate professor in the same university and his research focuses on powder technology including fluidization, caking and flowability testing methods.

Khashayar Saleh

Khashayar Saleh prepared a Ph.D. thesis on the coating of fine powders in the Chemical Engineering Laboratory of Toulouse and obtained his Ph.D. degree in 1998 from the Institute National Poly-technique de Toulouse (France). Professor Khashayar Saleh is currently the director of the Chemical Engineering Department at Compiègne University of Technology (Sorbonne Universities). His work is focused on powder technology including size enlargement technology, powder electrification and powder characterisation methods.

KONA Powder and Particle Journal No. 35 (2018) 172–185/Doi:10.14356/kona.2018003 Original Research Paper

Separation Characteristics of a Deflector Wheel Classifier in Stationary Conditions and at High Loadings: New Insights by Flow Visualization †

Christian Spötter *, Kurt Legenhausen and Alfred P. Weber

[1] *Institute for Particle Technology, Clausthal University of Technology, Germany*

Abstract

Although the deflector wheel classifier is the dominant separation device in the industrial separation of fine-grained particle fractions, the classifying mechanisms at high particle loadings are still not described and understood sufficiently. The existing models for the calculation of the separation efficiency, which are mostly based on a single particle's fate, fail to capture the behavior at high particle loading where particle-particle and particle-wall collisions are encountered. To overcome this knowledge gap, a high-speed camera was used to analyze the particle movement in the separation process of a deflector wheel classifier representing real physical conditions. It is shown that particle-particle and particle-wall collisions must be included in a consistent theoretical model to represent the effective particle behavior in the separation process. In addition, the influence of process parameters such as revolution rate and mass loading on the separation efficiency of a deflector wheel classifier at high loadings is presented here.

Keywords: particle size, deflector wheel classifier, cut point, separation efficiency, separation sharpness

1. Introduction

Air classification is an important step in the production of many industrial powders. According to *Rumpf* (Rumpf H. and Raasch J., 1962; Rumpf H. and Leschonski K., 1967; Rumpf H. et al., 1974), the basic task of this process is to classify a mixture of particles of different sizes into a fine and a coarse particle fraction. Since product characteristics and quality are closely related to the particle size, products with a narrow particle size distribution are desired, e.g. for color pigments and abrasive powders (Leschonski K., 1988, 1996). In contrast to classifiers with unrestricted flow such as the spiral air classifier with a free vortex, the deflector wheel classifier produces a forced vortex due to the rotating paddles; this has been stated as being less dependent on the mass loading (Leschonski K., 1988, 1996; Rumpf H. and Raasch J., 1962; Rumpf H. and Leschonski K., 1967; Rumpf H. et al., 1974).

The underlying conception is that the particles experience a centrifugal force in the rotational flow field which is counteracted by the drag of the air flowing inwards between the paddles (cf. **Fig. 1**) (Rumpf H. and Raasch J., 1962). Coarse particles are deflected on the outer edge of the deflector wheel, while fine particles follow the air flow through the deflector wheel and are separated later from the air flow by an aero-cyclone (Leschonski K., 1988, 1996; Rumpf H. and Raasch J., 1962; Rumpf H. and Leschonski K., 1967; Rumpf H. et al., 1974).

In the last century, *Rumpf* (Rumpf H. and Raasch J., 1962; Rumpf H. and Leschonski K., 1967; Rumpf H. et al., 1974), *Molerus* (Molerus O., 1967; Molerus O. and Hoffmann H., 1968), *Sender*, *Schubert* (Schubert H., 1968) and *Husemann* (Husemann K., 1998) developed separation models which describe the particle behavior and the separation efficiency of a deflector wheel classifier only on the basis of geometrical and equilibrium considerations. These models, which consider the behavior of a single particle under the influence of the centrifugal force and drag, are applicable for calculation of the cut point using several empirical coefficients, which can only be obtained from experiments. However, they suffer from several drawbacks. First, the dependency of the empirical parameters on the operating conditions cannot be attributed to a physically sound picture of the separation process. Second, the particle-paddle and particle-particle collisions which become significant at higher loadings are

---

† Received 17 May 2016; Accepted 16 September 2016

[1] Leibnizstrasse 19, 38678 Clausthal – Zellerfeld, Germany
* Corresponding author: Christian Spötter
E-mail : Christian.Spoetter@tu-clausthal.de
TEL : +49-5323-72-2576 FAX: +49-05323-72-2830

not taken into account. To overcome this knowledge gap *Galk* (Galk J., 1995) and *Füchsel* (Füchsel S., 2005) examined the influence of the particle loading on the separation characteristics of a deflector wheel classifier. During these experiments, *Galk* found a decrease in the ratio of the measured to the theoretical cut point at an increasing mass loading accompanied by a decrease of the separation sharpness. He explained this phenomenon with a retroactive effect of the feed over impulse exchange onto the fluid flow between the separating paddles. According to *Galk*, this momentum exchange leads to a deceleration of the drag flow near the feed inlet (Galk J., 1995).

Bauer (Bauer U., 2002) extended the studies into the submicron particle range and observed that in this regime also, the material mass flow has an influence on the position and slope of the calculated separation curves under otherwise constant experimental conditions. Based on his experimental results, he hypothesized that different sections of the separation efficiency curve are directly related to the geometry of different parts of the classifier (Stender M. et al., 2015). This interesting approach may explain our observations—which will be treated in future work but are out of the scope of the present contribution.

While for quite a while, little attention has been paid to the flow field through the paddles of the deflector wheel, *Legenhausen* (Legenhausen K., 1991) analyzed the flow behavior between the separation paddles using a Laser Doppler Anemometer (LDA) based on a water model. He found that the flow between two separation paddles detaches forming a flow vortex. Later, *Toneva* (Toneva P. et al., 2011) determined the gas flow behavior in a deflector wheel classifier using Particle Image Velocimetry (PIV) and Computational Fluid Dynamic (CFD) simulations. In agreement with *Legenhausen* they found a detachment of the gas flow from the paddles accompanied by a gas vortex between the separation paddles. Further, *Toneva* demonstrated that the vortex formation leads to a constriction of the particle flow and an increase in the inward radial gas velocity. Although they neglected the influence of particle-particle collisions on the separation behavior, their numerical calculations indicated that the particles frequently collide with the separation paddles where coarse particles leave the separation zone faster than fine particles. The calculations of *Tenova* have also shown that the coarse particles rebound in both inside and outside direction, which leads to a deterioration of the separation sharpness. Deduced from the calculated trajectories, a large proportion of the particle stream is not transported into the inside of the separation wheel. On the contrary, their calculations have shown that a particle accumulation in the flow stream near the outside edge of the separation wheel is possible. According to *Toneva*, this accumulation will lead to a deterioration of the separation sharpness due to long residence times and particle-particle interactions (Spötter C. et al., 2015; Stender M. et al., 2015; Toneva P. et al., 2011).

In order to transfer the simulation results of *Toneva* et al. to studies at high loadings, *Stender* et al. (Stender M. et al., 2015) reconstructed a deflector wheel classifier type Hosokawa Alpine ATP 50. By replacing the two-sided mounting of the wheel axis by a one-sided high-speed ball bearing, they achieved direct optical access to the front side of the separator wheel. With this optical access and using a high-speed camera, initial studies of the gas flow and particle movement in a real separation process of a deflector wheel classifier were carried out. During their experiments, *Stender* et al. found that at a revolution rate of the deflector wheel of 6000 rpm, a vortex forms near the leading separation paddles. This vortex moves into a separation area between the two separation paddles at an increasing revolution rate and finally reaches the area near the pursuing paddle at a revolution rate of 15,000 rpm. With increasing revolution rate, the vortex increasingly constricts the particle flow stream. Through this study, *Stender* et al. were able to confirm the model from *Legenhausen* for the first time under real process conditions. They pointed out that particle-particle and particle-wall collisions affect the separation process (Spötter C. et al., 2015; Stender M. et al., 2015).

To incorporate the real behavior of the gas flow and the particle motion during the separation process into the existing models, it is necessary to extend the considerations of *Legenhausen* and *Toneva* et al. to higher particle concentrations. Based on these studies, a better interpretation of feedback effects at higher material loadings and of the particle interactions under real process conditions may be achieved.

While performing separation studies on fly ash, *Eswaraiah* and *Narayanan* (Eswarajah C. and Narayanan S.S., 2005) also noticed that the separation process at high loadings is not sufficiently understood to enable development of reliable physically sound models. For this reason, this work aims at the presentation of systematic studies of the separation characteristics of a deflector wheel classifier by varying the revolution rate between 3000 and 15,000 rpm and the material loadings between 1 to 5 %, which may form the basis for an improved model taking into account particle-particle and particle-wall collisions.

2. Theoretical basics

2.1 The operation principle of a deflector wheel classifier

In 1939, *Rumpf* (Rumpf H. and Raasch J., 1962) described for the first time the extension of a spiral air clas-

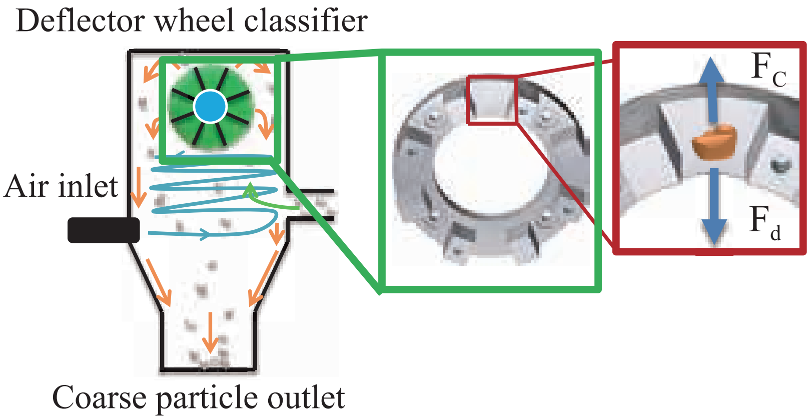

Fig. 1 Schematic diagram of a deflector wheel classifier.

sifier with a forced eddy sink flow, which is today known as a deflector wheel classifier (cf. **Fig. 1**). In this type of centrifugal counterflow air classifier, the flow field is formed by superposition of a sink flow and a vorticity flow induced by rotating paddles. The paddles are usually made out of thin plates, which are arranged vertically or obliquely to the separation wheel tangent (Rumpf H. and Raasch J.; 1962, Rumpf H. and Leschonski K., 1967; Rumpf H. et al., 1974).

The feed and the classifying air may be added separately or at the same time into the classifying zone of the deflector wheel classifier. The particles are then carried by the air flow towards the deflector wheel where the separation takes place. In the traditional approach, the particle movement between the paddles is determined by the opposing centrifugal force outwards and drag force inwards. For coarse particles, the centrifugal forces F_C dominate the drag forces so that the particles are rejected by the rotating wheel. For smaller particles, the centrifugal forces become less important compared to the drag forces F_d, and the particles are carried inwards where they are sucked into the fine particle outlet. In the following section, a simple model will be outlined which takes into account particle properties such as size and density and operation parameters such as air flow rate, material loading, revolution speed and wheel geometry

2.2 Classic model for cut point

For the following model, spherical particles with a given density are considered which neither interact nor influence each other, i.e. single particles in a uniform flow field, which is not affected by any walls. The flow field consists of a tangential velocity v_φ (circumferential direction) and a radial velocity v_r (inward direction). It is assumed that the particles initially have the same tangential u_φ and radial velocity components u_r as the classifying air ($u_\varphi = v_\varphi$ & $u_r = v_r$).

Due to the rotational movement, the particles experience the outwardly directed centrifugal force F_C

$$F_C = \rho_P \cdot V_P \cdot (u_\varphi^2/r) \tag{1}$$

where r is the distance to the rotation axis and u_φ is the particle tangential velocity which is assumed to be equal to v_φ (Bauer U., 2002; Legenhausen K., 1991; Spötter C. et al., 2015).

The drag force depends on the projection area of the particles, the drag coefficient and the relative velocity

$$v_{rel} = v_r - u_r \tag{2}$$

and can be written in the following way (Richardson J. F. and Zaki W.N., 1954; Rumpf H. and Raasch J., 1962):

$$F_d = c_w(Re) \cdot A_p \cdot (\rho_{Fl}/2) \cdot |v_{rel}| \cdot v_{rel} \tag{3}$$

For a certain particle size $x_{t,th}$, the radial velocity outwards induced by the superposition of centrifugal force and drag is equal to the radial gas velocity inwards so that particles of this size will describe circular trajectories without being classified to neither the fine nor the coarse fraction (idealized equilibrium). By assuming particle motion in the Stokes range, the cut point can be determined by equation (1) and (3) (Bauer U., 2002; Legenhausen K., 1991; Spötter C. et al., 2015):

$$x_{t,th} = \sqrt{\frac{18 \cdot \eta \cdot v_{r0} \cdot r_0}{\rho_p \cdot v_{\varphi 0}^2}} \tag{4}$$

where r_0 is the radial position where the equilibrium occurs. The calculated cut point $x_{t,th}$ at the radius r_0 is inversely proportional to the fluid circumferential velocity v_φ and proportional to the square root of the product $v_r r_0$. For a given deflector wheel geometry, a small cut point can only be achieved by a high peripheral speed and low radial velocities of the air flow. However, the separation grain size is distributed due to stochastic processes with identical shares into the fine and coarse material fractions (Bauer U., 2002; Legenhausen K., 1991).

2.3 Determination of separation curve and sharpness from experimental data

The separation efficiency $T(x)$ describes the fraction of a feed material, which is contained in the coarse material fraction after classification.

$$T(x) = \frac{m_C}{m_{\mathrm{Feed}}} \cdot \frac{q_{3,C}(x)}{q_{3,\,\mathrm{Feed}}(x)} \cdot 100\% \tag{5}$$

Here, feed and coarse materials were analyzed by laser diffraction in discrete size classes as a histogram or cumulative distribution. From the separation efficiency curve, the cut size is obtained for a separation efficiency of 50 % ($T(x_t) = 50$ %). The corresponding sharpness of cut is defined as (Stieß M., 2009):

$$\kappa = (x_{25}/x_{75}) \cdot 100\ \% \tag{6}$$

3. Material and method

3.1 Basic constriction and separation method of a deflector wheel classifier

In order to determine the separation characteristics, the modified deflector wheel classifier type Turboplex ATP 50 from Hosokawa Alpine with an aero cyclone and a bag filter system was used, as illustrated in **Fig. 2**.

As a feed material, limestone ($CaCO_3$) is introduced into the deflector wheel classifier (2) below the rotor via a feed screw attached to the side of the deflector wheel classifier (1). The cumulative particle size distribution of the feed material has an $x_{10,3}$ value of 5.86 μm, an $x_{50,3}$ value of 59.86 μm and an $x_{90,3}$ of 179,54 μm. From the bottom of the housing, the classifying air is supplied into the deflector wheel classifier tangentially via a classifying air pipe (3) equipped with an air filter. The aspirator produces a constant air flow of 75 m^3/h. The classifying wheel of the Turboplex ATP 50 has a wheel diameter of 50 mm and is powered by a horizontally positioned shaft. The peripheral speed of the separating wheel was varied using a frequency converter from 7.86 (3000 rpm) to 39.27 m/s (15000 rpm). The rejected coarse material leaves the separator downwards through the central particle lock system outlet (4). The fine material leaves the classifier wheel together with the classifying air stream via a fixed pipe (Spötter C. et al., 2015; Stender M. et al., 2015).

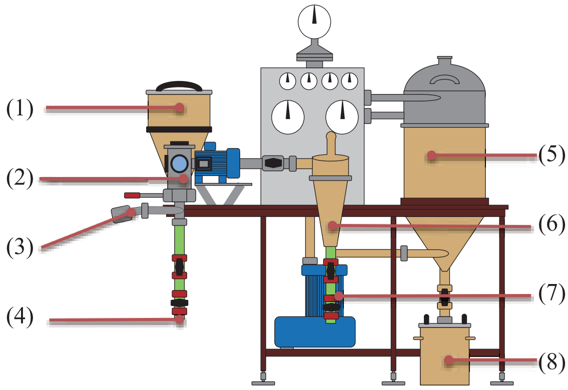

Fig. 2 Schematic of the Hosokawa Alpine ATP 50: (1) Feed screw, (2) deflector wheel classifier ATP, (3) separating air pipe, (4) particle lock system 1: coarse material outlet, (5) bag filter system, (6) aero cyclone (7) particle lock system 2: fine material outlet 1, (8) fine material outlet 2.

The fine particle fraction is separated from the classifying air by an aero cyclone (6). The fine particles leave the cyclone through a particle lock system into the fines outlet 1 (7). The very fine particles of the fine fraction leave the aero cyclone via the vortex finder and are finally separated in a bag filter system (5). The bag filters are periodically cleaned with compressed air and the particles are collected in a fines outlet 2 (8). By using the particle lock systems (4) and (7) for the separation of the coarse and fine particle fraction, it was possible to take samples while the separation wheel was still running. Therefore, it is possible to take and analyze samples from the starting point of the separation process and at different intervals until the separation process reaches stationary conditions (Spötter C. et al., 2015; Stender M. et al., 2015).

In the present study, an experimental protocol was used to recover the coarse and fine particle fractions. In different runs, the peripheral speed varied between 7.86 and 39.27 m/s, and the mass loading ranged from 1 to 5 %. The sampling procedure consisted of taking subsequent samples for 5 min each with a total collection time of 60 min using a particle lock system shown in **Fig. 2** ((4) and (7)). With this time-resolved system, it was possible to determine the time the deflector wheel classifier needs to reach stationary separation behavior.

3.2 Reconstruction of the deflector wheel classifier to permit optical accessibility

In order to determine the separation characteristics of a deflector wheel classifier, *Stender* et al. (Stender M., et al., 2015) reconstructed the ATP 50 so that an optical access onto the deflector wheel was achieved. In order to maintain the classification conditions and the flow of the separation air, *Stender* et al. did not change the geometry of the classifying wheel or the neighboring components. In order to realize this, the motor of the wheel and the outlet pipe of the fine particle fraction had to be moved to the same side of the deflector wheel. The outlet pipe of the fine particles was realized using a hollow shaft supported by two high-speed spindle bearings (A), driven by a flat belt (B) which is sealed with an oil-soaked gasket. The

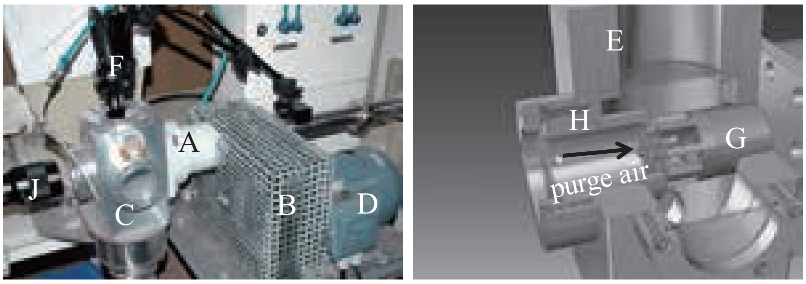

Fig. 3 Remodeled Turboplex ATP 50 deflector wheel: a) One-sided bearing for optical access on the opposite side, b) Installations to permit optical access and purge air for keeping the view of the deflector wheel free. (A = high-speed spindle bearings, B = flat belt, C = classifier chamber, D = three-phase asynchronous motor, E = top viewing window, F = light source, G = classifying wheel, H = side viewing window, I = transparent front wall, J = high-speed camera). Reprinted with permission from Ref. (Stender M. et al., 2015). Copyright: (2015) John Wiley & Sons Ltd.

drive of the hollow shaft takes place via a 1:3 gearing which is powered by a frequency-controlled three-phase asynchronous motor (D) (see **Fig. 3**) (Stender M. et al., 2015).

For the optical access to the classifying wheel, specially designed viewing windows were installed on the top (E) and on the side (H). The windows were placed in the side wall and the ceiling of the housing. Special glass discs of the type Mirogard were used for the windows which exhibit anti-reflective properties on both sides thus leading to a high transparency. A high-speed Keyence VW-600M camera was placed in front of the window (cf. **Fig. 3** (J)) to visualize the motions of the particles during the separation process. In order to prevent light reflections, the camera was aligned in a 90° angle to the illumination realized with a tripod lamp across the ceiling window (Spötter C. et al., 2015; Stender M. et al., 2015).

3.3 Calculation of the material loading

Besides the circumferential speed, also the mass loading (ML) was varied in this study. According to equation (7), the mass loading was calculated by dividing the feed mass flow rate by the separation air mass flow rate (Stieß M., 2009):

$$ML = \frac{feed\,mass\,flow\left[\frac{\mathrm{kg}}{\mathrm{h}}\right]}{separation\,air\,mass\,flow\left[\frac{\mathrm{kg}}{\mathrm{h}}\right]} \tag{7}$$

The aspirator of the deflector wheel classifier provided a constant air flow rate of 75 m^3/h, corresponding to an air mass flow rate of 90.13 kg/h. The mass loading was varied between 1 and 5 % (**Table 1**).

Table 1 Mass loading of the experiments at stationary conditions from 1 to 5 %.

Mass loading (ML)	Feed mass flow		Separation air mass flow
[%]	[kg/h]	[g/min]	[kg/h]
1	0.903	15.05	90.31
2	1.806	30.10	90.31
3	2.709	45.15	90.31
4	3.612	60.20	90.31
5	4.515	75.25	90.31

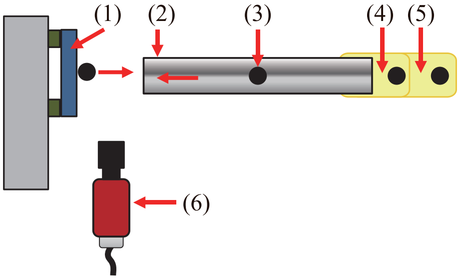

Fig. 4 Illustration of a particle cannon. (1) impaction plate, (2) metal tube, (3) particle, (4) relaxed ribbon, (5) tensioned ribbon and (6) high-speed camera.

3.4 Construction of a particle cannon

In section 5 of this study, a new model approach for the separation of a deflector wheel classifier will be presented. This model includes as a new parameter the thickness *H* of the particle layer which is formed by the impacting and rebounding particles close to the pursuing paddle. In order to determine this parameter, a particle cannon (cf. **Fig. 4**) was constructed which is able to image particles with sizes from 500 to 2000 µm at a velocity up to 80 m/s where the lower particle size is given by the camera resolution which also depends on the particle material. Since the limestone particles exhibited a mediocre contrast, the dependence of H on impact velocity and mass loading was investigated for quartz particles. During each experiment, particles were accelerated by means of an elastic ribbon under tension to different velocities (finger of a rubber glove). The particles leave the metal tube and collide with an impaction plate. While at very low loadings, the coefficient of restitution for single particles can be determined from the initial and rebounding velocity ($e_n = v_r/v_i$), at higher loadings, where significant particle-particle collisions occur, the particle layer thickness H is measured from images of the bulk behavior obtained with the high-speed camera.

Since the boundaries of the particle layer were not sharp but rather diffuse, the thickness was determined from the distribution of the gray scale values evaluated with the software ImageJ. As a criterion for the extension of the layer, the position was recorded where the gray scale value had dropped to 80 % of the maximum value.

4. Experimental results

4.1 Visualization and parametrization of gas and particle flow in the separation zone

The following results present the gas flow and the particle motion in the area between two separation paddles (separation zone). While for the visualization of the gas flow very fine limestone particles were used, the motion of coarser particles was visualized with coarser limestone particles ($x_{50,3}$ of 59.86 μm). As tracers, fine limestone particles with an $x_{50.3}$ of 2.15 μm were used which follow the gas flow without lag and without classification. To catch the gas flow behavior, due to some inhomogeneous distribution of the fine particles, the discernible contrast points were tracked on subsequent images. Using the software Motion analyzer VW 9000, the motion of these fine particle accumulations was represented by lines of arrows.

In **Fig. 5a)**, it is shown that at a revolution rate of 3000 rpm, the limestone tracer particles pass the whole separation area in an arc-like flow. The gas flow starts to be deflected slightly in the left/middle section of the classifying zone, while near the pursuing paddle, the gas flows in straight lines. Nevertheless, the gas flow of the very fine limestone particles passes the entire classification area at a revolution rate of 3000 rpm. At the beginning, the coarse limestone particles (**Fig. 6a)**) follow the gas flow into the separation zone, but later they continue their motion towards the pursuing paddle deviating from the gas flow due to their higher inertia. Only at this low revolution rate is the spatial distribution of the particles relatively homogeneous over the classification area as a consequence of the less deviated incoming particles and deflected larger particles (cf. **Fig. 6a)**).

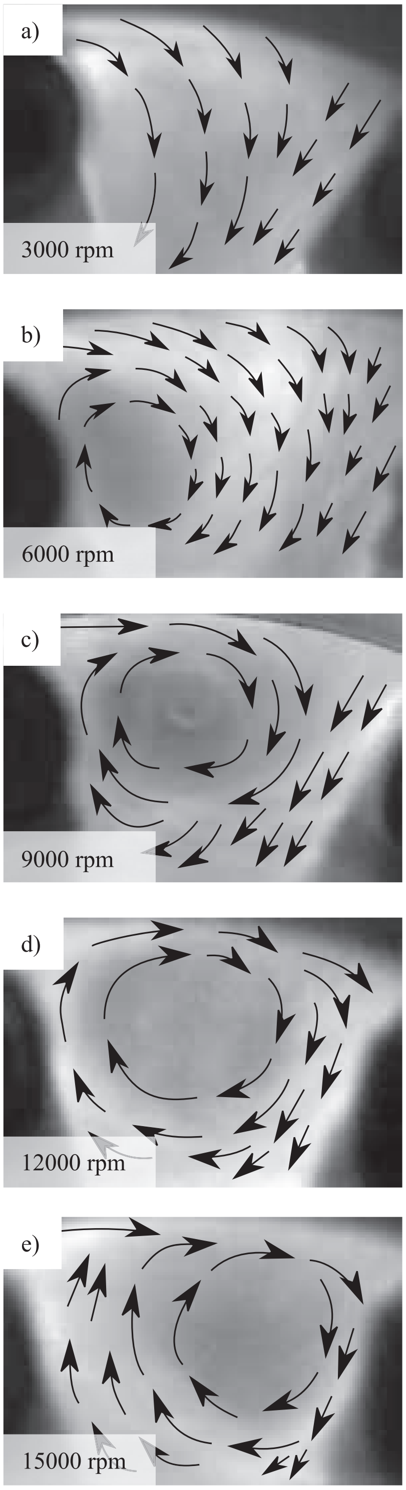

Fig. 5 Visualization of the gas flow (indicated by fine particles) between the separating paddles for increasing revolution rates from **a)** to **e)**. View onto the separation area between two deflection paddles (The separation wheel moves in anticlockwise direction). Reprinted with permission from Ref. (Stender M. et al., 2015). Copyright: (2015) John Wiley & Sons Ltd.

From subsequent images, the particle velocity relative to the pursuing paddle was measured using the Motion analyzer VW 9000 software. Interestingly, the particle

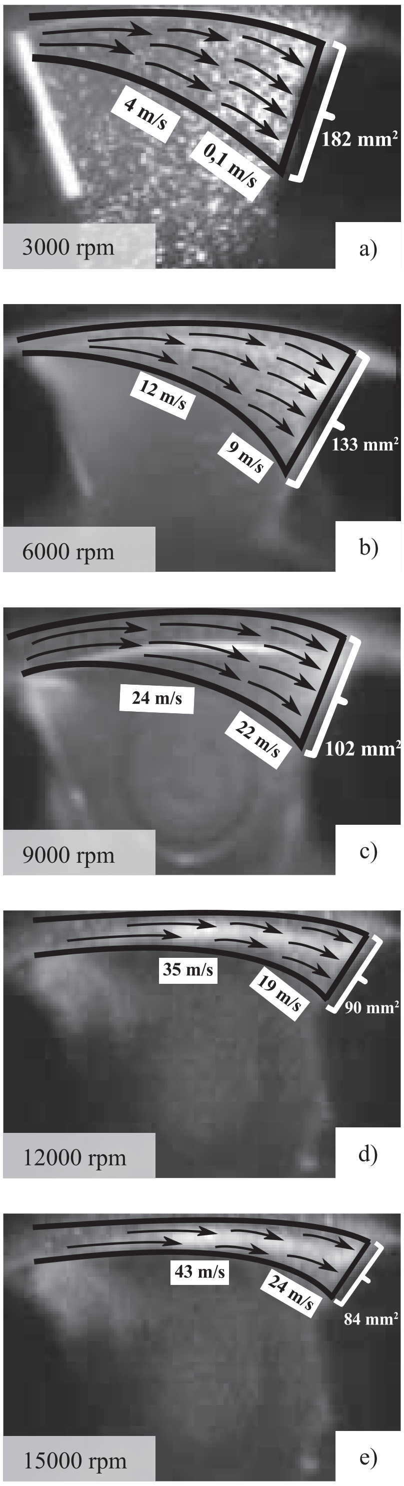

Fig. 6 Visualization of the coarse particle motion between the separating paddles for increasing revolution rates from **a)** to **e)**. View onto the separation area between two deflection paddles (The separation wheel moves in anticlockwise direction) [Reprinted with permission from Ref. (Stender M. et al., 2015). Copyright: (2015) John Wiley & Sons Ltd.

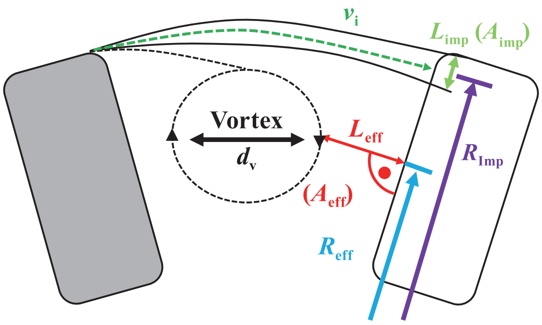

Fig. 7 2D model of the vortex formation and the particle flow in the separation zone of a deflector wheel classifier (paddle depth is D): L_{eff} = effective separation distance ($A_{eff} = L_{eff} \cdot D$ = effective separation area), L_{imp} = Impaction length ($A_{imp} = L_{imp} \cdot D$ = impaction area), d_v = vortex diameter, v_i = relative velocity between particle and pursuing paddle, R_{imp} = mean impaction radius (related to the axis of rotation) and R_{eff} = distance between the center of the vortex and the center of the deflector wheel.

velocity, initially close to the peripheral speed of the paddle, decreased as the paddle approached. This deceleration effect could be caused either by bouncing particles colliding with the approaching particles or by peripheral air flow created by the paddle motion, or a combination of both. In any case, the deceleration of the approaching particles was observed at all revolution rates, as indicated by the relative velocities given in **Fig. 6**.

For higher revolution rates, a vortex is formed (cf. **Fig. 5b–e**) which leads to a constriction of the particle flow, thereby focusing especially the coarse particles to hit the pursuing paddle on a smaller area (**Fig. 6b–e**) (Stender M. et al., 2015).

At an increased revolution rate of 6000 rpm, the tracer particle flow (**Fig. 5b**) begins to form a vortex on the left side of the separation area. This vortex leads to a constriction of the particle flow, thereby focusing it onto a smaller area of the impaction paddle (**Fig. 6b**) (Stender M. et al., 2015).

The vortex begins to move away from the leading separation paddle into the middle of the separation area if the revolution rate is increased further to 9000 rpm (**Fig. 5c**). With increasing revolution rate (**Fig. 5d–e**), the vortex moves closer and closer to the pursuing paddle. **Fig. 7** illustrates the model of the vortex formation and the particle motion in the separation zone.

Using the parametrization shown in **Fig. 7**, the flow field between the separation paddles was determined as a function of the revolution rate. The results illustrate the movement of the vortex leading to a constriction of the gas flow which depends on the revolution rate. Regarding the separation process, the constriction of the flow results in an increased inwards radial gas velocity. This should facilitate the entrainment of coarser particles according to the classic model outlined in chapter 2.2. However, this effect was not observed in the separation curves as discussed in chapter 4.3.

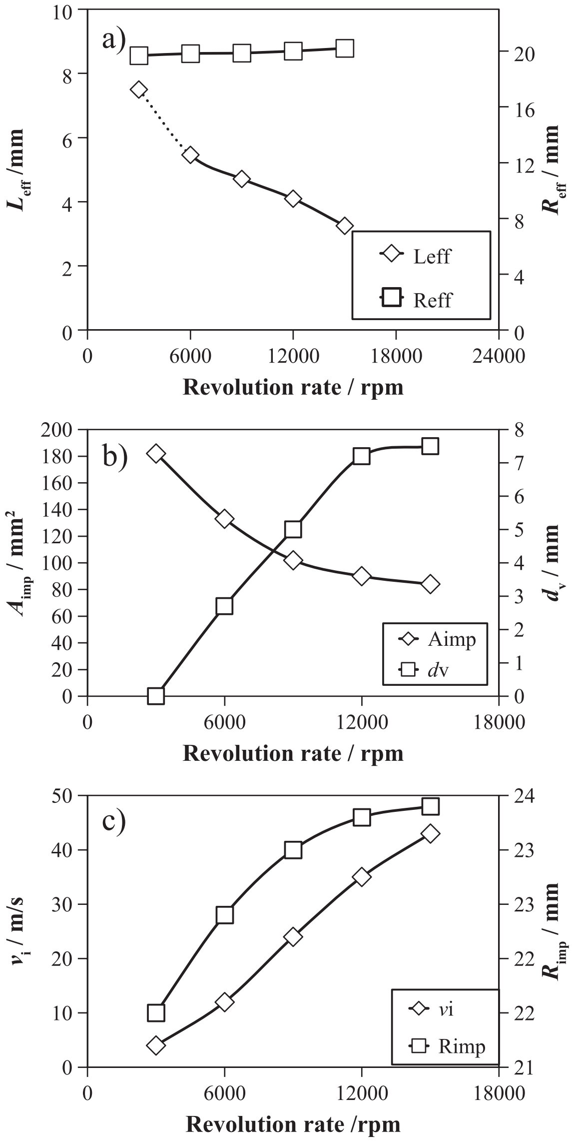

Fig. 8 **a)** Separation diameter L_{eff} and effective separation radius R_{eff} plotted against the peripheral speed of the deflector wheel; **b)** Impaction area A_{imp} and vortex diameter d_v plotted against the peripheral speed of the deflector wheel; **c)** Relative velocity between feed particle and pursuing paddle v_i and mean impact radius R_{imp} plotted against the peripheral speed of the deflector wheel.

While the lateral position of the vortex between the paddles depends on the peripheral speed, the radial position does not change (cf. **Fig. 8a**). At the same time, the size of the vortex d_v increases linearly with peripheral speed up to about 32 m/s, at which point it approaches a constant value given by the geometric constrictions of the paddles (cf. **Fig. 8b**). In all experiments performed here, the peripheral speed v_s of the separating wheel was higher than the circumferential component of the classifying air v_φ ($v_\varphi/v_s < 1$), leading to a clockwise rotating gas vortex for an anticlockwise rotating wheel in agreement with the results of the LDA measurements on a water model by *Legenhausen* (Legenhausen K., 1991).

For the classifier geometry used, it was observed that the particles were initially nearly at rest so that the relative velocity was mainly determined by the motion of the paddles as shown in **Fig. 8c**). As a consequence of the vortex behavior, the incoming particles are increasingly focused onto an impaction area A_{imp} of the pursuing paddle with increasing peripheral speed (cf. **Figs. 6 (b–e)** & **8b**). The impaction area is reduced in size and moves, on average, to the outer edge with increasing peripheral speed as indicated by the parameter R_{imp} (cf. **Fig. 8c**).

After the impaction, the coarse particles are reflected at a reduced speed relative to the pursuing paddle in random directions. However, in an absolute coordinate system, the particles experience much higher velocities after the rebound which is important for the centrifugal force. At low material charge, it is possible that a single particle bounces from the pursuing paddle almost unimpeded to the opposite leading paddle. With an increasing material charge and constriction of the particle flow (cf. **Figs. 6** and **8**), the rebounding particles collide with subsequent feed particles in a zone near the pursuing paddle. This interaction decelerates the approaching particles as well as the rebounding particles. With an increase in particle concentration, the frequency of particle-particle collisions also increases which reduces the extension of the collision zone as indicated by a particle layer in the vicinity of the pursuing paddle (cf. **Fig. 16**).

4.2 Transition from instationary to stationary separation behavior

In the following sections, the particle separation behavior will be discussed. Since the separation process between the paddles is very fast (in the ms range), it may be hypothesized that the overall separation process quickly reaches a steady state. However, in the following text it will be shown that, depending on the revolution rate and material loading, it may take several minutes up to over 50 min to reach a stationary separation behavior.

In **Fig. 9**, the mass fractions of fine and coarse material are shown as a function of the separation time for different mass loadings. For a revolution rate of 9000 rpm, the stationary separation is achieved faster with increasing mass loading and at a higher fraction of coarse material. The same behavior, however, in a mirror symmetrical way, applies for the fine material.

A similar observation was made for the separation curve as shown in **Fig. 10**. For a revolution rate of 9000 rpm and a mass loading of 3 %, a stationary separation behavior is not achieved before about 25 min.

In the following text, the time to reach stationary separation curves which are parametrized by the cut point and the sharpness of cut will be summarized for various revo-

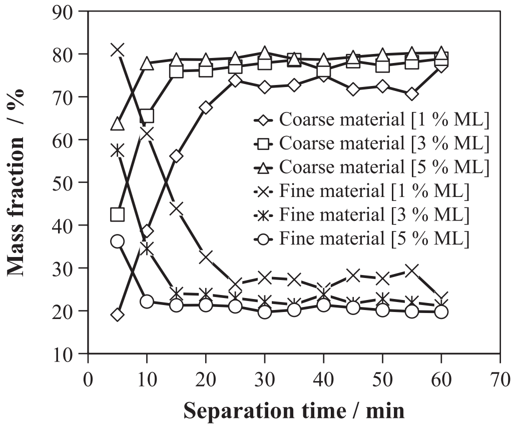

Fig. 9 Coarse and fine mass fraction plotted against the separation time for a material loading of 1 to 5 % and constant revolution rate of 9000 min^{-1}.

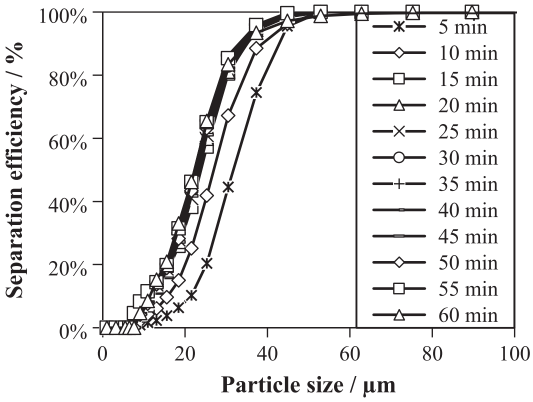

Fig. 10 Separation efficiency plotted against the separation time for a mass loading of 3 % and revolution rate of 9000 rpm.

lution rates and mass loadings. As shown in **Fig. 11a)** and **b)**, the cut point and sharpness reaches steady state faster with an increasing revolution rate and/or increasing mass loading. These results indicate that the particles accumulate in a hold-up ring around the deflector wheel which was in fact seen with the high-speed camera (**Fig. 12**). This hold-up ring consists of deflected and approaching particles with a concentration which increases significantly near the outer edge of the deflector wheel. When assuming that the capacity of this hold-up ring is constant, the dependence of the characteristic time to reach the steady state on the revolution rate and mass loading becomes obvious. The time to fill the hold-up ring scales inversely with the mass flow rate which in turn is determined by the particle velocity (peripheral speed) and the particle concentration (mass loading).

4.3 Separation behavior in stationary conditions

As shown in the last chapter, the deflector wheel classifier needs a certain time to reach stationary separation behavior, which may take up to 50 min in the worst case (3000 rpm). In the following text, the separation behavior at steady state conditions is outlined.

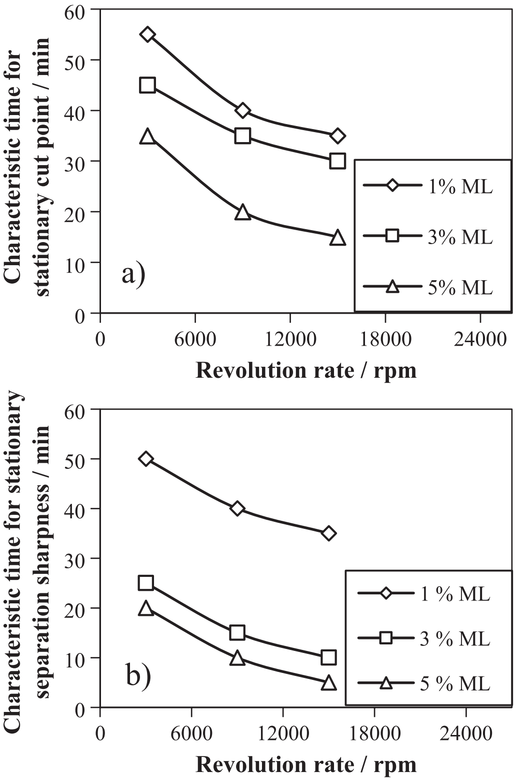

Fig. 11 **a)** Arrival of a stationary cut point & **b)** Arrival of a stationary separation sharpness plotted against the revolution rate for material loadings of 1 to 5 %.

Fig. 12 Image of the hold-up ring around the deflector wheel with high concentrations close to the outer edge of the wheel surrounded by a more diffuse zone.

In **Fig. 13**, the fractions of fine and coarse material are shown as a function of revolution rate and mass loading. With increasing revolution rate and mass loading, the fraction of the coarse material increases where, however, the influence of the revolution rate is dominating the effect of the mass loading. It is clear that the behavior of the fine material fraction is mirror-symmetrical to the coarse material. While the profile of the mass fraction curve remains unchanged, the absolute values of the mass fractions depend on the powder properties such as initial size distribution.

The dominating influence of the revolution rate is also

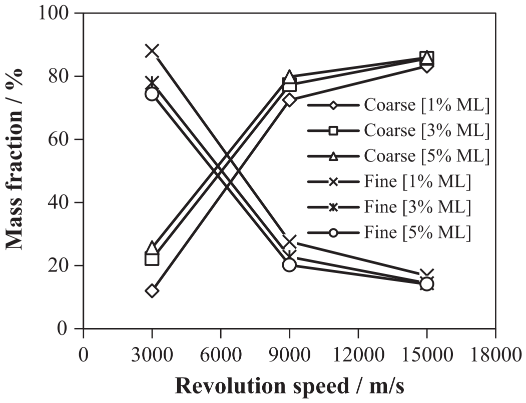

Fig. 13 Coarse and fine mass fraction plotted against the revolution rate in stationary conditions.

reflected in the separation curves shown in **Fig. 14a)**. While an increase of the revolution rate by a factor of 3 leads to an 83 % decrease of the cut point, an increase of the mass loading of the factor 3 results only in a reduction of 24 % (starting at 1 % and 3000 rpm). The evolution of the cut point for all investigated conditions is shown in **Fig. 14b)**.

In contrast to the cut point, the sharpness of cut is nearly independent of the revolution rate and mass loading. For the limestone particles with a median size of 70 µm, the values varied between 54 and 62 % (cf. **Fig. 14c)**). This uniformity of the sharpness was deemed to be a consequence of the hold-up ring around the deflector wheel which could act similarly to a pre-filter for the incoming particles. In addition, the particle layer formed at the pursuing paddle may also contribute to a constant sharpness, as further outlined in the discussion. Some experiments with finer limestone particles (median particle size of 40 µm) indicate a similar independence of the sharpness of cut on the revolution rate and mass loading, however, reaching higher average values in the range of 65 %.

5. Discussion

In industrial applications of deflector wheel classifiers, the operation time is usually so long that the time needed to reach the steady state separation may be considered as negligible. However, the reason for this induction time, i.e. the hold-up ring which needs to be filled for stationary operation, can also influence the feed delivery to the classifying wheel with respect to size distribution and initial particle velocity. While the detailed investigation of the characteristics of the hold-up ring is beyond the scope of this contribution, the motion of the particles in the deflector wheel will be treated in the following text. From the high-speed camera images presented in chapter 4.1, it is concluded that the particles are nearly at rest in an absolute coordinate system, i.e. the deflection paddles approach the particles which start to be drawn into the inter-paddle space by the radial gas flow. Therefore, in the approach phase, the particles have no peripheral speed so that they do not experience a centrifugal force. This result may be different for separators where the particles are accelerated to a certain circumferential speed before entering the classification zone. However, the deflector wheel classifier used here is representative for a significant class of separators. In the case of particles initially at rest, the classic model comparing centrifugal force and drag is not applicable and a physical sound cut size cannot be estimated. In fact, the particles would experience centrifugal forces only after being hit by the paddle. This phase will be discussed in more detail below. During the approach phase, however, the particles are accelerated in radial direction due to the constriction of the free flow area as a

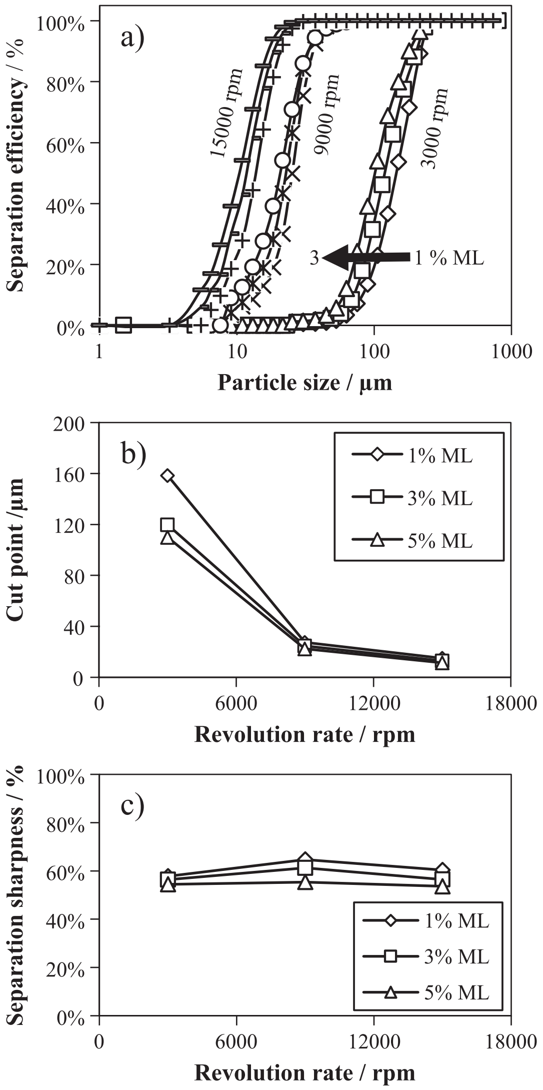

Fig. 14 **a)** Separation efficiency plotted against the particle size, **b)** Cut point & **c)** Separation sharpness against the revolution rate in stationary conditions.

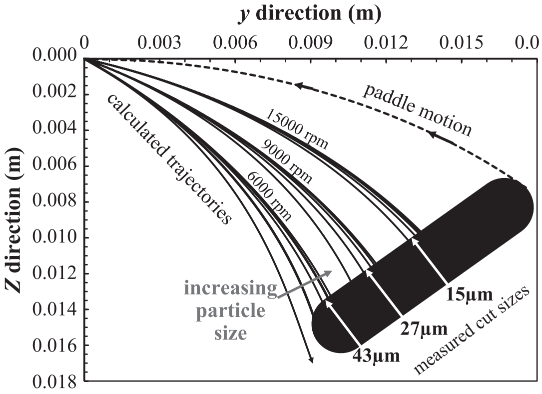

Fig. 15 Comparison of calculated limestone particle trajectories (black lines) for three revolution rates (6000, 9000, 15000 rpm) during the approach phase using a simple model with the measured cut sizes (43 µm, 27 µm, 15 µm) (white arrows). For each revolution rate, the calculated trajectories for particles with 10, 20, 40, 80 and 160 µm, respectively, are shown. The dashed line indicates the motion of the outer edge of the paddles, moving in anticlockwise direction.

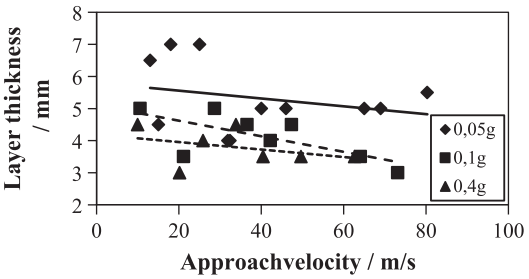

Fig. 16 Layer thickness of quartz particles plotted against approach velocity.

consequence of the vortex. Based on the geometric parametrization of the vortex (cf. chapter 4.1), the particle trajectories relative to the paddles were calculated by numerically integrating the equation of motion. To do so, it was assumed that the paddle approaches the particles at the given peripheral speed while the particles are accelerated in radial direction by the radial inwards gas flow. Since the revolution speed of the vortex and the gas flow at the initial zone between the paddles are not known, it was simply assumed that radial particle motion starts at the vortex in the presence of an accelerating radial gas flow. The radial component of the gas flow was approximated by the total gas flow divided by the cross-sectional area A given by:

$$A(r) = D{\cdot}L(r) = D{\cdot}[(R_\mathrm{v} - L_\mathrm{eff}) - (r{\cdot}(2R_\mathrm{v} - r))^{\frac{1}{2}}] \tag{8}$$

where R_V is the vortex radius (=$d_\mathrm{V}/2$).

The radial particle motion is then determined by:

$$\frac{\mathrm{d}u_r}{\mathrm{d}t} = \frac{18 \cdot \eta_\mathrm{eff}}{\rho_\mathrm{p} \cdot x^2} \cdot \left(v_r(r) - u_r(r)\right) \tag{9}$$

where Stokes' regime was assumed and the radial gas velocity was calculated by $v_r(r) = \dot{V} / A(r)$.

The calculated trajectories obtained from this simple model are shown in **Fig. 15** for three revolution speeds (6000, 9000, 15000 rpm), corresponding to peripheral speeds of 15.71, 23.56 and 39.27 m/s, respectively. In **Fig. 15**, the calculated particle motion is shown in the coordinate system where the origin is fixed on the outermost point of the leading paddle for limestone particles with sizes of 10, 20, 40, 80 and 160 µm.

From **Fig. 15** it is obvious that the particle trajectory in the approach phase depends on the particle Stokes' number (determined by the particle size and density and radial gas flow velocity) and the peripheral speed of the deflector wheel. However, the radial dispersion of the particles depends also on the effective viscosity η_eff, i.e. the drag coefficient encountered by the particle due to friction with the gas and to particle-particle collisions. Beside the gas properties, this effective viscosity is also a function of the peripheral speed and mass loading and can be approximated following the model of Richardson and Zaki (Richardson J. F. and Zaki W.N., 1954). Although the exact value of η_eff is not known for the particle system observed here, the particle trajectories calculated with the pure gas viscosity are in qualitative agreement with the experimental observations (cf. **Fig. 6**).

In addition to the calculated particle trajectories, the measured cut sizes (43 µm, 27 µm, 15 µm) for the three revolution rates (6000, 9000, 15000 rpm) are also indicated in **Fig. 15**. The white arrows indicate the locations of these cut sizes on the pursuing paddle in relation to the calculated trajectories. In this simple model for a given operating condition, the white arrow indicates the position where the feed is distributed in equal parts into the fine and coarse fraction. However, this size-dependent partitioning of the feed between the fine and coarse fraction could not be recorded with the high-speed camera used due to the limited size resolution which was further exacerbated by superposition effects at elevated concentrations.

In the rebound phase, the situation near the paddle is much more complicated. The particles bouncing from the paddle collide with the particles just approaching, leading to a very dense particle layer. Due to the limited resolution for the limestone particles, the thickness of this layer could not be determined directly at the paddle from the high-speed camera images. Therefore, off-line experiments with quartz particles which gave a better contrast were performed with the particle cannon (cf. chapter 3.4) to investigate the principal dependencies of the particle layer thickness on the mass loading and approach velocity.

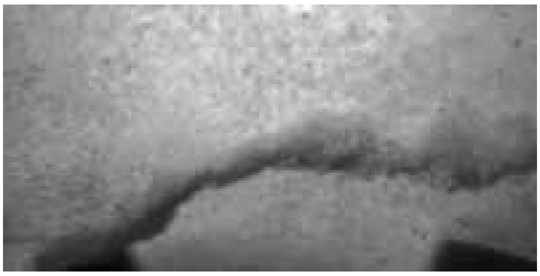

Fig. 17 High-speed camera picture of a particle streak at the outer edge of the deflector wheel.

As indicated in **Fig. 16**, the layer thickness depends more strongly on the mass loading than on the approaching velocity which corresponds to the peripheral speed of the paddle. In this particle layer, the concentration is extremely high so that the particles are prevented from free motion due to frequent particle-particle collisions. Therefore, we hypothesize that depending on the radial position, the different parts of the particle layer experience different centrifugal forces. It is then assumed that at a certain radial position, the centrifugal forces overcome the inwards directed drag on the particle layer. As especially well observed at low peripheral speed, the outer part of the particle layer discharges toward the hold-up ring while the inner part is drawn into the fine fraction. In **Fig. 15**, the measured cut sizes for the different revolution rates are indicated by white arrows. For each revolution rate, the arrow would indicate the separation of the feed material into a coarser fraction discharged to the outside in the form of streaks and a fine fraction reporting to the inside.

The formation of streaks on the periphery of the deflector wheel was already deduced by *Toneva* et al. (Toneva P. et al., 2011), who analyzed the gas flow field in a deflector wheel separator. They concluded that particles which are rejected from the pursuing paddle could build particle streaks in the periphery of the deflector wheel, exactly as observed in the high-speed camera images (cf. **Fig. 17**).

Surprisingly, the occurrence of streaks is periodical with a frequency which depends on peripheral speed and mass loading. So far, however, a detailed analysis of the streak characteristics has not been completed.

Since the detailed investigation of many open issues such as fine particle trajectories and motion, the thickness of the particle layer at the pursuing paddle and the circumferential speed of the vortex is currently restricted by the resolution of the high-speed camera, it is planned for the future to use a microscope objective and a Laser Doppler Anemometer to quantitatively evaluate these phenomena. These measurements, combined with ongoing CFD and DEM calculations, should provide a solid base for the development of a more quantitative separation model.

6. Summary

The performance of a deflector wheel classifier at steady state condition was studied experimentally with a limestone feed material. It was found that the time to reach stationary separation behavior may amount to several tens of minutes depending on mass loading and peripheral speed. In steady state, the separation efficiency curve, separation sharpness and cut point also depend on mass loading and peripheral speed.

The visualization of the separation zone between the paddles of the deflector wheel revealed that the classic separation models do not represent the physics of the separation process adequately. First, the formation and evolution of a vortex forming inside the separation zone as proposed by *Legenhausen*, *Toneva* et al. and *Stender* et al. has to be taken into account. This vortex causes a constriction of the radial fluid flow in the separation zone. Secondly, in an absolute coordinate system, the particles have nearly no peripheral speed in the approach phase towards the pursuing paddle and therefore they do not experience centrifugal forces in this phase. Third, the particles bouncing from the paddle collide with the incoming particles and form a dense layer close to the pursuing paddle. We hypothesize that the particles spread radially in the approach phase while the separation into coarse and fine fraction occurs in the dense layer close to pursuing paddle. In this model, the separation occurs at a special radial position on the pursuing paddle. Combining these considerations with the measured cut points may provide the base for more quantitative separation models taking into account operational and particle parameters.

As confirmed by high-speed camera images, the coarse fraction discharges as streaks to the periphery of the deflector wheel, probably contributing to the hold-up ring which forms around the deflector wheel. This hold-up ring which, to the best of our knowledge, is described here for the first time seems to be responsible for the induction time to reach stationary separation conditions.

Finally, the sharpness of cut was observed to be virtually constant, only marginally influenced by mass loading and peripheral speed. While this fact may facilitate the development of a separation model significantly, i.e. reducing the task to the determination of the cut point, the reason for the constant sharpness of cut is unclear so far. This phenomenon indicates that the interplay between particle approach, layer formation, streaks and hold-up ring is far from being understood and needs much more in-depth investigations.

Acknowledgements

The German research foundation is gratefully acknowledged for their financial support of this work in context of the priority program SPP 1679 (“Dyn. Simulation of cross-linked solid processes”) under the grand sign WE 2331/16-1.

In addition, special thanks go to B.Sc. Leonard Hansen for his work on the model approach and the particle cannon.

Abbreviations

CFD	Computational Fluid Dynamics
LDA	Laser Doppler anemometry
PIV	Particle image velocimetry

Greek letters

ρ_{Fl}	Fluid density
ρ_{P}	Particle density
η	Dynamic viscosity

Equation letters

A_{p}	[m^2]	Particle surface
$c_{\mathrm{w}}(Re)$	[–]	Coefficient of resistance
F_{c}	[N]	Centrifugal force
F_{W}	[N]	Drag force
g	[m/s²]	Gravity
g_{C}	[–]	Coarse material proportion
k	[%]	Separation sharpness
m_{C}	[kg]	Coarse material mass
m_{Feed}	[kg]	Feed material mass
q_{Feed}	[µm^{-1}]	Particle density distribution of the feed
q_{C}	[µm^{-1}]	Particle density distribution of the coarse particle fraction
Q_3	[–]	Particle size distribution
r_0	[m]	Separation radius
Re	[–]	Particle-Reynolds-number
$T(x)$	[%]	Separation efficiency
u_{p}	[m/s]	Particle circumferential velocity
V_{P}	[m^3]	Particle volume
v_{rel}	[m/s]	Relative velocity
v_{r0}	[m/s]	Radial fluid velocity at the radius r_0,
v_{φ}	[m/s]	Fluid circumferential velocity at radius r_0
x	[µm]	Particle size
x_{25}	[µm]	Particle size at 25 % of the separation efficiency curve
x_{75}	[µm]	Particle size at 75 % of the separation efficiency curve
x_{c}	[µm]	Median cut point

References

Bauer U., Zur trennscharfen Feinstsichtung in Fliehkraft-Abweiseradsichtern, Dissertation, TU Clausthal (2002).

Eswaraiah C. and Narayanan S.S., Studies on a rotating wheel air classifier for size classification of fly ash, Mineral process technology, Trichy India (2005) 465–472.

Füchsel S., Trockene Desagglomeration von Nanopartikelflocken in einer Gegenstrahlmühle mit kombinierter Onlineüberwachung, Dissertation, Clausthal (2012).

Galk J., Feinsttrennung in Abweiseradsichtern, Dissertation, TU Clausthal (1995).

Husemann K., Modelling of Dry Countercurrent Classification, Aufbereitungs-Technik 39, Freiberg (1998) 279–286.

Legenhausen K., Untersuchung der Strömungsverhältnisse in einem Abweiseradsichter, Dissertation, TU Clausthal (1991).

Leschonski K., Windsichter, verfahrenstechnische Maschinen zur Herstellung definierter pulverförmiger Produkte, Jahrbuch 1988 der Braunschweigischen Wissenschaftlichen Gesellschaft, Braunschweig (1988).

Leschonski K., Classification of particles in the submicron range in an impeller wheel air classifier, KONA Powder and Particle Journal, 14 (1996) 52–60.

Molerus O., Stochastisches modell der gleichgewichtssichtung, Chemie Ingenieur Technik, 39 (1967) 792–796.

Molerus O., Hoffmann H., Darstellung von windsichtertrennkurven durch ein stochastisches modell, Chemie Ingenieur Technik, 41 (1969) 340–344.

Richardson J.F., Zaki W.N., The sedimentation of a suspension of uniform spheres under conditions of viscous flow, Chemical Engineering Science, 3 (1954) 65–73.

Rumpf H. and Raasch J., Desagglomeration in Strömungen, Karlsruhe (1962).

Rumpf, H., Leschonski K., Prinzipien und neuere Verfahren der Windsichtung, Chemie Ingenieur Technik, 39 (1967) 1231–1241.

Rumpf H., Sommer K. and Stieß M., Berechnung von Trennkurven für Gleichgewichtsichter, Verfahrenstechnik (8), Karlsruhe (1974).

Schubert H., Aufbereitung fester mineralscher Rohstoffe—Band 1, Leipzig (1968).

Stender M., Legenhausen K. und Weber A.P., Visualisierung der Partikelbewegung in einem Abweiseradsichter, Chemie Ingenieur Technik, 87 (2015) 1392–1401..

Stieß M., Mechanische Vefahrenstechnik—Partikeltech-nologie 1, Springerverlag Konstanz (2009).

Spötter C., Stender M., Legenhausen K. und Weber A.P., Dynamische Trenncharakteristik von Abweiseradsichtern, Produktgestaltung in der Partikeltechnologie Band 7, Faunhofer Verlag (2015).

Toneva P., Epple P., Breuer M., Peukert W., Wirth K.-E., Grinding in an air classifier mill Part I: Characterisation of the one-phase flow, Powder Technology, 211 (2011) 19–27.

Toneva P., Wirth K.-E., Peukert W., Grinding in an air classifier mill—Part II: Characterisation of the two-phase flow, Powder Technology, 211 (2011) 28–37.

Author's short biography

Christian Spötter

Christian Spötter obtained his M.Sc. degree in 2014 from Clausthal University of Technology, Clausthal-Zellerfeld, with the study of environmental process engineering. For his master's thesis he researched the optimization of an ilmenite froth flotation by using new technologies. He graduated from the Institute of Mineral and Waste Processing, Clausthal University of Technology in 2014 headed by Prof. Dr.-Ing. D. Goldmann. His PhD work focuses on the characterization of the separation behaviour of a deflector wheel classifier by means of visualization of the separation of air and the particle flow.

Kurt Legenhausen

Dr.-Ing. Kurt Legenhausen studied mechanical engineering at Clausthal University of Technology and received his Dipl.-Ing. in 1981. In 1983, he joined the Institute of Particle Technology at Clausthal University of Technology (Head: Prof. Kurt Leschonski). He obtained his PhD in 1991 on the investigation of the flow field in a deflector wheel classifier. Afterwards he was chief engineer at the institute, which has been headed by Prof. Dr. Alfred Weber since 2005. He is managing editor of the Journal of Aerosol Science and assists Prof. Weber at the annual Clausthal course on "Particle Measuring Technologies".

Alfred P. Weber

Prof. Dr. Alfred Weber studied physics and obtained his PhD in aerosol physics at ETH Zurich in 1993. After a stay in the group of Prof. Sheldon Friedlander at UC Los Angeles (UCLA), he joined the group of Prof. Gerhard Kasper at the Karlsruhe Institute of Technology (KIT) in 1996. He received the Smoluchowski Award in 2001 for his work on aerosol nanoparticles. Since 2005, he is a full professor for Particle Technology at the Clausthal University of Technology. He is the editor-in-chief of the Journal of Aerosol Science. His research focuses on the gas-phase synthesis and applications of nanoparticles.

KONA Powder and Particle Journal No. 35 (2018) 186–199/Doi:10.14356/kona.2018001 Original Research Paper

Experimental Investigations of the Effect of Chemical Additives on the Rheological Properties of Highly Concentrated Iron Ore Slurries†

Assefa Kebede Melorie and Deo Raj Kaushal*

[1] *Department of Civil Engineering, Indian Institute of Technology Delhi, India*

Abstract

Chemical additives are widely used in iron ore industry in various processing steps such as classification, crushing, grinding, and pelletization. These additives are also used in transportation of iron ore through highly concentrated slurry pipelines which are currently operating and coming up in large number across the world. These additives are usually categorized by their functions rather than chemical composition. In this study, the effect of quick lime (QL), hydrated lime (HL), Sodium hexametaphosphate (SHMP) and Acti-Gel on the rheological behaviors of iron ore slurries at volumetric concentrations (C_v) of 18.8 %, 22.1 % and 25.8 % and dosages of additives ranging from 0.05–2 % were investigated. The rheological parameters were measured using computerized rotational rheometer. All the sample data were best represented by Herschel-Bulkley model. Minimum shear stress and viscosity were obtained at 2 % dosage of QL for 18.8 % and minimum flow behaviour index was obtained at 25.8 % with 2 % additive dosage. The addition of HL markedly increases all the rheological parameters. When SHMP is used, minimum shear stress and viscosity were obtained at dosage of 1.5 %, 2 % and 2 % for C_v of 18.8 %, 22.1 % and 25.8 % respectively. Acti-Gel resulted higher values of yield stress and flow behaviour indices at all solid concentrations.

Keywords: iron ore slurry, highly concentrated slurry, chemical additive, rheological property, Herschel-Bulkley fluid

1. Introduction

The demand of transporting a large quantities of iron ore fines, which are generated during mining and washing, through pipeline is increased very rapidly in the last decades. To mention one, recently in India the Essar Steel Company completed 253 km-long slurry pipeline that connects its ore washery plant at Dabuna, in Keonjhar district with its pelletization unit at Paradip. The design of this slurry pipeline entails predicting the power requirement per unit of solids delivered over a unit distance. This pump power demand is mainly a function of pressure drop. For establishing the pressure drop requirements the rheology of slurry has been identified as a critical parameter. Therefore, it would be useful to study the rheological behaviours of the slurry to estimate pressure drop and hence pumping capacity.

A number of factors influence the rheological behaviours namely the parent solid materials, the solid content, the particle size and its size distribution, slurry temperature, the pH and the presence of electrolytes and chemical additives (He et al., 2004). As stated by Jones and Harsley (2000) certain chemical additives enhance the fluidity of the slurries and hence enable the slurries to be pumped at much higher concentrations thus reducing the water requirements. So, the selection of appropriate additives should be recognized as one of the most essential factors in the preparation of slurries for transportation. It is, therefore, relevant to investigate the effects of chemical additives on the rheological behaviours of slurries. According to Schick and Villa (1983), the chemical additives must be chosen such that they should provide sufficient viscosity, electro-kinetic potential and the desired stability. A wide range of chemical additives have been used at various processing stages of iron ore mining industries in order to improve the rheological behaviours. These chemical agents might have been acted as a dispersants, coagulants, surfactants, or anti-settling agents.

Qiu G. et al. (2003) investigated the functions and molecular structure of ideal organic binders for iron ore pelletization based on the molecular design, interface chemistry, polymer science as well as failure model of a

---

† Received 23 September 2016; Accepted 27 December 2016
J-STAGE Advance published online 4 February 2017

[1] Hauz Khas, New Delhi - 110016, India
* Corresponding author: Deo Raj Kaushal;
E-mail: kaushal@civil.iitd.ac.in
TEL: +91-98-1828-0867 FAX: +91-11-2658-1117

binding system. Their investigations proved that -COO and -OH are ideal polar and hydrophilic groups of organic binders, respectively. They concluded that good organic binders for iron ore pelletization should contain structurally sufficient polar groups and hydrophilic groups.

He et al. (2004) reviewed the slurry rheology in ultrafine grinding, methods for the characterization of the slurry rheology, empirical equations for modelling the rheological behaviours and use of dispersants which affect the slurry rheology. They concluded that the effect of dispersant is crucial since the solids content of a ground material with an appropriate dispersant in a stirred media mill increases by about 30 wt.% and the fineness of the final product significantly enhances. They also concluded that for the slurry rheology control polyacrylic acid or its salts is the mostly used dispersant as a grinding aid. Pearse (2005) reviewed in detail the predominant reagents used and their mode of action in the mineral processing industry. According to this revision, lime and sulphuric acid are the highest volume bulk inorganic reagents used in mineral processing. Lime is being used for pH adjustment, coagulation, heavy metal precipitation, causticization and depression of pyrite in flotation whereas Sulphuric acid is used for pH adjustment as well as for leaching. He concluded that polyDADMAC (diallyldimethyl ammonium chloride) and quaternized polyamines are the main coagulants used in the minerals industry and low molecular mass polymers of sodium polyacrylate are used as the dispersing reagents.

Marcos and Antonio (2012, 2013) investigated the effects of the slurry's rheological behavior and the state of aggregation and dispersion on wet ultrafine grinding of an iron ore concentrate. They observed that the addition of lime caused an increase in specific energy consumption, with significant increase in yield stress and consistency index of the fluid. According to the review of Assefa and Kaushal (2015a) on the effects of various chemical additives on the flow behaviours of coal ash and iron ore slurries, all the chemical studied are capable of changing the flow behaviours of the slurries under considerations. They also concluded that the function of these chemical additives is almost always very specific in nature in which some additives are proprietary products with highly specific functions that work well in some systems but cannot be used in others. Hence, correct additive selection is important to get the intended results. Many other chemical additives are being used in the mineral processing industries such as in iron ore transportations (Mahiuddin et al., 1989; Sandra et al., 2013). A summary of some of the chemical additives and their functions are given in **Table 1**.

Generally speaking, the use of chemical additives in the iron ore processing varies from simple to the use of complex combinations of additives in classification, concentration, crushing, grinding, and pelletization. Many additional studies related to these have been published but there is still little understanding of the influence of chemicals on the flow behaviours of highly concentrated iron ore slurries. In the present study, the influence of four chemical agents, which have different nature, namely lime (quick lime and hydrated lime), Sodium hexametaphosphate (SHMP), and Acti-Gel®, on the rheological behaviours of high concentrate iron ore slurries were investigated.

2. Materials used

2.1 Parental solid material

The material used for this particular study was iron ore obtained from mine situated at the outskirt of Bangalore city, Karnataka state, India. The measured pH values are between 7.52–7.24 for slurry concentration of 18.8–25.8 % by volume without the addition of chemicals agents.

2.2 Chemical additives used

i) Lime

The two types of lime used for this study are quick lime (CaO) and hydrated lime ($Ca(OH)_2$). Usually both

Table 1 Some of the chemical additives and their functions on the iron ore slurries.

Name of the chemicals	Functions/effects	Parental solids	References
Tapioca, Potato and corn starch; Sodium Silicate & SHMP	Flocculants; Dispersants	Iron ore tailings	Hanumantha and Narasimhan, 1985
Magnafloc and Rishfloc; Sodium petroleum and CTAB	Flocculants; Surfactants	Iron ore fines	Singh & Besra, 1997
Calcium lignosulphonate	Surfactants	Ferrosilicon and magnetite	Mabuza et al., 2005
Magnafloc-1011-anionic and Magnafloc-333- non-ionic	Flocculants	Iron ore tailings	Dash et al., 2011
limestone	Increased reducibility	acid iron ore pellets	Iljana et al., 2015

Table 2 Typical physical properties of the chemical agents.

Properties	QL	HL	SHMP	Acti-Gel
Specific gravity	3.2–3.4	2.0–2.4	2.18	2.62
pH	~12.8	~12.4	5.5–7.7	7–9.5

lime act as a coagulants or flocculants and often added to the iron ore mixture to assist in binding the material to improve productivity and give a stronger sinter. The main difference between the two are their reactivity and chemical composition. Quick lime has a heavy density and is more reactive than hydrated lime. The pH values are much more alkaline (**Table 2**).

ii) Sodium Hexametaphosphate (SHMP)

It is mainly used as a deflocculant or as a dispersing agent. The dispersant reduces the particle-particle interaction by altering the surface charge, which prevents the particles from aggregating and effectively reduces the yield stress of the suspension. Several examples of viscosity modification in industrial slurries have been described although the cost of modifiers limits their general application. SHMP is more commonly used in laboratory procedures to sustain suspensions in the determination of particle size distribution.

iii) Acti-Gel

According to the Active Minerals International, LLC website (ActiveMinerals, 2016), Acti-Gel® 208 is a highly purified Magnesium Alumino-Silicate and used in a wide variety of water based industrial applications. It is chemically inert and stable between pH 2 and pH 13. It is a low-dose (–0.05 % to –0.20 % total dry weight material basis) rheology modifier and anti-settling agent that provides superior particle suspension, stabilizes mixtures, and dramatically improves the workability, flowability, pumpability and performance of slurries and pastes.

2.3 Water

In the real transportation of iron ore as slurries through pipelines, ordinary water is commonly used as a medium. Hence, ordinary tap water was chosen for the preparation of iron ore slurry for this particular investigation.

3. Measurement set up and range of parameters

3.1 Measuring device and sample preparations

The experiments were carried out in the Water Resources Simulation Laboratory of Civil Engineering Department, Indian Institute of Technology Delhi. The rheological data measurements were obtained with the help of an advanced computerized rotational rheometer, RheolabQC, manufactured by Anton Paar Company Ltd., Germany. It works according to the Searle principle in which the viscosity is proportional to the motor torque that is required for turning the measuring bob (rotor) against the fluid's viscous forces. It determines the required force for rotating a bob in a fluid at known speed and works by defining the exact volume of sample which is to be sheared within a test cell, the torque required to achieve a certain rotational speed is measured.

Table 3 Technical Specifications of RheoLabQC.

Property	Range
Speed	0.01 to 1200 L/min
Torque	0.20 to 75 mNm
Shear stress	0.5 to 30000 Pa
Shear rate	0.01 to 4000 L/s
Temperature	–20°C to 180°C
Angular resolution	2 μrad

The components of the rheometer and how the data can be read is explained in Assefa and Kaushal (2015b). Two setting options are available for test: controlled shear rate (CSR) and controlled shear stress (CSS). These options, together with the wide speed and torque ranges and very short motor response times, bring innumerable benefits for the application to investigate the conventional flow and viscosity behaviours of slurries and others. Details of the specifications of the rheometer geometry are shown in **Table 3**.

For the tests, around 80 to 100 g of the slurry was prepared by mixing the required quantity of solid materials with tap water to obtain the desired concentration by weight (C_w). The samples were weighed by an electronic balance with a deviation of ±10^{-4} g. Then, the volumetric solid concentration (C_v) is computed as:

$$C_v = \frac{100\,C_w}{C_w + S_g(100 - C_w)} \tag{1}$$

Where S_g is the specific gravity of the sample.

CSR between 30 to 300 s^{-1} at 10 equal intervals was applied for about 2 minutes to measure the corresponding shear stress and viscosity. All the measurements were repeated several times to minimize errors occur during tests. The repeated sets of sample data on shear stress and viscosity agreed within ±2 %. The pH were recorded at each measurements.

Once the sample is prepared and the measurement is done, different analysis method can be added in the analysis window interface. And hence, the measured data will be approximated using the chosen equations and the parameters are estimated by weighting of relative error. From the various equations inbuilt in the Rheoplus Software, Herschel-Bulkley and Bingham models have been chosen.

Using the given input data points of shear rate, in this particular study ranges from 30 to 300 s^{-1}, the parameters such as shear stress and apparent viscosity are estimated. After running the analysis, the model results are obtained together with the statistical results of correlation ratio, R and R^2, as well as standard deviations relation to yield stress. For a single data the model selection can be done using this value. But in this case, since for each samples data at least five replications have been made, the average of the series data were considered. Then, the rheological data obtained was fit to the Herschel-Bulkley and Bingham models and the best fit model was chosen using R^2.

3.2 Range of Parameters

The investigations were carried out at C_v of 18.8, 22.1 and 25.8 %. For all chemicals except Acti-Gel, the additive proportions of 0.05, 0.1, 0.5, 1, 1.5 and 2 % were used. But for Acti-Gel, proportions of 0.05, 0.1 and 0.2 % were used.

4. Results and discussions

Analysing the chemical reactions or change in the chemical properties of the slurry is not the intention of this particular study. It merely focuses on the influence of chemicals on the rheological properties of the iron ore slurries .

4.1 Physical properties of the sample

As shown in **Fig. 1**, the median particle diameter (d_{50}) is 12 μm. The maximum particle size is 300 μm and around 89 % of the particle sizes are below 75 μm. Hence, the sample can be categorized as finer particles. The specific gravity of iron ore fine was measured by sedimentation technique and found to be 4.32 and static settled concentration is 53.04 % by volume.

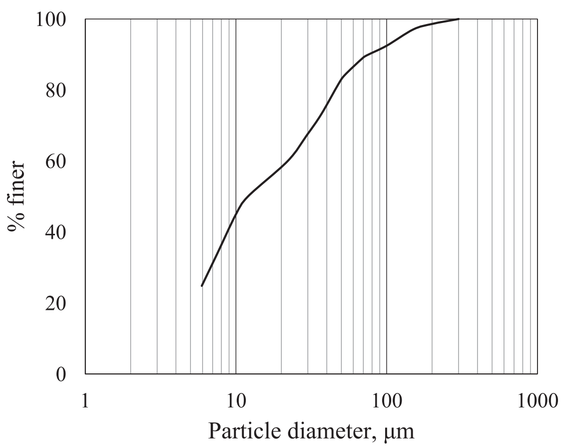

Fig. 1 Particle size distribution of the iron ore sample.

4.2 pH values

Fig. 2 shows the effects of concentration of chemical agents on pH values of iron ore slurries at different concentrations. From the figure, it is seen that pH values were highly affected by the addition of QL and HL.

Abrupt increase in the pH values was observed when these chemicals were added even in small proportions (0.05 %). But then onwards, the rate of increment was decreased as the amount of chemical agents increased. The minimum and the maximum values registered for both lime were 9.83 and 12.57 at 0.05 % on C_v of 25.8 % and at 2 % additives on C_v of 18.8 % respectively. When SHMP was used, the pH values were decreased as the additive proportion was increased for all slurry concentrations and

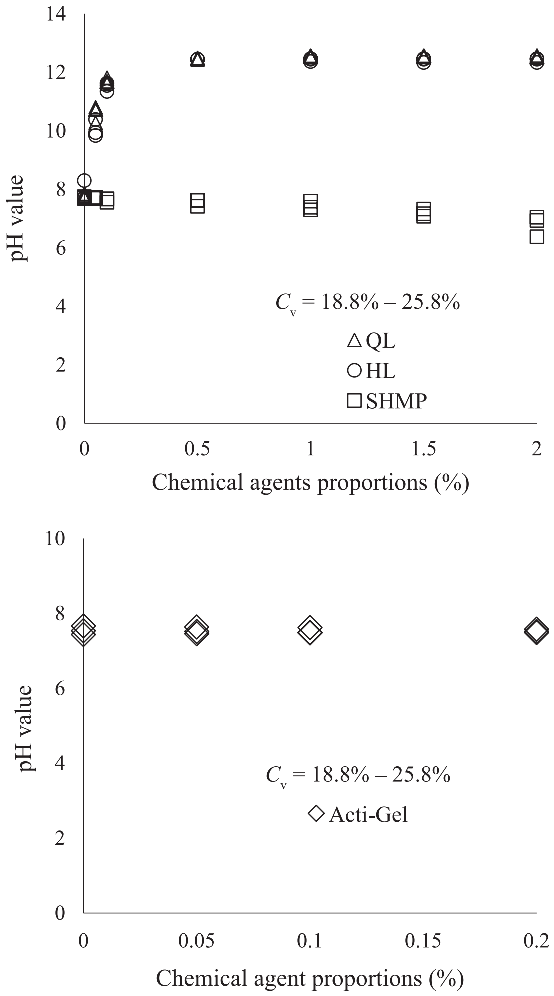

Fig. 2 pH values of the iron ore slurries at different solid concentration and chemical dosages.

a minimum and a maximum values of 7.72 and 6.37 were measured on C_v of 18.8 % at 0.05 % additive and on C_v of 25.8 % at 2 % additive respectively. In contrary, addition of Acti-Gel showed insignificant change in the pH values at all solid concentrations due to its inert properties.

4.3 Slurries rheological properties and model representation

The shear stress data were fitted to the models of Herschel-Bulkley and Bingham, which are expressed as:

Herschel-Bulkley model: $\tau = \tau_y + K\dot{\gamma}^n$ (2)

Bingham model: $\tau = \tau_y + \eta_p\dot{\gamma}$ (3)

Where, τ_y is the yield stress, K is a measure of the average viscosity of the fluid (or the flow consistency index) and n is a measure of the deviation of the fluid from Newtonian (or the flow behaviour index), η_p is the plastic viscosity and $\dot{\gamma}$ is the shear rate.

The average rheological data obtained from exact shear stress- shear rate data using the rotational rheometer and those obtained from the two models for C_v of 18.8, 22.1, and 25.8 % without chemical additives and C_v of 18.8 % with the addition of QL are shown in **Fig. 3(a–i)**. The same trends were followed for the rest of the data. For all the samples data, the range of R^2 were from 0.8993–0.9998 and from 0.4253–0.9997 for Herschel-Bulkley and Bingham model respectively. Hence, it is concluded that the variation of the shear stress with shear rate at all solid

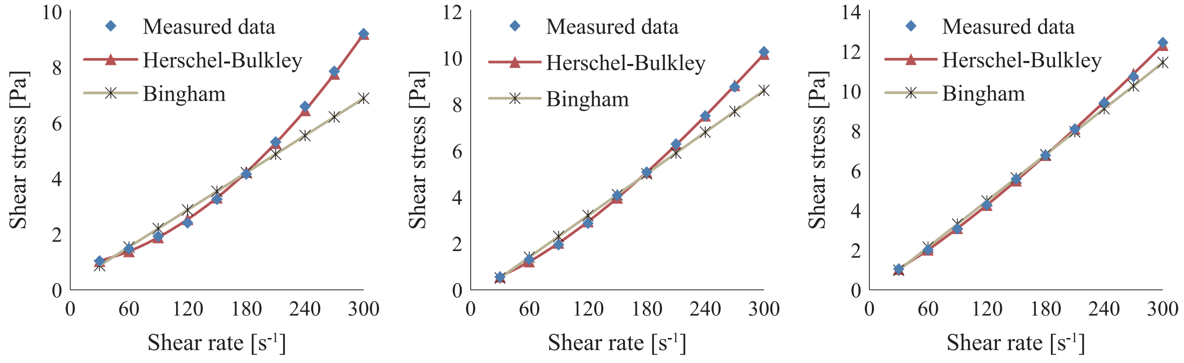

(a) C_v = 18.8%; QL = 0% (b) C_v = 22.1%; QL = 0% (c) C_v = 25.8%; QL = 0%

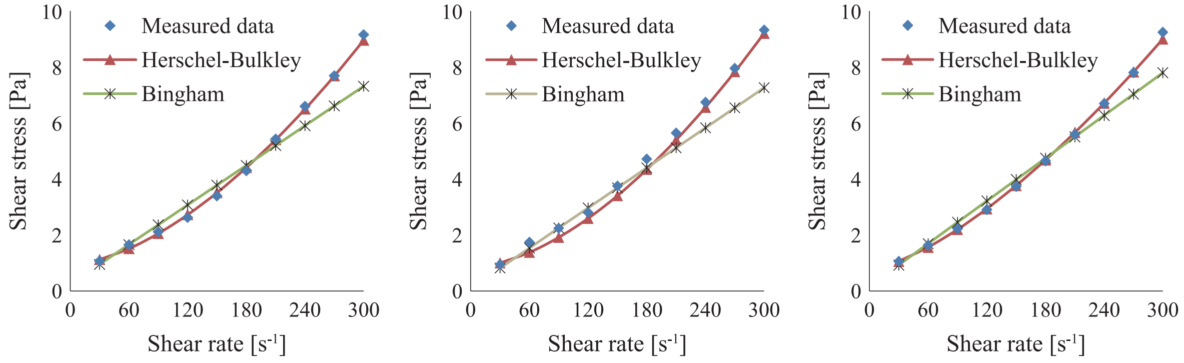

(d) C_v = 18.8%; QL = 0.05% (e) C_v = 18.8%; QL = 0.1% (f) C_v = 18.8%; QL = 0.5%

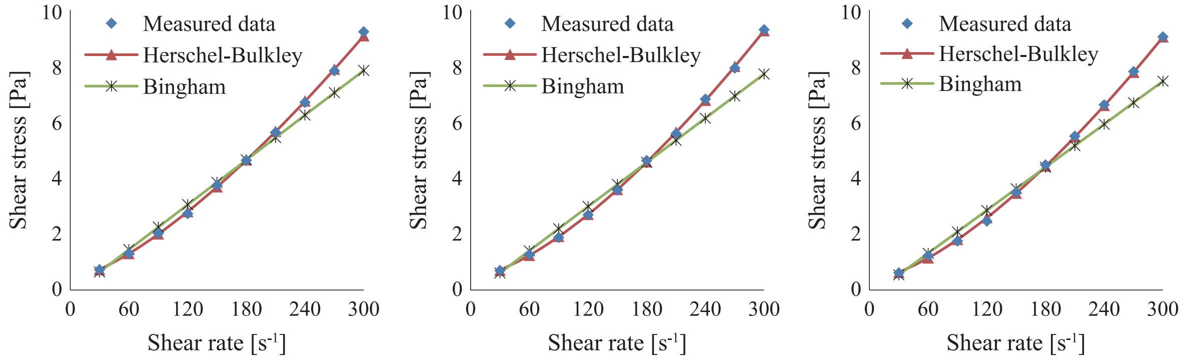

(g) C_v = 18.8%; QL = 1% (h) C_v = 18.8%; QL = 1.5% (i) C_v = 18.8%; QL = 2%

Fig. 3 (a–i). Selection of best fit model to the measured data of QL at different C_v and chemical proportions.

concentrations with and without the addition of chemicals follow a power law with yield stress and best represented by Herschel-Bulkley model.

The values of K and n were determined by regression analysis of the logarithmic form of Eqn. (2) using sets of shear stress and shear rate data read from the flow curves. For all data sets, the values of n are greater than one which indicate that the samples exhibit yield shear thickening behaviours (**Tables 4–7**). Furthermore, it shows an increasing degree of shear thickening with increase in solid contents. It may also be mentioned that the increase in apparent viscosity with iron ore content is almost proportional to the value of K.

4.4 The Effects of chemical additives

The Effects of different concentrations of chemical agents on the rheological behaviours of iron ore slurries are shown in **Figs. 4–15**. **Figs. 4–6** show the effects of QL on the shear stress and viscosity of iron ore slurries at C_v of 18.8 %, 22.1 % and 25.8 % and at additives concentrations of 0, 0.05, 0.1, 0.5, 1, 1.5 and 2 %.

It is showed that for all additives dosages the values of shear stress and viscosity registered were higher than the values without the chemical additives at C_v of 22.1 % and 25.8 %. Similarly, the increased in rheogram values were observed with increasing the solid concentrations and higher rate of increments were also shown in all additives dosages. But in the case of C_v of 18.8 %, the shear stress and viscosity were increased up to 0.5 % of additives and then deceased as the additives proportions increased and the minimum rheogram data were registered at the maximum additive concentration (2 %). The rate of decrement in viscosity at the lower shear rate ranges was higher than at higher shear rate ranges for all the solid concentrations and chemical additives proportions. **Table 4** displayed the results of the rheological parameters yield stress, flow behaviour index and consistency index as a function of proportions of QL. It is shown that the values of n were decreased as the solid concentrations increased for the same additives concentrations and minimum n values were registered at C_v of 25.8 %. Furthermore, for all solid concentrations, the additions of QL increased the yield stresses.

Figs. 7–9 present the shear stress and viscosity at C_v of 18.8, 22.1, and 25.8 % as a function of dosages of HL. Both the shear stresses and viscosities with the additions of this chemical agent were markedly higher compared

Table 4 Rheological parameters data at various concentrations and chemical additives of QL.

	C_v = 18.8 %			C_v = 22.1 %			C_v = 25.8 %		
QL (%)	τ_y (Pa)	n (–)	K (µPa.s^n)	τ_y (Pa)	n (–)	K (µPa.s^n)	τ_y (Pa)	n (–)	K (µPa.s^n)
0	0.086	1.7	5034	0.164	1.4	3361	0.307	1.21	11830
0.05	0.934	1.63	723	0.82	1.45	2548	0.856	1.25	9632
0.1	0.836	1.7	504	0.273	1.25	7851	1.28	1.42	3762
0.5	0.766	1.45	2119	0.521	1.4	3399	0.991	1.27	8760
1	0.369	1.39	3133	0.564	1.28	6794	0.759	1.17	16703
1.5	0.403	1.47	2031	0.783	1.32	5183	1.401	1.2	13265
2	0.329	1.47	1948	0.932	1.52	1724	1.25	1.19	13861

Table 5 Rheological parameters data at various concentrations and chemical additives of HL.

	C_v = 18.8 %			C_v = 22.1 %			C_v = 25.8 %		
HL (%)	τ_y (Pa)	n (–)	K (µPa.s^n)	τ_y (Pa)	n (–)	K (µPa.s^n)	τ_y (Pa)	n (–)	K (µPa.s^n)
0	0	1.26	6625	0	1.2	11197	0.134	1.11	22459
0.05	0	1.35	4482	0.143	1.26	8449	1.367	1.27	9605
0.1	0.755	1.57	1125	0.186	1.21	10965	1.8	1.48	2928
0.5	0.399	1.39	3330	0.108	1.21	10730	2.017	1.41	4217
1	0.604	1.36	3858	0.073	1.17	14197	1.264	1.32	7176
1.5	0.541	1.4	3185	0.413	1.2	11410	1.227	1.33	7068
2	0.548	1.42	2807	0.047	1.14	16711	1.57	1.32	7537

with the reference rheogram data (without the addition of chemical agents) at all solid concentrations and additive ranges. The same trends as that of QL were observed at low and high shear rates. Unlike the QL, the lower values of *n* were registered at C_v of 22.1 % for all additive dosages (**Table 5**).

Table 6 Rheological parameters data at various concentrations and chemical additives of SHMP.

	C_v = 18.8 %			C_v = 22.1 %			C_v = 25.8 %		
SHMP (%)	τ_y (Pa)	n (–)	K (μPa.s^n)	τ_y (Pa)	n (–)	K (μPa.s^n)	τ_y (Pa)	n (–)	K (μPa.s^n)
0	0	1.39	3760	0	1.31	6111	0.441	1.26	8736
0.05	0	1.64	940	0.559	1.53	5282	0.39	1.34	5546
0.1	0.087	1.44	2623	1.807	1.93	157	3.82	2.65	262
0.5	1.567	2.12	48.5	2.003	2.15	43.6	2.71	2.41	11.9
1	1.367	2.03	82.7	1.49	2.06	75.3	1.75	1.96	156
1.5	0.818	1.97	122	1.407	1.43	2207	1.92	2.02	116
2	1.297	1.85	219	1.321	2.76	2187	1.17	1.83	359

Table 7 Rheological parameters data at various concentrations and chemical additives of Acti-Gel.

	C_v = 18.8 %			C_v = 22.1 %			C_v = 25.8 %		
Acti-Gel (%)	τ_y (Pa)	n (–)	K (μPa.s^n)	τ_y (Pa)	n (–)	K (μPa.s^n)	τ_y (Pa)	n (–)	K (μPa.s^n)
0	0.106	1.43	2493	0.468	1.79	371.4	2.343	1.4	3424
0.05	0.72	1.81	277.2	0.7	1.79	350.2	0.514	1.38	4620
0.1	0.88	1.69	509.3	0.64	1.72	510.3	1.065	1.58	1454
0.2	0.668	1.84	231.5	1.013	1.67	678.6	1.54	1.69	757

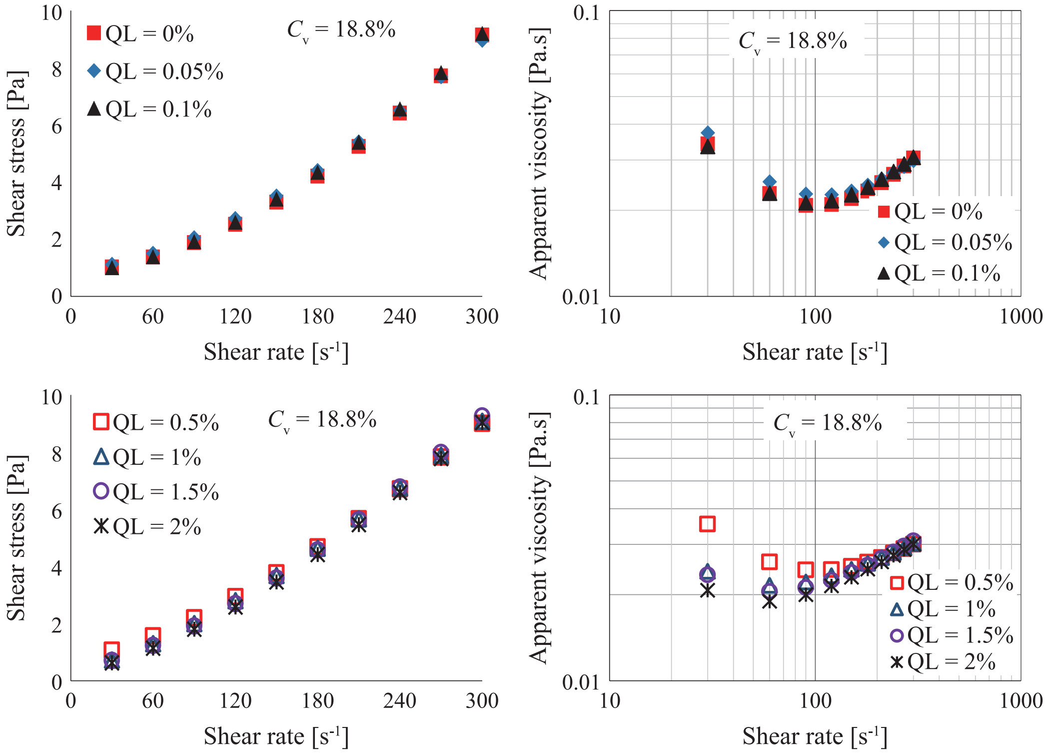

Fig. 4 Rheogram of iron ore slurries at QL dosages of 0 to 2 % and C_v of 18.8 %.

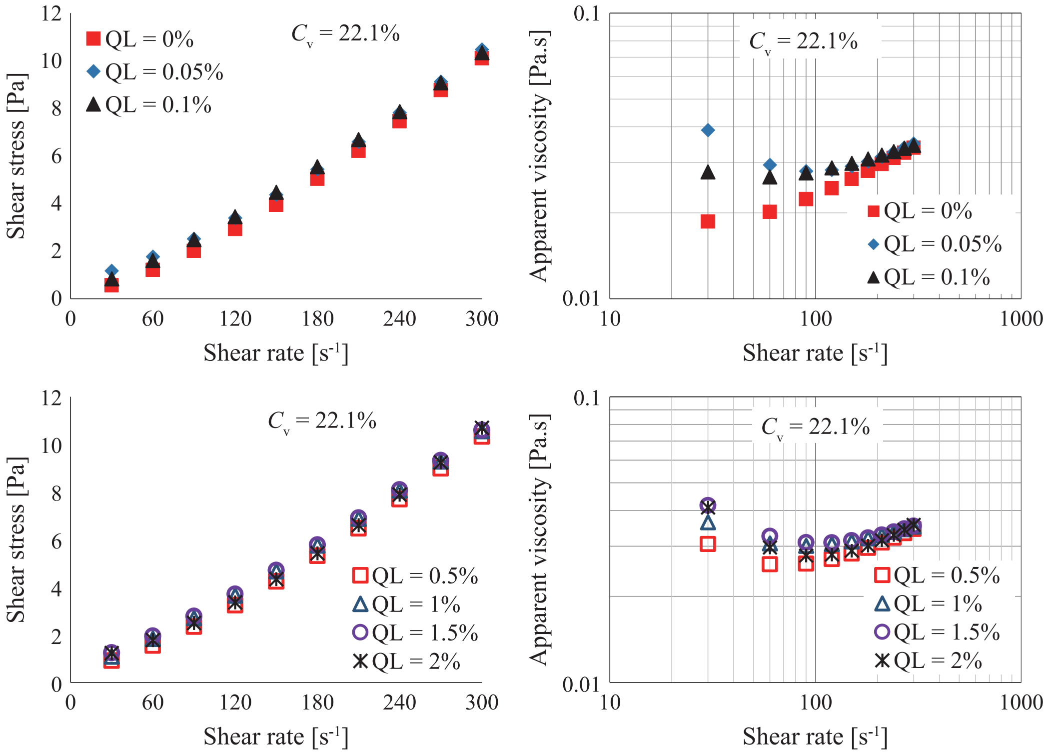

Fig. 5 Rheogram of iron ore slurries at QL dosages of 0 to 2 % and C_v of 22.1 %.

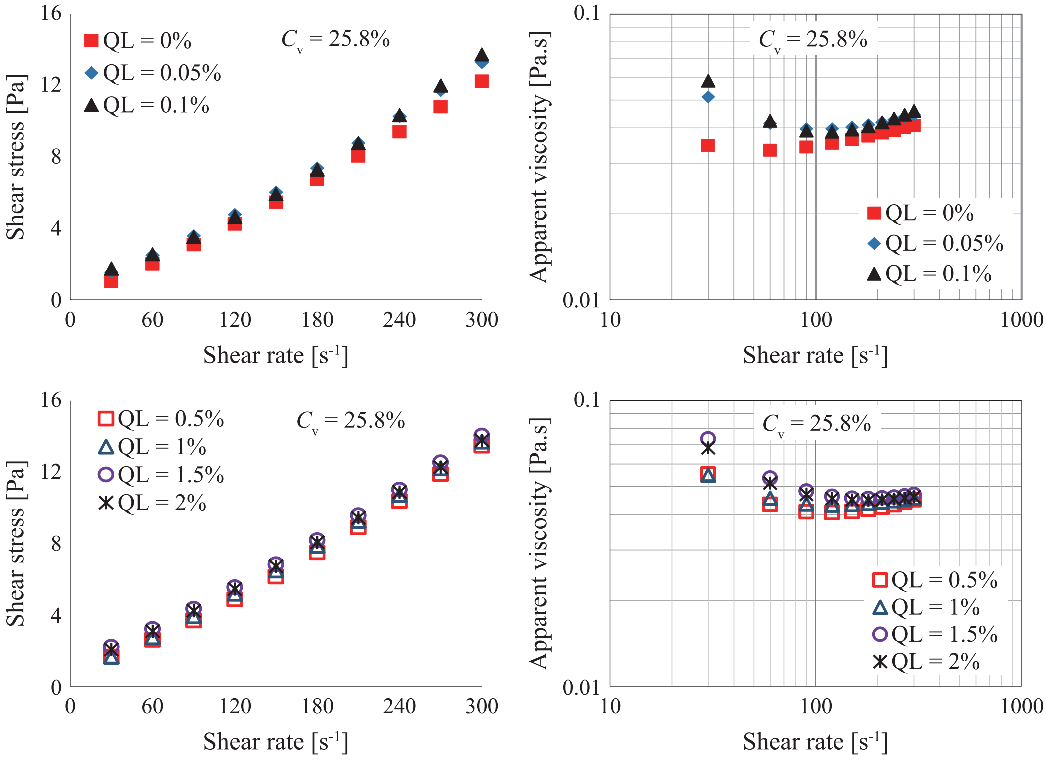

Fig. 6 Rheogram of iron ore slurries at QL dosages of 0 to 2 % and C_v of 25.8 %.

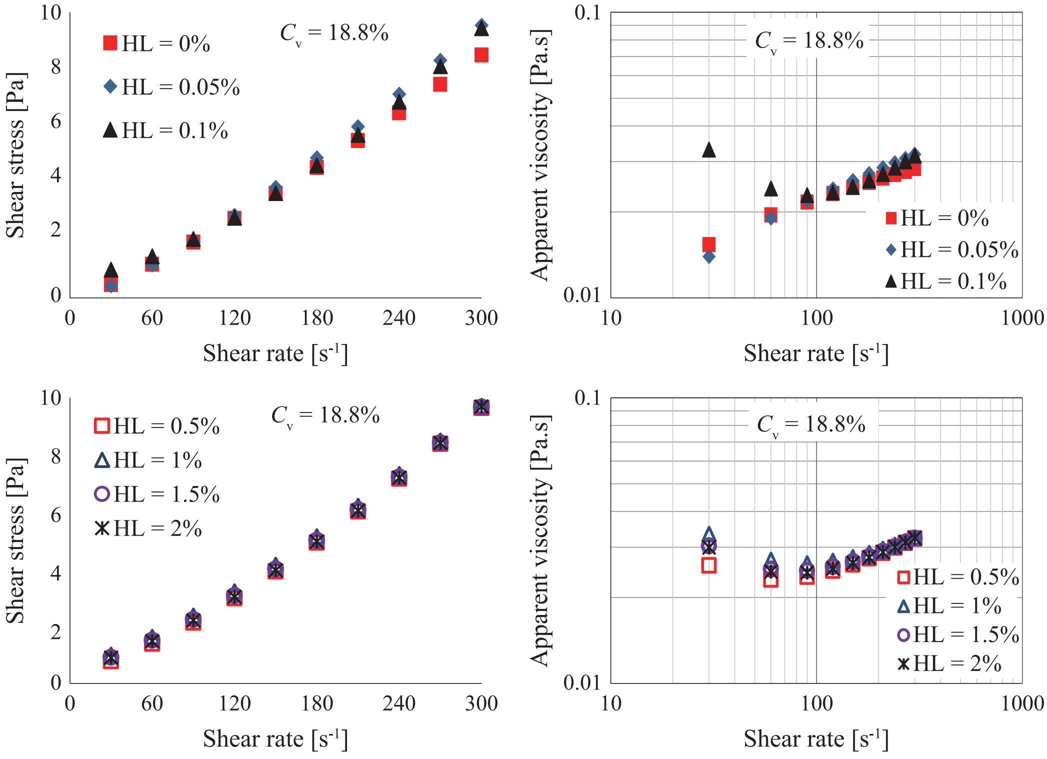

Fig. 7 Rheogram of iron ore slurries at HL concentrations of 0 to 2 % and C_v of 18.8 %.

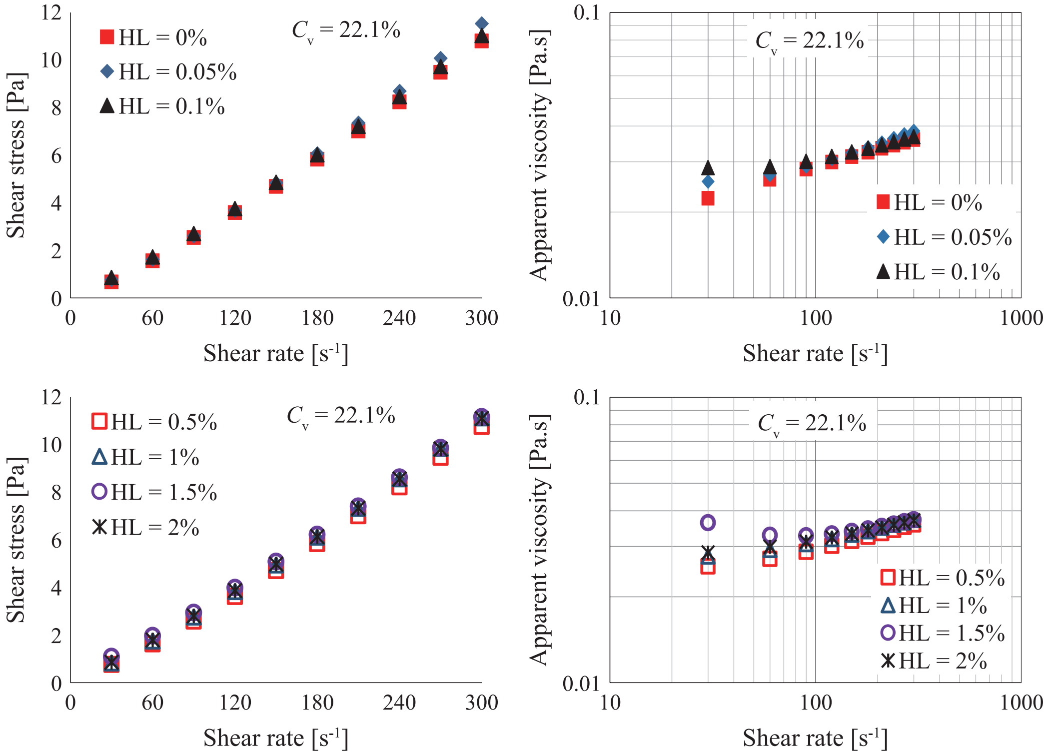

Fig. 8 Rheogram of iron ore slurries at HL concentrations of 0 to 2 % and C_v of 22.1 %.

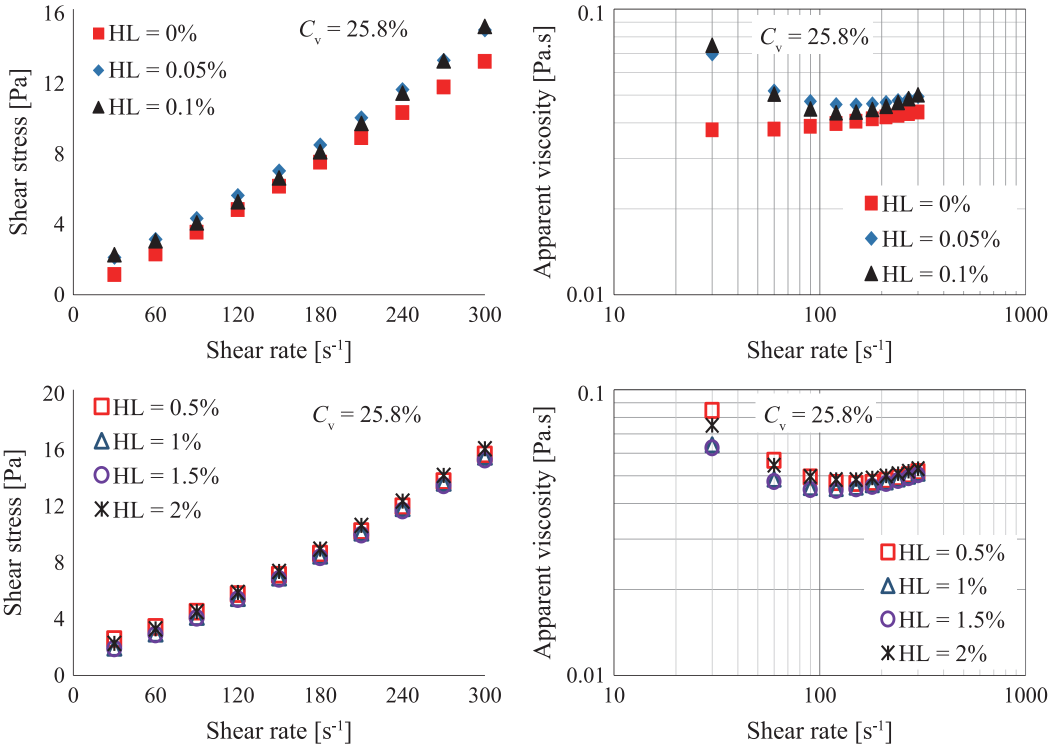

Fig. 9 Rheogram of iron ore slurries at HL concentrations of 0 to 2 % and C_v of 25.8 %.

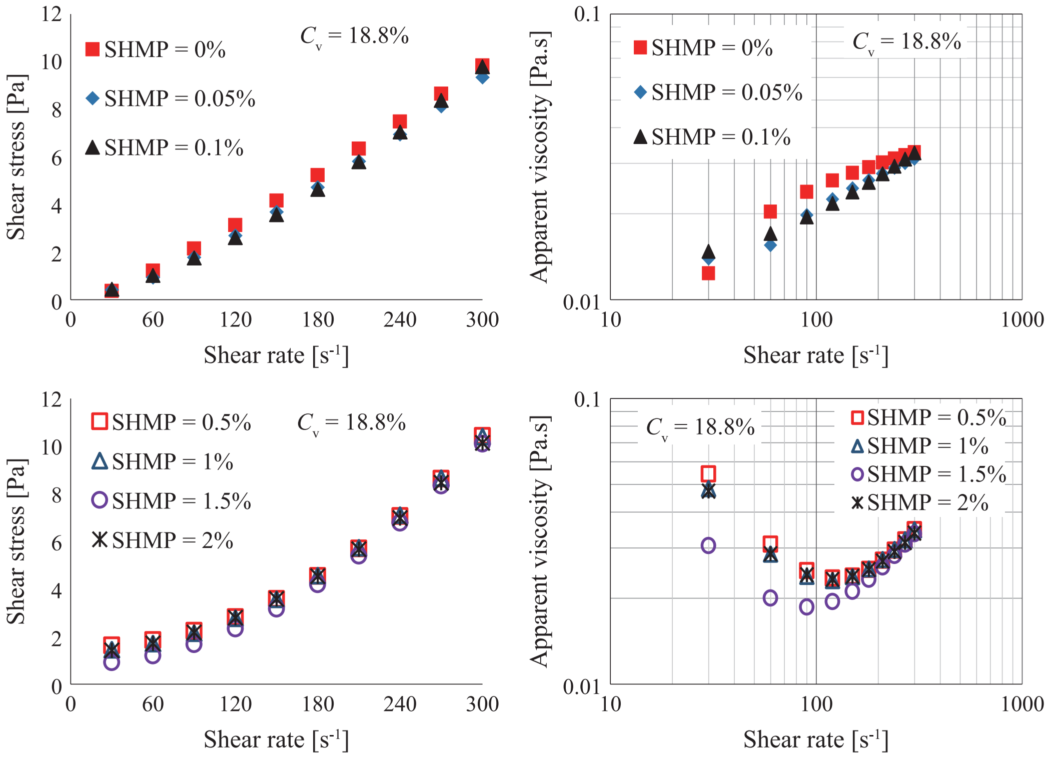

Fig. 10 Rheogram of iron ore slurries at SHMP concentrations of 0 to 2 % and C_v of 18.8 %.

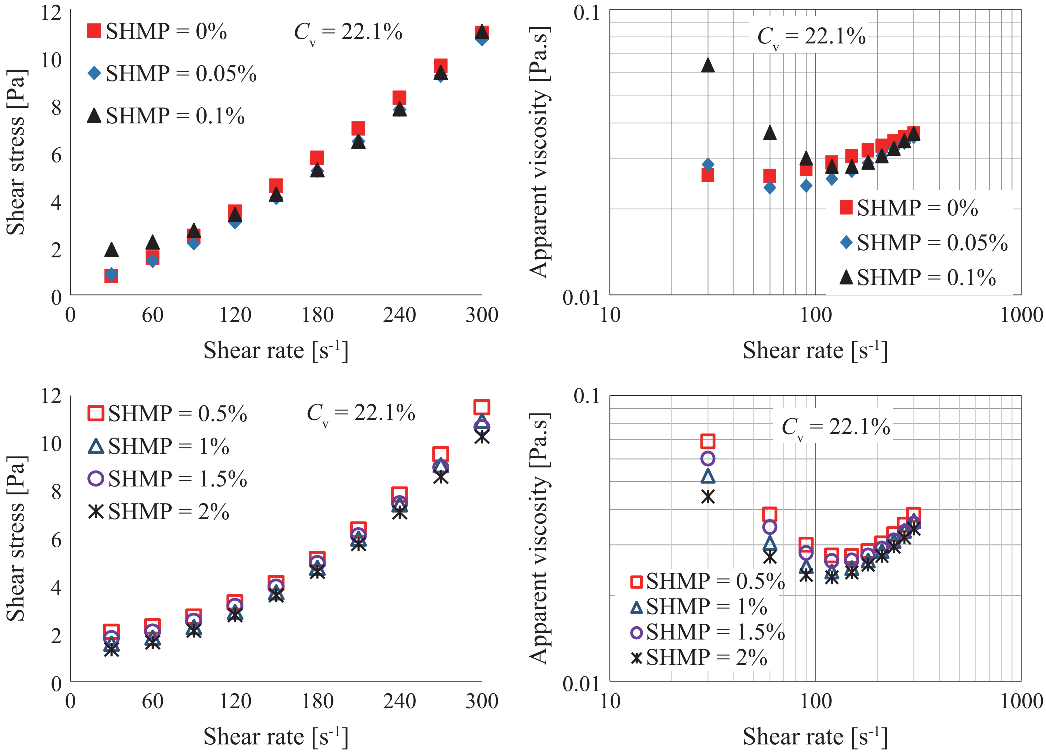

Fig. 11 Rheogram of iron ore slurries at SHMP concentrations of 0 to 2 % and C_v of 22.1 %.

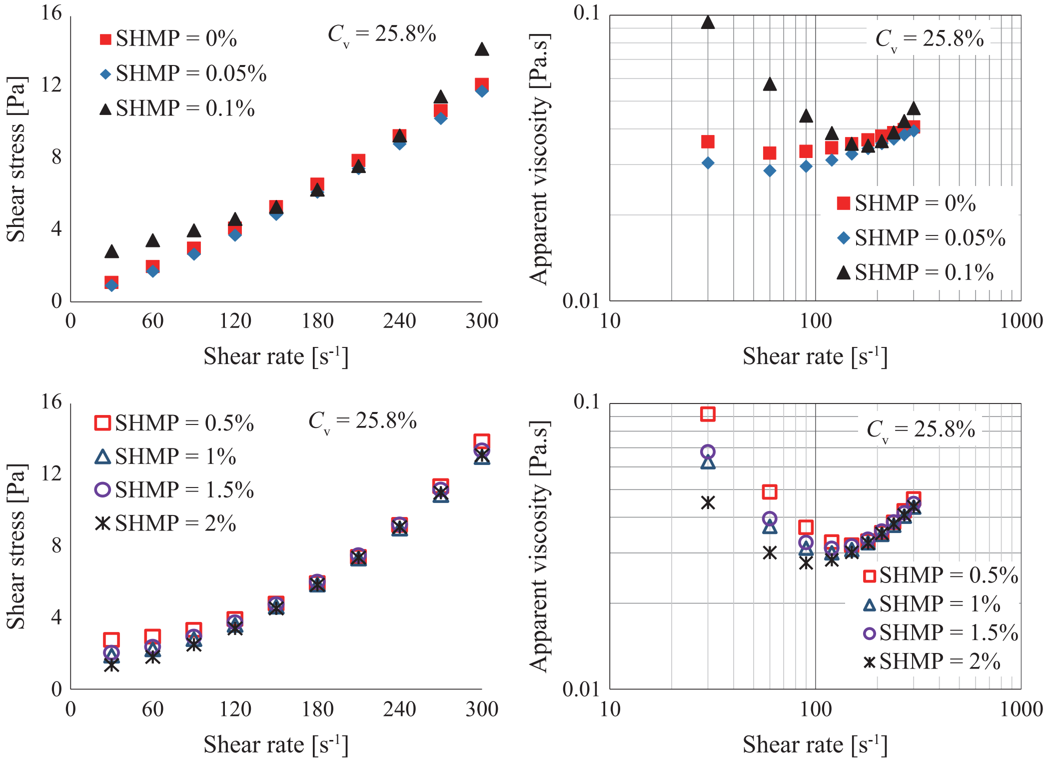

Fig. 12 Rheogram of iron ore slurries at SHMP concentrations of 0 to 2 % and C_v of 25.8 %.

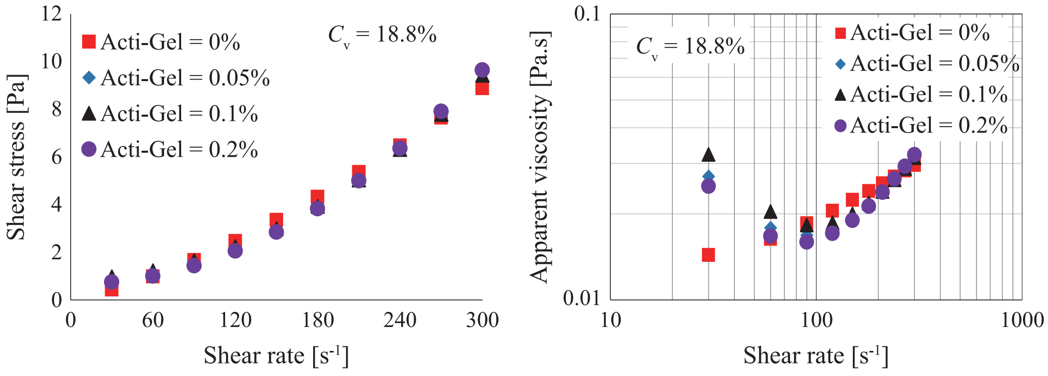

Fig. 13 Rheogram of iron ore slurries at Acti-Gel concentrations of 0 to 0.2 % and C_v of 18.8 %.

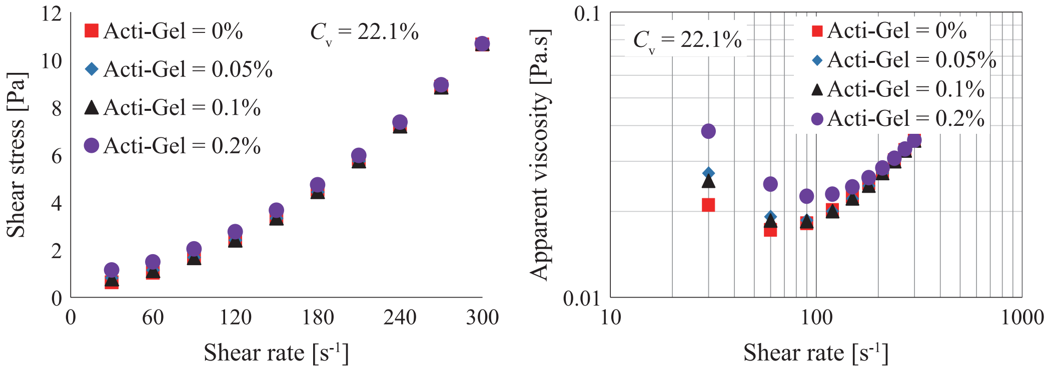

Fig. 14 Rheogram of iron ore slurries at Acti-Gel concentrations of 0 to 0.2 % and C_v of 22.8 %.

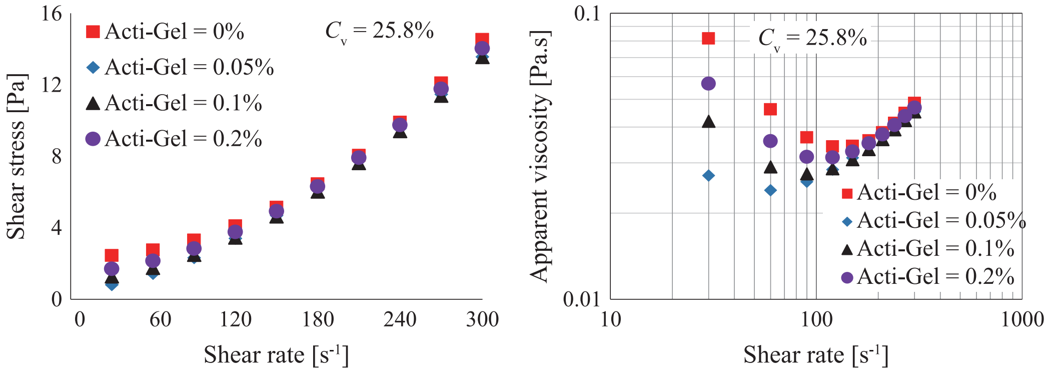

Fig. 15 Rheogram of iron ore slurries at Acti-Gel concentrations of 0 to 0.2 % and C_v of 25.8 %.

Figs. 10–12 illustrate the relationship between shear stress versus shear rate and viscosity versus shear rate for the iron ore slurries at C_v of 18.8 %, 22.1 % and 25.8 % using different dosages of SHMP as a dispersing agents. It can be seen that low shear stress and viscosity were obtained at additive dosage of 1.5 % for C_v of 18.8 % and at 2 % for C_v of 22.1 and 25.8 %. The same trends also observed as that of lime (QL and HL) at low shear, particularly less than 60 s^{-1}, the rheogram values increased at all solid concentrations and additives dosages but the rate of increment is higher than lime. Furthermore, the values of *n* were decreased as the solid concentrations increased for additives concentrations 0.05 % and then increased for the remaining dosages of additives for all concentrations (**Table 6**).

The effects of Acti-Gel dosages on the shear stress and viscosity of iron ore slurries at C_v of 18.8, 22.1 and 25.8 % are presented in **Figs. 13–15**. From these figures it can be observed that minimum shear stress was registered at 0.2 % of Acti-Gel for C_v of 18.8 % and at 0.1 % for 22.1 %

and 25.8 % of solid concentrations. It can also be seen that viscosity was increased drastically at the lower shear rate (usually less than 90 s^{-1}) for all additives and solid concentrations. A minimum yield stress was obtained at additive concentrations of 0.2 %, 0.1 % and 0.05 % for C_v of 18.8, 22.1 and 25.8 % respectively. But these minimum values were higher than the yield stress at 0 % additive (**Table 7**). Furthermore, it is also shown that the values of n were higher when this chemical was added for all range of solid concentrations which indicate that the slurry shows more yield thickening behaviours.

5. Conclusions

The iron ore slurries, with and without the additions of chemical agents, considered in this particular study exhibit shear thickening properties and best represented by Herschel-Bulkley model. The shear stress and viscosity were decreased beyond 0.5 % of QL and minimum results were registered at the maximum additive dosage (2 %) on 18.8 % solid concentration. Furthermore, the addition of QL increased the yield stress and minimum flow behaviour index was obtained at 25.8 % solid concentration with 2 % additive dosage. In contrary to the above, the addition of HL increased markedly the values of shear stress, viscosity, flow consistency and flow behavior indices. When SHMP is used, minimum shear stress and viscosity were obtained at a dosage of 1.5 % for C_v of 18.8 % and at 2 % for C_v of 22.1 % and 25.8 %. Acti-Gel resulted higher values of τ_y and n for all ranges of solid concentrations.

The pH values of the slurries were remarkably increased when QL and HL were used in all solid concentrations and additive dosages. On the other hand Acti-Gel showed negligible effect on pH due to its inert property and the friction factors increased at all solid concentration and Acti-Gel dosages.

Further investigation is needed on how these most effective chemical agents change the chemical composition and properties of the iron ore slurries for the intended purposes.

Acknowledgements

This scientific work was financed by the Ministry of Education, Ethiopia with the coordination of Indian Institute of Technology Delhi, India.

Nomenclature

C_w	Concentration by weight (%)
C_v	Volumetric solid concentration (%)
D	Pipe diameter (m)
f	Fanning friction factor (–)
f_0	Reference fanning friction factor (–)
f'	Normalized friction factor (–)
HL	Hydrated lime
K	Flow consistency index (Pa s^n)
n	Flow behaviour index (–)
QL	Quick lime
Re	Reynolds number (–)
S_g	Specific gravity (–)
SHMP	Sodium hexametaphosphate
U	Flow velocity (m/s)
ρ_m	Density of mixture (kg/m^3)
τ_y	Yield stress (Pa)
η_p	Plastic viscosity (Pa s)
$\dot{\gamma}$	Shear rate (s^{-1})

References

ActiveMinerals (Active Minerals International, LLC) <activeminerals.com/products/high-purity-magnesium-alumino-silicate/> accessed 20.02.2016.

Assefa K.M., Kaushal D.R., The influence of chemical additives on the flow behaviours of solid-liquid suspensions: a review, Conference Proceedings of RACEE-2015, International Journal of Engineering Research & Technology, 4.3 (2015a) 180–185.

Assefa K.M., Kaushal D.R., Experimental study on the rheological behaviour of coal ash slurries, Journal of Hydrology and Hydromechanics, 63.4 (2015b) 303–310.

Dash M., Dwari R.K., Biswal S.K., Reddy P.S.R., Chattopadhyay P., Mishra B.K., Studies on the effect of flocculant adsorption on the dewatering of iron ore tailings, Chemical Engineering Journal, 173 (2011) 318–325.

Qiu G., Jiang T., Li H., Wang D., Functions and molecular structure of organic binders for iron ore pelletization, Colloids and Surfaces A: Physicochemical and Engineering Aspects, 224 (2003) 11–22.

Hanumantha R.K., Narasimhan K.S., Selective flocculation applied to barsuan iron ore tailings, Inter. Journal of Mineral Processing, 14 (1985) 67–75.

He M., Wang Y., Forssberg E., Slurry rheology in wet ultrafine grinding of industrial minerals: A review, Powder technology, 147 (2004) 94–112.

Iljana M., Kemppainen A., Paananen T., Mattila O., Pisilä E., Kondrakov M., Fabritius T., Effect of adding limestone on the metallurgical properties of iron ore pellets, Inter. Journal of Mineral Processing, 141 (2015) 34–43.

Jones R.L., Horsley R.R., Viscosity modifiers in the mining industry, mineral processing and extractive, Metallurgy Review: An International Journal, 20.1 (2000) 215–223.

Mabuza N.T., Pocock J., Loveday B.K., The use of surface active chemicals in heavy medium viscosity reduction, Minerals Engineering, 18 (2005) 25–31.

Mahiuddin S., Bondyopadhyay S., Baruah J.N., A study on the beneficiation of Indian iron-ore fines and slime using chemical additives, International Journal of Mineral Processing, 26 (1989) 285–296.

Marcos G.V., Antonio E.C.P., Effect of reagents on the rheological behavior of an iron ore concentrate slurry, International Journal of Mining Engineering and Mineral Processing, 1.2 (2012) 38–42.

Marcos G.V., Antonio E.C.P., Effect of rheology and dispersion degree on the regrinding of an iron ore concentrate, Journal of Material Research and Technology, 2.4 (2013) 332–339.

Pearse M.J., An overview of the use of chemical reagents in mineral processing, Minerals Engineering, 18 (2005) 139 –149.

Sandra Lúcia de Moraesa, José Renato Baptista de Limaa, João Batista Ferreira Netob, Influence of dispersants on the rheological and colloidal properties of iron ore ultrafine particles and their effect on the pelletizing process—A review, Journal of Material Research and Technology, 2.4 (2013) 386–391.

Schick M.J., Villa J.L., Surfactants in coal technology, American Oil Chemical Society, (1983) 1349–1359.

Singh B.P., Besra L., The effect of flocculants and surfactants on the filtration dewatering of iron ore fines, Separation Science and Technology, 32.13 (1997) 2201–2219.

Author's short biography

Assefa Kebede Melorie

Mr Assefa received his BSc degree from Hawassa University (then Debub University), Ethiopia in 2004. In 2009, he obtained his MSc degree from Haramaya University, Ethiopia. Currently, he is a Ph.D. Scholar in the Department of Civil Engineering at Indian Institute of Technology (IIT) Delhi. His main research interests are in Rheology, Slurry/Sediment Transport, Multiphase Flows, Computational Fluid Dynamics and Hydraulics.

Deo Raj Kaushal

Dr. D. R. Kaushal was trained to be a slurry pipeline designer during his Ph.D. at IIT Delhi and Postdoctoral Research at KIT Japan. He has been an Associate Professor of Hydraulics in Water Resources Engineering Section of Civil Engineering Department at IIT Delhi since 2004. He has visited KIT Japan and KCT Japan as visiting Professor. During his teaching and Postdoctoral research, he has been carried out several researches and consultancy projects. He has worked with several mining, mineral-processing and production companies, either through direct consultation or through collaboration with other companies or research organizations.

KONA Powder and Particle Journal No. 35 (2018) 200–208/Doi:10.14356/kona.2018005 Original Research Paper

Compression and Relaxation Properties of Municipal Solid Waste Refuse-Derived Fuel Fluff[†]

Charley Sprenger, Lope G. Tabil* and Majid Soleimani

[1] *Department of Chemical and Biological Engineering, University of Saskatchewan, Canada*

Abstract

The compression and relaxation characteristics of municipal solid waste (MSW) refuse-derived-fuel (RDF) fluff were investigated with respect to biodegradable fraction, grind size, moisture content, applied load, and pelleting temperature. Experimental trials were performed by using a single pelleting unit mounted on an Instron universal testing machine. Two grind sizes of each sample were prepared, 3.18 mm and 6.35 mm, and moisture contents were increased to 8 %, 12 %, and 16 % w.b. The applied loads were set at 2 kN, 3 kN, and 4 kN at two temperature settings, 50 °C and 90 °C. The experimental data for these trials was collected and multiple compression and relaxation models were fitted to the applied pressure, compact density or volume data. The results indicated that the compact density of RDF improved by increasing the grind size, while the compact density of biodegradable pellets increased with increasing pelleting load and temperature. The compact density of pellets produced from RDF ranged from 880–1020 kg/m^3; the compact density of the biodegradable pellets ranged from 1120–1290 kg/m^3. The Walker and Jones models both indicated that the biodegradable material fraction has a higher compressibility than the RDF material, where neither moisture content nor grind size at all levels had a significant effect on the compressibility of either material. The Kawakita-Lüdde model estimated the porosity of the pelleted samples, while the Cooper-Eaton model indicated that the primary mechanism of densification was particle rearrangement. Application of the Peleg and Moreyra model for analysis of relaxation properties of the compressed materials determined the asymptotic modulus of the residual stress to be between 89 and 117 MPa for all experimental parameters; however, the RDF material produced more rigid pellets than the biodegradable material.

Keywords: densification, asymptotic modulus, visco-elastic properties, municipal solid waste, bio-processing, biofuels

1. Introduction

In an age of societal dependence on fossil-based resources, paired with concerns over environmental sustainability, researchers and policy makers are avidly looking towards biofuels as an alternative means to meet the demand for energy in future generations. In particular, 'advanced' biofuels—those that are made with materials that do not compete with food or land resources—are of high research and development interest as a means to achieve the energy goal in the most sustainable means possible (BioFuelNet, 2015). Biofuels are recognized with being carbon-neutral, slowing the exponentially rising consequences of greenhouse gas emissions, and are developed from renewable resources.

Municipal solid waste (MSW) consists of both organic and inorganic fractions and may include paper, plastic, glass, metal, food waste, wood, and other composite materials (Mor et al., 2006). There is potential for the utilization of MSW in the form of refuse derived fuel (RDF) as a feedstock for thermochemical conversion in this advanced biofuels industry. Typically, MSW is disposed of in landfills as garbage, as such the conversion to RDF would provide a more sustainable alternative disposal method for the waste. The City of Edmonton in collaboration with Enerkem Alberta Biofuels currently operates a Waste-to-Biofuels facility in which processed MSW (RDF-fluff) is converted into methanol through patented, low-severity gasification technology (EWMC, 2015). Densification of this RDF-fluff would produce a higher quality feedstock that is more durable, improving storage and handling as well as providing a more uniform product for conversion.

Literature indicates that there are numerous variables that influence biomass densification; these include both process conditions and material characteristics. The process variables imposed on the densification procedure

---

[†] Received 13 January 2017; Accepted 30 January 2017
J-STAGE Advance published online 31 March 2017

[1] 57 Campus Drive, Saskatoon, Saskatchewan, S7N 5A9, Canada,

* Corresponding author: Lope G. Tabil;
E-mail: lope.tabil@usask.ca
TEL: +1-306-966-5317 FAX: +1-306-966-4777

include temperature, applied pressure, hold time, die geometry, and application rate. The addition of heat results in a reduced resistance to applied load by biomaterials (Sokhansanj et al., 2005). Increased applied pressure will indeed result in higher densities, however there is an optimal pressure that should be utilized at which the mechanical strength of the material due to plastic deformation is reached (Yaman et al., 2000). Hold times are most significant in reducing the effect of 'spring-back' from elastic deformation during compression. Die geometry influences the amount of material that can be pelleted; smaller diameters will increase the restriction and therefore the energy required to produce a pellet. Material variables such as moisture content, particle size distribution, biochemical composition, and pretreatment are characteristic of particular biomass feedstocks. Several sources indicate that moisture contents between 8–12 % result in denser and higher quality pellets from cellulosic materials (Sokhansanj et al., 2005). Water acts as a binder in which the contact area of the particles is increased, allowing for the formation of bonds by van der Waal's forces (Mani et al., 2003). Particle size distribution in addition to geometric mean diameter has an effect on the quality and density of pellets (Payne, 1978). The biochemical composition of a feedstock (i.e. the fraction of starch, cellulose, protein, etc ...) will also affect the densification process and may indicate the necessity for pretreatment such as the case of lignocellulosic materials which are very resistant to deformation. Knowledge of the effects of these characteristics will assist in designing energy efficient compaction methods to produce high quality pellets for thermochemical conversion and provide understanding for the implementation of feasible waste management strategies.

Various models have been adapted in previous studies to examine the compression and relaxation characteristics of biomass feedstocks. The Jones, Walker, Kawakita-Lüdde, and Cooper-Eaton models are fitted to experimental compression data, while the Peleg and Moreyra model is fitted to relaxation data to determine a material's asymptotic modulus (Adapa, et al., 2010). Relationship between compression pressure and compact density, from both Walker and Jones models, indicates the compressibility of a material and points to an optimal pelleting pressure to be used for energy-efficient compaction of different samples (Mani, et al., 2006). Porosity of compacted samples estimated using the Kawakita-Lüdde model allows comparison to the solid density of the loose material; the solid density is the maximum value that can be achieved during compression where there is zero porosity. The Cooper-Eaton model hypothesizes the mechanisms of densification as particle rearrangement and deformation and that if the sum of these two parameters do not result in unity, then there must be another mechanism involved in the compaction process; thus, analysis of these parameters can assist in determining the ratio of the mechanisms involved in the densification of new materials (Adapa, et al., 2010). A material's asymptotic modulus, estimated by the Peleg and Moreyra model, implies its ability to sustain unrelaxed stresses or its rigidity (Talebi, et al., 2011). A material with a high compressibility resulting in a highly compact, rigid pellet is the desired outcome of a densification process, thus analysis of these parameters can result in optimizing the conditions for pelletization.

The objective of this study is to investigate how composition, grind size, moisture content, applied load, and processing temperature affect the compression and relaxation characteristics of MSW RDF-fluff.

2. Materials and Methods

2.1 Materials

Municipal solid waste (MSW) refuse-derived fuel (RDF) fluff was supplied by the Edmonton Waste Management Centre (EWMC), Edmonton, AB, Canada. The fluff upon receipt had a moisture content of 5.5 % wet basis (w.b.) and an average bulk density of 54.6 kg/m^3. It is to be noted that the EWMC facility experiences RDF-fluff moisture contents of upwards of 20–30 % w.b.

Pelleting characteristics were examined for two different fractions of the RDF-fluff material. The first material utilized the RDF in its raw composition; this consisted of approximately 35 % paper, 22 % plastics, 14 % textiles, 6 % wood/organics, and the remainder fines and inerts, determined by a composition sort. The second material consisted of only biodegradable components, wood and paper, after undergoing sorting to remove plastics and textiles.

Each material was ground in two screen sizes, 3.18 mm and 6.35 mm, of the knife mill (Retsch GmbH, Haan, West-Germany). The moisture content of each of the 4 material/grind size samples was determined according to ASABE Standard S358.3 (ASABE, 2008), then adjusted to 8 %, 12 %, and 16 %, w.b. Samples were allowed to equilibrate in air-tight containers for a minimum of 3 days prior to the start of the experiment.

2.2 Compression and relaxation tests

The compression tests were performed using a single pelleting unit (SPU) apparatus mounted on an Instron Universal Testing Machine (Model No. 3366, Instron Corp., Norwood, MA). This SPU consisted of a cylindrical die fixed to the base of the machine with a plunger attached to the moving crosshead of the Instron machine (Shaw, 2008). A heating element was attached to the pelleting die in order to control the temperature of the process; temperatures were compared at 50 °C and 90 °C, with the pelleting protocol allowing time for the material to preheat in the die before being compressed. Approximately 0.55 ± 0.05 g of biomass was fed into the die to produce each pellet. The Instron was then used to apply the load to compress the charged material at a rate of 50 mm/min until the desired compressive force (2, 3, and 4 kN) was achieved, at which point the plunger was held for 60 s as a retention time to avoid "spring-back" typical of densified biomass. A gate in the platform of the SPU apparatus was then opened manually to allow the plunger to eject the newly formed pellet from the die. The software programmed to control the Instron and complete the densification process recorded the time and force-displacement data for each pellet. Twelve pellets (replicates) were produced for each treatment combination; the dimensions and mass of each pellet was measured after each pellet was stored at room conditions for subsequent analyses.

2.3 Data analysis

The experimental data collected was analyzed using several compression and relaxation models for powders. All of the models were fitted to the experimental data using Microsoft Excel (Microsoft Corp., Redmond, WA) with the exception of the Cooper-Eaton model, in which SAS (Statistical Analysis System, Cary, NC) was employed. The Microsoft Excel analysis incorporated the solver tool and non-linear regression techniques, in which constants for the appropriate models were determined for each set of experimental data by the method of least squares. Acceptability of the correlation between the model constants and the experimental data was determined by the mean square error and the coefficient of determination (R^2) of the respective models.

The purpose of fitting the compression and relaxation data of the densification experiments was to determine the relationship between compression pressure and compact density in order to determine the most energy-efficient means of producing quality pellets for different material conditions.

Models proposed for analyzing the compressibility of powders have also been successfully applied to the compression of biomaterials such as timothy hay. Compression of non-metallic powders were modelled by Walker according to the volume ratio to applied pressure (Equation 1) (Walker, 1923).

$$\frac{V}{V_\mathrm{s}} = m \cdot \ln P + b \tag{1}$$

Where, V = volume of compacted hay, m^3; Vs = void-free solid volume, m^3; P = applied pressure, MPa; m, b = constants.

Jones (1960) described the compression of industrial metal powders through the linear relationship of the natural logarithm of both pressure and density (Equation 2).

$$\ln \rho = m' \cdot \ln P + b' \tag{2}$$

Where, ρ = compact density, kg/m^3; m', b' = constants.

Kawakita and Lüdde (1971) related pressure to the volume reduction of metallic powders (Equation 3).

$$\frac{P}{C} = \frac{1}{a_1 b_1} + \frac{P}{a_1} \tag{3}$$

$$C = \frac{V_0 - V}{V_0} \tag{4}$$

Where, C = volume ratio; V_0 = initial volume at zero pressure, m^3; a_1, b_1 = constants.

Cooper and Eaton (1962) attributed the compression of ceramic powders to two independent processes; the filling of large voids through material sliding past one another and slight fractures followed by the filling of small voids through plastic flow and fragmentation (Equation 5).

$$\frac{V_0 - V}{V_0 - V_\mathrm{s}} = a_2 e^{\frac{-k_1}{P}} + a_3 e^{\frac{-k_2}{P}} \tag{5}$$

Where, a_2, a_3, k_1, k_2 = constants.

The relaxation characteristics of solid foods are modelled by Peleg and Moreyra and can be used to compare different materials (Equation 6).

$$\frac{F_0 \cdot t}{F_0 - F(t)} = k_3 + k_4 \cdot t \tag{6}$$

Where, F_0 = initial relaxation force, kN; $F(t)$ = relaxation force at time t, kN; t = time, s; k_3, k_4 = constants.

A modified model by Peleg and Moreyra (1980) gives a slope index that describes the solidity of compressed materials; this can be used to determine the asymptotic modulus of solid foods and powders. The asymptotic modulus is defined as the ability of the compressed material to sustain un-relaxed stress, represented by the residual stress in the Peleg and Moreyra model (Equation 7).

$$E_\mathrm{A} = \frac{F_0}{A_\mathrm{a}\varepsilon}\left(1 - \frac{1}{k_4}\right) \tag{7}$$

Where, E_A = asymptotic modulus, MPa; ε = strain; A_a = cross-sectional area, m^2.

The percent average relaxation was calculated by using the initial force at the beginning of the relaxation phase and the final force after an elapsed time of 60 s (Equation 8).

$$\textit{Percent average relaxation} = \frac{100 \times (F_0 - F_\mathrm{e})}{F_0} \tag{8}$$

Where, F_e = final relaxation force, kN.

3. Results and discussion

The SPU trials resulted in data for 12 replicates of each material property and pelleting condition combinations. The aforementioned models were fitted to the data from these trials to evaluate the compression and relaxation characteristics for each sample. **Fig. 1** displays a typical compression curve for the biodegradable material fraction of RDF.

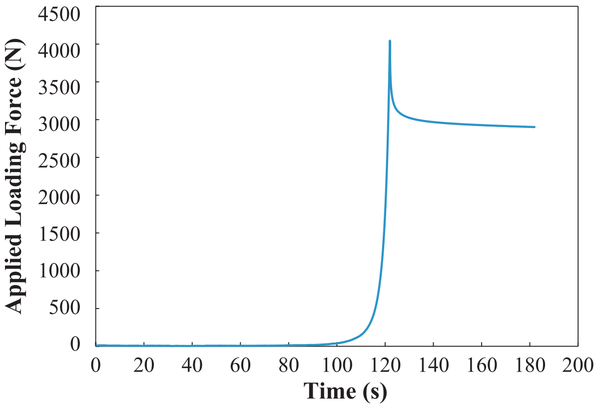

Fig. 1 Typical compression curve as a function of compression and relaxation time at preset loadings for 3.18 mm grind, 16 % m.c. (moisture content) biodegradable material at 50 °C.

The moisture content of the unprepared samples was determined to be 5.45 % w.b. for the RDF material and 7.15 % w.b. for the biodegradable fraction of the RDF material. These values were used to condition the samples, using the standard ASABE S358.3, to experimental moisture contents of 8, 12, and 16 %.

Prior to the experiments, the particle density of each material was determined for each moisture content and grind size combination using a pycnometer (Multipycnometer, Quantachrome Corp., Boynton Beach, FL); particle density is the maximum compact density that can be achieved during compression. Moisture content had little significance over the particle density; however, the densities for RDF ground by 3.18 and 6.35 mm screens were approximately 1350 and 1280 kg/m^3 (**Table 1**), respectively, while the densities for biodegradable material ground by 3.18 and 6.35 mm screens were approximately 1230 and 1140 kg/m^3, respectively.

3.1 Density

Table 1 shows the effects of material grind size, moisture content, pelleting load and temperature of the RDF and biodegradable materials, respectively. Densification of the RDF pellets was only affected by the material grind size, in which the material ground in a 6.35 mm screen in

Table 1 Effects of pelleting parameters on compact density (kg/m^3) of refuse derived fuel fluff and biodegradable material fraction.

Grind Size (mm)	Moisture Content (% w.b.)	Applied Load (kN)					
		2		3		4	
		Die Temperature (°C)					
		50	90	50	90	50	90
Refuse Derived Fuel Fluff							
3.18	8	938 (34)[a]	885 (28)	887 (32)	887 (34)	918 (47)	926 (37)
	12	898 (40)	870 (33)	896 (20)	913 (17)	937 (24)	929 (19)
	16	905 (20)	923 (40)	915 (23)	938 (19)	926 (13)	930 (45)
6.35	8	950 (36)	972 (36)	993 (47)	1000 (41)	1010 (29)	1010 (48)
	12	988 (44)	979 (40)	989 (49)	998 (42)	1007 (58)	990 (35)
	16	982 (36)	1014 (40)	991 (39)	1018 (34)	993 (59)	1010 (28)
Biodegradable material							
3.18	8	1126 (15)	1134 (21)	1194 (27)	1218 (18)	1206 (28)	1237 (22)
	12	1179 (19)	1190 (19)	1199 (12)	1232 (24)	1235 (22)	1250 (34)
	16	1154 (15)	1175 (13)	1194 (29)	1217 (16)	1219 (17)	1254 (29)
6.35	8	1122 (15)	1155 (38)	1181 (27)	1199 (14)	1253 (25)	1285 (18)
	12	1135 (25)	1184 (33)	1189 (29)	1227 (19)	1233 (23)	1255 (14)
	16	1161 (30)	1182 (20)	1204 (36)	1217 (21)	1227 (18)	1242 (21)

[a] Value in parentheses indicates the sample standard deviation where $n = 12$.

the knife mill resulted in greater compaction. Compact density of the biodegradable pellets increased with increasing pelleting load and temperature, while there was no significant effect of moisture content or grind size of the material. There were significant differences in the compact density of the two materials; the biodegradable material produced high density pellets; 1100–1250 kg/m^3, at all applied pressure and temperature combinations, while the RDF material produced pellets with densities of 850–1000 kg/m^3. Bulk density of the pellets produced during the single-pelleting trial was unable to be measured due to the small sample size, however a bulk density of pellets produced in a subsequent pilot-scale trial was determined to be approximately 590 kg/m^3 and 660 kg/m^3 for RDF and biodegradable materials, respectively. The bulk density of the raw RDF-fluff was 55 kg/m^3, therefore both the RDF and the sorted biodegradable materials produced a feedstock that was at least 10 times denser than the original product following pelletization.

3.2 Compression models

The relationship between pressure, volume, and density of the RDF and biodegradable material during the compression portion of the tests (i.e. until maximum loading was achieved) were fitted to models that have been developed for powders. The Walker model describes the relationship of volume ratio to pressure, which decreases linearly as the pressure increases. All test combinations resulted in a fitted Walker model that yielded an average coefficient of determination value (R^2) of greater than 0.90. **Fig. 2** shows a sample relationship between the volume ratio and the natural logarithm of applied pressure. The slope, m, of the fitted Walker model is referred to as the compressibility constant and it remained fairly constant for all parameter tests for each material type. For RDF samples, the slope had an average value of −0.3197 with a standard deviation of 0.0194; while the biodegradable fraction of RDF had an average slope value of –0.3410 with a standard deviation of 0.0235. The biodegradable samples showed a higher slope (absolute value) indicating higher compressibility than the RDF material. This variation could probably be attributed to the different compression properties of the additional plastic fraction in the RDF material. The value of ‘b’ was greater at lower grind size and for the RDF material.

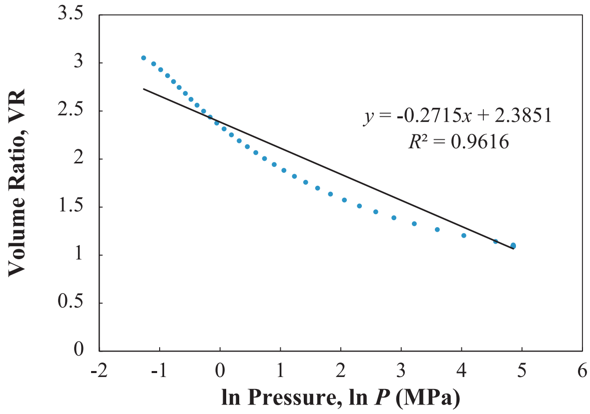

Fig. 2 Fitted Walker model relationship to compression data for 3.18 mm, 16 % m.c. biodegradable material under pelleting conditions of 4 kN applied force and 50 °C die temperature.

The Jones model describes the relationship of compact density to pressure, which increases linearly as the pressure increases. All test combinations resulted in a well-fitted Jones model, yielding an average R^2 value of greater than 0.97. The values of the slope, m', for the model indicates the compressibility of the material. For RDF samples, the slope had an average value of 0.1644 with a standard deviation of 0.0084; while the biodegradable samples had an average slope value of 0.1906 with a standard deviation of 0.0079. Similar to the results of the Walker model, the biodegradable samples showed a higher slope (m') indicating higher compressibility than the RDF material. For all moisture content/grind size combinations, the value of the slope appeared to decrease with an increase in either pelleting conditions, temperature or applied load. There was no significant difference in compressibility between trials with different material conditions, moisture content or grind size. The value of b' of the Jones model was relatively constant for all tests for both RDF and biodegradable materials at an average (standard deviation) of 7.2331 (0.1611) and 7.5622 (0.1509), respectively.

The Kawakita and Lüdde model indicated a good fit to the data, resulting in mean square error (MSE) values of less than 5×10^{-4}. However, there was no correlation found between the model constants and any of the experimental variables for either material. Established by Kawakita and Lüdde (1971), the model constant a_1 represents the initial porosity of the sample, while the parameter $1/b_1$ indicates the yield strength or failure stress of the compaction process (MPa). As such, the model indicates a higher average initial porosity for RDF material at a grind size of 6.35 mm, 0.899 compared to 0.753 at the 3.18 mm grind size. This is reasonable as the smaller particles would exhibit greater mechanical interlocking and thus, a lower initial porosity. The opposite observation is made for that of the biodegradable material, in which model determined initial porosities of 0.801 and 0.772 were for grind sizes of 3.18 mm and 6.35 mm, respectively. This contradiction may be attributed to the fact that while the materials were ground using a particular screen size, not all of the particles were exactly the same size; a particle size analysis indicated that the biodegradable material, once ground, consisted of a higher fraction of fine particles than the equivalent RDF ground material. Decrease in grind size resulted in a decrease in the yield stress ($1/b_1$) for both the RDF and biodegradable material, however the actual values (standard deviation) were similar at 2.59 (0.61) kPa and 2.65 (0.60) kPa, respectively.

Cooper-Eaton model speculates the two mechanisms involved in densification; particle rearrangement and deformation. The constants a_2 and a_3 in the Cooper-Eaton model, respectively represent the two mechanisms. Fitting the model to the experimental data yielded values for a_2 ranging from 0.66 to 0.97 and values for a_3 ranging from 0.00 to 0.23; this indicates that the majority of the compaction mechanism is resultant of particle rearrangement by the filling of large pores. The R^2 values for each sample were above 0.86 with most being at least 0.95, indicating a good fit of the model to the experimental data.

3.3 Relaxation characteristics

After the desired compression pressure was reached through the applied loading, the relaxation characteristics were observed for all trials. Noticeable relaxation was observed during the 60 s holding period; this indicates that complete plastic deformation was not fully achieved upon the applied loading.

The Peleg and Moreyra model was fitted to the linearized data of compressive pressure in relation to relaxation time. The slope of the model, k_4, is referred to as the solidity index and was used to calculate the asymptotic modulus, E_a, for the material. The asymptotic modulus indicates a material's ability to sustain unrelaxed stresses, such that a higher E_a leads to a more rigid restraint of a pellet's compact density (**Table 2**). Pellets produced from RDF material resulted in an asymptotic modulus of between 94 and 117 MPa, while the biodegradable pellets had an E_a value of 89 to 103 MPa. This indicates that the RDF material produces a more rigid pellet than the biodegradable material. The combined effects of pelleting temperature and initial moisture content have a positive correlation with the asymptotic modulus value for each material. Pellets produced at 90 °C had E_a values 3 to 17 percent larger than those produced at 50 °C; the highest percent difference was observed at 16 % m.c. (w.b.) for each grind size. The asymptotic modulus values calculated for the RDF-fluff samples were comparable to other biological materials according to literature; for example corn stover, barley straw, and wheat straw display E_a values between 20 and 160 MPa (Mani et al., 2006).

As previously noted, relaxation was observed during the experiment and was quantified as the percent average relaxation (PAR) (**Table 3**). Values ranging from 21 to 35 % and from 29 to 37 % were determined for the RDF and biodegradable pellets, respectively. These values are consistent with literature values for timothy hay, wherein PAR values of 27 to 53 % were published (Talebi, et al., 2011). As with the asymptotic modulus, die temperature has the highest positive correlation to PAR.

4. Conclusions

The compression and relaxation characteristics of RDF-fluff samples were investigated and the following conclusions were made:

1. The compact density of RDF pellets was only affected by grind size, in which it was greatest with material that was ground with a 6.35 mm screen in the knife mill; compact density of biodegradable pellets increased with increasing pelleting load and temperature, while there was no significant effect of moisture content or grind size of the material.
2. Both Walker and Jones model resulted in good fits to the experimental data and indicated that the biodegradable material had a higher compressibility than the RDF material for all conditions.
3. Fitting of the Kawakita-Lüdde model to the compres-

Table 2 Effects of experimental variables on asymptotic modulus, E_a (MPa).

Grind Size (mm)	Moisture Content (% w.b.)	Refuse Derived Fuel Fluff		Biodegradable Material	
		Die Temperature (°C)			
		50	90	50	90
3.18	8	102.31 (2.06)[a]	105.91 (0.98)	96.23 (0.39)	99.23 (12.10)
	12	94.33 (1.45)	99.76 (1.57)	98.06 (0.16)	102.07 (0.76)
	16	100.28 (9.40)	117.99 (3.92)	91.07 (0.87)	95.56 (0.49)
6.35	8	102.92 (1.06)	108.68 (1.55)	96.88 (0.49)	102.43 (2.17)
	12	100.24 (4.68)	104.10 (1.58)	93.82 (1.91)	99.88 (1.94)
	16	102.26 (8.68)	116.65 (2.04)	89.11 (3.56)	98.45 (3.89)

[a] Value in parentheses indicates the sample standard deviation where $n = 6$.

Table 3 Effects of experimental variables on percent average relaxation, PAR (%).

Grind Size (mm)	Moisture Content (% w.b.)	Refuse Derived Fuel Fluff		Biodegradable Material	
		Die Temperature (°C)			
		50	90	50	90
3.18	8	31.41 (1.15)[a]	28.00 (0.52)	33.47 (0.28)	34.58 (1.16)
	12	35.46 (0.71)	31.90 (1.20)	32.02 (0.19)	29.11 (0.51)
	16	31.86 (5.15)	21.65 (1.18)	36.52 (0.71)	33.40 (0.39)
6.35	8	31.53 (0.38)	27.44 (0.76)	32.29 (1.44)	29.16 (1.07)
	12	32.23 (2.65)	29.43 (0.39)	34.71 (1.30)	30.25 (1.34)
	16	31.17 (4.84)	22.62 (1.07)	37.68 (1.78)	31.52 (2.16)

[a] Value in parentheses indicates the sample standard deviation where $n = 6$.

sion data resulted in no significant correlation ($P = 0.05$) between the model parameters and the experimental variables.

4. The Cooper-Eaton model indicates that the primary mechanism in the densification of RDF derived biomass is attributed to particle rearrangement, with some secondary influence from plastic deformation or particle fragmentation.
5. Peleg and Moreyra's model, fit to the data, estimated the asymptotic modulus (E_a) for each sample and indicated that pellets formed from the RDF material had a higher E_a value than the biodegradable pellets; RDF-derived materials are determined to have comparable E_a values to literature values for other biological residues.

Acknowledgements

This research has been in collaboration with the Edmonton Waste Management Centre. Significant funding was provided by BioFuelNet Canada under the waste as feedstocks project.

Nomenclature

ASABE	American Society of Agricultural and Biological Engineers
BFN	BioFuelNet
EWMC	Edmonton Waste Management Centre
MSW	Municipal Solid Waste
PAR	Percent Average Relaxation
RDF	Refuse Derived Fuel
SPU	Single Pelleting Unit
A_a	cross-sectional area (m^2)
a_1	Kawakita-Lüdde model constant
a_2	Cooper-Eaton model constant
a_3	Cooper-Eaton model constant
b_1	Kawakita-Lüdde model constant
b	Walker model constant
b'	Jones model constant
C	volume ratio
E_a	asymptotic modulus, (MPa)
F_e	final relaxation force (kN)
F_0	initial relaxation force (kN)
$F(t)$	relaxation for at time t (kN)
k_1	Cooper-Eaton model constant
k_2	Cooper-Eaton model constant
k_3	Peleg-Moreyra model constant
k_4	Peleg-Moreyra model constant
m	Walker model constant
m'	Jones model constant
P	pressure (MPa)
t	time (s)
T	temperature (K)
V	volume of compacted material (m^3)
V_0	initial volume at zero pressure (m^3)
V_s	void-free solid volume (m^3)
ε	strain
ρ	compact density (kg/m^3)

References

Adapa P., Tabil L. Schoenau G., Compression characteristics of non-treated and steam-exploded barley, canola, oat, and wheat straw grinds. Applied Engineering in Agriculture, 26 (2010) 617–632.

ASABE (American Society of Agricultural and Biological Engineers Standards), ASAE S358.3 Moisture measurement—forages, ASABE, St. Joseph, Michigan, 2008.

BioFuelNet (BioFuelNet Canada), 2015, What are biofuels? <http://www.biofuelnet.ca/wp-content/uploads/2015/01/Infographics11.png> accessed 15.02.2017.

Cooper A., Eaton L., Compaction behavior of several ceramic powders, Journal of the American Ceramic Society, 45 (1962) 97–101.

EWMC (Edmonton Waste Management Centre), 2015, Waste-to-biofuels and chemicals facility: turning garbage into fuel <www.edmonton.ca/programs_services/garbage_waste/biofuels-facility.aspx> accessed 15.02.2017.

Jones W.D., Fundamental principles of powder metallurgy, Edward Arnold Publishers Ltd., London, 1960, pp. 242–370.

Kawakita K, Lüdde K., Some considerations on powder compression equations, Powder Technology, 4(1971) 61–68.

Mani S., Tabil L., Sokhansanj S., An overview of compaction of biomass grinds, Powder Handling & Processing, 15 (2003) 160–168.

Mani S., Tabil L., Sokhansanj S., Effects of compressive force, particle size, and moisture content on mechanical properties of biomass pellets from grasses, Biomass and Bioenergy, 30 (2006) 648–654.

Mor S., Ravindra K., Visscher A. De, Dahiya R., Chandra A., Municipal solid waste characterization and its assessment for potential methane generation: A case study, Science of the Total Environment, 371 (2006) 1–10.

Moreyra R., Peleg M., Compressive deformation patterns of selected food powders, Journal of Food Science, 45 (1980) 866–868.

Payne J.D., Improving quality of pellet feeds, Milling Feed and Fertilizer, 161 (1978) 3441.

Shaw M, Feedstock and process variables influencing biomass densification, M.Sc. Thesis, 2008.

Sokhansanj S., Mani S., Bi X., Zaini P., Tabil L., Binderless pelletization of biomass, Presented at the ASAE Annual International Meeting, July 17–20, 2005, Tampa, Florida. ASAE Paper No. 056061. ASAE, 2950 Niles Road, St. Joseph, MI 49085-9659 USA.

Talebi S., Tabil L., Opoku A., Shaw M., Compression and relaxation properties of timothy hay, International Journal of Agricultural and Biological Engineering, 4 (2011) 69–78.

Walker E., The properties of powders—Part VI: The compressibility of powders, Transactions of the Faraday Society, 19 (1923) 73–82.

Yaman S., Şahan M., Haykiri-açma H., Şeşen K., Küçükbayrak S., Production of fuel briquettes from olive refuse and paper mill waste, Fuel Processing Technology, 68 (2000) 23–31.

Author's short biography

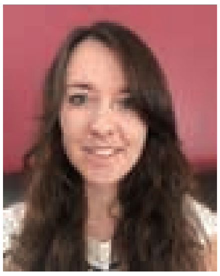

Charley Sprenger

Charley Sprenger is a MSc candidate in the Department of Chemical and Biological Engineering, University of Saskatchewan. Her thesis research is in the area of pre-processing of municipal solid waste for biofuels applications.

Lope G. Tabil

Lope G. Tabil, is a Professor of Biological Engineering in the Department of Chemical and Biological Engineering, University of Saskatchewan. The areas of research in which he works and maintains interest include bioprocess engineering, value-added engineering, biomass energy and postharvest handling of crops. He has also conducted research and development projects related to value-added processing of agricultural products including storage, drying and cooling, and physical properties of agricultural and biological materials.

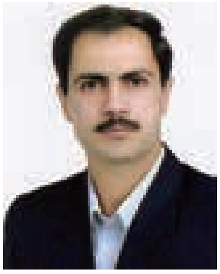

Majid Soleimani

Majid Soleimani is a PDF Research Associate at the Department of Chemical and Biological Engineering, University of Saskatchewan. His research interests are in bioproducts, biofuels, and biomaterials. He did his PhD in Industrial Biotechnology-Bioprocess Engineering. The title of his thesis was "Xylitol production in free- and immobilized-cell bioconversions from lignocellulosic biomass". The major focus of the thesis was on the kinetic study of xylitol production in homogeneous and heterogeneous bioreactors. In the last few years, he has been working on biomass densification (granulation and pelletization) and some thermochemical processes such as torrefaction for solid biofuel applications. Also, he has been involved in a few projects on biocomposites, including fully- and partially-degradable composites for structural applications or as cell support in biocatalysis.

KONA Powder and Particle Journal No. 35 (2018) 209–215/Doi:10.14356/kona.2018008 Original Research Paper

Photostability of Risperidone in Tablets[†]

Yuki Fujisawa[1]*, Yoshiteru Takahashi[1], Reiko Teraoka[2] and Shuji Kitagawa[2]

[1] *Pharmaceutical Technology Center, Sawai Pharmaceutical Co., Ltd., Japan*
[2] *Laboratory of Pharmaceutical Technology, Kobe Pharmaceutical University, Japan*

Abstract

The purpose of this study is to evaluate the photostabilization mechanism of risperidone tablets. Risperidone is widely used for sensory integration disorder. It is formulated as tablets, orally disintegrating tablets, fine granules, oral solutions, and intramuscular injections. We found that risperidone was unstable in tablets and generated oxidized products. Formation of the oxidized product R5 was promoted in the presence of hydroxypropylcellulose by photoirradiation. On the other hand, photostability improved greatly when carmellose (CMC) or carmellose calcium (CMC-Ca) was used as a disintegrant. Since CMC and CMC-Ca are acidic substances, the photostability of tablets may have been affected by pH. Therefore, the effects of different pHs were examined. Risperidone was dissolved in methanol and the buffer (in the presence or absence of hydroxypropylcellulose) at different pHs (1.2, 3.0, 4.0, 5.0, and 6.8) was added. The photodegradation of risperidone was not observed at less than pH 3.0 in the presence of hydroxypropylcellulose, and low pHs improved the photostability of risperidone. On the other hand, risperidone solution without hydroxypropylcellulose was stable at all pH values. Therefore, risperidone was photochemically oxidized in the presence of hydroxypropylcellulose at high pHs.

Keywords: photostability, risperidone, carmellose, pH, hydroxypropylcellulose, tablet

1. Introduction

Risperidone (3-{2-[4-(6-fluoro-1,2-benzisoxazol-3-yl)-1-piperidinyl]ethyl}-6,7,8,9-tetrahydro-2-methyl-4H-pyrido [1,2-α] pyrimidin-4-one) is a benzisoxazol derivative that is widely used for sensory integration disorder (Janssen P.A.J., 1987); it has both serotonin 5-HT$_2$ and dopamine D$_2$ antagonistic activities (Janssen P.A.J. et al., 1988; Leysen J.E. et al., 1988; Grant S. and Fitton A., 1994).

Risperidone was developed by Janssen Pharmaceutica Inc. and won FDA approval in the US on December 29, 1993 (where it is marketed as RISPERDAL^{TM}), and subsequently achieved worldwide acceptance (Germann D. et al., 2012).

9-Hydroxylation of risperidone is mainly generated by two cytochrome P-450 enzymes, CYP2D6 and CYP3A4. 9-Hydroxyrisperidone is the major metabolite of risperidone in plasma. 9-Hydroxyrisperidone has pharmacological activity as well as risperidone (Yasui-Furukori N. et al., 2001).

Risperidone is formulated as tablets, orally disintegrating (OD) tablets, fine granules, oral solutions (Berus P. et al., 2005), and intramuscular injections. It is practically insoluble in water, freely soluble in methylene chloride, and sparingly soluble in ethanol. It dissolves in dilute acid solutions (Merck Index, 14th ed., 2006).

This active pharmaceutical ingredient (API) is hydrolyzed into the R2 form in the presence of water, and is also oxidized into the R5 form during preservation (Tomar R.S. et al., 2004; Bharathi Ch. et al., 2008). R5 is an N-oxide product of risperidone and one of the major degraded substances that is generated by photoirradiation. The chemical structures of risperidone, R2, and R5 are shown in **Fig. 1**.

OD tablets are a new type of solid dosage form that are easily dispersed or dissolved in the oral cavity and are swallowed without water. The compliance and acceptability of patients are improved by OD tablets (Rahman Z. et al., 2010). The EP (European pharmacopoeia) describes OD tablets as uncoated tablets intended to be placed in the mouth where they disperse rapidly before being swallowed and as tablets which should disintegrate within 3 min. FDA defines OD tablet as a solid dosage form which contains a medicinal substance or active ingredient which disintegrates rapidly within a matter of seconds when placed upon a tongue (Bhatu P.B. et al., 2011).

In the case of tablets that are unstable to light, film coating technology may be performed to improve the sta-

---

[†] Received 30 July 2015; Accepted 26 April 2017
J-STAGE Advance published online 24 June 2017

[1] 3-8, Akagawa 1-chome, Asahi-ku, Osaka 535-0005, Japan
[2] 19-1 Motoyamakita-machi 4-chome, Higashinada-ku, Kobe 658-8558, Japan
* Corresponding author: Yuki Fujisawa
E-mail: y.fujisawa@sawai.co.jp
TEL: +81-6-6926-2650 FAX: +81-6-6922-5952

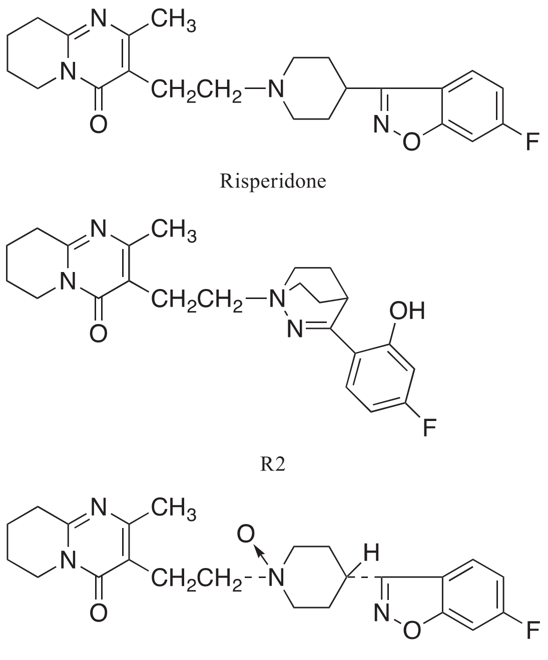

Fig. 1 Structural formulas of risperidone, R2, and R5.

bility. For example, titanium oxide, which is often formulated in the film has light shielding properties. However, film coating technology is not applicable to OD tablets because the film does not dissolve promptly with saliva. Also, the surface of the OD tablet is often brittle, the surface may collapse during film coating.

To develop the optimal formulation for risperidone OD tablets, the effects of excipients on the stability of risperidone were investigated.

When the risperidone OD tablets were previously formulated, the stability of risperidone against heat and photoirradiation was improved by adding carmellose (CMC) (Iwakura Y. et al., JP Patent, P2013-60392A).

It is well established that photochemical reactions of API are often affected by the excipients. Testing of the photostability of a drug substance and of the final dosage form is important to ensure the life span of the product (Tønnesen H.H., 2001).

The purpose of this study is to evaluate the stabilization mechanism of risperidone and other additives in risperidone OD tablets against photoirradiation.

2. Materials and methods

2.1 Formulation and manufacturing methods of risperidone orally disintegrating tablets

The formulation of risperidone OD tablets is shown in **Table 1**.

Table 1 Formulation of risperidone OD tablets.

	Ingredient	Weight (mg/tab)
1	Risperidone	0.5
2	D-Mannitol	q.s.
3	Corn Starch	3.0
4	Anhydrous Dibasic Calcium Phosphate	10.0
5	Carmellose (CMC)	5.0
6	Carmellose Calcium (CMC-Ca)	5.0
7	Hydroxypropylcellulose (HPC)	0.5
8	Light Anhydrous Silicic Acid	0.75
9	Magnesium Stearate	0.5
10	Aspartame	2.0
11	Flavor	0.15
	Total	50.0

Risperidone was obtained from Assia Chemical Industries Ltd. (Israel) for JP grade. Aspartame was JPE grade. Other materials were JP grade.

HPC was obtained for L grade of NISSO HPC (Nippon-Soda, Japan).

The OD tables were prepared by three different manufacturing methods as follows.

Method A: From No. 1 to No. 6 in **Table 1** were mixed in a fluidized bed granulator and then granulated by 1 % (w/w) HPC aqueous solution. The granules were sieved using a 710 μm screen and excipients from No. 8 to No. 11 were mixed. The mixture was compressed using a tablet press.

Method B: From No. 1 to No. 7 in **Table 1** were mixed in a fluidized bed granulator and then granulated using purified water. The granules were sieved using a 710 μm screen and excipients from No. 8 to No. 11 were mixed. The mixture was compressed using a tablet press.

Method C: From No. 1 to No. 6 in **Table 1** were mixed in a fluidized bed granulator and then granulated by purified water. Additionally, 1 % (w/w) HPC aqueous solution was sprayed for granulation. The granule was sieved using a 710 μm screen and excipients from No. 8 to No. 11 were mixed. The mixture was compressed using a tablet press.

Fluidized bed granulator: Multiplex Coater (MP-01, Powrex, Japan). Tablet press: PICCOLA (RIVA S.A., Argentina).

2.2 Irradiation test of risperidone OD tablets

Sample tablets of methods A, B, and C were stored in a light-irradiation tester with a D65 lamp (LT-120, Nagano Science, Japan), as previously demonstrated (Teraoka R.

et al., 2001).

Irradiation was carried at 1000 lx for 25 days. The temperature in the light-irradiation tester was kept at 298 K.

2.3 High-performance liquid chromatography (HPLC)

The analysis of risperidone and its degradation forms by an HPLC system in tablets has been reported (Suthar A.P. et al., 2009). The R5 formation rate was analyzed with an HPLC system (Prominence UFLC, Shimadzu, Japan) equipped with a UV detector (SPD-20AV, Shimadzu, Japan) operated at 275 nm. The packaged column was a reverse-phase C18 column (Zorbax SB-C18, 3.5 µm, 3.0×150 mm, Agilent, USA) operated at 298 K. The flow rate was kept at 1.1 mL/min. The mobile phase consisted of purified water:acetonitrile:trifluoroacetic acid (1600: 400:3) and the pH value was adjusted to 3.0 by adding NH_3 solution. After photoirradiation, 5 risperidone OD tablets were added into 25 mL of 0.1 mol/L hydrochloric acid/methanol mixture (3:2). After shaking, this solution was filtered using a polyolefin disposable syringe filter (Chromatdisk 25A, 0.45 µm, GL Science, Japan). A total of 10 µL of sample solution was subjected to HPLC analysis.

2.4 Colorimetric measurement

The color of a sample tablet was measured with a chromameter (Spectrophotometer SE6000, Nippon Denshoku, Japan) with the L*a*b* colorimetric system.

The average of 5 tablet measurements of ΔE^*, before and after photoirradiation in the 3-dimensional $L^*a^*b^*$ color space, was calculated as follows.

$$\Delta E^* = [(\Delta L^*)^2 + (\Delta a^*)^2 + (\Delta b^*)^2]^{1/2}$$

ΔL^*: the lightness difference
Δa^*: the red/green difference
Δb^*: the yellow/blue difference

2.5 Preparation of sample powders

The sample powders of risperidone and other additives were prepared as described in **Table 2**.

2.6 Solid-state UV-VIS spectra

UV-VIS solid-state absorption spectra of samples from a) to d) were measured on a UV-2450 system (Shimadzu, Japan) equipped with an integrating sphere unit (Shimadzu ISR-2200) at room temperature. A cell was filled with sample powder and the spectra were acquired with 0.2 nm sampling pitch in the wavelength range from 300 to 400 nm.

Table 2 Preparation of sample powders.

	Sample	Preparation Method
a)	RIS/CMC (powder)	7.5 g of risperidone and 7.5 g of CMC were mixed using a pestle in a mortar for 2 min.
b)	RIS/CMC (pellet)	7.5 g of risperidone and 7.5 g of CMC were mixed and granulated in a mortar with 3 mL of purified water. The granules were dried at 343 K for 2 h by a hot air circulation-type constant-temperature oven (MO-921, Toyama Sangyo, Japan).
c)	RIS/HPC (powder)	7.5 g of risperidone and 7.5 g of HPC were mixed using a pestle in a mortar for 2 min.
d)	RIS/HPC (pellet)	7.5 g of risperidone and 7.5 g of HPC were mixed and granulated in a mortar with 3 mL of purified water. The granules were dried at 343 K for 2 h by a hot air circulation-type constant-temperature oven (MO-921, Toyama Sangyo, Japan).

Table 3 Formulation of different amounts of CMC in risperidone OD tablets.

	Ingredient	Weight (mg/tab)		
	(Amount of CMC)	0	2.5	5.0
1	Risperidone	0.5	0.5	0.5
2	D-Mannitol	q.s.	q.s.	q.s.
3	Corn Starch	3.0	3.0	3.0
4	Anhydrous Dibasic Calcium Phosphate	10.0	10.0	10.0
5	CMC	0	2.5	5.0
6	CMC-Ca	5.0	5.0	5.0
7	HPC	0.5	0.5	0.5
8	Light Anhydrous Silicic Acid	0.75	0.75	0.75
9	Magnesium Stearate	0.5	0.5	0.5
10	Aspartame	2.0	2.0	2.0
11	Flavor	0.15	0.15	0.15
	Total	50.0	50.0	50.0

2.7 Solid-state NMR

^{13}C CP/MAS NMR spectra of samples a)~d) were measured on a Varian NMR System 500 with a zirconia sample tube (outer diameter: 5 mm, scanning speed: 20 kHz).

2.8 Formulation of sample tablets to examine the effect of CMC amount on stability

To examine the effect of CMC in tablets on photostability, three different amounts of CMC in tablets were prepared, as shown in **Table 3**. All formulations were manufactured by method C described in 2.1. Sample tablets were stored at 1000 lx for 14 days and R5 was measured by HPLC.

2.9 Formulation of sample solutions to examine the effect of pH on stability

A total of 1 mL of 0.5 mg/mL risperidone in methanol was mixed with 2 mL of 1 % (w/w) HPC buffer solution with various pHs (1.2, 3.0, 4.0, 5.0, 6.8). Sample solution was injected in a quartz cell and stored in a light-irradiation tester with a D65 lamp (3500 lx) for 14 days. The R5 formation rate was analyzed by HPLC. Each pH of buffer solution is shown as follows.

pH 1.2: 1st fluid for dissolution test (JP)
pH 3.0: Dilute McIlvaine buffer solution, pH 3.0
pH 4.0: Dilute McIlvaine buffer solution, pH 4.0
pH 5.0: Dilute McIlvaine buffer solution, pH 5.0
pH 6.8: 2nd fluid for dissolution test (JP)

2.10 Formulation of sample solutions to examine the effect of HPC concentration

A total of 1 mL of 0.5 mg/mL risperidone in methanol was mixed with 2 mL of each concentration (0 %, 0.01 %, 0.1 %, 1 %) of HPC buffer solution at pH 6.8. Sample solution was injected in a quartz cell and stored in a light-irradiation tester with a D65 lamp (3500 lx) for 14 days. The R5 generation rate was analyzed by HPLC.

3. Results and discussion

3.1 Photostability of risperidone OD tablets by different manufacturing methods

Tablets produced by methods A, B, and C were subjected to accelerated stability testing at 1000 lx for 25 days using a D65 lamp. The R5 formation rate was measured by HPLC and color differences were measured using a chromameter.

The results of photostability testing are shown in **Table 4**. Comparing these three manufacturing methods in terms of stability, method A was most unstable and method C was most stable. Similarly, the most color change was observed in method A. The color difference in method C was very limited.

It was considered that method C is the most stable manufacturing method among these three methods.

Table 4 R5 formation rate and color difference of risperidone OD tablets after photoirradiation.

Method	R5 formation (%)	Color difference (ΔE^*)
A	2.7	1.74
B	1.1	0.76
C	0.5	0.40

3.2 Measurement of solid-state UV-VIS spectra and solid-state NMR

There was a possibility that the change of photostability was due to a shift of the absorption wavelength (Kojima T. et al., 2007). Spectrum from 300 nm to 400 nm in a solid state was measured and the relative absorbance spectrum was plotted with the absorbance of 300 nm set as 1.0.

Sample d) was not measured because rubber-like pellets were obtained and these pellets were not suitable for the measurement because they were not solidified by the press.

As shown in **Fig. 2**, a shift of spectrum was not observed in any sample. Therefore, there was no change in the absorption wavelength.

Solid-state NMR has developed as an important technique for the characterization of pharmaceutical solids as well as DSC, FT-IR, and PXRD. Physicochemical information about both API and the formulated product was provided by the measurement (Berendt R.T. et al., 2006). It has been reported that risperidone has three polymorphs (Karabas I. et al., 2007; Krochmal B. et al., 2004). There was a possibility that the crystal form of risperidone was changed and a difference in the stability was observed. Measurements of samples a)~d) and risperidone were performed using solid-state NMR to determine whether the crystal form had changed or not and their spectra were compared. As shown in **Fig. 3**, changes in the spectra were not observed and it was suggested that there were no changes in the crystal forms.

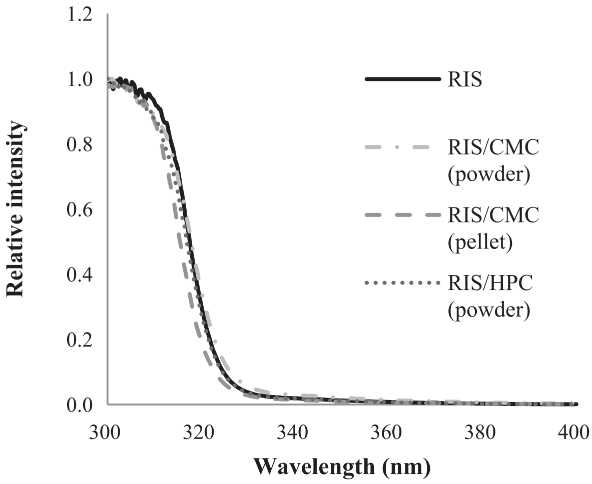

Fig. 2 Solid-state UV-VIS spectra of risperidone and samples a)~c).

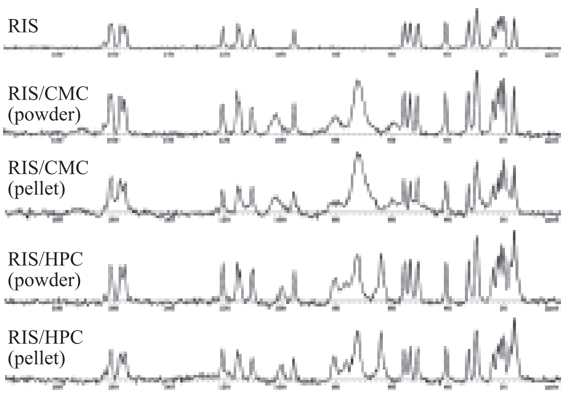

Fig. 3 Solid-state NMR spectra of risperidone and samples a)~d).

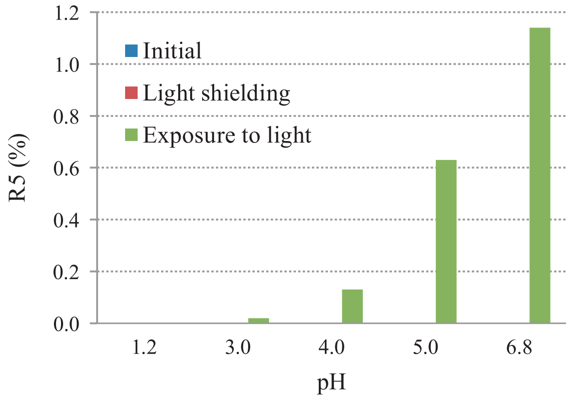

Fig. 4 R5 formation rate in different pH solutions (HPC concentration: 1 %).

3.3 Effect of CMC in tablets on the photostability

CMC is widely used as a relatively acidic disintegrant. A total of 1.0 g of CMC was dispersed in 100 mL of purified water and the suspension showed about pH 3.5 to 5.0 (European Pharmacopoeia 8th Edition, 2014).

To examine the effect of CMC on the photostability, three different amounts of CMC (0, 2.5, 5 mg) in OD tablets were formulated and stored at 1000 lx for 25 days. The pH of the tablet was also measured by dispersing the tablet in 20 mL of purified water for 20 min.

As the amount of CMC in the tablet increased, the pH value was lowered.

As shown in **Table 5**, No R5 was detected in any sample before photoirradiation by HPLC analysis. After photoirradiation, R5 was detected and its amount varied in a CMC-dependent manner.

Table 5 R5 formation rate at different amounts of CMC in OD tablets.

CMC (mg/tab)	pH	R5 formation rate (%)	
		Initial	1000 lx 25 days
0	7.6	N.D.	4.14
2.5	6.0	N.D.	1.31
5.0	5.1	N.D.	0.87

3.4 R5 formation rate in different pH solutions

The R5 formation rate of risperidone/HPC solution at different pHs was investigated. The results of photostability testing are shown in **Table 6** and **Fig. 4**. In light shielding conditions, all samples were stable. When samples were exposed to light, R5 was generated at high-pH conditions. It is considered that the photostability of risperidone was affected by the pH of the solution.

Table 6 R5 formation rate at different pH solutions (HPC concentration: 1 %).

pH	R5 formation rate (%)		
	Initial	3500 lx 14 days	
		Light shielding	Exposure to light
1.2	N.D.	N.D.	N.D.
3.0	N.D.	N.D.	0.02
4.0	N.D.	N.D.	0.13
5.0	N.D.	N.D.	0.63
6.8	N.D.	N.D.	1.14

3.5 R5 formation rate at different hydroxylpropylcellulose concentrations

To evaluate the effect of HPC on the stability of API, risperidone was dissolved in different concentrations of HPC aqueous solution. As shown in **Table 7**, R5 formation was not observed at any sample in light shielding conditions. On the other hand, R5 formation was increased with increasing HPC concentration when samples were exposed to light.

Table 7 R5 formation rate at different HPC concentrations (pH 6.8).

HPC (%)	R5 formation rate (%)		
	Initial	3500 lx 14 days	
		Light shielding	Exposure to light
0	N.D.	N.D.	N.D.
0.01	N.D.	N.D.	0.07
0.1	N.D.	N.D.	0.15
1	N.D.	N.D.	0.86

4. Conclusions

By the difference of manufacturing method, the photostability of risperidone in OD tablets was changed.

The photostability was significantly improved by adding purified water before granulation. These differences in stability suggested that risperidone and HPC reacted upon photoirradiation and formed degradation substances.

From the analysis of solid-state UV-VIS spectrum and solid-state NMR, no physical change was observed.

At low pH, risperidone in HPC solution was stable upon photoirradiation. On the other hand, risperidone in HPC solution was stable at any pH under light shielding conditions. It is suggested that this photo-reaction is suppressed at low pH because risperidone has mono- and di-protonated forms ($pK_1 = 8.1–8.6$, $pK_2 = 3.1$) (Alparone A., 2011).

The photostability of risperidone in HPC solution depended on the concentration of HPC.

To improve the photostability of risperidone OD tablets, it is important to use acidic excipients and a small amount of HPC.

Nomenclature

API	active pharmaceutical ingredient
CMC	carmellose (carboxymethylcellulose)
CMC-Ca	carmellose calcium
DSC	differential scanning calorimetry
EP	European pharmacopoeia
FDA	Food and drug administration
FT-IR	Fourier transform infrared spectroscopy
h	hour
HPC	hydroxypropylcellulose
JP	Japanese pharmacopoeia
lx	lux
min	minute
N.D.	not detected
NMR	nuclear magnetic resonance
OD	orally disintegrating
PXRD	powder X-ray diffraction
q.s.	quantum sufficiat
tab	tablet
w	weight

References

Alparone A., Spectroscopic properties of neuroleptics: IR and Raman spectra of Risperidone (Risperdal) and of its mono- and di-protonated forms, Spectrochimica Acta Part A: Molecular and Biomolecular Spectroscopy, 81 (2011) 631–639.

Berendt R.T., Sperger D.M., Isbester P.K., Munson E.J., Solid-state NMR spectroscopy in pharmaceutical research and analysis, TrAC Trends in Analytical Chemistry, 25 (2006) 977–984.

Berus P., Gartner A., Mlakar A., Puncuh K.A., Vrecer F., Preparation of a stable oral solution with risperidone, European Journal of Pharmaceutical Sciences, 25S1 (2005) S57–S58.

Bharathi Ch., Chary D.K., Kumar M.S., Shankar R., Handa V.K., Dandala R., Naidu A., Identification, isolation and characterization of potential degradation product in risperidone tablets, Journal of Pharmaceutical and Biomedical Analysis, 46 (2008) 165–169.

Bhatu P.B., Atish S.M, The technologies used for developing orally disintegrating tablets: A review, Acta Pharmaceutica, 61 (2011) 117–139.

European Pharmacopoeia 8th Edition, Carmellose, Carmellose calcium, The European Directorate for the Quality of Medicines & HealthCare, 2014, pp. 1773–1774.

Germann D., Kurylo N., Han F., Risperidone, Chapter 8 in: Brittain H. (Eds.), Risperidone, Profiles of drug substances, excipients, and related methodology, Academic Press, 37, 2012, pp. 313–361.

Grant S., Fitton A., Risperidone: A Review of its pharmacology and therapeutic potential in the treatment of schizophrenia, drugs, 48 (1994) 253–273.

Iwakura Y., Fujisawa Y., Toyonaga N., Oral disintegrant tablet containing risperidone and method for producing the same, JP Patent, (2013) JP2013060392A.

Janssen P.A.J., The development of new antipsychotic drugs: Towards a new strategy in the management of chronic psychoses, Journal for Drugtherapy and Research, 12 (1987) 324–328

Janssen P.A.J., Niemegeers C.J.E., Awouters F., Schellekens K.H.L., Megens A.A.H.P. and Meert T.F., Pharmacology of risperidone (R 64 766), a new antipsychotic with serotonin-S_2 and dopamine-D_2 antagonistic properties, Journal of pharmacology and experimental therapeutics, 244-2 (1988) 685–693.

Karabas I., Orkoula M.G., Kontoyannis C.G., Analysis and stability of polymorphs in tablets: The case of Risperidone, Talanta, 71 (2007) 1382–1386.

Kojima T., Onoue S., Katoh F., Teraoka R., Matsuda Y., Kitagawa S., Tsuhako M., Effect of spectroscopic properties of tamoxifen citrate polymorphs, International Journal of Pharmaceutics, 336 (2007) 346–351.

Krochmal B., Diller D., Dolitzky B., Aronhime J., Preparation of risperidone, US Patent (2004) US6,750,341B2.

Leysen J.E., Gommeren W., Eens A., de Chaffoy de Courcelles D., Stoof J.C., Janssen P.A., Biochemical profile of risperidone, a new antipsychotic, The Journal of Pharmacology and Experimental Therapeutics, 247 (1988) 661–670.

Merck Index, 14th ed., Merck Research Laboratories, division of Merck & Co., Whitehouse Station, N.J., , 2006, entry 8316, 1478.

Rahman Z., Zidan A.S., Khan M.A., Risperidone solid dispersion for orally disintegrating tablet: Its formulation design and non-destructive methods of evaluation, International Journal of Pharmaceutics, 400 (2010) 49–58.

Suthar A.P., Dubey S.A., Patel S.R., Shah A.M., Determination of Risperidone and forced degradation behaviour by HPLC in tablet dosage form, International Journal of PharmTech Research, 1 (2009) 568–574.

Teraoka R., Konishi Y., Matsuda Y., Photochemical and oxidative degradation of the solid-state tretinoin tocoferil, Chemical & pharmaceutical bulletin, 49 (2001) 368–372.

Tomar R.S., Joseph T.J., Murthy A.S.R., Yadav D.V., Subbaiah G., Krishna Reddy K.V.S.R., Identification and characterization of major degradation products of risperidone in bulk drug and pharmaceutical dosage forms, Journal of Pharmaceutical and Biomedical Analysis, 36 (2004) 231–235.

Tønnesen H.H., Formulation and stability testing of photolabile drugs, International Journal of Pharmaceutics, 225 (2001) 1–14.

Yasui-Furukori N., Hidestrand M., Spina E., Facciolá G., Scordo M.G., Tybring G., Different enantioselective 9-hydroxylation of risperidone by the two human CYP2D6 and CYP3A4 enzymes, Drug Metabolism and Disposition, 29 (2001) 1263–1268.

Author’s short biography

Yuki Fujisawa

Yuki Fujisawa graduated from Nagoya City University in 2002 and the Graduate School of the same university in 2004. He received a degree in organic and medicinal chemistry from the Graduate School. He has worked for Sawai Pharmaceutical Co., Ltd., since 2007. He is responsible for formulation development and scale-up study as a pharmaceutical researcher.

Yoshiteru Takahashi

Yoshiteru Takahashi is an executive corporate officer of Sawai Pharmaceutical Co., Ltd. He received BS degree (1975), Master degree (1977) and Ph.D. (1985) in pharmaceutical science from Kyoto University. He joined Sawai Pharmaceutical Co., Ltd. in 2003. His research interests include formulation development, scaling-up and improvement of the manufacturing technologies in a manner that allows for production on the market and enables registration.

Reiko Teraoka

Reiko Teraoka, Ph.D. is currently associate professor of laboratory of pharmaceutical technology in Kobe Pharmaceutical University.

Her research interests focus on:

- Stability evaluation and stabilization design of pharmaceutical drugs
Photostability of solid pharmaceutical drugs and cocrystals in particular
- Proper use of transdermal fentanyl for palliative care and anti-AIDS agent

Shuji Kitagawa

Shuji Kitagawa is a Professor in Department of Pharmaceutical Technology at Kobe Pharmaceutical University. Since April, 2013 he has also been a President of the same university. He holds a Ph.D. degree from Kyoto University in 1981. His research interests include percutaneous permeation of polyphenols and rheological study on ointments and creams. He has published more than 100 research papers during his research career.

KONA Powder and Particle Journal No. 35 (2018) 216–225/Doi:10.14356/kona.2018009 Original Research Paper

Simulation of Mechanical Degradation of Iron Ore Pellets in a Direct Reduction Furnace[†]

Fernando O. Boechat*, Rodrigo M. de Carvalho and Luís Marcelo Tavares

[1] *Department of Metallurgical and Materials Engineering, Universidade Federal do Rio de Janeiro – COPPE/UFRJ, Brazil*

Abstract

The increase in production of steel in electric arc furnaces in recent years influenced directly the world production of direct reduction iron (DRI). Amongst the most widely used technologies for DRI production is the MIDREX® process. The behavior of the metallic charge used in these furnaces, mainly made up of iron ore pellets, influences directly their productivity. Fines contained in the feed are typically removed by screening, in order to prevent them from impacting negatively the productivity of the furnace. However, fines still may be generated inside the furnace as a result of the collisions amongst pellets and between them and internals of the furnace as they move downwards from the feed to the discharge of the shaft furnace. Predicting and preventing such mechanical degradation is critical in the furnace operation. The present work deals with the prediction of degradation of iron ore pellets during reduction in a MIDREX furnace. Collision energies involved in the vertical flow of pellets along a MINIMOD® MIDREX direct reduction furnace were estimated using the discrete element method. Using this technique along with a model of degradation that considered assumptions based on information from the literature it was possible to estimate the proportion of fines generated inside the reactor, which was consistent with plant practice. Finally, it was predicted that the generation of fines in the reduction zone of the furnace would vary from 3.4 % to 4.6 % as the throughput of the furnace increased in 50 %.

Keywords: discrete element method, simulation, iron ore pellets, direct reduction, degradation

1. Introduction

Because of the reduced supply of good quality lump iron ore in the world market and the growing environmental constraints to sintering, iron ore pellets began to occupy an important role as raw material for primary iron production. Their participation in the production of pig iron and direct reduction iron (DRI) has increased year after year due to their advantages in comparison to lump ore. Some of the advantages are their higher uniformity in size, greater control of chemical composition, besides their reduced amenability to mechanical degradation during handling and under reduction.

The increase in production of steel using electric arc furnace impacted directly the production of DRI, raising it from 40 Mt in the beginning of this century to 74 Mt in 2014 (MIDREX, 2015). Several processes are used in the production of sponge iron, however the most widely used is the MIDREX (Midland Ross Experimental) process, which responds for more than half of the world's DRI production (MIDREX, 2014). In this process lump ore and/or iron ore pellets as used to compose the metallic charge, with iron ore pellets contributing to improve operational stability and increase productivity and/or metallization of charge, making this raw material the most attractive charge for producers of sponge iron in MIDREX furnaces (MIDREX, 2014).

In spite of their greater resistance to degradation, iron ore pellets still suffer from this problem, although to a more limited extent when compared to lump ore. Such degradation can take place either during handling from the pellet producer until loading the furnace, or under reduction, generating either coarse fragments or fines. Fines that are generated by handling prior to loading the furnace can be removed by screening. However, mechanical degradation can also occur inside the direct reduction furnace, as the result of the combined effect of weakening of the pellet structure due to reduction (Huang et al., 2012) and to the stresses which pellets withstand until they are discharged at the bottom of the furnace. When such mechanical degradation occurs inside the furnace, either coarse pellet pieces or fines may be produced. Indeed, such fines have been estimated to represent between 2 and 4 % in weight of the product, based on measurements

---

[†] Received 7 October 2016; Accepted 25 April 2017
J-STAGE Advance published online 24 June 2017

[1] Cx. Postal 68505, CEP 21941-972, Rio de Janeiro, Brazil
* Corresponding author: Fernando O. Boechat
E-mail: fboechat@globo.com
TEL: +55-21-2290-1544 Ext. 246

in plants that screen the furnace discharge (MIDREX, 2011). Such fragments can cause loss of furnace productivity because they affect negatively the permeability of the pellet bed, thus resulting in lower metallization of the charge. In addition to that, these fines can contribute to the pellets sticking to each other resulting in the formation of clusters, which besides contributing negatively to the permeation of reduction gasses, also create a disturbance in the flow of the charge (Wong et al., 1999; Basdag and Arol, 2002). Therefore, prediction of the amount of fines that are generated inside the reactor owing to the use of a particular type of iron ore pellet would be useful. This information could be used to assist in selecting the optimal feed blend to the direct reduction reactor, besides enabling the choice of the operational parameters that can reduce the impact of the formation of fines. However, no study in the published literature has been found that addressed simulating such mechanical degradation of iron ore pellets in direct reduction furnaces.

The present work uses a combination of the discrete element method (DEM) (Weerasekara et al., 2013) and models that describe pellet breakage and attrition to predict iron ore pellet degradation and fines generation in a vertical shaft direct reduction furnace in a one-way coupling strategy.

2. DEM simulation approach

The overview of the simulated direct reduction furnace is presented in **Fig. 1**. The furnace consists of a feeding system, containing 16 conduits (called legs), a first section, named reduction zone, on the bottom of which the reformed gases are introduced. The charge then travels downwards and encounters the upper burden feeders, which are axles that are meant to oscillate at predetermined angles at a speed that is adjusted to promote uniform transverse movement of the load and to limit the size of clusters formed. The identification of the sections and the corresponding numbers of pellets involved in the simulations can also be found in **Fig. 1**. The charge then encounters the region where the cooling gases are injected, to then find the sets of middle and lower burden feeders, until it is discharged from the bottom of the furnace.

The furnace simulated is designated MINIMOD®, and it has the smallest production capacity among the industrial furnaces that use the MIDREX technology (Atsushi, 2010). With 4.25 m in diameter, it can produce about half a million tons of sponge iron per year. The selection of this scale in the present work was due to challenges associated to the number of pellets that are present in this furnace at any time, which is in the order of several millions, which is only a fraction of the billions that occupy the 2-million ton-per-year Super Megamod® furnace measuring 7.15 m in diameter (Atsushi, 2010).

In spite of being the smallest industrial scale furnace, the MINIMOD® still contains an exceedingly large number of particles for a computationally cost-effective simulation using DEM. In order to reduce the number of parti-

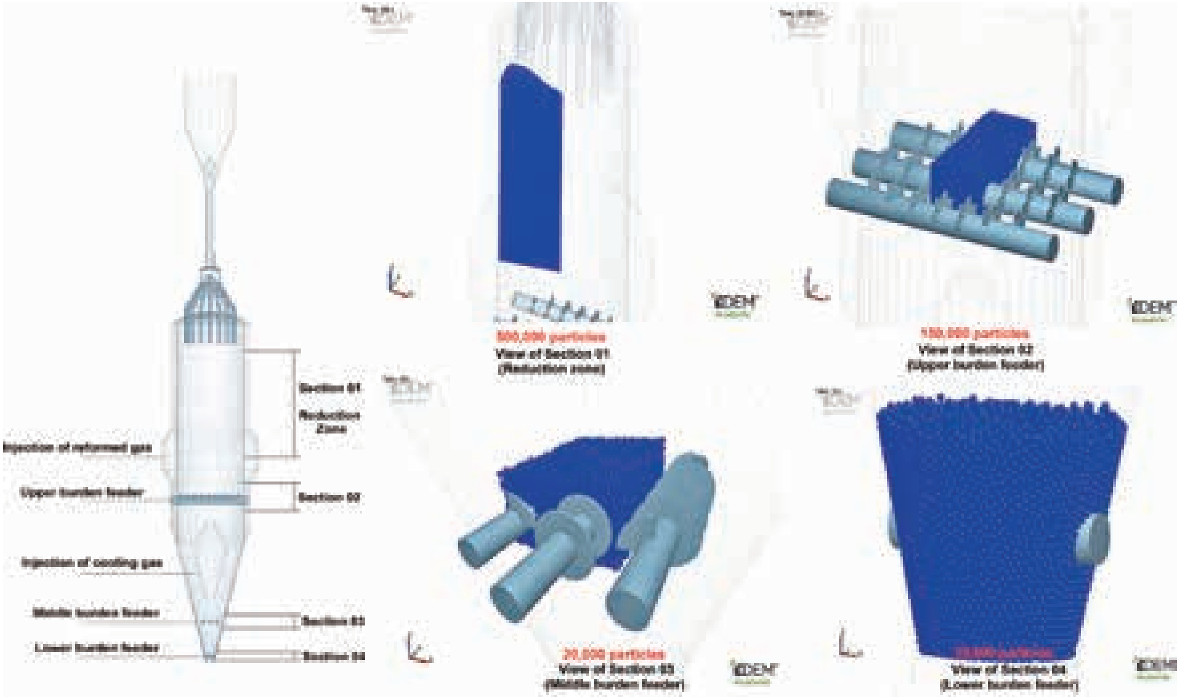

Fig. 1 Overview of the MINIMOD® MIDREX shaft furnace (left) and view of the simulated sections (middle and right). The number of particles corresponded to the 25 mm spheres simulated in each section.

cles within the simulation, the furnace was first split from top to bottom into four sections for simulation in separate, which were numbered 1 to 4 (**Fig. 1**). In order to further reduce the number of particles, only a fraction of the volume, with periodic boundaries, was simulated in sections #1 to #3. The region around the lower burden feeders (#4), on the other hand, was simulated with the full particle population.

Still with the aim of reducing the computation effort in the simulations pellets were assumed to present spherical geometry, which is a reasonable assumption in the case of iron ore pellets. In addition to that, pellets with nearly twice the average diameter of the actual pellets usually used industrially (9–19 mm), that is, 25 mm, were simulated. In spite of their uniform shape and size, no crystallization structures were identified in simulating the different sections of the furnace.

The software used in the DEM simulations was EDEM® by DEM Solutions (Edinburgh, UK), version 2.7. In all simulations the Hertz-Mindlin contact model available in EDEM® was adopted, and only gravity was considered as external force. The material parameters used in the simulations were those estimated on the basis of detailed testing by Barrios et al. (2013) with unreduced fired iron ore pellets. It is assumed that the contact properties would not change as pellets undergo reduction in the furnace. These and other material properties (density and shear modulus) are summarized in **Table 1**.

The speed of descent of metallic charge for each section was determined based on the simulated reactor with production of 58 t/h, which would correspond to an annual production in the order of half of a million tons. In addition to that, simulations were also conducted considering an increase in 50 and 100 % in the throughput of the system, resulting in simulated production of 86.8 and 116 t/h. These scenarios would correspond to cases when the residence time of the pellets in the furnace would be reduced significantly. The three systems of burden feeders were inserted in the model and the dimensions and modes of operation of these parts that turn were programmed on the basis of the parameters listed in **Table 2**.

For instance, the computational effort was such that in order to simulate 25 seconds of operation of the charge in section #1, approximately 240 hours of processing in a state-of-the-art workstation were required. Indeed, simulations were conducted until steady-state conditions were reached. Upon completion of the simulations, data from each collision, discriminated between the normal and the tangential component, were collected and processed using a post-processing routine developed in the authors' laboratory (Carvalho, 2013). Energies in the collisions were first equally split between each pair of pellets involved and then divided by the simulated particle weight, resulting in the specific collision energy. **Fig. 2** shows that the magnitudes of the specific collision energies are very similar for the 25 mm pellets simulated throughout the work and the 12.5 mm here analyzed in the lower burden feeder region of the furnace, thus demonstrating the validity of considering the larger pellet sizes in the remainder of the simulations.

Table 1 Hertz-Mindlin contact and material parameters of iron ore pellets (Barrios et al., 2013).

	Steel	Pellet
Poisson's ratio	0.3	0.25
Shear modulus (MPa)	7000	16
Density (kg/m^3)	7800	3948
	Steel-pellet	Pellet-pellet
Coefficient of restitution	0.48	0.39
Coefficient of static friction	0.49	0.50
Coefficient of rolling friction	0.21	0.25

Table 2 Operating parameters used for the burden feeders.

Position	Angle of rotation (°)	Period of rotation (s)	Frequency (rad/s)
Upper	45	180	0.0044
Middle	90	30	0.0524
Lower	60	10	0.1047
Position	Shaft radius (m)	Burdenfeeders radius (m)	
Upper	0.228	0.487	
Middle	0.080	0.175	
Lower	0.069	0.160	

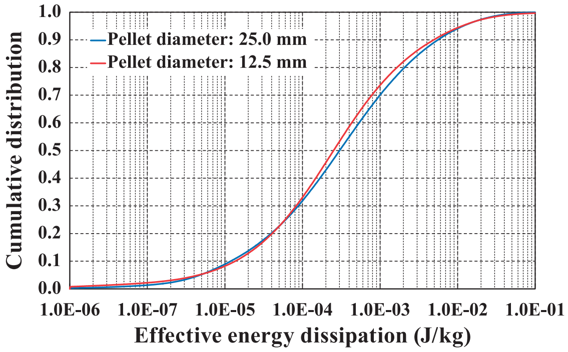

Fig. 2 Cumulative distribution of specific energy dissipation in the lower burden feeder section from simulations considering pellets of different diameters (12.5 and 25.0 mm).

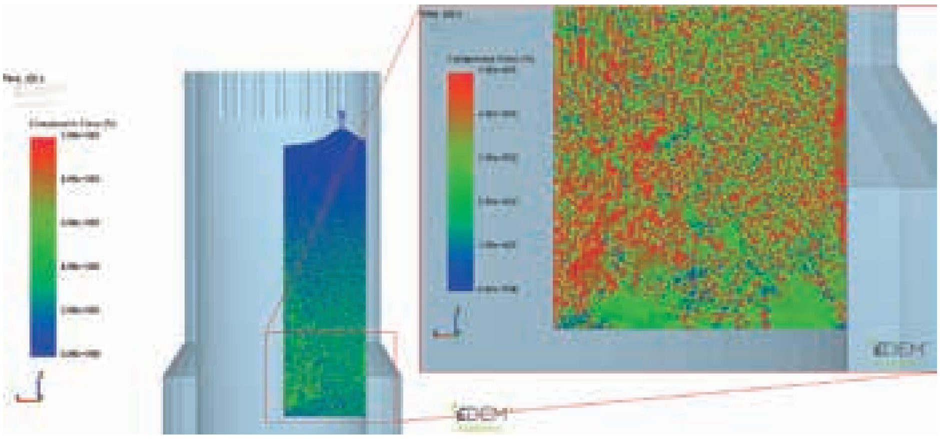

Fig. 3 Simulation of the reduction zone (section #1), showing detail in the bottom layer of the column with the profile of the compressive forces.

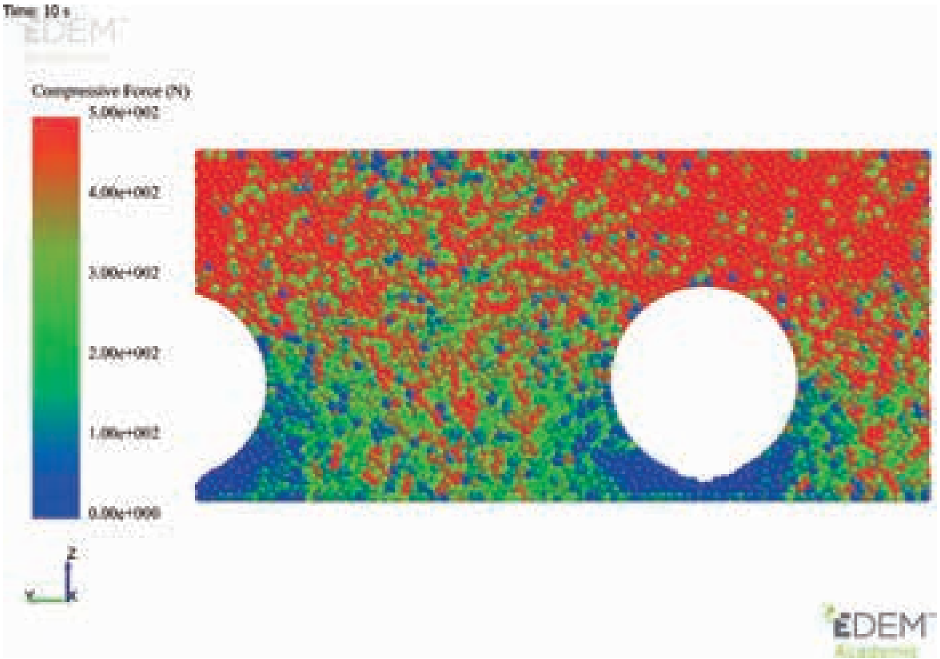

Fig. 4 Simulation showing the compression forces in section #2, influenced by the presence of the upper burden feeder.

3. DEM simulation results

From the DEM simulations it was possible to analyze the profile of the compressive forces in the sections studied. **Fig. 3** shows the influence of the depth in the pellet column inside the reduction zone (section #1) on the magnitude of compressive forces. In the following section (#2), shown in **Fig. 4**, the force applied was transferred from the previous section in order to allow simulating the entire column of pellets to which that section was subjected. In the figure it is observed that the magnitudes of the forces are similar to those presented on the basis of the column of reduction zone and the burden feeders work as a support to the column of pellets, withdrawing from the regions beneath it the effect of load from the column of pellets above. In sections #3 and #4, on the other hand, this method was not used, given the ability of the burden feeders of supporting the charge, reducing the magnitude of the contact forces (**Fig. 5**).

The energy dissipations in the collisions were analyzed in each section, with the larger frequency of higher energy collisions found closer to the bottom of the reduction column (**Fig. 3**), showing that there is a relative effect of depth of the pellets column. This effect becomes evident in **Fig. 6**, where the variation of the average normal energy dissipated in the collisions as a function of height and radius of furnace becomes evident.

A summary of the energy dissipation spectra in the dif-

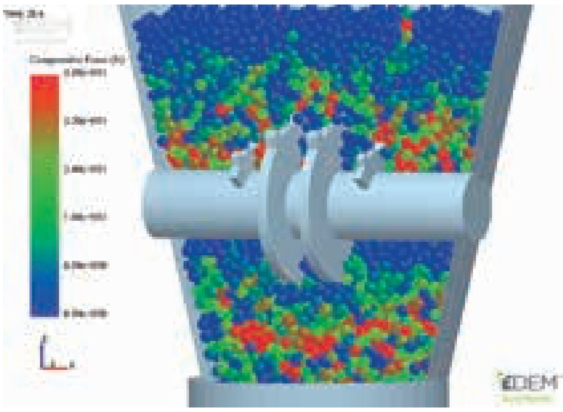

Fig. 5 Simulation showing the compressive forces in section #4 influenced by the presence of the lower burden feeder.

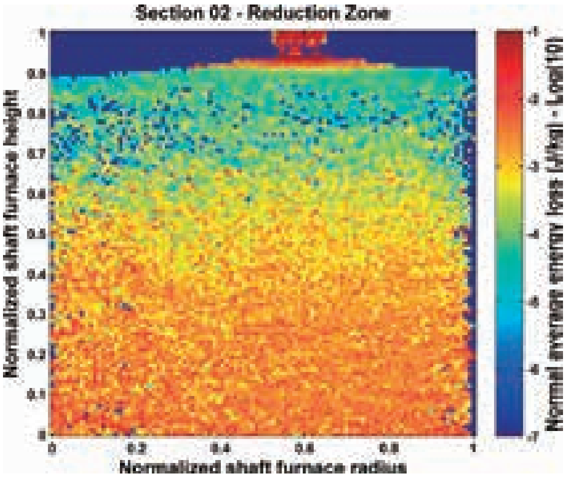

Fig. 6 Normal average energy transferred to particles as a function of normalized depth (0: bottom of reduction zone; 1: top) and radius of the section #1 of the reactor.

Table 3 Summary of the total energy dissipation distributions (in J/kg) of collisions by furnace section for a throughput of 58 t/h.

Statistic (J/kg)	Furnace section			
	#1—Reduction Zone	#2—Upper Burdenfeeder	#3—Middle Burdenfeeder	#4—Lower Burdenfeeder
Mean	0.214	0.0013	0.0018	0.0023
Median	0.0035	6.82E-05	1.85E-04	2.99E-04
95th percentile	0.294	0.0042	0.089	0.0103
Standard deviation	2.032	0.0094	0.0059	0.0093

ferent sections of the furnace is presented in **Table 3** for comparison. It becomes evident that the highest energy dissipation occurs in the reduction zone (section #1), whereas the sections around the burden feeders (sections #2–4) exhibit very low energy dissipations (**Fig. 7**).

An approach often used to increase the productivity in direct reduction furnaces is to increase the flow of reforming gases coupled to the throughput of the furnace. However, an adverse effect of this is the increase in the degradation of the pellets inside the furnace (MIDREX, 2011). **Table 4** compares predictions of the collision energy spectrum of the base case to two hypothetical cases in which the throughput was raised, showing that important increases in the average collision energies would result.

4. Modeling of pellet breakage

Depending on the magnitude of the collisions that happen amongst the pellets and between the pellets and the walls and furnace internals as the charge moves downwards from the feed to the discharge, breakage of pellets may occur. Breakage of pellets can occur catastrophically, which is called body breakage, every time a pellet loses more than 10 % of its original weight in any event (Tavares et al., 2015). On the other hand, pellets may suffer only surface breakage or attrition, also called breakage by abrasion or chipping, which results in generation of fines, besides leaving the core of the original pellet nearly undisturbed, since it contains no less than 90 % of the mass of the original pellet prior to the collision event. In this later case, it is possible that the pellet becomes more amenable to breakage in a future stressing event. A model framework that has been developed to describe this in the context of degradation of ores during handling is described elsewhere (Tavares and Carvalho, 2011) and elements of it are here used to predict breakage in the MINIMOD MIDREX furnace.

The threshold between these two modes of breakage efined above is given by the mass-specific particle fracture energy of the pellets (Tavares et al., 2015). **Fig. 8** presents the distributions of specific fracture energies for fired pellets contained in different size classes under slow compression conditions. A comparison between these and

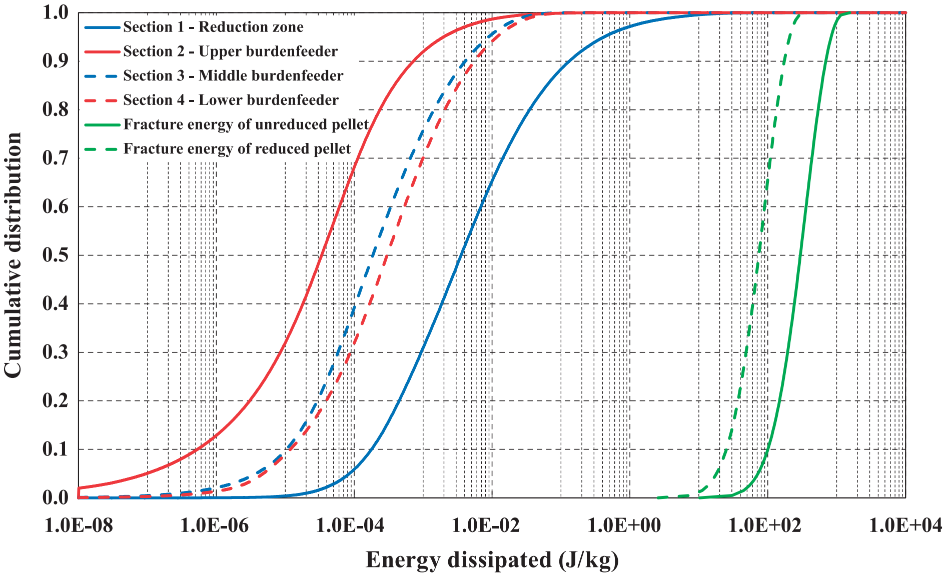

Fig. 7 Cumulative distribution of total energy dissipated in the four sections of the furnace simulated. Also shown for comparison are the fracture energy distributions of unreduced and estimated values after complete reduction.

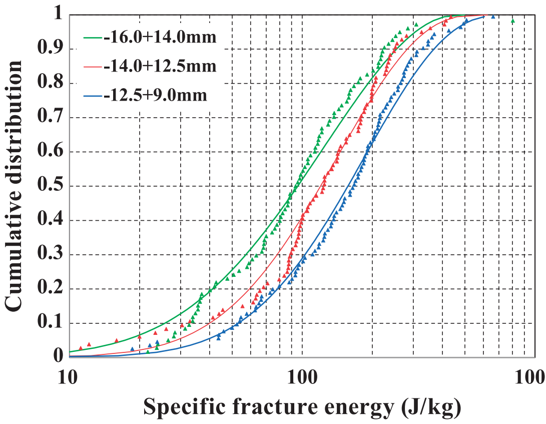

Fig. 8 Distribution of specific fracture energies of fired iron ore pellets.

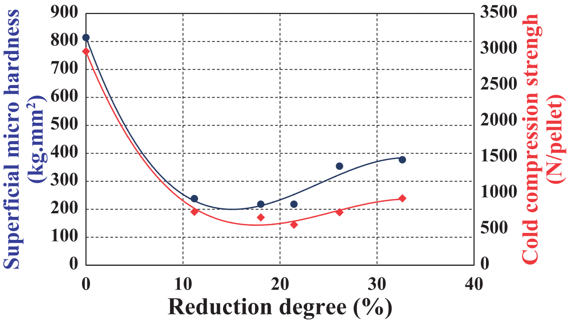

Fig. 9 Effect of degree of reduction on the compressive strength and surface hardness of iron ore pellets (data from Huang et al., 2012). Copyright: (2012) Powder Technology.

Table 4 Summary of the energy dissipation spectra (in J/kg) of collisions for section #1 of the furnace as a function of throughput.

Statistic (J/kg)	Estimated throughput		
	58 t/h	87 t/h	116 t/h
Mean	0.214	0.238	0.251
Median	0.0035	0.0039	0.0038
95th percentile	0.294	0.318	0.321
Std. dev.	2.032	2.536	2.539

the distributions presented in **Fig. 7** suggests that no pellets would suffer catastrophic breakage inside the furnace, since the energy required to break the weakest fired pellet is higher than the collision energy of highest magnitude inside the furnace. However, as pellets move downwards in the furnace, they undergo reduction, having their strength reduced. Work by Huang et al. (2012) demonstrated that the compressive strength—and therefore the fracture energy—of iron ore pellets drops significantly as reduction occurs (**Fig. 9**). As such, considering such estimate that particles loose in the order of 75 % of their compressive strength upon reduction (Huang et al., 2012) and assuming that the mass-specific fracture energies would be reduced in the same magnitude, it would be more likely that breakage of pellets might occur in the reduction section of the furnace (section #1). However, even considering that reduced pellets would further lose their fracture energies upon undergoing repeated stresses in the furnace, this effect may be considered negligible under the conditions simulated (**Fig. 7**).

It is important to recognize, however, that the presence

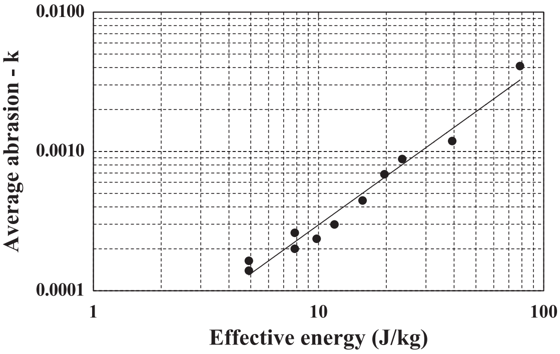

Fig. 10 Experimental results and model fit for fines generation due to attrition of fired pellets as a function of effective collision energy (Cavalcanti, 2015). Model coefficient of correlation (R^2) of 0.97. Copyright: (2015) Universidade Federal do Rio de Janeiro.

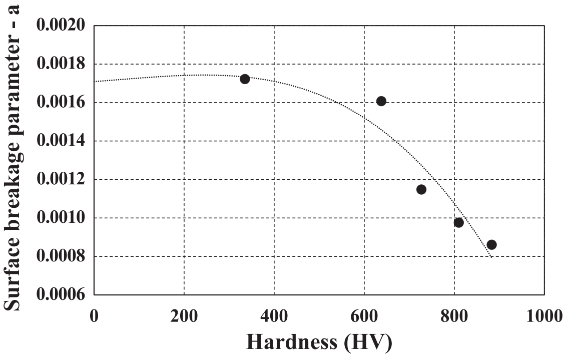

Fig. 11 Relationship between parameter *a* from Eqn. 1 and Vickers hardness in the periphery of unreduced iron ore pellets (Cavalcanti, 2015). Copyright: (2015) Universidade Federal do Rio de Janeiro.

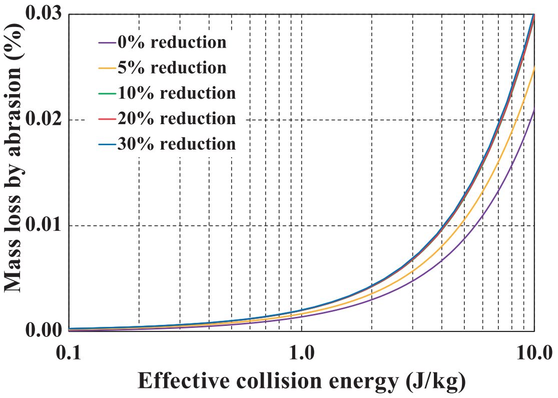

Fig. 12 Predicted percentage of fines generated in pellets with different levels of reduction as a function of effective collision energy.

of coarse fragments, generated during handling prior to feeding the furnace, may be responsible for the appearance of lower fracture energies particles than well-formed pellets, which could still undergo body breakage inside the furnace.

Although unlikely to suffer body breakage, pellets inside the furnace will be subjected to stresses that will certainly be responsible for surface breakage or attrition. A model that describes the relationship between the stressing energy and the generation of fines as the result of surface breakage is (Cavalcanti, 2015)

$$k = a\left(\frac{E}{E_o}\right)^{\lambda} \tag{1}$$

where k is the proportion of fines generated in each collision event, E_o is a reference specific collision energy, taken as 10 J/kg, and a and λ are dimensionless fitting parameters to be calibrated from experimental data. It is worth noting that in the case where the constant λ is equal to 1, this model becomes equivalent to the one proposed by Ghadiri and Zhang (2002). E is the effective mass-specific energy in each collision, obtained from a combination of the normal component of the energy dissipated in the normal direction of the collision added to 57 % of the contribution from the shear component. This composition of the collision energy was estimated on the basis of impacts of pellets against angled targets (Cavalcanti, 2015). **Fig. 10** presents data for an unreduced iron ore pellet, comparing it to the model fit, resulting in the values of a and λ equal to 0.00029 and 1.16, respectively. The fitted model parameters, however, are only valid for unreduced pellets. Huang et al. (2012) demonstrated that the hardness of an outer layer of the pellet reduces as pellets undergo reduction (**Fig. 9**). Recent work in the authors' laboratory (Cavalcanti, 2015) proposed a relationship between the Vickers hardness of the region close to the surface of unreduced iron ore pellets to their amenability to surface breakage (**Fig. 11**).

Combining now the results from Huang et al. (2012) and **Fig. 11**, it is possible to estimate the change in abrasion response as a function of degree of reduction. This is illustrated in **Fig. 12**, which shows predictions on the effect of effective collision energy on the mass loss in a single collision of a pellet inside the furnace with different levels of reduction.

A comparison of **Fig. 7** and **Fig. 10** demonstrates that the collision energies found in the furnace are still comparatively low, so that significant extrapolation in the model became necessary.

5. Simulation of pellet degradation in the MINIMOD furnace

Degradation in the furnace, assuming stresses are insufficient to cause body breakage, only surface breakage (attrition), can then be predicted considering that pellets will undergo collisions from the feed to the discharge of

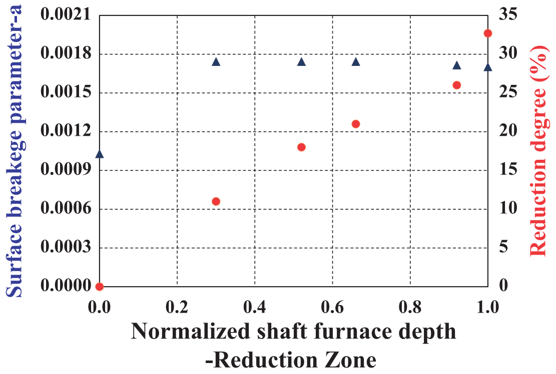

Fig. 13 Variation of the degree of reduction (based on Parisi and Laborde model) and the surface breakage parameter a in Eqn. 1 as a function of depth in the reduction section of the furnace.

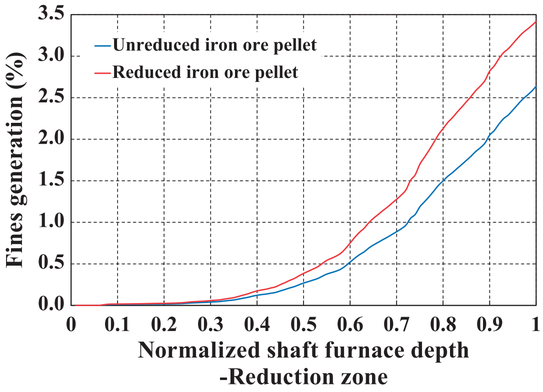

Fig. 14 Prediction of the evolution of fines generation relative to the depth of the furnace in reduction zone with the effect of loss of mechanical strength caused by the reduction.

the furnace flowing like a piston, so that

$$w_{i,\text{out}} = w_{i,\text{in}} \int_0^1 \int_0^\infty p_i(E,h)[1-k_i(E,h)]\,\mathrm{d}E\,\mathrm{d}h, \text{ for } i \neq n \qquad (2)$$

$$w_{n,\text{out}} = 1 - \sum_{i=1}^{n-1} w_{i,\text{out}} \qquad (3)$$

where w_i is the fraction of pellets in size class i, n is the number of size classes, E is the effective specific energy applied to each pellet in each collision and h is the fractional depth in the furnace.

The proportion of material contained in the finer size range (fines) generated is then calculated by

$$\text{Fines generated} = w_{n,\text{out}} - w_{n,\text{in}} \qquad (4)$$

The challenge in applying the equations above lies in the fact that k_j, the proportion of degraded material by surface breakage, not only varies with collision energy, but also with the degree of reduction and, therefore, the vertical normalized position in the furnace h. Fortunately, work by Parisi and Laborde (2004) made it possible to estimate the degree of reduction of the pellets along the vertical axis of the furnace, from the feed to the end of the reduction section, that is, the entrance of the point of entry of the reforming gases. Parisi and Laborde (2004) proposed this model on the basis of data from two industrial MIDREX plants. **Fig. 13** shows outputs of their simulations, which were used as the basis for the present work. The figure also presents predictions of the surface breakage parameter a from Eqn. 1, now considering the model described in **Fig. 11**, which nearly doubled in magnitude from the feed to the end of the reduction section.

The assumptions considered in the present work were:

- The variability of the fracture energies as well as the stiffness of iron ore pellets do not change with the degree of reduction

Table 5 Summary of the predictions of fines generation for the different sections of the furnace for the feedrate of 58 t/h.

Section	Estimated fines generation (%)
#01—Reduction zone	3.42
#02—Upper Burdenfeeder	0.07
#03—Middle Burdenfeeder	0.01
#04—Lower Burdenfeeder	0.03
Total	3.53

- All characteristics of the pellets remain unchanged after the charge passes the zone of introduction of reforming (reducing) gases

Simulations were carried out considering the base case (**Table 4**), which resulted in **Fig. 14**. It shows that the fines generation in the reduction zone is 3.4 %. Considering this, as well as the additional contribution of fines generation in the other sections (#2 to #3, of the burden feeders), the final predicted value for the amount of fines generated inside the reactor is estimated as 3.5 % (**Table 5**). This result shows good agreement with those seen in industrial plants that produce cold DRI and perform screening of discharge (2 to 4 %) (MIDREX, 2011). With this value considered for fines generation, the resulting production loss would be 17600 t/year approximately.

It is important to remember that the reference value mentioned only corresponds to discharge and other fines generated inside the reactor, e.g. in take-off, for correct comparison with the value found by the model, must also be computed. As such, the predictions by the model may still be conservative. If the change in the amenability of the pellets to surface breakage resulting from reduction is not accounted for, then predictions would be of only 2.64 % of fines, which very likely underestimates the proportion of fines generated in the furnace.

Simulations have also considered the case when the throughput of the furnace is increased (**Table 4**). The increase in throughput by 25 and 50 % would increase the fines production to 4.26 and 4.63 % in the reduction zone, demonstrating the increased importance of this problem.

6. Conclusions

Based on simulations of motion of iron ore pellets in a MIDREX MINIMOD furnace using the discrete element method and to the application of a simple degradation model, it was possible to conclude that:

- Body breakage is unlikely to occur with well-formed pellets, but surface breakage has a significant role in degradation inside the furnace studied in the reduction zone.
- The reduction zone, especially the region closest to the injection of reducing gases, is the greatest responsible for the most severe collisions, with magnitudes capable of generating fines due to attrition. Indeed, the dissipation of energy of the collisions was found to have direct influence of the height of the column of pellets. Simulation of the increase of production, corresponding to the increase of descent of the charge demonstrated an increase in severity of the collisions.
- In the region around the burden feeders, the dissipation of energy in collisions of the pellets showed was very low. Because of this, little additional fragmentation due to collisions takes in these regions. Such degradation, however, can increase with the use of higher speeds of rotation of the burden feeders.
- Simulations demonstrated that about 3.4 % fines for normal operation and up to 4.6 % at higher throughputs would be generated in the reduction zone of the MINIMOD furnace.

Acknowledgements

The authors would like to thank Vale S.A. for sponsoring the research and for permission to publish the work and for CNPq for partially sponsoring the work. The authors also thank DEM Solutions for the use of the software EDEM under the Academic Program.

References

Atsushi M., Uemura H., Sakaguchi T., MIDREX Processes, KOBELCO TECHNOLOGY REVIEW, 29 (2010) 50–57.

Barrios G.K.P., Carvalho R.M., Kwade A., Tavares L.M., Contact parameter estimation for DEM simulation of iron ore pellet handling, Powder Technology, 248 (2013) 84–93.

Basdag A., Arol A.I., Coating of iron oxide pellets for direct reduction, Scandinavian Journal of Metallurgy, 31 (2002) 229–233.

Cavalcanti P.P.S., Calibration and validation of a mathematical model of degradation of fired pellets during transportation and handling, M.Sc. thesis, Universidade Federal do Rio de Janeiro, 2015 (in Portuguese).

Carvalho R.M., Mechanistic modeling of semi-autogenous grinding, Ph.D thesis, Universidade Federal do Rio de Janeiro, 2013.

Ghadiri M., Zhang Z., Impact attrition of particulate solids. Part 1: A theoretical model of chipping, Chemical Engineering Science, 57 (2002) 3659–3669.

Huang Z., Yi L., Jiang T., Mechanisms of strength decrease in the initial reduction of iron ore oxide pellets, Powder Technology, 221 (2012) 284–291.

MIDREX, Direct from Midrex–3rd/4th Quarter 2011, Midrex Technologies, Inc., p. 9, 2011, <www.midrex.com/assets/user/media/DFM2011Q3-4.pdf> accessed 15.08.2013.

MIDREX, World direct reduction statistics, Midrex Technologies, Inc., p. 14, 2015, <http://www.midrex.com/assets/user/news/MidrexStatsbook201411.pdf> accessed 10.05.2016.

MIDREX, Shaft Furnace Technologies—Solutions for Steelmakers, Midrex Technologies, Inc., p. 10, 2014, <www.midrex.com/assets/user/media/MIDREX_Process-Brochure.pdf> accessed 10.05.2016.

Parisi D.R., Laborde M.A., Modeling of counter current moving bed gas-solid reactor used in direct reduction of iron ore, Chemical Engineering Journal, 104 (2004) 35–43.

Tavares L.M., Carvalho R.M., Modeling ore degradation during handling using continuum damage mechanics, International Journal of Mineral Processing, 101 (2011) 21–27.

Tavares L.M., Carvalho R.M., Pereira H.C., Bianchi M.R., Otaviano M.M., Predicting iron ore pellet degradation due to handling from pellet plant to steel mill, Proc. 2nd European Steel Technology and Application Days, Düsseldorf, 2015.

Weerasekara N.S., Powell M.S., Cleary P.S., Tavares L.M., Evertsson M., Morrison R.D., Quist J., Carvalho R.M., The contribution of DEM to the science of comminution, Powder Technology, 248 (2013) 3–24.

Wong P.L.M., Kim M.J., Kim H.S., Choi C.H., Sticking behaviour in direct reduction of iron ore, Ironmaking & Steelmaking, 26 (1999) 53–57.

Author's short biography

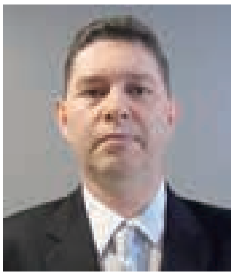

Fernando Oliveira Boechat

Fernando Oliveira Boechat is PhD student at Universidade Federal do Rio de Janeiro. He completed his bachelor's degree in Industrial Engineering from Faculdade Integradas Espirito Santense and his master's degree in Metallurgical and Materials Engineering from Universidade Federal do Rio de Janeiro. He is currently a lecturer at Centro Universitário Católico de Vitória, teaching courses in Industrial Engineering. His research interests include modeling of industrial, mainly metallurgical processes.

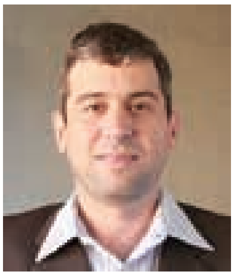

Rodrigo Magalhães de Carvalho

Rodrigo Magalhães de Carvalho is an Associate Professor at Universidade Federal do Rio de Janeiro. He holds a bachelor's degree in Chemical Engineering and Metallurgical and Materials Engineering master's and D.Sc. degrees at Universidade Federal do Rio de Janeiro, under Prof. Luís Marcelo M. Tavares supervision. He joined the faculty of the Department of Metallurgical and Materials Engineering at Universidade Federal do Rio de Janeiro in 2014, where he is the deputy-head of the Laboratório de Tecnologia Mineral. His research interests include discrete element method in mineral processing and steelmaking applications, mathematical modeling and simulation of comminution processes. He received Minerals Engineering International Young Person's award and International Mineral Processing Congress Young Authors Award in 2014 and has received a number of awards from Brazilian Association of Metallurgy, Materials and Mining (ABM) as a co-author with Prof. Luís Marcelo Tavares.

Luís Marcelo Tavares

Luís Marcelo Tavares is a Professor at Universidade Federal do Rio de Janeiro. He received his bachelor's degree in Mining Engineering (honours) and his master's degree from Universidade Federal do Rio Grande do Sul. He was awarded a Ph.D. degree in Extractive Metallurgy at the University of Utah under the supervision of the late Professor R.P. King. He has been a member of the faculty of the Universidade Federal do Rio de Janeiro (Brazil) since 1998, where he is head of the Laboratório de Tecnologia Mineral and has been Department chairman. His research interests include advanced models of comminution, particle breakage, physical concentration, classification, iron ore processing and development of pozzolanic materials. He is a founding member of the Global Comminution Collaborative (GCC) and has received a number of awards from the Brazilian Association of Metallurgy, Materials and Mining (ABM).

KONA Powder and Particle Journal No. 35 (2018) 226–250/Doi:10.14356/kona.2018014 Original Research Paper

Effect of Particle Size and Cohesion on Powder Yielding and Flow[†]

Hao Shi [1]*, Rahul Mohanty [2,4], Somik Chakravarty [3], Ramon Cabiscol [2], Martin Morgeneyer [3], Harald Zetzener [2], Jin Y. Ooi [4], Arno Kwade [2], Stefan Luding [1] and Vanessa Magnanimo [1]

[1] *Multi-Scale Mechanics (MSM), Faculty of Engineering Technology (ET), MESA+, University of Twente, The Netherlands*
[2] *Institute for Particle Technology (iPAT), TU Braunschweig, Germany*
[3] *Laboratoire Transformations Intégrées de la Matière Renouvelable (TIMR), Université de Technologie de Compiègne (UTC) Sorbonne Universités, France*
[4] *Institute of Infrastructure and Environment, School of Engineering, University of Edinburgh, UK*

Abstract

The bulk properties of powders depend on material characteristics and size of the primary particles. During storage and transportation processes in the powder processing industry, the material undergoes various modes of deformation and stress conditions, e.g., due to compression or shear. In many applications, it is important to know when powders are yielding, i.e. when they start to flow under shear; in other cases it is necessary to know how much stress is needed to keep them flowing. The measurement of powder yield and flow properties is still a challenge and will be addressed in this study.

In the framework of the collaborative project T-MAPPP, a large set of shear experiments using different shear devices, namely the Jenike shear tester, the ELE direct shear tester, the Schulze ring shear tester and the FT4 powder rheometer, have been carried out on eight chemically-identical limestone powders of different particle sizes in a wide range of confining stresses. These experiments serve two goals: i) to test the reproducibility/consistency among different shear devices and testing protocols; ii) to relate the bulk behaviour to microscopic particle properties, focusing on the effect of particle size and thus inter-particle cohesion.

The experiments show high repeatability for all shear devices, though some of them show more fluctuations than others. All devices provide consistent results, where the FT4 powder rheometer gives lower yield/steady state stress values, due to a different pre-shearing protocol. As expected, the bulk cohesion decreases with increasing particle size (up to 150 µm), due to the decrease of inter-particle cohesion. The bulk friction, characterized in different ways, is following a similar decreasing trend, whereas the bulk density increases with particle size in this range. Interestingly, for samples with particle sizes larger than 150 µm, the bulk cohesion increases slightly, while the bulk friction increases considerably—presumably due to particle interlocking effects—up to magnitudes comparable to those of the finest powders. Furthermore, removing the fines from the coarse powder samples reduces the bulk cohesion and bulk density, but has a negligible effect on the bulk friction.

In addition to providing useful insights into the role of microscopically attractive, van der Waals, gravitational and/or compressive forces for the macroscopic bulk powder flow behaviour, the experimental data provide a robust database of cohesive and frictional fine powders for industrially relevant designs such as silos, as well as for calibration and validation of models and computer simulations.

Keywords: cohesive powders, shear testers, yield locus, bulk friction, bulk cohesion, particle size effect, T-MAPPP, database

1. Introduction

Granular materials are omnipresent in our daily life and widely used in various industries such as food, pharmaceutical, agriculture and mining. Interesting granular phenomena like yielding and jamming (Liu and Nagel, 1998; Bi et al., 2011; Luding, 2016; Kumar and Luding, 2016), dilatancy (Cates et al., 2005; Van Hecke, 2009; Yang et al., 2015), shear-band localization (Alshibi and Sture, 2000; Singh et al., 2014), history-dependence (Thakur et al., 2014), and anisotropy (Radjai et al., 1996; Majmudar and Behringer, 2005) have attracted significant scientific interest over the past decades (Savage and Hutter, 1989; Cundall, 1989; Radjai et al., 1999; Wolf et al., 2000;

[†] Received 10 May 2017; Accepted 27 June 2017

[1] P.O. Box 217, 7500 AE Enschede, The Netherlands
[2] Volkmaroder Str. 4-5, 38104 Braunschweig, Germany
[3] Rue Roger Couttolenc, CS 60319, 60203 Compiègne Cedex, France
[4] Edinburgh EH9 3JY, Scotland, UK
* Corresponding author: Hao Shi
E-mail: h.shi-1@utwente.nl
TEL: +31(0)53-489-6445

GDR-MiDi, 2004; Tomas, 2005; Alonso-Marroquin and Herrmann, 2004; Luding 2005a, b, 2008). Various laboratory element tests can be performed to study the bulk behaviour of granular materials (Schwedes, 2003). Element tests are also a valuable tool to understand the influence of particle properties, e.g. density, size-distribution and shape, on the macroscopic bulk response. Moreover, such element tests are commonly used for the industrial designs of silos (Jenike, 1967; Schwedes and Schulze, 1990; Schulze, 2003a).

Element tests are (ideally homogeneous) macroscopic tests in which the force (stress) and/or displacement (strain) path are controlled. The most widely performed element test in both industry and academia is the shear test, where a granular sample is sheared until failure is reached and the material starts to flow. Shear testers are usually classified into two groups: direct and indirect methods (Schwedes, 2003; Schwedes and Schulze, 1990). In direct shear testers, the shear zone is pre-defined by the device design, and the shear failure is forced in a specific physical location. On the contrary, in the indirect devices, the shear zone develops according to the applied state of stress. The most common indirect devices are the uni-axial compression tester (Russell et al., 2014; Thakur et al., 2014; Imole et al., 2016) and bi-axial shear box (Morgeneyer et al., 2003; Morgeneyer and Schwedes, 2003; Feise and Schwedes, 1995). Direct devices can be further categorised into two sub-groups: translational and rotational. Typical translational shear testers include the direct shear tester (Casagrande, 1936; Schwedes, 1979; Shibuya et al., 1997) and the Jenike shear tester (Jenike, 1964), while torsional or rotational shear testers include the FT4 powder rheometer (Freeman, 2007), the Schulze ring shear tester (Schulze, 1994) and the Brookfield powder flow tester (Berry et al., 2015). Detailed reviews of testers have been presented by several authors (Schwedes, 2003; Tsunakawa and Aoki, 1982; Schulze, 2008), and more (non-commercial) shear testers with higher complexity can be found in literature (Harder and Schwedes, 1985; Janssen and Zetzener, 2003; Bardet, 1997).

Quality and reproducibility of results are key aspects for proper material characterization. Although shear testing technologies have been developed and studied extensively, significant scatter in measurements is still common when testing powder flowability using different devices in different labs/environments (Freeman, 2007; Schulze, 1994; Berry et al., 2015; Schulze, 2001; Kamath et al., 1993; Kamath et al., 1994). Previous studies have been focusing on this problem by performing round-robin experimental studies on the Jenike tester (Akers, 1992), the Schulze ring shear tester (Schulze, 2001) and the Brookfield powder flow tester (Berry et al., 2015) as well as comparing different devices (Koynov et al., 2015). The earliest round-robin study (Akers, 1992) resulted in a certified material (CRM-116 limestone powder) and a common standard experimental testing procedure for determining the yield locus. Schulze (Schulze, 2011) has collected 60 yield loci obtained using the small Schulze shear tester RST-XS (21 labs) and 19 yield loci using the large Schulze shear tester RST-01 (10 labs) on one limestone powder (CRM-116). Results have been compared among them as well as with the results from reference Jenike tester. While results from RST-01 and RST-XS are in good agreement, a considerable deviation (up to 20 %) was observed when comparing results from the Schulze ring shear tester to the Jenike shear tester. Similar outputs are found by other researchers (Berry et al., 2015; Koynov et al., 2015; Salehi et al., 2017), where yield loci from the Brookfield powder flow tester, the Schulze ring shear tester, the FT4 powder rheometer and the Jenike shear tester are compared. The Brookfield powder flow tester and the FT4 powder rheometer show systematically lower shear responses in comparison to the other two shear testers.

Other studies have compared different industrially relevant powders but only in a single device (Teunou et al., 1999; Fitzpatrick et al., 2004). Moreover, these comparative studies have been limited to relatively low stresses. A deeper understanding of the flow behaviour of powders in several shear devices over a wide stress range is still missing.

Our collaborative network, EU/ITN T-MAPPP (www.t-mappp.eu), offers the unique possibility to shed light on the complex topic of powder yielding and flow, extending beyond the boundaries of previous projects. The network involves 16 partners in both academia and industry across Europe. The present study has multiple goals. Firstly, we want to investigate the consistency and repeatability of yield loci measurements between commonly used shear testers. This can provide a robust platform to establish the reliability of the testing methodology and procedures. Secondly, we aim to study the influence of cohesion on powder flowability by testing powders that have same chemical composition but different particle size, leading to different degrees of bulk cohesion. Finally, once the agreement between the shear devices is established, measurements can be combined to characterise the powders over a wider stress range, which is not achievable with a single device. To achieve this goal, a systematic study has been carried out by testing 8 powders (Eskal limestone with median particle diameter from 2.2 to 938 μm) in 5 shear testers (the Jenike Shear Tester, the Direct Shear Tester, the Schulze Ring Shear Tester with two shear cell sizes, and the FT4 Powder Rheometer) at 4 partner locations by different operators. Limestone powder has been chosen due to its negligible sensitivity towards humidity and temperature changes.

The work is structured as follows: In section 2, we provide information on the limestone samples/materials, in section 3 the description of the experimental devices and in section 4 the test procedures. Sections 5 and 6 are devoted to the discussion of experimental results with focus on shear devices and materials, respectively, while conclusions and outlook are presented in section 7.

2. Material description and characterization

In this section, a brief description of the limestone samples along with their material properties is provided. Eight size grades with the same chemical composition, i.e. Eskal limestone (calcium carbonate), are used, with median particle sizes that almost span three orders of magnitude from µm to mm.

The Eskal series (KSL Staubtechnik GmbH, Germany) is extensively used in many fields including construction and automotive industries. Eskal is also used as a reference powder for standard testing and calibration of equipment in powder technology, for instance, shear testers (Feise, 1998; Zetzener and Schwedes, 2002) and optical sizing systems due to the favourable physical properties: high roundness, low porosity and an almost negligible sensitivity towards humidity and temperature changes, which allows to avoid sample pretreatment.

Table 1 summarizes the physical properties of the Eskal samples. Median particle size d_{50} ranges from 2.22 µm (cohesive, sticky primary particles that form clumps) to 938 µm (free-flowing primary particles). In this study, all powders are named with their original commercial name (e.g. Eskal150, Eskal300), except for Eskal K0.1–0.5 and K0.5–0.8 (original product names are Eskal Körnung 0.1–0.5 and Körnung 0.5–0.8), which for sake of brevity, is referred to as "K". The particle size distributions were determined by laser diffraction (HELOS + RODOS, Sympatec GmbH) with the dry dispersion unit. The span of the particle size distribution decreases with increasing particle size from 1.52 to 0.7, whereas the initial bulk density (bulk density measured directly after filling) increases from 540 to 1400 kg/m^3. Primary particle density ρ_p is measured using a helium pycnometer at 0.9 % moisture content and is found to be independent of size. Particle roundness, which is the ratio of the perimeter of the equivalent circle to the real perimeter of the projected primary particle, was measured with the Sympatec-QICPIC imaging system. The working principle of this technique consists of a high-speed image analysis sensor capable of capturing 500 frames per second with low exposure time below 1 ns; this set-up allows to capture and measure with a high detail size and shape information of an extremely large number of particles in the size range of 1 µm to 30 mm (Witt et al., 2006). Values are the average over approximately the range between 20000 and 8000000 particles, depending on the median size of primary particles in the powders. The median particle size, d_{50}, is used in the following as reference to the different Eskal samples.

Figs. 1 and **2** show the scanning electron microscopy images of Eskal30 and Eskal K0.1–0.5, in two different length scales. The topography of the surfaces are created using secondary electron imaging (SEI) method. In **Fig. 1**, we see that all the Eskal30 primary particles have similar shapes (left) and rough surfaces (right). But for Eskal K0.1–0.5, in **Fig. 2**, we observe more fines between the coarse particles (left) as well as on the surface (right). The other Eskal samples have mostly similar shapes (difference

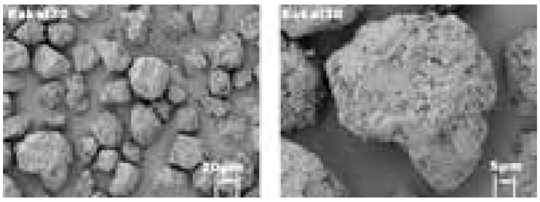

Fig. 1 SEM topography images of Eskal30 ($d_{50} = 30$ µm) in two different length scales as shown in the scale bars.

Table 1 Material parameters of the experimental samples. The initial bulk density represents bulk density from raw materials. Here, K0.1–0.5 means Körnung 0.1–0.5, which follows the commercial product naming. The initial bulk density values are provided by the manufacturer.

Property (Eskal)		Unit	300	500	15	30	80	150	K0.1–0.5	K0.5–0.8
Particle size	d_{10}	µm	0.78	1.64	12	21	39	97	4.5	738
	d_{50}	µm	2.22	4.42	19	30	71	138	223	938
	d_{90}	µm	4.15	8.25	28	43	106	194	292	1148
Span	$(d_{90}–d_{10})/d_{50}$	[–]	1.52	1.50	0.84	0.73	0.94	0.70	1.29	0.44
Particle density	ρ_p	kg/m^3	2737	2737	2737	2737	2737	2737	2737	2737
Moisture content	w	%	0.9	0.9	0.9	0.9	0.9	0.9	0.9	0.9
Roundness	Ψ	[–]	0.75	0.55	0.48	0.66	0.84	0.88	0.74	0.85
Initial bulk density	ρ_0	kg/m^3	540	730	1110	1230	1330	1370	1400	1276

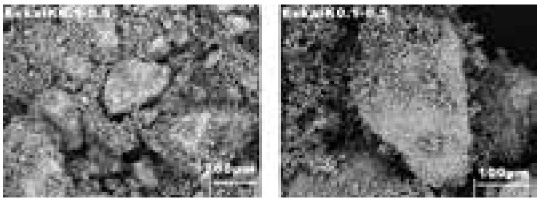

Fig. 2 SEM topography images of Eskal K0.1–0.5 ($d_{50} = 223$ µm) in two different length scales as shown in the scale bars.

in the range of 20 %, considering the mean values of roundness) irrespective of median particle size of the samples.

3. Experimental set-up

Many testers have been devised for measuring the yielding and flow properties of bulk solids in the last 70 years, ranging from the Jenike Shear Tester to the semi-automated or fully automated testers that are being developed in the present days (Carr and Walker, 1968). Here we present a comparison between measurements in five direct shear devices, specifically the two "translational" devices, namely the ELE direct shear tester and the Jenike shear cell, and three "rotational" devices (The Schulze ring shear testers and the FT4 powder rheometer).

A detailed comparison between the main features of all testers is shown in **Table 2** and a comparison of results from all these testers is presented in section 5. Two main characteristics of these devices are the degree of automation and the normal stress regime. The Schulze ring shear tester and the FT4 powder rheometer are in most of the operational stages completely automated, which strongly reduces the operator influences. The ELE direct shear tester can reach the highest normal stress among all the devices we investigated.

3.1 Jenike shear tester

The Jenike tester is a direct translational shear tester, developed in the 1960s (Jenike, 1964) and it is recognized as one of the industrial standards for designing reliable bulk solids handling equipment such as storage bins, silos and hoppers. The tester consists of a shear cell ($D = 93$ mm) which includes a closed-bottom hollow base fitted to a fixed bearing plate. A shear ring capable of moving horizontally is placed over the base with a top lid, used to close the cell, see **Fig. 3(a)**. The shear cell is filled with

Table 2 Specification comparison of the Schulze ring shear tester (RST-1), ELE direct shear tester (DST), FT4 powder rheometer (FT4) and Jenike shear cell (Jenike). The actual shear velocities used are indicated in parentheses, stars refer to the default value from control softwares.

Property	Jenike	DST	RST-01	RST-XS	FT4
Cell volume (cm^3)	189	126	204	31.4	86.4
Cell geometry	cylinder	box	ring	ring	cylinder
Wall material	aluminium	stainless steel	aluminium	aluminium	borosilicate glass
Diameter (D) or Length (L) (cm)	9.3	6	6 (inner) 12 (outer)	3.2 (inner) 6.4 (outer)	5
Height (H) (cm)	2.8	3.5	2.4	1.3	4.4
Aspect ratio H/D or H/L	0.30	0.58	0.27	0.27	0.88
Shear displacement limit (mm)	8	10	unlimited	unlimited	unlimited
Test control	Manual	Manual	Computer	Computer	Computer
Sample weighing	offline	offline	offline	offline	on-board
Compression device	top lid	top lid	top ring	top ring	vented piston
Driving velocity	1–3 (2) (mm/min)	0.001–2 (2) (mm/min)	0.0038–22.9 (*) (°/min)	0.0038–22.9 (*) (°/min)	6–18 (6) (°/min)
Max. normal stress (kPa)	10–30	2778	50	20	22
Sample conditioning before pre-shear	pluviation (manual)	pluviation (manual)	pluviation (manual)	pluviation (manual)	rotated blade (automatic)
Yield locus test duration	2 hours	2 hours	20 mins	20 mins	30 mins
Stress measure direction	horizontal	horizontal and vertical	rotational and vertical	rotational and vertical	rotational

the test sample, which rests within the base and the shear ring, as shown in **Fig. 3(b)**. A normal force is applied to the shear lid by loading weight on a hanger. A shear force is then applied using a bracket and a pin on the shear ring. The bulk solid undergoes shear deformation due to the simultaneous displacement of the upper ring and the lid against the stationary bottom ring. The stem is moved by a motor at a constant speed of around 1–3 mm/minute and the shear force is measured by a force transducer and is recorded on a computer.

For conducting a shear test, a sample of powder is uniformly filled into the shear cell using a spatula and/or a sieve. The sample is initially pre-consolidated by twisting a special lid covering the powder bed under a certain normal load. Then the lid and the filling ring are replaced with a shear lid and the pre-consolidated sample is presheared until a steady state flow is reached, which is defined as a state of constant shear force and bulk density for a given normal stress. After retracting the shear stem and reducing the normal load, the shearing process is re-initiated under a reduced normal load until a maximum shear stress is recorded. This peak value represents a single point on the yield locus. The pre-shear and shear process is repeated for lower normal loads in order to get the complete yield locus. A more detailed description of the standard testing procedure is reported in the ASTM standard D-6128 (ASTM-D6128, 2006). The laborious work of filling and sample conditioning as well as a potential influence of the operator are the major drawbacks of this technique.

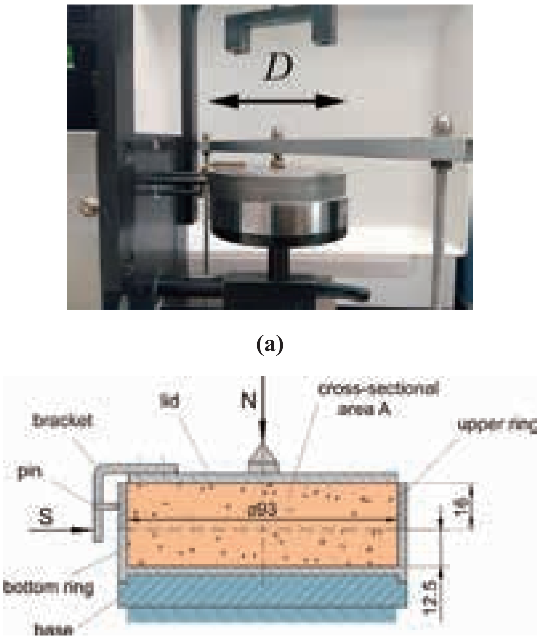

(a)

(b)

Fig. 3 **(a)** Jenike direct shear tester and **(b)** the schematic representation of the Jenike shear cell. For technical details see **Table 2**. **Fig. 3(b)**, reprinted with permission from author (Schulze, 2002). Copyright: (2002) Dietmar Schulze.

3.2 ELE direct shear tester (DST)

The second direct shear tester (ELE International, United Kingdom), is illustrated in **Fig. 4(a)**. It operates with specimens with a square cross-section of 60 mm × 60 mm and a height of 30 mm. The apparatus is enclosed in a robustly constructed case. It is designed for and can reach shear stress up to 1250 kPa and normal stress up to 2778 kPa. The speed range is between 0.0001 to 2 mm/min. The ELE direct shear tester is designed for much higher load in soil testing, employs a simple shear principle as the Jenike shear cell, has a larger shear displacement range (up to 12 mm in horizontal direction) and the possibility of reverse box movement.

The shear test sequence starts with the filling of the shear box by dry pluviation of the powder into the box until a height of approximately 40 mm is reached; then

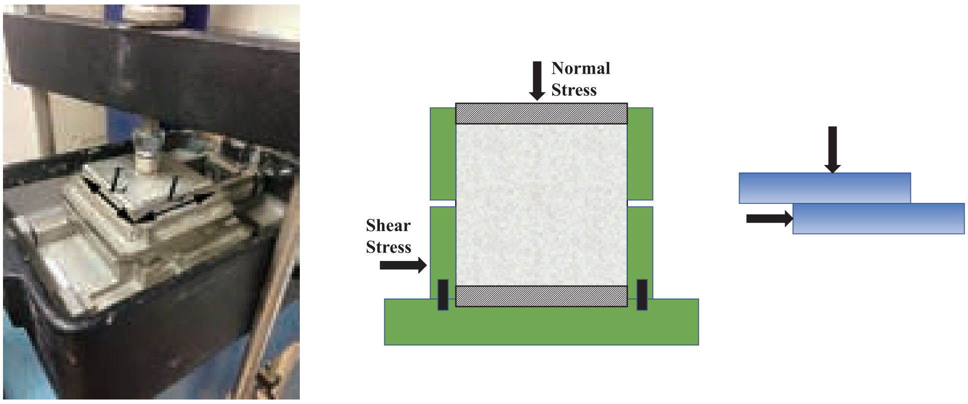

(a)

(b)

Fig. 4 **(a)** The ELE direct shear tester and **(b)** the schematic representation of the ELE direct shear cell set-up. For technical details see **Table 2**.

the top excess powder is removed by a scraper to ensure that the top surface of the sample is flat. Finally the top lid is mounted and the powder sticking to the sides of the box is removed carefully using a small paint brush. In addition to the typical direct shear testers as listed in Sec. 3.1, the main drawback for this tester is the possible ejection of powder through the inter-quadrate opening. In order to compare results in DST with other devices properly, shear tests in this study are performed following the same ASTM standard D-6128 (ASTM-D6128, 2006) as in Jenike shear tester. For the steady state test, in analogy to the normal wall friction procedure, the sample is first sheared to steady state at the highest normal load chosen. Then step by step the normal load is decreased and shear is continued until steady state is reached.

3.3 Schulze ring shear tester—RST-01 and RST-XS

Among the shear devices for powder characterization, the Schulze rotational ring shear tester (1994) is one of the most widely used testers. The Schulze ring shear tester (RST-01) operates connected to a personal computer running a control software that allows the user to obtain, among other things, yield loci and wall yield loci. A smaller version of the ring shear tester with exactly the same working principle is the so-called RST-XS, developed for smaller specimen volumes (3.5 ml to 70 ml, rather than 204 ml for the RST-01). For both testers, ring-shaped (annular) bottom ring of the shear cell contains the bulk solid specimen. An annular-shaped lid is placed on top of the bulk solid specimen and it is fixed at a cross-beam (**Fig. 5**).

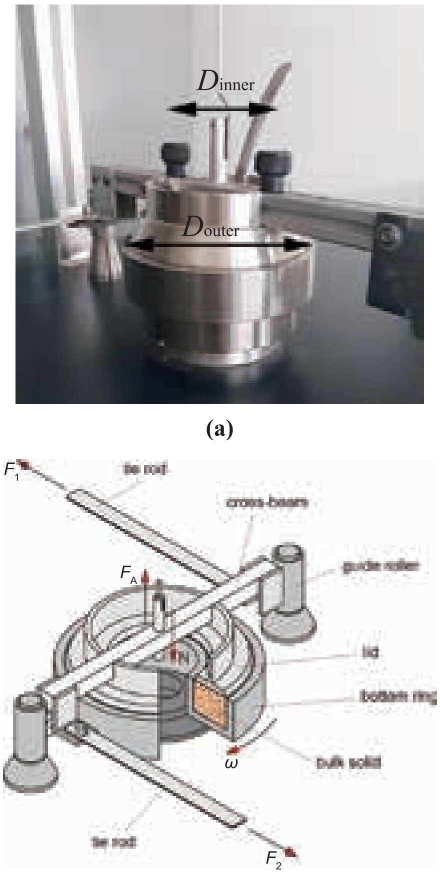

(a)

(b)

Fig. 5 **(a)** The Schulze ring shear tester RST-01 and **(b)** the working principle of the Ring shear cell set-up. The difference between RST-XS and RST-XS is the shear cell size. For technical details see **Table 2**. **Fig. 5(b)**, reprinted with permission from author (Schulz, 2003b). Copyright: (2003) Dietmar Schulze.

A normal force, F_N, is exerted on the cross-beam in the rotational axis of the shear cell and transmitted through the lid onto the specimen. Thus a normal stress is applied to the bulk solid. In order to allow small confining stress, the counterbalance force, F_A, acts in the centre of the cross-beam, created by counterweights and directed upwards, counteracting the gravity forces of the lid, the hanger and the cross-beam. Shearing of the sample is achieved by rotating the bottom ring with an angular velocity ω, whereas the lid and the cross-beam are prevented from rotation by two tie-rods connected to the cross-beam. Each of the tie-rods is fixed at a load beam, so that the forces, F_1 and F_2, acting on the tie-rods can be measured. The bottom of the shear cell and the lower side of the lid are rough in order to prevent sliding of the bulk solid on these two surfaces. Therefore, rotation of the bottom ring relative to the lid creates a shear deformation within the bulk solid. Through this shearing the bulk solid is deformed, and thus a shear stress τ develops, proportional to the forces on the tie-rods ($F_1 + F_2$). All the tests performed here follow the ASTM standard (ASTM-D6773-16, 2008).

3.4 FT4 powder rheometer

The last experimental equipment used in this work is the FT4 Powder Rheometer (Freeman technology Ltd., UK), depicted in **Fig. 6(a)**. Standard accessories for the shear test include the 50-mm-diameter blade for sample conditioning, the vented piston for compression, the shear head for the shearing process and the 50-mm-high with 50 mm diameter borosilicate test vessel. One advantage of the commercial FT4 Powder Rheometer is the automated nature of the test procedure requiring minimal operator intervention.

The shear test sequence under the ASTM standard D7891 (ASTM-D7891-15, 2015) can be summarized as follows: the test vessel is carefully filled with the powder of interest using a spatula after obtaining the tare weight. The conditioning procedure involves the movement of the conditioning blade into the test sample to gently disturb the powder bed for a user-defined number of cycles before it is removed slowly. A cycle consists of the inward and outward movement of the conditioning blade into the powder bed with a constant rotation movement all the time. In order to prevent the conditioning blade from touching the base of the vessel, the direction of the blade movement is reversed as soon as it is within 1 mm of the vessel base. It is believed that this creates a uniform, loosely packed test sample that can be readily reproduced (Freeman, 2007).

In this study, we perform three pre-conditioning cycles before the shear tests are carried out (pre-conditioning does not involve a confining stress like in the other 3 testers). The portion of the base insert of the test vessel are excluded from the calculation of the vessel height, leading to a maximum vessel height of 44 mm instead of 50 mm and an aspect ratio α of 0.88. Subsequent to pre-conditioning, the blade is replaced with a vented piston, which incorporates a stainless steel mesh to allow the enclosed air in the powder to escape uniformly across the surface of the powder bed. The vessel assembly is then split (and thus levelled) after the vented piston executes the compression until the pre-shear normal stress level is reached. Then the powder mass is recorded after splitting to compute the bulk density before the shear tests start. A detailed description of the vessel split-and-levelling procedure is reported by Freeman et al. (2009).

A shear test begins after changing the vented piston to the shear head as shown in **Fig. 6(b)**. The shear head moves downwards inserting the blades into the powder and induces a normal stress as the shear head bottom surface is in contact with the top of the powder. The shear head continues to move downwards until the required pre-shear normal stress is reached. At this point slow rotation of the shear head begins, inducing an increasing shear stress. As the powder bed resists the rotation of the shear head, the shear stress increases until failure, at the point a maximum shear stress is observed. As a consequence, a shear plane is formed just below the ends of the blades. The shear head is kept moving until the shear stress does not change anymore for the pre-shear step and is stopped immediately after the maximum is reached for each shear step. A constant normal stress is maintained throughout each pre-shear or shear step. Note that pre-shear in FT4 is a multi-stage process and will be discussed in the next section. All the tests performed with the FT4 powder rheometer follow ASTM standard (ASTM-D7891-15, 2015).

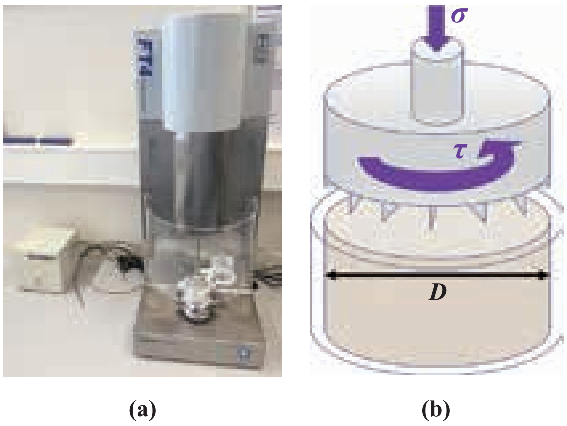

(a) (b)

Fig. 6 **(a)** The FT4 Powder Rheometer and **(b)** the working principle of the FT4 shear cell set-up. For technical details see **Table 2**.

4. Test procedures

In this section, an overview of the testing procedures as well as all the details of the tests performed using shear devices for different limestone specimens are presented.

The diagram in **Fig. 7** illustrates the common testing procedures used for measuring the yield locus. The Schulze ring shear tester RST-01 only requires one single pre-shear cycle before the first shear point and the steady state is reached (**Fig. 7** top). And this pre-shear determination is also similar in the DST and Jenike. However, the FT4 powder rheometer involves multiple pre-shear cycles before the first shear is initiated, and it determines the steady state only when the difference between the end point shear stress values from two consecutive pre-shear cycles is within 1 % (**Fig. 7** bottom). The number of multiple pre-shear cycles in the FT4 usually varies from 4 for cohesive powders to 6 for free-flowing powders. And the influence of this difference on powder flow properties will be further elaborated in Sec. 5.3.

The main quantities referred to in this study (linearised effective yield locus, yield locus and steady state/termination locus) are explained in **Fig. 8**, where the pre-shear and shear points are the measured values as indicated in **Fig. 7**. According to these three loci, three different angles can be determined: effective angle of internal friction,

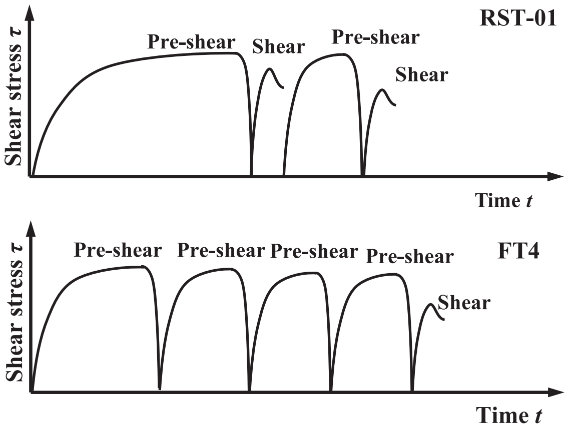

Fig. 7 Schematic drawing of typical yield locus measurement steps for RST-01 (top) and FT4 (bottom).

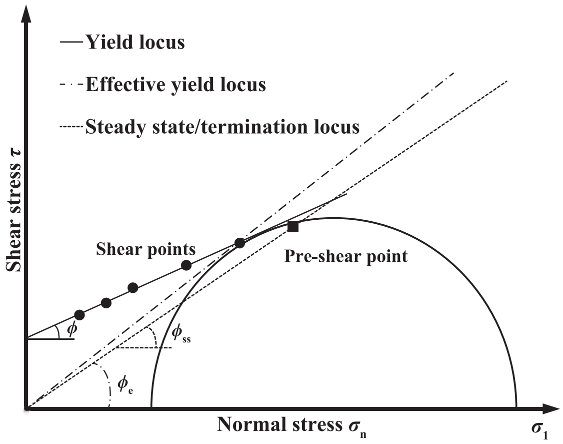

Fig. 8 Schematic drawing of effective yield locus, yield locus and steady state locus.

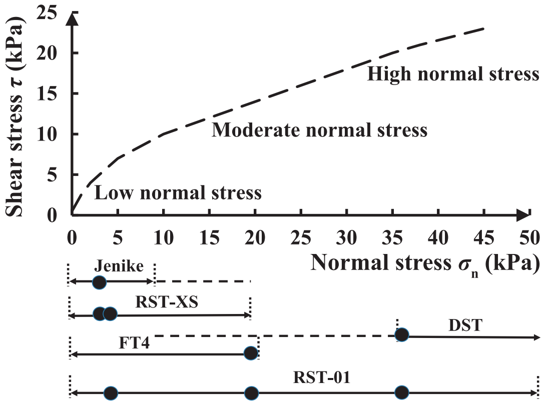

Fig. 9 Schematic drawing of typical yield locus. Black arrows at the bottom: typical normal stress ranges used for each device; dashed lines are extended normal stress limits. Black points indicate the actual normal stress levels used for different shear testers.

ϕ_e, angle of internal friction, ϕ, and steady state angle of internal friction, ϕ_{ss} as depicted in **Fig. 8** and the details are given by Schulze (2008). The intercept of yield locus for normal stress equals to zero is named as cohesive strength, and it qualitatively indicates the bulk cohesion of a given sample under a given normal stress. Note that all the quantities measured from different testers are using the same definition here.

Since all the devices investigated here have been designed for different purposes, they are adapted to test the materials in preferable normal stress ranges. In **Fig. 9**, we show schematically the range of normal stress that each device can cover with acceptable accuracy. In the same plot, we indicate the extended normal stress ranges of Jenike and DST (dashed lines). For Jeinke in higher normal stress range, the data are highly difficult to acquire and less reliable due to insufficient shear path available in shearing direction. On the other hand, low/intermediate normal stress results from DST are less accurate due to the limit of the force sensor. The actual normal stresses used for this study are also highlighted with black dots on the solid lines and summarized in **Table A1**. In **Fig. 9**, we divide the whole normal stress range into three regimes: i) low normal stress, where Jenike, RST-01/RST-XS and FT4 can be used; ii) moderate normal stress, where RST-01 and FT4 are available; iii) high normal stress that DST and RST-01 can be relied on.

The Schulze RST-01 was chosen as a reference device and used to test all 7 Eskal samples at 3 different pre-shear normal stress levels since it covers the widest stress range. A limited number of cases were tested with the other devices depending on the accuracy and material availability. However, for each pre-shear normal stress, tests on one powder have been performed using at least two devices in order to check the reproducibility of the results between the testers. Each test was repeated three times (3 fresh samples) to investigate the repeatability within a single device. Details on the pre-shear and shear normal stress levels used are given in **Table A1**. In addition, we have also performed steady state locus study using 4 powders in DST. We have chosen a pre-shear normal stress values between 1.4 and 36.1 kPa. The test details are summarized in **Table A2**.

5. Comparison of shear devices

In this section, we compare the measurement from different shear devices and a general overview of the repeatability and reproducibility of the test results is given. In order to compare the yield loci from different testers, two limestone powders were chosen as reference powders (see **Table 3**), namely cohesive Eskal300 (2.22 μm) and free flowing Eskal150 (138 μm).

Table 3 Summary of the tests performed. The numbering in the table are the number of powders tested with a certain device under a certain pre-shear stress level. For more details, see **Table A1**. Note that the values in the parentheses refer to the pre-shear normal stress values used for a specific device.

Stress in kPa Device	Low stress 5 (4.3)	Moderate stress 20	High stress 35 (36.1)
Jenike	2 (4.3)	[–]	[–]
DST	[–]	[–]	4 (36.1)
RST-01	7	8	7
RST-XS	4 (4.3)	[–]	[–]
FT4	[–]	4	[–]

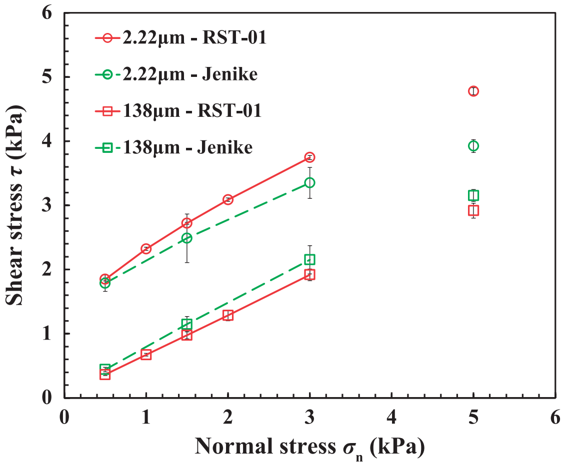

Fig. 10 Yield locus (shear stress versus normal stress) of Eskal150 (138 μm) and Eskal300 (2.22 μm) using RST-01 and Jenike. The pre-shear normal stress is kept at 5 kPa for both devices. Points with and without lines are shear and pre-shear points, respectively. Lines are guides to the eye.

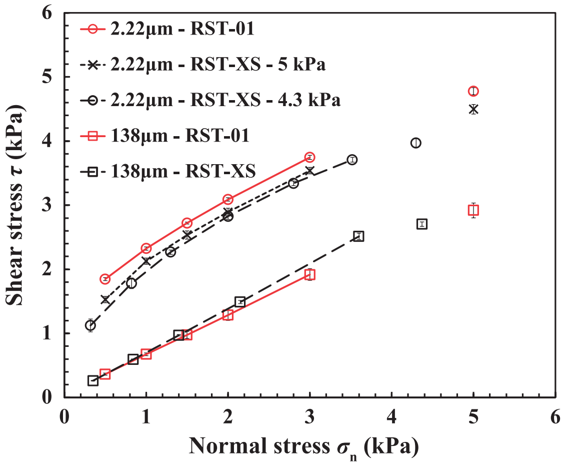

Fig. 11 Yield locus (shear stress versus normal stress) of Eskal150 (138 μm) and Eskal300 (2.22 μm) using RST-01 and RST-XS. The pre-shear normal stresses are set to 5 and 4.3 kPa for RST-01 and RST-XS, respectively (Eskal300 has one extra 5 kPa pre-shear using RST-XS). Points with and without lines are shear and pre-shear points, respectively. Lines are guides to the eye. Note that here the data for RST-01 are the same as in **Fig. 10**.

5.1 Low normal stress: Schulze ring shear tester (RST-01) vs Jenike tester

In the low normal stress regime, we first compare the RST-01 with the standard Jenike tester at pre-shear normal stress of 5 kPa. Each shear point is measured with 3 fresh samples to acquire the standard deviations. The yield loci for Eskal150 (138 μm) and 300 (2.22 μm) are shown in **Fig. 10**. Both testers show quite good repeatability with a higher standard deviation from the Jenike tester. When we look at the individual powders, the agreement between the two shear testers for Eskal150 is good, with the difference increasing slightly with increasing normal stress. The pre-shear stress values are also close within the deviation range. For the finer Eskal300, the discrepancy between the two devices becomes higher, but still within the standard deviation. A big discrepancy is observed for the pre-shear points, where the Jenike shows lower values and higher standard deviations compared to RST-01. This may be related to the manual control procedure of the Jenike shear cell. Often the pre-shear must be stopped to prevent the risk of running out the shear displacement.

5.2 Low normal stress: Schulze ring shear tester (RST-01) vs (RST-XS)

In the same low normal stress range, we have also tested the two reference powders using the smaller RST-XS, and the data are compared to RST-01 as shown in **Fig. 11**. For both devices, the repeatability is very high, with the standard deviations within the symbol size. For the free flowing Eskal150, the yield loci measured by the two devices demonstrate a very good agreement although a slightly different pre-shear normal stresses are used. For the cohesive Eskal300, data from RST-XS are consistently lower than data from RST-01. However, both devices show a non-linear behaviour with the slope (decreasing with increasing normal stress).

To further investigate RST-XS, we have tested Eskal300 in the RST-XS using the same pre-shear and shear stress levels as in RST-01, and results are also plotted in **Fig. 11**. We observe that, also in this case of same pre-shear normal stress, the RST-XS values are systematically lower than the RST-01 values (around 5 %). As the only known difference between RST-XS and RST-01 is the shear cell size, our results indicate that the powder response may be influenced by the system size in the case of cohesive material.

5.3 Moderate normal stress: Schulze ring shear tester (RST-01) vs FT4 powder rheometer

In the moderate normal stress regime, we compare the most commonly used rotational shear testers, the RST-01 and the FT4 rheometer. Both testers are automated and allow selection of a pre-shear normal stress value, σ_{pre}, which was set to 20 kPa for our comparison.

The yield loci for Eskal300 and Eskal150 are shown in **Fig. 12**. Both the RST-01 and the FT4 show good repeatability for each measurement point, with the standard deviations within the symbol size. For the free-flowing Eskal150, the yield loci measured by the two devices are in very good agreement except for the pre-shear points,

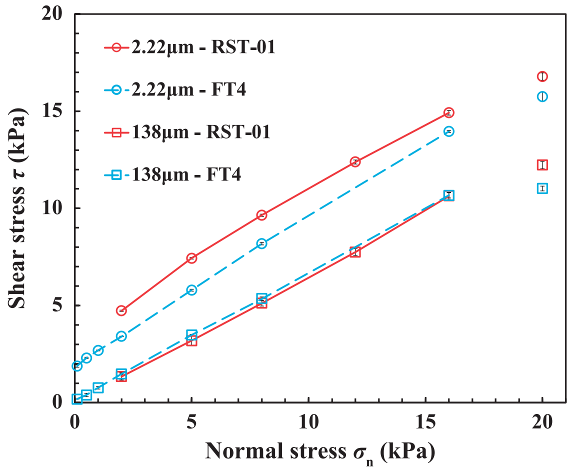

Fig. 12 Yield locus (shear stress versus normal stress) of Eskal150 (138 µm) and Eskal300 (2.22 µm) using RST-01 and FT4. The pre-shear normal stress is kept at 20 kPa for both devices. Points with and without lines are shear and pre-shear points, respectively. Lines are guides to the eye.

where the FT4 gives a much lower value than the RST-01. However, for the cohesive Eskal300, we see a pronounced difference between results obtained by the two devices (around 10–20 %), although the angle of internal friction (slope) between the two devices stays almost the same. A similar trend is observed with the other two cohesive samples: Eskal500 and Eskal15, with the values measured by FT4 systematically lower than the ones from RST-01 (data not shown here, for details see **Tables B1** and **B2**).

We associate the difference in the behaviour between the two devices to the test protocols as explained in Sec. 4. The Schulze ring shear tester, based on the ASTM standard D-6773 (ASTM-D6773-16, 2008), uses the conventional pre-shear determination criterion: the steady state shear stress plateau is determined in one pre-shear stage and the following pre-shear stages after incipient flow follows this one pre-shear state value. On the other hand, for the FT4 powder rheometer, based on the ASTM standard D7891 (ASTM-D7891-15, 2015), several pre-shear cycles are performed until the steady state reaches a constant shear stress value (within 1 % difference). This value is the assumed as pre-shear steady state and the shear stage starts. In the case of cohesive powders, the samples need 3–10 repetitions for the pre-shear to fulfil the steady state criterion in the FT4. This may lead to formation of a pre-defined shear failure plane in the sample that reduces its shearing resistance along the shear direction. We point out here that both shear devices are automated using their own test software where the test protocols are in-built and therefore impossible to change by the users. In addition, there is another significant difference between the two testers in that the Schulze ring shear tester has an annular cross-section where the shear displacement is applied fairly uniformly over the solid shearing surface; whilst the FT4 rheometer has a circular cross-section where the shearing displacement is highly non-uniform with values decreasing towards zero at the centre of the cross-section. It is thus probable that critical shearing state may not be fully achieved particularly near the central zone of the cross-section, thereby producing a smaller overall critical shear stress.

5.4 High normal stress: Schulze ring shear tester (RST-01) vs direct shear tester (DST)

In the high normal stress regime, we compare the reference Schulze ring shear tester (RST-01) with the direct shear tester (DST) as shown in **Fig. 13**. The pre-shear stress σ_{pre} is set to 35 kPa for the RST-01 and 36.1 kPa for the DST. This small difference in the pre-shear normal stress applied is due to the design limitation of DST, where one can only change the normal stress discontinuously.

As we can see clearly from the figure, the results from DST and RST-01 are in good agreement for both powders. The standard deviation of DST data is higher than the RST-01, and becomes more prominent for low stress levels as well as for the free-flowing sample Eskal150. In the case of pre-shear points, the DST shows a slightly lower value compared to the RST-01, but the difference is negligible. For the yield locus of Eskal150, data from the two devices overlap within the error bars. When we focus on Eskal300, DST underestimates the shear stress values on the yield locus with respect to the RST-01, especially for low normal stresses. We want to point out that the low stress data from DST may be less reliable that the shear

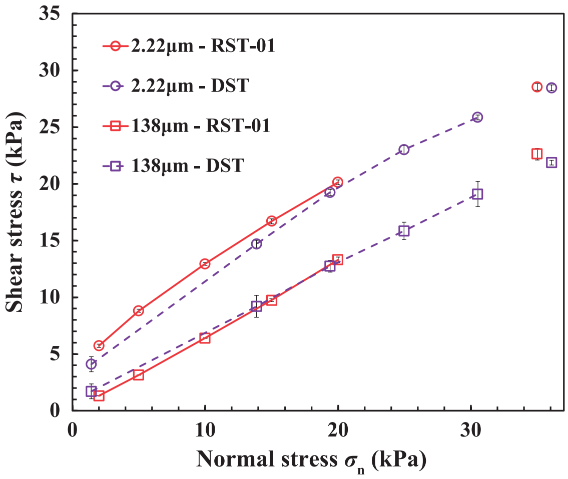

Fig. 13 Yield locus (shear stress versus normal stress) of Eskal150 (138 µm) and Eskal300 (2.22 µm) using RST-01 and DST. The pre-shear normal stresses are kept at 35 and 36.1 kPa for RST-01 and DST, respectively. Points with and without lines are shear and pre-shear points, respectively. Lines are guides to the eye.

force measurement system of DST has a lower limit value of 1 N (1 kPa).

Finally, in order to confirm the reproducibility between the two devices, we further test the steady state shear responses for Eskal K0.1–0.5 and Eskal K0.5–0.8, as shown in **Fig. 14**. Results from the two shear devices show good agreements for the tested two powders, with the data points following the two linearised yield loci within the standard deviations.

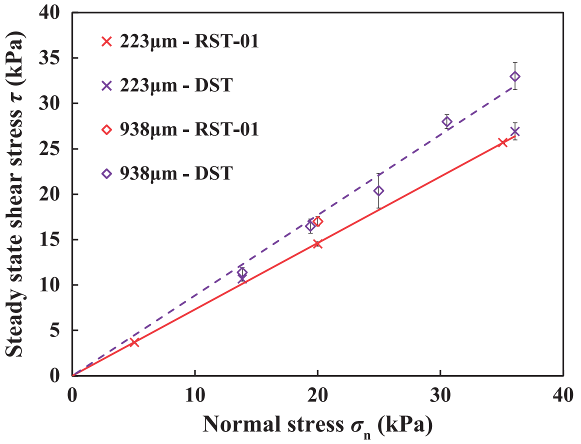

Fig. 14 Steady state locus (shear stress versus normal stress) of Eskal K0.1–0.5 (223 µm) and K0.5–0.8 (938 µm) using RST-01 and DST. The lines are the least mean square linear regression to the data with angle $\phi_{ss} = 36.2°$ for Eskal K0.1–0.5 and 41.5° for Eskal K0.5–0.8.

5.5 Summary of device comparison

In order to validate the consistency of the results obtained from different shear devices, we extrapolate the linearised yield loci and compare both angle of internal friction as well as cohesive strength (interception of linearised yield locus on y-axis) for the two reference powders (**Figs. 15** and **16**). The data from different shear testers are interpreted in different ways. In the case of the yield locus from the Jenike tester and DST, the shear points are linearised using a least square method, while the RST-01, RST-XS and FT4 are linearised using the default software with pro-rating method. For a free-flowing powder, Eskal150 (138 µm), we get a good agreement among the RST-01, the RST-XS and the FT4 for the cohesive strength, *c*, but higher values from the Jenike and es-

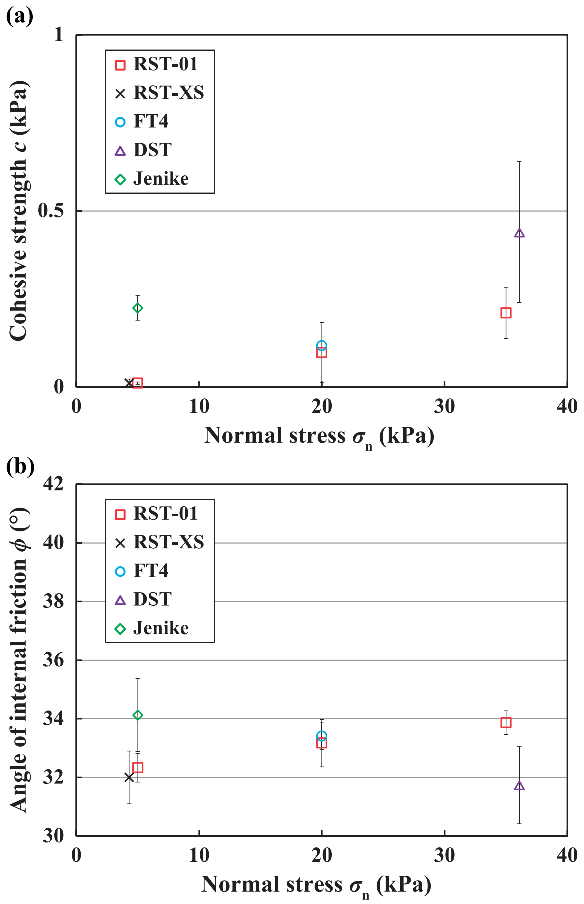

Fig. 15 **(a)** Cohesive strength, *c* and **(b)** angle of internal friction, ϕ, plotted against normal stress, σ_n, for Eskal150 (138 µm tested using all the devices in this study.

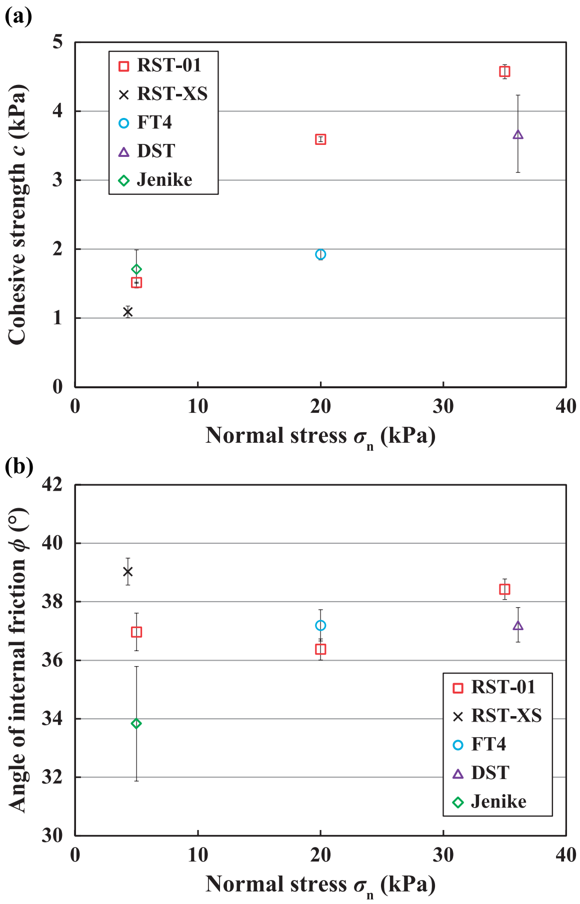

Fig. 16 **(a)** Cohesive strength, *c* and **(b)** angle of internal friction, ϕ, plotted against normal stress, σ_n, for Eskal300 (2.22 µm) tested using all the devices in this study.

pecially from the DST with also larger standard deviations (**Fig. 15(a)**). A similar observation is also found for the angle of internal friction as shown in **Fig. 15(b)**, but the ϕ value obtained from the DST is lower than the other devices. This is caused by the limit of the direct shear tester in the low stress range (below 1.0 kPa). The direct shear tester is initially designed for measuring the strength of soil samples in civil engineering, where the stresses applied are usually high, whereas our tests were performed at much lower stress levels, close to the accuracy limit (around 0.5 kPa) of the force ring on direct shear tester, resulting in a decrease in measurement accuracy for the direct shear tester using free-flowing powders. In the case of the Jenike shear tester, the ϕ value is higher than the other devices, but still within the deviation range.

In **Fig. 16**, we investigate the reproducibility of all the devices by looking at the most cohesive Eskal300 powder (2.22 µm). DST shows a good agreement with the highest standard deviation for cohesive strength, c, (**Fig. 16(a)**). However, the difference between the DST and the RST-01 is around 20 %. The RST-XS, Jenike and the RST-01 have a good agreement but FT4 shows a relatively lower value for c, thus underestimating the flowability of very cohesive powders. When we look at the ϕ value as shown in **Fig. 16(b)**, Jenike unexpectedly gives the lowest value with the highest standard deviation. The DST shows slightly lower values than the RST-01 and the FT4 has a good agreement with the RST-01 (within deviation range). Similar behaviour is observed for two other Eskal powders tested using RST-01, RST-XS, FT4 and DST: cohesive Eskal500 and easy-flowing Eskal15 (data are not shown here, see the **Tables** in Appendix B). Note that the vertical axes of cohesive strength are different in **Fig. 15** and **Fig. 16**.

6. Effects of varying particle size

In this section, we present the comparison of seven Eskal powders tested by the Schulze ring shear tester (RST-01) at different pre-shear stresses as given in **Table 3**. For the analysis of RST-01 data, we used the standard RST-CONTROL 95 software with “N-RHOB-correction” activated (Schulze, 2011). The powder have sizes ranging from 2.22 to 938 µm, and identical chemical composition as explained in **Table 1**. We characterize the above-mentioned seven powders in terms of bulk density, angle of internal friction, cohesive strength, steady state angle of internal friction, effective angle of internal friction and flow function.

6.1 Bulk density at steady state

As a first step, we look at the dependence of the bulk density on the normal stress and particle size for all the powders. Data are shown in **Fig. 17(a)**. Zero normal stress (arrows on bulk density axis) corresponds to the initial bulk density of the fresh samples before applying any stresses (provided by the manufacturer). By increasing normal stress, the bulk density increases for all powders with different rates, higher for small-particle-size powder and almost zero for Eskal80 (71 µm) and 150 (138 µm). However, for Eskal K0.1–0.5 (223 µm), the bulk density increases with increasing normal stress. We associate this trend to the wider particle size distribution (large span value 1.29 as shown in **Table 1**) and the visible huge amount of fines as shown in **Fig. 2**. A wider particle size distribution allows easy rearrangement of the packing structure when applying external load.

In **Fig. 17(b)**, we plot the bulk density with respect to

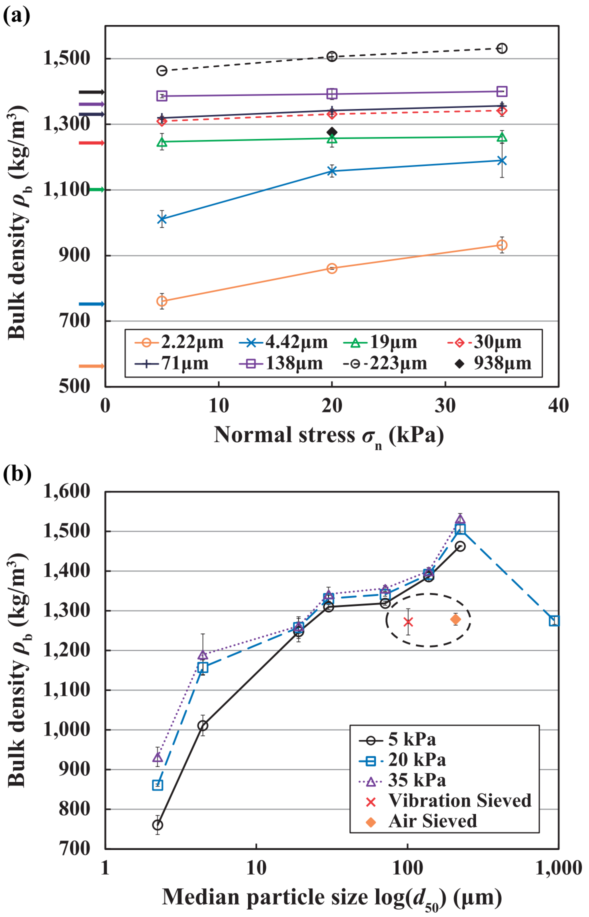

Fig. 17 Bulk density in steady state, ρ_b, plotted against **(a)** normal (pre-shear) stress, σ_n, **(b)** median particle size, d_{50}. Arrows represent the initial bulk density of the raw samples before stress and shear are applied. Symbols in the dashed area are sieved Eskal K0.1–0.5 (223 µm) sample sheared at $\sigma_n = 20$ kPa. Lines are guides to the eye.

the median particle size for different normal stresses. We observe an increasing trend with increasing particle size consistent for all normal stresses. This can be explained by the presence of cohesive forces (van der Waals) between primarily particles other than gravitational forces. Since Eskal powders are relatively dry, the presence of liquid bridging and other forces are expected to be small, the dry cohesive interaction will result in forming clusters and create many voids in the bulk, and therefore decrease the bulk density. As cohesive forces become smaller with increasing size, particles will have mainly frictional and gravitational forces without forming clusters and therefore the material can form a denser bulk solid. One extra powder, Eskal K0.5–0.8 (938 μm), is also tested under 20 kPa normal stress. This powder breaks the trend seen previously and shows a lower bulk density associated with the largest median particle size. In order to investigate further the role of the span in the bulk density behaviour, we perform sieving on the sample with largest span, Eskal K0.1–0.5 (223 μm). Two sieving methods are used: standard vibration sieving and high pressure air sieving. The median particle sizes reduce to 101 μm and 208 μm, in the case of vibration sieving and air sieving, respectively. The vibration sieving is only effective in removing the coarse particle but not the fines and thus leads to an increase of the span from 1.289 to 2.173. While the air sieving is effective enough to remove both coarse and fines and decrease the span to 0.395. The bulk densities for Eskal K0.1–0.5 (223 μm) after sieving are plotted in the dashed area of the same **Fig. 17(b)**. The bulk density of the sieved samples both decrease to values that are similar to the values of the largest median particle size powder, Eskal K0.5–0.8 (938 μm). This indicates that for a given median particle size, the span has a dominating effect on the bulk density of a powder.

6.2 Bulk responses from incipient and steady state flow

6.2.1 Angle of internal friction from incipient flow

The angle of internal friction describes the bulk friction during incipient flow of a powder, which is determined from the linearised yield locus as shown in **Fig. 8**. Although the yield locus for cohesive powder is nonlinear by nature, the linearised yield locus can still be used to estimate the angle of internal friction in a certain stress range. This estimated value is one important property that determines the maximum bulk friction of a powder from a given pre-consolidation history. Here, unless specified, all angles of internal friction originate from linearised yield loci.

In **Fig. 18**, we plot the angle of internal friction against normal stress at three different pre-shear normal stress and particle size for the 7 powders studied (Eskal K0.5–0.8 is also included here but with only one point). Within the stresses investigated, there is no apparent dependence of the angle of internal friction on the normal stress (**Fig. 18(a)**). However, if we focus on the dependence on the particle size as shown in **Fig. 18(b)**, we observe that when d_{50} is lower than approximately 30 μm, ϕ decreases with increasing particle size. Then, for $30 < d_{50} < 150$ μm, we observe that the ϕ is almost constant with changing particle size for the three pre-shear normal stresses chosen. Interestingly, if the particle size keeps rising to $d_{50} < 150$ μm, ϕ follows a parallel rise and achieves similar values to the ones obtained for samples smaller than 30 μm. For Eskal K0.1–0.5 ($d_{50} = 223$ μm), the angle of internal friction increases back to around 38°.

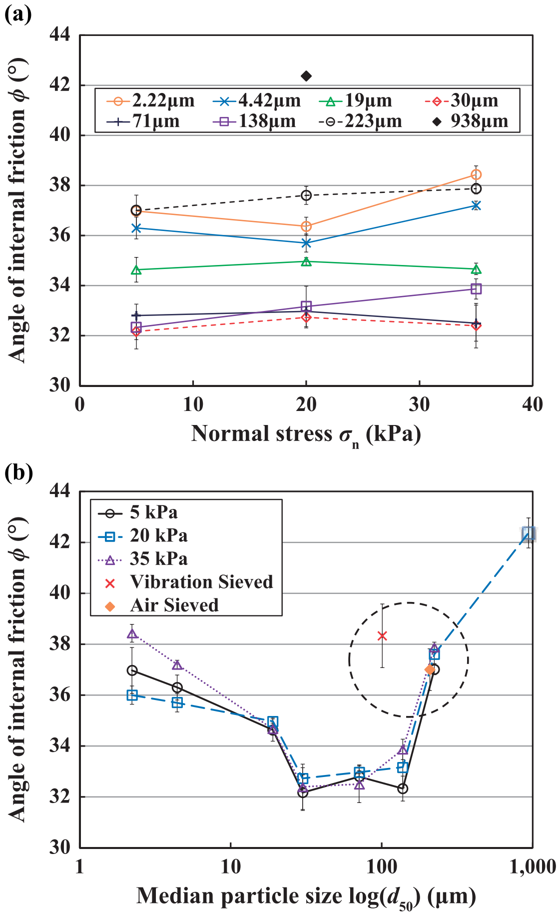

Fig. 18 Angle of internal friction, ϕ, plotted against **(a)** pre-shear normal stress, σ_n, **(b)** median particle size, d_{50}. Symbols in the dashed area are sieved Eskal K0.1–0.5 (223 μm) sample sheared at $\sigma_n = 20$ kPa. Lines are guides to the eye.

We have run several tests/checks with the goal of elucidating the non-monotonic behavior that observed in **Fig. 18(b)**. First, we further test another sample in the range of $d_{50} > 150$ μm, namely Eskal K0.5–0.8 ($d_{50} = 938$ μm), at 20 kPa pre-shear stress. The ϕ value of Eskal K0.5–0.8 increases even further to around 42°. This confirms that the increasing trend is not limited only to a specific sample. As second step, we have measured the angle of internal friction for the two sieved samples obtained after sieving Eskal K0.1–0.5 (223 μm) via vibration and air methods that are already introduced in Sec. 6.2.1. While the bulk density strongly reduces after sieving, the angle of internal friction remains unaffected as shown in the dashed area of **Fig. 18(b)**, which indicates that the span of particle size distribution is not the primary factor influencing the bulk friction. Finally, in order to check the influence of the devices, we have further tested Eskal K0.1–0.5 (223 μm) and K0.5–0.8 (938 μm) in the direct shear tester (DST), and the results are reported in **Fig. 14**. The flow behaviour of both powders are very similar using RST-01 and DST. This agreement clarifies that the behaviour originates from material properties rather than from a specific shear device.

One possible explanation of this interesting behaviour on bulk friction would be that the different size particles have a similar shape (this is visible by comparing the roundness between Eskal K0.1–0.5 and K0.5–0.8 in **Table 1**) but different surface roughness/asperity, but this has to be further investigated and it is far beyond the scope of this study. Another possibility is the competition between the inter-particle cohesion and inter-particle friction (caused by shape). When the particles are small, the inter-particle cohesion dominates the flow behaviour and enhances the shear resistance. Also when a sample is confined under a given confining stress, if the inter-particle cohesion is high, the sample bulk density will be low, which gives more free spaces for particles to move around. Therefore, the geometrical interlocking does not play an important role here. When the particle size is large, we have almost no influence from inter-particle cohesion and the whole powder is more densely packed, so that the inter-particle friction/interlocking (shape/geometry) is the ruling mechanism of the bulk friction behaviour. For an intermediate particle size, these two effects are both reducing but still competing with each other, and they cannot be distinguished.

6.2.2 Cohesive strength from incipient flow

As a complement to the angle of internal friction, one has to also look at the cohesive strength, which is the extrapolated intercept from the linearised yield locus, and gives an indication of the strength of the powder under zero confining stress (σ_n). In **Fig. 19(a)**, we plot the cohesive strength against the pre-shear normal stress. As expected, the values of cohesive strength at given stress levels are higher for powders with finer particle size. The cohesive strength of all powders increases with increasing normal stress, but with different slopes. The cohesive strength of the two finest powders, Eskal300 (2.22 μm) and Eskal500 (4.42 μm), increase conspicuously with normal stress.

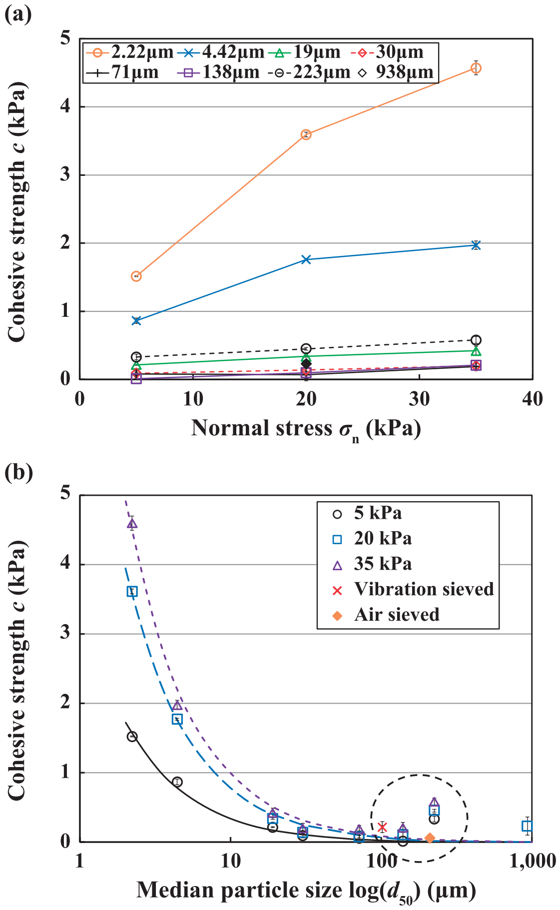

Fig. 19 Cohesive strength, c, plotted against **(a)** pre-shear normal stress, σ_n, **(b)** median particle size, d_{50}. Symbols in the dashed area are sieved Eskal K0.1–0.5 (223 μm) sample sheared at $\sigma_n = 20$ kPa. Lines are from the fitted function: $c(d_{50}) = \sigma_{pre} * d_c/d_{50}$ with $d_c = 0.6919$, 0.3953 and 0.2809 μm for $\sigma_{pre} = 5$, 20 and 35 kPa, repectively.

As we focus on the particle size dependence in **Fig. 19(b)**, we see a monotonically decreasing bulk cohesion with increasing particle size for all the normal stress levels investigated. However, the cohesive strength for raw Eskal K0.1–0.5 (223 μm) increases above this trend (as shown in the dashed area in the figure). This apparent discrepancy was also observed in the bulk density and the angle of internal friction, as explained earlier. We further investigated this behaviour by sieving the sample using different techniques. It seems that our air sieving procedures are effective and reduce the cohesive strength of the powder by separating the fines from the coarse fractions. The theory that smaller particles have the strongest cohesive forces, acting most effectively on each other, is consistent with the strongest decrease in cohesion for the air-sieved samples in which the fines are most effectively removed. The observation of removing fines reduces bulk cohesion but does not affect bulk friction supports the hypothesis that frictional flow behaviour of powders in the range of $d_{50} > 150$ µm is governed by particle interlocking.

In **Fig. 19(b)**, we have also given fitted lines based on the equation as shown in the caption. All our data fitted well with a power law dependence and this power has its origin from the adhesive forces between two particles, as introduced by Rumpf in 1990 (Rumpf 1990, Rabinovich et al. 2000), where the adhesion force between two particles is linearly proportional to particle diameter: $F_{\mathrm{ad}} \propto d$. While for the cohesive strength, it is a bulk property with an unit of stress. Therefore, cohesive strength is proportional to the adhesion force divided by effective contact area: $c \propto F_{\mathrm{ad}}/d^2$, and finally we get $c \propto d^{-1}$, which is the relation used for our fitting.

6.2.3 Bulk friction from steady state flow

Along with the bulk density (volume fraction), angle of internal friction and cohesive strength, the steady state angle of internal friction, ϕ_{ss}, also plays a major role in determining the powder flow behaviour. The steady state flow does not depend on time change or sample history and one could get a unique bulk friction response to shearing for each normal stress level for a given sample. We first look at the ϕ_{ss} with respect to the applied normal stress in **Fig. 20(a)**. For samples with median particle size higher than 20 µm (Eskal30, 80, 150 and K0.1–0.5), the ϕ_{ss} behaves similarly as ϕ, no clear dependence on normal stress is observed. However, for samples smaller than 20 µm (Eskal300, 500 and 15), ϕ_{ss} decreases with increasing normal stress.

When we look at the size influence on ϕ_{ss} in **Fig. 20(b)**, we observe a very similar trend to the angle of internal friction in **Fig. 18(b)**. However, the value of ϕ_{ss} for largest size powder is lower than the value of the finest powder, where ϕ of the coarsest powder exceeds the finest. This indicates that the inter-particle cohesion contributes more to the shear resistance at steady state flow than at incipient flow. When looking at the behaviour of the two sieved samples, ϕ_{ss} stay almost unchanged after sieving, which is consistent with **Fig. 18(b)**.

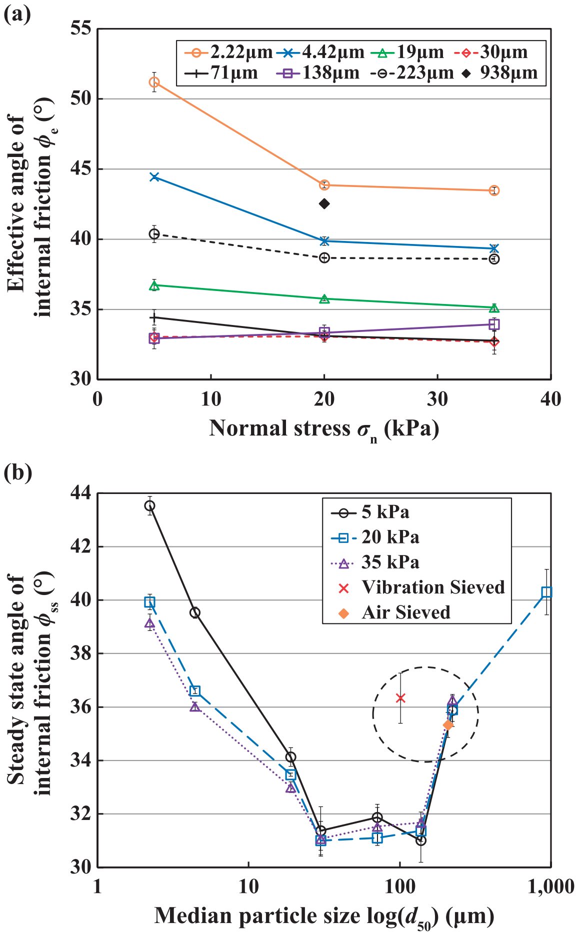

Fig. 20 Steady state angle of internal friction, ϕ_{ss}, plotted against **(a)** pre-shear normal stress, σ_{n}, **(b)** median particle size, d_{50}. Symbols in the dashed area are sieved Eskal K0.1–0.5 (223 µm) sample sheared at $\sigma_{\mathrm{n}} = 20$ kPa. Lines are guides to the eye.

6.3 Quantities relevant for silo design

The parameters mentioned in the sections above are determined directly from the physical response of powders in the shear tester, e.g., bulk friction values can be directly calculated from the measured normal and shear stresses, and are very useful for understanding the powder's physical behaviour. However, for designing a silo, some additional parameters play an important role (Jenike, 1976; Schulze, 2008, 2014b). These will be discussed in the following sections.

6.3.1 Effective angle of internal friction

The effective angle of internal friction is defined as the angle of the effective yield locus, which is the line starting at the origin of the $\sigma_{\mathrm{n}} - \tau$ plane and tangent to the Mohr circle (see **Fig. 8**). And this property is crucial for designing the hopper angle in order to achieve mass flow in a silo.

In **Fig. 21**, the effective angle of internal friction is plotted against the normal stress and median particle size. Within the stress levels investigated, ϕ_{e} decreases with increasing normal stress, except for two intermediate size powders—Eskal30 (30 µm) and 150 (138 µm), which shows a consistent behaviour with ϕ_{ss} independent of the normal stress. Interestingly, for even higher particle size, Eskal K0.1–0.5 (223 µm), ϕ_{e} again decreases with applied normal stress.

When we focus on the dependence of the effective angle of internal friction on the particle size as shown in **Fig. 21(b)**, we observe a very similar trend as ϕ and ϕ_{ss}, especially with values of ϕ_{e} consistently higher than ϕ_{ss} for both very fine and very coarse powders. Also in this

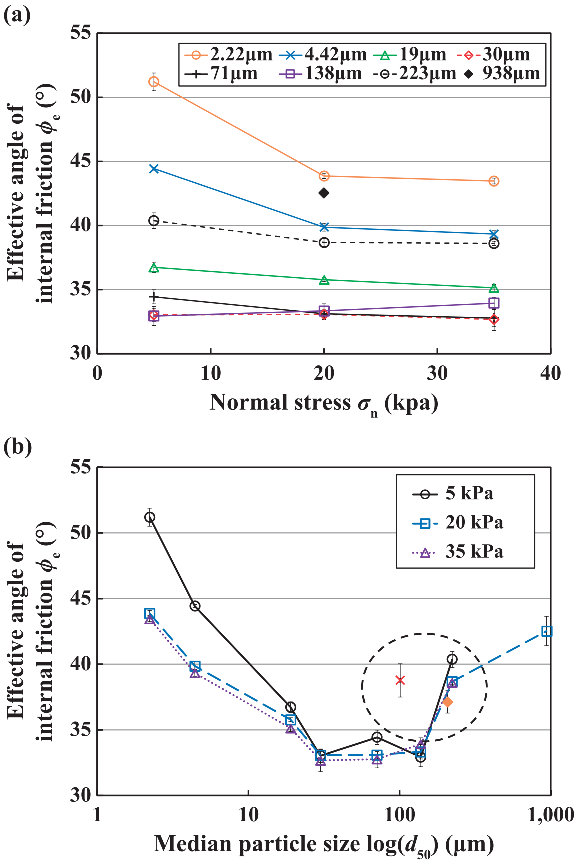

Fig. 21 Effective angle of internal friction, ϕ_e, plotted against **(a)** pre-shear normal stress, σ_n, **(b)** median particle size, d_{50}. Symbols in the dashed area are sieved Eskal K0.1–0.5 (223 µm) sample sheared at $\sigma_n = 20$ kPa. Lines are guides to the eye.

case, sieving barely affects the behaviour of the powders, see dashed area in **Fig. 21(b)**.

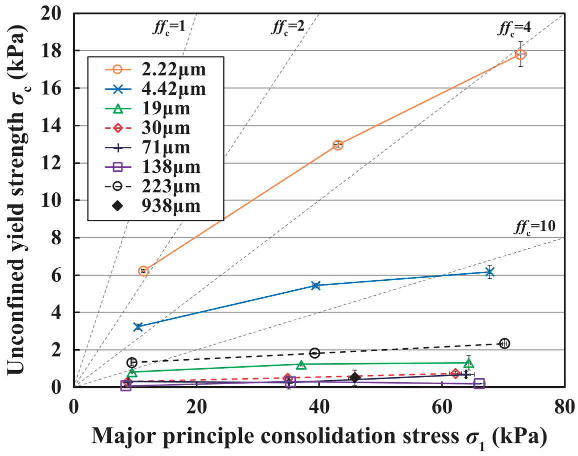

Fig. 22 Flow function: unconfined yield strength, σ_c, plotted against major consolidation stress, σ_1 under 3 different pre-shear stresses using RST-01. Different symbols/colours represent different materials. Note that for Eskal K0.5–0.8, there is only one point, and we have error bars with both σ_c and σ_1. Lines are guides to the eye.

6.3.2 Flow function and powder flowability

Finally, we process the results to look at the powder flowability in the form of the flow function to evaluate how a given powder would fail/flow under a given major consolidation stress (see **Fig. 8**). This is also of great significance for designing the outlet diameter of a silo (Schulze, 2014a). When a powder sample is compressed in a confined geometry, e.g. a cylinder in a uni-axial tester, the major consolidation stress is named as σ_1, which indicates the maximum compressive stress achieved in the sample. If the powder is sufficiently cohesive, it will form an intact bulk/block after the confinement is removed. If the block is compressed again, the minimum stress needed to achieve sample failure/breakage is called the unconfined yield strength, σ_c. Note that the sample stress paths in uni-axial testers and shear testers are different, but the stress states could be linked using Mohr's Circle. The curve $\sigma_c = f(\sigma_1)$ is called flow function in powder engineering, which can be used to characterize material flowability, $ff_c = \sigma_1/\sigma_c$ (Schulze, 2008). The flowability is defined as follows:

- $ff_c < 1$ not flowing
- $1 < ff_c < 2$ very cohesive
- $2 < ff_c < 4$ cohesive
- $4 < ff_c < 10$ easy flowing
- $ff_c > 10$ free flowing

In **Fig. 22**, we plot the flow functions for 7 limestone powders. As we can see, our powders cover almost the whole range of flowability, from cohesive to free flowing. In the stress range we investigated, σ_c increases for all the samples with increasing σ_1. As expected, the slope of the increase trend becomes higher with decreasing particle size, with the maximum slope of Eskal300 (minimum particle size). The flowability of a certain powder depends not only on the major consolidation stress σ_1, but also on particle size.

7. Conclusion and outlook

In this study, we have systematically examined the powder flow behaviour of limestone powder samples with varying median particle sizes in different shear testers at different confining stress levels. The major goal is to understand the relation between microscopic properties such as particle size and contact cohesion and macroscopic, bulk properties such as bulk density, cohesive strength and shear resistance (characterized by the effective angle of internal friction, the internal friction at steady state flow, and the internal friction).

All shear testers investigated show highly repeatable/

reproducible results and good overall, consistent agreement among each other. Direct shear devices (Jenike and ELE direct shear tester) give the highest standard deviations. The yield loci obtained by the Schulze ring shear tester (RST-01) are consistently slightly higher than the results from other testers, which, on the practical side, results in a more conservative but safer silo design. The shear protocol evidently influences the measurements as shown by comparing the RST-01 and the FT4, where the latter gives a significantly lower yield locus, which we attribute to a different pre-shear protocol. As a conclusion, while the automated devices minimize the operator influence, the output should be carefully interpreted, as differences in the protocol can result in considerable deviations in the measured material response even if the qualitative trends are found to be consistent among different testers.

In order to study the material behaviour, eight limestone powders with identical chemical composition and median particle size ranging from 2.2 μm to 938 μm have been tested in a wide range of normal stresses (5, 20 and 35 kPa). Both factors, size and stress, are found to influence the bulk flow significantly. As expected, the bulk density and cohesive strength increase with increasing normal stress, the effect being stronger for finer particles. On the other hand, the angle of internal friction seems to be unaffected by the normal stress (at least in the range investigated here), while the effective angle of internal friction and the steady state angle of internal friction show a decreasing trend with normal stress.

When we look at the dependence of the macroscopic flow on particle size, two regimes can be distinguished, above and below the median particle size of about 150 μm. For the fine particle regime, contact cohesion dominates the bulk behaviour, the effect getting smaller with increasing particle size. The bulk density increases monotonically with particle size, and the bulk cohesion (cohesive strength) decreases to nearly zero. The friction angles (effective angle of internal friction, angle of internal friction and steady state angle of internal friction), follow a similar decreasing trend as bulk cohesion.

In the coarse particle regime (150 to 938 μm), the bulk behaviour is less obvious. The bulk cohesion slightly increases while bulk density increases, then decreases. The bulk friction angles increase with increasing particle size up to values comparable to those of the finest powders. In order to check the effect of small particles in this regime, fines are removed from the coarse samples via air sieving. This results in a significant reduction in bulk density and bulk cohesion, while the bulk friction angles are barely affected. This proves that the fine particles being the main source of cohesion. The competition between contact cohesion and geometrical effects can explain the transition between the two regimes. For dry powders consisting of large particles, the inter-particle cohesive forces, especially the van der Waals forces, become negligible. The interlocking between particles due to the surface roughness and shape dominates the bulk behaviour of coarse samples, while cohesion is the key contribution that governs the shear strength of fine powders. The geometrical interlocking effect is further enhanced by the increase of the bulk density for coarse samples. On the other hand, low density is associated with small median particle size, due to the presence of clusters and large pores.

For the sake of completeness, we also look at the flow behaviour of our powders, as relevant for the silo-design procedure. Overall, the flowability increases when increasing normal stress (powders become more free flowing) for finer samples, with the effect becoming weaker for coarse samples that are more free flowing anyway.

The present paper is the beginning of a collection of experimental data that, in the future, can be enriched with more data from many more materials of both industrial and academic interest. Our speculations on the interesting bulk cohesion and friction behaviour with increasing particle size have to be further investigated. Furthermore, this experimental database can be used as a source for design (e.g. silo) procedures and as a benchmark for further experimental studies. Last but not least, the development, calibration and validation of particle models and simulations, especially the DEM contact models, and simulations of element tests (shear tests), require experimental data as presented here.

Acknowledgement

Helpful discussions with Abhinendra Singh and Bert Scheper as well as the help from Bruno E. Chávez Montesareon on experimental set-ups are gratefully acknowledged. This work is financially supported by the T-MAPPP project of the European-Union-funded Marie Curie Initial Training Network FP7 (ITN607453); see http://www.t-mappp.eu/ for more information.

Nomenclature

ρ_p	Particle density (kg/m^3)
ρ_0	Initial bulk density (kg/m^3)
ρ_b	Bulk density (kg/m^3)
w	Moisture content (%)
d_{10}	Particle diameter where 10 % of distribution is below this value (μm)
d_{50}	Particle median size where 50 % of distribution is below this value (μm)

d_{90}	Particle diameter where 90 % of distribution is below this value (µm)
Ψ	Roundness ([–])
τ	Shear stress (kPa)
τ_{ss}	Steady state shear stress (kPa)
τ_{p}	Peak failure shear stress (kPa)
σ_{n}	Normal stress (kPa)
σ_{pre}	Pre-shear normal stress (kPa)
c	Cohesive strength of yield locus or bulk cohesion (kPa)
c_{ss}	Cohesive strength of steady state locus (kPa)
σ_{c}	Unconfined yield strength (kPa)
σ_1	Major consolidation stress (kPa)
σ_2	Minor consolidation stress (kPa)
ϕ	Angle of internal friction (°)
ϕ_{e}	Effective angle of internal friction (°)
ϕ_{ss}	Steady state angle of internal friction (°)
ff_{c}	Flowability ([–])

References

Akers R.J., The certification of a limestone powder for Jenike shear testing (CRM 116), *EUR (Luxembourg)*, 1992.

Alonso-Marroquin F., Herrmann, H.J., Ratcheting of granular materials, Physics Review Letter, 92 (2004) 54301.

Alshibli K.A., Sture, S., Shear band formation in plane strain experiments of sand, Journal of Geotechnical and Geoenvironmental Engineering, 126 (2000) 495–503.

ASTM-D6128-16, Standard test method for shear testing of bulk solids using the Jenike shear cell, West Conshohocken, PA: ASTM International, 2006.

ASTM-D6773-16, Standard shear test method for bulk solids using the Schulze ring shear tester, West Conshohocken, PA: ASTM International, 2008.

ASTM-D7891-15, Standard test method for shear testing of powders using the freeman technology FT4 powder rheometer shear cell, West Conshohocken, PA: ASTM International, 2015.

Bardet J.P., Experimental Soil Mechanics, Prentice-Hall, Upper Saddle River, New Jersey, 1997.

Berry R.J., Bradley M.S.A., McGregor R.G., Brookfield powder flow tester-Results of round robin tests with CRM-116 limestone powder, Proceedings of the Institution of Mechanical Engineers, Part E: Journal of Process Mechanical Engineering, 229 (2015) 215–230.

Bi D., Zhang J., Chakraborty B., Behringer R.P., Jamming by shear, Nature, 480 (2011) 355–358.

Carr J.F., Walker D.M., An annular shear cell for granular materials, Powder Technology, 1 (1968) 369–373.

Casagrande A., The determination of the pre-consolidation load and its practical significance, Proceedings of the international conference on soil mechanics and foundation engineering, 3 (1936) 60–64.

Cates M.E., Haw M.D., Holmes C.B., Dilatancy, jamming, and the physics of granulation, Journal of Physics: Condensed Matter, 17 (2005) S2517.

Cundall P.A., Numerical experiments on localization in frictional materials, Ingenieur-Archiv, 59 (1989) 148–159.

Feise H.J., A review of induced anisotropy and steady-state flow in powders, Powder Technology, 98 (1998) 191–200.

Feise H., Schwedes J., Investigation of the Behaviour of Cohesive Powder in the Biaxial Tester, KONA Powder Particle Journal, 13 (1995) 99–104.

Fitzpatrick J.J., Barringer S.A., Iqbal T., Flow property measurement of food powders and sensitivity of Jenike's hopper design methodology to the measured values, Journal of Food Engineering, 61 (2004) 399–405.

Freeman R., Measuring the flow properties of consolidated, conditioned and aerated powders—A comparative study using a powder rheometer and a rotational shear cell, Powder Technology, 174 (2007) 25–33.

Freeman R.E., Cooke J.R., Schneider L.C.R., Measuring shear properties and normal stresses generated within a rotational shear cell for consolidated and non-consolidated powders, Powder Technology, 190 (2009) 65–69.

GDR-MiDi, On dense granular flows, European Physical Journal E–Soft Matter, 14 (2004) 341–365.

Harder J., Schwedes J., The development of a true biaxial shear tester, Particle & Particle Systems Characterization, 2 (1985) 149–153.

Imole O.I., Paulick M., Magnanimo V., Morgeneyer M., Montes B.E., Ramaioli M., Kwade A., Luding S., Slow stress relaxation behavior of cohesive powders, Powder Technology, 293 (2016) 82–93.

Janssen R.J.M., Zetzener H., Measurements on cohesive powder with two biaxial shear testers, Chemical Engineering & Technology, 26 (2003) 147–151.

Jenike A.W., Storage and Flow of Solids, Bulletin No. 123, Bulletin of the University of Utah, 53 (1964).

Jenike A.W., Quantitative design of mass-flow bins, Powder Technology, 1 (1967) 237–244.

Jenike A.W., Storage and flow of solids. bulletin no. 123, vol. 53, no. 26, November 1964, Technical report, Utah University, Salt Lake City (USA), 1976.

Kamath S., Puri V.M., Manbeck H.B., Flow property measurement using the Jenike cell for wheat flour at various moisture contents and consolidation times, Powder Technology, 81 (1994) 293–297.

Kamath S., Puri V.M., Manbeck H.B., Hogg R., Flow properties of powders using four testers-measurement, comparison and assessment, Powder Technology, 76 (1993) 277–289.

Koynov S., Glasser B., Muzzio F., Comparison of three rotational shear cell testers: Powder flowability and bulk density, Powder Technology, 283 (2015) 103–112.

Kumar N., Luding S., Memory of jamming–multiscale models for soft and granular matter, Granular Matter, 18 (2016) 1–21.

Liu A.J., Nagel S.R., Nonlinear dynamics: Jamming is not just cool any more, Nature, 396 (1998) 21–22.

Luding S., Anisotropy in cohesive, frictional granular media, Journal of Physics: Condensed Matter, 17 (2005a) S2623–S2640.

Luding S., Shear flow modeling of cohesive and frictional fine powder, Powder Technology, 158 (2005b) 45–50.

Luding S., Cohesive, frictional powders: contact models for tension, Granular Matter, 10 (2008) 235–246.

Luding S., Granular matter: So much for the jamming point, Nature, 12 (2016) 531–532.

Majmudar T.S., Behringer R.P., Contact force measurements and stress-induced anisotropy in granular materials, Nature, 435 (2005) 1079–1082.

Morgeneyer M., Brendel L., Farkas Z., Kadau D., Wolf D.E., Schwedes J., Can one make a powder forget its history?, Proceedings of the 4th international conference for conveying and handling of particulate solids, Budapest, 2003, pp. 12–118.

Morgeneyer M., Schwedes J., Investigation of powder properties using alternating strain paths, Task Quarterly, 7 (2003) 571–578.

Rabinovich Y.I., Adler J.J., Ata A., Singh R.K., Moudgil B.M., Adhesion between nanoscale rough surfaces: I. Role of asperity geometry, Journal of Colloid and Interface Science, 232 (2000) 10–16.

Radjai F., Jean M., Moreau J.J., Roux S., Force distribution in dense two-dimensional granular systems, Physical Review Letters, 77 (1996) 274–277.

Radjai F., Roux S., Moreau J.J., Contact forces in a granular packing, Chaos: An Interdisciplinary Journal of Nonlinear Science, 9 (1999) 544–550.

Rumpf H., Particle technology, Chapman & Hall, London/New York, 1990.

Russell A., Müller P., Shi H., Tomas J., Influences of loading rate and preloading on the mechanical properties of dry elasto-plastic granules under compression, AIChE Journal, 60 (2014) 4037–4050.

Salehi H., Barletta D., Poletto M., A comparison between powder flow property testers, Particuology, 32 (2017) 10–20.

Savage S.B., Hutter K., The motion of a finite mass of granular material down a rough incline, Journal of Fluid Mechanics, 199 (1989) 177–215.

Schulze D., Entwicklung und Anwendung eines neuartigen Ringschergerätes, Aufbereitungs-Technik, 35 (1994) 524–535.

Schulze D., Flow properties of bulk solids (v), Deutsche Keramische Gesellschaft und Nederlandse Keramische Vereniging, Annual Meeting 2002, Eindhoven., 2002, pp. 21–23.10.

Schulze D., Time- and velocity-dependent properties of powders effecting slip-stick oscillations, Chemical Engineering & Technology, 26 (2003a) 1047–1051.

Schulze D., Towards more reliability in powder testing (v), Proceedings of the 4th international conference for conveying and handling of particulate solids (CHoPS), Budapest, 2003b, pp. 5–31.

Schulze D., Powders and bulk solids: behavior, characterization, storage and flow, Springer, 2008.

Schulze D., Round robin test on ring shear testers, Advanced Powder Technology, 22 (2011) 197–202.

Schulze D., Beispiele gemessener Fließeigenschaften, in ‘Pulver und Schüttgüter’, Springer, 2014a, pp. 249–268.

Schulze D., Verfahrenstechnische Siloauslegung, in ‘Pulver und Schüttgüter’, Springer, 2014b, pp. 335–360.

Schwedes J., Vergleichende Betrachtungen zum Einsatz von Schergeräten zur Messung von Schüttguteigenschaften, Proceedings of PARTEC, Nürnberg, 1979, pp. 278–300.

Schwedes J., Review on testers for measuring flow properties of bulk solids, Granular Matter, 5 (2003) 1–43.

Schwedes J., Schulze D., Measurement of flow properties of bulk solids, Powder Technology, 61 (1990) 59–68.

Shibuya S., Mitachi T., Tamate S., Interpretation of direct shear box testing of sands as quasi-simple shear, Geotechnique, 47 (1997) 769–790.

Singh A., Magnanimo V., Saitoh K., Luding S., Effect of cohesion on shear banding in quasistatic granular materials, Physical Review E, 90 (2014) 022202.

Teunou E., Fitzpatrick J.J., Synnott E.C., Characterisation of food powder flowability, Journal of Food Engineering, 39 (1999) 31–37.

Thakur S.C., Ahmadian H., Sun J., Ooi J.Y., An experimental and numerical study of packing, compression, and caking behaviour of detergent powders, Particuology, 12 (2014) 2–12.

Tomas J., Product design of cohesive powders – Mechanical properties, compression and flow behavior, Chemical Engineering & Technology, 27(6) (2005) 605–618.

Tsunakawa H., Aoki R., Measurements of the failure properties of granular materials and cohesive powders, Powder Technology, 33 (1982) 249–256.

Van Hecke M., Jamming of soft particles: geometry, mechanics, scaling and isostaticity, Journal of Physics: Condensed Matter, 22 (2009) 033101.

Witt W., Altrogge D., Rutsch O., High speed image analysis and dispersion for size and shape characterisation on fibres, Proceedings of 5th World Congress of Particle Technology, 2006.

Wolf B., Scirocco R., Frith W.J., Norton I.T., Shear-induced anisotropic microstructure in phase-separated biopolymer mixtures, Food Hydrocolloids, 14 (2000) 217–225.

Yang Y., Fei W., Yu H.-S., Ooi J., Rotter M., Experimental study of anisotropy and non-coaxiality of granular solids, Granular Matter, 17 (2015) 189–196.

Zetzener, H. Schwedes, J., Relaxation and creep of dry bulk solids, Particle & Particle Systems Characterization, 19 (2002) 144–148.

Appendix A. Test details on yield locus and steady state locus

Table A1 Summary of pre-shear/shear normal stress values used in each shear device to measure yield locus.

Device	Samples	Normal stress applied (kPa)
RST-01	Eskal 300, 500, 15, 30, 80, 150, K0.1–0.5	Pre-shear at 5 Shear at 0.5, 1, 1.5, 2, 3
	Eskal 300, 500, 15, 30, 80, 150, K0.1–0.5, K0.5–0.8	Pre-shear at 20 Shear at 2, 5, 8, 12, 16
	Eskal 300, 500, 15, 30, 80, 150, K0.1–0.5	Pre-shear at 35 Shear at 2, 5, 10, 15, 20
RST-XS	Eskal 300, 500, 15, 150	Pre-shear at 4.3 Shear at 0.35, 0,85, 1.4, 2.1, 3.6
DST	Eskal 300, 500, 15, 150	Pre-shear at 36.1 Shear at 1.4, 13.9, 19.4, 25, 30.5
FT4	Eskal 300, 500, 15, 150	Pre-shear at 20 Shear at 0.1, 0.5, 1, 2, 5, 8, 16
Jenike	Eskal 300, 150	Pre-shear at 5 Shear at 0.5, 1.5, 3

Table A2 Summary of normal stress values applied using direct shear tester (DST) to measure steady state locus.

Samples	Normal stress applied (kPa)
Eskal 300, 500, 15, 150	1.4, 2.8, 4.2, 5.5, 6.9, 8.2, 9.6, 11, 12.3, 13.9, 19.4, 25, 30.5, 36.1
Eskal K0.1–0.5	13.9, 36.1
Eskal K0.5–0.8	13.9, 19.4, 25, 30.5, 36.1

Appendix B. Test results of all the powders and devices shown in this paper

Table B1 Data measured from RST-01 for several Eskal powders and different pre-shear stresses.

Device	Sample	d_{50} (μm)	σ_{pre} (kPa)	c (kPa)	σ_1 (kPa)	σ_c (kPa)	ρ_b (kg/m^3)	ϕ_e (°)	ϕ (°)	ϕ_{ss} (°)
RST-01	K0.5–0.8	938	5	0.08	11.49	0.33	1288.00	41.37	40.57	38.97
			20	0.23	45.77	0.51	1275.67	42.53	42.37	40.30
			35	0.06	88.49	0.27	1299.67	42.30	42.23	41.20
	K0.1–0.5	223	5	0.33	9.47	1.33	1463.33	40.37	37.00	35.87
			20	0.45	39.23	1.82	1506.00	38.67	37.60	35.90
			35	0.58	70.17	2.33	1531.67	38.60	37.87	36.27
	Eskal150	138	5	0.01	8.53	0.06	1386.00	32.93	32.22	31.00
			20	0.10	35.34	0.31	1392.33	33.33	33.17	31.37
			35	0.21	66.07	0.19	1400.33	33.93	33.87	31.67
	Eskal80	71	5	0.08	8.88	0.31	1319.33	34.43	32.80	31.87
			20	0.07	35.02	0.25	1341.67	33.10	32.97	31.10
			35	0.19	63.9	0.68	1356.33	32.77	32.50	31.53
	Eskal30	30	5	0.09	8.83	0.31	1309.67	33.03	32.17	31.37
			20	0.14	34.84	0.49	1331.00	33.07	32.73	31.00
			35	0.20	62.20	0.74	1342.00	32.67	32.40	31.07
	Eskal15	19	5	0.21	9.44	0.82	1247.00	36.73	34.63	34.13
			20	0.34	37.08	1.23	1257.67	35.77	34.97	33.77
			35	0.42	64.34	1.31	1262.00	35.13	34.67	33.00
	Eskal500	4.42	5	0.86	10.47	3.25	1011.33	44.43	36.30	39.53
			20	1.76	39.45	5.44	1157.67	39.87	35.70	36.60
			35	1.97	67.79	6.17	1190.00	39.33	37.20	36.03
	Eskal300	2.22	5	1.52	11.33	6.21	760.67	51.20	36.97	43.53
			20	3.59	43.06	12.97	861.00	43.87	36.37	39.93
			35	4.57	72.81	17.82	932.33	43.47	38.43	39.17

Table B2 Data measured from RST-XS, FT4 and DST for several Eskal powders and different pre-shear stresses.

Device	Sample	d_{50} (μm)	σ_{pre} (kPa)	c (kPa)	σ_1 (kPa)	σ_c (kPa)	ρ_b (kg/m^3)	ϕ_e (°)	ϕ (°)	ϕ_{ss} (°)
RST-XS	Eskal150	138	4.3	0.01	7.67	0.13	1447.67	34.13	32.00	29.93
	Eskal15	19		0.07	7.91	0.26	1416.67	34.57	33.80	32.53
	Eskal500	4.42		0.41	8.70	0.93	1015.00	40.83	38.33	37.50
	Eskal300	2.22		1.09	9.39	4.16	767.67	50.90	39.03	42.97
FT4	Eskal150	138	20	0.12	30.88	0.43	1441.45	33.75	33.41	24.91
	Eskal15	19		0.20	32.57	0.75	1297.10	33.51	32.95	29.82
	Eskal500	4.42		0.75	36.68	2.94	1081.57	37.59	35.68	34.16
	Eskal300	2.22		1.92	41.06	7.75	782.16	41.82	37.20	38.21
DST	Eskal150	138	36.08	0.86	59.83	1.95	1429.09	32.61	31.00	31.22
	Eskal15	19		1.30	60.83	3.10	1281.59	35.83	34.08	34.91
	Eskal500	4.42		2.13	61.33	7.40	1204.08	37.60	34.61	35.24
	Eskal300	2.22		3.67	64.47	10.07	952.30	42.01	37.21	38.27
Jenike	Eskal150	138	5	0.22	18.17	0.35	1445.63	35.31	34.13	32.09
	Eskal300	2.22		1.71	11.30	7.17	788.91	47.95	33.83	37.95

Appendix C. The explanation on the graphical abstract

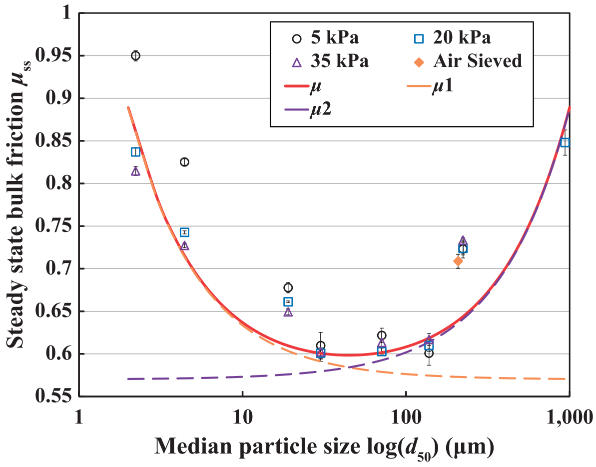

Fig. C1: Steady state bulk friction, $\mu_{ss} = \tan(\phi_{ss})$, plotted against median particle size, d_{50}. Solid line is the fitted function, μ, in Eq. (1C). Orange and purple dashed lines represent contributions from inter-particle cohesion and geometrical/inter-locking, respectively.

In Fig. C1, we have plotted the same data as shown in Fig. 20(b), but with a proposed theory which fits the data with $\sigma_{pre} = 20$ kPa:

$$\mu = \mu_0 \left(1 + \frac{d_{c\mu}}{d_{50}} + \frac{d_{50}}{d_{g\mu}} \right) \tag{1C}$$

where, the fitted values are $\mu_0 = 0.57$, $d_{c\mu} = 1.12$ µm and $d_{g\mu} = 1790$ µm with "c" denoting cohesion and "g" geometry. In Fig. C1, the curve $\mu 1$ represents the first contribution inversely proportional to d_{50} due to inter-particle cohesion, which decays to zero with increasing particle size and it has the same power law as the cohesive strength, see Fig. 19(b). In contrast, the second term $\mu 2$ is an empirical relation due to contributions from particle geometrical/inter-locking, which increases with particle size. The combination of these two contributions gives the total steady state bulk friction of the limestone powders in Eq. (1C).

Author's short biography

Hao Shi

Hao Shi is a PhD candidate in the MSM (Multi-Scale Mechanics) group at the faculty of engineering technology (ET) chaired by Prof. Stefan Luding at University of Twente, the Netherlands. He completed his BEng degree in refrigeration and air-conditioning engineering at Nanjing Institute of Technology (2011), China. He received his MSc degree in chemical and energy engineering at Otto-von-Guericke University (2013), Magdeburg, Germany, where he worked in the mechanical process engineering group chaired by Prof. Jürgen Tomas. Later, he joined the MSM group in 2014 for his PhD study which is based on the Marie Curie training network "T-MAPPP". His research interests range from tabletting processes for cohesive powders to discrete element simulations of granular assemblies with the development of calibration and validation protocols as well as other industry-relevant research studies. He collaborates with other researchers in various institutions and industries including TU Braunschweig in Germany, UT Compiegne in France, P&G in UK and the university of Edinburgh in UK.

Rahul Mohanty

In 2013, Rahul Mohanty completed his master studies in Material Resource Engineering at AcSIR University, India. In the same year, he joined CSIR-IMMT, India, as a Quick Hire Scientist for a one-year internship. In September 2014, he joined iPAT—research group "Bulk Solids and Granular Matters" as a research associate in TU Braunschweig, Germany. Later in September 2015, he moved to P&G UK, Newcastle, continuing his research as a research scientist based on the Marie Curie training network "T-MAPPP". His research interest is to investigate the dry as well as wet contact adhesion for the chosen processes, in order to develop a DEM model for quasi-static and dynamic processes and validation against simple tests, and to develop an upscaling procedure from a DEM particle model to process a scale compartment model.

Somik Chakravarty

Somik Chakravarty completed his BEng in mechanical engineering at the University of Sheffield and MSc in Thermal power and fluids engineering at the University of Manchester, UK. He is presently on an EU FP7 Marie Curie fellowship (T-MAPPP) working as an early stage researcher at the University of Technology of Compiègne (UTC), France, in the field of characterization of mechanical properties of bulk solids. His research interests include powder handling and processing, characterization of powders by their flow properties and dustiness. He collaborates with researchers in academia and industry including TU Braunschweig, BASF, INERIS, and the University of Twente.

Author's short biography

Ramon Cabiscol Martinoli

Ramon Cabiscol studied chemical engineering from 2008 to 2013 at the Institut Químic de Sarrià in Barcelona. He received a DAAD scholarship in 2013 for postgraduate students to perform a research internship at the Technische Universität Braunschweig. His scientific interests include powder handling and flowability, tableting technology and numerical modelling of compaction. He is currently part of the Marie Curie training network "T-MAPPP". He is carrying out his PhD on "Modelling of abrasion of pharmaceutical tablets" at the Institute for Particle Technology and the Center for Pharmaceutical Engineering (PVZ), both in Braunschweig.

Martin Morgeneyer

Martin Morgeneyer works at Compiègne University of Technology (UTC), France, and his research focuses on powder and particle properties. He studied in Braunschweig, Compiègne and Zaragoza, received his degree in mechanics and his PhD in powder mechanics from the Technical University of Braunschweig, Schwedes' group. Prior to joining UTC as VP International Relations, Morgeneyer worked at Unilever in Warrington, and was responsible for internationalization at the Faculty of Mechanical Engineering at Braunschweig, of which he became the managing director later on. He now serves as chair of the Working Party on Characterization of Particulate Systems at the EFCE.

Harald Zetzener

Harald Zetzener studied mechanical engineering from 1989 to 1996 at the Technische Universität Braunschweig. He finished his PhD thesis on "Determination of rate-dependent deformation behaviour of cohesive powders in a bi-axial test" in 2002. He performed a post-doc at the Telemarks Technical Research and Development Centre in Porsgrunn, Norway. Afterwards he worked as Supply Quality Manager for Reckitt Beckinser before assuming the position of Deputy Director of the Institute for Particle Technology. His field of expertise is particle technology and design of equipment.

Jin Ooi

With a BEng (Hons) degree from the University of Auckland and a PhD from the University of Sydney, Jin Ooi joined the University of Edinburgh in 1990 and has been the professor of Particulate Solid Mechanics since 2005. His research covers both computational and experimental studies of of powders and solids, from particle phenomena to bulk characteristics, and applications in industrial processes. Jin enjoys collaboration with academic and industrial partners. He has published extensively with over 150 journal and conference papers and several book chapters. He is on the editorial board for Canadian Geotechnical Journal and Acta Geotechnica, and has co-founded DEM Solutions Ltd. and Particle Analytics Ltd.

Author's short biography

Arno Kwade

Arno Kwade studied mechanical engineering from 1986 to 1992 at the Technische Universität Braunschweig and the University of Waterloo. He finished his PhD thesis on "Autogenous Grinding in Stirrred Media Mills" in 1996. Afterwards he worked as general manager and executive director before he started his career as full professor for mechanical process engineering in 2005 at the Institute for Particle Technology. He is the head of the Centre of Pharmaceutical Engineering (PVZ) and member of the board of the Automotive Research Centre Niedersachsen (NFF). His main research focuses on experimental and numerical investigations in the fields of grinding and dispersing, flow and compression of powders as well as preparation of particulate coatings.

Stefan Luding

Stefan Luding studied physics at the University of Bayreuth, Germany, on reactions on complex and fractal geometries. He continued his research and moved to Freiburg for his PhD on simulations of dry granular materials in the group of polymer physics with-Prof. A. Blumen. Then he spent his postdoc time in Paris VI, Jussieu, with E. Clément and J. Duran before he joined the group of Computational Physics with Prof. Herrmann, where he did his habilitation. In 2001, he moved to DelftChemTech at the TU Delft in Netherlands as Associate Professor in Particle Technology. Since 2007 he holds the chair on Multi-Scale Mechanics (MSM) at the Faculty of Engineering Technology, ET, at the University of Twente, the Netherlands, with ongoing research on fluids and solids, particles and their contacts, granular materials and powders, asphalt, composites, bio- and micro-fluid systems and self-healing materials. Since 1998 he is managing Editor in Chief of the journal Granular Matter and since 2005 president of AEMMG, the scientific organizing committee of the Powders & Grains conference series.

Vanessa Magnanimo

Vanessa Magnanimo is an Assistant Professor (UD1) in the Department of Thermal and Fluid Engineering within the Faculty of Engineering Technology at the University of Twente. She is part of the Multi-Scale Mechanics group. Vanessa received her MSc degree in construction engineering from the Politecnico of Bari, Italy, and received her PhD in Continuum Mechanics from the same university. After her PhD and before joining the University of Twente as a postdoc in 2010, she worked as a consultant in a structural engineering firm. She was a visiting scientist at the Levich Institute—CCNY and at T&AM—Cornell University. Vanessa is currently principal investigator in EU- and industrially-funded projects. She was part of the editorial board for Géotechnique and Powder Technology and is presently chair of the Female Faculty Network Twente. Vanessa's broad research interests are primarily in the area of theoretical analysis and modern simulation techniques applied to constitutive modelling of materials with an internal micro-structure such as soils and powders.

KONA Powder and Particle Journal No. 35 (2018) 251–257/Doi:10.14356/kona.2018016 Original Research Paper

Forces on Particles in Time-Varying Magnetic Fields[†]

Jaclyn D. Ray, James R. Nagel, Dave Cohrs and Raj K. Rajamani[*]
[1] *Department of Metallurgical Engineering, University of Utah, USA*

Abstract

Electrodynamic sorting is a process that sorts metals based on conductivity, density, and geometry. The process works by inducing electrical eddy currents within particles placed in a time-varying magnetic field. For the special case of a perfect, uniform sphere, an approximate equation can be used to predict the net force under a linear magnetic gradient. This paper explores the accuracy of that model by measuring the net force on spherical samples of copper, brass, and aluminum with varying sizes and excitation frequencies. Results consistently show strong agreement with the approximate models over all conditions. We also explore several non-spherical geometries, including cylinders, cubes, and disks. We found that they could be modeled as equivalent spheres, given an appropriate radius, and had reasonable accuracy over frequency.

Keywords: electrodynamics, eddy current, time-varying magnetic field, scrap metal waste

1. Introduction

Scrap metal recycling is a high-value industry that reduces pollution from primary production. As it can potentially be recycled an infinite number of times, scrap metal may even eliminate the mining of some metals altogether. This factor alone is significant since reducing the primary production of metals is becoming an essential means of decreasing man-made pollutants that aggravate the environment (Förstner et al., 2012). In 2016, for example, aluminum recovered from old scrap was equivalent to about 31 % of apparent consumption while copper scrap contributed similar values to the total US supply (USGS, 2017). Such low percentages of recycled material reveal the importance of investing in scrap metal recycling.

Since the value of scrap metal depends heavily on purity, a key aspect of the recycling process is sorting. Obtaining high-grade metal, however, can be economically difficult for many reasons. Alloys, for example, often have nearly indistinguishable properties and are thus difficult to tell apart. Furthermore, the material feedstock might vary from day-to-day. Automobiles, for instance, have changed dramatically in composition since the 1980s and continue to do so today (Wernick and Themelis, 1998). Consequently, there is strong economic incentive to find efficient new methods for purifying scrap metal.

To meet this challenge, several technologies exist to recover metals from mixed material streams. Magnetic separators, for example, remove ferrous material through the use of fixed permanent magnets (Oberteuffer, 1974). Dense media separation recovers certain nonferrous metals by separating light elements from the heavy (Weiss, 1985). Mechanical eddy current separators recover electrically conductive metals from non-conductive materials by rotating a drum of alternating north/south magnets (Rem et al., 1998). Metallic particles entering the magnetic field are excited with electrical eddy currents, which in turn accelerate the particle due to magnetic forces against the moving electrical charge. Even hand sorting by visual inspection can be effective in certain developing countries where the cost of human labor is very low (Wilson et al., 2006).

Despite the many available technologies, material recovery is still very limited. For example, magnetic separators can only recover ferrous materials from nonferrous. Density separation cannot distinguish between alloys with similar densities. Mechanical eddy current separators are generally only effective on particles greater than an inch in size and when the materials that are being separated have significantly different conductivity (Norrgran and Wernham, 1991). Hand sorters cannot easily distinguish between metals that look alike nor can they effectively process small particles in large quantity.

One emerging technology that addresses many of these problems is electrodynamic sorting (EDX) (Dholu et al., 2017; Smith et al, 2017). The process is similar to mechanical eddy current separation but, rather than spin an array of permanent magnets, it utilizes a fixed electromagnet.

[†] Received 8 May 2017; Accepted 1 August 2017
J-STAGE Advance published online 30 September 2017

[1] 135 S 1460 E, ROOM 412, Salt Lake City, UT 84112-0102, USA
[*] Corresponding author: Raj K. Rajamani
E-mail: raj.rajamani@utah.edu
TEL: +01-801-587-8329

Unlike mechanical eddy current separators, however, EDX can reach far higher frequencies of excitation and thus operate on particles well below an inch in size. The tunability of frequency and intensity also allows for separation as a function of density, conductivity, and even geometry.

Although the basic principle of EDX has been demonstrated empirically, there does not yet exist a clear mathematical framework by which to model the forces on scrap metal particles. The most relevant contributions to date appear to stem from Peter Rony (1964) and George Lohöfer (1989), both of whom studied the heating effects of eddy current induction on uniform spheres. More recently, Bidinosti et al. (2007), developed a workable model for the eddy current distribution throughout a uniform metal sphere in a time-varying magnetic field. The recent work of Nagel (2017) has also helped to formalize the theory of eddy current induction in various canonical geometries. To date, however, there still has yet to be any direct application of this theory to the field of scrap metal recycling.

This paper seeks to validate the theoretical predictions of forces acting on metal particles in a time-varying magnetic field. We begin by reviewing the relevant theory on the subject and modeling the net force acting on a uniform metal sphere. We then test that model by measuring the forces on several spherical particles under excitation by an EDX magnet. Lastly, we expand on that analysis by fitting the same equations to non-spherical geometries in an effort to quantify the behavior of more realistic particles. Results show that even non-spherical particles can be reasonably represented by spheres, thus greatly enhancing our ability to predict the behavior of scrap metal particles as they travel through an EDX magnet.

2. Theory

We consider a sphere with known radius a and conductivity σ situated in a uniform magnetic field $\boldsymbol{B} = B_0 \cos(\omega t)\hat{\boldsymbol{z}}$. Since the excitation field is in a sinusoidal steady state, we can express this using phasor notation as simply $\boldsymbol{B} = B_0\hat{\boldsymbol{z}}$. Building on the work done by Rony (1964), the magnetic dipole moment $\boldsymbol{m}$ of the sphere can be shown to satisfy

$$\boldsymbol{m} = \frac{2\pi B_0 a^3}{\mu_0}\left[1 - 3\frac{ka\cosh(ka) - \sinh(ka)}{(ka)^2\sinh(ka)}\right]\hat{\boldsymbol{z}} \tag{1}$$

$$\boldsymbol{m} = m_z\hat{\boldsymbol{z}}, \tag{2}$$

where $k = \sqrt{j\omega\mu_0\sigma}$ and μ_0 is the permeability of free space. Due to the presence of the applied magnetic field $\boldsymbol{B}$, there also exists a net force $\boldsymbol{F}$ acting on $\boldsymbol{m}$, given by Jackson (1999)

$$\boldsymbol{F} = \nabla(\boldsymbol{m}\cdot\boldsymbol{B}). \tag{3}$$

It is important to note that Eqn. 2 is only a first-order approximation derived under the assumption of a linear magnetic field gradient. It also shows that a uniform magnetic field will produce no net force since the quantity $\boldsymbol{m}\cdot\boldsymbol{B}$ becomes constant. We therefore introduce a linear gradient α to the magnetic field such that $\boldsymbol{B} = (B_0 + \alpha x)\hat{\boldsymbol{z}}$. The gradient α is assumed to introduce only a small perturbation, meaning that $\boldsymbol{m}$ does not change significantly in the applied gradient. Substituting back into Eqn. 2 therefore reveals

$$\boldsymbol{F} = \nabla[m_z(B_0 + \alpha x)] \tag{4}$$

$$\boldsymbol{F} = \frac{\partial}{\partial x}[m_z B_0 + m_z \alpha x]\hat{\boldsymbol{x}} \tag{5}$$

$$\boldsymbol{F} = m_z \alpha \hat{\boldsymbol{x}}. \tag{6}$$

Noting that $\boldsymbol{F}$ is still a phasor quantity in sinusoidal steady state, we next calculate the time-averaged force using

$$\boldsymbol{F}_{\text{avg}} = \frac{1}{2}Re\{\boldsymbol{F}\}, \tag{7}$$

where $Re\{x\}$ denotes the real part of x. After some lengthy derivation, the time-averaged force finally evaluates to

$$\boldsymbol{F}_{\text{avg}} = -\frac{3\pi B_0 \alpha a^3}{\mu_0}\left[\frac{1}{3} - \frac{1}{q}\frac{\sinh(q) - \sin(q)}{\cosh(q) - \cos(q)}\right]\hat{\boldsymbol{x}}, \tag{8}$$

where $q = 2a/\delta$ and $\delta = \sqrt{2/(\omega\mu_0\sigma)}$ is the skin depth.

3. Method

Fig. 1 shows a diagram of the experimental configuration. A signal generator sets a desired frequency and voltage, which is then fed to a high-current amplifier. In order to negate the high impedance from the magnetic induc-

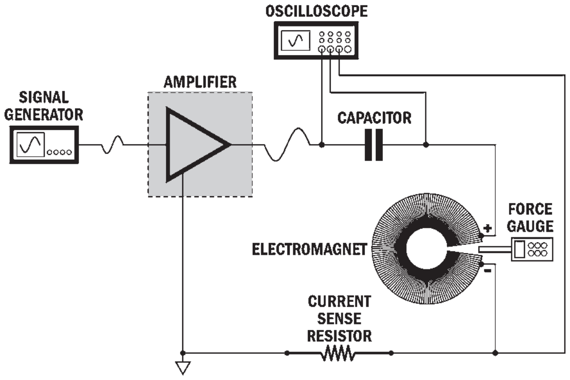

Fig. 1 Schematic representation of the force measurement circuit.

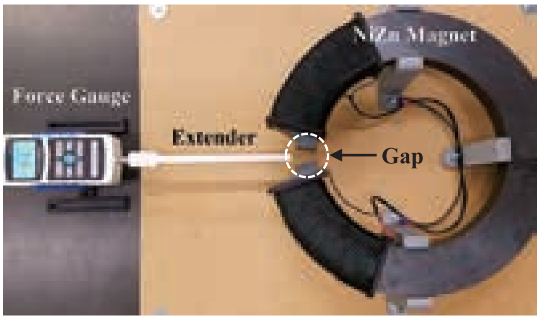

Fig. 2 NiZn magnet and force gauge used for experiment.

tance, a capacitor bank is placed in series with the inductor to create a resonant RLC circuit. A 1.0-Ω resistor is also placed in series with the capacitors to serve as a current-sense resistor for the entire circuit.

A custom-built 360-mm NiZn toroid magnet and a Mark-10 force gauge were used for our measurements. Depicted in **Fig. 2** the magnet is wound with 300 turns, using 18-gauge Teflon-insulated stranded-copper wire. At one end of the magnet, a specialized air gap was cut out so as to channel the magnetic field into a small volume of space. Once the system was activated, any test particles placed inside the gap were accelerated into the force gauge, thereby producing a force measurement. To negate gravity, the test particles were also glued to non-conductive string and suspended in the gap.

Because the probe on the force gauge is made out of metal, it could not be placed near the magnetic gap during excitation. To address this issue, a 3D-printed plastic extender was attached to the force gauge. The extender was then placed directly in front of the test particle, thereby catching it as soon as it was acted on by the magnetic field. The force then transferred directly down the rigid extender and into the gauge, resulting in a reliable force measurement.

Fig. 3 shows some metal samples used for our measurements. Though the theoretical model is technically only supposed to apply to spheres, industrial scrap metals rarely present as such perfect shapes. We were therefore particularly interested in testing the validity of Eqn. 8 on non-spherical geometries. The particle sizes used in this experiment ranged from 5 to 13 mm to represent typical sizes of fine scrap material. Each sample was also made from different metals and alloys, including copper, brass, and aluminum, which are commonly found in industrial scrap. For each metal shape, we likewise printed a unique plastic extender to fit the geometry. For example, an extender with a concave end would fit the spheres and cylinders, a flat end would hold the cubes, and a U-shaped end would steady the disks.

Fig. 4 shows the magnetic field profile that was measured at 10-A DC down the centerline of the gap. The peak of the field at $x = 0$ indicates the rear of the gap at the inner radius to the toroid. Measurements at several frequencies between 0–10 kHz also showed a fairly consistent field profile over the bandwidth of interest. The vertical bars indicate the region where test particles were inserted and measured. This specific region was chosen due to its approximate linearity, high field intensity, and physical space into which the particles could fit.

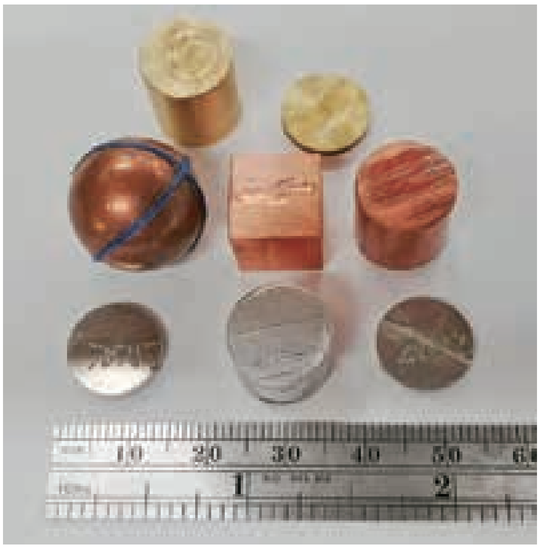

Fig. 3 Some test particles used in the force experiment.

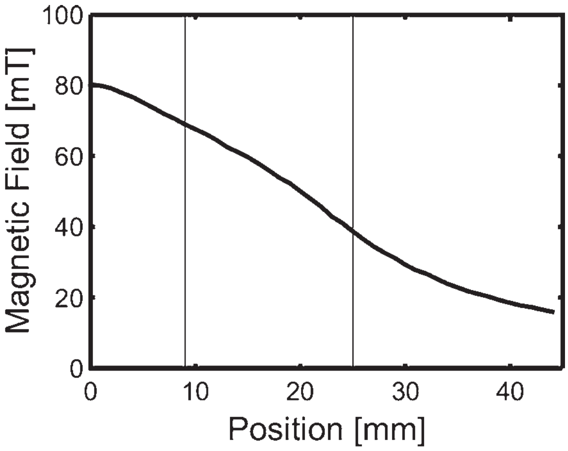

Fig. 4 Magnetic field versus position at DC. The vertical lines indicate the volume of space where test particles were measured.

Though the field profile was consistent across frequency, we did notice that the magnetic field decreased when particle samples were placed within the gap. This problem was caused by the eddy currents induced in the test sample itself, which tended to oppose the applied magnetic field of excitation. As a result, less magnetic flux would bridge the gap, thereby lowering the total inductance of the circuit. With the inductance lowered, the resonant frequency of the RLC circuit would shift slightly and thus lower the total drive current across the coils.

Since the excitation field is directly proportional to drive current, we compensated for it by simply increasing the drive voltage until the current reached its pretest amplitude.

Another problem we encountered during our measurements was thermal instability. When excited by a magnetic field, induced eddy currents tended to dissipate a great deal of heat throughout the particles. Even though measurements lasted for only a few seconds, the particle's temperature would often jump to over 100 °C. Since conductivity tends to somewhat vary with temperature, there was some worry about thermal consistency over the course of several measurements. To alleviate such concerns, all particles were immersed in a cup of ice water to ensure stable and reproducible temperatures before each test. Measurements were then repeated four times to ensure accuracy.

4. Results and Discussion

The first set of experiments focused solely on the spherical particles, with parameters displayed in **Table 1**. The radius r of each sphere was measured using a caliper. The magnetic field intensity $\boldsymbol{B}$ was measured from the center of the sphere using a Gauss probe and fixed to a value of 49.5 mT peak (or equivalently, 35 mT RMS) over all experiments. The field gradient α was then obtained by calculating the central difference around the center of each sphere. Note that there are small differences in α even though each measurement had the same magnetic field intensity. These differences are due to variations in the particle's placement in the gap, which was primarily determined by its size. Lastly, electrical conductivity σ of each particle was measured with a Fisher Sigmascope conductivity probe. Results from the spherical force measurements are summarized in **Fig. 5** and strongly agree with the predictions of Eqn. 8.

Table 1 Test parameters used in the force calculations of sphere samples.

Material	r [mm]	$\boldsymbol{B}$ [mT]	α [T/m]	σ [MS/m]
Al 2017	2.8	49.5	–1.7	16.1
Al 6061	6.1	49.5	–1.8	25.5
Al 2024	6.3	49.5	–1.7	17.3
Al 1100	6.3	49.5	–1.7	24.3
Brass	3.2	49.5	–1.7	13.8
Brass	9.5	49.5	–1.8	12.7
Copper	2.8	49.5	–1.8	46.6
Copper	7.5	49.5	–1.8	49.6

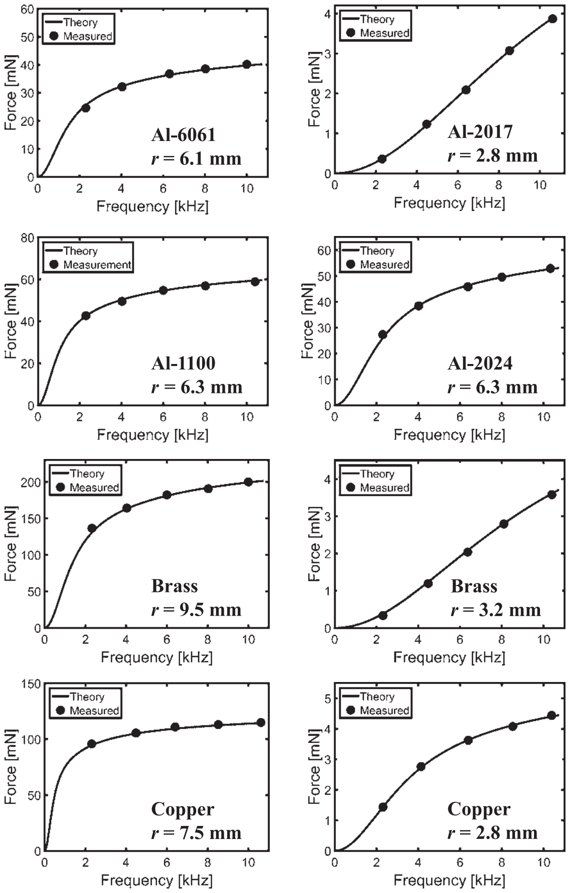

Fig. 5 Spherical force measurements compared to analytic calculations.

While encouraging, it is important to remember that scrap metal waste is rarely spherical. At the same time however, due to the strong predictability and convenience of Eqn. 8, we would still like to try and approximate non-spherical geometries as spheres. To that end, we note that for any arbitrary geometry at a given excitation frequency, there exists a hypothetical sphere which will experience the same force under identical conditions. If the radius of such a sphere were to remain consistent over a large bandwidth, then we can use that sphere as an approximate model for the non-spherical particle. To test this hypothesis, we measured the force on several non-spherical geometries and plotted their frequency response against an ideal sphere with an appropriate radius.

To derive an equivalent spherical radius, we began by calculating the equivalent volume of some non-spherical particle. For example, a cylinder could satisfy

$$\pi r_{\text{cyl}}^2 h = \frac{4}{3}\pi r_{\text{s}}^3, \tag{9}$$

where r_{cyl} is the measured radius of the cylinder, h is the cylinder height, and r_{s} is the radius of some equal-volume sphere. Solving for r_{s}, we have

$$r_\mathrm{s} = \sqrt[3]{\frac{4}{3} r_\mathrm{cyl}^2 h} \ . \tag{10}$$

We then multiply r_s by a correction coefficient ε to find

$$r_0 = \varepsilon r_\mathrm{s} \ , \tag{11}$$

where r_0 is the equivalent radius of a sphere that would produce the same force as the measured particle under identical conditions. If $\varepsilon < 1$, then it can be understood that $r_0 < r_\mathrm{s}$, thus implying a lower force density than would have been achieved if the particle were compacted into a sphere of equal volume. Likewise, for $\varepsilon > 1$, the particle has a higher force density than its equal-volume sphere. To find ε for a given particle, we simply searched over increments of 0.01 until the theoretical curve generated by Eqn. 8 reasonably fit the measured data.

Results of this experiment are summarized in **Fig. 6–8** with the parameters for each experiment summarized in **Tables 2–4**. For the cylinders, we found that ε was generally between 0.95–1.05. The only exception was a small brass cylinder, which may have been an experimental outlier. Cubes, however, were consistently between 0.92–0.99. The disks consistently resulted in ε values well above 1.2, which is most likely the result of their high cross-sectional area relative to their volume. If the disks were instead oriented along their minimum cross-section, then ε would naturally decrease accordingly. The key finding here, however, is that once a suitable r_0 was derived, Eqn. 8 seemed to produce a very good fit to the measured data. This seems to strongly indicate that even non-spherical particles can, in principle, be modeled in terms of some equivalent sphere over a large bandwidth.

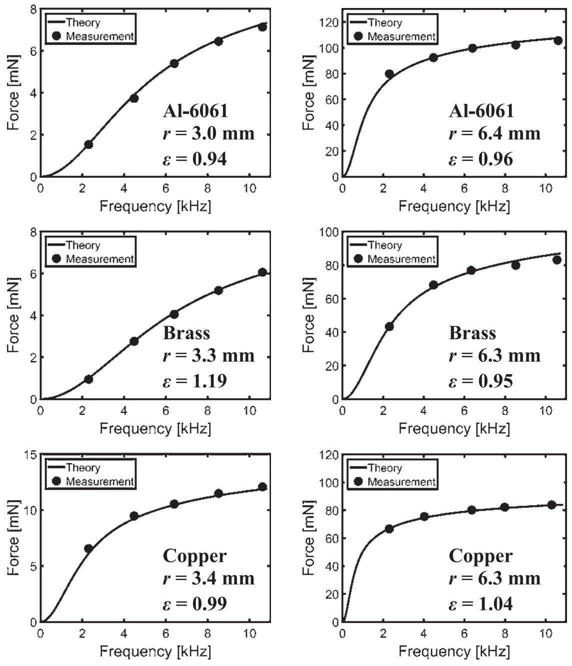

Fig. 6 Cylinder force measurements compared to analytical calculations.

In summary, we found that Eqn. 8 very accurately predicts the expected force on conductive spheres in the presence of a time-varying magnetic field. We also found that, given the appropriate equivalent radius, non-spherical geometries could likewise follow curves similar to Eqn. 8. Such knowledge has tremendous practical application in the field of magnetic separation of nonferrous metals.

To illustrate, consider the limit as $F \to \infty$. Since the net force found in Eqn. 8 is a function of the product between conductivity and frequency, all particles of similar geometry must eventually converge to the same value. Density, however, is a fixed property of the material itself and does not vary. For example, copper is roughly three times denser than aluminum, meaning an aluminum particle

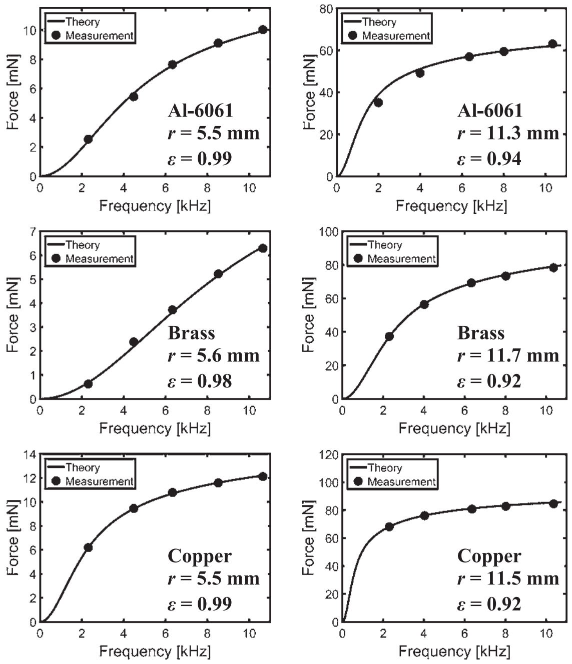

Fig. 7 Cube force measurements compared to analytical calculations.

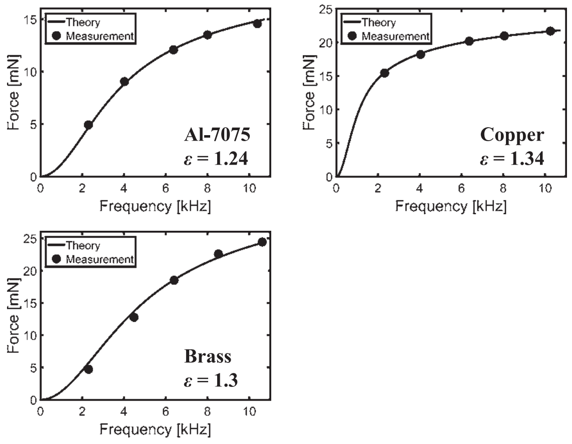

Fig. 8 Disk force measurements compared to analytical calculations.

Table 2 Test parameters used in the force measurements of cylinder samples with radius r and height h.

Material	r [mm]	h [mm]	$\boldsymbol{B}$ [mT]	α [T/m]	σ [MS/m]
Al 2017	3.0	6.1	49.5	–1.7	25.1
Al 6061	6.4	13.1	49.5	–1.8	12.8
Brass	3.3	6.2	49.5	–1.8	12.8
Brass	6.3	13.1	49.5	–1.7	12.8
Cu alloy	3.4	6.2	49.5	–1.7	54.1
Cu alloy	6.3	12.4	49.5	–1.7	50.1

Table 3 Test parameters used in the force measurements of cube samples with side length ℓ.

Material	ℓ [mm]	$\boldsymbol{B}$ [mT]	α [T/m]	σ [MS/m]
Al 6061	5.5	49.5	–2.3	25.1
Al 6061	11.3	49.5	–2.0	25.0
Brass	5.6	49.5	–2.3	12.8
Brass	11.7	49.5	–2.3	12.8
Copper	5.5	49.5	–2.3	54.0
Copper	11.5	49.5	–2.0	54.1

Table 4 Test parameters used in the force measurements of disk samples with radius r and height h.

Material	r [mm]	h [mm]	$\boldsymbol{B}$ [mT]	α [T/m]	σ [MS/m]
Al 7075	4.5	1.7	49.5	–1.5	18.2
Copper	5.0	1.7	49.5	–1.3	54.1
Brass	4.7	1.9	49.5	–1.9	12.8

will experience three times the acceleration under the same magnetic field. As was demonstrated by Dholu (2017), this allows us to separate aluminum from copper by simply throwing the aluminum particles a much further distance. Further research will be necessary to explore the practical limits of this concept on real-world industrial applications.

Acknowledgements

This work was funded by the United States Advanced Research Project Agency – Energy (ARPA-E) METALS Program under cooperative agreement grant DE-AR0000411. We would also like to thank Jake Salgado for 3D printing many of the necessary equipment and Dawn Sweeney for her insightful edits.

References

Bidinosti C.P., Chapple E.M., Hayden M.E., The sphere in a uniform RF field—Revisited, Concepts in Magnetic Resonance Part B: Magnetic Resonance Engineering, 31B (2007) 191–202.

Dholu N., Nagel J.R., Cohrs D., Rajamani R.K., Eddy current separation of nonferrous metals using a variable-frequency electromagnet, KONA Powder and Particle Journal, 34 (2017) 241–247.

Förstner U., Wittmann G.T.W., Eds., Metal Pollution in the Aquatic Environment, Springer Science & Business Media, 2012.

Jackson J.D., Ed., Classical Electrodynamics, 3rd Edition, Wiley, 1999.

Lohöfer G., Theory of an electromagnetically levitated metal sphere I: absorbed power, SIAM Journal on Applied Mathematics, 49 (1989) 567–581.

Nagel J.R., Induced eddy currents in simple conductive geometries due to a time-varying magnetic field, IEEE Antennas and Propagation Magazine (accepted, 2017).

Norrgran D.A., Wernham J.A., Recycling and secondary recovery applications using an eddy-current separator, Minerals & Metallurgical Processing, 8 (1991) 184–187.

Oberteuffer J., Magnetic separation: A review of principles, devices, and applications, IEEE Transactions on Magnetics, 10 (1974) 223–238.

Rem P.C., Beunder E.M., Akker A.J.v.d., Simulation of eddy-current separators, IEEE Transactions on Magnetics, 34 (1998) 2280–2286.

Rony P.R., The Electromagnetic Levitation of Metals, California. Univ., Berkeley. Lawrence Radiation Lab. and California. Univ., Berkeley, Tech. Rep., 1964.

Smith Y.R., Nagel J.R., Rajamani R.K., Electrodynamic eddy current separation of end-of-life PV materials, in: Zhang L., Drelich J.W., Neelameggham N.R. et al. (Eds.), Energy Technology 2017: Carbon Dioxide Management and Other Technologies, Springer International Publishing, Cham (2017) pp. 379–386.

USGS (United States Geological Survey), 2017, Mineral Commodity Summaries 2017 <minerals.usgs.gov/minerals/pubs/mcs/> accessed 03.08.2017.

Weiss N.L., Ed., SME Mineral Processing Handbook, Vol. 2, Society of Mining Engineers of the American Institute of Mining, Metallurgical, and Petroleum Engineers, 1985.

Wernick I.K., Themelis N.J., Recycling metals for the environment, Annual Review of Energy and the Environment, 23 (1998) 465–497.

Wilson D.C., Velis C., Cheeseman C., Role of informal sector recycling in waste management in developing countries, Habitat International, 30 (2006) 797–808.

Author's short biography

Jaclyn Ray

Jaclyn Ray completed her undergraduate degree in Physics from the University of Utah in Salt Lake City, in 2015. In 2016, she graduated with MS degree in Metallurgical Engineering also from the University of Utah. She currently works for Lockheed Martin Aerospace Skunk Works.

James Nagel

Dr James Nagel completed his undergraduate degree in 2004 and MS degree in 2006, both in Electrical Engineering, from Brigham Young University in Provo, Utah. He then completed his PhD in 2011, also in Electrical Engineering, from the University of Utah in Salt Lake City, Utah, and was awarded the Stockham Medal of Excellence for conspicuously effective teaching. He now works as a research associate for the University of Utah, where his research focuses on applied electromagnetics with a specialty in numerical methods.

Dave Cohrs

Dave studied Environmental Science with emphasis on Analytical Chemistry at University of Maryland, Baltimore County in Maryland. He managed water quality laboratories at public aquariums for 16 years and has consulted for aquariums, zoos, and academia on water chemistry and life support topics. He now works for the University of Utah as a research associate.

Raj Rajamani

Raj Rajamani has been on the faculty of the Metallurgical Engineering department of the University of Utah, Salt Lake City, Utah, USA since 1980. Currently he holds the position of professor. His research interest include population balance modeling of tumbling mills, computational fluid dynamics of hydrocyclones, discrete element modeling of semi-autogenous grinding mills, eddy current sorting of metallic particles and modeling of high pressure grinding rolls. He received the Antoine M. Gaudin Award, presented by the Society of Mining, Metallurgy and Exploration Engineers Inc. in the year 2009.

KONA Powder and Particle Journal No. 35 (2018) 258–272/Doi:10.14356/kona.2018017 Original Research Paper

Applicability of Probabilistic Nucleation Modelling for the Analysis of Microfluidics Data[†]

Florent Bourgeois[*], **Sébastien Teychené and Béatrice Biscans**

[1] *Laboratoire de Génie Chimique, Université de Toulouse, CNRS, INPT, UPS, Toulouse, France*

Abstract

Microfluidics tools have been developing rapidly over the past decade, as they offer unparalleled ability for controlling nucleation and tracking crystallisation events inside very large numbers of individual nanolitre-size droplets. They have demonstrated a significant potential for screening protein crystallization conditions and for the direct determination of inorganic products solubility curves. The accepted basis for analysing microfluidics data is the probabilistic nucleation model originally proposed by Pound and La Mer (1952). Given the significance of this model for the purpose of analysing microfluidics data, the paper conducts a review of its hypotheses, usage and applicability. A step-by-step derivation of the model equations confirms that the time variation of the proportion of empty droplets which microfluidics experiments can provide with high accuracy is indeed the recommended method for estimation of nucleation kinetic parameters from microfluidics experiments. The paper shows that, depending on its implementation, the model predicts different rates of appearance of crystals inside individual droplets. The paper focuses on two distinct implementation modes, referred to as constant supersaturation and single nucleation event modes. By confronting model prediction with microfluidics measurements for eflucimibe in octanol, the paper finds that both modes yield different model predictions, shedding light on the potential and limits of the probabilistic nucleation model for the analysis of microfluidics data.

Keywords: microfluidics, nucleation, modelling

1. Introduction

Microfluidics devices have become key research tools in recent years for the screening of the crystallization conditions of proteins (Selimović et al., 2009), the determination of crystallization kinetics (Laval et al., 2009; Teychené and Biscans, 2012) and precipitation kinetics (Vitry et al., 2015). The principle of this method is to divide the volume of the studied solution into a large number of small, independent droplets in an inert oil. These droplets can be produced in specific microfluidics geometries and their volume and chemical composition can be fixed in a controlled way. In addition, microfluidics devices allow a rapid mixing of the different compounds, help prevent hydrodynamic dispersion and cross-contamination, and the droplets can be stored in microchannels.

For nucleation studies, this experimental technique generates a great deal of data that permit reliable access to the kinetics of nucleation. Typically, the frequency of nucleation events is obtained by counting over time the number of drops without crystals (Laval et al., 2009). When the number of droplets is larger than the number of impurities initially present in the solution, one can observe homogeneous nucleation in some droplets. Moreover, when all the droplets have the same volume V and for a small enough V, it is in principle possible to relate the probability that a droplet contains a crystal to the nucleation rate (Kashchiev et al., 1994). Measurements of the temporal evolution of the fraction of droplets that contain crystals thus permit an estimation of the nucleation kinetics.

The processing of the data generated by such techniques remains limited, however. Indeed, because of the presence of a surfactant, an interface as well as some dust or impurities, the majority of published experimental studies show that the appearance of crystal nucleation in these systems is due to two concomitant mechanisms, namely heterogeneous and homogeneous nucleation. In general, nucleation data that originate from such experiments are treated either by neglecting the first instance of nucleation (Dombrowski et al., 2010), by treating the nucleation process in a comprehensive manner without

---

[†] Received 18 May 2017; Accepted 7 July 2017

[1] 4, allée Emile Monso CS84234, 31432 Toulouse, France

[*] Corresponding author: Florent Bourgeois
E-mail: florent.bourgeois@ensiacet.fr
TEL: +33-(0)5-34-32-36-00 FAX: +33-05-34-32-37-00

differentiating between possible nucleation mechanisms (Goh et al., 2010) or by averaging the influence of impurities on the crystallization process (Laval et al., 2009; Teychené and Biscans, 2011). In addition to the models developed by Goh et al. (2010) in the case of protein crystallization by evaporation, we propose a probabilistic model of the nucleation process that allows us to have access to the different nucleation kinetics that are observed experimentally, to deduce the temporal evolution of the number of crystals within the droplets, and also to trace the influence of "active sites" on nucleation.

2. Probabilistic nucleation model for analysis of microfluidics experiments

2.1 Nucleation model derivation

The nucleation process inside individual droplets can be analysed using a probabilistic nucleation model. Such an approach appears in a number of published studies in the context of microfluidics systems, albeit through different forms and uses. It is revisited here in some detail with the objective of establishing a sound basis for its applicability and usage in the context of microfluidics nucleation analysis.

The model first considers two distinct types of droplets, namely droplets with active nucleation sites and droplets without any nucleation site. Only homogeneous nucleation events can occur inside droplets devoid of nucleation sites, whereas both homogeneous and heterogeneous nucleation events can possibly take place inside droplets that bear active nucleation sites.

The nucleation model that results, whereby the first account of the probabilistic nucleation model is credited to Pound and La Mer (1952), uses only 3 macroscopic parameters, all of which have solid theoretical bases.

The first model parameter m is the mean number of active nucleation sites inside the system's droplets. Considering that active nucleation sites are identical in all respects and that they nucleate independently of each other inside a droplet, the probabilistic model considers that active nucleation sites have the same nucleation kinetic rate k (time^{-1}), the model's second parameter. The third model parameter is the homogeneous nucleation kinetic rate k_0 (time^{-1}), which applies to all droplets devoid of nucleation sites, and also to droplets with active nucleation sites if they undergo homogeneous nucleation.

To avoid any ambiguity, the term "homogeneous nucleation" that is used throughout this paper was chosen to keep consistent with the original definition by Pound and La Mer (1952). It refers to nucleation that occurs in the volume of the droplet, as opposed to "heterogeneous nucleation" which is understood to take place on the surface of nucleation sites. The nucleation mechanism associated with the term k_0 is therefore not to be mistaken for the homogeneous nucleation rate defined in Classic Nucleation Theory (CNT). This point, which has already been pointed out by several authors (Laval et al., 2009; Akella et al., 2014) in relation to probabilistic nucleation modelling, will be further discussed in section 3 of the paper.

Since we have no reason to expect interdependence of the droplets inside our microfluidics system – the system is designed so that two droplets have no interaction with each other – then a Poisson process is a suitable candidate for describing the statistics of nucleation events that occur within individual droplets. This simple statement justifies application of the Poisson statistics, as initially proposed by Pound and La Mer (1952) to model the nucleation process in microfluidics systems.

Considering a system with N_T droplets in total, the number N_p of droplets with p active nucleation sites is predicted by the Poisson distribution with mean m such that:

$$N_p = N_\mathrm{T} \times dpois(p,m) \quad \text{where } p \in [0,\infty] \tag{1}$$

where $dpois()$ denotes the probability density function of the Poisson distribution. Since $dpois(p,m) = \frac{m^p}{p!}\mathrm{e}^{-m}$, the expected fraction of droplets without active nucleation sites is therefore e^{-m} and the number of droplets with active sites is $1 - \mathrm{e}^{-m}$. Sear (2014) indicates that m should lie in the range 0.1 to 1. This means that the maximum number of active nucleation sites per droplet that can be expected, with a confidence level of 99 %, is in the range 1 to 4. These values correspond to the 99 % quantiles of the Poisson distribution with mean $m = 0.1$ and $m = 1$, respectively. Given that $k_0 t$ is the mean number of nucleation events to occur inside a droplet without active nucleation sites during time period t, the probability that r nucleation events take place inside such a droplet during time period t is:

$$dpois(r, k_0 t) \quad \text{where } r \in [0,\infty] \tag{2}$$

Such a droplet may produce any number r of nuclei. Thus, the number of droplets without nucleation sites that contain r crystals at time t is:

$$N_0(r,t) = N_\mathrm{T} \times dpois(0,m) \times dpois(r,k_0 t) \quad \text{where } r \in [0,\infty] \tag{3}$$

The nucleation event that takes place inside a droplet that carries p active nucleation sites is a Bernoulli random variable with probability $q = \left(\frac{k_0}{k_0 + pk}\right)$ for homogeneous nucleation and $1 - q = \left(\frac{pk}{k_0 + pk}\right)$ for heterogeneous nucleation.

The probability of homogeneous nucleation is expected to be significantly lower than that of heterogeneous nucleation, typically one or two orders of magnitude lower. This explains why Pound and La Mer (1952) neglected the possibility that a droplet with active nucleation sites may nucleate homogeneously. Akella et al. (2014) corrected this assumption and justly accounted for this possibility in their work. Finally, the probability that r nucleation events take place inside such a droplet during time period t is:

$$\left(\frac{k_0}{k_0+pk}\right) dpois(r,k_0t)+\left(\frac{pk}{k_0+pk}\right) dpois(r,pkt) \qquad \text{where } r\in[0,\infty] \tag{4}$$

The second Poisson density distribution $dpois(r, pkt)$ could be upper truncated at p, if one assumes that one active nucleation site can produce one nucleus only. The authors chose not to truncate this distribution, assuming that a nucleation site can produce any number of nuclei. The number of droplets with p nucleation sites that contain r crystals at time t is therefore:

$$\begin{aligned} N_p(r,t) &= N_\mathrm{T}\times dpois(p,m) \\ &\times\left(\left(\frac{k_0}{k_0+pk}\right) dpois(r,k_0t) + \left(\frac{pk}{k_0+pk}\right) dpois(r,pkt)\right) \\ &\text{where } r\in[0,\infty] \end{aligned} \tag{5}$$

Finally, the total number of droplets with r crystals at time t is given by:

$$\begin{aligned} N(r,t) &= N_\mathrm{T}\times dpois(0,m)\times dpois(r,k_0t) \\ &+\sum_{p=1}^{\infty} N_\mathrm{T}\times dpois(p,m)\times\left(\left(\frac{k_0}{k_0+pk}\right) dpois(r,k_0t) + \left(\frac{pk}{k_0+pk}\right) dpois(r,pkt)\right) \\ &\text{where } r\in[0,\infty] \end{aligned} \tag{6}$$

and the number fraction $f_r(t)$ of droplets that bear r crystals at time t is:

$$\begin{aligned} f_r(t) &= dpois(0,m)\times dpois(r,k_0t) \\ &+\sum_{p=1}^{\infty}\left[dpois(p,m)\times\left(\left(\frac{k_0}{k_0+pk}\right) dpois(r,k_0t) + \left(\frac{pk}{k_0+pk}\right) dpois(r,pkt)\right)\right] \\ &\text{where } r\in[0,\infty] \end{aligned} \tag{7}$$

This equation is the main equation for predicting the state of the microfluidics system at any time t. For all practical uses, there is no need to use the analytical expression of the probability density function (PDF) of the Poisson distribution since it is easily computed by numerical software programs.

However, in order to relate this expression to the analytical expressions that can be found in the literature, some of which are referred to in the following section, equation (8) gives the analytical equivalent for the number fraction $f_r(t)$ of droplets that bear r crystals at time t.

$$\begin{aligned} f_r(t) &= \mathrm{e}^{-m}\times\frac{(k_0t)^r}{r!}\mathrm{e}^{-k_0t} \\ &+\sum_{p=1}^{\infty}\left[\frac{m^p}{p!}\mathrm{e}^{-m}\times\left(\left(\frac{k_0}{k_0+pk}\right)\frac{(k_0t)^r}{r!}\mathrm{e}^{-k_0t} + \left(\frac{pk}{k_0+pk}\right)\frac{(pkt)^r}{r!}\mathrm{e}^{-pkt}\right)\right] \\ &\text{where } r\in[0,\infty] \end{aligned} \tag{8}$$

2.2 The case of empty droplets

The time variation of the fraction of empty droplets is well accepted as a means of estimating nucleation parameters m, k_0 and k from microfluidics experimental data. This section reviews this important practical issue.

From equation (7), the number fraction $f_0(t)$ of empty droplets ($r = 0$) at time t is:

$$\begin{aligned} f_0(t) &= dpois(0,m)\times dpois(0,k_0t) \\ &+\sum_{p=1}^{\infty}\left[dpois(p,m)\times\left(\left(\frac{k_0}{k_0+pk}\right) dpois(0,k_0t) + \left(\frac{pk}{k_0+pk}\right) dpois(0,pkt)\right)\right] \end{aligned} \tag{9}$$

Or, from equation (8):

$$\begin{aligned} f_0(t) &= \mathrm{e}^{-m}\times\mathrm{e}^{-k_0t} \\ &+\sum_{p=1}^{\infty}\left[\frac{m^p}{p!}\mathrm{e}^{-m}\times\left(\left(\frac{k_0}{k_0+pk}\right)\mathrm{e}^{-k_0t} + \left(\frac{pk}{k_0+pk}\right)\mathrm{e}^{-pkt}\right)\right] \end{aligned} \tag{10}$$

This expression appears different from those published by Pound and La Mer (1952), and later by Akella et al. (2014). The differences are clarified in the following text.

First of all, let us suppose that the droplets are either without or with active nucleation sites, as was assumed by Pound and La Mer (1952). Equation (10) becomes:

$$\begin{aligned} f_0(t) &= \mathrm{e}^{-m}\times\mathrm{e}^{-k_0t} \\ &+\sum_{p=1}^{\infty}\left[\frac{m^p}{p!}\mathrm{e}^{-m}\times\left(0\times\mathrm{e}^{-k_0t}+1\times\mathrm{e}^{-pkt}\right)\right] \\ &= \mathrm{e}^{-m}\times\mathrm{e}^{-k_0t}+\sum_{p=1}^{\infty}\left[\frac{m^p}{p!}\mathrm{e}^{-m}\mathrm{e}^{-pkt}\right] \end{aligned} \tag{11}$$

Besides the case where $k \gg k_0$, which hails back to Pound and La Mer’s assumption, there is no simplification to equations (9) and (10), recalling that they apply to the situation where droplets with nucleation sites can nucleate homogeneously or heterogeneously. Akella and Fraden (2014), however, published the following equation under these assumptions:

$$f_0(t) = \mathrm{e}^{-m} \times \mathrm{e}^{-k_0 t} \times \exp\left(m\mathrm{e}^{-kt}\right) \tag{12}$$

It can be shown that this expression is the analytical expression for $f_0(t)$ that corresponds to the following nucleation model:

$$\begin{aligned} &f_r(t) = dpois(0,m) \times dpois(r,k_0 t) \\ &+\sum_{p=1}^{\infty}\left[dpois(p,m) \times dpois(r,(k_0+pk)t)\right] \\ &\quad \text{where } r \in [0,\infty] \end{aligned} \tag{13}$$

This equation assigns a nucleation rate ($k_0 + pk$) to the probability of nucleation of droplets with active sites, when in actual fact, the probabilities of nucleation are different depending on whether these droplets nucleate homogeneously or heterogeneously. This oversight is of no consequence when predicting the time variation of $f_r(t)$ in the case $k >> k_0$. However, it becomes increasingly significant when the difference between homogeneous and heterogeneous nucleation rates decreases, leading to incorrect estimates of nucleation parameters from the measured variation $f_0(t)$.

While providing the reader with a step-by-step derivation of the probabilistic nucleation model, this section has highlighted that one must be careful and use the model that precisely matches the assumptions.

This simplifies to the expression derived by Pound and La Mer (1952):

$$f_0(t) = \mathrm{e}^{-m} \times \left(\mathrm{e}^{-k_0 t} + \exp\left(m\mathrm{e}^{-kt}\right) - 1\right) \tag{14}$$

whose equivalent in terms of Poisson distribution is:

$$\begin{aligned} &f_0(t) = dpois(0,m) \times dpois(0,k_0 t) \\ &+\sum_{p=1}^{\infty}\left[dpois(p,m) \times dpois(0,pkt)\right] \end{aligned} \tag{15}$$

This is particularly critical when using the model to estimate nucleation model parameters from which phenomenological analysis of the nucleation process can be inferred.

2.3 Analysis of probabilistic nucleation model usage

In addition to differences that may arise from model assumptions on the final form of the probabilistic nucleation model, differences will also occur depending on how it is implemented.

Assuming that droplets with active sites can nucleate homogeneously or heterogeneously, and that nucleation events can yield any number of nuclei, equations (7) and (8) give the time variation of droplets with r crystals given nucleation parameters m, k_0 and k.

For the sake of clarity, the behaviour and possible uses of this model are discussed below through numerical examples. The mean number of active nucleation sites per droplet is set to $m = -\ln(0.5)$, which corresponds to an equal proportion of droplets with and droplets without active nucleation sites. The values of the nucleation rates for homogeneous and heterogeneous nucleation, noted k_0 and k, respectively, will be varied in the examples that follow.

For the sake of readability, only predictions of $f_0(t)$ through $f_4(t)$ are plotted, that is the fractions of droplets that bear up to 4 crystals. This is deemed sufficient to reveal the pattern of the models. **Fig. 1** shows the nucleation model behaviour for a decreasing ratio between homogeneous and nucleation kinetic constants k_0/k.

What these curves all have in common is that the proportion of droplets with a given number of crystals increases, goes through a maximum (or two), and then drops back to zero. When the ratio between homogeneous and heterogeneous kinetic constants k_0/k is low, the curves exhibit 2 modes. Theses modes relate to the occurrence of homogeneous and heterogeneous nucleation events, and the more different their nucleation rates the more separate and distinct the 2 modes. These curves evolve gradually towards single mode curves as the ratio k_0/k increases; this is the behaviour that is most often portrayed in the literature (Dombrowski et al., 2010; Goh et al., 2010). The limiting case for this ratio corresponds to $k = 0$, which is that of purely homogeneous nucleation. **Fig. 2** shows the result of the model for $k = 0$.

The underlying assumption behind all the model predictions presented above is that droplets which have undergone a nucleation event at time t can sustain other nucleation events at a later time, with the same nucleation kinetics. This is equivalent to saying that the state of supersaturation inside individual droplets remains constant as time advances (i.e. the crystal growth rate is zero). We shall refer to this use of the nucleation model as *constant supersaturation mode*.

Another way of using the nucleation model consists of allowing droplets to undergo only one nucleation event, with the outcome in terms of number of crystals determined by the Poisson statistics of the model. This mode may offer a better representation of reality in microfluidics experiments where the constant supersaturation mode does not apply. We shall refer to this mode as the *single nucleation event mode*. In this case, model predictions can no longer be made analytically as they require using a Monte Carlo (MC) simulation scheme that predicts the nucleation of every single droplet in the system. **Fig. 3** explains implementation of the nucleation model by Monte Carlo.

Case a

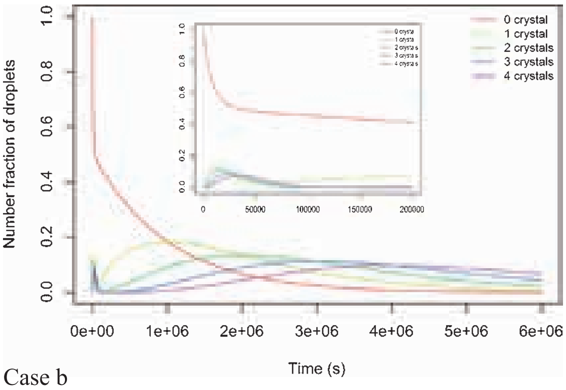

Case b

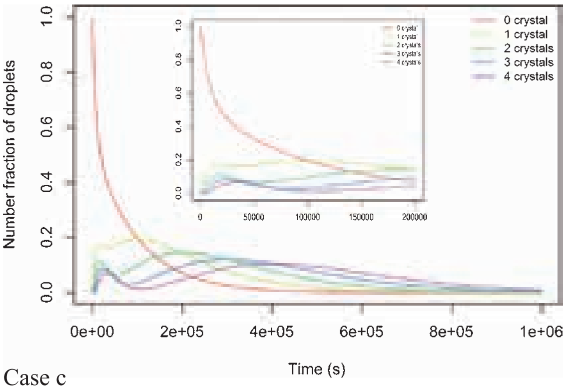

Case c

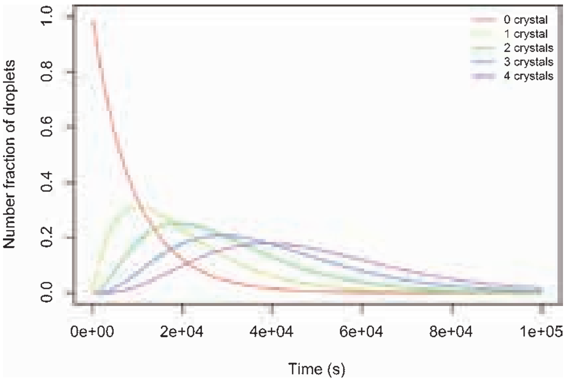

Fig. 1 Illustration of the probabilistic nucleation model behaviour. **Cases a**, **b** and **c** show the effect of a decreasing ratio between homogeneous and heterogeneous nucleation kinetic constants k_0/k. Inserts are used to zoom on the heterogeneous nucleation period.
Case a: Mixed homogeneous/heterogeneous nucleation with $k_0/k = 0.01$ ($m = -\ln(0.5)$, $k_0 = 10^{-6}\ \mathrm{s}^{-1}$, $k = 10^{-4}\ \mathrm{s}^{-1}$)
Case b: Mixed homogeneous/heterogeneous nucleation with $k_0/k = 0.1$ ($m = -\ln(0.5)$, $k_0 = 10^{-5}\ \mathrm{s}^{-1}$, $k = 10^{-4}\ \mathrm{s}^{-1}$)
Case c: Mixed homogeneous/heterogeneous nucleation with $k_0/k = 1$ ($m = -\ln(0.5)$, $k_0 = k = 10^{-4}\ \mathrm{s}^{-1}$)

Fig. 4 shows the output of the probabilistic nucleation model, used in single nucleation event mode, for **Fig. 1**, **Case a** (mixed homogeneous/heterogeneous nucleation), and **Fig. 2** (homogeneous nucleation only), recalling that they were obtained using the model in constant supersaturation mode.

Predictions using the single nucleation event mode or the constant supersaturation mode are totally different, as one would expect. Where the model with constant supersaturation predicts any number of crystals inside the droplets, the single nucleation event mode rarely predicts more than 1 crystal per droplet with the nucleation parameters used.

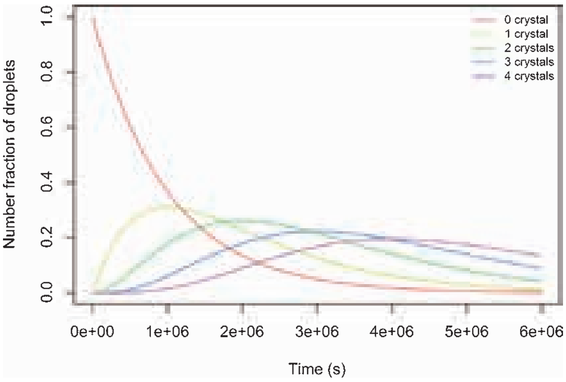

Fig. 2 Model prediction with homogeneous nucleation only ($m = -\ln(0.5)$, $k_0 = 10^{-6}\ \mathrm{s}^{-1}$, $k = 0$).

It is important to recognise that $f_0(t)$ is the same regardless of the model used, i.e. whether it is used in single nucleation event mode or in constant supersaturation mode. This can be demonstrated analytically, and comes from the fact that the nucleation rate of droplets is independent of the path followed by the nucleation events that follow. This is confirmed in the previous figures, which show that the prediction for $f_0(t)$ using analytical equation (9) is indistinguishable from that calculated by the MC simulation scheme. This result fully endorses using the variation of empty droplets to estimate the nucleation parameters from microfluidics experiments.

3. Application of the probabilistic nucleation model to the analysis of microfluidics nucleation data

As discussed in section 2, the probabilistic nucleation model can be used to estimate nucleation parameters m, k_0 and k, directly from the measured variation of $f_0(t)$. Once the nucleation parameters have been estimated, the model can then be applied to predict the variation of $f_r(t)$ for any value of the number r of crystals. This section reviews application of the model to both endeavours, and discusses the behaviour and validity of the probabilistic nucleation model through the prism of actual microfluidics experimental data sets.

3.1 Experimental data

The applicability of the probabilistic nucleation model, which includes estimation of nucleation parameters and

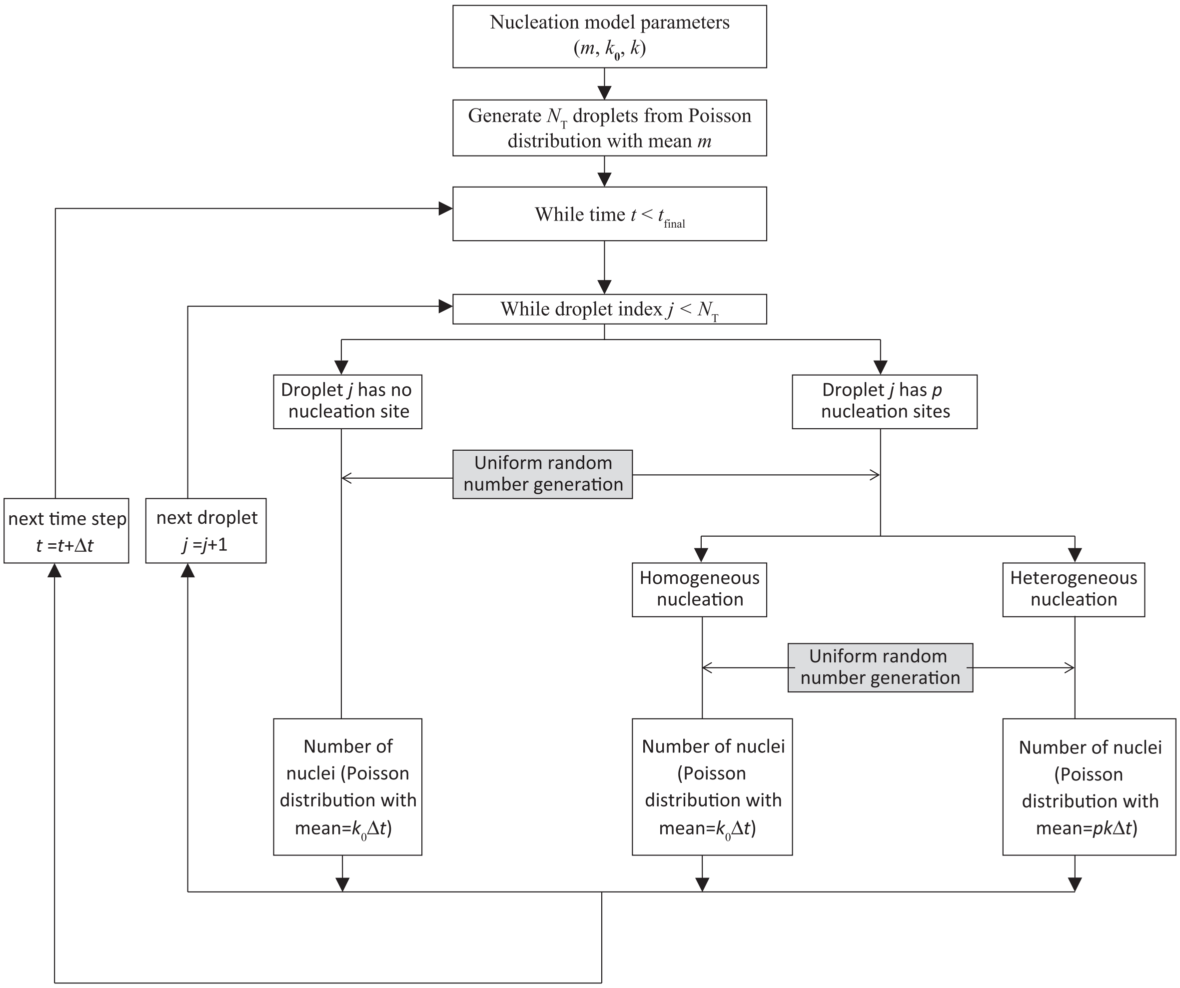

Fig. 3 Principle of the MC simulation scheme implementing equation (7), for one set of nucleation parameters (m, k_0, k).

prediction of nucleation events inside individual droplets, was tested using 4 data sets from the authors (see Teychené and Biscans, 2011), and two additional data sets from Akella et al., Figs. 25 and 29 (Akella et al., 2014). The latter are used in section 5. **Table 1** summarises the experimental conditions used to generate the microfluidics data. The experimental protocol is summarised below, however, the reader is invited to refer to Teychené et al. (2011) for details. The data were generated using a glass microfluidics platform in the context of a study about the nucleation of eflucimibe crystals in octanol. Undersaturated droplets of eflucimibe dissolved in octanol were generated with water as the carrier fluid. These droplets were generated using a flow-focusing geometry that generates highly monodispersed droplets. In these experiments, the variation of volume between droplets is less than 0.1 nL.

Glass syringes, equipped with patterned filters (Millipores, pore diameter < 0.2 µm), are used to inject the fluids into the devices. The temperature of the syringe and the tubing that contain the organic solution are controlled to avoid crystallization by means of a small flexible heater. Flow rates are controlled by syringe pumps (PhD 2000, Harvard apparatus). The temperature of the microfluidic platform is precisely controlled using Peltier elements. Platinum temperature sensors, which are embedded in the microfluidics chip, provide precise temperature monitoring. Owing to this temperature control, the droplets are generated at a temperature 5 °C above the saturation temperature (denoted as T^* in **Table 1**) for all the experiments. As soon as the desired amount of droplets is obtained on the microfluidics chip, typically 600 to 800, the flow is stopped and the system is rapidly cooled (i.e. in less than 1 minute) down to the desired temperature in order to induce supersaturation (denoted as $T_{\text{nucleation}}$ in **Table 1**).

Digital images of the whole microfluidics chip were acquired using an inverted light microscope (Zeiss AXIO observer) equipped with a CCD colour camera (PCO Sensicam QE) at a frame rate ranging from 5 to 30 minutes. The optical resolution of the system is 1 µm/pixel with the 10′ objective, and the particle detection threshold is around 5 µm.

As unfrozen droplets can be identified without ambiguity, their number was determined automatically by image

Case a

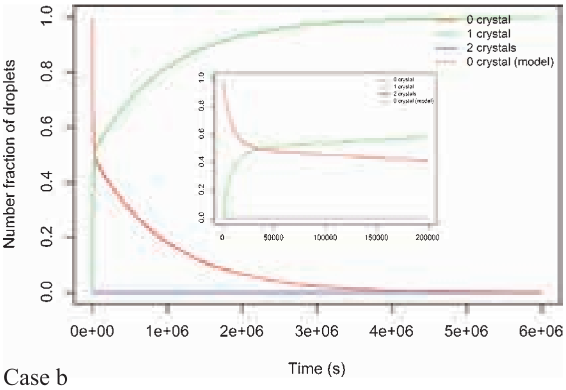

Case b

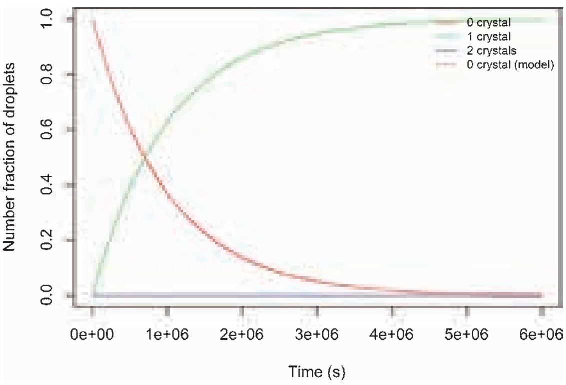

Fig. 4 Model prediction using single nucleation event mode. The dotted lines represent the analytical prediction of $f_0(t)$ from model equations (9) or (10).
Case a: Simulation run output for the mixed homogeneous/heterogeneous nucleation case. $m = -\ln(0.5)$, $k_0 = 10^{-6}\ \mathrm{s}^{-1}$, $k = 10^{-4}\ \mathrm{s}^{-1}$, $N_\mathrm{T} = 10000$ droplets, $\Delta t = 100$ s. At $t = 10^6$ seconds, the model predicts 18.29 % empty droplets, 81.67 % droplets with 1 crystal, 0.15 % droplets with 2 crystals, 0 % with 3 crystals.
Case b: Simulation run output for the pure homogeneous case. $m = -\ln(0.5)$, $k_0 = 10^{-6}\ \mathrm{s}^{-1}$, $k = 0\ \mathrm{s}^{-1}$, $N_\mathrm{T} = 10000$ droplets, $\Delta t = 100$ s. At $t = 10^6$ seconds, the model predicts 36.1 % empty droplets, 63.9 % droplets with 1 crystal, 0 % droplets with 2 crystals.

analysis. The number of crystals in frozen droplets, however, was counted by visual inspection. With each experiment, the time at which the first visible crystallization event occurred was recorded. It varied between 25 and 70 minutes. This value was ultimately used to rescale the experimental time.

3.2 Estimation of nucleation kinetic parameters

Under the assumption of normality of experimental errors, the model parameters m, k_0 and k are estimated by non-linear least squares minimization. Given the large amount of data points obtained at the end of a microfluidics experiment, the more so for empty droplets, the experimental data can confidently be bootstrapped in order to provide an estimate of the confidence intervals of nucleation model parameters, as well as the model confidence and prediction intervals. **Fig. 5** illustrates one bootstrap iteration of the parameter estimation scheme applied to data set D. Typically, 1000 bootstrap iterations are carried out for a data set that comprises over one hundred data points.

Table 1 Experimental conditions used to produce the microfluidics experimental data. The average droplet volume is 11.5 ± 0.1 nL.

Data sets	T^* (°C)	$T_\mathrm{nucleation}$ (°C)	$10^3 \times x°$	$10^3 \times x^*$	S_x
A	47	20	4.202	1.870	2.25
B	40	5	2.847	1.411	2.02
C	50	5	5.536	1.411	3.92
D	60	5	8.088	1.411	5.73

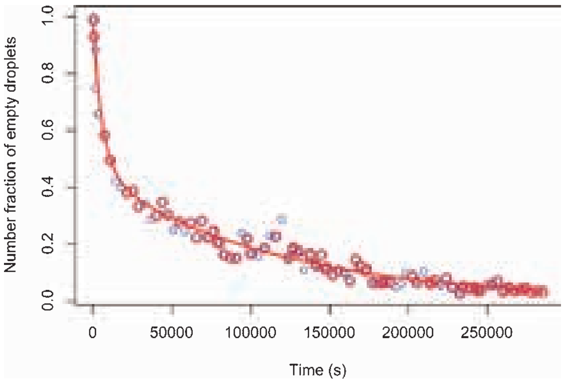

Fig. 5 Example of a bootstrap estimation of the nucleation model parameters. The blue symbols are the experimental data points, the red symbols the bootstrap sample, and the solid line is the model regression for the bootstrap sample.

Each bootstrap iteration gives a set of model parameters (m, k_0, k), and the combined bootstrap estimations yield the model confidence and prediction intervals. **Fig. 6** gives the estimated 95 % prediction intervals for data sets A through D, using 1000 bootstrap estimates in each case.

The bootstrap estimations yield the distribution of individual model parameters from which their confidence intervals can also be obtained. **Table 2** gives the results that were obtained from the 4 selected data sets.

For all data sets, the relative standard deviation (RSD) of the estimated parameter k_0, defined by Pound and La Mer (1954) as the rate of volume nucleation (i.e. $k_0 = J_\mathrm{v}V$, cf. Eqn. 15), is small. This means that the experimental sampling frequency was high enough to capture the essential features of the homogeneous nucleation kinetic component of the nucleation model.

Parameters m and k relate to the heterogeneous nucleation kinetic component of the nucleation model. **Table 2** shows that parameter k is not estimated with the same

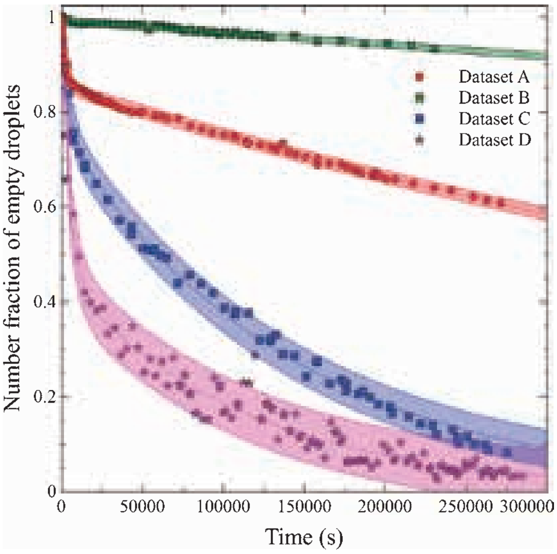

Fig. 6 Nucleation model 95 % prediction interval estimated for data sets A through D.

Table 2 Estimated nucleation model parameters (m, k_0, k) for data sets A through D, and number fraction $N_{\text{act.}} = 1-e^{-m}$ of droplets with active nucleation sites. The table indicates the estimated mean and relative standard deviation (RSD).

Data sets		A	B	C	D
$k_0 \times 10^6$ (s^{-1})	mean	1.26	0.26	7.05	8.78
	RSD	0.9 %	5.5 %	1.6 %	3.0 %
$k \times 10^4$ (s^{-1})	mean	4.55	9.61	2.24	1.71
	RSD	17.9 %	91.5 %	16.5 %	14.7 %
m	mean	0.16	0.01	0.28	0.85
	RSD	1.0 %	70.7 %	3.5 %	4.0 %
$N_{\text{act.}}$	mean	0.147	0.008	0.248	0.573
	RSD	0.9 %	66.7 %	3.1 %	2.5 %

precision as parameter k_0. Heterogeneous nucleation is a process that proceeds very fast at the beginning of the experiment because the energy barrier to form a critical nucleus is lower with surface nucleation than it is with volume nucleation. Moreover, the lower the number of impurities per drop, the rarer the occurrence of nucleation events. Sampling frequency at the start of an experiment is therefore critical for capturing the salient features of heterogeneous nucleation. The frame rate used to conduct the microfluidics experiments was not always sufficient and sometimes yielded only a handful of experimental points inside the heterogeneous nucleation period. This observation, which can be readily observed in **Fig. 6**, explains that the lower the mean number of impurities per droplet, the broader the confidence interval associated with estimation of parameter k. The worst case occurred with data sets A and B. This result is exacerbated by sampling statistics. Indeed, the fact that data set B contains $N_{\text{act.}} = 0.8$ % of droplets with active nucleation sites means that in a microfluidics experiment that uses 600 to 800 droplets, the number of droplets with active nucleation sites is on average no more than 7. Such a number is clearly too low to expect precise estimates of heterogeneous nucleation rate parameters k and m. When the amount of impurities is high enough, as with data sets C and D, the sampling frame rate is sufficient and nucleation rate parameter k and m are estimated with good precision.

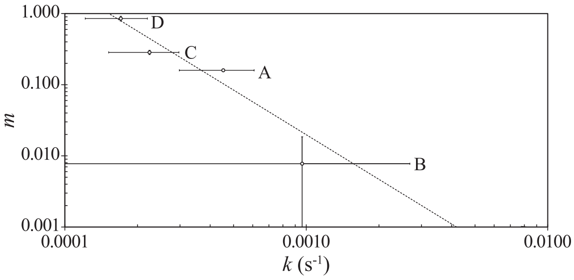

Fig. 7 Illustration of the strong correlation between heterogeneous nucleation rate parameters m and k. The correlation plotted is: $\log_{10}k = -3.82 - 0.48\log_{10}m$.

Notwithstanding the difficulty with estimation of k at low levels of impurities, **Fig. 7** shows that the heterogeneous nucleation parameters m and k are negatively correlated. The interpretation of the correlation between the estimated values of k and m, where the latter increases with supersaturation as one would expect, is unclear. It is emphasised that the variation of k between experiments does not contradict the model assumption that k is the same for all active nucleation sites; it just indicates that the nature of active nucleation sites differs between experiments.

Although the purpose of this paper was not to venture into nucleation theory, it seemed justified to give some interpretation of the values of the estimated nucleation model parameters that were obtained.

In the framework of CNT, the homogeneous nucleation rate is related to the parameter of the nucleation model by the following equation (Kashchiev, 2000):

$$J_v = A_0 \exp\left(-\frac{16\pi\sigma^3 v_m^2}{3(k_B T)^3 \ln^2 S}\right) = A_0 \exp\left(-\frac{\Delta G_v^*}{k_B T}\right) \equiv \frac{k_0}{V} \tag{16}$$

According to equation (16), k_0 is the product of the volume of the solution V where nucleation occurs and the rate of nucleation J (number of particles per unit time and unit volume). So, CNT for homogeneous nucleation implies that nucleation kinetics parameters are related to the volume of the droplets, and therefore the size, or size distribution of the droplets. In the context of this study, droplets are monodisperse and their volume is invariant during any given microfluidics experiment.

A_0 is the nucleation rate prefactor which can be written as (Kashchiev, 2000):

$$A_0 = \rho_{\mathrm{N}} Zj = \rho_{\mathrm{N}} Z 4\pi \rho D r^* \exp\left(-\frac{\Delta F}{k_{\mathrm{B}} T}\right) \tag{17}$$

Where $j = 4\pi \rho D r^* \exp\left(-\frac{\Delta F}{k_{\mathrm{B}} T}\right)$ is the rate at which a monomer is added to the critical cluster, ρ is the number density of a monomer in the solution, D the diffusion coefficient, r^* the critical radius of the nuclei, $\exp\left(-\frac{\Delta F}{k_{\mathrm{B}} T}\right)$ is the probability of effective collision between a cluster and a monomer, and ρ_{N} is the number density of nucleation sites. As with homogeneous nucleation, every monomer can be a nucleation site $\rho = \rho_{\mathrm{N}}$.

Similarly, the heterogeneous surface nucleation rate is written as (Kashchiev, 2000):

$$J_{\mathrm{s}} = A_0' \exp\left(-\frac{\Delta G_{\mathrm{s}}^*}{k_{\mathrm{B}} T}\right) \equiv k \tag{18}$$

As the main assumption of CNT is that the properties (shape, surface tension, etc.) of the pre-critical nuclei are the same as those of the post-critical nuclei and of the crystal, the pre-exponential factor has the same expression. However, in that case, the number density of nucleation site is directly related to the number density of impurities and is much smaller than the number density of monomers.

The evolution of the nucleation rate (k_0) as a function of temperature and supersaturation is given in **Fig. 8**. As predicted by CNT, it is found that $\ln(k_0)$ varies linearly with the term $T^{-3}\ln^{-2}S$. The crystal solution interfacial tension is calculated from the slope of the line, giving a value of 3 $\mathrm{mJ \cdot m^{-2}}$ that is consistent with the data already published (Teychené and Biscans, 2008). From the intercept, the pre-exponential factor of the nucleation rate was found to be in the range of 10^7, which is very low for a purely homogeneous nucleation rate. Estimation of this factor from CNT in the case of a purely homogeneous nucleation yields values in the range 10^{10} to 10^{13} $\mathrm{s^{-1}}$. Because the number of nucleation sites is smaller than the number of monomers in solution, the discrepancy can be attributed either to heterogeneous nucleation (with static heterogeneities present in the solution from the start of the experiment, but with a lower activity than the impurities responsible for the fast nucleation rate), or to the inability of CNT to capture the complexity of crystal nucleation from solution (i.e. nucleation is catalysed by dynamic heterogeneities, which are formed during the nucleation process, for instance). The limits of CNT have already been pointed out by a number of authors, including Vekilov (2010) for protein nucleation, Jawor-Baczynska et al. (2015) for organic molecules and Gebauer et al. (2014) for salts.

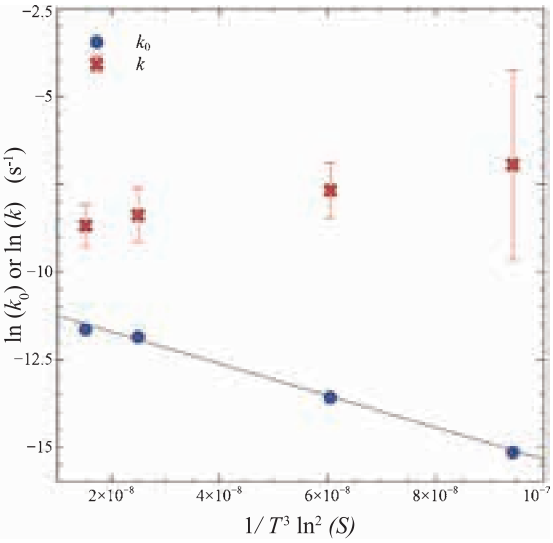

Fig. 8 Evolution of the nucleation rates k and k_0 as a function of supersaturation S and temperature T.

Fig. 8 also displays the variation of the heterogeneous surface nucleation rate k as a function of $T^{-3}\ln^{-2}S$. Because m and k are strongly correlated, and because of the large uncertainty associated with data set B in particular, it is difficult to interpret the measured trend of the heterogeneous nucleation rate k. Nevertheless, the upward trend of $\ln(k)$ vs $T^{-3}\ln^{-2}S$ (which is directly related to the energy barrier of the nucleation process) is lower than the one obtained in the case of volume nucleation. As the nucleation process is fast, it can be inferred that the energy barrier for heterogeneous nucleation is very low.

For the same reasons, it is difficult to interpret the evolution of the mean number of impurities m. Based on Pound and La Mer's original paper (1954), this number depends both on temperature and concentration. For data sets A through D, it appears that m is proportional to the concentration of solute, which implies that the impurities come with the solute molecules. They are probably associated with molecules with a molecular structure that resemble the solute molecules and cannot be purified.

This section has confirmed that provided the sampling frame rate is commensurate with the heterogeneous nucleation rate and that the number of observed droplets is high enough to eliminate sampling statistics issues, the measured variation of unfrozen droplets can yield good estimates of nucleation parameters. Discussion about the parameter estimates led to the assertion that nucleation microfluidics experiments should be performed at the same initial concentration but with a different final temperature in order to decorrelate the heterogeneous nucleation parameters m and k, and to study conclusively the influence of supersaturation and temperature on nucleation kinetics.

4. Prediction of the appearance of crystals

Model predictions of $f_r(t)$ were obtained using the probabilistic model employed in single event nucleation mode and using the MC simulation scheme presented earlier for the selected experimental data sets. The output of the MC scheme is dependent on the time step Δt used as well as the total number N_T of droplets. The MC simulation requires using as small a time step Δt as possible, which impacts computation time. The choice of time step Δt used in the simulations is such that it is no greater than $1/k$, the heterogeneous nucleation giving the fastest kinetics.

Fig. 9 shows the prediction of the fraction of empty droplets output by the MC simulation against the experimental microfluidics data. The prediction is good, as one would expect since the nucleation model parameters were estimated from the measured fraction of empty droplets. However, the point here is to recognise that the predictions are obtained by the MC simulation scheme, not from the analytical expressions for $f_0(t)$, which confirms the correctness of the Monte-Carlo simulation code developed by the authors to simulate the probabilistic nucleation model.

Fig. 9 also shows the predicted prediction intervals for data set D for two different total numbers N_T of droplets. The prediction intervals obtained for the simulation performed using 700 droplets (which correspond to the number of the droplets analysed during the experiment) captures nicely the spread of the experimental data. As expected, the model predicts that had a lower number of droplets been observed, the spread of the experimental data would have been higher. This expected trend shows that the model can also be used to guide the experimentation in terms of setting the number of droplets to be observed. This is an important issue as the spread of the data controls the precision of the estimates of the nucleation model parameters.

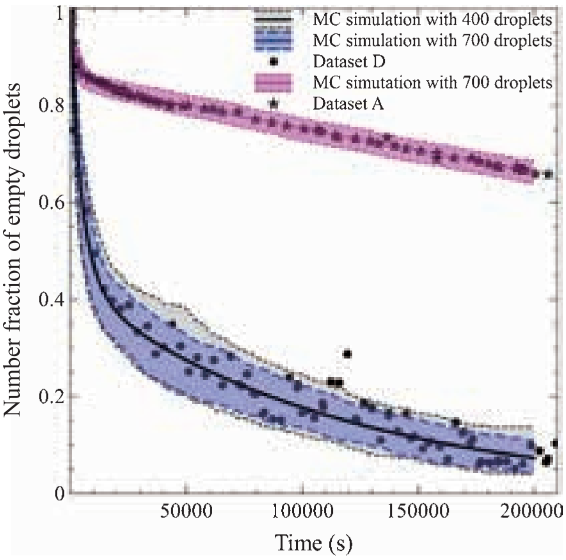

Fig. 9 Prediction of the fraction of empty droplets as a function of time using MC simulation for two representative experiments and two total numbers of droplets.

The point was made in section 2.3 that the prediction of the number of crystals inside a droplet depends on the mode chosen to implement the nucleation model. The following text analyses the capacity of the nucleation model to predict the appearance of crystals. It is worthy of note that, to the best of the authors' knowledge, application of the probabilistic nucleation model to predict the appearance of crystals in microfluidics experiments has not yet been reported.

Experimentally, it was observed that for experiments performed at relatively low supersaturation, most of the droplets contained 1 crystal and very few droplets contained two crystals. This is the case for data set A, which produced 33 % of droplets with 1 crystal, 2 % with 2 crystals and 65 % without crystals. With experiment B, droplets that had nucleated contained only 1 crystal. Simulation results of the probabilistic nucleation model used in single nucleation event mode are given in **Fig. 10** for data sets A and B. It is emphasised here that the predictions use the parameters (k_0, k, m) that were estimated in section 3 from the time variation of empty droplets. The agreement between simulations and measurements is good, confirming that the single nucleation event mode gives a good account of the nucleation events that took place in experiments A and B. One explanation is that as supersaturation is low, when one crystal appears, it starts growing and consumes all the supersaturation. The depletion of solute induces a decrease in nucleation probability such that no new nucleation event can occur inside the droplet. Such a situation will prevail when crystal growth kinetics are very fast, or when the ratio between the crystal nucleation rate and the crystal growth rate is small.

It can be noticed in **Fig. 10** that the measured fraction of droplets which bear one crystal is mainly inside the upper portion of the model's prediction interval, and that it is the opposite for the droplets with 2 crystals. One may recall that crystal number counting was done by visual inspection, and it is believed that the visual counting biased the data by overestimating the number of droplets with 1 crystal at the expense of those with 2 crystals. Visual counting of the number of crystals inside a droplet is difficult, and this nucleation-model-based analysis stressed the importance of this issue for analysis of microfluidics experiments.

When the crystal nucleation rate to crystal growth rate ratio is high (with the limiting case of no crystal growth), not all the supersaturation is consumed by a single crystal, and successive nucleation events may occur over time. Let us consider data set D for which the initial supersaturation was twice that of data sets A and B. **Fig. 11** shows

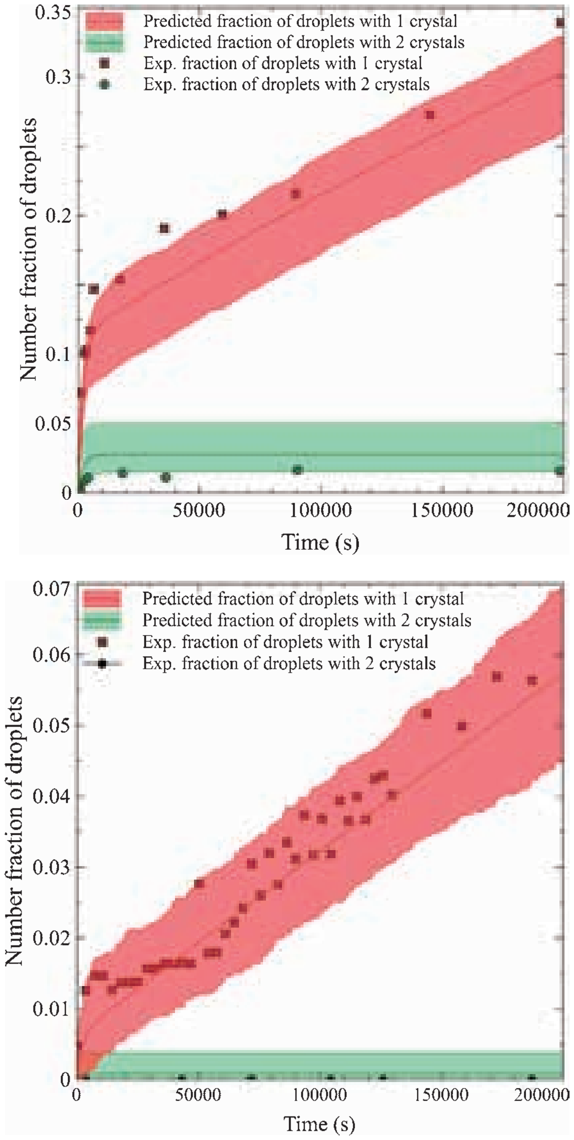

Fig. 10 Predicted and measured temporal evolution of the fraction droplets containing one or two crystals in the droplets for data set A (upper) and data set B (lower).

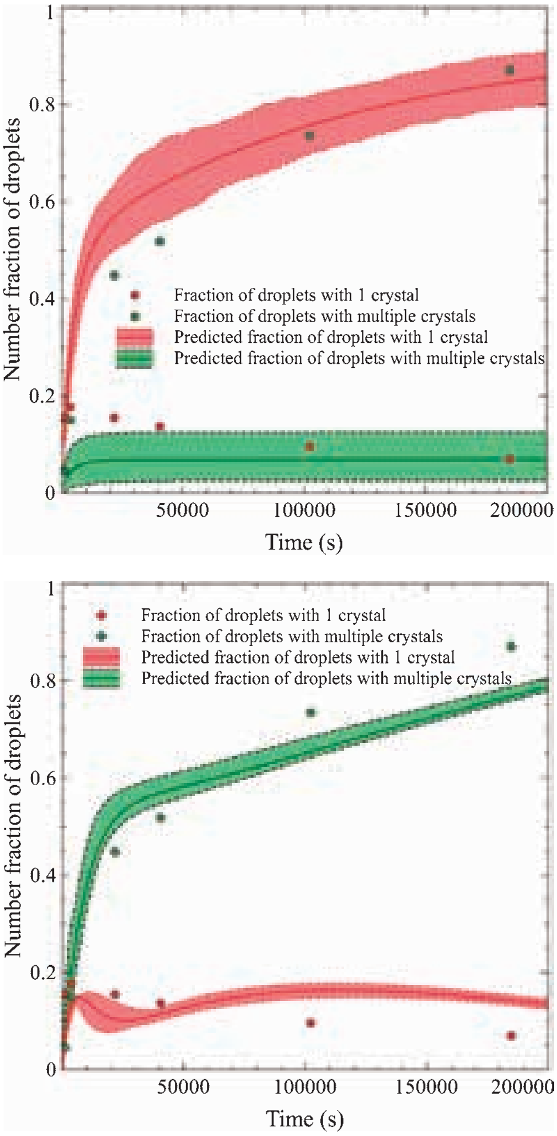

Fig. 11 Predicted and measured temporal evolution of the number fractions of droplets containing one or more crystals for data set D. Upper figure: single nucleation event mode. Lower figure: constant supersaturation mode.

Table 3 Values of the k_0/k ratio for data sets A through D.

Data sets	A	B	C	D
k_0/k	0.0028	0.0003	0.0314	0.0515

the predictions of the probabilistic nucleation model used in both single nucleation event mode and constant supersaturation mode.

The variation of the number fraction of droplets that contain one crystal bears no resemblance with data sets A and B. Indeed, it shows a rapid increase at the beginning of the experiment to a maximum value, then a slow decrease. The measured number fraction of droplets with 2 crystals or more shows a continuous increase over time. The upper plot in **Fig. 11** shows the nucleation model prediction in single nucleation event mode. It is clear that this implementation mode of the nucleation model does not capture at all the nucleation events of data set D. The lower plot in **Fig. 11** gives the prediction of the nucleation model in constant supersaturation mode. Notwithstanding the counting bias between droplets with one or more crystals, it is clearly apparent that the constant supersaturation mode gives a much closer match to the measured data. With data set D, given its higher state of supersaturation and its higher k_0/k ratio, which is more than 1 order of magnitude higher than that of data sets A and B as seen in **Table 3**, it is not surprising to find that the hypotheses of the constant supersaturation mode give a better account of the measured microfluidics data.

Even though the single nucleation event mode can be a close match to microfluidics data, as found with data sets A and B, both the single nucleation event and the constant supersaturation modes are limited in their ability to predict nucleation in that they do not account for the crystal growth that follows nucleation. To further improve our ability to model microfluidics systems and gain even more value out of the valuable data produced by such systems, it is necessary to couple the probabilistic nucleation model with a crystal growth model that accounts for the consumption of supersaturation inside individual droplets. The Monte-Carlo simulation scheme, in which droplets are individualised, provides just the right environment for such a development. This requires both accurate measurements of crystal growth inside droplets, and a valid thermodynamic model of the liquid phase.

5. Application to microfluidics data from literature

For the sake of rounding off the paper, it was deemed relevant to apply the probabilistic nucleation model to high-quality data published by researchers other than the present authors. The data selected was that of Figs. 25 and 29 from Akella et al. (2014). The estimated nucleation parameters, using the non-linear parameter estimation scheme presented earlier, are given in **Table 4**. The values are close to those published by Akella et al., however, they differ due to the difference between equation (10), proposed by the authors and equation (14) used by Akella et al.

Figs. 12 and **13** show the corresponding 95 % prediction intervals for the number fraction f_0 of empty droplets. The prediction intervals are narrower compared to those of data sets A through D. This is due to Akella et al. using a high number of droplets, typically 1200 to 4000 in each of their experiments, so that their raw measurements of f_0 are extremely smooth.

Figs. 14 and **15** show the predictions made using both single nucleation event mode ($N_T = 1000$ drops) and constant supersaturation mode for the production of crystals.

The results show that the single nucleation event mode predicts that after 15 hours, most droplets contain 1 crystal, with no more than 0.24 % and 0.62 % of droplets containing 2 crystals for the data from Figs. 25 and 29, respectively. The constant supersaturation mode predicts a significant proportion of droplets that bear 2 or more crystals.

It is anyone's guess as to the actual number of crystals observed by Akella and co-workers (2014), as they did not report this information. The predictions are so distinct that it should be rather simple for them to decide whether their system behaves more like one mode or the other. By examining the images and movie frames provided in their paper, and considering that their experiment is carried out at a low level of supersaturation, it is probable that their system follows the single nucleation event mode and produced no more than 1 crystal per droplet.

Table 4 Estimated nucleation model parameters (m, k_0, k) for Akella et al's data sets (Akella et al., 2014, Figs. 25 and 29), and number fraction of droplets with active nucleation sites.

Data sets		**Fig. 25**	**Fig. 29**
$\boldsymbol{k_0} \times 10^6$ (s^{-1})	mean	6.93	10.2
	RSD	1.7 %	1.1 %
$\boldsymbol{k} \times 10^4$ (s^{-1})	mean	0.66	3.55
	RSD	5.7 %	38.4 %
$\boldsymbol{m}$	mean	0.48	0.20
	RSD	3.4 %	2.4 %
$\boldsymbol{N_{act.}}$	mean	0.383	0.181
	RSD	2.7 %	2.2 %

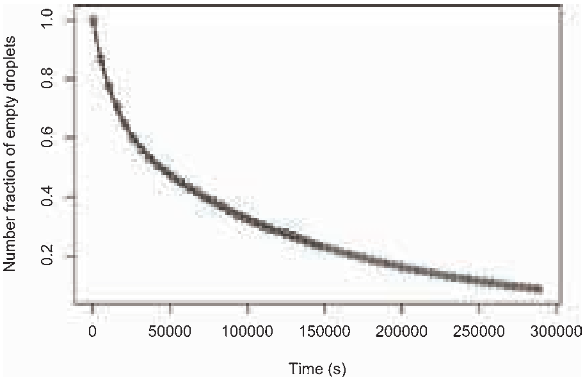

Fig. 12 Nucleation model 95 % prediction interval for the number fraction of empty drops using Akella et al.'s data (Akella et al., 2014, Fig. 25, p. 4500).

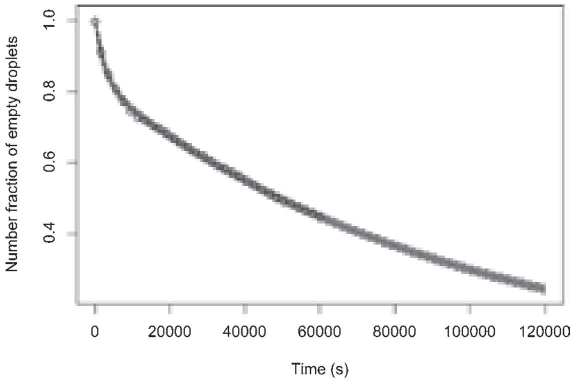

Fig. 13 Nucleation model 95 % prediction interval for the number fraction of empty drops using Akella et al.'s data (Akella et al., 2014, Fig. 29, p. 4502).

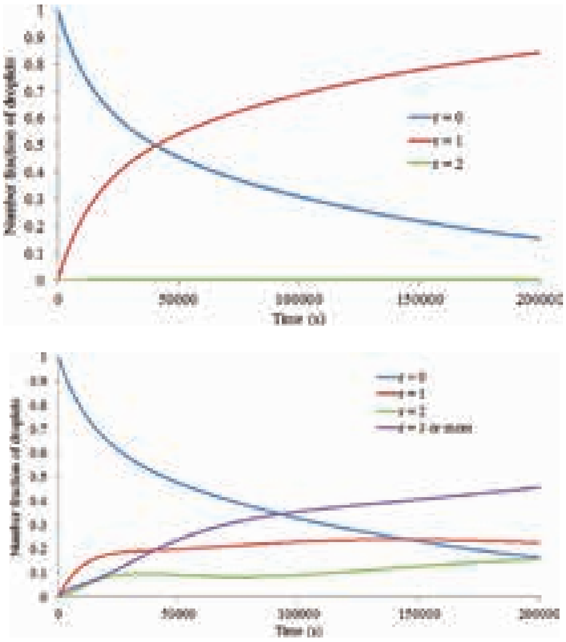

Fig. 14 Prediction of crystal formation for Akella et al.'s data from Fig. 25. (top: single nucleation event mode; bottom: constant supersaturation mode)

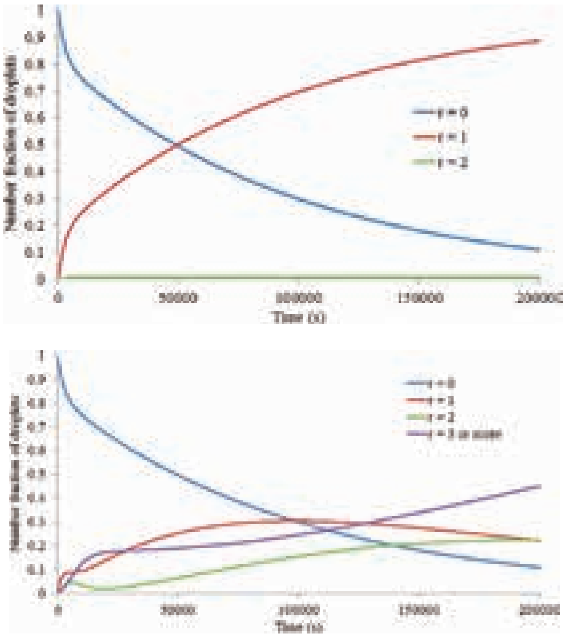

Fig. 15 Prediction of crystal formation for Akella et al.'s data from Fig. 29. (top: single nucleation event mode; bottom: constant supersaturation mode)

6. Conclusions

The probabilistic nucleation model originally proposed by Pound and La Mer (1952) was revisited with the objective of clarifying its underlying hypotheses and associated behaviour. The nucleation model considers two types of droplets, i.e. droplets without nucleation sites which can only undergo homogeneous nucleation events, and droplets with active nucleation sites which can undergo homogeneous and heterogeneous nucleation events. Analytical expressions were derived for predicting the variation of the fraction of droplets that contain a given number of crystals, both in terms of Poisson distribution functions and exponential functions.

The paper emphasises that the same model can be implemented in different ways which yield different outcomes. The model was applied in constant supersaturation and single nucleation event modes. The first mode, which is often portrayed in the literature, corresponds to the droplets with no crystal growth, whereas the second one corresponds to droplets having a supersaturation that is just sufficient for one nucleation event and associated crystal growth.

Regardless of the implementation mode, the model prediction for the time variation of the fraction of empty or unfrozen droplets is the same, confirming that nucleation kinetic parameters m, k_0 and k should indeed be estimated using the experimental measurements of the fraction of empty droplets. This is a particularly favourable situation given that this is the fraction that is most accurately measured in practice. Indeed, identifying droplets that contain 1 or more crystals is obviously more prone to measurement errors than identifying empty droplets. The estimation of nucleation model parameters showed the importance of frame rate and number of droplets as they impact the precision of the parameter estimates.

In the context of microfluidics studies, it was confirmed that both modes of implementation of the nucleation model are applicable. The probabilistic nucleation model was used, possibly for the first time, to predict the rate of appearance of crystals for microfluidics systems. Experimental results with low supersaturation levels were well predicted by the single nucleation event mode. The single nucleation event mode was shown to yield droplets with no more than one or two crystals, a desirable situation from an industrial perspective. The constant supersaturation mode accounted better for the nucleation events observed for data sets with excess supersaturation. Comparison between predicted and measured number fractions of droplets with one or more crystals indicated the possibility of bias in the number counting of crystals inside individual droplets, emphasising the need to develop reliable crystal counting methods for harvesting the full benefit of microfluidics systems.

The analysis confirmed the value and applicability of the probabilistic nucleation model for analysis of microfluidics data, particularly for estimation of nucleation parameters. The model showed limitations in its applicability for predicting the appearance of crystals inside droplets, although it gave reasonable predictions at low supersaturation levels. As the probabilistic nucleation model alone cannot account for the consumption of the supersaturation inside droplets, the nucleation model cannot predict the number of crystals inside droplets. As the real situation is somewhere between the single nucleation event and the constant supersaturation modes, it is necessary for prediction of the rate of appearance of crystals inside individual droplets to merge the probabilistic nucleation model with a crystal growth model.

Nomenclature

$dpois(k,\lambda)$	Probability density function of the Poisson distribution with mean λ
D	Diffusion coefficient ($m^2 \cdot s^{-1}$)
$f_r(t)$	Number fraction of droplets containing r crystals at time t
k	Nucleation rate constant of an active nucleation site (s^{-1})
k_B	Boltzmann constant $k_B = 1.38064852 \times 10^{-23}$ m^2 $kg \cdot s^{-2} \cdot K^{-1}$
k_0	Homogeneous nucleation rate constant (s^{-1})
j	Droplet index used in Monte-Carlo simulation (s)
J_s	Heterogeneous surface nucleation rate (s^{-1})
J_v	Homogeneous nucleation rate ($s^{-1} \cdot m^{-3}$)
m	Mean number of active nucleation sites per droplet
$N_{act.}$	Number fraction of droplets that contain active nucleation sites at the start of a microfluidics experiment
N_p	Number of droplets with p active nucleation sites
N_T	Total number of droplets counted in a microfluidics experiment
p	Number of active nucleation sites in a droplet
r	Number of nucleation events inside a droplet
r^*	Radius of the critical nuclei (m)
S_x	Supersaturation defined as $S_x = x°/x^*$
t	Time (s)
T	Temperature (K)
T^*	Saturation temperature (°C)
$T_{\mathrm{nucleation}}$	Final quench temperature (°C)
V	Droplet volume (m^3)
$x°$	Initial molar fraction of eflucimibe in octanol or solubility molar fraction at T^*
x^*	Solubility molar fraction at $T_{\mathrm{nucleation}}$
Z	Zeldovich factor
Δt	Time increment used in the Monte-Carlo simulation (s)
ΔG^*	Free energy barrier of nucleation (J)
ρ	Number density of monomers per unit of volume (m^{-3})
ρ_N	Number density of nucleation sites (m^{-3})
σ	Crystal solution interfacial tension ($mJ \cdot m^{-2}$)

References

Akella S.V., Mowitz A., Heymann M., Fraden S., Emulsion-based technique to measure protein crystal nucleation rates of lysozyme, Crystal Growth & Design, 14 (2014) 4487–4509.

Dombrowski R.D., Litster J.D., Wagner N.J., He Y., Modeling the crystallization of proteins and small organic molecules in nanoliter drops, AIChE Journal, 56 (2010) 79–91.

Gebauer D., Kellermeier M., Gale J.D., Bergstrom L., Colfen H., Pre-nucleation clusters as solute precursors in crystallisation, Chemical Society Reviews, 43 (2014) 2348–2371.

Goh L., Chen K., Bhamidi V., He G., Kee N.C.S., Kenis P.J.A., Zukoski C.F., Braatz R.D., A stochastic model for nucleation kinetics determination in droplet-based microfluidic systems, Crystal Growth & Design, 10 (2010) 2515–2521.

Jawor-Baczynska A., Moore B.D., Sefcik J., Effect of mixing, concentration and temperature on the formation of mesostructured solutions and their role in the nucleation of DL-valine crystals, Faraday Discussions, 179 (2015) 141–154.

Kashchiev D., Clausse D., Jolivet-Dalmazzone C., Crystallization and critical supercooling of disperse liquids, Journal of Colloid and Interface Science, 165 (1994) 148–153.

Kashchiev D., Ed., Nucleation – Basic Theory with Applications, Butterworth-Heinemann, Oxford (2000).

Laval P., Crombez A., Salmon J.-B., Microfluidic droplet method for nucleation kinetics measurements, Langmuir, 25 (2009) 1836–1841.

Pound G.M., Lar Mer V.K., Kinetics of crystalline nucleus formation in supercooled liquid tin, Journal of the American Chemical Society, 74 (1952) 2323–2332.

Sear R.P., Quantitative studies of crystal nucleation at constant supersaturation: Experimental data and models, CrystEngComm, 16 (2014) 6506–6522.

Selimović Š., Jia Y., Fraden S., Measuring the nucleation rate of lysozyme using microfluidics, Crystal Growth & Design, 9 (2009) 1806–1810.

Teychené S., Biscans B., Nucleation kinetics of polymorphs: induction period and interfacial energy measurements, Crystal Growth & Design, 8 (2008) 1133–1139.

Teychené S., Biscans B., Microfluidic device for the crystallization of organic molecules in organic solvents, Crystal Growth & Design, 11 (2011) 4810–4818.

Teychené S., Biscans B., Crystal nucleation in a droplet based microfluidic crystallizer, Chemical Engineering Science, 77 (2012) 242–248.

Vekilov P.G., The two-step mechanism of nucleation of crystals in solution, Nanoscale, 2 (2010) 2346–2357.

Vitry Y., Teychené S., Charton S., Lamadie F., Biscans B., Investigation of a microfluidic approach to study very high nucleation rates involved in precipitation processes, Chemical Engineering Science, 133 (2015) 54–61.

Author's short biography

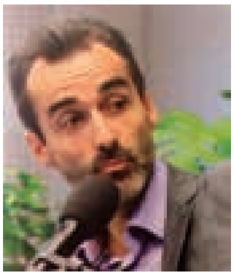

Florent Bourgeois

Prof. Bourgeois received his PhD in extractive metallurgy from the University of Utah in 1993. He was affiliated to the University of Queensland from 1994 to 2000 with research and teaching activities related to mineral and coal processing, after which he spent 5 years with the French Geological Survey's processing department. In 2006, he joined the Laboratoire de Génie Chimique at the University of Toulouse (France). His field of competence is particulate process design and modelling, with emphasis on solid-liquid separation, comminution, liberation and sampling, as they apply to mineral and waste beneficiation.

Sébastien Teychené

Dr Sébastien Teychené is assistant professor in chemical engineering at the Laboratoire de Génie Chimique of the University of Toulouse (France). He received his B. Eng. degree in chemical and environmental engineering from the Institut National de Sciences Appliquées (INSA, Toulouse) in 2000, and a master's degree in chemical engineering in 2001. He was awarded his PhD in chemical engineering from the University of Toulouse in 2006, after which he joined Dr. Béatrice Biscans' research team at the Laboratoire de Génie Chimique. His research work focuses on thermodynamics and kinetics aspects of nucleation and phase transitions in the crystallization processes of organic compounds.

Béatrice Biscans

Dr. Béatrice Biscans obtained her engineering degree in chemical engineering from the University of Toulouse in 1982 and was awarded her PhD in chemical and process engineering in 1985. From 1987 onwards, following a post-doctoral position, she worked for the National Centre for Scientific Research (CNRS) at the Laboratoire de Génie Chimique (Toulouse, France). Her research focuses on particle technology and processing. She leads a research group working on crystallization, formulation processes and the production of nanoparticles. Until recently, she was head of the Laboratoire de Génie Chimique. She is currently president of the Working Party on Crystallization of the European Federation of Chemical Engineering and of the Working Party on Powders and Particles of the French Society of Chemical Engineering. She is also the CNRS' representative expert in chemical engineering.

KONA Powder and Particle Journal No. 35 (2018) 273–282/Doi:10.14356/kona.2018019 Original Research Paper

The Friction Stress Distribution of Loose Materials to Silo Walls in Deep Pyramidal Silos[†]

Xuewen Wang*, Zhaojian Yang and Bo Li

[1] *Shanxi Key Laboratory of Fully Mechanized Coal Mining Equipment, College of Mechanical Engineering, Taiyuan University of Technology, China*

Abstract

Referring to the classification of vertical silos, the classification rules for deep silos and shallow silos on pyramidal silos and conical silos have been established. Based on the basic assumptions of Janssen Formula, the friction stress distribution of loose materials to silo walls was discussed in detail on deep pyramidal silos. An analytic equation was established used the slice method. Finite element model was developed to simulate the friction stress distribution. The analytic result was almost the same with the simulation result. However, the equation yielded a minor error mainly because there were some differences between the assumptions presented in the equation and the real state of materials. Based on the simulation results, the analytic equation was revised. The results showed that the friction stress distribution of loose materials to silo walls in deep pyramidal silos was related to the material characteristics and design parameters of silo walls, as well as the material powder attribute. The revised equation precisely indicated the contact friction stress behaviors of loose materials and provided a shortcut method of calculation for related research.

Key words: loose material, pyramidal silos, friction stress, contact, finite element

1. Introduction

As a special industry thin-shell structure, silos have many advantages, ranging from having a simple structure that is low cost, space efficient, and stable, having an easy loading and unloading process that can be conveniently managed. Silos are widely used in many fields to stockpile loose materials, such as mineral, grain, foodstuff, coal, chemical fertilizer, and concrete. In the state of stockpiling loose materials, the mechanics behavior of the silos and the loose materials are all very complex (Jansseune A. et al., 2016a,b; Park H.W. et al., 2016; Jagtap P. et al., 2015; Colonnello C. et al., 2014). However, with the mature development of the finite element method and discrete element method, the numerical simulation method managed to contribute greatly to the silo research (Ding S. et al., 2015; Wang Y. et al., 2014; Gallego E. et al., 2010) and the loose materials or the solid particle behavior, including the powder friction angles, forces, stresses and so on (Hua X. et al., 2013; 2015). Basing on relevant literature, many scholars are interested in studying the lateral pressure of stored loose material in silos. Although the famous static deep-silo lateral pressure formula has already been put forward by JANSSEN over 100 years ago (Janssen, H.A. 1895), the JANSSEN formula is still being widely cited, used and discussed (Matchett A.J. et al., 2015; LI Z.F. et al., 2014). In the meantime, many new research results on lateral pressure have been put forward (Wang Y. et al., 2014; Couto A. et al., 2013; Nascimento J.W.B.d. et al., 2013).

In general, these research works are mainly concerned with cylindrical silos (Iwicki P. et al., 2016; Jansseune A. et al., 2016a,b; Sadowski A.J. et al., 2014), particularly on the pressure (Wang Y. et al., 2014; Couto A. et al., 2013; Nascimento J.W.B.d. et al., 2013), stability (Sondej M. et al., 2016; Iwicki P. et al., 2015; Lozano C. et al., 2015), and fluidity effect or discharge flow (Ding S.et al., 2015; Gallego E. et al., 2015; Benyamine M. et al., 2014) of the loose material on the silos. The square platform silos have already been studied by some scholars (Goodey R.J. et al., 2006; Guines D. et al., 2001; Brown C.J. et al., 2000). However, there are only a few studies so far which analyze the mechanical behavior of loose materials in pyramidal silos. Comparing with the general cylindrical silos, the structure of the pyramidal silos is special. It has been applied in some engineering fields because of its simple structure and easy manufacture. The friction stress distribution of loose materials in these silos is helpful to study

---

[†] Received 16 May 2017; Accepted 23 August 2017

[1] 79 Yingze W St, Wanbailin Qu, Taiyuan, Shanxi 030024, China
* Corresponding author: Xuewen Wang
E-mail: wxuew@163.com
TEL: +86-351-6010414

the force obtained in storing and unloading, optimize the design structure and cut down the manufacturing cost.

In this paper, an analytic equation of loose material friction stress distribution was established used the slice method in deep pyramidal silos with reasonable assumptions and simplifications. The friction stress was solved by a finite element contact analytic method, and the contact-friction state was discussed in deep pyramidal silos. Lastly, a more reasonable equation was published after verification and modifying to provide foundation for the deep pyramidal silos' structure design and storage efficiency.

2. The analytic formula of friction stress distribution

2.1 The silo structure

"EN 1991-4. Eurocode 1: actions on structures, Part 4: silos and tanks" (CEN, 2004) prescribed that a deep cylindrical silo was the one with aspect ratios (the ratio of h to D) greater than or equal to 2.0; a shallow cylindrical silo was the ratio of h to D greater than or equal to 0.4 and less than 1.0; otherwise, it was a medium deep silo [see **Fig. 1(a)**]. However, there was no rule for conical silos and pyramidal silos. Here, such a rule was prescribed for them with reference to "EN 1991-4. Eurocode 1: actions on structures, Part 4: silos and tanks" (CEN, 2004), as shown in **Fig. 1**.

(1) As far as the conical silo was concerned, it was a deep conical silo when $h/(D/2) \geq 2.0$; it was a shallow conical silo when $h/(D/2) < 2.0$ [see **Fig. 1(b)**]. It was a deep conical silo when $\alpha \leq 0.462$ rad (α was the obliquity of the conical silo, cotangent 0.462 rad ≈ 2.0); otherwise, it was a shallow conical silo [see **Fig. 1(b)**].

(2) As far as the pyramidal silo was concerned, it was a deep pyramidal silo when $h/[\min(A,B)/2] \geq 2.0$; it was a shallow pyramidal silo when $h/[\min(A,B)/2] < 2.0$ [see **Fig. 1(c)**]; It was a deep pyramidal silo when $\min(\phi_1, \phi_2) \leq 0.462$ rad; otherwise, it was a shallow pyramidal silo [see **Fig. 1(c)**].

A pyramidal silo has some features as follows: (1) it has a simple structure (see **Fig. 2**) and is easy to manufacture; (2) the friction stress of the materials varies with the obliquity of silo walls; (3) the contact friction behaviors of loose materials in deep silos as presented in this paper is different from those of the shallow silos.

In this paper, the friction stress distribution of loose materials to silo walls was investigated for the case of the deep pyramidal silos.

2.2 The friction stress distribution

In 1895, according to two basic assumptions, the German civil engineer JANSSEN gave the famous calculation formula of the static pressure in a cylindrical silo, namely, the JANSSEN Formula (Janssen H.A., 1895). The two as-

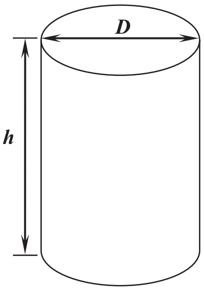

(a) The cylindrical silo

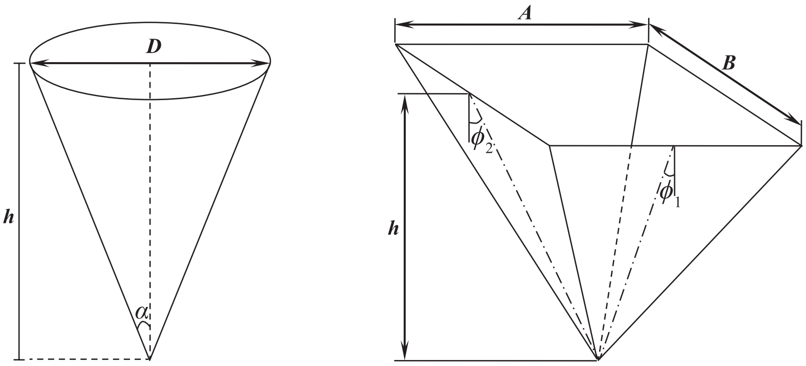

(b) The conical silo

(c) The pyramidal silo

Fig. 1 The diagram of deep silo and shallow silo.

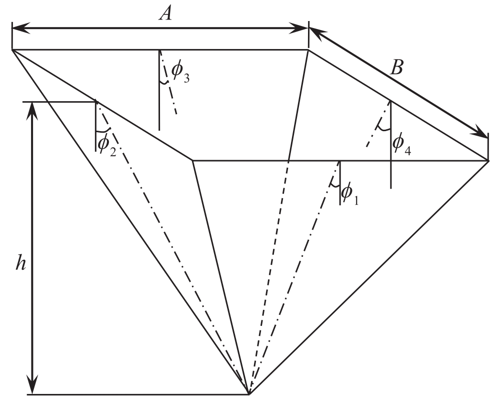

(a) The pyramidal silo geometrical parameters

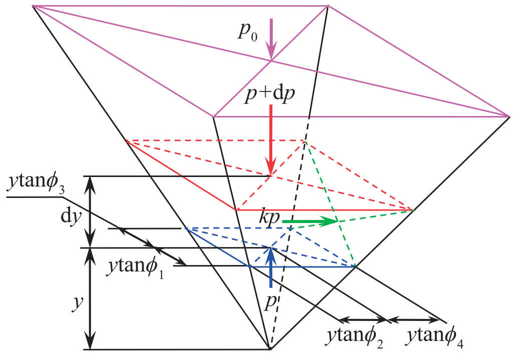

(b) The vertical pressure distribution of loose materials in deep pyramidal silo

Fig. 2 The diagram of the vertical pressure distribution of loose materials in deep pyramidal silo.

sumptions were expressed in the following: (1) the vertical pressures were equally distributed in the same depth; (2) the ratio of horizontal pressure to vertical pressure was a constant k, which was the lateral pressure coefficient.

Below are some of the assumptions in this paper based on above:

(1) Loose materials are in an ultimate stress state. Before or after the state, the external force on the loose materials approached a limiting value and the loose materials will suddenly collapse. At this moment, the lateral pressure coefficient k reflects the force exerted from another direction when the force is acted upon by the loose materials either horizontally or vertically.

(2) Particles are minute (the diameter is less than 1 mm), indicating that the loose materials are homogeneous.

(3) The loose materials must have unified physical properties and be in a uniformly filling state to assure a constant internal friction factor.

(4) The vertical pressure is equal on the same plane.

As shown in **Fig. 2**, we supposed that the horizontal cross section was rectangular, the height was h, the obliquities of the four walls to the axis vertical curve were ϕ_1, ϕ_2, ϕ_3 and ϕ_4, respectively, and the bulk density of loose materials was ρ. Starting at the lowermost peak, a thin layer unit with vertical thickness dy was the research object. The thin layer unit was approximated as a cuboid.

Let the areas of the four walls of the thin layer unit be dA_1, dA_2, dA_3, and dA_4, and the friction forces of the loose materials in walls be $f_{\mathrm{d}A1}$, $f_{\mathrm{d}A2}$, $f_{\mathrm{d}A3}$ and $f_{\mathrm{d}A4}$. Thus, along the vertical direction, the force balance of the loose materials in the thin layer unit could be expressed in the following:

$$\begin{aligned}&[(p+\mathrm{d}p)+\rho g\mathrm{d}y]\cdot[(y\tan\phi_1+y\tan\phi_3)(y\tan\phi_2+y\tan\phi_4)]\\&=p\cdot[(y\tan\phi_1+y\tan\phi_3)(y\tan\phi_2+y\tan\phi_4)]\\&+(f_{\mathrm{d}A_1}+f_{\mathrm{d}A_2}+f_{\mathrm{d}A_3}+f_{\mathrm{d}A_4})\end{aligned} \tag{1}$$

$$f_{\mathrm{d}A_i}=\mu kp\cdot\mathrm{d}\,A_i \qquad i=1,2,3,4 \tag{2}$$

$$\begin{cases}\mathrm{d}A_1=(y\tan\phi_2+y\tan\phi_4)\mathrm{d}y\\\mathrm{d}A_2=(y\tan\phi_1+y\tan\phi_3)\mathrm{d}y\\\mathrm{d}A_3=(y\tan\phi_2+y\tan\phi_4)\mathrm{d}y\\\mathrm{d}A_4=(y\tan\phi_1+y\tan\phi_3)\mathrm{d}y\end{cases} \tag{3}$$

Upon combining Eq. (1), (2), and (3), a relationship relating dp to dy could be expressed in the form of Eq. (4):

$$\frac{\mathrm{d}p}{\mathrm{d}y}=\frac{2k(\tan\phi_1+\tan\phi_2+\tan\phi_3+\tan\phi_4)\mu}{(\tan\phi_1+\tan\phi_3)(\tan\phi_2+\tan\phi_4)}\cdot\frac{p}{y}-\rho g \tag{4}$$

Note that $p=p_0$ if $y=h$ from **Fig. 2**. By solving the differential Eq. (4), the vertical pressure p of the loose materials in deep pyramidal silos could be determined in Eq. (5):

$$\begin{cases}p=\rho gy\cdot\ln\left(\dfrac{h}{y}\right)+p_0\dfrac{y}{h} & (\lambda=1)\\[2ex] p=\dfrac{\rho gy}{\lambda-1}\left[1-\left(\dfrac{y}{h}\right)^{\lambda-1}\right]+p_0\left(\dfrac{y}{h}\right)^{\lambda-1} & (\lambda\neq1)\\[2ex] \lambda=\dfrac{2k(\tan\phi_1+\tan\phi_2+\tan\phi_3+\tan\phi_4)\mu}{(\tan\phi_1+\tan\phi_3)(\tan\phi_2+\tan\phi_4)}\end{cases} \tag{5}$$

In most cases, $\lambda\neq1$.

If there were no loose materials or other pressures at the top of the silos, $p_0=0$.

In the engineering practice, most pyramidal silos were symmetrically designed, namely $\phi_1=\phi_3$, and $\phi_2=\phi_4$. Thus, the λ might be simplified in Eq. (6) in the following:

$$\lambda=\frac{k(\tan\phi_1+\tan\phi_2)\mu}{\tan\phi_1\cdot\tan\phi_2} \qquad (\phi_1=\phi_3,\phi_2=\phi_4) \tag{6}$$

In some cases, the design parameters of the pyramidal silos were the length A and B of silo top opening as **Fig. 2** showed rather than the dip angle of the silo walls. If the pyramidal silos were symmetrically designed, namely $\phi_1 = \phi_3$ and $\phi_2 = \phi_4$, the λ might be expressed as Eq. (7) in the following:

$$\lambda = \frac{k(A+B)\mu}{A \cdot B \big/ 2h} \quad (\phi_1 = \phi_3, \phi_2 = \phi_4) \tag{7}$$

The vertical pressure shown in Eq. (5) must be disassembled to study the friction stress between loose materials and silo walls. In the current study, the lateral pressure coefficient k was an important constant when the vertical force was changed into the horizontal force. Furthermore, the lateral pressure coefficient k could be sampled with different methods prescribed by the code for the design of silos in different countries (SAG, 2001; ACI, 1997; Jaky J., 1948; CEN, 1995; DIN 1055, 1987). In this paper, the lateral pressure coefficient k was prescribed in Eq. (8) according to Rankine's earth pressure theory (SAG, 2001).

$$k = \tan^2\left(45^\circ - \frac{\phi_\text{f}}{2}\right) \tag{8}$$

In Eq. (8), ϕ_f is the internal friction angle of loose materials.

Taking a piece of triangular prism as an object for investigation (**Fig. 3**). We supposed that plane A was an internal wall, ϕ_i ($i = 1, 2, 3, 4$) was the dip angle of plane A to the vertical plane, p was the vertical pressure, pA_i was the pressure of p to A_i, and $pA_i \sin \phi_i$ was the disassembled pressure perpendicular to plane A. Similarly, the lateral pressure kp might be disassembled. The disassembled pressure of the perpendicular pressure to surface A was $kpA_j \cos \phi_i$. Therefore, the friction force on plane A was Eq. (9):

$$\begin{aligned} f_\text{A} &= \mu\left(pA_i \sin\phi_i + kpA_j \cos\phi_i\right) \\ &= \mu\left(pA \sin\phi_i \sin\phi_i + kpA \cos\phi_i \cos\phi_i\right) \\ &= \mu pA\left(\sin^2\phi_i + k\cos^2\phi_i\right) \end{aligned} \tag{9}$$

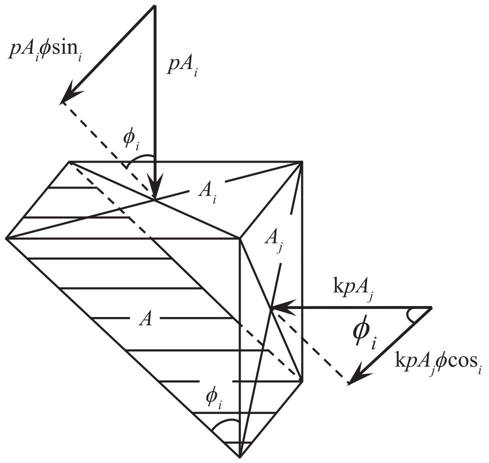

Fig. 3 The diagram of the vertical pressure disassembling.

Thus, the friction stress distribution on plane A could be indicated as Eq. (10):

$$p_\text{f} = \mu p\left(\sin^2\phi_i + k\cos^2\phi_i\right) \tag{10}$$

3. Contact Analysis and Verification

Eq. (10) could be verified numerically using finite element contact analysis.

3.1 Contact conditions and iterative processes

Contact conditions established when two separated surfaces touched at normal direction while maintaining tangential relative movement. In general physical meaning, the surfaces in contact status had the following characteristics:

(1) No penetration between each other.

(2) The normal pressure and tangent friction force might be transferred during contact.

(3) Generally the normal pulling force could not be transferred when surface separation occurred.

All the above three characteristics introduced significant physical variations of silo-loose material system in terms of normal and tangential stiffness. In fact, this highly nonlinear contact mechanics between silo and loose materials formed a major concern of silo engineers or civil engineers. This paper studied the contact friction stress.

Nonlinear contact problems could be solved through a series of repetitive iterative processes to accomplish accurate contact analysis. The procedure could be divided into four steps: (1) a particular contact status type was initially presumed; (2) finding out the contact stresses and displacement of contact point based on the presumed contact status; (3) checking if the contact condition could be met for all contact points; (4) if the contact condition was not satisfied, then the contact status was modified and another iteration started until all contact conditions could be met at all contacting points.

3.2 Contact analysis

Due to the symmetric property of silo structures, simplified two-dimensional contacting simulations were carried out in this paper, nonlinear finite element software ANSYS was used and the contacting surfaces between loose materials and silos were defined with rigid-to-flexible surface-to-surface contact pair. Target surfaces of silos were modeled with TARGE169 element and the contact surfaces of loose materials were modeled with CONTA171 element.

The ANSYS TARGE169 element could be used to represent various 2-D "target" surfaces together with the associated contact elements (CONTA171). The contact elements, CONTA171, were overlaid on top of the relevant solid elements in order to describe deformable loose material boundary and possible contact silo surface with target elements, TARGE169. This target surface was discretised by a set of target segment elements (TARGE169) and was paired with its associated contact surface via a shared real constant set. Any translational or rotational displacement or even temperature could be imposed on the target segment element. Moments and Forces could also be applied on target elements.

CONTA171 was used to represent contact and sliding between 2-D "target" surfaces (TARGE169) and a deformable surface, defined by this element. The element was applicable to 2-D structural and coupled field contact analyses. This element was located on the surfaces of 2-D solid, shell, or beam elements without midside nodes (such as PLANE42). It had the same geometric characteristics as the attached solid, shell, or beam element. In ANSYS numerical model, contact occurred when surface elements penetrated into target segment elements (TARGE169) at allowable normal distance. Coulomb and shear stress friction could be used to simulate the tangential contact behavior.

Although no penetration occurred in real silos, numerical technique only allowed a stiffness-penetration law to simulate the contacting physics (see **Fig. 4**). Hence, penetration Δ must be small enough so that high accuracy could be obtained, which meant larger contact stiffness must be used. But large contact stiffness added simulation cost and convergence difficulties. To overcome this, contact stiffness in this paper was defined as the silo element stiffness multiplied by a normal contact stiffness factor. It was found that accurate results could be obtained when the normal contact stiffness factor was set to 1.0. It should be noted that this factor also indicated the contact stiffness equaled to the silo element stiffness. The maximum penetration was only δ = 0.001 m (see **Table 1**) when the normal contact stiffness factor was set to 1.0. Since only a brief summary of analysis method was given here, more detailed discussions and method could be found elsewhere (Wang X.W. et al., 2015).

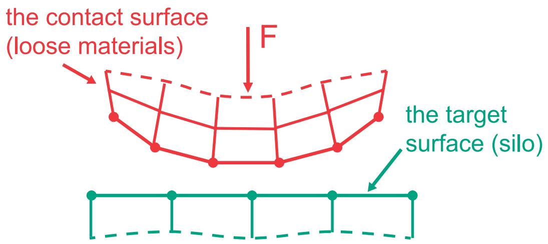

(a) In non-contact state

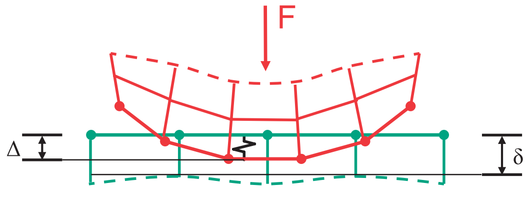

(b) In contact state

Fig. 4 The penetration tolerance δ and the penetration Δ **(a)** In non-contact state; **(b)** In contact state.

During FE analysis, silos and loose materials were meshed with 2D solid element, PLANE42. Such element could be used either in 2D plane model (plane stress or plane strain) or axi-symmetric model. The element was defined by four corner nodes, each had two degrees of freedom: translations in the nodal x or y directions. The element could simulate plasticity, creep, swelling, stress stiffening behavior with large deflection and large strain capabilities.

The full Newton-Raphson solver was used in this study, due to its improved convergence efficiency for highly nonlinear problems, especially to the contact between granulate materials and silo surfaces. Moreover, ANSYS Newton-Raphson solver could automatically improve. Its convergence efficiency by tracing back system residual errors.

In FE contact analysis, correlation parameters on the loose materials and the silo were indicated in **Table 2**.

Table 1 The contact parameters.

The item	The parameters
The mesh element	Plane42
The contact elements	Targe169 and conta171
The contact form	Rigid-to-flexible surface-to-surface contact
The normal contact rigid factor	1
The maximum penetration depth	0.001 m

Table 2 Applied parameters of a pyramidal silo.

1) bulk density: $\rho = 700\ \text{kgm}^{-3}$, cohesion: $P_n = 10000$ Pa;
2) gravity acceleration: $g = 9.8\ \text{ms}^{-2}$;
3) the dip angles of the silo walls: $\phi_1 = \phi_3 = 0.227$ rad;
4) friction factor: $\mu = 0.5$;
5) internal friction angle: $\phi_f = 0.349$ rad;
6) silo roof pressure: $p_0 = 6432$ Pa;
7) vertical height: $h = 11.0$ m;
8) calculation ranges: $y = 0.3–11$ m.

Then, $k = 0.49$;

$$\lambda = \frac{2k\left(\tan\phi_1 + \tan\phi_2 + \tan\phi_3 + \tan\phi_4\right)\mu}{\left(\tan\phi_1 + \tan\phi_3\right)\left(\tan\phi_2 + \tan\phi_4\right)} = 1.49$$

3.3 The results

Taking an engineering silo as an example (**Fig. 5**), the contact analysis were carried out. The analysis object is the narrow-wall of the engineering silo (**Fig. 5**).

Correlation parameters on the narrow-wall and the loose materials in the engineering silo were indicated in **Table 2**. The k and λ were determined by these parameters, where $k = 0.49$, $\lambda = 1.49$. The results were shown in **Fig. 6**, **Fig. 7**, and **Table 3**. In **Fig. 6**, different width represents different friction zone (sliding and sticking). The curves of **Fig. 7** shown the contact friction stress value and its location.

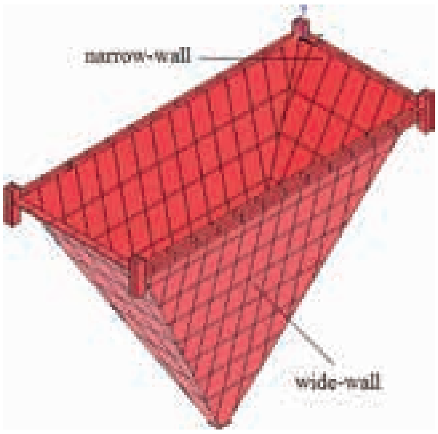

Fig. 5 An engineering silo.

3.4 Modification

Fig. 6 indicated that the contact friction zone could be divided into two parts: sliding contact friction zone and sticking contact friction zone. The interval dividing point between the sliding zone and sticking zone was approximately in the middle. The location varied with different parameters. In **Fig. 6**, the location is located in the middle of node 103 and node 104. The contact friction stress reached the minimum (near 0) at the top of the pyramidal silo, and the stress gradually increased from the sliding contact friction zone to the interval dividing point (**Fig. 7**). The contact friction stress was at the max in the interval dividing point, and it gradually decreased from the interval dividing point to the bottom.

Comparing the FEA results value with the analytic value of the 11 nodes in **Table 3** (node location shown in **Fig. 6**), it showed that above the interval dividing point, the FEA results was a little greater than the analytic solution for most of the nodes. The FEA results were about 1.1 times that of the analytic solution. However, the FEA results below the interval dividing point were about 0.95

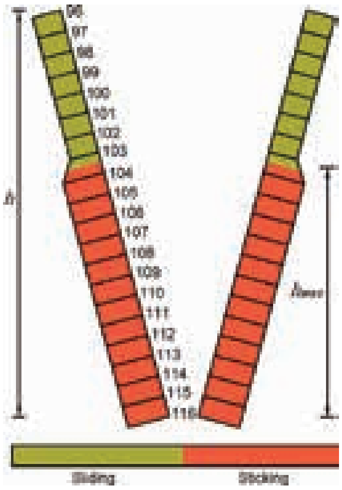

Fig. 6 The contact friction zone and the node location.

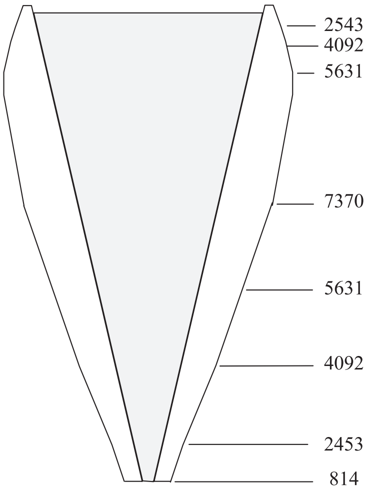

Fig. 7 The contact friction stress (Pa).

Table 3 Results comparison.

Node number	96	98	100	102	103	104	107	110	114	115	116
Vertical height coordinate: y (m)	11	9.93	8.86	7.79	7.255	6.72	5.115	3.51	1.37	0.835	0.3
FEA results: m (Pa)	1573.4	3803.6	5322.8	6291.9	6923.7	6912.4	6650.9	6177.6	3523.9	2492.1	1822.0
Analytic results: n (Pa)	1658.8	3331.2	4709.7	5776.0	6185.4	6508.2	6917.6	6379.9	3761.8	2631.5	1181.7
(m/n)	0.95	1.14	1.13	1.09	1.12	1.06	0.96	0.97	0.94	0.95	1.54

times or less that of the analytic solution. Near the discharge opening (node No. 116), the FEA results were a little greater because of the dynamic discharge pressure. For dynamic discharge, more complex phenomena, such as material sticking or blocking in the form of a rat hole, arching and bridging were likely to happen. This paper did not discuss the complex phenomena near the discharge opening.

As a whole, the analytic results roughly conformed to the FE contact calculation results. It had been pointed out that the analytic method was still reasonable. The error was in 10 % or less, because there were some differences between the assumptions and the real state.

Moreover, different states in the sliding contact friction zone and sticking contact friction zone had not been fully taken into account in the assumptions. In the sliding contact friction zone, the friction was introduced by external forces. The energy dissipation by friction was mainly due to the relative movement between the loose materials and the silo at the contact surfaces. In the sticking contact friction zone, the friction was internal friction. The friction energy dissipation was mainly due to the elastic deformation because of the contact. In general, the impact of external forces was a little greater than internal friction.

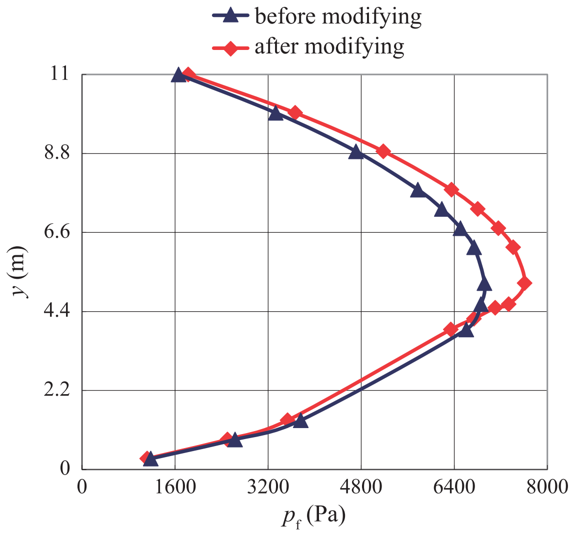

Fig. 8 The friction stress distribution curve.

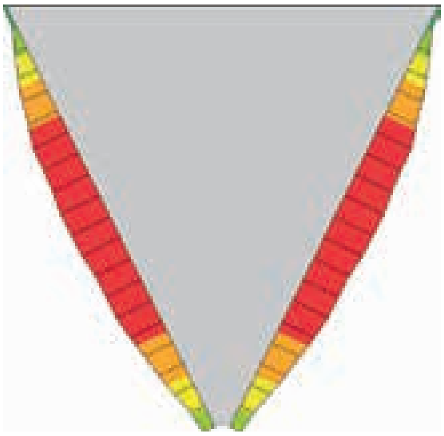

Fig. 9 The contact friction stress curve (on wide-wall).

Taking the wide-wall of the engineering silo as analysis object, and changing attribute parameters of the loose materials, a similar contact friction stress curve and similar conclusion were obtained (**Fig. 9**). Thus, Eq. (10) might be modified. Based on **Table 3** and **Fig. 6**, taking the discharge opening as a starting point, supposing the height of pyramidal silo was h, the modified formula of the combination of Eq. (5) and Eq. (10) were as follows:

$$\begin{cases} \begin{cases} p'_f = 1.1\mu p\left(\sin^2\phi_i + k\cos^2\phi_i\right) & h_{\max} < y < h, i = 1, 2, 3, 4 \\ p'_f = 0.95\mu p\left(\sin^2\phi_i + k\cos^2\phi_i\right) & 0 < y < h_{\max}, i = 1, 2, 3, 4 \end{cases} \\ \begin{cases} p = \dfrac{\rho g y}{\lambda - 1}\cdot\left[1 - \left(\dfrac{y}{h}\right)^{\lambda-1}\right] + p_0\left(\dfrac{y}{h}\right)^{\lambda-1} \qquad (\lambda \neq 1) \\ \lambda = \dfrac{2k\left(\tan\phi_1 + \tan\phi_2 + \tan\phi_3 + \tan\phi_4\right)\mu}{\left(\tan\phi_1 + \tan\phi_3\right)\left(\tan\phi_2 + \tan\phi_4\right)} \end{cases} \end{cases} \tag{11}$$

Here, $y = h_{\max}$ when p is at the max, and ϕ_i is the obliquity (see **Fig. 2** and **Fig. 3**).

In addition, the force of loose materials in the discharge opening could not be regarded as the static force. In here, dynamic pressure would be acted upon during the unloading process of the loose materials. Eq. (11) would not be applied in the discharge opening where the friction stress distribution was more complex. Hence, further research would be needed, or the values near the discharge opening would increase by 1.5–2 times that of the results obtained by Eq. (11) in the practical engineering calculations.

The modified distribution curve (shown in **Fig. 8**: after modifying) was drawn according to Eq. (11). In fact, there was a mutation near $h_{\max}$. The curve in **Fig. 8** was made a smooth processing.

4. Discussions and prospects

(1) For the purpose of engineering application, this study focused on the pyramidal silos which other researchers paid less attention. The lateral pressure coefficient k and the assumptions based on Janssen formula were also applied during the calculation to provide a convenient way for structure calculation of pyramidal silos and improve the design efficiency of field application engineers. Obviously, the stress conditions of pyramidal silos could have been some different from the cylindrical silo that Janssen formula applied on, and the mechanical

properties of loose materials were complex at the edge and corner part. Therefore, this study only did the approximate research on silo walls. More precise behavior and mechanism research of loose materials, and the friction stress distribution around the edges of the pyramid silos were beyond the scope of this study.

(2) Pyramidal silos are mainly used on the field of storing industrial bulk material (such as coal, gravel, concrete). According to the data obtained from field engineers, the main problems of this kind of silo were the poor flow during the unloading process and the wear of walls. To solve these problems, this study mainly researched on the friction stress distribution and the contact state between the loose materials and silo walls. For the normal pressure (or stress) distribution and the behavior study, the related papers were recommended (Goodey R.J. et al., 2017; Li Z.F., et al., 2014; Rotter J.M. et al., 2002; Brown C.J. et al., 2000).

(3) The slice method, based on the limit equilibrium theory, took the loose materials as the rigid body. When establishing equilibrium equations, some acceptable assumptions were used to increase the known conditions and transformed the statically indeterminate problem into the static problem. The complex boundary conditions of non-continuous, heterogeneity, anisotropy and external load of loose materials could be conveniently processed and finally derived the quantitative calculation model for field applications.

However, the slice method ignored the deformation and strength of the material itself and the complex behavior was simplified which would inevitably cause some error. In addition, the slice method could not provide accurate friction stress distribution graphics and images. The finite element analysis and software technology could make up for this defect and validate and correct the quantitative model. The combination of them could correct the calculation error to a certain extent.

(4) The finite element method was used in this study to simulate the contact and friction between the bulk material and the pyramidal silo. The discrete element method could be applied combining test researches to study the discrete characteristic of material, particle behavior and the influence mechanism of material on the silo in the future.

5. Conclusions

(1) The analytic equation of loose material friction stress distribution was established in deep pyramidal silos with reference to the basic assumptions of the JANSSEN Formula.

(2) The friction stress distribution of loose materials in deep pyramidal silos was studied with the finite element contact analysis. We concluded that the friction behaviors included sliding contact friction and sticking contact friction, and that the friction stress was maximum at the interval dividing point between the sliding zone and sticking zone. The friction stress decreased gradually to the roof and the bottom separately.

(3) The FEA results and the analytic result were compared and analyzed. The error was 10 % or less. The main reason was that some differences existed between the assumptions and the real state. Moreover, the different states in the sliding contact friction zone and sticking contact friction zone had not been fully taken into account in the assumptions.

(4) The analytic equation had been modified by comparing the results. It showed that the friction stress distribution of loose materials in deep pyramidal silos was related to the material and design parameters of silos, as well as the powder attribute of the loose material. The modified equation reflected precisely the contact-friction behaviors of loose materials in deep pyramidal silos and provided a shortcut method for calculation in related research.

Acknowledgements

The project was supported by the Young Scientists Fund of the National Natural Science Foundation of China (51105266), Program for the Outstanding Innovative Teams of Higher Learning Institutions of Shanxi (2014) and the Basic Condition Platform Project of Shanxi (2014091016).

Nomenclature

A, B	internal side length of silo top opening (see **Fig. 1**)
D	internal diameter of silo top opening (see **Fig. 1**)
g	gravity acceleration, $g = 9.8\ \mathrm{ms}^{-2}$
h	vertical height of the conical silo or the pyramidal silo (see **Fig. 1** and **Fig. 2**)
k	lateral pressure coefficient [see Eq. (2)]
p	vertical pressure [see Eq. (5)]
p_0	silo roof pressure (see **Fig. 2**)
p_f, p'_f	friction stress [see Eq. (10) and Eq. (11)]
P_n	cohesion of loose material
α	obliquity of the conical silo (see **Fig. 1**)
ϕ_1, ϕ_2, ϕ_3, ϕ_4	obliquity of the pyramidal silo walls (see **Fig. 1** and **Fig. 2**)

ρ	bulk density of loose material
μ	friction factor
ϕ_f	internal friction angle
λ	a coefficient

$$\lambda = \frac{2k\left(\tan\phi_1 + \tan\phi_2 + \tan\phi_3 + \tan\phi_4\right)\mu}{\left(\tan\phi_1 + \tan\phi_3\right)\left(\tan\phi_2 + \tan\phi_4\right)}$$

[see Eq. (11)]

References

ACI (American Concrete Institute), ACI 313-97 & ACI 313R-97, Standard practice for design and construction of concrete silos and stacking tubes for storing granular materials (ACI 313-97) and Commentary—ACI 313R-97, ACI International, 1997.

Benyamine M., Djermane M., Dallozdubrujeaud B., Aussillous P., Discharge flow of a bidisperse granular media from a silo, Physical Review E Statistical Nonlinear & Soft Matter Physics, 90 (2014) 032201(8pp). https://doi.org/10.1103/PhysRevE.90.032201

Brown C.J., Lahlouh E.H., Rotter J.M., Experiments on a square planform steel silo, Chemical Engineering Science, 55 (2000) 4399–4413.

CEN (the European Committee for Standardization), ENV 1991-2-2: Eurocode 1: Basis of design and actions on structures. Actions on structures exposed to fire (together with United Kingdom National Application Document), Brussels, Belgium, 1995.

CEN (the European Committee for Standardization), EN 1991-4: Eurocode 1: actions on structures, Part 4: silos and tanks, Brussels, Belgium, 2004.

Colonnello C., Reyes L.I., Clément E., Gutiérrez G., Behavior of grains in contact with the wall of a silo during the initial instants of a discharge-driven collapse, Physica A: Statistical Mechanics and its Applications, 398 (2014) 35–42.

Couto A., Ruiz A., Herráez L., Moran J., Aguado P.J., Measuring pressures in a slender cylindrical silo for storing maize. Filling, static state and discharge with different material flow rates and comparison with Eurocode 1 part 4, Computers & Electronics in Agriculture, 96 (2013) 40–56.

DIN 1055, Design loads for buildings: Loads in silo bins, Beuth Verlag, Berlin, Part 6, 1987.

Ding S., Li H., Ooi J.Y., Rotter J.M., Prediction of flow patterns during silo discharges using a finite element approach and its preliminary experimental verification, PARTICUOLOGY, 18 (2015) 42–49.

Gallego E., Rombach G.A., Neumann F., Ayuga F., Simulations of granular flow in silos with different finite element programs: ANSYS vs. SILO, Transactions of the Asabe, 53 (2010) 819–829.

Gallego E., Ruiz A., Aguado P.J., Simulation of silo filling and discharge using ANSYS and comparison with experimental data, Computers & Electronics in Agriculture, 118 (2015) 281–289.

Goodey R.J., Brown C.J., Rotter J.M., Predicted patterns of filling pressures in thin-walled square silos, Engineering Structures, 28 (2006) 109–119.

Goodey R.J., Brown C.J., Rotter J.M., Rectangular steel silos: Finite element predictions of filling wall pressures, Engineering Structures, 132 (2017) 61–69.

Guines D., Ragneau E., Kerour B., 3D Finite-Element Simulation of a Square Silo with Flexible Walls, Journal of Engineering Mechanics, 127 (2001) 1051–1057.

Hua X., Curtis J., Guo Y., Hancock B., Ketterhagen W., Wassgren C., The internal loads, moments, and stresses in rod-like particles in a low-speed, vertical axis mixer, Chemical Engineering Science, 134 (2015) 581–598.

Hua X., Curtis J., Hancock B., Ketterhagen W., Wassgren C., The kinematics of non-cohesive, sphero-cylindrical particles in a low-speed, vertical axis mixer, Chemical Engineering Science, 101 (2013) 144–164.

Iwicki P., Rejowski K., Tejchman J., Stability of cylindrical steel silos composed of corrugated sheets and columns based on FE analyses versus Eurocode 3 approach, Engineering Failure Analysis, 57 (2015) 444–469.

Iwicki P., Sondej M., Tejchman J., Application of linear buckling sensitivity analysis to economic design of cylindrical steel silos composed of corrugated sheets and columns, Engineering Failure Analysis, 70 (2016) 105–121.

Jagtap P., Chakraborty T., Matsagar V., Nonlinear dynamic behavior of granular materials in base excited silos, Mechanics of Advanced Materials & Structures, 22 (2015) 313–323.

Jaky J., Pressure in silos. In Proc. 2nd International Conference on Soil Mechanics and Foundation Engineering, Rotterdam, June 21–30 (1948), 1, 103–107.

Janssen H.A., Versuche über getreidedruck in silozellen, Zeitschrdvereines Deutscher Ingenieure, 39 (1895) 1045–1049.

Jansseune A., Corte W.D., Belis J., Elastic failure of locally supported silos with U-shaped longitudinal stiffeners, Engineering Failure Analysis, 70 (2016a) 1041–1049.

Jansseune A., Corte W.D., Belis J., Imperfection sensitivity of locally supported cylindrical silos subjected to uniform axial compression, International Journal of Solids & Structures, 96 (2016b) 92–109.

Li Z.F., Peng Z., Jiang Y.M., Measurements of granular pressure in silo: Janssen behaviour and deviation, Physics, 63 (2014) 104503.

Lozano C., Zuriguel I., Garcimartín A., Stability of clogging arches in a silo submitted to vertical vibrations, Physical Review E Statistical Nonlinear & Soft Matter Physics, 91 (2015) 062203.

Matchett A.J., Langston P.A., Mcglinchey D., A model for stresses in a circular silo with an off-centre circular core, using the concept of a principal stress cap: Solution for a completely filled silo and comparison with Janssen and DEM data, Chemical Engineering Research & Design, 93 (2015) 330–348.

Nascimento J.W.B.d., Lopes Neto J.P., Montross M.D., Horizontal pressures in cylindrical metal silos and comparison with different international standards, Engenharia Agrícola, 33

(2013) 601–611.

Park H.W., Kim S.T., Choung M.G., Han W.Y., Yoon W.B., Analysis of grinding kinetics and flow behavior of adzuki bean (phaseolus angularis) flour for hopper design, Journal of Food Process Engineering, 39 (2016) 366–376.

Rotter J.M., Brown C.J., Lahlouh E.H., Patterns of wall pressure on filling a square planform steel silo, Engineering Structures, 24 (2002) 135–150.

Sadowski A.J., Rotter J.M., Modelling and behaviour of cylindrical shell structures with helical features, Computers and Structures, 133 (2014) 90–102.

SAG (State Administration of Grain), GB50322-2001, Grain steel silo design standard, China Planning Press, Beijing, China (in Chinese), 2001.

Sondej M., Iwicki P., Wójcik M., Tejchman J., Stability analyses of a cylindrical steel silo with corrugated sheets and columns, Steel & Composite Structures, 20 (2016) 147–166.

Wang X., Qin Y., Li J., Tian Y., Yang Z., Static contact statuses between conical silos and granular materials and its influential factors, Transactions of the Chinese Society of Agricultural Engineering, 31 (2015) 65–70.

Wang Y., Lu Y., Jin Y.O., Finite element modelling of wall pressures in a cylindrical silo with conical hopper using an Arbitrary Lagrangian–Eulerian formulation, Powder Technol, 257 (2014) 181–190.

Xia H., Wassgren C.R., Curtis J.S., Hancock B.C., Ketterhagen W.R., Yu G., Sphero-Cylindrical Particle Dynamics and Stresses in a Vertical Axis Mixer, AIChE Annual Meeting, Pittsburgh, PA, USA, 2012.

Xia H., Wassgren C.R., Curtis J.S., Hancock B.C., Ketterhagen W.R., Yu G., Internal Load and Moment Distributions of Rigid, Sphero-Cylindrical Particles in a Stirred Vessel, 14 Aiche Meeting, Atlanta, GA, USA, 2014.

Author's short biography

Xuewen Wang

Xuewen Wang received the PhD in mechanical design and theory in 2008. He is a full professor of mechanical engineering in Taiyuan University of Technology, Taiyuan, China. His research interests include granular material mechanics, modern mechanical design theory and method and mechanical CAD/CAE.

Zhaojian Yang

Zhaojian Yang received the PhD in mechanical design and theory in 1997. He is a full professor of mechanical engineering in Taiyuan University of Technology, Taiyuan, China. His research interests include modern design theory and method, mechanical equipment status monitor and fault diagnosis and mechanical dynamics.

Bo Li

Bo Li received the PhD in mechanical design and theory in 2016. He is a lecturer of mechanical engineering in Taiyuan University of Technology, Taiyuan, China. His research interests include granular material mechanics.

Symposium Reports

The 51st Symposium on Powder Technology

The 51st Symposium on Powder Technology was held at Senri Hankyu Hotel, Osaka, Japan on Wednesday, September 13, 2017. It was organized by Hosokawa Powder Technology Foundation with the sponsorship of Hosokawa Micron Corporation. Over 160 people from the industries and universities attended this symposium. The theme of the symposium this year was "Powder Technology Required for Creation of Advanced Materials". There were six lectures with questions and answers followed by a get-acquainted party for further free discussions.

The first lecture was given by Prof. Adschiri, who was presented the KONA Award last year, on his lifework research in the field of production and applications of nanoparticles prepared by the Supercritical Hydrothermal Synthesis method. The further three lectures were carried out by the professors with the diversity of the fields including solid-liquid separation of colloids, particle packing of the particles in the coated film during drying and preparation of materials for all-solid-state batteries via a mechanochemical process.

The other two lectures were from the industries and concerned about the development of engineered smart particles for the functional pharmaceutical products by use of a granulation technology and the introduction of new machines for the wide range of powder processing including grinding mills, air classifies, driers and so on.

The contents of the symposium are shown in the followings.

The 51st Symposium on Powder Technology

Theme: Powder Technology Required for Creation of Advanced Materials

Opening address Mr. Yoshio Hosokawa (President of Hosokawa Powder Technology Foundation)

Session 1 Chaired by Prof. emeritus Ko Higashitani (Kyoto University)

- Lecture 1
  "Continuous Production of Nanoparticles by Supercritical Hydrothermal Synthesis
  —Nanoparticles Synthesis, Nanohybrid Materials, and Surface Controlled Nanocatalysts—"
  Prof. Tadafumi Adschiri (WPI-AIMR, Tohoku University)
- Lecture 2
  "Developments on Solid-Liquid Separation of Colloids"
  Prof. Eiji Iritani (Graduate School of Engineering, Nagoya University)

Session 2 Chaired by Prof. Hirofumi Takeuchi (Gifu Pharmaceutical University)

- Lecture 3
  "Particle Packing Process in the Coated Film of Particle Dispersions during Drying"
  Assoc. Prof. Yoshiyuki Komoda (Graduate School of Engineering, Kobe University)
- Lecture 4
  "Smart Particle Design for Advanced Functional Formulations
  —Creation and Evaluation of Opusgran®—"
  Mr. Yasushi Ochiai (CMC based Drug Development, Sumitomo Dainippon Pharma Co., Ltd.)

Session 3 Chaired by Prof. Satoshi Watano (Osaka Prefecture University)

- Lecture 5
  "Preparation of Materials for All-Solid-State Batteries via a Mechanochemical Process"
  Prof. Akitoshi Hayashi (Graduate School of Engineering, Osaka Prefecture University)
- Lecture 6
  "The Latest Trend of Development of Powder Equipment"
  Dr. Akira Watanabe (Technology Research Institute, Hosokawa Micron Corporation)

Closing remarks Prof. emeritus Fumiyoshi Saito (Tohoku University)

Symposium on Powder Technology

Get-acquainted Party

2nd International Hosokawa Powder Technology Symposium

As a part of special events to celebrate the 25th anniversary of the establishment of Hosokawa Powder Technology Foundation, the 2nd Hosokawa Powder Technology Symposium was held at Hosokawa Micron Powder Systems in Summit, New Jersey, USA on Wednesday, October 4, 2017. This symposium was the second overseas conference on powder and particle technology organized by Hosokawa Foundation and supported by Hosokawa Micron Corporation as well as Hosokawa Micron Powder Systems, which is a division of Hosokawa Micron International, Inc. The number of attendees was nearly 100 including more than 10 people from the universities. Most attendees came from various locations in USA and also included some from Mexico as well as Japan.

The main subject of this symposium was "Challenges & Opportunities in Particle Characterization & Processing" and there were four lectures by the speakers from both academic and industrial fields after the welcome address from Mr.Yoshio Hosokawa, the President of Hosokawa Powder Technology Foundation and Hosokawa Micron Corporation, with the closing remarks from Mr. Rob Voorhees, President of Hosokawa Micron International, Inc.

The symposium consisted of lectures of different aspects from bio and nano particle technology, grinding processing, particle characterization and application to the dry powder inhalation as seen in the program below. Additionally the history and activities of Hosokawa Foundation were introduced using poster panels together with the KONA Powder and Particle Journal exhibited. During the lunch time, discussions were also made among the attendees in front of the actual powder processing machines and characterization devices.

2nd International Hosokawa Powder Technology Symposium

Theme: Challenges & Opportunities in Particle Characterization & Processing

Welcome address Mr. Yoshio Hosokawa (President of Hosokawa Powder Technology Foundation)

◆1 Leveraging Particle and Nano Bio Technologies for Product and Process Innovations
Dr. Brij M. Moudgil – Center for Particulate and Surfactant Systems (CPaSS), University of Florida

◆2 Size Reduction Technologies for Efficient Powder Processing Systems
Mr. Bill Brown – Hosokawa Micron Powder Systems

◆3 Particle Shape Analysis – Sometimes It's Very Important
Dr. Raymond S. Farinato – Solvay Technology Solutions

◆4 Particle Technology for Dry Powder Inhalers
Dr. Anthony J. Hickey – RTI International, Research Triangle Park

Closing remarks Mr. Rob Voorhees (President of Hosokawa Micron International, Inc.)

At a lecture

Speakers and organizers

The 24th KONA Award

Prof. Adschiri graduated from The University of Tokyo in 1981, and received his Doctorate in Engineering from the same institution in 1986. He worked as a Special Research Fellow at JSPS (Japan Society for the Promotion of Science), following which he was appointed as an Assistant Professor in The University of Tokyo in 1987. As a visiting scholar, he has had the opportunity to carry out research work at the University of Waterloo (1991, Canada), University of Hawaii (1996, US), and University of Delaware (1997, US).

Prior to joining Tohoku University, the primary focus of his research was on coal conversion technology. In 1989, he moved to Tohoku University and began studying reactions in supercritical fluids for biomass conversion, chemical recycling of wastes, new organic reactions, and materials synthesis. He is the inventor of the "supercritical hydrothermal synthesis" method for nanoparticles (NPs). This method enables the in-situ organic modification of the surface of NPs, as well as the direct synthesis of NPs. He led a major national project (30 million USD) in Japan entitled "Super Hybrid Nanomaterials" for fabricating new composite materials of surface-controlled NPs and polymers that simultaneously show properties of ceramics and polymers, based on his supercritical fluid method. This method enables the control of the morphology of NPs, and allows for the exposure of the most reactive surface for use as a nano-catalyst. The impact of his research is not just constrained to academia; it also has significant application potential in industry. Some of his proposed processes have been commercialized in Japan and elsewhere. In particular, the first chemical recycling process of waste polymers and the synthesis of supercritical NPs have attracted significant industrial attention.

He has published more than 250 papers, with more than 9000 citations, and has an h-index of over 50. He has been invited more than forty times to major international conferences in a variety of research fields as a plenary/keynote/invited lecture. For his research excellence, he has been awarded many prizes, including awards from the Chemical Society Japan (Science Award), Society of Chemical Engineering of Japan (Best Research Award, and SCEJ Society Award), Japan Energy Society (Progress Award), etc. In addition to academic societies, he is the recipient of the honorable Japan Invention Award from the Japanese government and three-time winner of the Minister's awards of MEXT (Ministry of Education, Culture, Sports, Science and Technology) as well. Ten years ago, the Japanese government selected five (now nine) distinguished research teams as part of the World Premier Research Center Initiative (WPI), and he had the honor to be selected as a principal researcher for the Advanced Institute of Materials Research (WPI-AIMR) in Tohoku University.

Currently, Prof. Adschiri serves as the Vice President of ISHA (International Solvothermal Hydrothermal Association), Vice President of IASCF (International Society for Advancement of Supercritical Fluids), Chairman of the Asian Society of Supercritical Fluids, and Vice President of the Society of Chemical Engineers, Japan. In 2014 he was assigned as a member of Science Council of Japan (six-year appointment followed by a conjunction membership for an additional twelve years). In 2016, he became a member of the Engineering Academy of Japan (life time).

KONA Powder and Particle Journal No. 35 (2018) 287/Doi:10.14356/kona.2018025 Infomation Article

General Information

History of the Journal

In the history of KONA Powder and Particle Journal, two organizations have been playing an important role. The one is the Council of Powder Technology, Japan (CPT) and the other is the Hosokawa Powder Technology Foundation (Hosokawa Foundation). The CPT was established in 1969 by Hosokawa Micron Corporation as a nonprofit organization to enhance the activities of research and development on powder science and technology. The Hosokawa Foundation was established in 1991 as a public-service corporation approved by the Ministry of Education, Culture, Sport, Science and Technology of Japan. The issues from No.1 (1983) to No.12 (1994) of KONA were published by CPT and the issues from No.13 (1995) by the Hosokawa Foundation.

The aim of KONA in the early days was to introduce excellent Japanese papers to the world and thus KONA consisted of papers recommended by some Japanese academic societies and translated from Japanese to English. From the issue of No.8, the CPT changed its editorial policy to internationalize the KONA and to incorporate papers by authors throughout the world in addition to translated papers. In response to this change, three editorial blocks have been organized in the world; Asian-Oceanian, American and European. The policy and system have not changed even after the Hosokawa Foundation has taken over from the CPT. From the issue of No.27 (2009), publication of translated papers has been terminated and only original papers have been published. The CPT is active still today and collaborates with the Hosokawa Foundation.

Aims and Scope

KONA publishes papers in a broad field of powder science and technology, ranging from fundamental principles to practical applications. The papers describing technological experiences and critical reviews of existing knowledge in special areas are also welcome.

The submitted papers are published only when they are judged by the Editor to contribute to the progress of powder science and technology, and approved by any of the three Editorial Committees.

The paper submitted to the Editorial Secretariat should not have been previously published.

Category of Papers

- Invited articles
  Review papers and special articles invited by the KONA Editorial Committees.
- Contributed papers
  Original research and review papers submitted to the KONA Editorial Committees, and refereed by the reviewers and editors.

Submission of Papers

It is now possible to submit your paper online via **Editorial Manager® for KONA Online Paper Submission and Peer Review System**. For all further information, please go to the journal's homepage on http://www.kona.or.jp/jp/journal/info.html.

- Asian/Oceanian Editorial Secretariat
  Dr. T. Yokoyama or Dr. L. Cui
  Hosokawa Powder Technology Foundation
  1-9, Shodaitajika, Hirakata-shi, Osaka, 573-1132 Japan
- European / African Editorial Secretariat
  Dr. S. Sander or Ms. L. Kneisl
  Hosokawa Alpine AG
  Peter-Dörfler-Straße 13-25, D - 86199 Augsburg, Germany
- American Editorial Secretariat
  Dr. C. C. Huang
  Hosokawa Micron Powder Systems
  10 Chatham Road, Summit NJ 07901 USA

Publication in KONA is free of charge.

Publication Schedule

KONA is published annually. The publication date is around January 10th.

Subscription

KONA is distributed free of charge to senior researchers at universities and laboratories as well as to institutions and libraries in the field throughout the world. The publisher is always glad to consider the addition of names of those, who want to obtain this journal regularly, to the mailing list.

Instructions to Authors

(1) Manuscript format

- Electric files should be submitted to the Editorial Secretariat by online. Authors' short biography with less than 100 words per person and color photographs of all the authors should be attached to the final version.
- The structure of manuscripts should follow the following order; title, authors, affiliations, abstract, graphical abstract, keywords, main text, (acknowledgement), (appendix), (nomenclature), references. The items with parentheses are not mandatory.
- Full postal addresses must be given for all the authors. Indicate the corresponding author by the mark"*" after the name. Telephone and fax numbers and e-mail address should be provided for the corresponding author.
- Abstract should not exceed 200 words.
- Graphical abstract should be a concise, visual summary of the article which will be displayed in the contents list both online and print.
- The appropriate number of keywords is 5 or 6.
- The maximum pages printed in KONA are supposed to be:
  15 for an original paper and 25 for a review paper.
- Symbols and units should be listed in alphabetical order with their definition and dimensions in SI units.
- The color figures will appear in color both on the KONA Website (http://www.kona.or.jp) and also in the paper version.
- Concerning references, the alphabetical system should be adopted. Please use reference management software such as Endnote to manage references as far as possible.
  List: References should be arranged first alphabetically and then further sorted chronologically if necessary. More than one reference from the same author(s) in the same year must be identified by the letters "a", "b", "c", etc., placed after the year of publication.
  Examples:
  - Reference to a book:
  Strunk Jr. W., White E.B., The Elements of Style, fourth ed., Longman, New York, 2000.
  - Reference to a chapter in an edited book:
  Mettam G.R., Adams L.B., How to prepare an electronic version of your article, in: Jones B.S., Smith R.Z. (Eds.), Introduction to the Electronic Age, E-Publishing Inc., New York, 2009, pp.281–304.
  - Reference to a journal publication:
  Tsuji Y., Tanaka T., Ishida T., Lagrangian numerical simulation of plug flow of cohesionless particles in a horizontal pipe, Powder Technology, 71 (1992) 239–250.
  Text: All citations in the text should refer to:
  1. Single author: the author's name (without initials, unless there is ambiguity) and the year of publication;
  2. Two authors: both authors' names and the year of publication;
  3. Three or more authors: first author's name followed by "et al." and the year of publication.
  Citations may be made directly (or parenthetically). Groups of references should be listed first alphabetically, then chronologically.
  Examples: "as demonstrated (Hidaka J. et al., 1995; Tsuji Y., 1992a, 1992b, 1993). Mori Y. and Fukumoto Y. (2002) have recently shown ...."

(2) Copyright and permission

- The original paper to be submitted to KONA has not been published before in any language or in any journal or media; it is not submitted and not under consideration for publication in whole or in part elsewhere.
- Authors are responsible for obtaining permission from the copyright holders to reproduce any figures, tables and photos for which copyright exists.
- The KONA Journal applies the **Creative Commons Attribution License** to all works published by the Journal. Copyright stays with the agreed copyright owner, and the Hosokawa Powder Technology Foundation is granted the exclusive right to publish and distribute the work, and to provide the work in all forms and media.
- Users of the journal will be able to reuse the contents in any way they like, provided they are accurately attributed. No permission is required from either the authors or the publisher.

Free electronic publication of KONA is available at http://www.kona.or.jp


picoline
HOSOKAWA ALPINE
Start out small and hit it really big.


Mixing, Drying &
Agglomeration Solutions


MAJSx
MIKRO AIR JET SIEVE

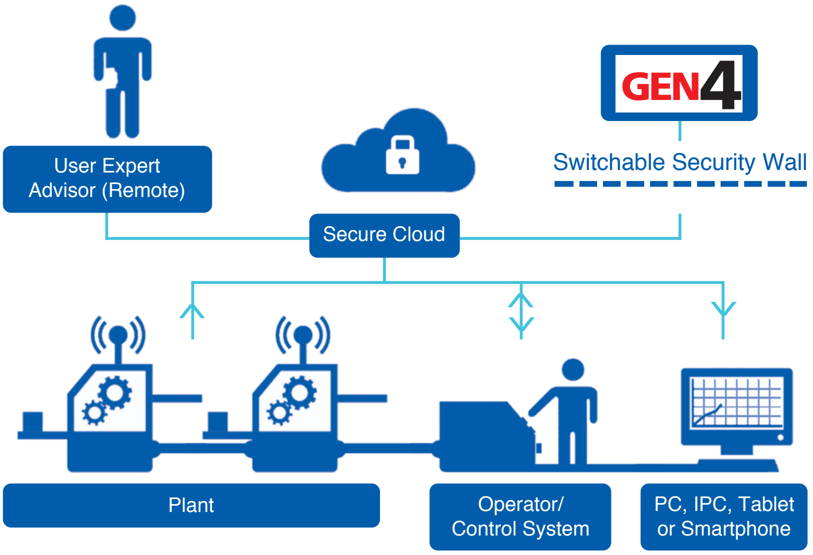
User Expert Advisor (Remote)
GEN4
Switchable Security Wall
Secure Cloud
Plant
Operator/ Control System
PC, IPC, Tablet or Smartphone